Cape Peninsula University of Technology
creating futures

Domestic and Commercial Fuel Cell / Battery / Ultra-capacitor / Thermoelectric Hybrid Power Energy Conversion and Energy Storage Management CCHP System

by

Nganyang Paul Bayendang

Thesis submitted in fulfilment of the requirements for the degree

Doctor of Engineering: Electrical Engineering

in the Faculty of Engineering & Built Environment

at the Cape Peninsula University of Technology

Supervisor: **Prof Mohamed Tariq Kahn**

Co-supervisor: **Dr Vipin Balyan**

Bellville Campus

Date submitted: **31 December 2021**

CPUT copyright information

The thesis may not be published either in part (in scholarly, scientific or technical journals), or as a whole (as a monograph), unless permission has been obtained from the University.

DECLARATION

I, Nganyang Paul Bayendang, declare that the contents of this thesis represent my own unaided work, and that the thesis has not previously been submitted for academic examination towards any qualification. Furthermore, it represents my own opinions and not necessarily those of the Cape Peninsula University of Technology.

Signed:  Date: March 15, 2022

Official Version

ABSTRACT

South Africa and by and large Africa, have been experiencing dire electrical energy crisis with unstable national grids which have led to load shedding (power rationing) from time to time and consequently inconveniencing many people's lives and livelihoods. As a result of this, various sustainable energy initiatives focusing on renewable/alternative energy, have been commissioned to supplement the national grid and for private use. However, renewable energy systems suffer from inefficiency at various levels, since it involves various hybrid power and energy conversion technologies and systems. In light of these developments, my research was undertaken to investigate the energy conversion inefficiency problem and the objectives were defined which include; to propose and model an innovative hybrid power energy conversion scheme, enhance the energy / power inefficiency at component(s) or system levels and if possible justify the merits practically. To achieve this, an extensive literature review was conducted on combined, cold, heat and power (CCHP) systems, fuel cells, thermoelectricity and power converters as well as energy management systems. A research design and methodology was devised which constitutes a proton exchange membrane fuel cell and thermoelectricity CCHP system aided with Lithium ion battery and ultra-capacitor as well as power converters and energy management system. The postulated system was modeled and simulated using MATLAB and Simulink and deeper research was focused on the thermoelectricity section − which became the primal point of my research. Thermoelectric devices (generators and coolers) can produce power, cold and heat; however, their efficiencies are limited by their i) intrinsic figure of merit and further, their ii) practical design and implementation. Only the manufacturers can improve the former; however, the latter can be enhanced by the system or application researcher, hence thermoelectricity with and without heatsinks was comprehensively modeled using MATLAB / Simulink to understand their theoretical and practical functioning, optimal operations and configurations at module and system levels. Various unique findings and novel results were presented on how to improve the thermoelectric generator (TEG) output power and thermoelectric cooler (TEC) cooling power as well as their respective conversion efficiency and coefficient of performance. My research scientific contributions are summed up in ten research articles, in which numerous MATLAB / Simulink models of thermoelectricity were created and validated, new formulas were derived and validated as well as the proffered innovative CCHP system was modeled. However, due to procurement delays, the practical system was not designed and tested to demonstrate physically my research findings and hence, it is recommended as the next logical step for further studies.

ACKNOWLEDGEMENTS

I wish to sincerely thank the followings:

- Prof Mohamed Tariq Kahn for the supervision and keeping up with my research pace − even very late at night!
- Dr Vipin Balyan for the co-supervision, keeping up with my research pace as well as organising extra funding!
- CPUT CPGS for the 2020 and 2021 bursaries!
- UWC HySA Systems for 2019 and 2022 bursaries, funding my research publications and some research items!
- CPUT and Technical University (TU) of Sofia, Bulgaria for the 2020 Erasmus+ student mobility award!
- TU-Sofia 2020 Erasmus+ staff and particularly Prof Ivo Draganov for hosting me and very well, at TU Sofia!
- To anyone / entity not mentioned who / that directly / indirectly added value to my PhD research!

Opinions expressed in this thesis and the conclusions arrived at, are those of the author, and are not necessarily to be attributed to those acknowledged.

DEDICATION

For my family home and abroad, especially my late father Pa Bayendang Samson Nkwa, my late siblings particularly my late sister Bayendang Mercy Arrey, my late friend Suinyuy Derrick Ngoran and most importantly to my living mother Ma Bayendang Elizabeth Akor Taboko (whom unfortunately passed unto glory on February 10, 2022: may her soul RIPPP) and to my ancestors in my village of Tali 2, to the people of my home town of Mamfe and the Manyu land!

PREFACE

NB: my thesis is written based-on my PhD journal /conference articles that are /will be published.

My thesis report is organised as follows: Chapter 1 introduces my research and constitutes the research overview, the research problem, the research problem background, the research problem literature review, the research project objectives, the research project design and methodology, the research project delineations and the research summary. Chapter 2 covers in-depth the research problem literature review which contains four review articles covering in details CCHP systems, fuel cells, thermoelectricity, power converters and energy management systems. Chapter 3 constitutes the first set of two research articles on thermoelectricity generator (TEG) and thermoelectricity cooler (TEC) modeling using Matlab and Simulink. Chapter 4 composes of another set of two research articles on TEG with heatsinks and TEC with heatsinks modeling and simulation based on dimensional analysis using Matlab and Simulink. Chapter 5 consists of the final set of two research articles on TEGs and TECs optimal operation points investigation and TEGs optimum configurations determination using Matlab and Simulink. Chapter 6 discusses holistically my research to conclude the study and Chapter 7 proffers further recommendations.

ABBREVIATIONS / GLOSSARY / SYMBOLS

Π	The Peltier constant and is the product of the Seebeck coefficient and absolute temperature
ΔT	TEG(s)/TEC(s) temperature difference ($T_h - T_c$) in °C or kelvin
ΔT	Temperature difference between hot and cold sides of a thermoelectric device in K or °C
ΔT_{max}	TEC(s) maximum temperature difference in °C
ΔT_n	TEC(s) normalized temperature difference
ΔV	The super-capacitor output voltage dropped during fuel cell starvation
A	TEG / TEC p-n junction thermocouple area in m^2
a	TEG p-n junction thermocouple area in m^2
A_1	TEG hot side heatsink1 total surface area in m^2
A_2	TEG cold side heatsink2 total surface area in m^2
Ab	Heatsink base area in m^2
AC	Alternating Current
AOCA	Adaptive Optimal Control Algorithm
Bat	Battery
BDC	Bidirectional DC-DC Converter
BDCMG	Bipolar DC Micro-grid
C	Configuration
C1-10	Configuration 1 to 10
CCHP	Combined Cold, Heat and Power or Combined Cooling, Heating and Power
CDE	CO_2 Emission
CFD	TEC(s) cold flux density in W/m
CHP	Combined Heat and Power
CMMC	Current-fed Modular Multilevel Converter
CoP	TEC(s) coefficient of performance
COP	Coefficient of Performance
CoP	Coefficient of Performance
CoP_e	TEC(s) CoP expression
CoP_{max}	TECs maximum CoP
CoP_{mid}	TEC(s) midpoint CoP
CoP_n	TEC(s) normalized CoP TEC(s)
CPC	Conventional Phase-shift Control
CPUT	Cape Peninsula University of Technology
C_{scv}	The super-capacitor capacitance needed during during fuel cell starvation
D	Duty cycle of the power converter
DAFB	Dual Active Full Bridge
DC	Direct Current
DC-IBC	Direct Coupled-Interleaved Boost Converters
DG	Distributed Generation
DHB	Dual Half Bridge
DHSIC	Dual-Input High Step-Up Isolated Converter
DMFC	Direct Methanol Fuel Cell
DoD	Department of Defence
DPP	Differential Power Processing
DT_s	TEG dimensionless temperature difference
ECE	External Combustion Engine
Eff*	TEG dimensionless conversion efficiency
EGS	Energy Generation System
EIS	Electrochemical Impedance Spectroscopy
EMI	Electromagnetic Interference
EMS	Energy Management Systems / Energy Management & Storage
EMU	Energy Management Unit
FC	Fuel Cell
FCEV	Fuel Cell Electric Vehicle
FCS	Fuel Cell Stack
FCs	Fuel Cells
FEL	Following the Electric Load
FHL	Following the Hybrid Thermal-Electric Load
FIC	Full-bridge Isolated Converter
FLC	Fuzzy Logic Controller
FPGA	Field Programmable Gate Array
FTL	Following the Thermal Load

GaN	Gallium Nitride
GSHP	Ground Source Heat Pump
h_1	TEG hot side heatsink1 convection coefficient
h_2	TEG cold side heatsink2 convection coefficient
H_2	Hydrogen
HC	Hill Climbing
HEV	Hybrid Electric Vehicles
HF	High Frequency
HFD	TEG heat flux density in W/m^2 or TEG(s) heat flux density in W/m^2
HIC	Half-bridge Isolated Converter
HIL	Hardware In the Loop
HPS	Hybrid Power Source
HS	Heatsinks
HSU	Heat Storage Unit
HT PEM FC	High Temperature Polymer Electrolyte Membrane Fuel Cell
I	TEGs output current in ampere through the TEG(s)
IAT	Inlet Air Throttling
IBC	Interleaved Boost Converters
ICE	Internal Combustion Engine
IC-IBC	Inverse Coupled-Interleaved Boost Converters
I_{conv_out}	TEGs booster converter output current
I_{cop}	TEC(s) current in ampere to yield CoP
Icp_{max}	TEC(s) maximum cooling power current in ampere
IES	Integrated Energy System
I_e	TEC electrical current
I_{in}	TEC module(s) input current in ampere
Iin_n	TEC(s) normalized input current is the ratio of I_{cop} and I_{max}
I_{max}	TEC(s) maximum input current in ampere when $Q_c = 0$
I_{Max}	TEG(s) maximum output current in ampere
I_{mid}	TEC(s) midpoint current in ampere
I_n	TEG(s) normalized output current
I_{TEG_Ci}	TEG converter input current in ampere
I_{TEG_Co}	TEG converter output current in ampere
I_{TEG_Int} = ITEGRtint	TEG internal resistance current in ampere
I_{TEG_OC} = TEGIoc	TEG ideal current in ampere
I_{TEG_Out}	TEGs generated current (input current to the boost converter)
$ITEG_{Rtint}$	TEG ohmic current − results to TEG Ohmic or Joule heating
ITESC	Ionic Thermoelectric Super-capacitor
k	TEG / TEC thermal conductivity in W/mK
K	TEG / TEC thermal conductance in (W/K)
K	TEG(s) / TEC(s) thermal conductance in (W/K)
K_1	TEG hot side heatsink1 thermal conductance
K_2	TEG cold side heatsink2 thermal conductance
k_e	TEG(s)/TEC(s) effective thermal conductivity in W/mK
$k_{ec} = k_E$	Thermal conductivity charge carrier contribution (W/mK)
L	TEG / TEC p-n junction thermocouple length in meter
LF	Low Frequency
LGH	Low Grade Heat
LHS	Left hand side
LiBr	Lithium Bromide
Li-ion	Lithium Ion
L_o	Constant known as the Lorenz number ($2.44x10^{-8}$ $W\Omega K^{-2}$)
LP	Linear Programming
LT PEM FC	Low Temperature Polymer Electrolyte Membrane Fuel Cell
LTHS	Low Temperature Heat Source
MFC	Model Free Control
MIC	Modular-Integrated Converter
MIL	Model In the Loop
MIMO	Multi-Input Multi-Output
MPP	Maximum power point
MPPT	Maximum power point tracking
MPT	Maximum Power Transfer
n	TEG / TEC manufacturer p-n thermocouples amount used in a TEG / TEC

η	TEG thermal / electrical / conversion efficiency
η	TEG(s) thermal / electrical / conversion efficiency
N	TEG number of modules required
η_1	TEG hot side heatsink1 fin efficiency
$\eta_1 h_1 A_1$	TEG hot side heatsink1 convection conductance
η_2	TEG cold side heatsink2 fin efficiency
$\eta_2 h_2 A_2$	TEG cold side heatsink2 convection conductance
η_c	Carnot efficiency
η_e	TEG(s) conversion efficiency expression
N_h	TEG dimensionless convection conductance
ηhA	TEG convection conductance
N_i	TEG-HS dimensionless output current
NiMH	Nickel Metal Hydride
N_k	TEG dimensionless thermal conductance
NLP	Nonlinear Programming
η_m	TEG(s) maximum conversion efficiency
η_{mp}	TEGs max power conversion efficiency at the TEGs max P_o
η_n	TEG(s) conversion efficiency normalized
N_v	TEG-HS dimensionless output voltage (V_{os})
NZEB	Nearly Zero Energy Building
η_{TEG}	TEG thermal or electrical or conversion efficiency
η_{max}	TEG maximum efficiency determined by ZT
O_2	Oxygen
OCV	Open Circuit Voltage
ORC	Organic Rankine Cycle
P&O	Perturb and Observe
PAFC	Phosphoric Acid Fuel cell
PBI	PolyBenzImidazole
PCM	Phase Change Material
P_{conv_out}	TEGs booster converter output power
PCS	Power Conditioning Stage
PEC	Principal Energy Consumption
PEM	Proton Exchange Membrane or Polymer Electrolyte Membrane
PGU	Power Generation Unit
PI	Proportional Integral
PID	Proportional Integral Derivative
PIL	Processor In the Loop
P_{in}	TEC module(s) input power in watt
Pin_{mid}	TEC(s) midpoint input power in watt
PLL	Phase Lock Loop
PMFC	Plant Microbial Fuel Cell
P_n	TEG normalized output power or TEG(s) normalized output power
Po	The difference between the FC output power and load power during t_p
Po	TEG(s) output power in watt − which is $Q_h - Q_c$
P_o	TEG(s) output power in watt, is the difference between Q_h and Q_c
Po_{max}	TEG(s) maximum output power in watt
P_{os}	TEG dimensionless output power, is the difference between $Q_h*(Q_{s1})$ and $Q_c*(Q_{s2})$
PSO	Particle Swarm Optimization
P_{TEG_Ci}	TEG converter input power in watt
P_{TEG_Co}	TEG converter output power in watt
P_{TEG_Int} = PTEGRtint	TEG internal resistance power in watt
P_{TEG_OC} = TECPocM	TEG ideal power in watt
P_{TEG_Out}	TEGs generated power (input power to the boost converter)
$PTEG_{Rtint}$	TEG generated power loss − due to TEG internal resistance
PV	Photovoltaic
PWM	Pulse Width Modulation
ρ	TEG / TEC electrical resistivity in Ω.m
ρ_e	TEG / TEC effective electrical resistivity in Ω m
ρ_e	TEG(s) / TEC(s) effective electrical resistivity in Ω.m
Q_c	TEG heat emitted on its cold side in watt
Q_c	TEG(s) heat emitted on TEG module(s) cold-side in watt
Q_c	TEC(s) cooling power on TEC module(s) cold-side in watt
Qc_{max}	TECs maximum absorbable heat in watt, when $\Delta T = 0°C$

Qc_{mid}	TEC(s) midpoint cooling power in watt
Qc_n	TEC(s) normalized cooling power is the ratio of Q_c and Qc_{max}
Qcp_{max}	TEC(s) Icop maximum cooling power in watt
Q_h	TEG(s) heat absorbed on TEG module(s) hot-side in watt
Q_h	TEC(s) heat emitted on TEC module(s) hot-side in watt
Q_{s1}	TEG hot side dimensionless heat absorbed (Q_h*)
Q_{s2}	TEG cold side dimensionless heat released (Q_c*)
Q_t	The TEC thermal current
R	TE device (TEG and TEC) module unit resistance in ohm
RHS	Right hand side
RIC	Resonance Isolated Converter
R_L	TEG(s) electrical load resistance in Ω connected to the TEG(s) output
R_r	TEG dimensionless internal electrical resistance -- also denoted as rr
R_s	Power source resistance in ohms connected to the TECs
R_t	TEG / TEC module internal resistance in ohm -- also denoted as R_R
R_t	TEG / TEC module(s) total resistance in ohms
R_{TEG_Int} = TEGRtint	TEG internal resistance in ohm
r	TEG / TEC thermocouples p-n junction unit resistance in ohm (Ω)
S	TE device Seebeck coefficient in V/K or Seebeck voltage per unit of temperature in (V/K)
SA	Simulated Annealing
SC	Super-capacitor
S_e	TEG / TEC effective Seebeck coefficient in V/K
Se	TEG(s) / TEC(s) effective Seebeck coefficient in V/K
SiC	Silicon Carbide
SIL	Software In the Loop
SMC	Sliding Mode Control
SoC	State of Charge
SOFC	Solid Oxide Fuel Cell
SPWM	Sinusoidal Pulsed Width Modulation
ST	Solar Thermal
STC	Standard Test Condition / Solar Thermal Collector
σ	Electrical conductivity (Siemens/m) is the inverse of electrical resistivity ρ (Ω.m)
$S^2\sigma$	Known as TEG electrical power factor (W/mK^2)
T	Absolute temperature in kelvin (273.15 K) or 0°Celsius
T_1	TEG hot side temperature (T_h)
T_2	TEG cold side temperature (T_c)
T_c	Temperature on TEG / TEC cold-side in °C
T_c	Temperature on thermoelectric device or material cold side (kelvin or Celsius)
TE	Thermoelectric
TEC	Thermoelectric Cooler
TEC_{COP}	TEC Coefficient of Performance
TECsa	TEC cold-side surface area
TEG	Thermoelectric generator
TEG_{Ioc}	TEG ideal generated current − assuming there is no TEG_{Rtint}
TEG-P = T_p	TEG in parallel
TEG_{PocM}	TEG ideal generated power − assuming there is no TEG_{Rtint}
TEG_{Pout}	TEG generated electrical output power delivered to the load (W)
TEG_{Rtint}	TEG internal resistance (R_t) − responsible for the power loss
TEG-S = T_s	TEG in series
TEGs DT	TEGs temperature difference
TEGs T_c	TEGs cold side temperature
TEGs T_h	TEGs hot side temperature
TEGsa	TEG hot-side surface area
TEG_{Voc}	TEG ideal generated voltage − assuming there is no TEG_{Rtint}
TER	Thermoelectric Heat-flux Regulator
T_h	Temperature on TEG / TEC hot side in °C
T_h	Temperature on thermoelectric device or material hot side (kelvin or Celsius)
THD	Total Harmonic Distortion
THRS	Thermoelectric Heat Recovery System
T_i	TEG hetasinks fluid dimensionless temperatures (Tis)
T_{i1}	TEG hot side heatsink1 fluid dimensionless temperature
T_{i2}	TEG cold side heatsink2 fluid dimensionless temperature
TIM	Thermal Interface Material

T_{off}	The off cycle of the FC power converter switching period Ts.
T_p	TEG(s) / TEC(s) module quantity in parallel
t_p	FC fuel starvation period
TRCC	Trans-critical CO2
Ts	The FC power converter switching period
T_s	TEG(s) / TEC(s) module quantity in series
T_{s1}	TEG hot side dimensionless temperature
T_{s2}	TEG cold side dimensionless temperature
T_t	TEG(s) / TEC(s) modules total quantity
$\overline{T}$	TE device average temperature $(T_h + T_c)/2$ in K or °C
UC	Ultra-capacitor
UC-IBC	UnCoupled-Interleaved Boost Converters
V_{act}	FC activation loss
V_{conc}	FC concentration loss
V_{comv_out}	TEGs booster converter output voltage
V_{FC_Stack}	FC stack voltage when loaded
Vi	DC-DC power converter input voltage
Vin	TEC module(s) input voltage in volt
Vin_{max}	TEC's max V_{in} in (V) that produces max ΔT_{max} when $I_{in}=I_{max}$
Vin_n	TEC(s) normalized input voltage is the ratio of V_{in} and Vin_{max}
V_n	TEG normalized output voltage
Vn	TEG(s) normalized output voltage
V_o	TEG module output voltage in volt
Vo	TEG module(s) output voltage in volt
Vo	DC-DC power converter output voltage
V_{oc}	TEG ideal output voltage (consider it as EMF = electromotive force) in volt
V_{ohmic}	FC Ohmic loss
Vo_{max}	TEG(s) maximum output voltage in volt
Vopen	FC stack unloaded voltage
V_{os}	TEG dimensionless output voltage (N_v)
VSC	Voltage Source Converter
V_{TEG_Ci}	TEG converter input voltage in volt
V_{TEG_Co}	TEG converter output voltage in volt
V_{TEG_Int} = VTEGRtint	TEG internal resistance voltage in volt
V_{TEG_OC} = TEGVoc	TEG ideal voltage in volt
V_{TEG_Out}	TEGs generated voltage (input voltage to the boost converter)
$VTEG_{Rtint}$	TEG generated voltage drop − due to TEG internal resistance
WADALINE	Wavelet Adaptive Linear Neuron
Z	TE device Figure of Merit measured in per K (K^{-1})
z	TE material Figure of Merit measured in per K (K^{-1})
ZCS	Zero Current Switching
Z_e	TEG / TEC effective figure of merit in per K
Ze	TEG(s) / TEC(s) effective figure of merit in per K
ZSI	Z-Source Inverter
ZT	TE device dimensionless Figure of Merit at absolute temperature (273.15 K)
$Z\overline{T}$	TE device dimensionless Figure of Merit at mean temperature $\overline{T}$
zT	Thermoelectric material dimensionless Figure of Merit at absolute temperature (0°Celsius)
ZTA	TEG dimensionless figure of merit at temperature TA ($\overline{T}$)
ZT_{i2}	TEG dimensionless figure of merit at temperature T_{i2}
ZVS	Zero Voltage Switching

Table of Contents

List of Figures

List of Tables

CHAPTER 1

INTRODUCTION

1.1 Overview

South Africa (and at large Africa), is experiencing an ongoing unstable national electricity grid (Eberhard *et al*., 2017). As per ratification of the Paris agreement (Van der Walt *et al.*, 2017), renewable energy and energy efficiency integration, as well as the policies and regulatory frameworks have been progressively refined following the commitments towards a low carbon footprint and green economy, with focus on energy mix to ensure energy security and sustainability. This however has been hampered by Eskom (South Africa's national electrical energy provider) ongoing intermittent electrical power-cuts due to its apartheid legacy aging infrastructure (NPC, 2018) inadequate new power station designs, poor administrations, unscrupulous contracts, high pressure on the national grid from rising demands from increase distributions to previously disadvantaged areas and new establishments, electricity theft and tampering, technical break downs, inadequate supply of raw materials as well as incompetent staff. In this context, the penetration of renewable energy sources and sustainable energy solutions, are enforced to complement the national grid as well as for private use. As a result, sustainable energy options such as hydro electric power, solar energy, wind energy and as well fuel cells (Bessarabov *et al.*, 2017; Eberhard *et al*., 2017; Van der Walt *et al.*, 2017; NPC, 2018) are mostly being considered and employed at various levels. In light of this, I alternatively advance the case for thermoelectricity and how it can be applied as a green energy efficient source and energy load for an innovative combined cold, heat and power (CCHP) system. However, hybrid power energy systems have various challenges and therefore must be improved.

1.2 Research Problem Statement

The problem of inefficiency in hybrid power energy conversion systems.

1.3 Research Problem Background

Hybrid power energy conversion simply means combining, normally different renewable energy and power technologies to produce power and energy. In such a setup, the various technologies augment each other, as well as provide different utilities from a combined system. Usually, the power technologies have high dynamics response and therefore complements the hybrid system to provide quick peak power during transient load conditions, whereas the energy technologies have low dynamics response and therefore complements the hybrid system to provide energy for longer duration. Such an augmented system can reliably supply and sustain large electrical loads.

Most renewable energy systems such as solar and wind energy are designed as augmented systems, whereby the energy harnessed from the sun and or wind, is stored in an energy reservoir (e.g. a battery) (Leahy *et al*., 2010) connected to power converters/inverters to provide power during energy harnessing outages or to a balance of plant. This is then used to supply the various electrical loads which could be lighting, heating, cooling as well as other electrical appliances. Such a renewable energy system can only generate electricity which has to be further converted / stored and later used for other applications and this process is usually inefficient and expensive.

As an alternative, is a renewable energy system based on fuel cells (FCs) − which are clean electro-chemical devices that can continuously convert chemical energy into electrical energy (with water and heat as by-products), provided they are continuously fueled with reactant gases, normally Hydrogen and Oxygen − in the case of polymer electrolyte membrane (PEM) FC (Chandan *et al.*, 2013). As evident, a FC renewable energy system can wholly provide electricity, heat as well as water − which is clearly a more energy efficient system; as from a single process, three energy utilities are produced. However, this has to be managed properly with energy storage and management systems to further improve the efficiency, such that excess electricity when unused can be stored in battery banks and use later or the electricity can be used to supply heating loads, likewise the heat produced can be directly used for heating applications or stored (dumped in water) when not in use or converted to cold or harnessed to produce electricity. However, fuel cells are costly and prone to a phenomenon called 'fuel starvation' – the lack / delay of hydrogen flow during high current demand (Thounthong & Sethakul, 2007).

The case for thermoelectricity is advance – whereby waste heat can be cleanly converted to power or reversibly, cold and or heat can be produced from power (Champier, 2017; He & Tritt, 2017; Petsagkourakis *et al.*, 2018; Jouhara *et al.,* 2021). However, thermoelectric devices intrinsically have low figure of merit which makes them inefficient, especially if improperly applied. In light of this, a CCHP system constituting a fuel cell (PEM), Lithium ion battery, ultra-capacitor, thermoelectricity and energy management system is proffered and the inefficiency with focus on power/energy associated in this hybrid system, is the research problem.

1.4 Research Problem Literature Review

CCHP systems, fuel cells, thermoelectricity and fuel cells power converters and energy management systems were extensively reviewed to ascertain the various research gaps and to determine novel practices that are sumarised in Tables 1.1-1.5 and summarily outlined as follows:

1.4.1 Thermoelectricity Literature Review

The thermoelectricity literature reviewed is summarised in Table 1.1 and detailed in Chapters 2-5.

Table 1.1: Summary of eighteen thermoelectricity case studies reviewed (adapted from Bayendang *et al.*, 2020b)

Case Studies Analysed	Highlights, Advantages and Disadvantages
Case Study 1.4.1.1 (Bell L.E., 2008)	- The principle of thermoelectricity: Construction, TEG and TEC. - ZT: TE device dimensionless figure of merit. More ZT, the better.
Case Study 1.4.1.2 (Gao X., 2014)	Showed that TEG can be used as TERs to harvest exhaust heat and boost HT PEM FC efficiency with emphasis on i) heat exchanger surface type, ii) its housing dimensions and iii) power conditioning.
Case Study 1.4.1.3 (Huston J. *et al*., 2004)	- About 40 specific applications of TEG were researched and it was noticed that TEG form factor is key to enable mounting anywhere. - TEG was used with various FCs to boost output power by 7-10%.
Case Study 1.4.1.4 (Zhao D. *et al*., 2016)	Showed how energy was harnessed from intermittent heat sources and converted into stored charge via the ionic Soret Effect in an ITESC. Max efficiency is very low compared to TEG of same ZT.
Case Study 1.4.1.5 (Mahmud K.H. *et al*., 2017)	Demonstrated that TEGs connected in series and parallel, generate more voltage and current respectively, that also increases with Tc.
Case Study 1.4.1.6 (Qu Z. *et al*., 2018)	Developed a thermodynamic model for the TEG and micro-turbine. Showed that TEG almost doubled the hybrid CHP output power.
Case Study 1.4.1.7 (Katkus T., 2015)	The manufacturing of a TEG involve choosing a TE material with good ZT (>1), electrodes insulating plate, adhesives and module architecture. A real system was built to characterise TEG modules.
Case Study 1.4.1.8 (Sullivan O.A., 2012)	Modeled TEGs and TECs on a chip. TECs are more efficient using more and better if operated at steady state for frequent hotspot. For infrequent hotspots, TECs maybe cooled with square root transient pulses of very short duration. TEG MPT occurred at greater load resistance. TEG useful power is firstly linear and later parabolically proportional to the heat flux. More TEGs increase output power but decrease later. Thinner TIM improves TECs and TEGs capabilities.
Case Study 1.4.1.9 (Teffah K. *et al*., 2018)	- TEC was used as a TEG cooler in simulated and practical setups. - The ΔT was directly proportional to the TEC V_{in} and TEG V_{out}.
Case Study 1.4.1.10 (Stockholm J., 2016)	Demonstrated that the output power from TEG when pulsed, doubles the conversion efficiency. An 8.4% increase was attained.
Case Study 1.4.1.11 (Kiziroglou M.E. *et al*., 2016)	Proved that thicker TEGs with good area coverage can be used to harvest electricity from environment with fluctuating temperatures.
Case Study 1.4.1.12 (Sulaiman S.M. *et al.*, 2017)	Showed the use of a TEG with FC under simulated natural (static) and forced convection cooling (dynamic) to convert heat to power. However, very high ΔT is required to generate significant power.
Case Study 1.4.1.13 (Hasani M. & Rahbar N., 2015)	Demonstrated the duality of TECs as TEGs in a FC CHP using a THRS. Low ΔTs gave low V_{outs}. MPT occurred at R_{load} of 1 – 10 **Ω**.
Case Study 1.4.1.14 (Park J. *et al*., 2014)	Showed the use of a low-cost microcontroller and temperature sensor based circuit, to track TEG MPP with a 1.1% tracking error.
Case Study 1.4.1.15 (Yildiz F. *et al*., 2013)	Compared TEG and Solar energy conversion. A TEG generates more power relative to solar module of same size but more costly.
Case Study 1.4.1.16 (Apertet Y. *et al*., 2014)	Deduced that a TEG output power and efficiency in a thermal environment, can be simultaneously maximised if its heat flux is constant but not the case if its temperature difference is constant.
Case Study 1.4.1.17 (Ebrahimi M. & Derakhshan E., 2018)	Proved that a TEC LT-PEM FC hybrid CCHP system is capable of producing 2.79kW of electricity, 3.04kW of heat and 26.8W of cooling with a total efficiency of ~77% and fuel saving of 43.25%.
Case Study 1.4.1.18 (Mamur H. & Çoban Y., 2020)	TEGs have no moving parts, have long service life, operate quietly and are green. TEGs have low efficiency and are expensive. By using the manufacturer datasheets, TEGs were modeled, simulated, experimented and results correlated. Impedance matching with boost converter and P&O MPPT schemes gave 98.64% efficiency.

1.4.2 Power Converters and Energy Management Systems (EMS) Literature Review

The power converters literature reviewed is summarised in Table 1.2 and detailed in Chapter 2.

Table 1.2: Power converters studies examined summary (adapted from Bayendang *et al.*, 2020a / 2021a)

Power Converters	Highlights, Merits and Demerits
Study 1.4.2.1 (Kolli A. *et al*., 2015a)	Various FCs DC-DC power converters setups. Emphasis on different types of interleaved converters for high, medium and low power uses. FCs in parallel /series raise output power.
Study 1.4.2.2 (Kabalo M. *et al*., 2010)	FC vehicles cutting edge DC-DC converters. High voltage ratio, compactness and efficiency with affordability, should be used to implement power converters. Presented different schemes.
Study 1.4.2.3 (Delshad M. & Farzanehfard H., 2011)	ZVS current fed push-pull DC-DC converter. When power is off, voltage surge across the switch is absorbed. This improve its efficiency and compactness to enable basic PWM control.
Study 1.4.2.4 (Bizon N., 2011)	A new architecture of FC HPS for efficient functioning and better steadfastness. HPS with active MPPT and hysteretic current controls were used to minimize ripple current from FC.
Study 1.4.2.5 (Ahmed O.A. & Bleijs J.A.M., 2013)	For an UC in DC micro-grids, a bidirectional voltage-fed setup is preferred for quick dynamic response, though for a broad input voltage instability at the UC, there is greater circulating power flow and conduction losses.
Study 1.4.2.6 (Carvalho A. *et al*., 2011)	Modeled a PEM FC using Matlab. Noted the preferred model must take control and optimise the FC operation points. Soft switching based on series resonant and SA was used, as it reduces switching losses and boost efficiency.
Study 1.4.2.7 (Mwaniki F.M., 2014)	Multi-phase tapped-coupled inductor suited for varying high power DC-DC converter uses. Showed less input & output power ripples.
Study 1.4.2.8 (Huangfu Y. *et al*., 2015)	High power efficiency step-down converter for discrete wind power supply scheme, akin PV. Achieved a 2kW supply with 96% efficiency with step-down ZVS/LCD scheme with MPPT.
Study 1.4.2.9 (Seyezhai R. *et al*., 2013)	Interleaved converters with switched capacitor are considered the suitable topology for FC systems, because of reduced ripple power in the input and output, quicker transient reaction, small EMI, enhanced efficiency and reliability.
Study 1.4.2.10 (Nymand M. & Andersen M.A.E., 2008)	A new low-leakage inductance low-resistance design approach to low-voltage high-power isolated boost converters. Poorest efficiency at minimum input voltage with maximum power was ~97%. The maximal efficiency was ~98%.
Study 1.4.2.11 (Eckardt A. *et al*., 2005)	FC automotive power-train application using high current buck-boost DC-DC converter with digital control to render apt protection against over-current, over-voltage & over-temperature.
Study 1.4.2.12 (Kirubakaran A. *et al.*, 2009)	PEM FC setup with DC-DC step-up converter: Design, modeling and simulation. For instant load fluctuation from 0.6 – 1.1kW, the FC current and voltage took ~50 - 70ms (fuel starvation) to attain a new steady state. The altering voltage was tracked with PI controller.
Study 1.4.2.13 (Outeiro M.T. & Carvalho A., 2013)	A method to devise power converters for fuel cell rooted schemes using resonant technique. Independent voltage and PEMFC controllers. Enhanced FC efficiency by managing FC P_{out}.
Study 1.4.2.14 (Wang H., 2019)	Devise and management of a 6-phase IBC rooted in SiC with EIS functionality for FC HEV. IBC dynamic model with HIL real-time.
Study 1.4.2.15 (Fanjul L.M.P., 2006)	Design deliberations for DC-DC converters in FC schemes. Used analytical and experimental schemes to achieve a steady and efficient FC & power converter system. A modular FC stack and DC-DC converter were pioneered by dividing it into autonomous optimal sections.

Study 1.4.2.16 (Ravi D. *et al*., 2018)	IBC and BDC were researched. IBC improves power ripples. The more the interleaving, the better the ripple reduction; though, the more costly. BDC can charge storage devices and furthermore, the isolated types offer galvanic protection in high power uses; however, their large size makes them unfit for portable uses.
Study 1.4.2.17 (Gao J. *et al*., 2019)	FCs have various challenges and the best solution is one that is inclusive with various hardware and software solutions to optimize better FCs costs, performance and longevity.
Study 1.4.2.18 (Liu H. *et al*., 2020)	Investigated a high power fuel cell system. Two test setups were used; a i) rated and ii) cycle working condition tests and found that fuel cell power engine reached 80kW at rated power with the peak power exceeding 100kW.
Study 1.4.2.19 (Miyazaki R. *et al*., 2020)	A current-fed snubber-less ZCS FC high step-up DC-DC converter was studied. It achieved a greater voltage boost ratio and low power ripple, making it suitable for smart homes use.
Study 1.4.2.20 (Bhaskar M.S. *et al*., 2020)	Reviewed extensively and comprehensively in theory and topologically, the different types of fuel cells with focus on the use of fuel cells in FCEV power-trains. Miscellaneous types of power converters were also assessed in details.
Study 1.4.2.21 (Rathode K.S. *et al*., 2019)	Researched a hybrid PV and FC system. The power electronics used a DC-DC converter, a three phase DC-AC inverter for interfacing to the electrical grid and AC loads with P&O MPPT as well as reference frame theory and PLL to enable a reliable power supply system.
Study 1.4.2.22 (Kavyapriya S. & Kumar R.K., 2020)	Modeled and simulated four step-up power converters schemes. Found that the ZETA topology offers the best THD, followed by LUO, SEPIC and Boost with THD of 31.22%, 53.83 %, 65.38 % and 80.22 % respectively.
Study 1.4.2.23 (Bazin P. *et al*., 2020)	Implemented a smart FC with built-in DC-DC power converter. The classic boost converter with 6-phase interleaving was chosen, as it fitted well, efficient & offered least parts used. The efficiency was >95% for a nominal output power of ~1.5kW and output voltage of 240V.
Study 2.24 (Gonnet, A., *et al.* 2019)	Studied power converter topology for FC battery voltage conditioning. The classic boost converter inductor was replaced with a LCL filter. Gave good performance at varying loads.
Study 1.4.2.25 (Corcau J. *et al*., 2019)	Modeled & simulated a hybrid aerodrome FC power source consisting of a FC stack, a boost and buck-boost DC to DC converters as well as super-capacitor to provide clean, stable, peak power and energy dynamics during transients.
Study 1.4.2.26 (Abdelhakim A. & Blaabjerg F., 2020)	Proposed a CMMC single-stage solution to interface a low voltage PV and fuel cells DC power supplies to a higher voltage AC load or grid. This offers better performance and is less bulky, contrary to a two-stage boost converter.
Study 1.4.2.27 (Prabhakaran P. & Agarwal V., 2020)	Presented a BDCMG power supply system based on a novel 4-port dual-input dual-output DC-DC converter to interface fuel cells, PV and wind power sources to a low voltage BDCMG. The converter was reliable, compact, versatile and unidirectional with a 93% peak efficiency and a ~87% rated power efficiency.
Study 1.4.2.28 (Youn H.S. *et al.*, 2020)	Investigated a high power hybrid hydrogen FC railway system with focus on designing an efficient and high power density DC-DC converter. Two DC-DC power converters, namely the IBC and three-level boost converter were researched to determine the most suitable DC-DC boost power converter architecture. The three-level boost converter out performed the IBC in terms of efficiency, power density and dynamic current response and was chosen.

1.4.3 Combined Cold, Heat and Power (CCHP) Systems Literature Review

The CCHP systems literature reviewed is summarised in Table 1.3 and detailed in Chapter 2.

Table 1.3: Reviewed CCHP systems case studies summary (adapted from Bayendang *et al.*, 2020a)

CCHP Research Reviewed	Highlights, Advantages and Disadvantages	CCHP Research Reviewed	Highlights, Advantages and Disadvantages
Case Study 1.4.3.1 (Bozchalui M.C. & Sharma R., 2012)	ICEs CCHP system: Has advanced with comparatively fast start-up time, high efficiency and affordability. Fuels can be petrol, natural gas and gasoline. However, it is noisy, noxious & need high servicing.	Case Study 1.4.3.10 (Cozzolino R., 2018)	LT PEM FC CCHP: The results revealed better execution based on exergy and energy in the overall functional field of the CCHP (tri-generation) scheme. However, LT PEMFC requires expensive Pt catalyst.
Case Study 1.4.3.2 (Badea N. *et al*., 2010)	Stirling Engine CCHP: Green and more efficient. Suitable mostly for motionless or non-stop working applications. Works by re-using the fuel (gas) back and forth.	Case Study 1.4.3.11 (Wang Z. *et al.,* 2018)	Inlet Air Throttling Gas-turbine CCHP: Findings showed that the CCHP scheme is better than the discrete scheme on yearly review, regardless of the working system that is employed. Needs high temperature.
Case Study 1.4.3.3 (Maraver D. *et al*., 2013)	Biomass CCHP: A thermodynamic model that takes into account various sizes of CHP and cooling units was advanced. It however needs lots of space to implement.	Case Study 1.4.3.12 (Lu S. *et al*., 2018)	PV CCHP and GSHP Micro Gas-turbine: A multi-energy regional energy supply system optimization was accomplished. It is nonetheless very expensive to install.
Case Study 1.4.3.4 (Xu A.D. *et al*., 2014)	Micro-turbine CCHP system: By means of pressure, air is then pumped to the recuperator cold side to ably combine with heat for cold production. It requires high temperature to produce more power.	Case Study 1.4.3.13 (Li B. *et al*., 2019)	GSHP and ICE CCHP: The hybrid scheme execution having heat exchanger was superior to the same system not having heat exchanger. It is environmentally not friendly – high temperature, noisy & large.
Case Study 1.4.3.5 (Su Z. *et al*., 2016)	Biomass & solar CCHP: Utilized genetic algorithm to realize a model to acquire an optimum operation technique; considering energetic criteria, the environment and economics. It dismally requires sunlight.	Case Study 1.4.3.14 (Jiang R. *et al*. 2017)	ICE with cooling and dehumidification CCHP system: A thermo-economic model was instituted and a constrained NLP resolve was employed to maximize the system blueprint and functioning strategy.
Case Study 1.4.3.6 (Wongvisanupong K. & Hoonchareon N., 2013)	Gas-turbine and Photovoltaic CCHP: Optimum execution having smallest cost modeled as a LP based-on Matlab. An online economic optimum functioning was simulated. Needs sunlight to function.	Case Study 1.4.3.15 (Chen X. *et al*., 2018)	A 5kW PEM FC CCHP: The outcomes revealed that inlet gases small working temperature, more pressure and relative humidity are paramount for enhancing system competence, exergy and emission. It was optimized with evolution algorithm.
Case Study 1.4.3.7 (Zhao H. *et al*., 2018)	Micro-turbine, PV and wind turbine CCHP system: Used HOMER to model an optimum economic operation model of a micro-grid having net current cost as the optimization purpose. It has a reasonable energy saving and contamination effects.	Case Study 1.4.3.16 (Ebrahimi M. & Derakhshan E., 2018)	LT-PEM FC TEC hybrid CCHP scheme is proficient in producing 26.8W of cold, 3.04kW of heat and 2.79kW of power with an overall efficiency of ~77% and 43.25% fuel saving. Has water management issues and requires costly catalyst because of LT.
Case Study 1.4.3.8 (Wang R. *et al*., 2018)	PAFC and SOFC CCHP system: Thermal, electrolysis and technical economies as well as including factors that protect the environment were investigated. PAFC produces less power relative to other fuel cells of the same size and weight. SOFC has high CHP efficiency but needs high temperature that slows the start-up time.	Case Study 1.4.3.17 (Mehrpooya M. *et al*., 2017)	Stirling Engine and MCFC CCHP system: MCFC is the primary source of power and its exhaust heat was utilized to provide the Stirling engine, from which it delivers heat to the cold generator absorption chiller. The combined cold, heat and power that were generated are respectively 1372kW, 2137kW and 6482kW. Usually very high temperature involved. No catalyst needed.
Case Study 1.4.3.9 (Wang J.L. *et al*., 2014)	ICE & TEG CCHP system: Utilized ICE to produce power, cold and heat – which is stored in hot water. The heat exchanger and TEG were employed to effectively recuperate the ICE's exhaust gas emitted heat. It is power efficient due to TEG incorporation; however, may have environmental issues because of ICE usage.		

CCHP Research Reviewed	Highlights, Advantages and Disadvantages	CCHP Research Reviewed	Highlights, Advantages and Disadvantages
Case Study 1.4.3.18 (Wu D. *et al*., 2019)	CCHP-ST-ORC system harmonizes fossil fuel with renewable energy and its performance was assessed based on thermodynamics. Their findings revealed that their CCHP-ST-ORC system could produce an extra 5.1kW electricity. CCHP-ST-ORC has similar exergy efficiency of 40% compared to the traditional CCHP and CCHP-ST systems.	Case Study 1.4.3.27 (Lingmin C. *et al*., 2021)	A wind, solar and natural gas CCHP system for a remote tourist area with energy hub for electric power and heat with cold from the chillers. The PGU supply the bulk of the power during wind and solar outages and the heat and power storage devices as well assisted in these regards to reduce wastage and to enhance the system performance. Complex system.
Case Study 1.4.3.19 (Mao Y. *et al*., 2020)	CHP is becoming promising technology to provide cascaded efficient energy and the system performance can be enhanced by integrating PV / thermal panels as well as energy storage. Their system has better cost and primary energy savings of ~17%.	Case Study 1.4.3.28 (Lombardo W. *et al.,* 2020)	A CCHP system based on PV, micro-ORC plant and an adsorption chiller with built in real bio-climatic NZEB, modeled with TRNSYS. The system effectiveness is affected by weather condition. The system yearly efficiency ranged from 32 to 42%.
Case Study 1.4.3.20 (Lingmin C. *et al*., 2020)	CCHP multi-energy system incorporating gas, solar and wind energy as well as power storage controlled by PSO method. Power generation under FEL can reach above 50% during peak load periods.	Case Study 1.4.3.29 (Wu D. *et al*., 2021)	Integrated multi-scenario CCHP system theoretical model. A novel self-adaption technique based on exhaustive search algorithm was suggested for a least / hour operation cost, reduced yearly by 0.67%.
Case Study 1.4.3.21 (Cao Y. *et al*., 2020)	CCHP system routed in a developed owl search technique. In the proposed system, wasted heat from hot gases is recycled while at the same time producing power, enabling > 85% system energy efficiency.	Case Study 1.4.3.30 (Ma H. *et al.*, 2020)	CCHP-ORC system to stabilize irregular power and heat demands and enhance the versatility and changeability of the heat to power ratio on the source side. Used TRNSYS to develop a simulation model.
Case Study 1.4.3.22 (Farmani F. *et al*., 2018)	A smart EMS concept of a micro grid CCHP system for buildings, to control the schedules of its energy storage and renewable systems. The conclusion drawn is the use of CCHP system fitted with a smart controller, could significantly lowers a building energy operating cost.	Case Study 1.4.3.31 (Miao N. *et al*., 2020)	Cascaded CCHP systems reduce emission, but their provisions are challenging for optimal setup. Thus, analysis is required and two operating modes namely "fixing power based on heat" and "fixing heat based on power" were assessed with the latter the better having a lower yearly cost.
Case Study 1.4.3.23 (Zare V. & Takleh H.R., 2020)	A geothermal CCHP system with the ejector TRCC fitted with a traditional Rankine cycle. The findings noted that replacing the gas cooler resulted to 30.9% exergy efficiency, 49.1% net power output and 75.8% cooling output rise, but with a 39.1% loss in the heating output.	Case Study 1.4.3.32 (Ji J. *et al*., 2020)	A novel CCHP system with in-built hybrid energy storage system and ORC, with the research goal to evaluate its performance. In one of the case studies, the efficiency varied between 35.70% and 42.70% with the efficiency improvement above 40% relative to the traditional CCHP systems, having 3.61 kWh and 1.86 kWh energy savings in summer & winter respectively.
Case Study 1.4.3.24 (Mohammadi K. & Powell K., 2020)	New integrated co-generation and tri-generation systems configurations using a CO_2 parallel compression economization-vapor compression refrigeration cycle with a 1MW capacity. Their research main contribution is an in-depth techno-economic assessment of the numerous possible variations for these systems.	Case Study 1.4.3.33 (Jia J. *et al*., 2021)	A CCHP-ORC-ST system was studied and had better thermodynamic performance, as they are versatile with greater power production capability, more energy and more waste heat efficient. Relative to conventional CCHP systems, the yearly cost saving increase was 15.0% in commercial and 27.0% in office buildings.
Case Study 1.4.3.25 (Chahartaghi M. & Sheykhi M., 2019)	Dual Stirling engine CCHP system with H_2 and Helium as the functioning gases. The power, cold, heat productions, CCHP efficiency and CoP results using H_2 were respectively 15.24 kW, 19.65 kW, 12.65 kW, 70% and 64.4% and Helium 22.52 kW, 21.65 kW, 14.43 kW, 72.29% and 66.7%. Helium offered better results.	Case Study 1.4.3.34 (Li J. *et al*., 2021)	Assessment of traditional CCHP systems based on fossil fuels and modern types based on IES with renewable energy. However, unlike fossil fuel, renewable energy is unstable due to outages and may affect the energy security; as a result, an IES approach is paramount to coordinate and maximize the various energy flows.
Case Study 1.4.3.26 (Parikhani T. *et al*., 2020)	A novel ammonia-water mixture CCHP system driven by a low temperature heat source (LTHS) − which is a tailored version of a Kalina cycle. Thermodynamics and thermo-economics balance equations for performance analysis of the thermal system were used to investigate the viability of the recommended system. The energy and exergy efficiencies were respectively calculated to be 49.83%, 27.68%. The electrical, cooling and heating optimum capacities were respectively 0.253 MW, 1.610 MW and 1.972 MW.		

1.4.4 Fuel Cells Literature Review

The fuel cells literature reviewed is summarised in Tables 1.4 and 1.5 and detailed in Chapter 2.

Table 1.4: Fuel cell types and comparisons (adapted from Bayendang *et al.*, 2020a)

FC Types	Electrolyte	Reactions	Advantages	Disadvantages
Polymer Electrolyte Membrane (PEM) FC	Solid organic polymer poly-perfluorosulfonic acid. LT: [50 – 100℃] Polybenzimidazole (PBI) HTPEM: [100 – 200℃]	Anode: $4H_2 \rightarrow 8H^+ + 8e^-$ Cathode: $2O_2 + 8H^+ + 8e^- \rightarrow 4H_2O$ Cell: $4H_2 + 2O_2 \rightarrow 4H_2O$	• Solid electrolyte lowers decay & servicing. • Low – mid temperature. • Rapid startup (LT-PEM) • Trivial or no effluence. • Power efficiency 45%.	• Low temperature needs costly catalysts (Pt). • High reaction to fuel contaminants such as CO. • HT-PEM not durable. • LT-PEM water deluge.
Alkaline FC (AFC)	Aqueous solution of KOH drenched in a matrix Temp: [60 – 200℃]	Anode: $2H_2 + 4(OH)^- \rightarrow 4H_2O + 4e^-$ Cathode: $O_2 + 2H_2O + 4e^- \rightarrow 4(OH)^-$ Cell: $2H_2 + O_2 \rightarrow 2H_2O$	Cathode reaction faster in alkaline electrolyte; therefore, high execution. >55% power efficiency.	Very costly CO_2 extraction from the fuel requiring air streams, thus prone to CO_2 emission. Requires pure H_2.
Phosphoric Acid FC (PAFC)	Liquid Phosphoric Acid doused in a matrix Temp: [175 – 200℃]	Anode: $2H_2 \rightarrow 4H^+ + 4e^-$ Cathode: $O_2 + 4H^+ + 4e^- \rightarrow 2H_2O$ Cell: $2H_2 + O_2 \rightarrow 2H_2O$	• Approx 85% efficiency if use CHP systems. • ~40% power efficiency • Use impure H_2 fuel.	• Needs pricey Pt catalyst. • Low power & current. • Bulky size and weight. • Aggressive electrolyte.
Molten Carbonate FC (MCFC)	Liquid solution of Lithium or Sodium or Potassium Carbonates drenched in a matrix Temp: [600 – 1000℃]	Anode: $H_2 + CO_3^{2-} \rightarrow H_2O + CO_2 + 2e^-$ Cathode: $0.5O_2 + CO_2 + 2e^- \rightarrow CO_3^{2-}$ Cell: $H_2 + 0.5O_2 + CO_2 \rightarrow H_2O + CO_2$ (CO_2 is made at the anode and used at the cathode)	High temperature, thus no need for over-priced catalysts. Flexibility to use other fuels. Power efficiency is >50%.	High temperature speeds rust and degradation of FC components. Long start-up time. Expensive thermal management.
Solid Oxide FC (SOFC)	Solid Zirconium Oxide with added small Ytrria (Y_2O_3) amount Temp: [600 – 1000℃]	Anode: $H_2 + O^{2-} \rightarrow H_2O + 2e^-$ Cathode: $1/2O_2 + 2e^- \rightarrow O^{2-}$ Cell: $H_2 + 1/2O_2 \rightarrow H_2O$	Can use contaminated fuels. Akin to PEM, has solid electrolyte merits. Power efficiency >50%.	High temperature enhances decay and destruction of FC parts. Sluggish starting up. Poor capability at ~ 600℃.
Plant Microbial FC (PMFC)	Different soil types, wetland sediments, rhizo-deposits, microbes, compose Ambient Temp (±20℃)	Anode: $(CH_2O)_6 + 6H_2O \rightarrow 6CO_2 + 24H^+ + 24e^-$ Cathode: $6O_2 + 24e^- + 24H^+ \rightarrow 12H_2O$ Cell: $6H_2O + 6CO_2 \rightarrow 6O_2 + (CH_2O)_6$	Eco-friendly, organic (B N_2, NH_4 etc) removal in wastewater treatments, plant bio-sensing, used in wetlands / agricultural lands to generate power.	Bioelectricity generation is relatively very low, regular maintenance to replace plants, natural operational conditions need observing, photosynthesis dependent.

Table 1.5: Fuel cells assisted techniques comparison summary (adapted from Bayendang *et al.*, 2020a)

Fuel Cells Assisted Schemes	Highlights, Advantages and Disadvantages
Fuel Flow-rate Control	H_2 and O_2 are continually controlled to track the FC current variations, by noticing the FC current slope and by sustaining a steady flow-rate of the fuel to make sure the FC at all times has sufficient fuel flow. Although this method ensures the fuel cell is not deprived of H_2 and O_2, it is nevertheless not efficient, because the fuel flow is usually stable particularly at the highest value.
Battery (e.g. Li-ion)	Battery has a higher specific power relative to FCs, thus retorts swiftly & provides the peak power should there be a transient current. Batteries unlike FCs, store energy. Conversely, battery needs time to charge and will degrade if discharge and charge faster and frequently in high current uses.
Ultra-capacitor (UC) or Super-capacitor (SC)	SCs / UCs have the fastest transient response and highest power density compared to batteries and FCs; hence, they're the most ideal energy storage devices for peak current uses, since they charge rapidly & helps circumvent FC slowness but they've the least energy density (discharges fastest).
Battery and SC or UC	The most suitable FC assisted technique is this, as using both aids the FC when peak power and utmost energy are needed at the same time. Drawback is it's a bit costly due to more components.
CombiLit	CombiLit is a composite device that stores energy, by merging in same cell, the electrodes of a lofty energy density Li-ion battery and a peak power density SC. Need costly repairs when faulty.
Solar Cell and SC	Solar cell has max energy density and SC has peak power density that assists the FC during transients. However, constant sunlight is required and the response performance depends on SC.

1.5 Research Project Objectives

From the literature review, it's evident inefficiency exists at many levels in a CCHP system; as a result, the research objectives are defined as follows: i) model a fuel cell-thermoelectricity CCHP system aided with battery and ultra-capacitor as well as energy management system ii) improve the energy / power efficiency on one or more components of the modeled CCHP system and iii) optionally implement in practice the modeled CCHP system and validates the added efficiency.

1.6 Research Project Design and Methodology

The research project methodology was designed in-line with the research respective three objectives and summarised in Figure 1.1 is the overview of the proffered system concept design.

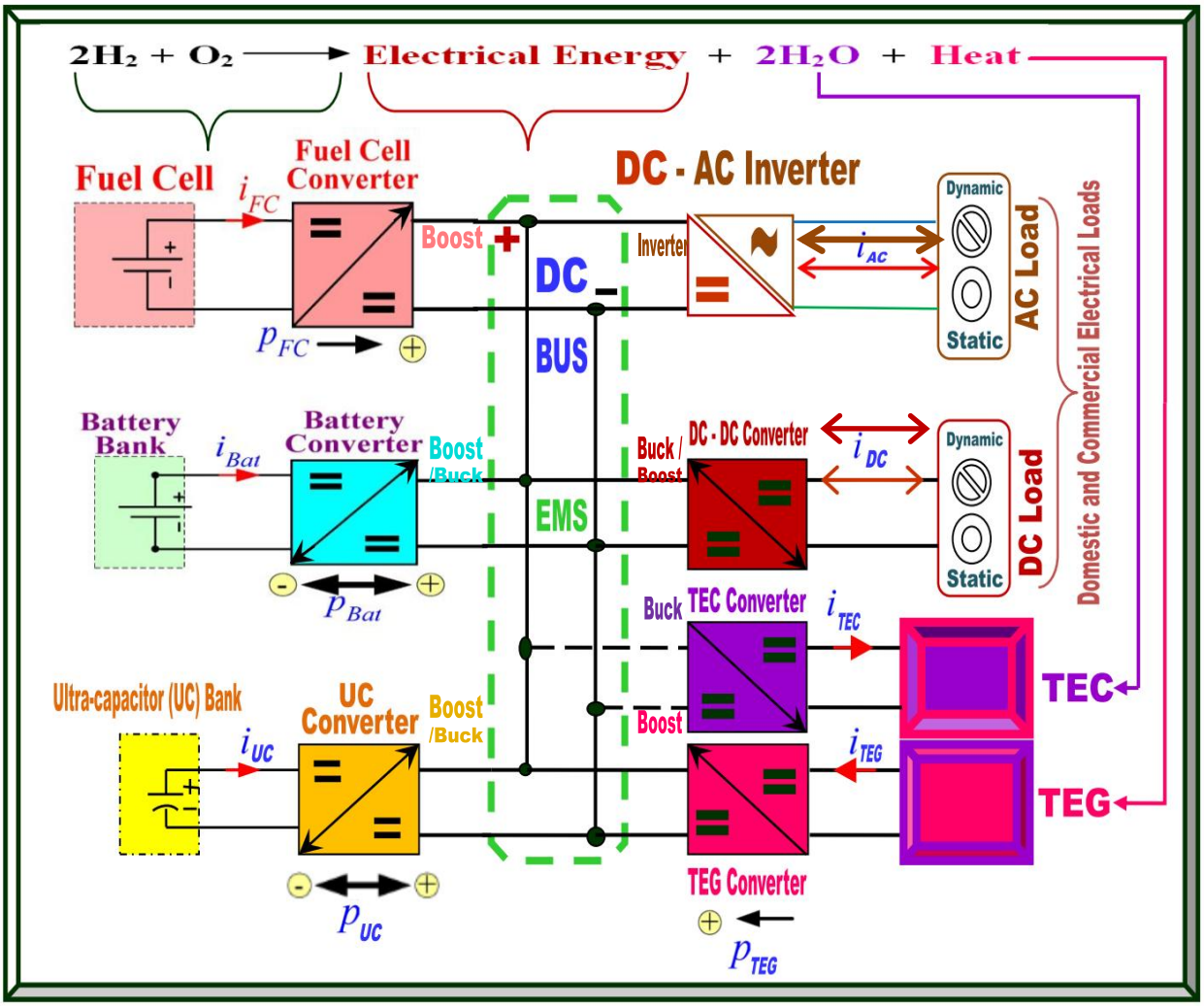

Figure 1.1: Postulated CCHP system and design methodology overview

1.7 Research Project Delineations

The research project shall be practically implemented and tested provided resources / time permit.

1.8 Research Project Scientific Contributions / Outcomes: Models and Articles

The research project outcomes are various simulated models in Matlab / Simulink, ten accredited articles (nine published and one currently under peer review) and the final thesis documentation.

A) Bayendang, N.P., Kahn, M.T., Balyan, V. & Draganov I. 2020. CCHP systems analysis with emphasis on fuel cells, thermoelectricity and power converters. *2020 5th International Conference on Smart and Sustainable Technologies (SpliTech)*; Split, Croatia; 1–9. http://dx.doi.org/10.23919/SpliTech49282.2020.9243720. ***Chapter 2: Section 2.2.**

B) Bayendang, N.P., Kahn, M.T. & Balyan, V. 2021. Power converters and EMS for fuel cells CCHP applications: A structural and extended review. *Adv. Sci. Technol. Eng. Syst. J.* 6(3): 54-83. http://dx.doi.org/10.25046/aj060308. ***Chapter 2: Section 2.3.**

C) Bayendang, N.P., Kahn, M.T. & Balyan, V. 2020. A structural review of thermoelectricity for fuel cells CCHP applications. *Hindawi Journal of Energy*, Volume 2020, 1-23. https://doi.org/10.1155/2020/2760140. ***Chapter 2: Section 2.4.**

D) Bayendang, N.P., Kahn, M.T. & Balyan, V. 2022. Combined cold, heat and power (CCHP) systems and fuel cells for CCHP applications: A topological review. *Undergoing peer review*. ***Chapter 2: Section 2.5.**

E) Bayendang, N.P., Kahn, M.T., Balyan, V., Draganov, I. & Pasupathi, S. 2020. A comprehensive thermoelectric generator (TEG) modelling. *AIUE Congress 2020: Energy and Human Habitat Conference*, Cape Town, South Africa, 1-7. http://doi.org/10.5281/zenodo.4289574. ***Chapter 3: Section 3.2.**

F) Bayendang, N.P., Kahn, M.T., Balyan, V., Draganov, I. & Pasupathi, S. 2020. A comprehensive thermoelectric cooler (TEC) modelling. *AIUE Congress 2020: International Conference on Use of Energy*, Cape Town, South Africa, 1-7. http://dx.doi.org/10.2139/ssrn.3735378. ***Chapter 3: Section 3.3.**

G) Bayendang, N.P., Kahn, M.T. & Balyan, V. 2021. Simplified thermoelectric generator (TEG) with heatsinks modeling and simulation using Matlab and Simulink based-on dimensional analysis. *AIMS Energy*, 9(6): 1213-1240. 10.3934/energy.2021056. ***Chapter 4: Section 4.2.**

H) Bayendang, N.P., Kahn, M.T. & Balyan, V. 2021. Simplified thermoelectric cooler (TEC) with heatsinks modeling and simulation using Matlab and Simulink based-on dimensional analysis. *AIUE Conference 2021: 2nd Energy and Human Habitat Conference*, Cape Town, South Africa, 1-8. http://dx.doi.org/10.2139/ssrn.3900757. ***Chapter 4: Section 4.3.**

I) Bayendang, N.P., Kahn, M.T. & Balyan, V. 2022. Thermoelectric generators (TEGs) and thermoelectric coolers (TECs) modeling and optimal operation points investigation. *Adv. Sci. Technol. Eng. Syst. J.* 7(1): 60-78. DOI: 10.25046/aj070107. ***Chapter 5: Section 5.2.**

J) Bayendang, N.P., Kahn, M.T. & Balyan, V. 2022. Thermoelectric generators (TEGs) modules − Optimum electrical configurations and performance determination. *Undergoing publication production.* [Accepted: March 9, 2022]. *AIMS Energy*. ***Chapter 5: Section 5.3.**

K) Bayendang, N.P. 2021. Domestic and commercial fuel cell / battery / ultra-capacitor / thermo-electric hybrid power energy conversion and energy storage management CCHP system. *CPUT CPGS 2020 / 2021 Postgraduate Conference*. Abstract / Poster Presentations. https://cputpgconf.org.za/wp-content/uploads/2021/08/POSTGRAD-CONF-ABSTRACT-PROGRAMME-2020.pdf

1.9 Research Summary

Energy insecurity is an ongoing national problem in South Africa. Renewable CCHP energy system is proffered as a sustainable solution. However, hybrid power energy conversion systems have many facets which are inefficient. A thorough literature review was done from which the research objectives and methodology were defined. The study outcome is ten accredited articles.

CHAPTER 2

LITERATURE REVIEW

2.1 Overview

Energy insecurities in South Africa and by extension Africa, are no new news on our continent. In Chapter 1, the study was briefly introduced with focus on the various aspects of my research. Literature review is the most vital aspect on any research, as it gives a broad base understanding with respect to the past, present and posterity of the topic under investigation. The success of a research and its novel outcomes lie squarely on the quality of the literature review. As a result, various sources of information, predominantly scholarly publications and books were consulted.

This chapter identifies and examines in details past research and publications on five main areas of my research − which includes CCHP systems, fuel cells, thermoelectricity, power converters and energy management technologies. This in-depth literature review was performed to have a better understanding on the subject matter and also to find the research gaps and ascertain the best practices that can be applied and or developed further individually, as well as systematically. This is to address or offer new innovative approaches to improve or resolve the research problem of inefficient energy conversion at component and or at system levels. This is because inefficiency at component level, definitely translates to inefficiency at system level, therefore the problem must be looked into holistically. Since my PhD thesis report is written based-on my PhD articles, the detailed literature review is adapted from my four below articles and it should be noted that three of the review articles have already been published and one is currently undergoing peer review.

- Bayendang, N.P., Kahn, M.T., Balyan, V. & Draganov, I. 2020. CCHP systems analysis with emphasis on fuel cells, thermoelectricity and power converters. *2020 5th International Conference on Smart and Sustainable Technologies (SpliTech)*; Split, Croatia; 1 – 9. http://dx.doi.org/10.23919/SpliTech49282.2020.9243720.

- Bayendang, N.P., Kahn, M.T. & Balyan, V. 2021. Power converters and EMS for fuel cells CCHP applications: A structural and extended review. *Adv. Sci. Technol. Eng. Syst. J.* 6(3): 54-83. http://dx.doi.org/10.25046/aj060308.

- Bayendang, N.P., Kahn, M.T. & Balyan, V. 2020. A structural review of thermoelectricity for fuel cells CCHP applications. *Hindawi Journal of Energy*, Volume 2020, 1-23. https://doi.org/10.1155/2020/2760140.

- Bayendang, N.P., Kahn, M.T. & Balyan, V. 2022. Combined cold, heat and power (CCHP) systems and fuel cells for CCHP applications: A topological review. *Undergoing peer review*.

2.2 CCHP Systems Analysis with Emphasis on Fuel Cells, Thermoelectricity and Power Converters

This section highlights the ongoing electricity crisis in South Africa and in general Africa as the bases for the research, whereby in an effort for potential innovative / green alternative solutions, various combined cooling, heating and power (CCHP) systems are analysed; with henceforth focus on fuel cells (FC), thermoelectricity (TE) and power converters. Five trendy fuel cell types are compared and the proton electrolyte membrane (PEM) FC is of interest; however, like all fuel cells, it is prone to the inherent fuel cell fuel starvation. Therefore, viable solutions were examined, from which in addition, TE is postulated here as a possible hybrid solution to the FC fuel starvation problem, further to its established tri-generation (CCHP) potentials with fuel cells. Moreover, FCs and TE cannot reliably operate without assisted with suitable power converters, energy storage and management; hence, these technologies are further investigated as well. This study therefore determines and presents some best practices that can be applied to devise, model and implement an efficient and innovative fuel cell CCHP system.

2.2.1 Introduction

Faced with the ongoing electrical energy and power crises in South Africa (Bessarabov *et al.*, 2017; NPC, 2018) and by extension in Africa (Eberhard *et al*., 2017); this literature review study extensively investigates various research on i) combined cooling, heating and power (CCHP), ii) fuel cells (FC), iii) thermoelectricity (TE) and iv) power converters (PC). This is to establish and present some best practices that can be applied to devise, develop and implement an energy efficient FC-TE hybrid power CCHP system for domestic and commercial applications / users, who are currently suffering from periodic power cuts. Summarised in Table 2.1, CCHP also termed tri-generation, is principally a concurrent combined heat and power (CHP) energy scheme (cogeneration) with now cooling included. It summarily constitutes a prime mover and energy conversion mechanisms to generate Power, Heat and Cold at once when fueled, enabling it to directly cater for average households fundamental energy requirements (e.g. in South Africa / Africa). As stated in Wu (2006), Ming *et al.* (2015) and Zhang *et al.* (2018); CCHP systems as illustrated in Figure 2.1, are becoming very popular of recent due to their size, flexibility, applicability, reliability, energy-saving, efficiency, environmental friendliness and costs saving characteristics.

From the CCHP systems analysed, those based-on FCs and thermoelectricity as well as their applicable power converters, are of most interests and are therefore introduced here and covered in details in the subsequent sections that follow. According to Thomas *et al*. (1999) and Hoogers (2002); William Grove in 1839 discovered FC principle in which he called it “gaseous voltaic battery” and later modestly informed Michael Faraday in 1842. As indicated in Table 2.3, Figure 2.2 and equation (2.1); FCs are electro-chemical devices that can continuously convert chemical energy into electrical energy (with water and heat as by-products), as long as they are continuously supplied with fuel and reactant gases – usually Hydrogen (H_2) and Oxygen (O_2) in the

case of polymer electrolyte membrane (PEM) FC. However, FCs are prone to FC fuel starvation phenomenon – which is a drop in the FC voltage due to absent of fuel (H_2), caused by high transient current load conditions. Thermoelectricity as per the studies summarised in Table 2.4, is a thermal and or electrical process, whereby a material based-on its thermal and or electrical properties, can either generates cold and or heat depending on the voltage polarity across the material or this same material is capable of generating electricity from heat, when there is a temperature difference (ΔT) across the material surfaces. There are commonly three effects governing thermoelectricity, generally called thermoelectric effects, which are i) the Seebeck effect (discovered in 1821 by Thomas Seebeck), effected by thermoelectric generators (TEG); ii) the Peltier effect, (discovered in 1834 by Jean Peltier), effected by thermoelectric coolers (TEC) and iii) the Thomson effect (discovered in 1851 by William Thomson aka Lord Kelvin). FCs and TEGs are very low DC voltage sources which could be erratic when loaded, thus they warrant power conditioning to the DC bus and eventually to the various AC and or DC loads. As per the studies examined and summarised in Table 2.5, power converters are therefore required to either step-up, step-down and or invert these DC power sources and then maintained a reliable power henceforth. FCs and TEGs are also usually assisted with batteries and or super-capacitors to provide energy storage and faster energy and power dynamic responses when loaded. Hence, CCHP systems, fuel cells, thermoelectricity and power converters are analysed in brief details in the following sections.

2.2.2 CCHP Systems

A CCHP system generates power and heat simultaneously in a single process while the cooling is subsequently derived from the heat or at times from the power, depending on the CCHP system design employed as shown in Figure 2.1. If the CCHP system is designed properly, the overall system energy efficiency could be above 90%. CCHP systems prime mover normally make use of different energy sources and energy conversion mechanisms. From the literature review and highlighted in Badea *et al.* (2010) and Bozchalui and Sharma, (2012); the name or type of a CCHP system is derived from its power generation unit (PGU) or prime mover. Various CCHP systems case studies relevant to my study, were reviewed and the summary of the findings is given in Table 2.1.

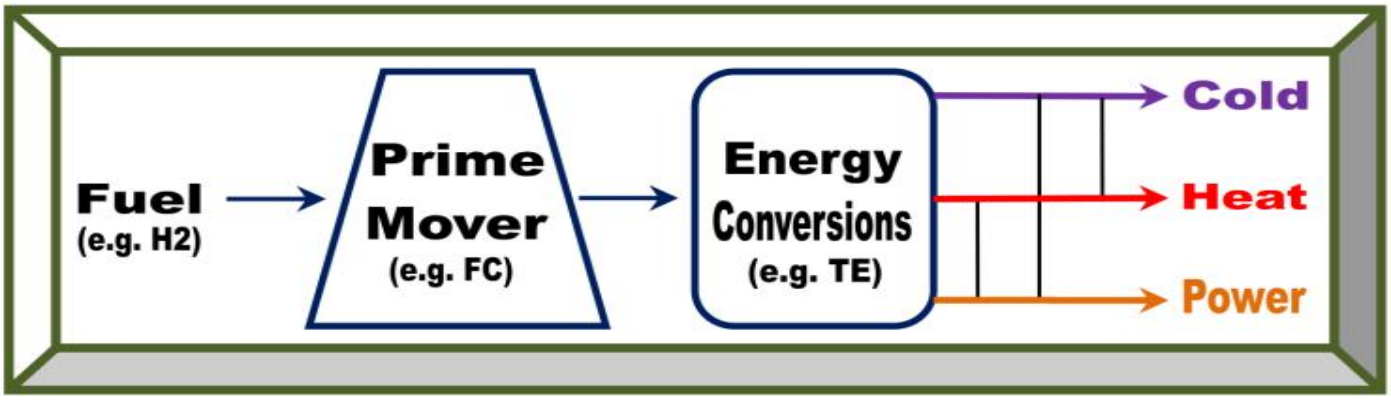

Figure 2.1: CCHP systems overview

Table 2.1: Analyzed CCHP systems summary (adapted from Bayendang *et al.*, 2020a)

CCHP Research Analysed	Highlights, Advantages and Disadvantages
Analysis A (Bozchalui M.C. & Sharma R., 2012)	ICEs CCHP: Have evolved with relatively high efficiency, low-cost and quick start-up time. Can be powered by natural gas, gasoline fuels and petrol. Noisy, toxic and high maintenance.
Analysis B (Badea N. *et al.*, 2010)	Stirling Engine CCHP: More efficient and green. Mostly suited for stationary or constant running applications. Works by recycling gas.
Analysis C (Maraver D. *et al.*, 2013)	Biomass CCHP: A thermodynamic model that considers the integration of different sizes of cogeneration and cooling units was developed.
Analysis D (Xu A.D. *et al.*, 2014)	Micro-turbine CCHP: Air is first pressurized and pumped to the cold side of the recuperator to efficiently mix with heat to produce cooling.
Analysis E (SU Z. *et al.*, 2016)	Biomass and solar CCHP: Used genetic algorithm to implement a model to obtain an optimal operation strategy factoring economic, environmental as well as energetic criteria.
Analysis F (Wongvisanupong K. & Hoonchareon N., 2013)	Photovoltaic and Gas-turbine CCHP: Optimal operation with minimum cost modeled as a linear program (LP) using Matlab. Online economic optimal operation was simulated.
Analysis G (Zhao H. *et al.*, 2018)	Wind Turbine, PV and Micro-turbine CCHP: Used HOMER to model an optimal economic operation model of a micro-grid with net present cost as the optimization objective. Has a better energy saving and pollution effects.
Analysis H (Wang R. *et al.*, 2018)	Phosphoric acid (PAFC) and solid oxide (SOFC) Fuel Cells (FCs) CCHP: Researched electrolysis, thermal and technical economies as well as environmental protection factors.
Analysis I (Wang J.L. *et al.*, 2014)	ICE and TEG CCHP: Used ICE to generate electricity, cold and hot water; whereas TEG and heat exchanger were used to efficiently recover the ICE's exhaust gas waste heat.
Analysis J (Cozzolino R., 2018)	Low temperature (LT) PEM FC CCHP: The findings showed a good performance in terms of energy and exergy in the complete operating field of the tri-generation (CCHP) system.
Analysis K (Lu S. *et al.*, 2018)	Ground source heat pump (GSHP) Micro Gas-turbine and PV CCHP: Multi-energy regional energy supply system optimization.
Analysis L (Wang Z. *et al.,* 2018)	Inlet Air Throttling Gas-turbine CCHP: Results showed the CCHP system is superior to the separate system on annual evaluation, irrespective of which operation scheme used.
Analysis M (Li B. *et al.*, 2019)	ICE and GSHP CCHP: The hybrid system performance with heat exchanger was better to similar CCHP system without heat exchanger.
Analysis N (Jiang R. *et al.*, 2017)	ICE with Dehumidification and Refrigeration CCHP: A thermo-economic model was established and a constrained nonlinear programming solution was used to optimize the design and operation plan of the system.
Analysis O (Chen X. *et al.*, 2018)	5kW PEM FC CCHP: The results indicated that low operating temperature, high relative humidity and pressure of inlet gases are helpful for improving system exergy, efficiency and emission; optimized using evolution algorithm.
Analysis P (Ebrahimi M. & Derakhshan E., 2018)	A TEC LT-PEM FC hybrid CCHP system is capable of generating 2.79kW of power, 3.04kW of heat and 26.8W of cold with a total efficiency of ~77% and fuel saving of 43.25%.
Analysis Q (Mehrpooya M. *et al.*, 2017)	Stirling Engine and molten carbonate fuel cell (MCFC) CCHP: MCFC is the main power source and its exhaust heat was used to supply the Stirling engine, which in turn supplies heat to the absorption chiller's cold generator. The combined cold, heat and power generated were respectively 1372kW, 2137kW and 6482kW.

2.2.3 Fuel Cells

As per Thomas *et al*. (1999), Hoogers (2002), Thounthong and Sethakul, (2007) and Chandan (2013); Hydrogen FCs based-on proton exchange membrane (PEM) as shown in Figure 2.2 and equation (2.1), are gradually becoming alternative energy sources, which are furthermore clean and renewable with diverse applications. However, as detailed in Thounthong and Sethakul, (2007) and depicted in Figure 2.3, FCs are generally susceptible to a phenomenon known as 'fuel starvation' – the absence or delay of H_2 and or O_2 flow, resulting in difficulties of FCs handling a peak demand in current when loaded, hence a dip in the FC voltage. As demonstrated in Taniguchi *et al.* (2004), fuel (H_2) and or O_2 starvation, even for a second must be avoided, as it can cause serious and lasting damages to the electro-catalyst of the fuel cell and henceforth reducing its energy and power supplies capability, efficiency, durability and reliability. As investigated by Sulaiman *et al.*, (2015), FCs have high energy density but low power density; as a result, FCs can not a) supply the initial high electric power required to instantly switch-on a load (e.g. hybrid electric vehicle (HEV), b) quickly respond when there is a sudden fluctuation in load current (e.g. when accelerating in the case of a HEV (Boettner, 2002 and Khaligh & Li, 2010) or varying heater temperature and c) absorb HEV regenerative power generated when it is decelerating or braking. Therefore, an extra energy storage device such as a rechargeable battery and or a power source with very fast dynamic response such as an ultra-capacitor (UC) or a super-capacitor (SC) bank, which is coupled to energy and power conversion devices with energy management system (EMS), are needed to aid the FC. As a result, various attempts to address this critical FC fuel starvation phenomenon problem have been researched over the years and presented in Table 2.2, is a summary of several investigations which include but not limited to the following six main methods: a) FC aided with fuel flow-rate control, b) FC aided with battery, c) FC aided with SC, d) FC aided with battery and SC or UC, e) FC aided with CombiLit and f) FC aided with a solar cell and SC or UC. The review findings on typical fuel cells is summarised in Table 2.3.

$$H_2 + 0.5O \longrightarrow H_2O + \text{Electrical Energy} + \text{Heat} \qquad (2.1)$$

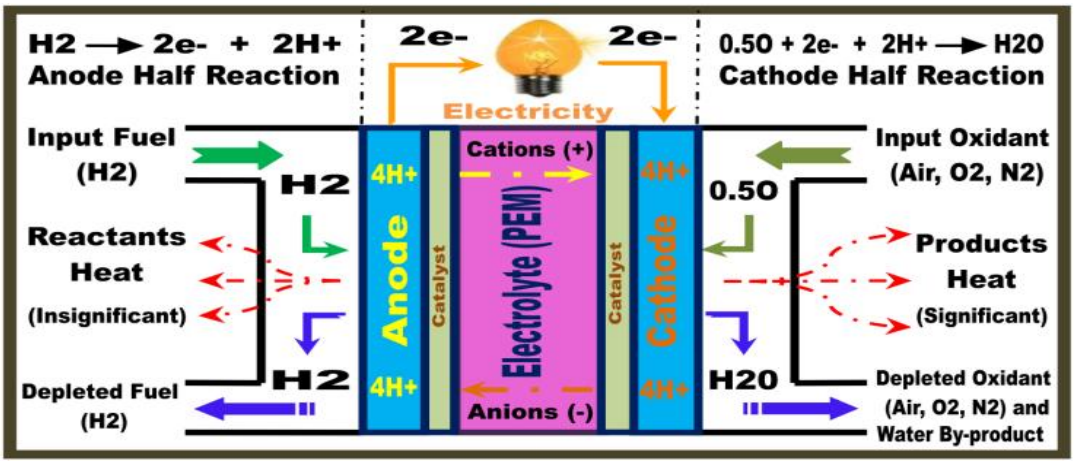

Figure 2.2: PEM fuel cell operation principle overview

Table 2.2: FC fuel starvation aiding techniques summary (adapted from Bayendang *et al.*, 2020a)

FC Aiding Types	Highlights, Advantages and Disadvantages
Fuel Flow-rate Control	H_2 and O_2 are constantly controlled to follow the fuel cell current fluctuations, by observing the FC current gradient and by maintaining a constant fuel flow-rate to ensure the FC always have enough flow of fuel. This technique is however inefficient, since the flow of fuel is always constant especially at maximum value.
Battery (e.g. Li-ion)	Has a higher power density compared to a FC, thus reacts faster and supplies the high current when there is a transient current. Battery stores energy that FC can't. However, batteries take long to charge & degrades if dis/charged faster.
Super-capacitor (SC) or Ultra-capacitor (UC)	SCs / UCs have the highest power density and fastest transient response relative to batteries and FCs; thus, this makes them the desired energy storage device for high current uses, as they charge quickly and also avoid FC inertia. However, they have the lowest energy density.
Battery and SC or UC	This is the most popular FC aiding approach, having both augment the FC when high power and high energy are simultaneously required.
CombiLit	CombiLit is a hybrid energy storage device that combines a high power density super-capacitor electrode and a high energy density Li-ion battery electrode housed in one cell.
Solar Cell and SC	Solar cell has high specific energy and SC has high specific power which augments the FC during transients, though not without sunlight.

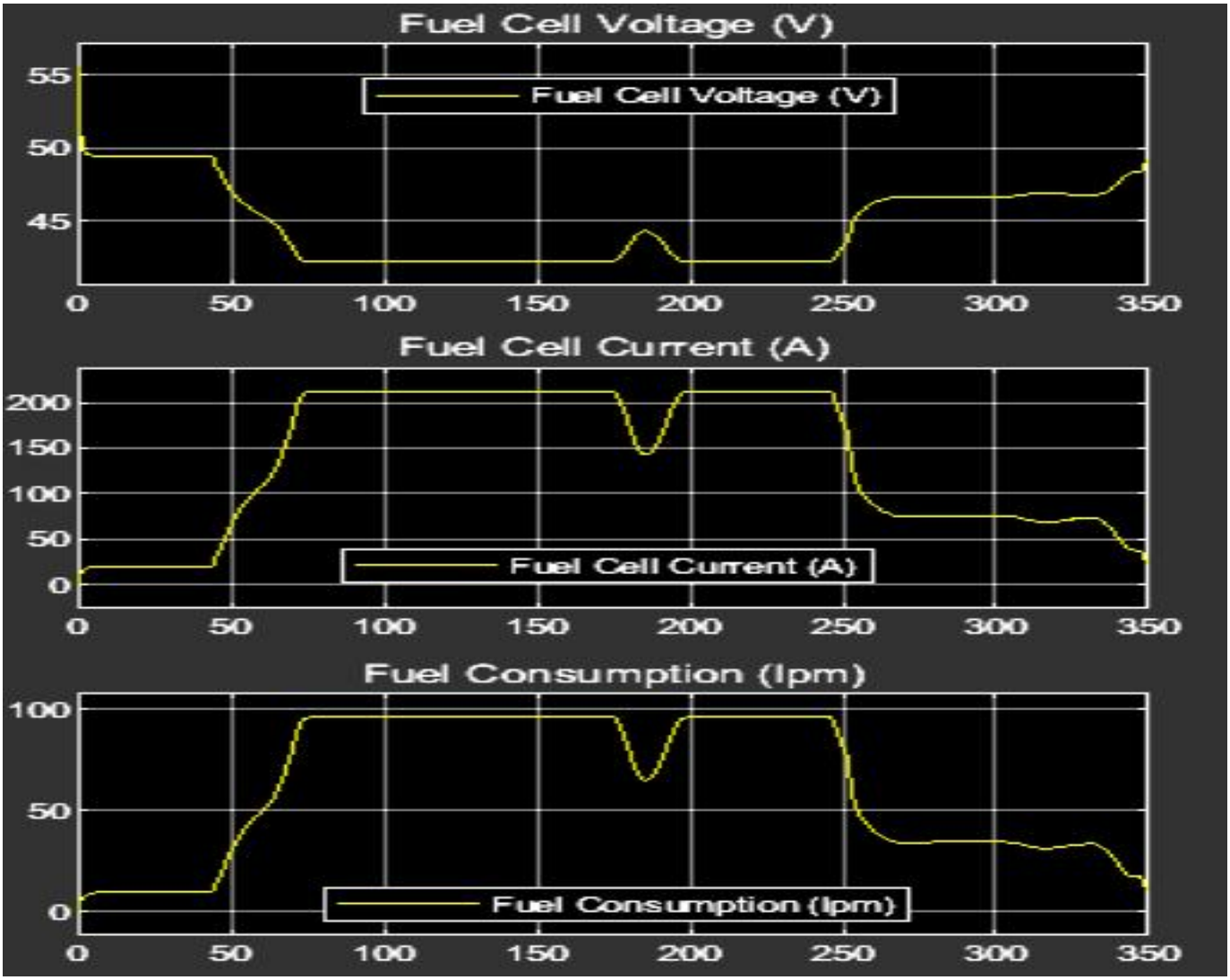

Figure 2.3: PEM fuel cell fuel starvation phenomenon

Table 2.3: Fuel cell types and comparisons summary (adapted from Bayendang *et al.*, 2020a)

FC Types	Electrolyte	Reactions
Polymer Electrolyte Membrane (PEM) FC	Solid organic polymer poly-perfluorosulfonic acid. LT: [50 – 100°C] Polybenzimidazole (PBI) HTPEM: [100 – 200°C]	Anode: $2H_2 \rightarrow 4H^+ + 4e^-$ Cathode: $O_2 + 4H^+ + 4e^- \rightarrow 2H_2O$ Cell: $2H_2 + O_2 \rightarrow 2H_2O$
Alkaline FC (AFC)	Aqueous solution of Potassium Hydroxide soaked in a matrix Temp: [60 – 200°C]	Anode: $H_2 + 2(OH)^- \rightarrow 2H_2O + 2e^-$ Cathode: $O_2 + 2H_2O + 2e^- \rightarrow 2(OH)^-$ Cell: $2H_2 + O_2 \rightarrow 2H_2O$
Phosphoric Acid FC (PAFC)	Liquid Phosphoric acid soaked in a matrix Temp: [175 – 200°C]	Anode: $H_2 \rightarrow 2H^+ + 2e^-$ Cathode: $0.5O_2 + 2H^+ + 2e^- \rightarrow H_2O$ Cell: $H_2 + 0.5O_2 \rightarrow H_2O$
Molten Carbonate FC (MCFC)	Liquid solution of Lithium or Sodium or Potassium Carbonates soaked in a matrix Temp: [600 – 1000°C]	Anode: $H_2 + CO_3^{2-} \rightarrow H_2O + CO_2 + 2e^-$ Cathode: $0.5O_2 + CO_2 + 2e^- \rightarrow CO_3^{2-}$ Cell: $H_2 + 0.5O_2 + CO_2 \rightarrow H_2O + CO_2$ (CO_2 is produced at anode and consumed at cathode)
Solid Oxide FC (SOFC)	Solid Zirconium Oxide with added small Ytrria (Y_2O_3) amount Temp: [600 – 1000°C]	Anode: $H_2 + O^{2-} \rightarrow H_2O + 2e^-$ Cathode: $0.5O_2 + 2e^- \rightarrow O^{2-}$ Cell: $H_2 + 0.5O_2 \rightarrow H_2O$
FC Types	**Advantages**	**Disadvantages**
Polymer Electrolyte Membrane (PEM) FC	• Solid electrolyte lowers decay & maintenance. • Low – mid temperature • Fast start-up (LT-PEM) • Little or no pollution. • Power efficiency 45%.	• Low temperature needs expensive catalysts (Pt). • High sensitivity to fuel impurities such as CO. • HT-PEM not durable • LT-PEM water flooding
Alkaline FC (AFC)	Cathode reaction faster in alkaline electrolyte; thus, high performance. Power efficiency >55%.	Expensive CO_2 removal from the fuel needing air streams, thus prone to CO_2 emission. Needs pure H_2.
Phosphoric Acid FC (PAFC)	• Up to 85% efficiency in CHP applications. • Power efficiency ~40% • Use impure H_2 fuel.	• Needs costly Pt catalyst. • Low current and power. • Large weight and size. • Aggressive electrolyte
Molten Carbonate FC (MCFC)	High temperature, thus no need for expensive catalysts. Flexibility to use other fuels. Power efficiency is >50%.	High temperature speeds rust and breakdown of FC components. Long start-up time. Expensive thermal management.
Solid Oxide FC (SOFC)	Can use impure fuels. Has solid electrolyte benefits akin to PEM. Power efficiency is >50%.	High temperature speeds corrosion and damage of FC parts. Slow start-up. Poor ability at ~ 600°C.

2.2.4 Thermoelectricity

According to the literature review in Table 2.4, thermoelectricity can be applied practically to a) cogenerate DC power as TEG and or b) provide thermal management (cooling / heating) as TEC. Thermoelectric (TE) devices exhibit duality – can be used interchangeably within limits as TEG or as TEC and this is depicted in Figure 2.4.

2.2.4.1 Thermoelectric Generator (TEG): Seebeck Effect

Seebeck effect is DC electricity generation from heat and the devices that do perform such a process are known as TEGs. There are various types of TEGs depending on their design (stages), material, shapes and applications.

2.2.4.2 Thermoelectric Cooler (TEC): Peltier Effect

Depending on the direction of current flow (power supply voltage polarity), TECs are thermoelectric (TE) devices that can generate cold and or heat from DC electricity and the process is called the Peltier effect.

TEGs and TECs thermal and electrical conductivities are related through the Wiedemann-Franz relationship, defined as:

$$k_{ec} = \sigma T L_o \qquad \text{(W/mK)} \tag{2.2}$$

where k_{ec} is the thermal conductivity electronic charge carrier contribution, σ is the electrical conductivity, T the absolute temperature (273.15 K) in kelvin (or 0°C) and L_o is a constant known as the Lorenz number (2.44×10^{-8} $W\Omega K^{-2}$).

Furthermore, the thermoelectric materials are categorized based-on their dimensionless figure of merit (zT), given as:

$$zT = S^2 \sigma T / k \tag{2.3}$$

where S is the Seebeck voltage per unit of temperature in kelvin.

The TE device maximum efficiency (η_{max}) determined by the TE device temperatures and device dimensionless figure of merit (ZT) – which is not the same as zT, is defined as:

$$\eta_{max} = \eta\left(\frac{\sqrt{1+Z\overline{T}}-1}{\sqrt{1+Z\overline{T}}+T_c/T_h}\right) \tag{2.4}$$

where the device Carnot efficiency is $\eta = (T_h - T_c)/T_h$, the TE device average temperature is $\overline{T} = (T_h+T_c)/2$, the device temperature difference is $\Delta T = T_h - T_c$, $Z\overline{T}$ is the TE device dimensionless figure of merit at average temperature $\overline{T}$ and T_h and T_c are respectively the TE device hot and cold sides temperature. When $ZT = zT$, the relationship reduces to:

$$Z = z = S^2 \sigma / k \qquad (K^{-1}) \tag{2.5}$$

where $S^2\sigma$ is known as the TEG electrical power factor.

The TEG DC output voltage (V_{out}) to the load is computed as:

$$V_{out} = n\,(S\Delta T - IR) \quad \text{(V)} \tag{2.6}$$

where n is the quantity of the TEG p-n junction thermocouples used, I is the DC current in ampere flowing through the TEG and R is the TEG p-n junction thermocouple unit resistance in ohm.

The TEG electrical or conversion efficiency (η_{TEG}) is:

$$\eta_{TEG} = P_{out}/Q_h \tag{2.7}$$

where P_{out} is the TEG DC electrical output power in watt to the load and Q_h is the heat absorbed in watt on the TEG hot side at temperature T_h.

The TEC DC input voltage in volt is:

$$V_{in} = n\,(S\Delta T + IR) \quad \text{(V)} \tag{2.8}$$

The TEC coefficient of performance (CoP) is given as;

$$CoP = Q_c/P_{in} \tag{2.9}$$

where Q_c in watt is the cooling power or heat absorbed on the TEC cold side at temperature T_c and P_{in} is the TEC DC input power ($P_{in}=IV_{in}$) in watt.

Figure 2.4 summarises the Seebeck-Peltier effects and Table 2.4 summarises the thermoelectricity case studies reviewed.

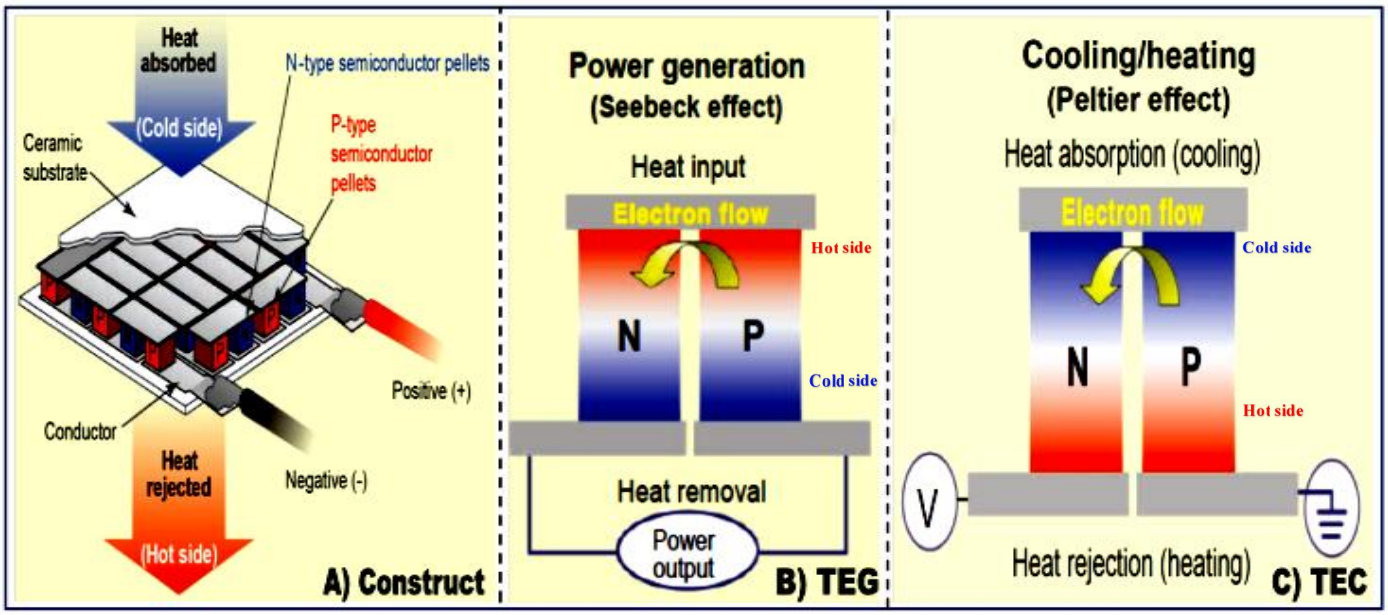

Figure 2.4: Thermoelectric device: Construct, TEG & TEC (adapted from Bell, 2008)

Table 2.4: Reviewed thermoelectricity studies summary (adapted from Bayendang *et al.*, 2020b)

Thermoelectricity Studies Analyzed	Highlights, Advantages and Disadvantages
Analysis A (Bell L.E., 2008)	Thermoelectricity: Construction, TEG & TEC. *Z* is TEG figure of merit. The more *Z* the better.
Analysis B (Gao X., 2014)	TEG can be used as TERs to harvest exhaust heat and boost HT PEM FC efficiency with emphasis on i) heat exchanger surface type, ii) housing dimensions & iii) power conditioning.
Analysis C (Huston J. *et al.*, 2004)	Observed from ~ 40 specific TEG applications that TEG form factor is crucial to enable mounting anywhere. TEG was used with different FCs to boost efficiency by 7 to 10%.
Analysis D (Zhao D. *et al.*, 2016)	Harnessed energy from intermittent heat sources and converted into stored charge via the ionic Soret effect in an ITESC. Max efficiency is very low compared to TEG of same *ZT*, since ITESC power isn't continuous.
Analysis E (Mahmud K.H. *et al.*, 2017)	TEGs connected in series and parallel, generate more voltage and current respectively that also increases with decrease cold side temperature.
Analysis F (Qu Z. *et al.*, 2018)	Developed a thermodynamic model for the TEG and micro-turbine. Showed that TEG almost doubled the hybrid CHP output power.
Analysis G (Katkus T., 2015)	TEG manufacturing involve choosing a TE material / device with good *ZT* (>1), electrodes insulating plate, adhesives and module architecture. A real world system was built to physically characterize various TEG modules.
Analysis H (Sullivan O.A., 2012)	Modeled TEGs and TECs on a chip. TECs are more efficient using more and even better if operated at steady state for frequent hotspot. For infrequent hotspots, TECs maybe cooled with square root transient pulses of very short duration. TEG MPT occurred at greater load resistance. TEG useful power is firstly linear and later parabolic proportional to the heat flux. More TEGs increase output power but decrease later due to overcrowding. Thinner TIM improves TECs and TEGs capabilities.
Analysis I (Teffah K. *et al.*, 2018)	TEC was used as a TEG cooler in simulated and practical setups. The ΔT was directly proportional to the TEC V_{in} and the TEG V_{out}.
Analysis J (Stockholm J., 2016)	Demonstrated that the electrical output from TEGs when pulsed, can doubles the conversion efficiency – an ~8.4% increase was realized.
Analysis K (Kiziroglou M.E. *et al.*, 2016)	Proved that thicker TEGs with good area coverage can be well used to harvest electricity from environment with varying temperatures.
Analysis L (Sulaiman M.S. *et al.,* 2017)	Used TEG with FC in simulated natural (static) and forced convection cooling (dynamic) to convert heat to power. However, very high ΔT is required to generate some significant power.
Analysis M (Hasani M. & Rahbar N., 2015)	Demonstrated the duality of TECs as TEGs in a FC CHP using a THRS. Low ΔTs gave very low V_{outs}. MPT occurred at R_{load} of 1 – 10 Ω.
Analysis N (Park J. *et al.*, 2014)	Employed a low-cost microcontroller and temperature sensor based circuit to track TEG max output power with a 1.15% tracking error.
Analysis O (Yildiz F. *et al.*, 2013)	Compared TEG and Solar energy conversion. A TEG generates more power relative to solar module of the same size but do so more costly.
Analysis P (Apertet Y. *et al.*, 2014)	A TEG output power and efficiency in a thermal environment can be simultaneously maximized if its heat flux is constant (Norton TEG model) but not the case if its temperature difference (Thevenin TEG model) is constant.
Analysis Q (Mamur H. & Çoban Y., 2020)	TEGs have no moving parts, have long service life, operate quietly and are green. TEGs have low efficiency and are expensive. By using the manufacturer datasheets, TEGs were modeled, simulated, experimented and results correlated. Impedance matching with boost converter and P&O MPPT schemes gave 98.64% efficiency.

2.2.5 Power Converters (PCs)

In DC-DC power converters (see varieties in Figure 2.5) and summarized in Table 2.5, the basic switching types are buck, boost and buck-boost as well as Cuk, from which different and or enhanced types are developed to give isolated versions with one or more switches as well as including soft-switching types. Under continuous conduction, beginning with the buck converter, its output voltage is less than its input voltage, calculated as:

$$V_o = D\ V_i \qquad \text{(V)} \qquad (2.10)$$

where V_i and V_o are the power converters input and output voltages respectively and D the duty cycle.

In contrast, the boost converter output voltage is always more than its input voltage and its conversion ratio is:

$$V_o = V_i\ /\ (1-D) \qquad \text{(V)} \qquad (2.11)$$

The $1 - D$ value is relative to the ON position time of the switching device and the boost rate is defined as:

$$V_o = V_i\ (T_s\ /\ T_{off}) \qquad \text{(V)} \qquad (2.12)$$

where Ts is the switching period and T_{off} the off cycle of Ts.

The buck-boost converter depending on the D value, it can either decrease ($D < 0.5$) or increase ($D > 0.5$) the output voltage and the conversion ratio is: $V_o = DV_i\ /\ (1-D)$ (V) (2.13)

The FC stack voltage (V_{FC_Stack}) when loaded is a function of its activation loss (V_{act}), concentration loss (V_{conc}) and Ohmic loss (V_{ohmic}) which is expressed by the Nernst equation as:

$$V_{FC\_Stack} = V_{open} - V_{act} - V_{ohmic} - V_{conc} \qquad \text{(V)} \qquad (2.14)$$

During FC fuel starvation, V_{FC_Stack} normally drops (see Figure 2.3) and the load current and the indicated FC parameters, determine the extent and duration of this volt drop. This problem is addressed variously as summarized in Table 2.2 and together with a DC - DC power converter; one of the quick solutions is by using a super/ultra-capacitor shown in Figure 2.5 and its value (C_{scv}) is computed in terms of the energy that it can provide during the FC fuel starvation period (t_p) using: $C_{scv} = 2\Delta P_o t_p\ /\ \Delta V^2$ (Farads) (2.15)

where P_o is the FC power and load power difference during t_p; and ΔV is the SC output voltage dropped.

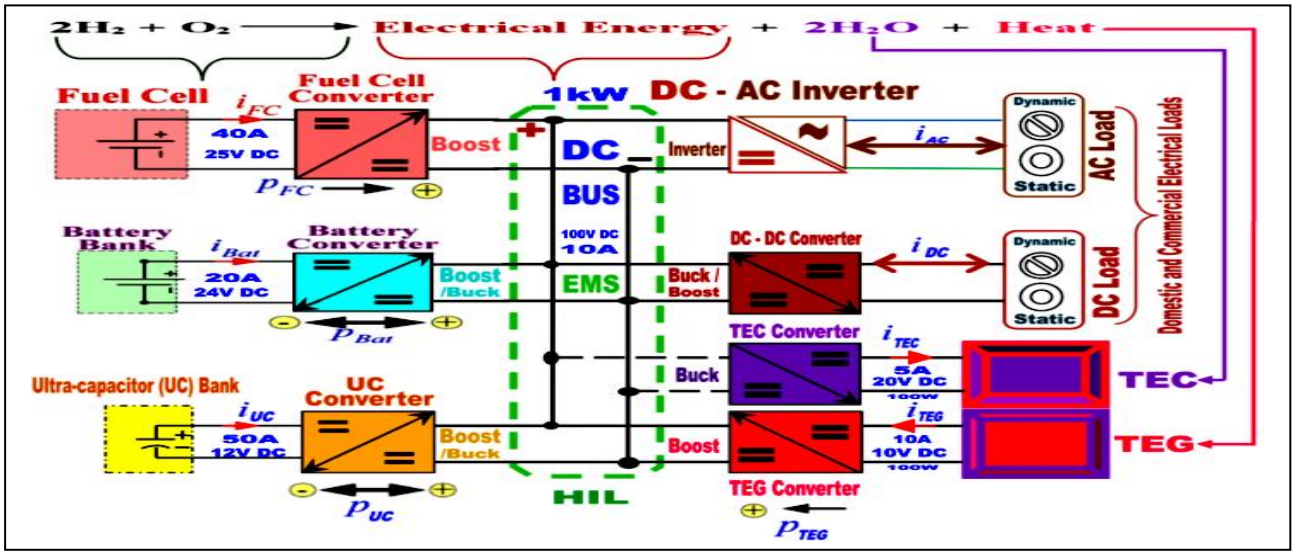

Figure 2.5: Power conversion illustration in proposed CCHP system

Table 2.5: Examined power converters studies summary (adapted from Bayendang *et al.*, 2020a)

Power Converters Research Analyzed	Highlights, Advantages and Disadvantages
Analysis A (Kolli A. *et al.*, 2015a)	DC-DC power converters architectures for FCs applications: Focused on IBC, FIC, HIC, RIC and ZSI power supplies for low, mid and high power uses. FC in series and parallel gives more power.
Analysis B (Kabalo M. *et al.*, 2010)	State-of-the-art of DC-DC converters for FC vehicles: Converters should be implemented with high voltage ratio, efficiency & compact-ness with low-cost. Various schemes depicted.
Analysis C (Delshad M. & Farzanehfard H., 2011)	A new soft switched push-pull current fed converter for FC applications: Proposed a ZVS current fed push-pull DC–DC converter. Used simple PWM control. Efficient and compact.
Analysis D (Bizon N., 2011)	A new topology of FC hybrid power source for efficient operation & high reliability: FC ripple current was reduced by the HPS with active MPPT as well as hysteretic current controls.
Analysis E (Ahmed O.A. & Bleijs J.A.M., 2013)	A comparative study of power flow control methods for an UC bidirectional converter (BDC) in DC micro-grids: CPC modulation was applied to derive alternative techniques to improve the BDC performance and efficiency.
Analysis F (Carvalho A. *et al.*, 2011)	Matlab/Simulink were used to model a power converter and PEM FC. Simulated annealing (SA) optimization algorithm was used to model accurate PEMFC static and dynamic behaviours with a series resonant converter to curb ripples.
Analysis G (Mwaniki F.M., 2014)	High voltage boost multiphase tapped-coupled inductor DC-DC converter for variable voltage sources (FCs & TEGs) & high power PV uses.
Analysis H (Huangfu Y. *et al.*, 2015)	High power efficiency buck converter design for standalone wind power supply system, akin PV & TEGs. Used buck LCD or ZVS topology with MPPT to attain 2kW with 96% efficiency.
Analysis I (Seyezhai R. *et al.*, 2013)	High gain IBC with switched capacitors for FC was modeled with Matlab /Simulink. Reduced electromagnetic emissions & ripple currents in input/output circuits, faster transient response, improved reliability & efficiency was attained.
Analysis J (Nymand M. & Andersen M.A.E., 2008)	A new approach to high efficiency in isolated boost converters for high-power low-voltage FC applications. The worst case efficiency at min input voltage with max power was 96.8% and the maximum efficiency was up to 98%.
Analysis K (Eckardt B *et al*, 2005)	High power buck-boost DC-DC converter for FC automotive power-train application with digital control to provide full protection against overvoltage, over-current & over-temperature.
Analysis L (Kirubakaran A. *et al.,* 2009)	PEMFC system with DC-DC boost converter: design, modeling and simulation. For load variation from 600 to 1100W instantaneously, the FC voltage & current took about 50 - 70ms to reach a new steady state – fuel starvation. PI controller was used to track the varying voltage
Analysis M (Outeiro M.T. & Carvalho A., 2013)	Methodology to design power converters for FC based systems: a resonant approach. Autonomous voltage and PEMFC controllers. Improves FC efficiency by controlling FC P_{out}.
Analysis N (Wang H., 2019)	Design and control of a 6-phase IBC based on SiC semiconductors with EIS functionality for FC HEV. HIL real-time IBC dynamic model.
Analysis O (Fanjul L.M.P., 2006)	Design considerations for DC-DC converters in FC systems. Attained analytically & verified experimentally to enable an efficient and stable FC & power converter system. A modular FC stack & DC-DC converter were introduced by partitioning into autonomous optimal sections.
Analysis P (Motapon S.N. *et al.*, 2014)	Developed a simulation model & experimental test bench for comparative analysis of different EMS schemes for a FC hybrid power system.
Analysis Q (Sulaiman N. *et al.*, 2015)	Extensive review on fuel cell fuel starvation and energy management system for FC hybrid electric vehicles: In-depth issues & challenges.

2.2.6 CCHP System, FC, TE, PCs, Battery, UC and EMS Modeling and Operation

The modeling of a complete CCHP system involves various sections and aspects which are beyond the scope of this literature review study. However, some fundamental modeling and results of a PEM FC, TE and PCs sections as well as a storage battery, an UC (or SC) and EMS are presented to substantiate the analysis. Figure 2.6 depicts a partial Matlab / Simulink model of the postulated CCHP system under research (shown in Figure 2.5) with focus on the FC, battery and UC power dynamics. The results are illustrated in Figure 2.7 in which initially at power-on, the FC switches on gradually while the battery and UC are charging. Once current is instantaneously drawn, the UC having the fastest power dynamics, will quickly supply power till its energy is exhausted and it is then aided by the battery until the FC power gradually rises and reaches steady state to sustain the power demands till the load is switched-off. Thereafter, the FC power level returns to normal and the battery and UC return to charging mode as controlled by the proportional−integral−derivative (PID) EMS.

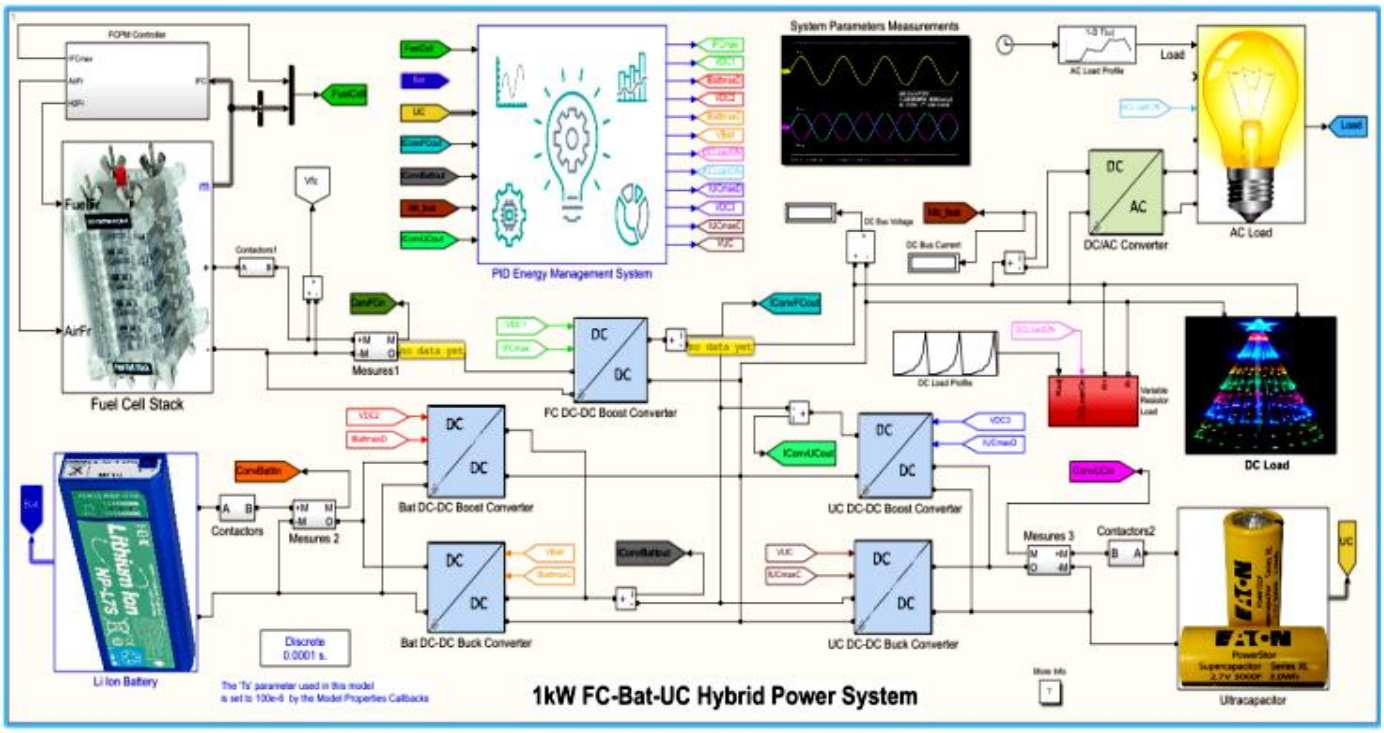

Figure 2.6: FC, battery and ultra-capacitor hybrid power system model

Depicted in Figures 2.8 and 2.9, are respectively a Matlab / Simulink TEG model and its simulated result. Once there's heat flux on the TEG hot-side resulting to temperature difference across it, DC power is generated and can be sustained with MPPT at varying electrical loads. TEGs when combined with FCs, can convert the waste heat produced (in the FC electrochemical reactions) to power, hence also aiding the FC in power and or energy dynamics. Figures 2.10 and 2.11 exemplify a Matlab / Simulink TEC model that can generates cold when DC power is applied to it. All these power and energy sources together with heat exchangers (not discussed herein) as well as an EMS controller; present a clean, efficient and innovative renewable energy FC-TE CCHP system.

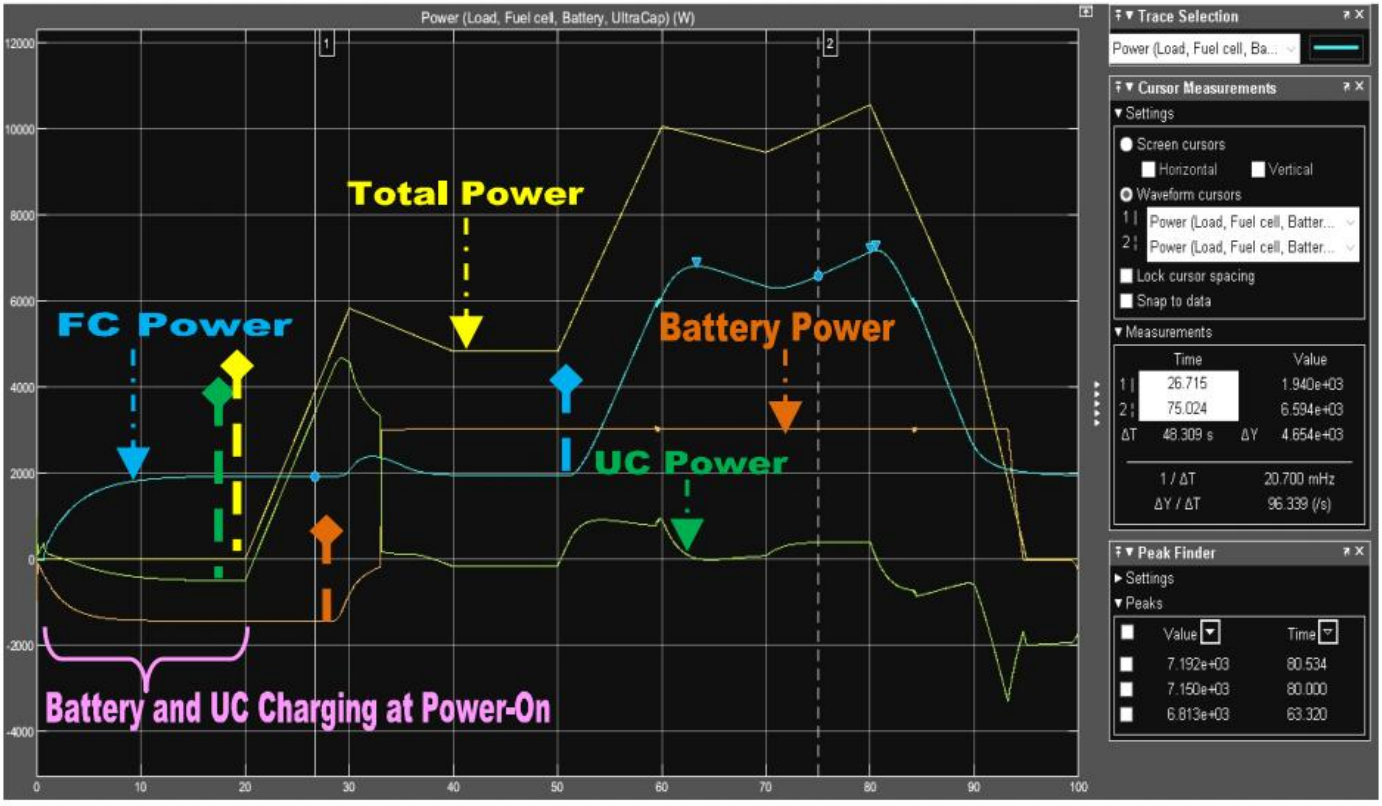

Figure 2.7: Fuel cell, battery and ultra-capacitor power-energy dynamics analysis

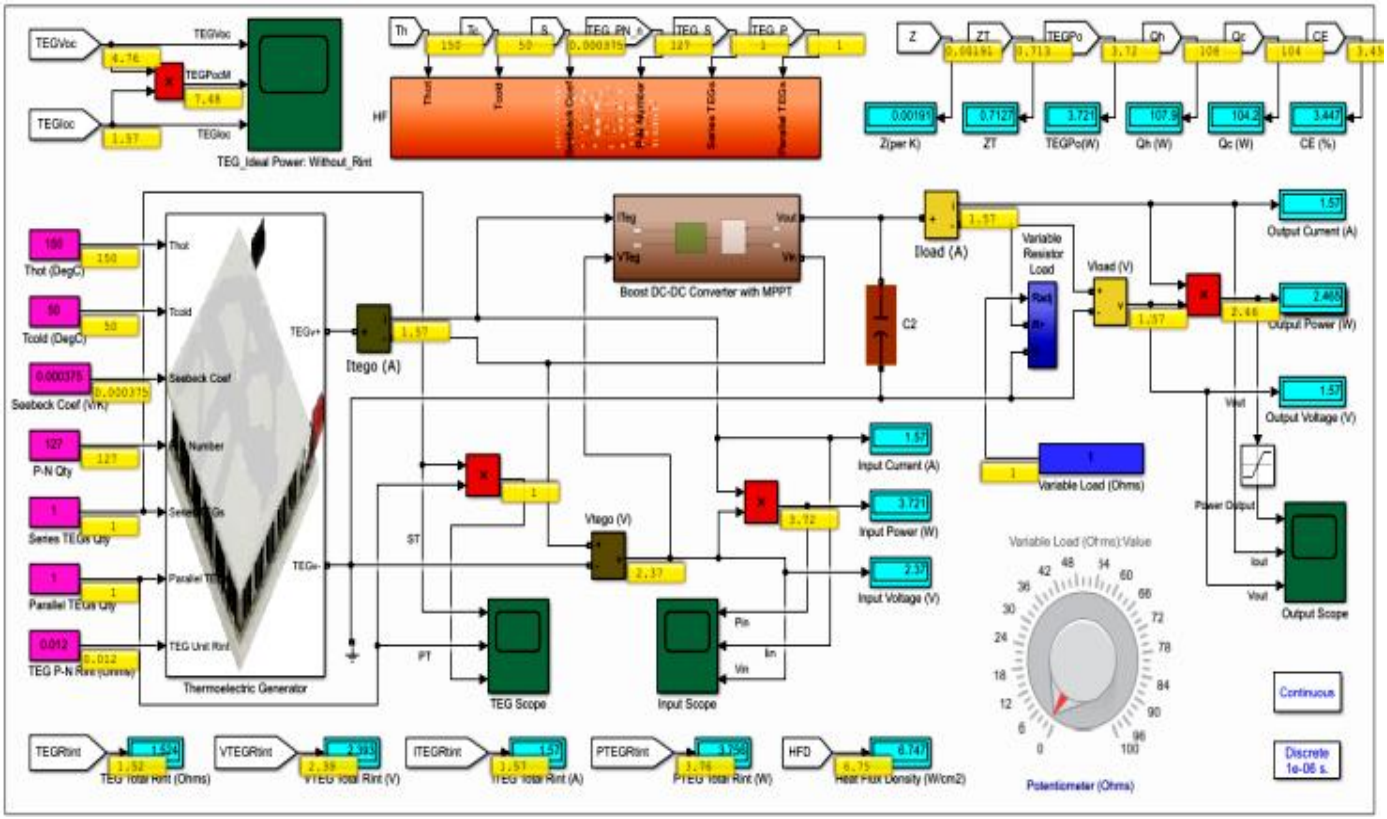

Figure 2.8: TEG and power converter modeling with a variable DC load

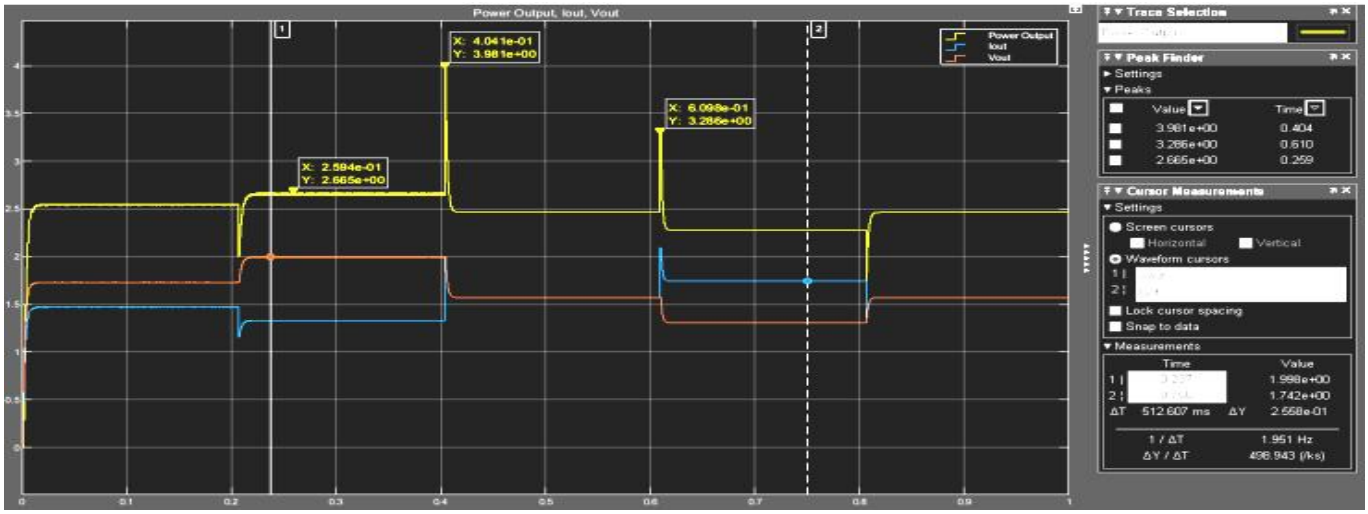

Figure 2.9: TEG & power converter modeling results with varying DC loads

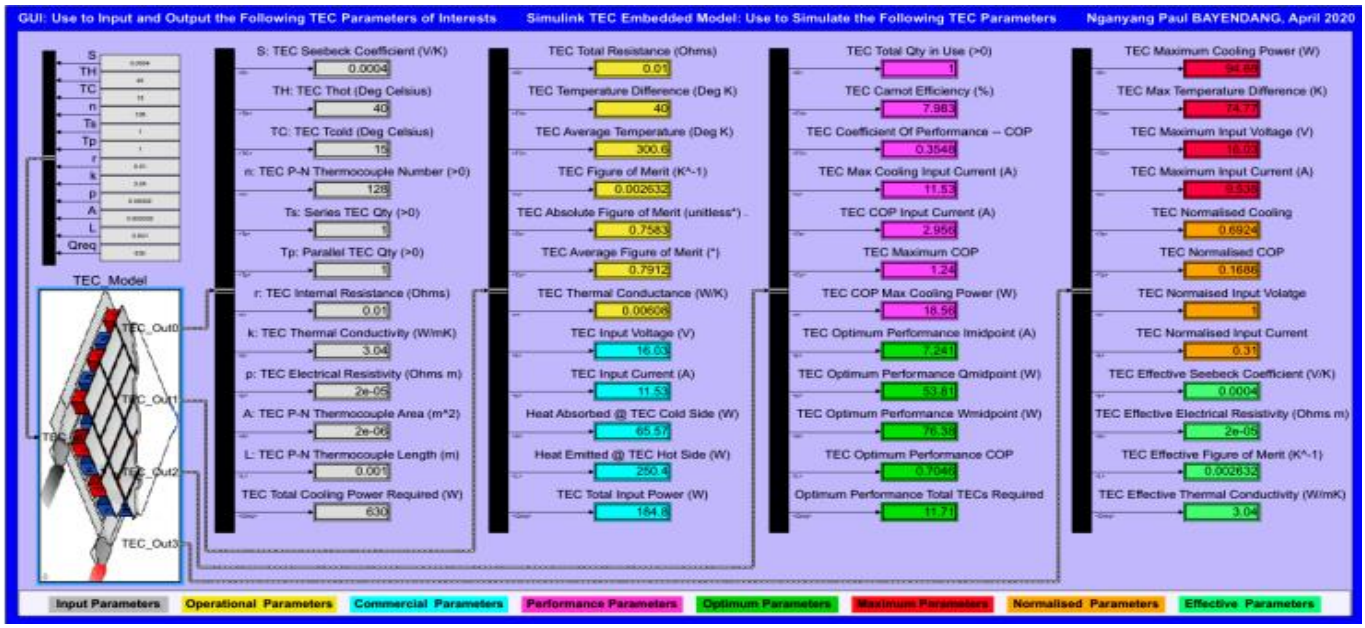

Figure 2.10: TEC various parameters comprehensive modeling

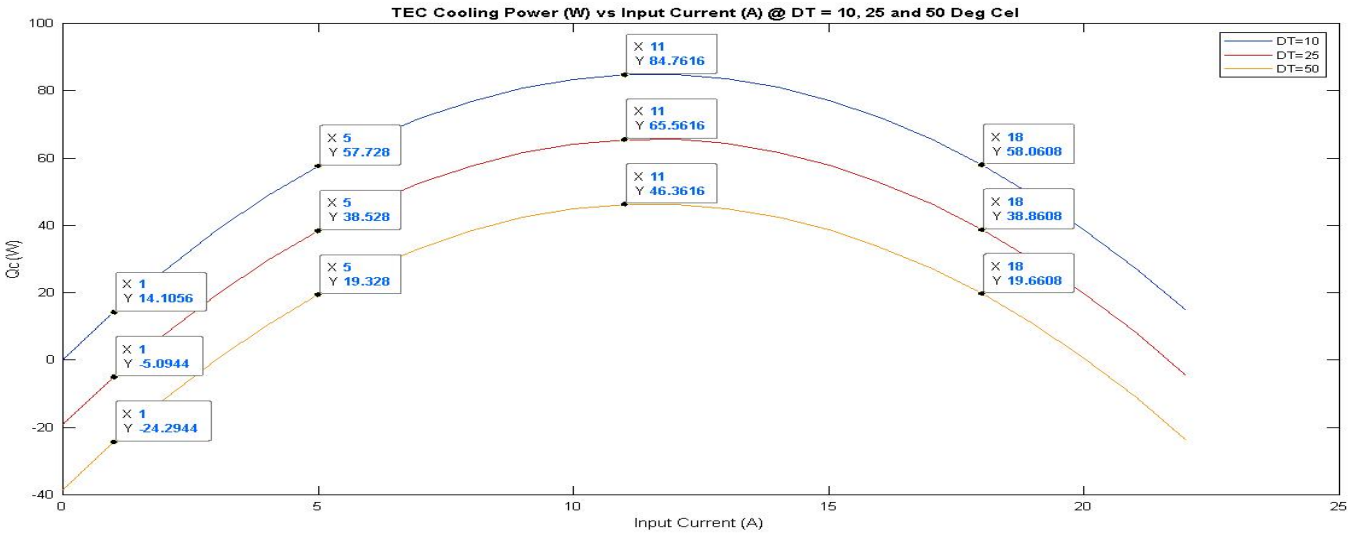

Figure 2.11: TEC cooling power (Q_c) and input current (I) @ various ΔTs

2.2.7 Summary

From the above analyses, some of the best practices (highlights, pros and cons) that can be applied when considering CCHP systems, fuel cells, thermoelectricity and power converters, are summarised as follows:

2.2.7.1 CCHP Systems

- Generates cold, heat and power simultaneously.
- Depending on type, can use different fuels, prime movers and energy / power conversion mechanisms.
- ICE is traditionally noisy, toxic and needs high maintenance; though it has evolved and relatively has now high efficiency, low-cost and quick start-up time.
- Stirling engine are fairly efficient and green. Mostly suited for stationary or constant running applications.
- Micro-turbines are also comparatively popular and applicable in various hybrid energy applications.
- Fuel cells are becoming very popular and are the future especially in transportation (HEV).

2.2.7.2 Fuel Cells

- Popularly five types (PEMFC, AFC, PAFC, MCFC and SOFC) excluding Direct Methanol (DM) FC – which practically is still a PEMFC, except that it uses methanol directly as fuel but its electrolyte is PEM.
- Generates clean power continuously (as long there are fuel / reactant gases) with heat and water as clean by-products − both of which can be transformed / recycled as per the renewable energy system design.
- FCs are generally environmentally friendly and requires very minimal operational maintenance.
- FCs, especially high temperature types, have very poor power dynamics responses and are therefore susceptible to FC fuel starvation phenomenon – a fall in the FC voltage due to hindrance or inadequate flow of gases (H_2 and O_2), during transient load (high current) conditions.
- This FC fuel starvation problem is popularly addressed with a hybrid cascaded battery, super/ultra-capacitor FC augmentation and suitable power converters with power tracking and energy management algorithm – usually MPPT, PI controller and fuzzy logic schemes.
- FCs can be stacked in series to increase voltage and in parallel to increase current. However, the reliability and performance could be better but expensive and complex, if a good modular approach is employed – whereby each FC unit before stacking, could have its own autonomous power converter at module level.
- The PEM FC is the most popular and widely used because of its simpler and non-hazardous chemistry.

- The LT PEM FC is gaining traction, however its low temperature makes it to require expensive Platinum catalyst, as well as considerable management of the water by-product. In addition, it may not be suitable for CCHP system with TEG, due to the low reaction temperatures (very low grade waste heat) involved.
- The HT PEM FC using the PBI membrane, suits CCHP application; as its maximum temperature range falls in line with TEG temperature (>99°C) needed for fair power generation and less water management is needed.

2.2.7.3 Thermoelectricity

- Generates power, cold and heat depending on the use − if used as TEG and or TEC.
- TEGs generate electricity based-on Seebeck effect.
- TEG max efficiency is determined by its figure of merit (Z) or by $ZT \geq 1$, ΔT and by the heat absorbed at T_h.
- Large and constant temperature difference ($\Delta T \geq 100°C$) is needed to generate appreciable DC power. However, high and constant heat flux also plays a vital role. In other words, two TEGs may have the same $\Delta T = 100°C$, but the TEG with a higher hot side temperature (T_h) and with lesser thermal resistance, will be far more better to generate and deliver efficient maximum power to the electrical load.
- TEGs can be connected in series and or in parallel to respectively boost the generated voltage and current. However, maximum power can be delivered to the load when the TEG and load resistances are matched. This is however hardly the case in practice, thus, this mismatch warrants power converters with tracking techniques.
- TEG and TEC exhibit duality – TEC device can be used as TEG at preferably temperatures less than 200 ℃.
- TECs generate cold and or heat based-on the Peltier effect.
- Depending on the applied voltage polarity, the generated cold / heat is directly proportional to the TEC input current within certain maximum operational limits and inversely proportional to its temperature difference ΔT.
- Thomson effect synergizes and enhances the Seebeck and Peltier effects. It is practically trivial. Thomson effect is different from Joule or Ohmic heating – the former is reversible while the latter is irreversible.

2.2.7.4 Power Converters

- DC-DC power converters are needed to regulate, increase and or decrease DC voltages from the FC and TEG to and fro the DC bus, from which the DC power can also be converted to AC depending on the system design.
- There are various types of topologies such as the buck, boost, buck-boost, resonant but most often interleave boost converter are employed, though the type chosen vary according to an application or system resources.
- To maintain reliable operations, the DC-DC power converters are normally complemented with energy management system techniques, to ensure efficient and peak power delivery and control to the electrical load.

2.3 Power Converters and EMS for Fuel Cells CCHP Applications: A Structural and Extended Review

Fuel Cells (FCs) and Combined Cooling, Heating and Power (CCHP) systems are becoming very popular due to their environmental friendliness and immense applications. This extended review commenced by introducing the rampant South Africa's electricity crisis as the basis for the study, followed by some structural analyses of up to forty four miscellaneous power electronics converters case studies applicable to fuel cells including at least sixteen FCs energy management systems (EMS) applicable case studies. The review rationale is to determine innovative best practices that can be applied to devise an efficient power converter and EMS for an energy efficient FC CCHP system. From these analyses, it is realized that each power converter and EMS scheme has its merits and demerits depending on the targeted applications and most importantly the research project objectives − that is, whether the goals are to reduce costs, enhance efficiency, reduce size, boost performance, simplicity, durability, reliability, safety etc. Therefore, the conclusion drawn is, there is no "one size fits all" approach, as all the various reviewed case studies reported relatively good results based on their chosen schemes for their targeted applications. Notwithstanding, this review highlights are, i) the interleaved boost converter and variants as well as ii) the maximum power point tracking (MPPT) technique; are the most widely used schemes, as they are reasonably effective and simple to implement. The contributions brought forward are i) an apt single reference study that presents a quick and concise topological insight and synopsis of assorted FCs power converters as well as EMS and ii) my proffered FC CCHP system with the chosen power converters and EMS undergoing research to offer an innovative energy efficient solution for basic commercial and household energy needs such as DC electricity, heating, cooling and lighting. This study is introduced next, followed by various powers converters and EMS studies reviewed and finally the main points are summarised.

2.3.1 Introduction

Compounded with re-occurring electrical energy and power problems in South Africa and at large Africa (Bessarabov *et al.*, 2017; Eberhard *et al*., 2017; NPC, 2018); this extended study to Bayendang *et al*. (2020a), extensively investigates with emphasis on fuel cells (FCs), some assorted research on power converters and energy management systems / storage (EMSs) techniques. Currently, there's up to 2 hours of daily electricity rolling blackouts in South Africa (RSA), due to RSA national energy utility company (ESKOM) inability to generate and supply enough energy to meet its local electricity demands. This sporadic power cut is due to the legacy apartheid energy system being over-stretched with more underprivileged areas / users now having access to electricity, old energy infrastructures being upgraded, poorly designed and inefficient new energy infrastructures, poor technical maintenance, inadequate technical abilities, periodic technical breakdowns, electricity theft / tampering, maladministration as well as corrupt and illicit business deals and political reasons.

Thus, various optional renewable energy sources, especially solar and wind powers are being commissioned to augment and or stabilize the South African national grid supply and also for personal use. Alternative energy sources such as i) FCs − which produce power and heat as well as water when fueled with H_2 and O_2 and ii) thermoelectricity − which simply generates a) electricity based-on the Seebeck effect and b) heat / cold based-on the Peltier effect, are of interests. In this regard, my research focuses on FCs and thermoelectricity; however, these clean energy sources need supporting technologies and techniques to operate well. In light of this, i review applicable best practices that can be developed to execute an energy efficient fuel cell alternative power / energy system for domestic and commercial combined cooling, heating and power (CCHP) applications − since electricity, heat / cold and light are the most commonly used forms of energy in most households and businesses in RSA. Fuel cells CCHP systems are versatile, clean and are becoming very fashionable; hence, discussed next are miscellaneous power converters and EMS research applicable to FCs and by extension to FC CCHP systems.

Typically, a fuel cell stack closed-circuit voltage is a function of the FC activation, concentration and Ohmic losses governed by the Nernst equation. This FC loaded condition draws more current resulting to a voltage dip / drop, as a result of sluggish Hydrogen / Oxygen flow to sustain it and this phenomenon is called the fuel cell fuel starvation. This voltage drop and the load current together with other FC parameters, establish the degree and duration of the problem. This issue is tackled diversely as analyzed / asserted briefly in Bayendang *et al*. (2020a).

As reviewed and summarised in Table 2.6, DC-DC power converters are paramount to either boost and or reduce DC power sources (e.g FCs) levels and then regulate a consistent power flow thereafter. FCs typically produce low DC voltage but high DC current, which combined with the possibility to fluctuate when connected to a load, especially if big, demands power regulations to the DC bus and ultimately to the different DC and or AC loads.

In DC-DC power converters, with the exception of linear regulators, the fundamental three switching kinds are the step-down, step-up and step-up / step-down − from which various and or improved versions are derived to give isolated derivatives having one or multiple switches and including the advanced soft-switching versions.

In continuous conduction mode, the voltage output from step-down DC-DC power converters, is always lesser than its voltage input. Contrarily, the voltage output from a step-up DC-DC converter is always more than its voltage input. The step-down / step-up power converter based-on its duty cycle value; can respectively either decrease (if the duty cycle is < 0.5) or increase (if the duty cycle is > 0.5) the power converter voltage output.

As examined and summarised in Table 2.7, EMSs are essential to control the power converters to ensure i) maximum power is transferred to the load(s), the ii) bus is stable and iii) energy /power supply system is efficient.

2.3.2 Power Converters (PCs)

Power converters are simply needed to buck, boost and provide the required, regulated and reliable voltage to the DC bus and subsequently to the DC and or AC loads. In what follows and summarized in Table 2.6, are miscellaneous case studies that structurally analyzed in brief details, some power converters for use with FCs.

2.3.2.1 DC-DC Power Converters Architectures for Fuel Cells Applications

Presented in Kolli *et al.* (2015a), power sources based on fuel cells are now trendy devices. They offer reliability, flexibility as well as efficiency through multi-stack topologies. To access the market requires simplifying further the FCs design and its supporting components, which among others include the power converters which ensure the output voltage is regulated. Their research thus focused on DC-DC power converters by giving an inclusive outline on the interfaces of PCs for use in aircraft, railways, automotive and small static areas such as households.

The significance of selecting the correct power converters topology and the related technology is crucial, as its facets allow thermal compatibility with various methods for integrating the DC-DC power converters to the fuel cells. These topological and technological features that have been examined and displayed in Figures 2.12a − 2.12f with highlights in Figures 2.12e − 2.12f, are some popular PCs topologies. In their study, they indicated how connecting a fuel cell stack to DC-DC power converters in parallel and or in series, increase the current and or voltage outputs respectively.

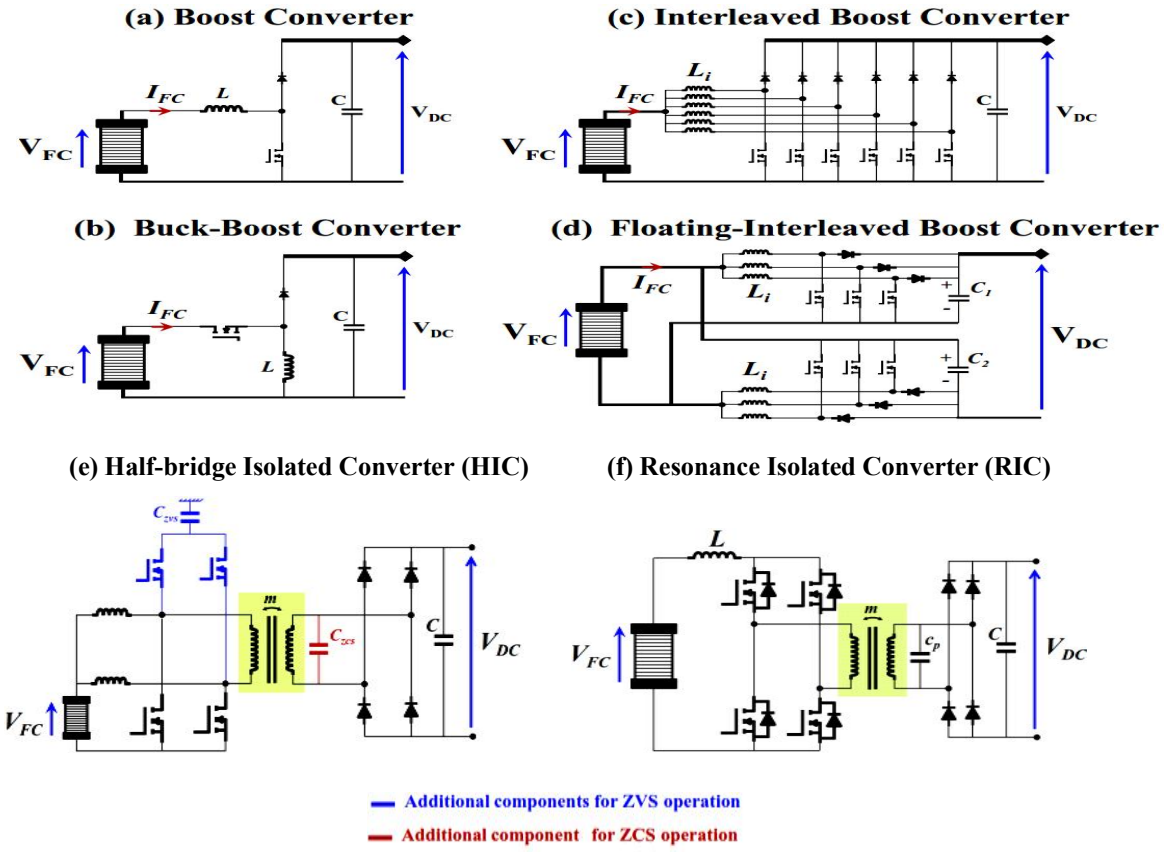

Figure 2.12: DC-DC power converters architectures for fuel cells applications (adapted from Kolli *et al.*, 2015a)

Explained in their research and portrayed in Figures 2.12c and 2.12d, are non-isolated multi-phase boost converters, which are mainly appropriate for applications that require low DC bus voltage. The interleaved topologies shown, meet the prerequisite for curbing low FC ripple currents. The depicted standard interleaved boost converter (IBC) shown in Figure 2.12c and the floating interleaved converter (FIC) depicted in Figure 2.12d, show similar merits. Z-sources inverters (ZSI) were also articulated, in which their features and merits make them suitable choices for 3-phase electric drives − for instance automotive and railway applications. Furthermore, the study indicated that the isolated converters based-on high frequency planar transformer (which according to Kolli *et al.*, 2015b), only one quantity was left in the market in 2014), is beneficial in high DC link voltage applications such as railway. Contrarily, the isolated converters give a low efficiency for medium power applications. However, the soft-switching function enables the enhancement of the converter efficiency but at the cost of using supplementary components in the converter configurations. These improvements are shown in Figures 2.12e and 2.12f − whereby the half-bridge isolated converter (HIC) and the current-fed full-bridge resonant isolated converter (RIC), respectively illustrate the zero voltage switching (ZVS) and zero current switching (ZCS) operations, in which both increase the efficiency by reducing the devices switching losses. The technological review on the other hand focused on the new wideband-gap semiconductor materials and the utilization of Silicon Carbide (SiC) and Gallium Nitride (GaN) devices with low on-resistance, high power densities and high speed switching with less losses, which could transcend to major improvements in the power converters performance. Nowadays, GaN devices are suited for low/mid power applications, whereas SiC technology is more desirable for designing high power fuel cells DC-DC converters.

2.3.2.2 State-of-the-Art Fuel Cells DC-DC Converters

According to Kabalo *et al.* (2010), fuel cells are current intensive sources that have become popular. The study presented various suitable topologies of DC-DC power converters for FCs output voltage conditioning. The goal of the main DC-DC power converter between the FC and DC bus was emphasized, which demands the power converter be designed and operated using high efficiency, high voltage ratio and high density with low-cost. As a result, their paper highlighted some pointers in this regard, as well as some positives and negatives. Some of the excerpted schemes are shown in Figures 2.13a - 2.13c.

2.3.2.3 A Soft Switched Push-pull Current-fed Converter for FC Applications

Examined in Delshad and Farzanehfard (2011), a zero-voltage switching (ZVS) current-fed push pull DC–DC converter is suggested for fuel cells power generation system as pictured in Figure 2.14. In the study, the auxiliary circuit in this converter supplies ZVS condition for all converter switches which reduces switching losses and further absorbs at turnoff instances, the voltage surge across the switches.

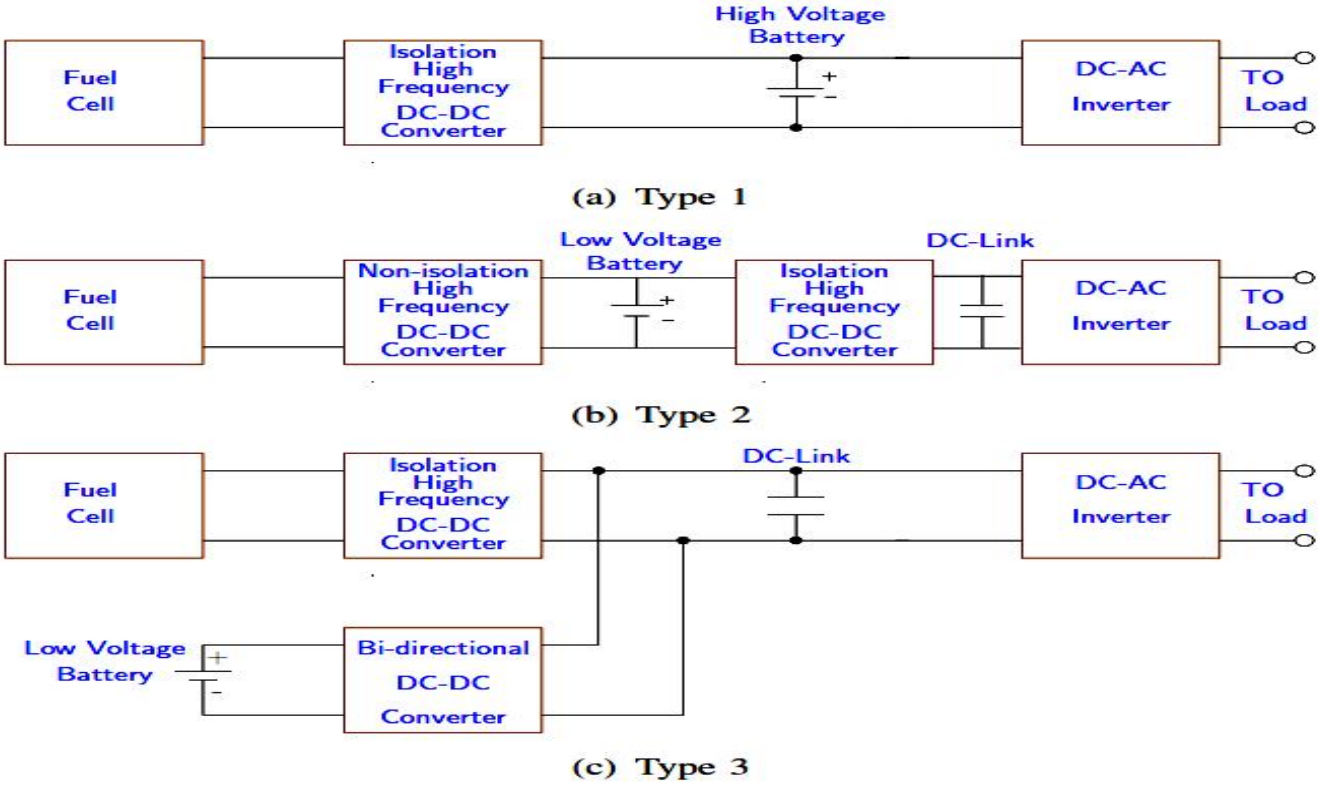

Figure 2.13: Fuel cells DC-DC power converters (adapted from Kabalo *et al.*, 2010)

This merit enhances the converter efficiency and reduces its size and weight – which henceforth enables the implementation of a very simple control circuit based on pulse width modulation (PWM). This setup was then used to analyse and validate the operation of the converter using a lab prototype. The projected DC-DC power converter experimental results, the various operating modes as well as their corresponding timing waveforms, are presented in detailed in their published paper.

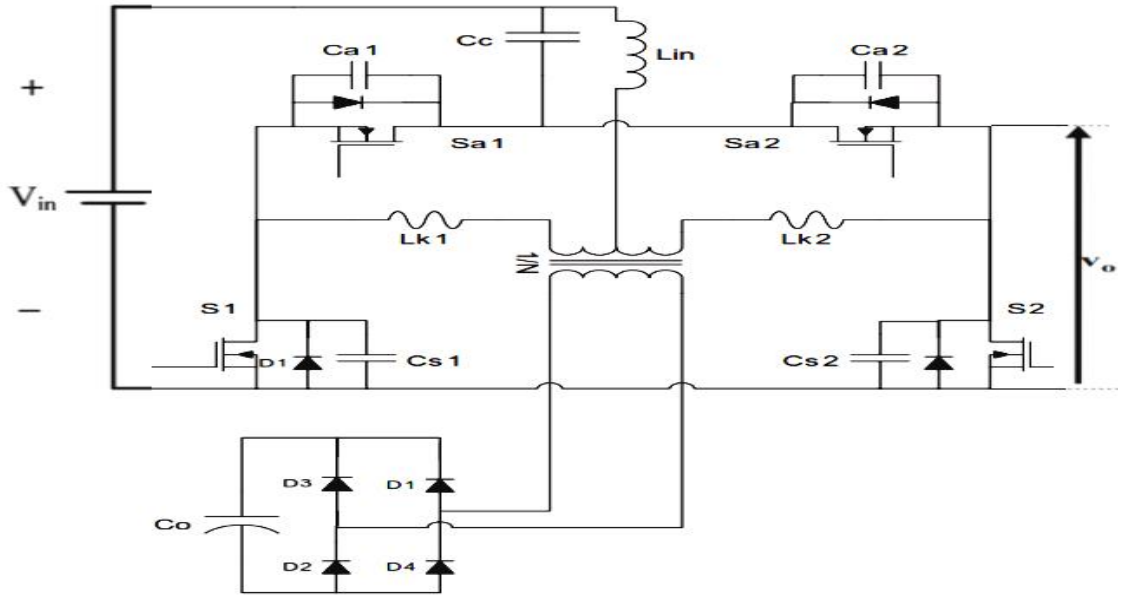

Figure 2.14: Soft switched push-pull current-fed converter (adapted from Delshad & Farzanehfard, 2011)

2.3.2.4 Topology of FC Hybrid Power Source for Efficient Operation and High Reliability

Proposed in Bizon (2011), is a fuel cell hybrid power source (HPS) topology with the attribute to curb the ripple current of the FC inverter system. The ripple current usually occurs at the DC port of the FC HPS when operating the inverter system − which is connected to the grid or which supplies AC motors in vehicular applications. As a result, if the alleviation measures are not implemented, this ripple current is propagated back to the FC stack. The suggested FC HPS has other good performance features; such as the maximum power point tracking (MPPT), high steadfastness in operation during transient power pulses and finally improved energy efficiency in peak power applications.

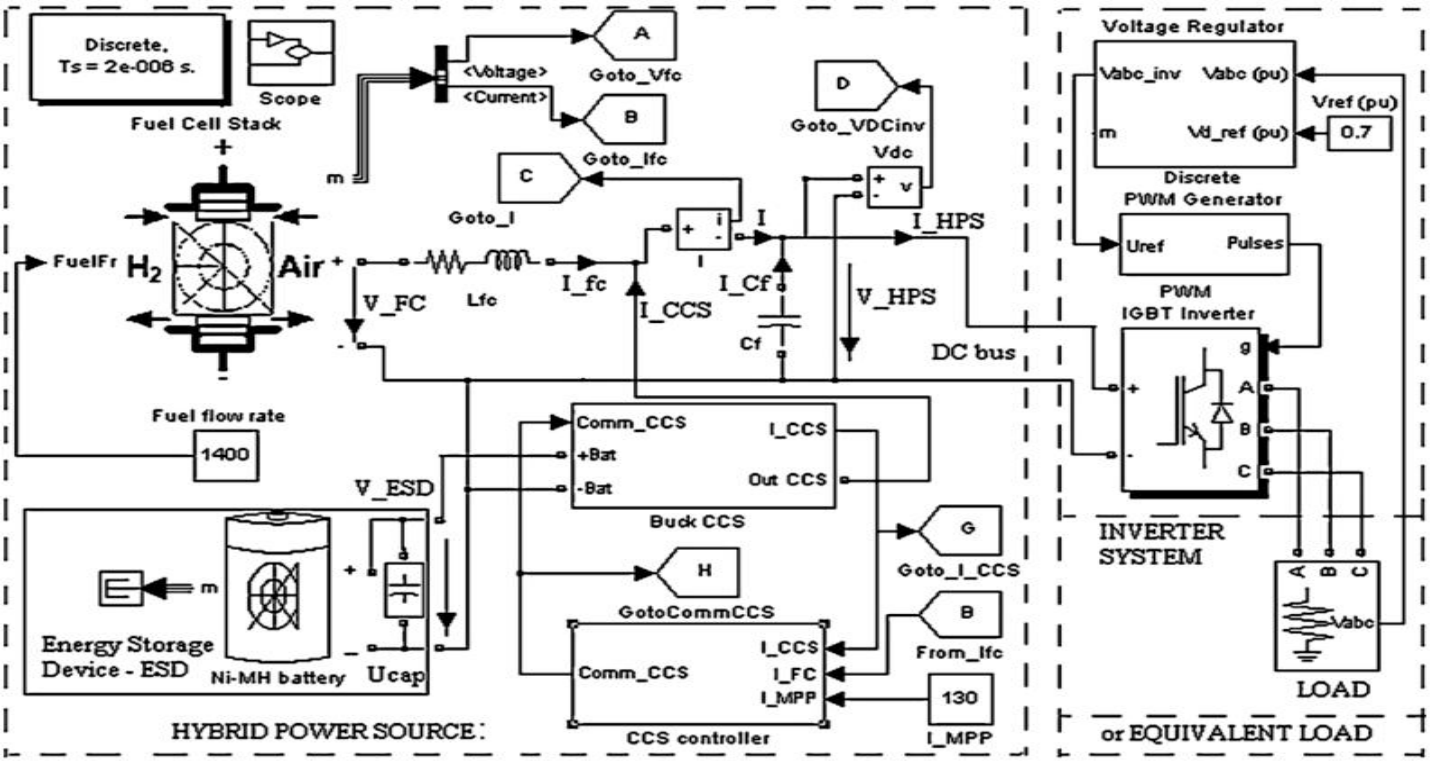

Figure 2.15: Hybrid power source topology (adapted from Bizon, 2011)

To mitigate the ripple, this approach made use of an inverter system powered directly from the FC stack with a controlled buck current source that was used as the low power source. The low frequency (LF) ripple reduction is rooted in active control, whereby the anti-ripple current is injected in HPS output node and this has the LF power spectrum similar to the inverter ripple. In light of this, the fuel cell ripple current was curbed by the designed active control. Indicators defined to evaluate the mitigation ratio of the LF harmonics were used to assess the ripple current alleviation performances. The relatively good performances shown were attained with the use of a hysteresis current control, but better if a devoted nonlinear controller is used, which can be designed in two ways as follows i) simulation trials that assist to draw the attributes of ripple mitigation ratio verse fuel cell ripple current and ii) fuzzy logic controller (FLC). The ripple factor was ~ 1% in both cases. Figure 2.15 depicts it.

2.3.2.5 Power Flow Control Methods for Ultra-capacitor Bidirectional Converter in DC Micro-grid

Postulated in Ahmed and Bleijs (2013), distributed generation (DG) in the form of DC micro-grids depicted in Figure 2.16, has recently attracted increasing research interests. A bidirectional DC-DC converter (BDC) shown in Figure 2.17, is required to incorporate renewable energy resources and energy storage devices such as an ultra-capacitor (UC) to the DC bus of a DC micro-grid to sustain the charging and discharging states of the ultra-capacitor. For the quick dynamic response of the ultra-capacitor, a bidirectional voltage-fed setup is suitable, though for a broad input voltage fluctuation of the ultra-capacitor, this setup manifests a greater circulating power flow and greater conduction losses in the end. Presented in this study are a comprehensive overview on the numerous modulation schemes that are employed to manage the power flow of the bidirectional voltage-fed DC-DC converter for the ultra-capacitor applications. An in-depth analysis of the bidirectional converter investigating the impact of the circulating power flow interval was developed and analytical methods such as the conventional phase-shift control (CPC) modulation were applied to develop alternative modulation schemes to advance the efficiency and performance of the bidirectional power converter.

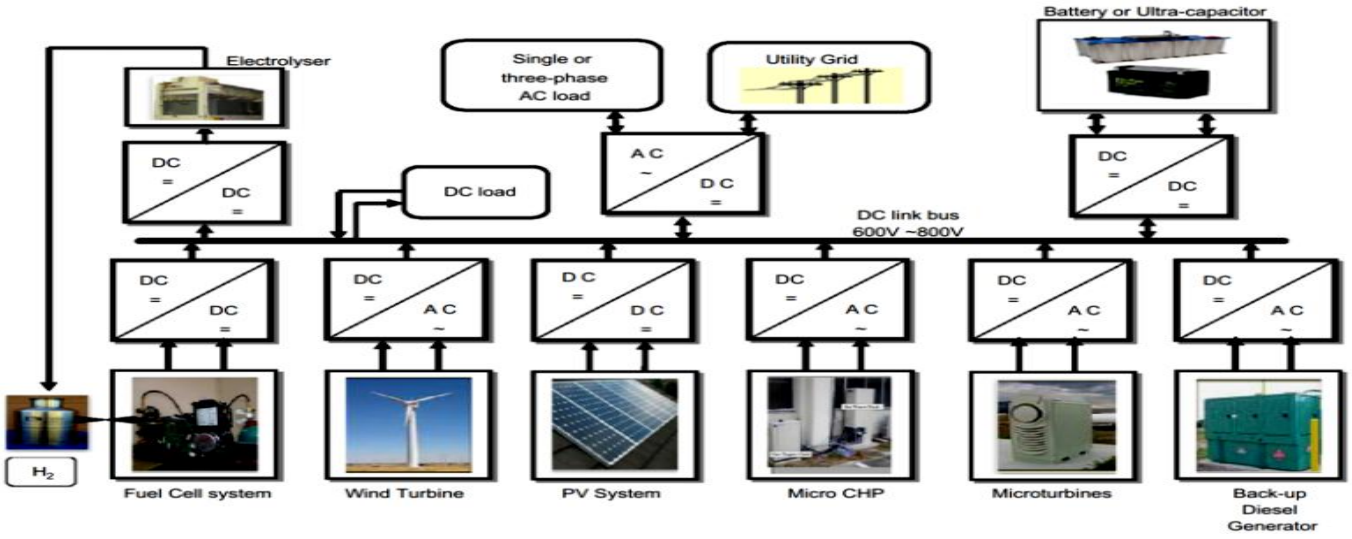

Figure 2.16: DC Micro-grid distributed generation (adapted from Ahmed & Bleijs, 2013)

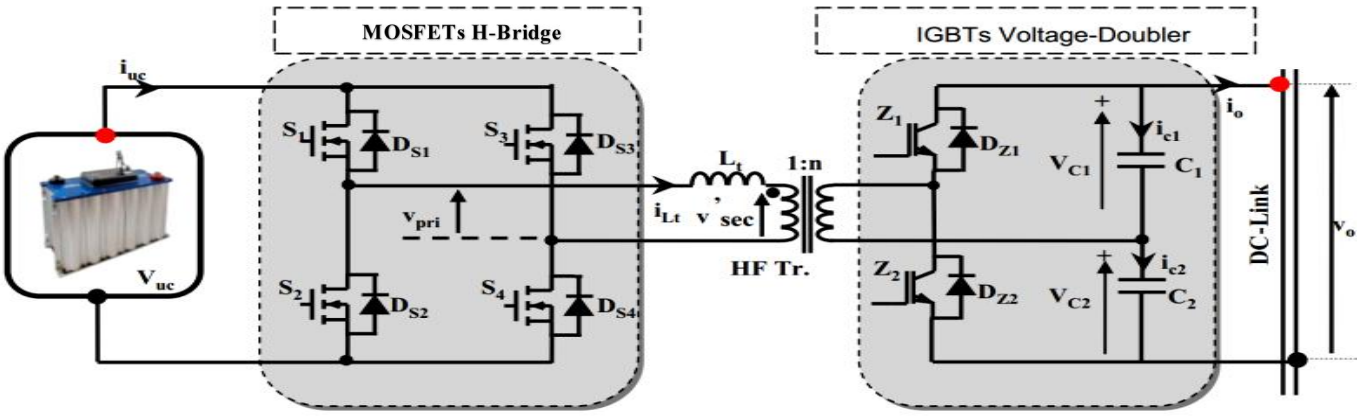

Figure 2.17: BDC power flow control methods for ultra-capacitor in DC micro-grid (adapted from Ahmed & Bleijs, 2013)

2.3.2.6 Fuel Cell and Power Converter Models in Matlab / Simulink

Studied in Carvalho *et al.* (2011), Matlab and Simulink were employed to model a power converter and PEM FC. Depicted in Figure 2.18, the first section of the research discussed the methodology for an accurate model for the fuel cell stack, as well as its static and dynamic behaviors − which form a crucial aspect in the design of electrical power generation founded on fuel cells. The technique applied was simulated annealing (SA) optimization algorithm, which justifies its customization to meet the goal of a speedy convergence to institute the correct values for the fuel cell parameters. The correlation between the simulated and experimented results proved that the suggested model provided an accurate depiction of the static and dynamic behaviors for the PEM FC. The second section of the study engaged on feasible architectures that can be tailored for the DC-DC power converter.

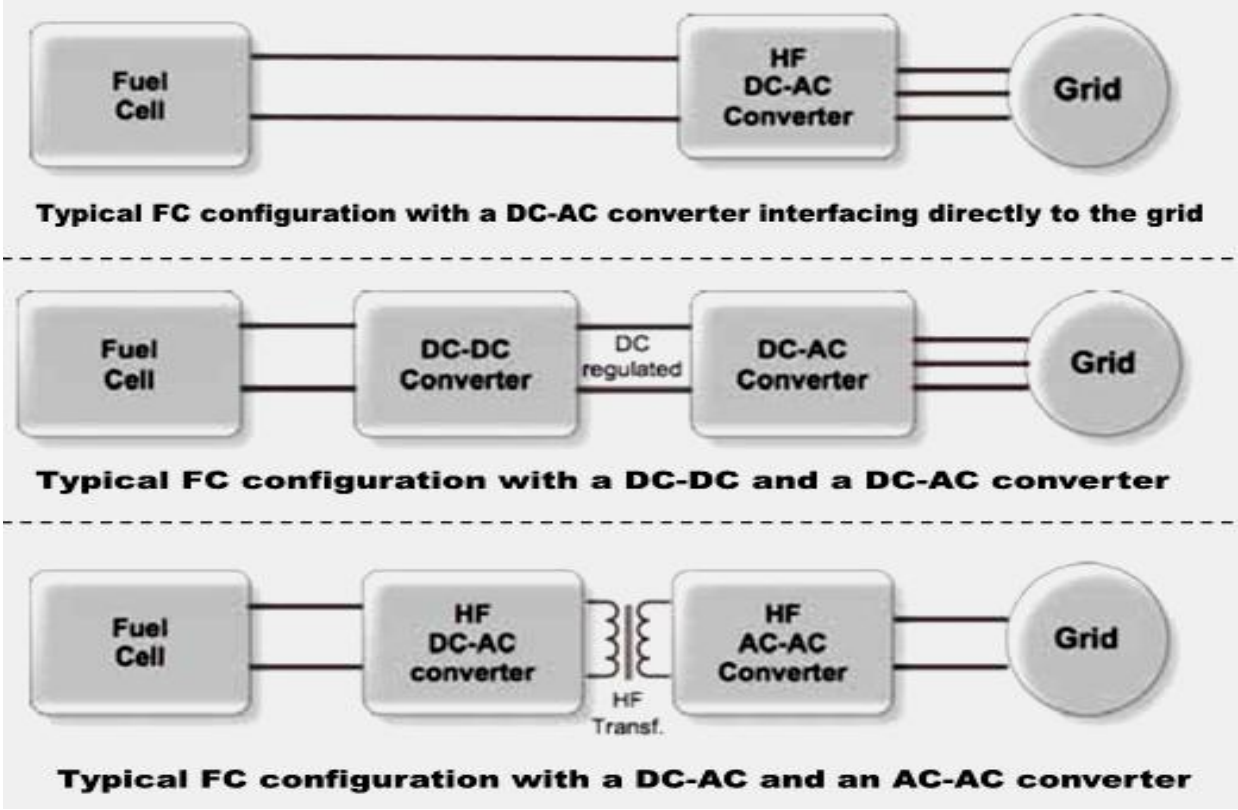

Figure 2.18: FC power converters models in Matlab/Simulink (adapted from Carvalho *et al.*, 2011)

The preferred topology must be suitable to take control and optimize the operation point of the fuel cell; as a result, the soft switching attests to be particularly fitting, especially the series resonant topology converters − because it reduces the switching losses and consequently increasing the efficiency. This converter execution can be explained as follows: the supplied voltage by the stack, which is normally low (29V - 42V), is changed to a constant and high amplitude, in this case, a 400VDC bus is used to generate power to the grid through an inverter.

The high frequency (HF) transformer is a boost voltage transformer, which is as well used to offer galvanic isolation between the low and high voltage levels of the circuits. In the primary side of the transformer, the resonant converter with its inductor-capacitor (LC) series resonant circuit, provides the sinusoidal waveforms of voltage and current. The circuit resonant frequency is determined by choosing suitable values for the L and C elements, from which the FC DC voltage is initially inverted to AC in the primary side of the HF transformer and then rectified to DC on the secondary side. The PEM FC is protected from the ripple voltage and current the converter produces by the LC filter in the primary side, which as well stores the DC bus energy. The secondary side LC filter reduces the ripple voltage and current to the load. In conclusion, the simulation results were correlated using actual data acquired from a commercial system. As a result, it was justified that, the hybridization of a suitable power converter using a well-defined controller in conjunction with a well-optimized fuel cell stack model, makes fuel cell good for power generation.

2.3.2.7 High Voltage DC-DC Boost Converter Suitable for Varying DC Voltage Sources

Researched in Mwaniki (2014), is a high voltage step-up converter appropriate for varying voltage sources such as photovoltaic (PV) and by extension fuel cells as well as thermoelectric generators (TEGs). Different varying voltage boost sources were assessed to institutes their limits, from which a multi-phase tapped-coupled inductor DC-DC boost converter that can attain high voltage boost ratios from a variable power supply (PV in this case) and without adversely compromising the performance, was then postulated as pictured in Figure 2.19. The suggested converter achieved minimal voltage and current ripples at both the input and output as well as exhibited reasonable performance at high power levels making it preferred for high power applications. The simulated and practical results correlated to confirm their research.

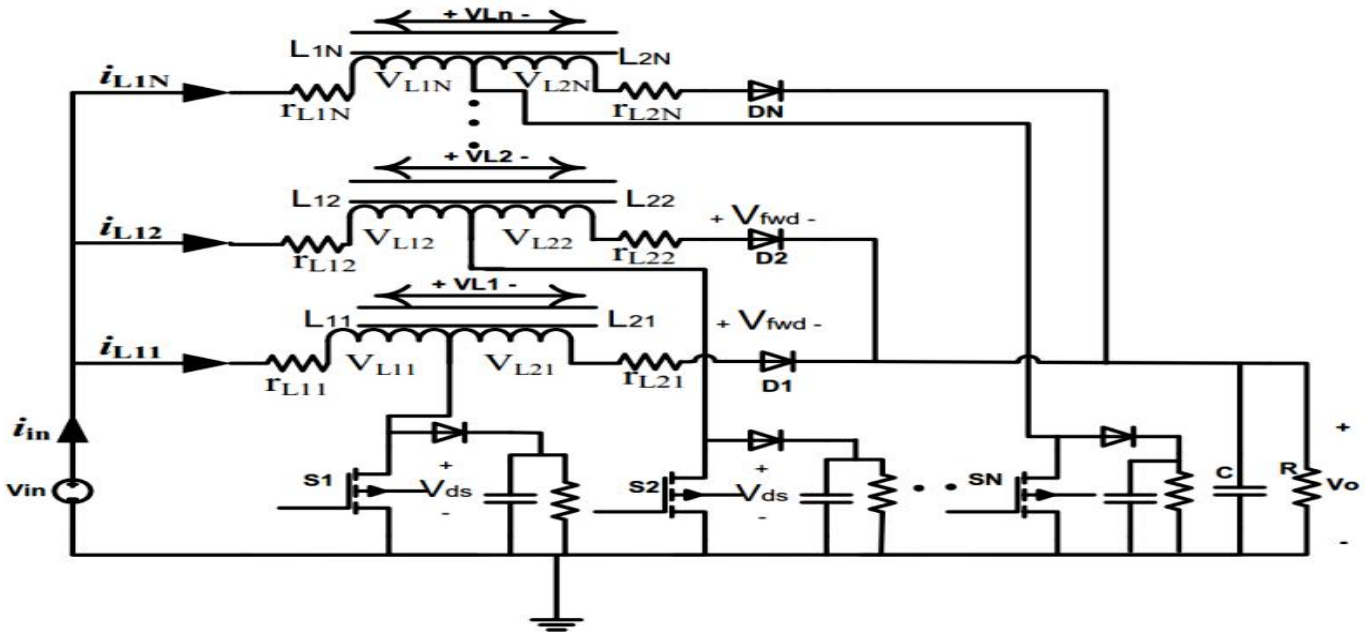

Figure 2.19: High voltage DC-DC boost converter suitable for varying voltage sources (adapted from Mwaniki, 2014)

2.3.2.8 High Power Efficient DC-DC Buck Converter Suitable for Varying Voltage Sources

According to Huangfu *et al.* (2015), in a varying power generation source such as wind (likewise solar-cells and TEGs as well as fuel cells), the power converter efficiency is one of the crucial aspects for the performance of the system. In such systems, the DC-DC step-down converter is usually used for high power systems. Taking into account the cost and efficiency of a converter, their research focus was mainly on the devise of enhanced buck converter topologies with interest on the (inductor, capacitor and diode) LCD converter depicted in Figure 2.20 – which is to be used for a peak power standalone wind power generation system. A (resistor, capacitor and diode) RCD and an improved RCD buck converter could also remove the voltage spikes; however, it unfortunately further depletes the stored voltage amplitude when the power is switched-off − this is because C_1 discharges the voltage stored through R_1. Therefore, the need for a LCD version portrayed in Figure 2.20.

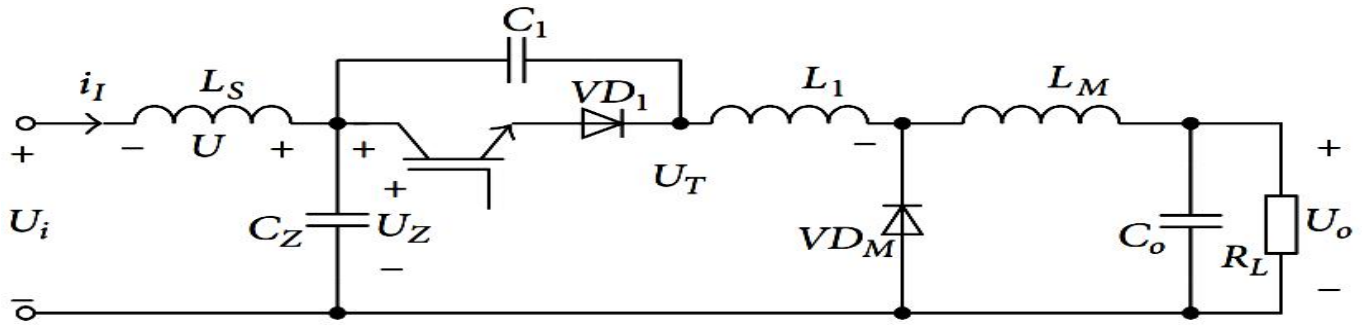

Figure 2.20: High power efficiency DC-DC buck converter suitable for varying voltage sources (adapted from Huangfu *et al.*, (2015)

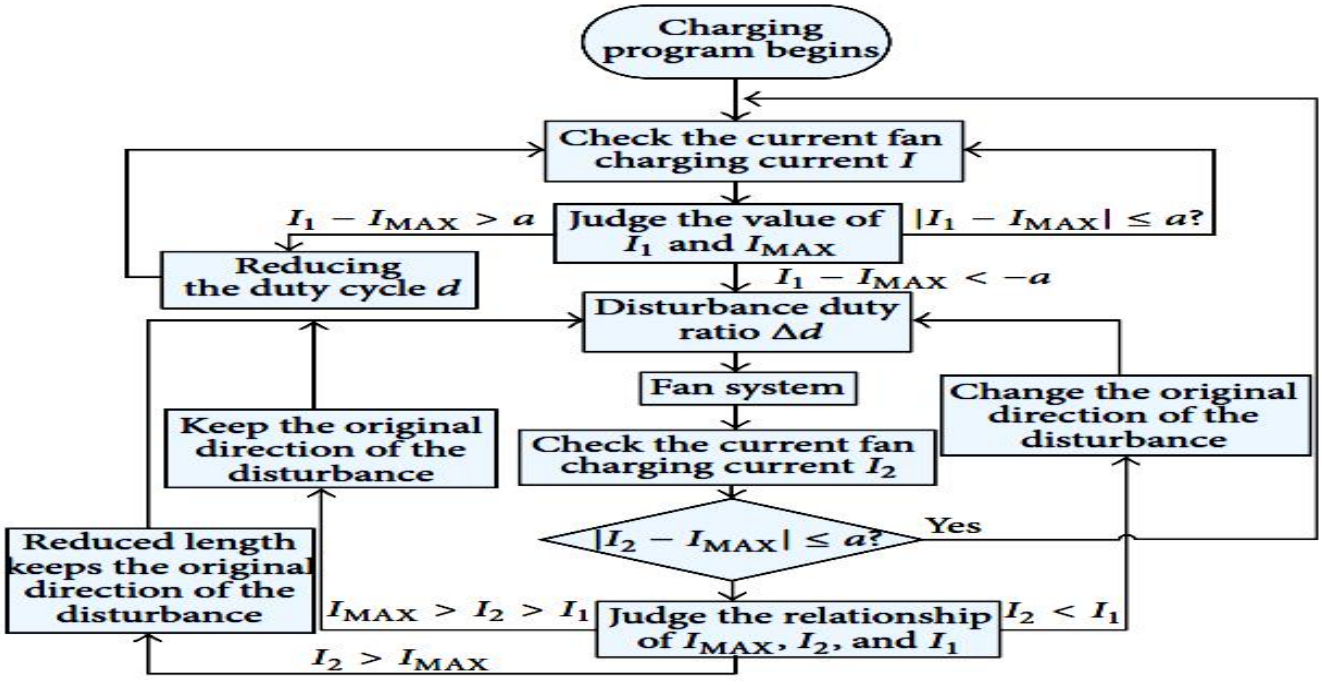

Figure 2.21: DC-DC buck converter climbing mountain MTTP algorithm flowchart for varying voltage sources (adapted from Huangfu *et al.*, 2015)

This issue was addressed by using a better improved buck converter − the LCD version as shown in Figure 2.20. This version does not have any resistor but an inductor with negligible energy loss as displayed in their test result. This LCD architecture is also known as zero-voltage switching (ZVS). At resonance, L_1 and C_1 cancel out, reducing the voltage spike and increasing the switching speed. The practical designed LCD converter instead of using IGBTs, it uses multi-MOSFETs in parallel to boost the current and the switching speed of the converter. By employing MPPT, the practical utmost efficiency of the designed 2kW DC - DC step-down converter was approximately 96%.

MPPT algorithm ensures the maximum power generated stays constant by monitoring the desired reference output with the generated output and adjusting the duty cycle or PWM signal to the active switch(es) of the power converter. The common MPPT techniques according to Huangfu *et al.* (2015), includes i) optimum tip speed ratio, ii) power curve control and iii) climbing mountain – the latter was used in their study and its flowchart is illustrated in Figure 2.21.

2.3.2.9 High Gain IBC for Fuel Cells Applications

As researched by Seyezhai *et al.* (2013), distributed generation most capable technologies is fuel cell and to design a high efficiency power system using fuel cell, a fitting DC-DC converter is necessary. Among the different DC-DC converters, interleaved converters with switched capacitor are considered a preferred topology for FC systems because of reduced ripple currents in the input and output circuits, quicker transients reaction, small electromagnetic emissions, enhanced efficiency and reliability. This improved conversion efficiency is attained by dividing the output current into 'n' parts, to significantly eliminate I^2R losses and inductor losses. Their research aim was to devise and implement a high gain IBC based-on switched capacitors (to improve converter voltage gain) for fuel cell systems. In their interleaved boost converter proposed, the front-end inductors are magnetically cross-coupled to enhance the electrical performance and reduce the weight and size. By using switched capacitors interfaced with FCs, Matlab and Simulink were used to simulate an interleaved converter, from which a prototype was developed to validate the simulation results. Figure 2.22 depicts their IBC.

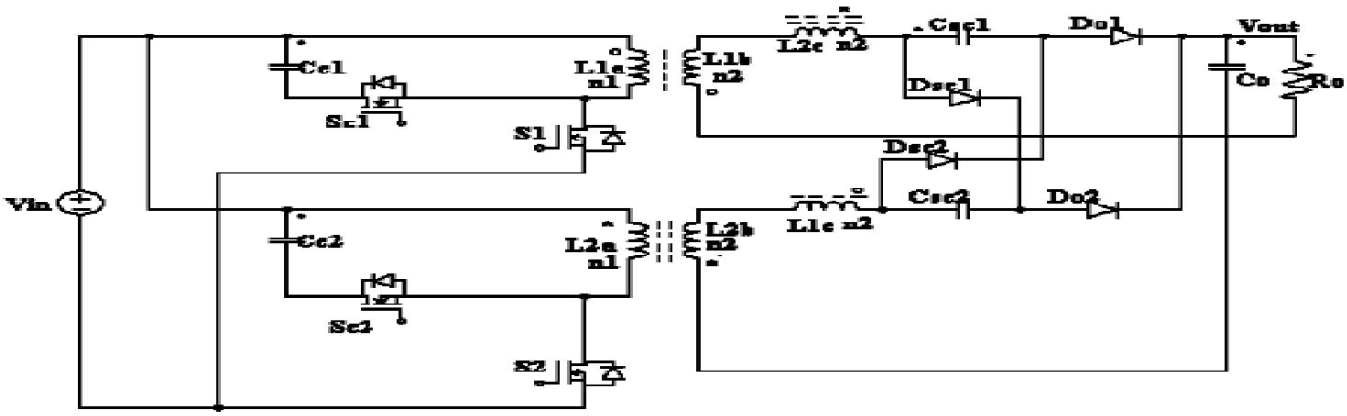

Figure 2.22: High gain IBC for fuel cells applications (adapted from Seyezhai *et al.*, 2013)

2.3.2.10 High Efficiency Isolated Boost Converters for High-Power Low-Voltage FC Uses

As investigated in Nymand and Andersen (2008), fuel cells power systems, as portrayed in Figure 2.23, show significant output impedance which reduces the output voltage with increased in the output power; as a result, system peak power is attained at converter smallest input voltage. In light of these drawbacks, a new low-leakage inductance low-resistance to low-voltage high-power isolated boost converter design technique, was presented as shown in Figure 2.24. By optimizing the transformer design and circuit lay-out, very low levels of parasitic circuit inductance were attained. Power MOSFETs fully rated for recurring avalanche, were used to eliminate primary side voltage clamp circuits and switch on-state losses. Furthermore, extensive interleaving of the primary and secondary transformer windings, reduced the transformer proximity effect losses.

Silicon Carbide rectifying diodes are not prone to reverse recovery and therefore allow fast diode turn-off, hence were used to further reduce losses. As illustrated in the study, test results from a 1.5kW full-bridge step-up converter confirmed theoretical analysis and demonstrated a very high efficiency. The maximum efficiency was up to 98% whereas the worst-case efficiency with maximum power and at minimum input voltage was ~ 96.8%.

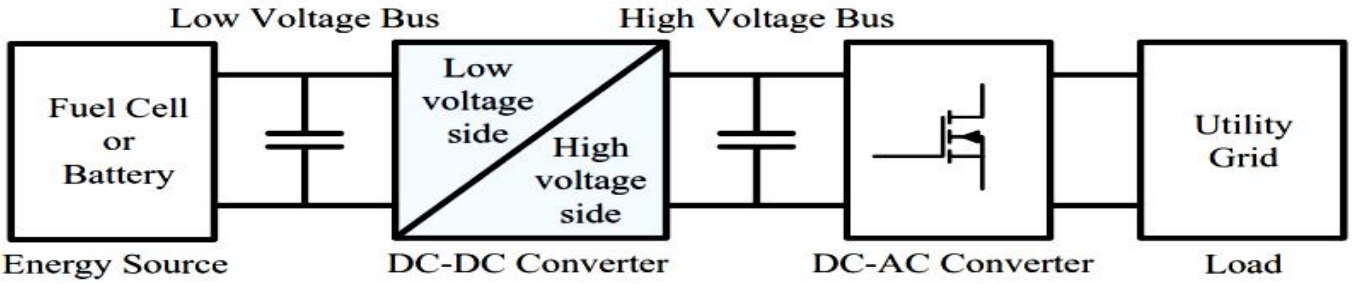

Figure 2.23: Fuel cell power supply system (adapted from Nymand & Andersen, 2008)

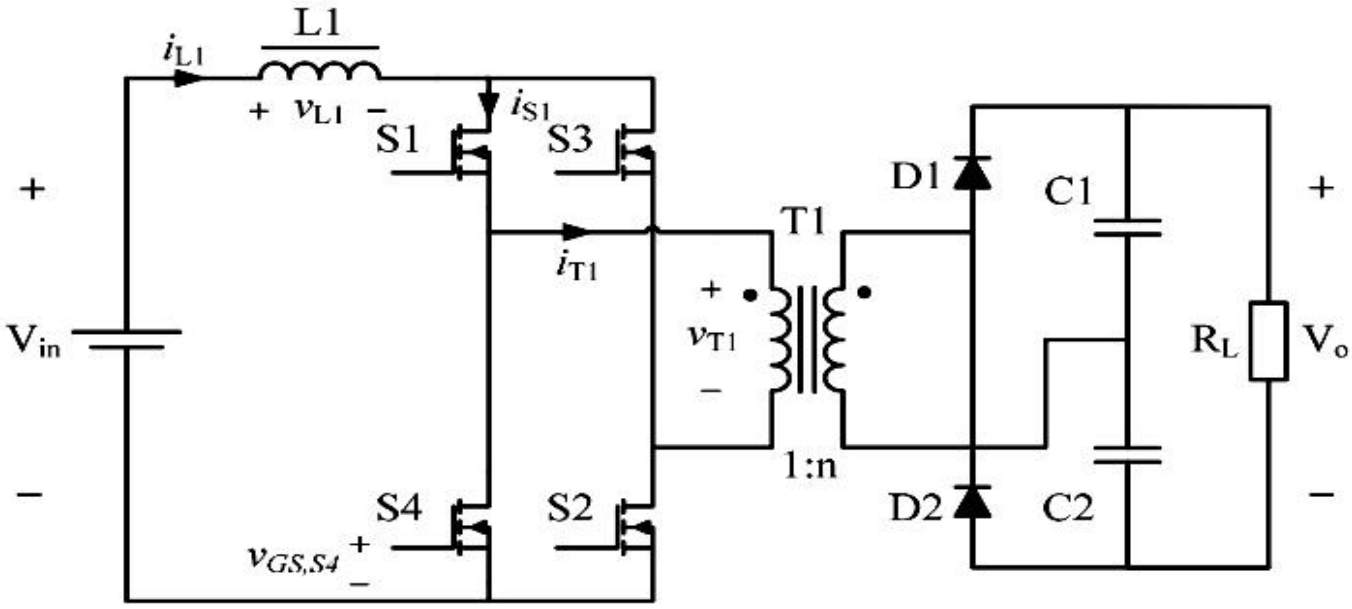

Figure 2.24: FC high-power low-voltage high efficiency isolated boost converters (adapted from Nymand & Andersen, 2008)

2.3.2.11 High Power Buck-Boost DC-DC Converters: Automotive Power-train Applications

Investigated in Eckardt *et al.* (2005), is a high-power buck-boost DC-DC converter for use in the power-trains of hybrid cars as shown in Figures 2.25 and 2.26. To enable smooth transitions between both energy transfer directions, a special digital control strategy was implemented. Equipped with this feature, the converter can obtain the energy management in the electric power-train. The digital control provides full protection against over-voltage, over-current and over-temperature. Two efficient prototypes of 24kW and 70kW bidirectional (buck-boost) DC-DC converters were developed and evaluated. The presented measurements show that higher voltages for the power-train and storage battery assure higher efficiency due to lower current losses by the use of IGBTs. Using integrated liquid cooling of up to 85°C with very low losses, a high-power density of up to 5W/cm³ was achieved. Characterization data of the converter and measurements in the target application (a hybrid fuel cell car) with test parameters and values of passive components used, are shown in the study as well as what happens when the converter transits from boost to buck mode. Finally, presented in the full manuscript are voltage and current dynamics as well as the efficiencies and output power in the various operation modes. NB: though this application relates to power trains, the power converters can also be used with other FC applications.

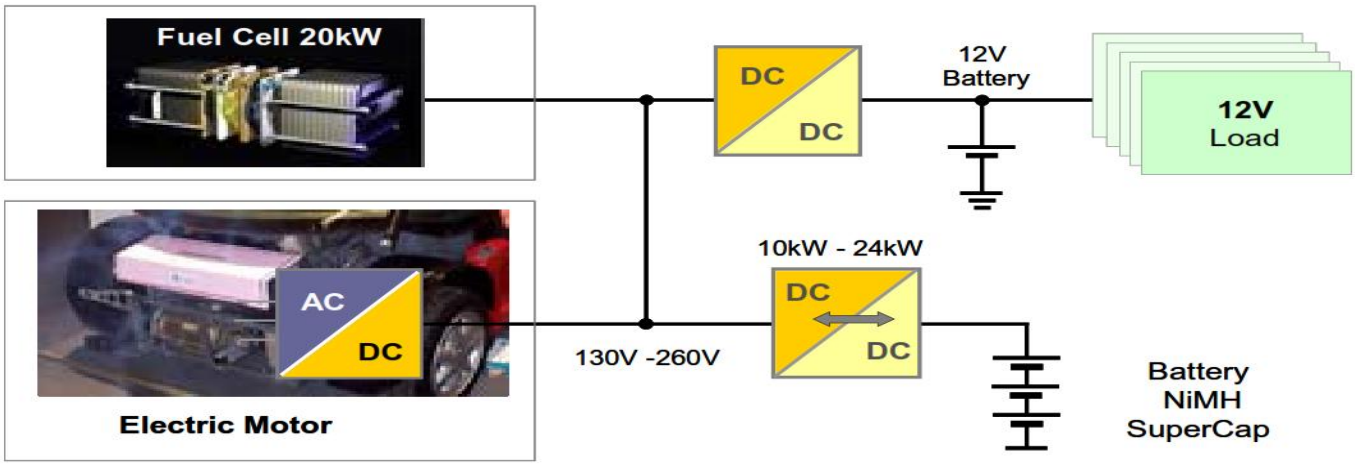

Figure 2.25: Concept overview (adapted from Eckardt *et al.*, 2005)

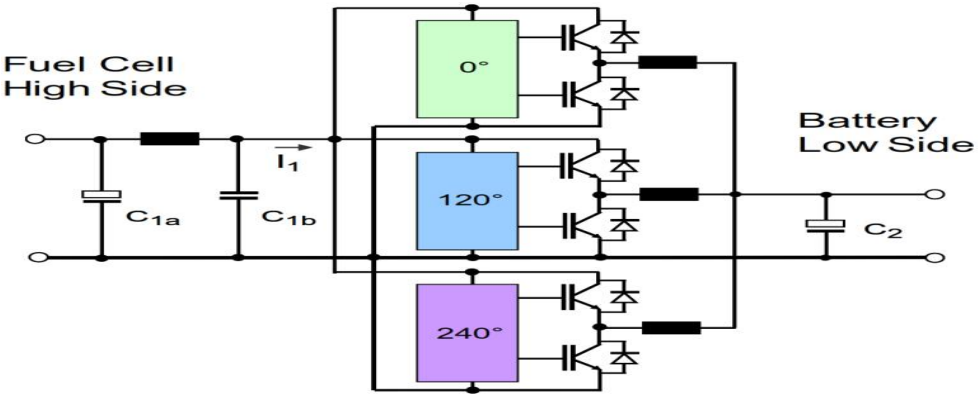

Figure 2.26: High power buck-boost DC-DC converters: Automotive power-train applications (adapted from Eckardt *et al.*, 2005)

2.3.2.12 PEM FC System with DC-DC Boost Converter: Design, Modelling and Simulation

Indicated in Kirubakaran *et al.* (2009), fuel cells as exemplified in Figure 2.27, are regarded as one of the most proficient devices for standalone and grid connected distributed generations (DGs), due to their environmental friendliness, modularity and high energy potential capability. The drawbacks in the extensive use of FCs are their i) sluggish dynamic response to abrupt load changes and ii) costly installation. As a result, their research focused on the simulation of dynamic behaviour of a Nexa 1.2kW PEM FC using DC-DC step-up converter, which was correlated with cascaded 2-stack FC model. The performance of the basic DC-DC boost converter as a power converter for the Nexa TM 1.2kW PEM FC model was analyzed for changing loads to manage the power flow for improved performance. As the FC pressure or temperature rises, the power density of the FC stack also increases for rising loads; therefore, to analyse this dynamic behaviour for changes against temperature, an advanced parametric model based on circuit simulator PSpice for a class of PEM FC was also developed in addition to the fuel cell models based on thermodynamics and electrochemical equations. The fuel cell performance is governed by its electrical and thermal efficiencies − the electrical efficiency of the fuel cell relies on the fuel cell activation and concentration losses besides the natural Joule heating (Ohmic loss), whereas the thermodynamic efficiency relies on the fuel cell fuel processing, water management and the fuel cell system's temperature control.

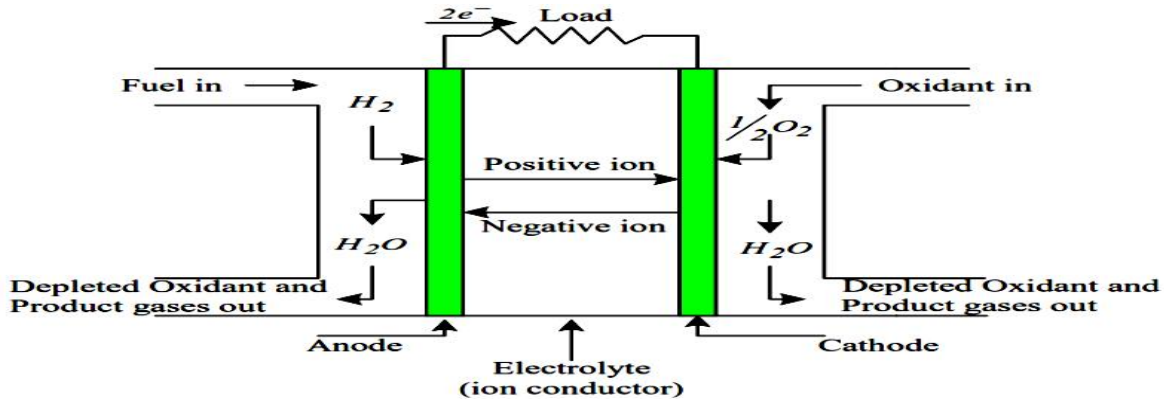

Figure 2.27: Fuel cell overview (adapted from Kirubakaran *et al.*, 2009)

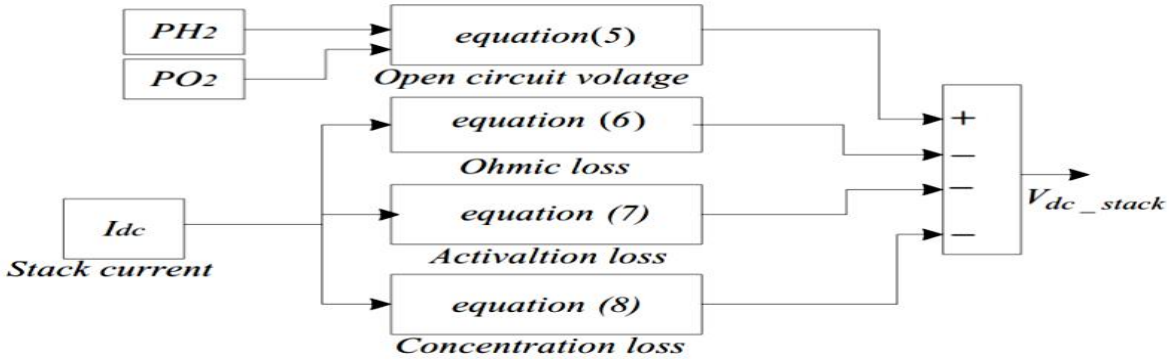

Figure 2.28: PEM FC system with DC-DC boost converter: Design, modeling and simulation (adapted from Kirubakaran *et al.*, 2009)

All these factors were taken into consideration when the design was done using Matlab / Simulink as in Figure 2.28. It was noticed that for instantaneous loads variation from 0.6 - 1.1kW, the fuel cell current and voltage took about 50 - 70ms to attain a new steady state. This delay is known as the fuel cell fuel starvation phenomenon – this makes the fuel cells non-linear and should not be operated, because the electrolyte membrane of the FC can be destroyed. The FCs must be operated only in its linear region. The DC-DC converter used was a basic boost converter with PI controller, which gave better performance for load variations without using any storage devices. A constant bus voltage of 80V was maintained in the converter output, regardless of changes in the load and fuel cell terminal voltages. Steady state error was reduced to zero by the proportional integral (PI) controller. In their conclusion, operating fuel cells with a basic step-up converter using PI controller, can give better performance for standalone / grid connected low power applications. This claim is evident in their measured and simulated results shown in their full research paper.

2.3.2.13 Methodology to Design FC Based Systems Power Converters: A Resonant Approach

Presented in Outeiro and Carvalho (2013), is the evaluation, devise and implementation of a fuel cell-based power generation scheme, which necessitates suitable selection of i) the FC model and ii) the power electronics converters shown in Figure 2.29. The fuel cell model used is semi-empirical based on PEM FC Mark 1020 with static and dynamic properties as well as the FC limited current and voltage supply ratings − irrespective of the converter used. The power converter employed a resonant technique that provides high frequency operation, less component stresses, soft switching etc.

The power converter controller was split into two functions, namely: i) the voltage controller − which stabilizes the converter output voltage during loading fluctuations and ii) the PEM controller − which enhances the performance by maintaining the PEM FC in its optimal point of operation. The outcome confirmed that the researched converter is a good choice to enhance the efficiency of a PEM FC, because it permits a sufficient control of the power delivered by the fuel cell while sustaining the requirements dictated by the load to maximize the gains with soft-switching control. The FC DC is converted either to DC then to AC (DC-DC-AC) or FC DC to direct AC or FC DC to DC and AC-AC isolated by a transformer. The operation mode of the DC power conversion can be divided into i) linear, ii) switching and iii) soft-switching or resonant. The four non-isolation buck, boost, buck-boost and Cuk converters can be respectively converted to forward, boost, flyback and Cuk; by adding isolation transformer and when the isolation converters use more than a switch; it could be a push-pull, half bridge or full bridge as portrayed in Figure 2.30. The results showed that the chosen power converter is suitable to improve the PEM FC efficiency, as it allows proper control of the power delivered by the FC, by satisfying the criteria enforced by the load regulation with minimal losses as a result of adopting soft switching.

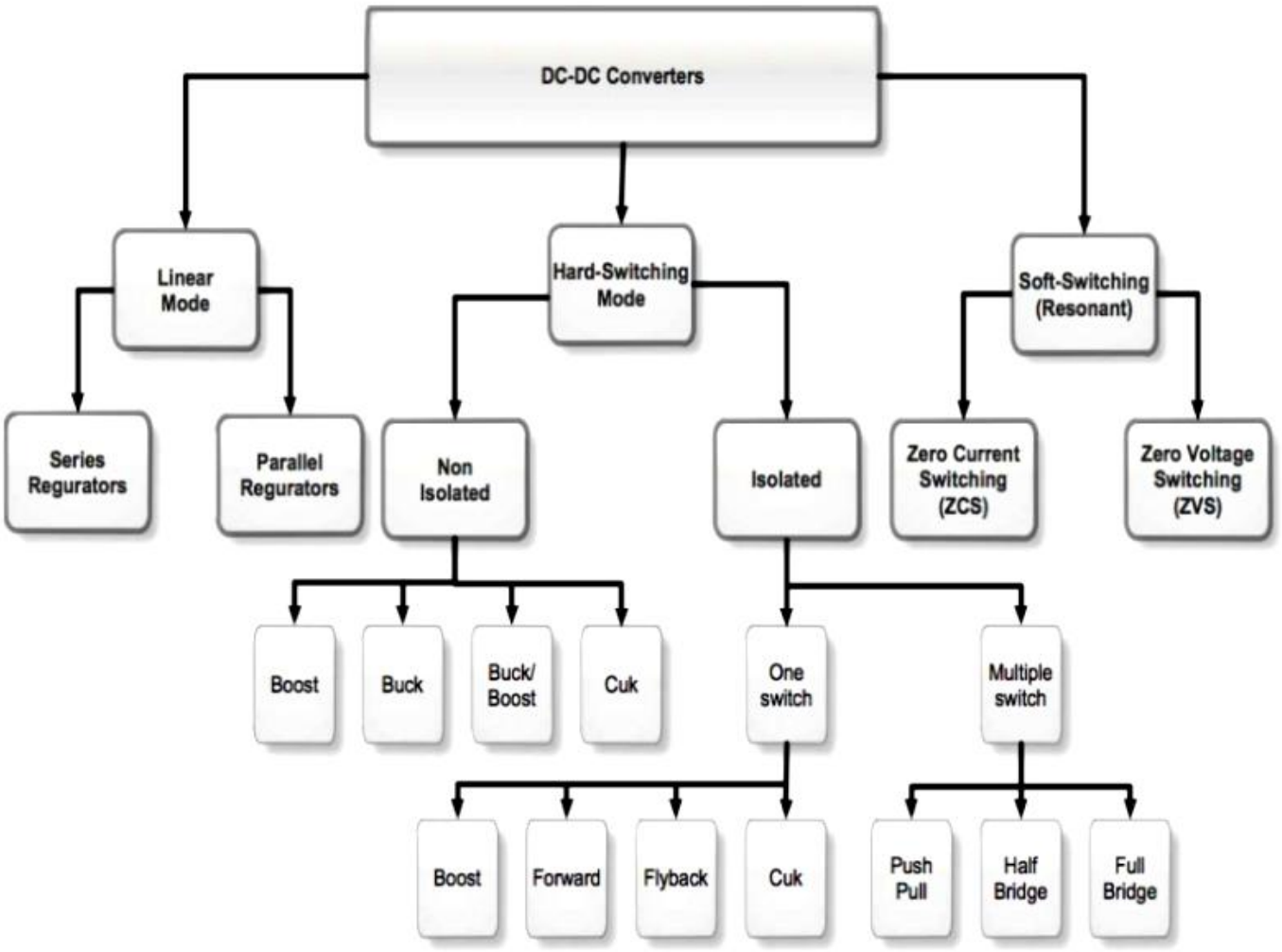

Figure 2.29: DC-DC converters overview (adapted from Outeiro & Carvalho, 2013)

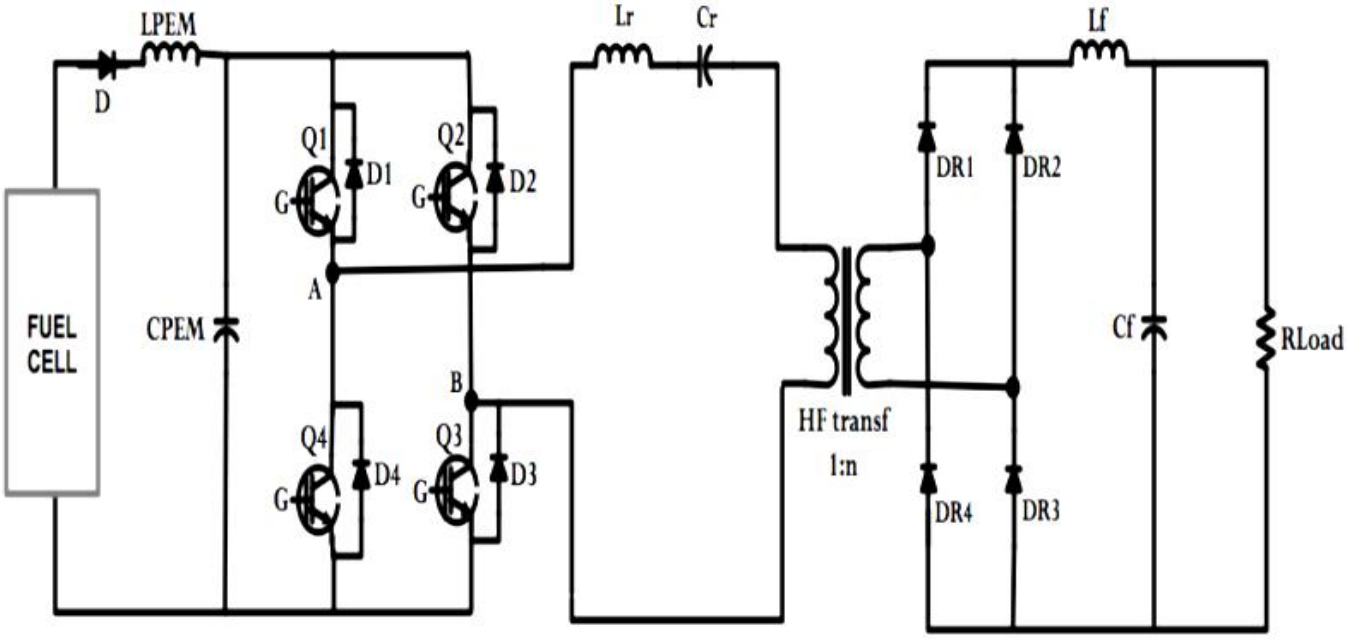

Figure 2.30: Methodology to design FC based power converters systems: A resonant approach (adapted from Outeiro & Carvalho, 2013)

2.3.2.14 Design and Control of a 6-phase IBC Based-on SiC Semiconductors with EIS Functionality for Fuel Cell Electric Vehicle

Researched by Wang (2019) indicates that, in today's FC Electric Vehicle (FCEV), DC-DC converter is paramount to step-up the PEM FC output voltage to a high level (400 - 700V). As a result, the research aim was to design a 6-phase IBC based on SiC semiconductors and inverse coupled inductors of cyclic cascade structure having high compactness, high efficiency and high voltage gain ratio. The reliability and durability have to be enhanced to advance the consumption and commercialization of FC technologies. Electrochemical Impedance Spectroscopy (EIS) is typically used for PEM FC's diagnosis. To eliminate additional equipment and sensor, the on-line EIS detection functionality incorporated with the control technique of the suggested PEM FC linked to the DC-DC step-up converter was also investigated. The interleaved topology helped decreased the FC current ripple to ensure an extended FC lifespan. Furthermore, the multi-phase topology shared the high input current, hence reducing Joule heating, which allays the electrical stress of the power switches; thus, this redundancy ensures the reliability and robustness of the converter. The magnetic core design is also critical, as it controls the amount of ripple; as a result, the three types Uncoupled (UC)-IBC, Direct Coupled (DC)-IBC, and Inverse Coupled (IC)-IBC were experimented. The SiC-based semiconductors increased the switching frequency and decreased power losses. The on-line EIS detection functionality was integrated with sliding mode control (SMC) of the postulated DC-DC step-up converter. Fuel cells most common problems of membrane drying and flooding were estimated based on PEM FC's equivalent electric circuit model. The real-time hardware-in-the-loop (HIL) validation of the proposed converter was achieved. MicroLabBox (embedded real-time processor with (Field Programmable Gate Array (FPGA)), was used as the real-time platform for prototyping. In all, a 21kW PEM FC's voltage model was developed as the power source and the HIL framework provided in real-time, a benefit to monitor the converter's dynamic working process that was not viable with the offline simulation. Figures 2.31a−2.31c summarize their study.

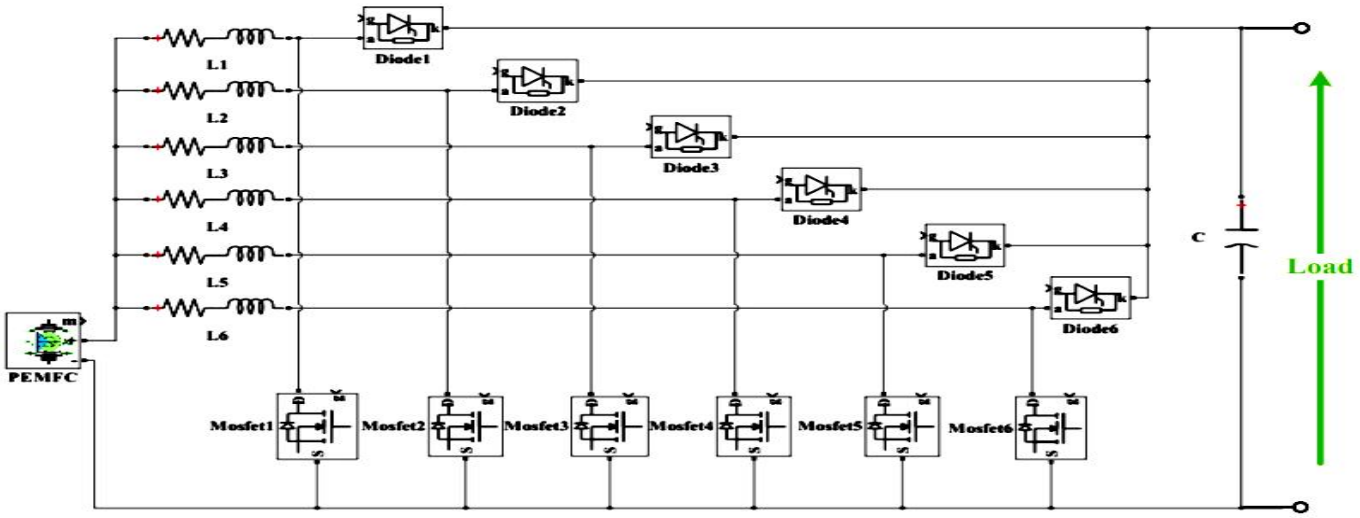

(a). 6-phase IBC (UC-IBC)

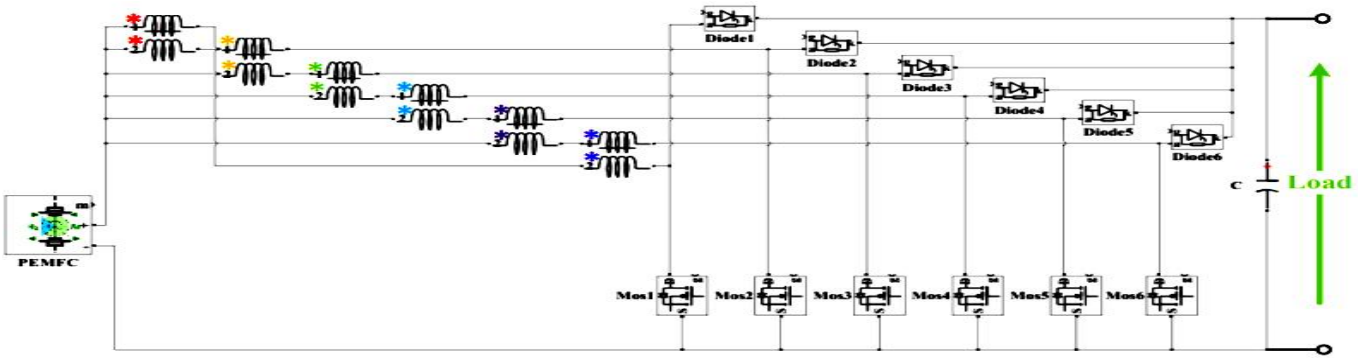

(b). 6-hase IBC based on direct coupled inductor of cyclic cascade structure (DC-IBC)

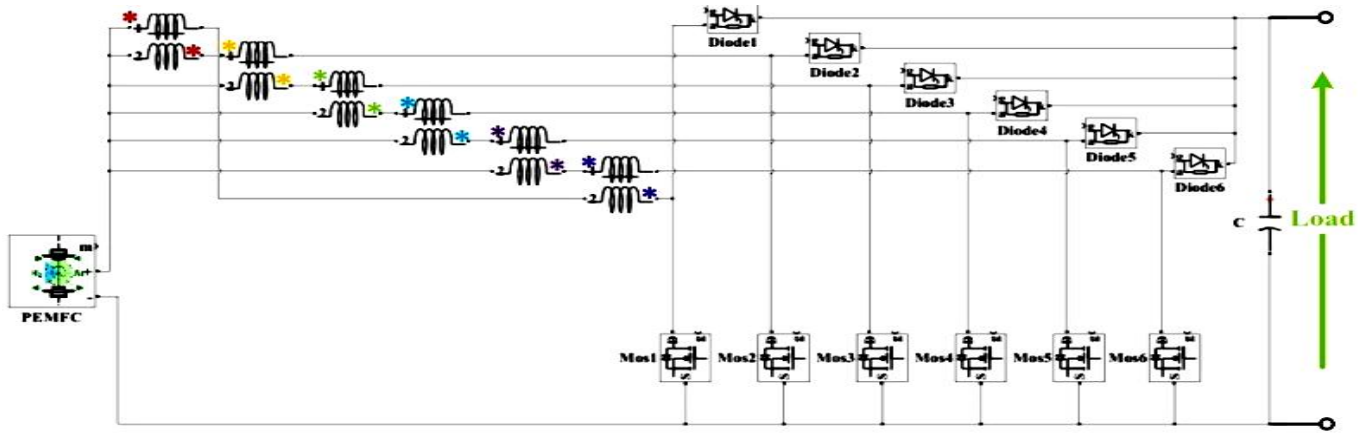

(c). 6-hase IBC based on inverse coupled inductor of cyclic cascade structure (IC-IBC)

Figure 2.31: Six-phase IBC based on SiC semiconductors with EIS (adapted from Wang, 2019)

2.3.2.15 Design Considerations for DC-DC Converters in Fuel Cells Systems

As examined in Fanjul (2006), the development of alternative energy sources, has been improved by the fast increase of fossil fuel costs along with a rise in environmental education – which include but unlimited to fuel cells, wind, solar and ocean tidal-wave power. Among them, fuel cells due to their high modularity, efficiency and basic design have received increased interests in recent years. However, their low voltage output and wide variation from unloaded to fully loaded, demands the need of a power converter to interface the FC to its loads. In light of this, their research was undertaken, in which design considerations were attained analytically and experimentally verified to enable an efficient and stable fuel cell as well as power converter system. Further to the design guidelines, investigated also were new power converter layouts that do not need the use of transformers to accomplish a large voltage gain. Their research general outcomes are means of i) mathematical analysis and ii) experimental prototypes, that contributed to the lessening of the cost and size of the power converter as well as to raise the efficiency of the system. It was discovered that when the FC load current is not purely DC, the Hydrogen usage of the stack increased and the power output of the FC decreased. This effect importance is a function of the ripple current frequency as demonstrated in their full research.

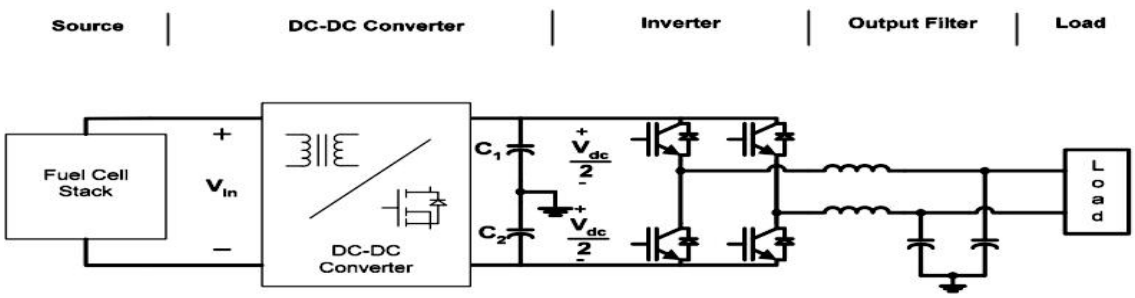

(a) Typical fuel cell power conversion system for residential applications

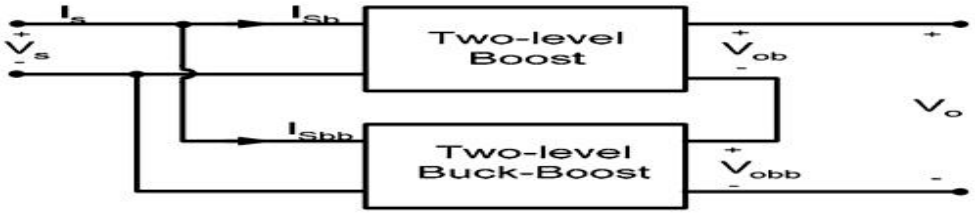

(b) Block diagram of the proposed DC-DC converter

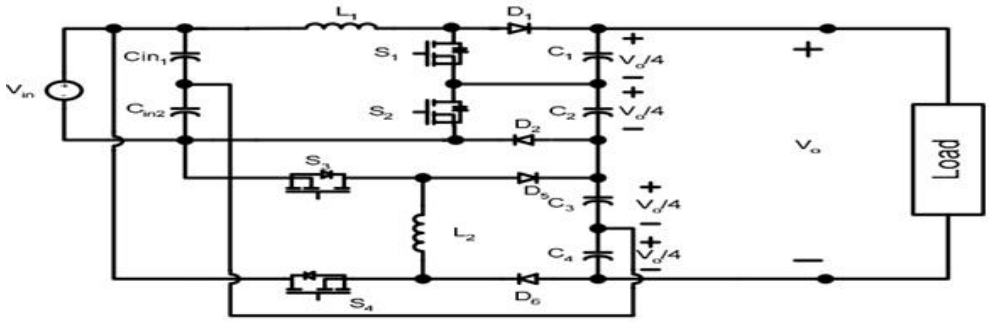

(c) Circuit schematic of the proposed two level boost and buck-boost converter

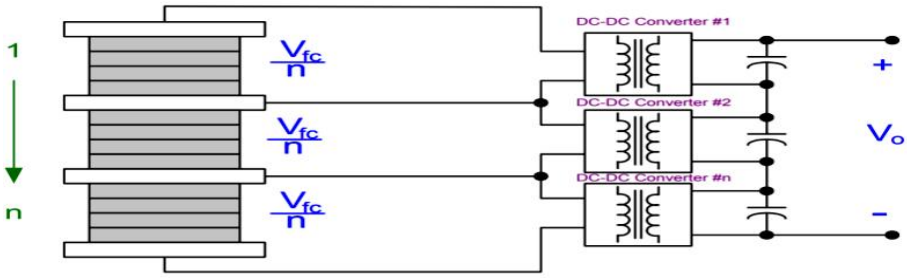

(d) Fanjul proposed sectioned / taped FC stacked with modular DC-DC converter

Figure 2.32: Design considerations for DC-DC converters in FCs systems (adapted from Fanjul, 2006)

Furthermore, by using analytical and experimental methods, it was demonstrated that for load currents with low frequency ripple (<1kHz), the Hydrogen usage increased up to 7% whereas the power output of the FC decreased up to 30%. In addition, if the frequency of the ripple current is high, >20kHz, the Hydrogen utilized by the FC also increased in the range from 1 - 3%, whereas its power output dropped by 5%. It was further realized that the FC thermal performance was not rigorously affected by high frequency ripple currents presence – due to

discontinuous operation mode. It was also found that the FC internal impedance can considerably affect the dynamics of the DC-DC converter. Also, the diminished power left during purging of the FC stack has been shown to be another possible cause for instability. To allay these problems, super-capacitors were connected in parallel to the FCs and a method to compute the value of the super-capacitor to attain stability was derived. A 30W boost converter system experimental results confirmed the validity of the suggested solution. Finally, good dynamic behaviour and stability were proven to be feasible with the use of super-capacitors connected to the output of the FCs. To lessen the cost and volume of the system, a high gain transformer-less DC-DC converter was researched – it employed a two level boost and a two level buck-boost converter in cascade to achieve a high voltage gain and low input ripple current, which contributed to lower electromagnetic interference (EMI). Experimental results demonstrated the viability of the DC-DC converter and showed a possible voltage gain of 5. Normally, FCs are constructed by stacking many cells which limit the generated power to the weakest cell in the stack. In addition, if one or more FCs fail, the entire system must be overhauled. To address these shortcomings, a new modular FC stack and DC-DC converter were pioneered – the FC stack was partitioned into different sections with autonomous operations. This has increased system reliability at a reduced output power should a section failed. Additionally, the generated power from the system was optimized by adjusting the drawn current from each section based on the voltage they produced, which resulted in a 10-14% extra power generation. Common mode noise due to transients was also noticed and was resolved by using shielded transformers. Figures 2.32a-2.32d exposit the study highlights.

2.3.2.16 An Overview of Various Fuel Cell DC-DC Converters

According to Ravi *et al.* (2018), fuel cells are now becoming the preferred alternative renewable energy source, as their power production process is not affected by fluctuating environmental factors, contrary to solar cells and wind power plants. However, fuel cells produce low DC output voltage which requires stepping-up and interfacing them to the DC bus. Thus, the need for DC-DC boost power converters, which could be interleaving to help minimize the power ripples as well as bidirectional to charge storage devices such as a battery. In this regard, their paper discussed various interleaved (2, 3, 4 and 6 phases) and bidirectional (non-isolated and isolated) DC-DC boost converters architectures. The non-isolated BDC DC-DC boost converters covered include i) buck-boost converter, ii) cascaded buck-boost converter, iii) CUK converter, iv) SEPIC-ZETA converter and v) switched capacitor. The isolated BDC DC-DC boost converters covered include i) dual half bridge (DHB) and ii) dual active full bridge (DAFB). Figure 2.33 illustrates the research overview and the conclusion drawn is interleaved boost converters improve power ripples and the more the interleaving, the better the ripple reduction; however, the more costly and bulky it becomes due to the many components used. BDC can additionally charge storage devices and furthermore, the isolated types can offer galvanic protection in high power applications; however, their large size due to the extra isolating transformer, makes them unsuitable for portable and or compact applications.

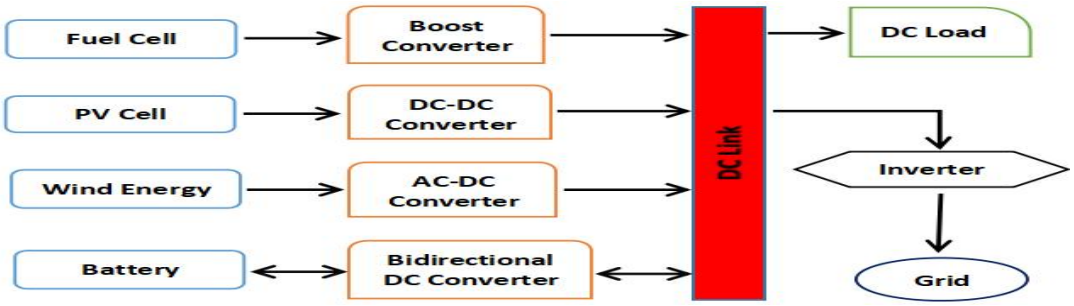

Figure 2.33: An overview of various fuel cell DC-DC converters (redrawn from Ravi *et al.*, 2018)

2.3.2.17 Challenges and Developments of Automotive Fuel Cell Hybrid Power System and Control

As assessed in Gao *et al.* (2019), fuel cells are the future replacement for internal combustion engine in vehicles, though the current costs and Hydrogen supply infrastructure are the limiting factors. In their analysis, they noted that FCs in hybrid power systems have energy control, inertia, power, model and optimization problems which were summarized briefly with emphasis on the electro-chemical reactions, dynamics and the core parameters affecting FCs efficiency and durability. Their review concludes by highlighting that fuel cells have various challenges and the best solution is one that is inclusive by incorporating various hardware and software solutions to optimize the fuel cells costs, performance and longevity. Figure 2.34a exemplifies a typical FC system and Figure 2.34b illustrates a simplified FCEV architecture.

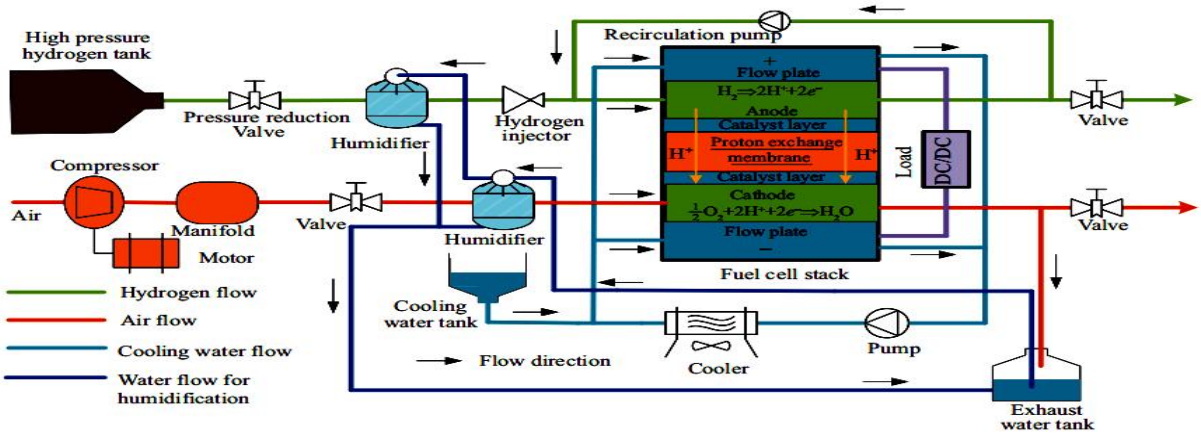

(a) Typical fuel cell system

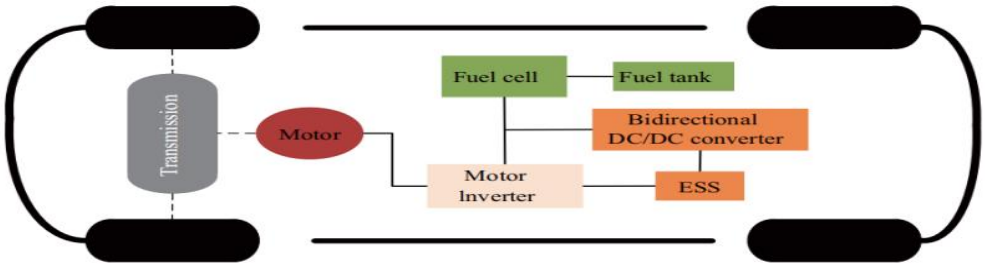

(b) Fuel cell electric vehicle power-train

Figure 2.34: Fuel cell system and FCEV Power-train (adapted from Gao *et al.*, 2019)

2.3.2.18 Experimental Study and Performance Analysis on High Power Fuel Cell System

In Liu *et al.* (2020), it's affirmed that PEM fuel cell for use in vehicles requires high power density — normally during starting-up and accelerating. As a result, their study presented an experimental research of a 100kW fuel cell power supply system with focus on measuring the system parameters such as voltage, current, temperature, pressure and hydrogen consumption. Two test set-ups were used; a i) rated and ii) cycle working condition tests. In the former, the system operates for an hour at a rated point with constant working conditions and the outcomes revealed stable operations when working constantly at the rated output power. In the latter, the test is conducted based-on their specified national standard, in which the fuel cell voltage is regulated to be a fixed value and the output current is varied with the working conditions. The conclusion arrived at is the researched fuel cell power engine reached 80kW at rated power with peak power exceeding 100kW. Figures 2.35a and 2.35b exemplify the researched FC power schemes.

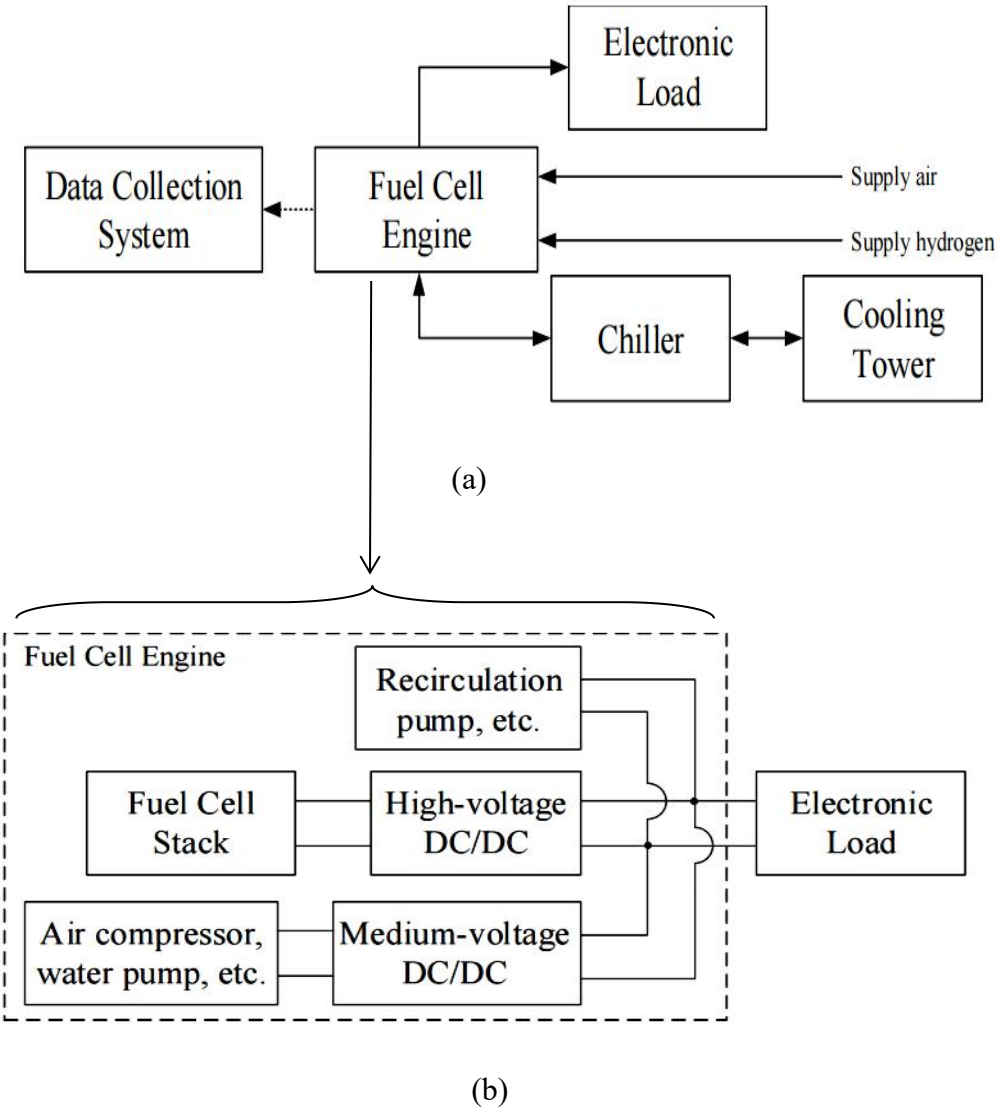

Figure 2.35: (a) The power system overview and (b) fuel cell power engine (adapted from Liu *et al.*, 2020)

2.3.2.19 Coupled Inductor-assisted Current-Fed Snubber-less Zero-Current-Soft Switching High Step-up DC-DC Converter for FC Power Interface

Presented in Miyazaki *et al.* (2020), is a ZCS current-fed isolated DC-DC boost converter for a fuel cell smart home power system. To avoid ripple current from damaging the fuel cell electrodes and to ensure good boost voltage ratio, their design incorporated a magnetically coupled interleaved inductors with a 180◦ phase shift and a small number of passive components. A 50/60W 1MHz prototype based on 600V GaN-HFETs, was performance tested focusing on the design efficiency, ripple and voltage ratio.

Figure 2.36a illustrates the concept design and Figures 2.36b and 2.36c, portray the DC-DC converter with a full bridge and voltage doubler outputs respectively. Normally, the primary side of the high-frequency transformer (HF-X) windings constitutes a two-phase current-fed high-frequency resonant inverter with complementary *Q1 / Q2* as the active switches and *L1 / L2* as the coupled inductors. HF-X leakage (*Lr*) and magnetizing inductances (*Lm*) produce the multi-resonant transitions with *Cp*, to generate the high voltage boost ratio and quasi-resonant sub-interval for soft commutations. The leakage inductance operates as a snubber inductor to reduce the high di/dt rate at *Q1* and *Q2* switched-on transitions. For a higher boost ratio, the full bridge rectifier output can be substituted with a voltage doubler rectifier. Their findings showed that the postulated power converter can attain a snubber-less ZCS commutations, a greater voltage boost ratio and low power ripple; making it suited for smart homes use.

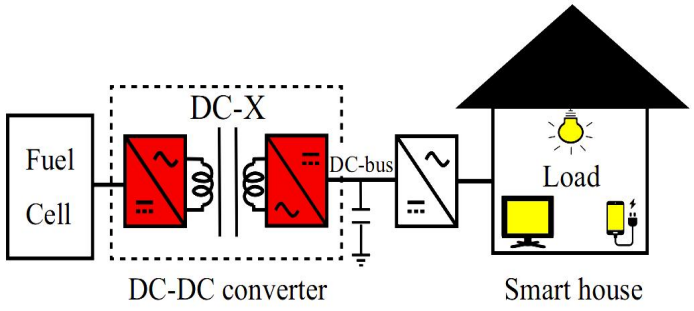

(a) Concept overview

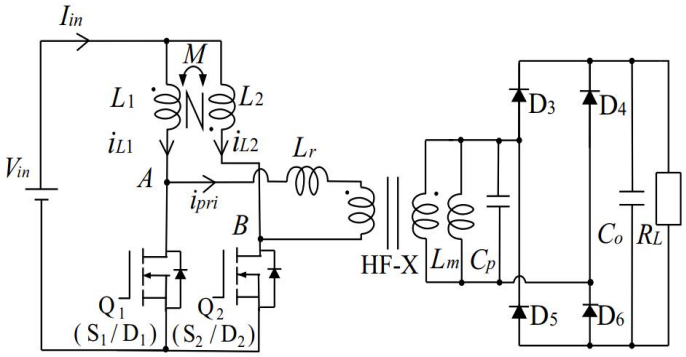

(b) High step-up DC-DC converter with full-bridge rectifier

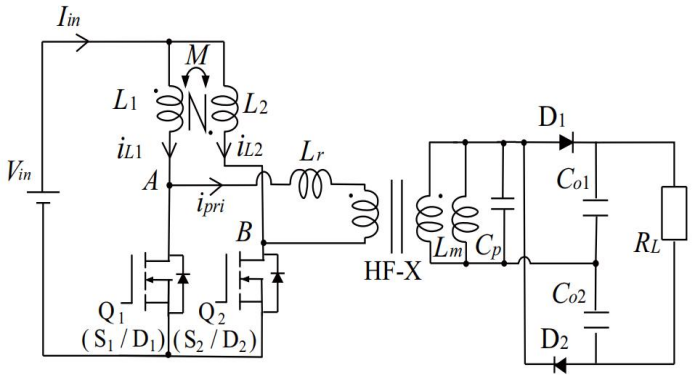

(c) High step-up DC-DC converter with voltage doubler rectifier

Figure 2.36: System concept design and high step-up DC-DC converter types (adapted from Miyazaki *et al.*, 2020)

2.3.2.20 Survey of DC-DC Non-Isolated Topologies for Unidirectional Power Flow in FC Vehicles

Investigated in Bhaskar *et al.* (2020), is an outstanding research on fuel cells power-trains and power converters. Its extensively discussed in details the theoretical and architectural frameworks of fuel cells. Figures 2.37a and 2.37b respectively depict in totality a summary of fuel cell types and power electronics converters classifications.

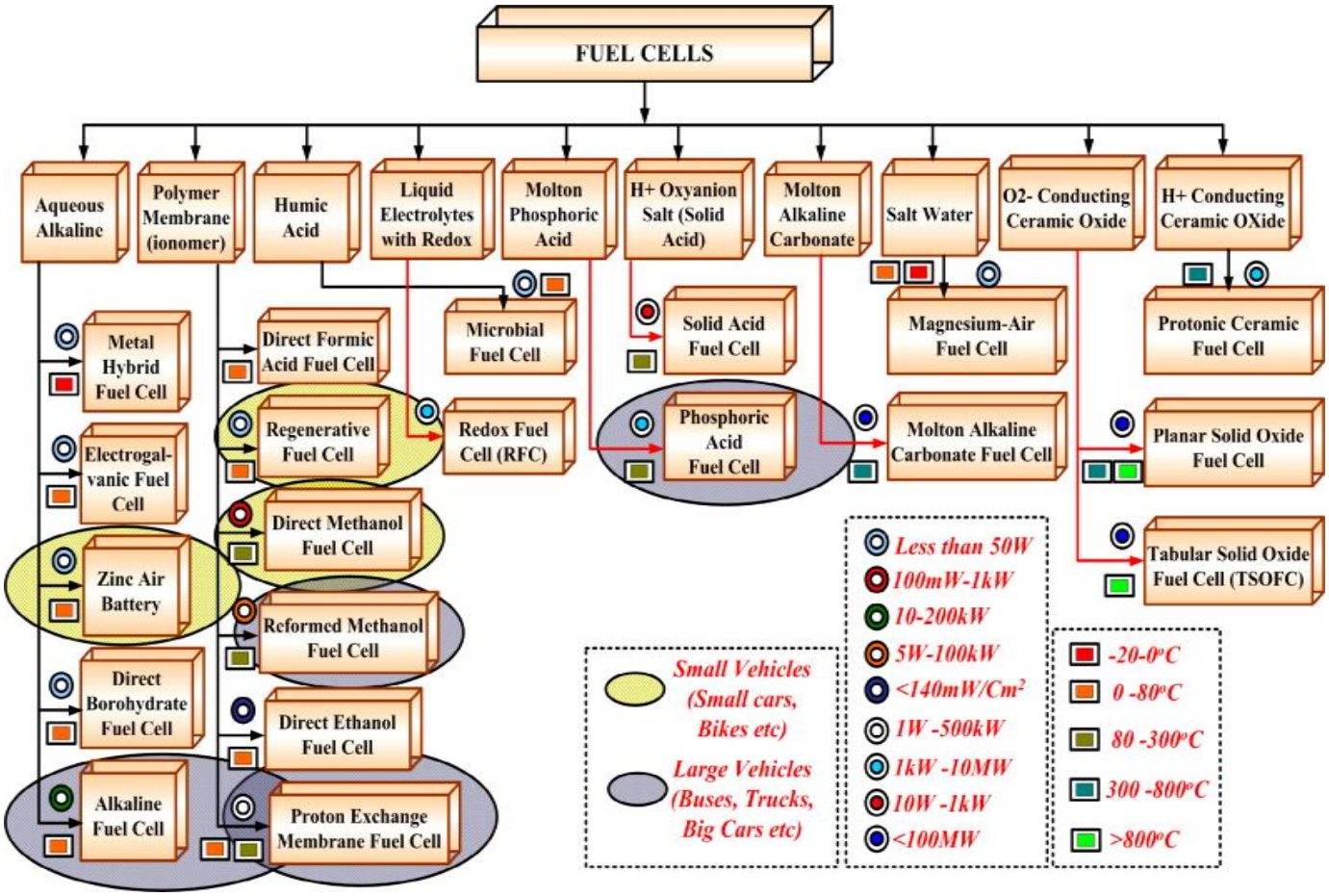

(a) Fuel cells classification

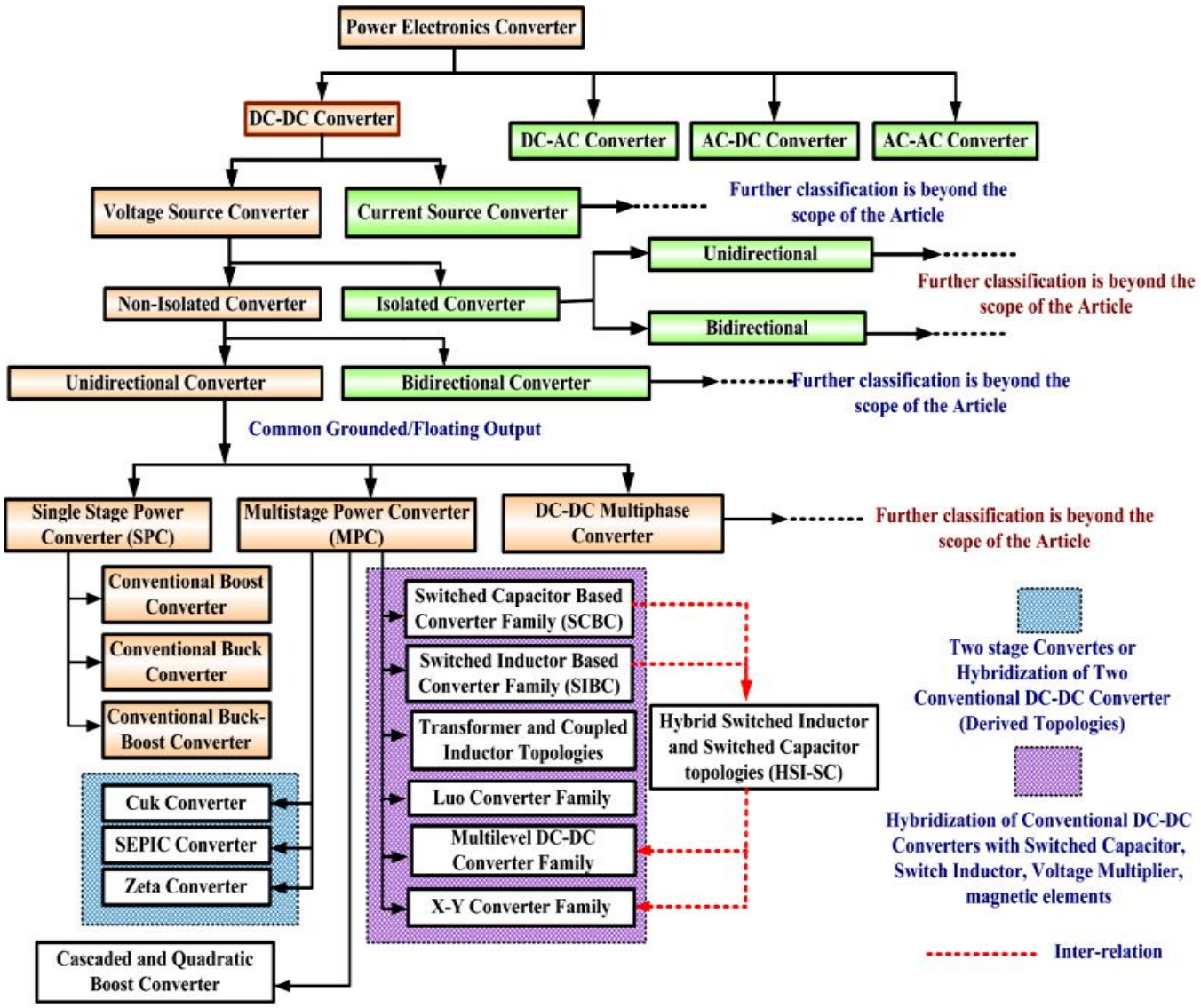

(b) Power converters classification

Figure 2.37: Fuel cells and power converters classifications (adapted from Bhaskar *et al.*, 2020)

2.3.2.21 Performance Analysis of PV and Fuel Cell-based Grid Integrated Power System

Studied in Rathode *et al.* (2019), is a smart grid power generation system constituting solar cells and solid oxide fuel cells (SOFC) hybrid system as shown in Figure 2.38a. The SOFC augments the PV system during power outages due to fault and non-sunny periods. Alternative to SOFC; biomass and wind power systems can be used by integrating them with phase lock loop (PLL) to maintain a constant output supply. The power electronics made used of a DC-DC converter, a three phase DC-AC inverter for interfacing to the electrical grid and AC loads. In addition, is a LC filter to eliminate unwanted signals in the power system. The energy management techniques used include P&O MPPT as well as reference frame theory and PLL to enable a reliable power supply. Figures 2.38b-2.38c respectively show the PV and SOFC schemes.

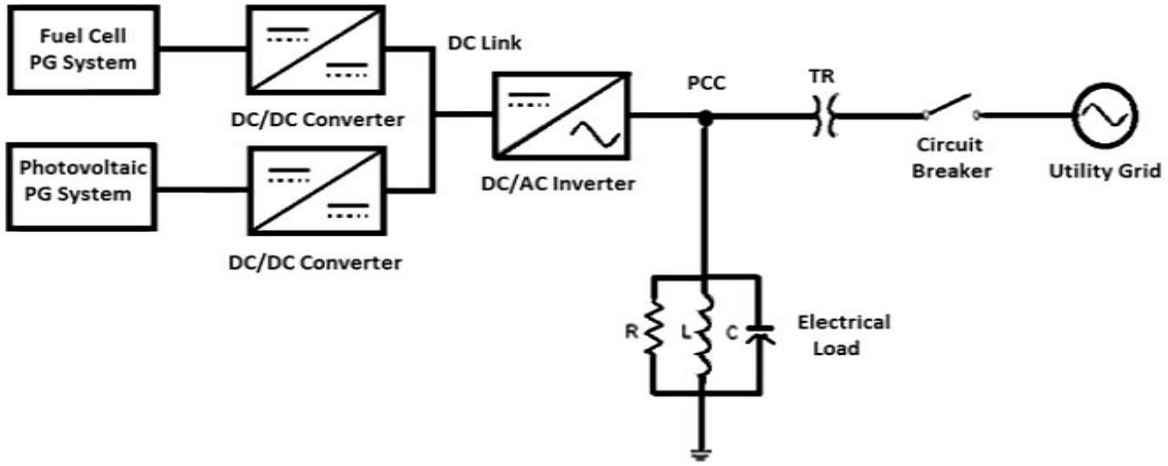

(a) Concept overview

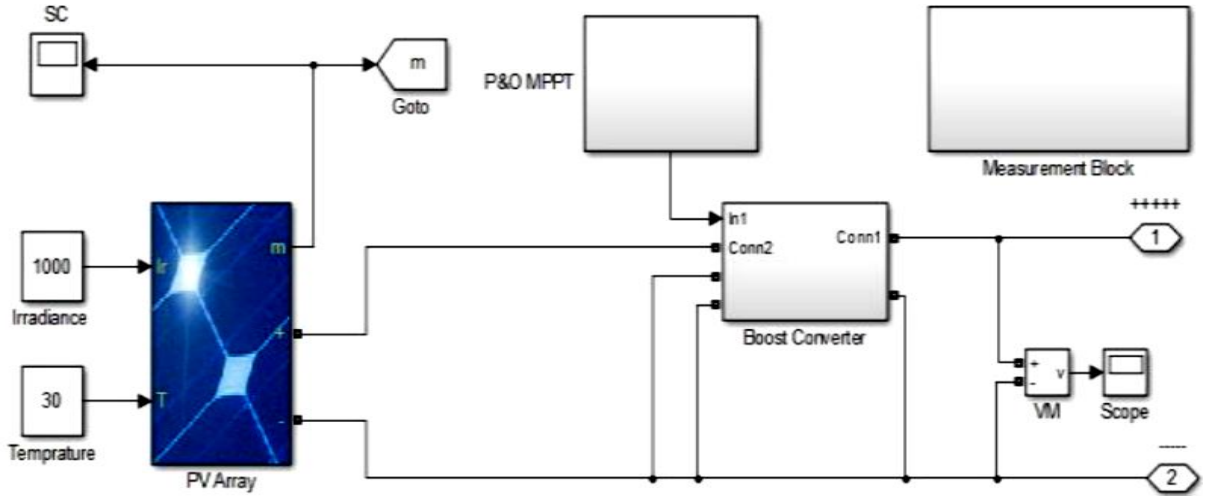

(b) Solar cell power system modeled with Matlab

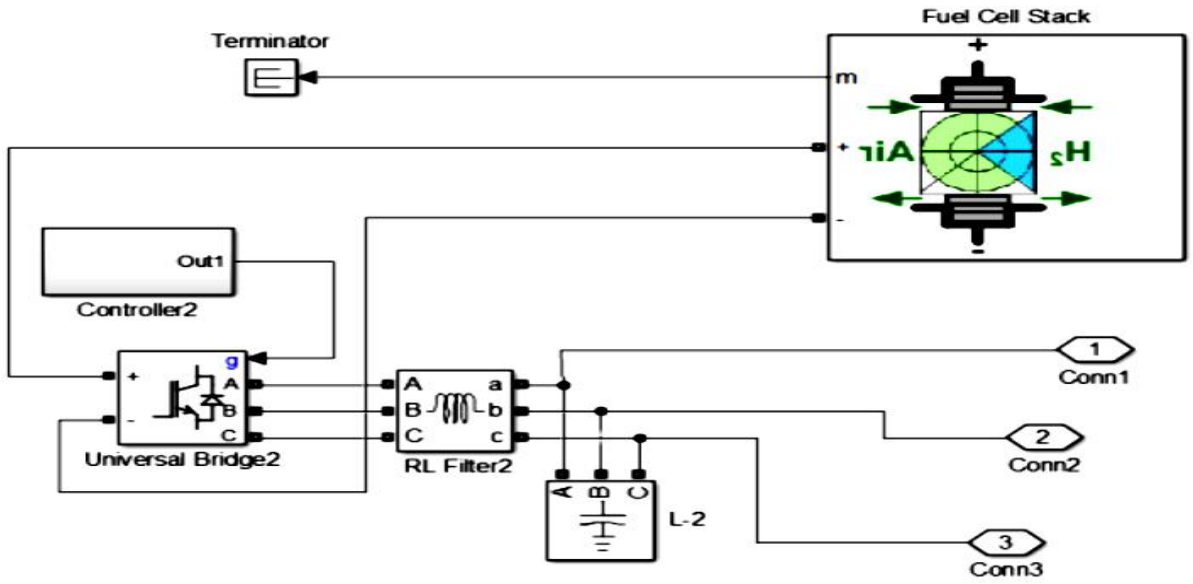

(c) Fuel cell power system modeled with Matlab

Figure 2.38: System concept design, PV and fuel cell power systems depictions (adapted from Rathode *et al.*, 2019)

2.3.2.22 Modeling and Simulation of DC-DC Converters for Fuel Cell Systems

Affirmed in Kavyapriya and Kumar (2020), FC is the future renewable energy source, especially for portable applications. Fuel cells as a result of their low output voltage, require highly efficient power converters; thus, their research using Matlab, focused on the modeling and simulations of four types of DC-DC converters, namely i) boost, ii) SEPIC, iii) LUO and iv) ZETA. Their study was tested using the same fuel cell output voltage of 12V, connected to each converter input with each converter output voltage set at 48V. It was found that the ZETA topology offers the best total harmonic distortion (THD), followed by LUO, SEPIC and Boost with respective THD of 31.22%, 53.83 %, 65.38 % and 80.22 %. It was furthermore concluded that the ZETA topology THD performance can be improved with the addition of more filtering components. Figures 2.39a - 2.39c embody the SEPIC, LUO and ZETA DC-DC power converters modeled using Matlab and Simulink.

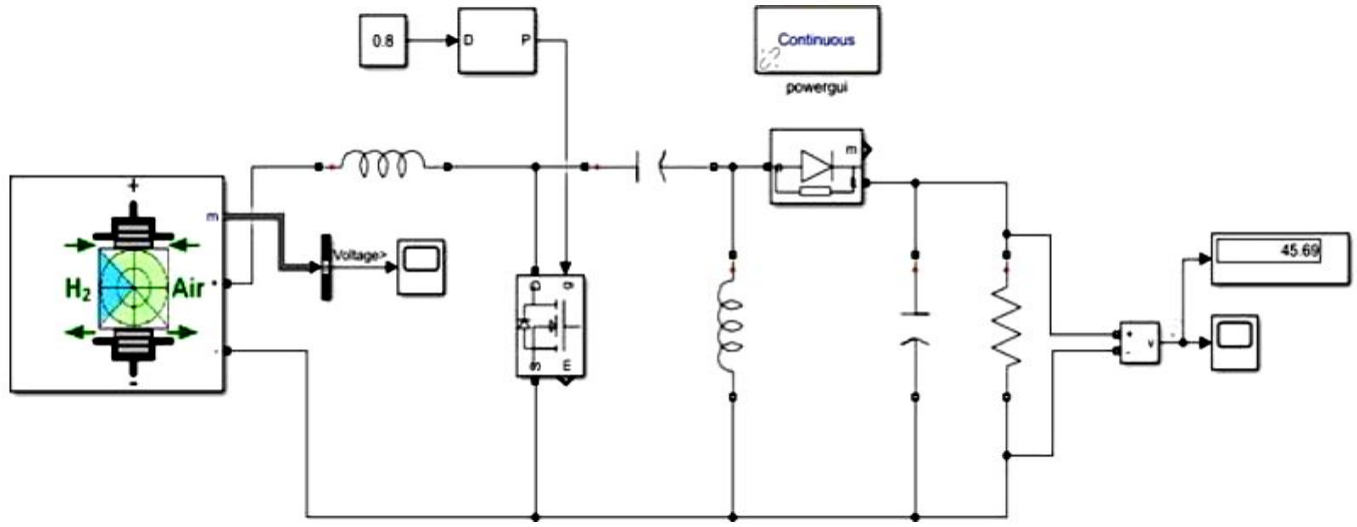

(a) Fuel cell with SEPIC DC-DC converter simulation model

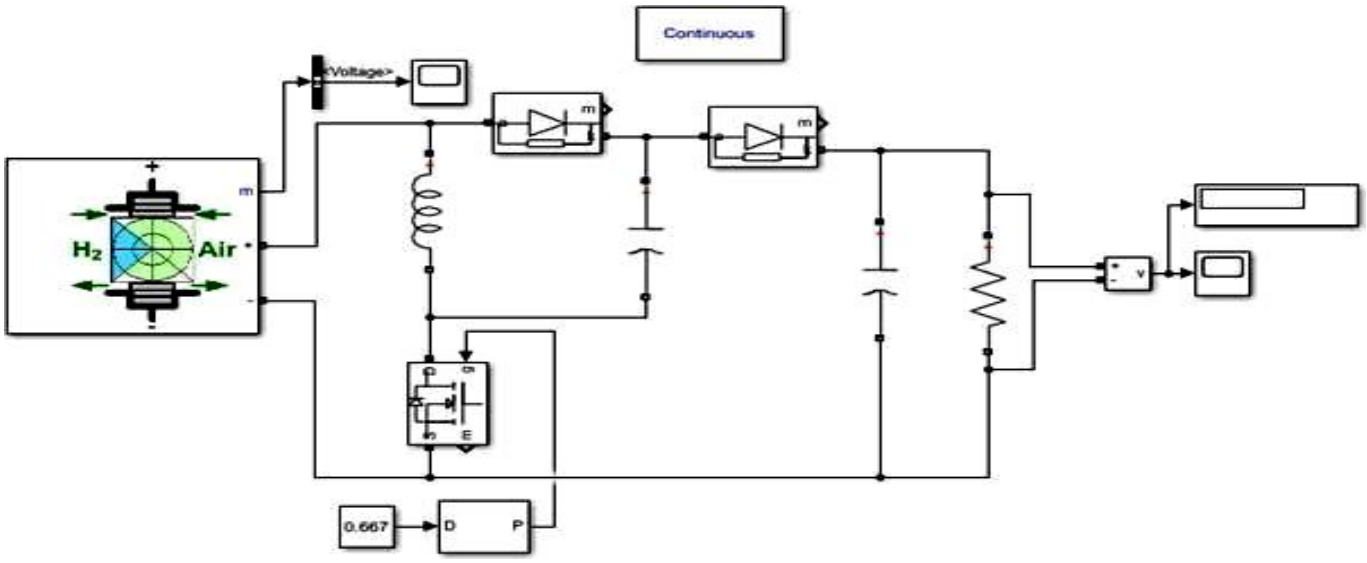

(b) Fuel cell with LUO DC-DC converter simulation model

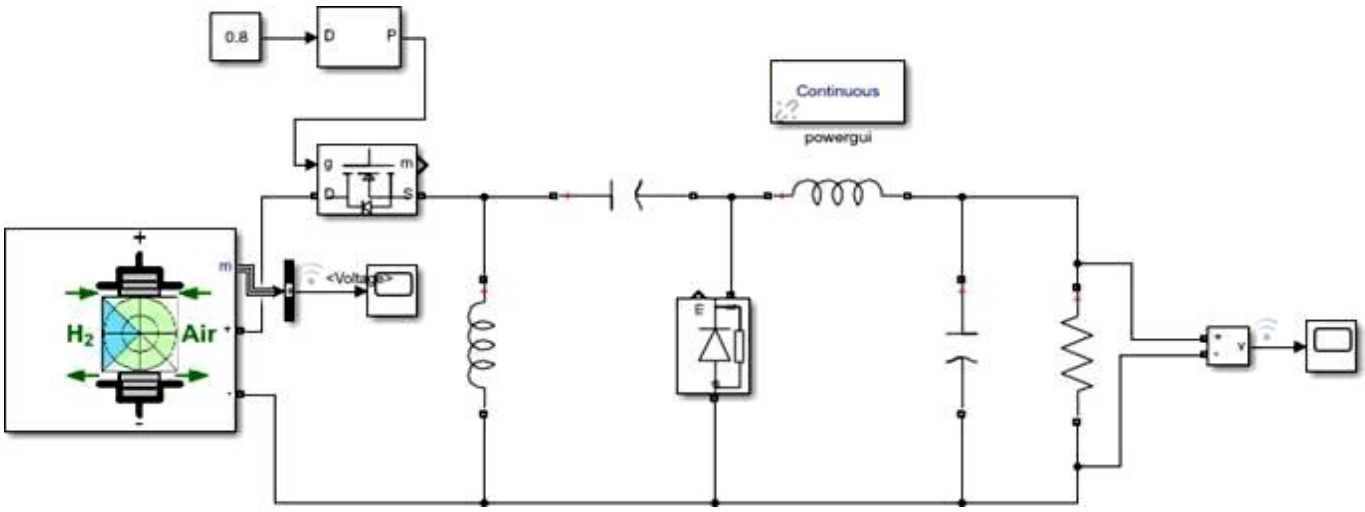

(c) Fuel cell with ZETA DC-DC converter simulation model

Figure 2.39: Simulink model of FC with SEPIC, LUO and ZETA DC-DC power converters topology (adapted from Kavyapriya & Kumar, 2020)

2.3.2.23 Smart Fuel Cell Module (6.5 kW) for a Range Extender Application

Researched in Bazin *et al.* (2020) using SolidWorks, is a 6.5kW fuel cell model with a mechanically integrated 6-phase interleaved DC-DC boost converter for electric vehicles applications. The design constraints were such that the power converter was mounted on the fuel cell terminal plates and cooled using the same FC cooling system as shown in Figures 2.40a and 2.40b. The choice of the power converter topology was driven by the simplicity of its design, since the converter must fit on the FC terminals as well as the fuel cell configuration. As a result, the classic boost converter was chosen, as it employed the minimum components count and furthermore the phase inductors and switching devices can be respectively connected directly on the FC positive and negative plates as pictured in Figure 23b. Continuous conduction mode was chosen for the converter and the ripple was minimal. To conclude their study, the measured converter efficiency was >95% for a minimum output power of 1.5kW and output voltage of 240V. Future work for an aircraft use was considered.

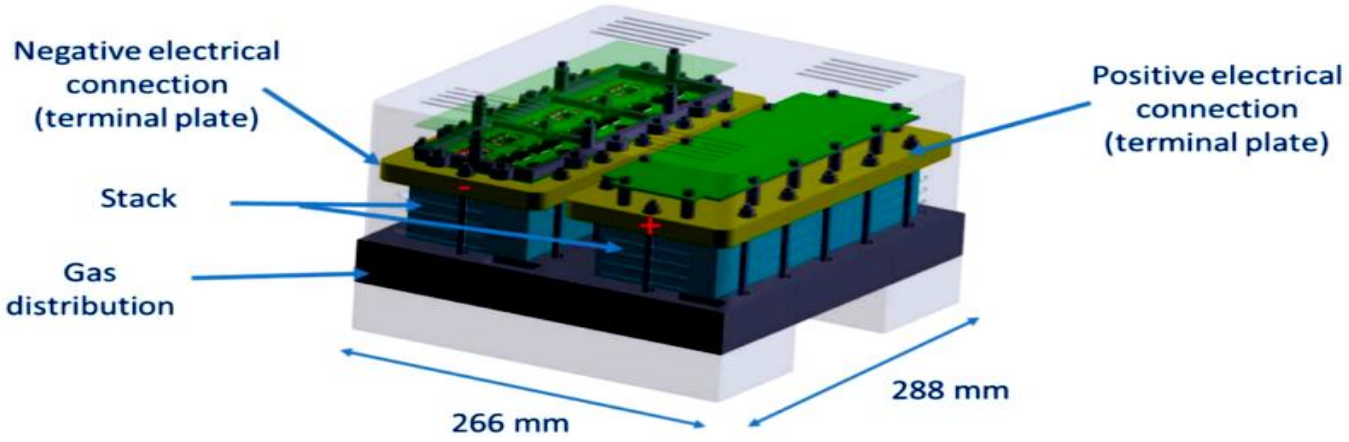

(a) Fuel cell concept design modeled with SolidWorks

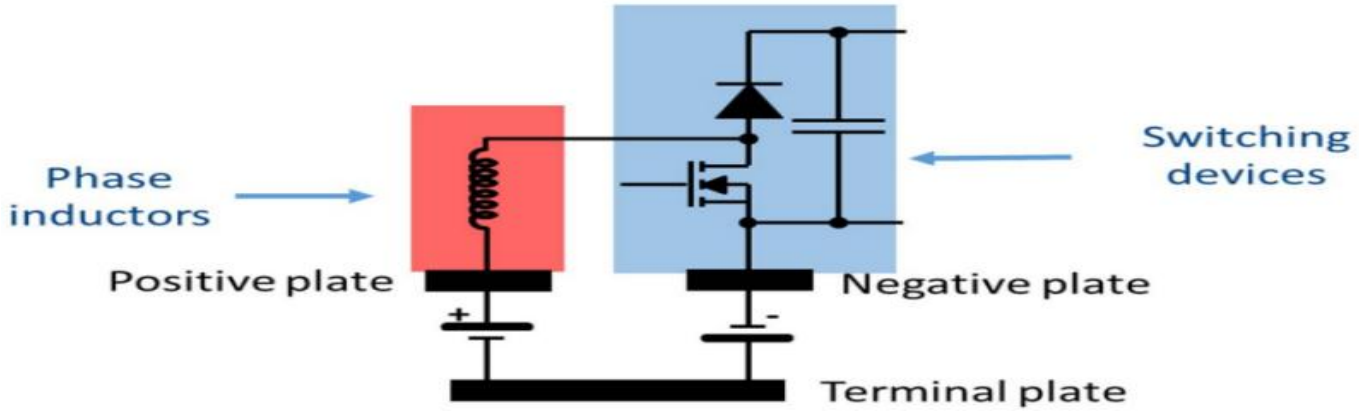

(b) Integration of the power converter on the fuel cell plates

Figure 2.40: SolidWorks model of the FC with integrated power converter (adapted from Bazin *et al.*, 2020)

2.3.2.24 Power Converter Topology for Conditioning a Fuel Cell Battery Voltage

Stated in Gonnet *et al.* (2019), their research conditioned the output voltage of a FC battery using DC-DC boost converter. The main novelty was to substitute the classic boost converter inductor (L) with an inductor-capacitor-inductor (LCL) filter topology as shown in Figure 2.41. The output voltage was then controlled using a sliding mode strategy including a load impedance observer. The simulated results showed good performance with varying loads.

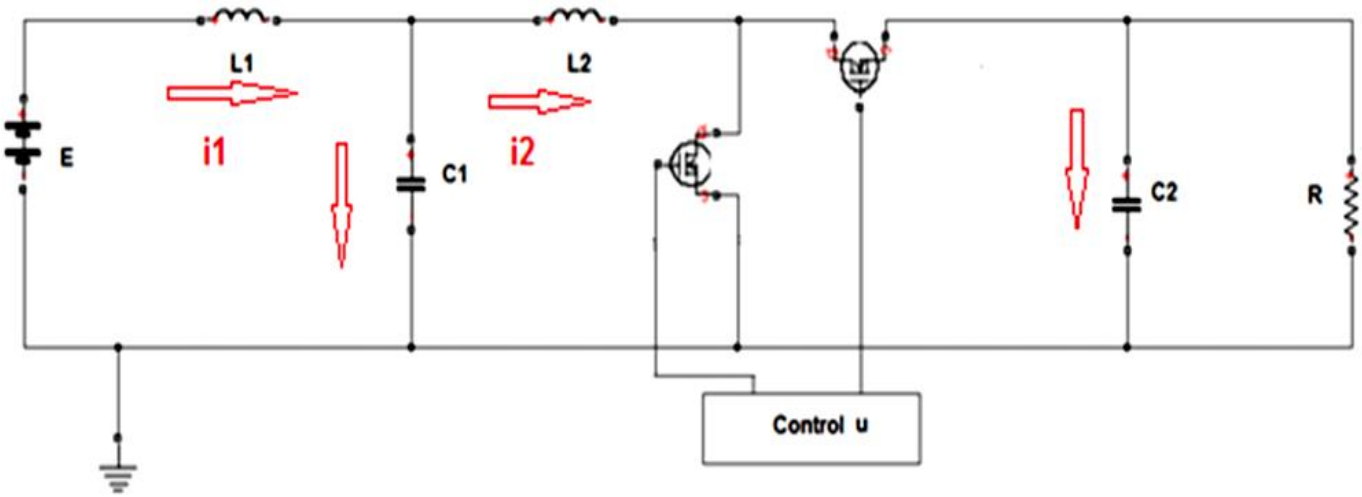

Figure 2.41: LCL boost DC-DC power converter (adapted from Gonnet *et al.*, 2019)

2.3.2.25 Modeling and Simulation of an Aerodrome Electrical Power Source Based-on Fuel Cells

Examined in Corcau *et al.* (2019), reducing fuel usage and emissions such as NO_x, is aviation present challenge. As a result, there is the need to develop latest power sources using non-polluting sources such as Hydrogen fuel cells. Their work presented the modeling and simulation of a potential configuration for a hybrid aerodrome fuel cell power source. Their postulated architecture consists of a fuel cell stack, DC to DC set-up converter, super-

capacitor and a buck-boost converter. The fuel cell and super-capacitor are respectively connected to a boost and buck-boost converter as correspondingly shown in Figures 2.42a and 2.42b. With this set-up, the fuel cell with slower power dynamics, supplies the bulk of the power during steady state operation, whereas the super-capacitor with a faster power dynamics, assist the fuel cell during peak power transient demand as well as stores power from the DC bus. The suggested configurations were simulated using Matlab, Simulink and Simscape Power Systems and it can be summed that the hybrid power aerodrome source shown in Figure 2.42c, can work efficiently, enabling its use for such long-term applications.

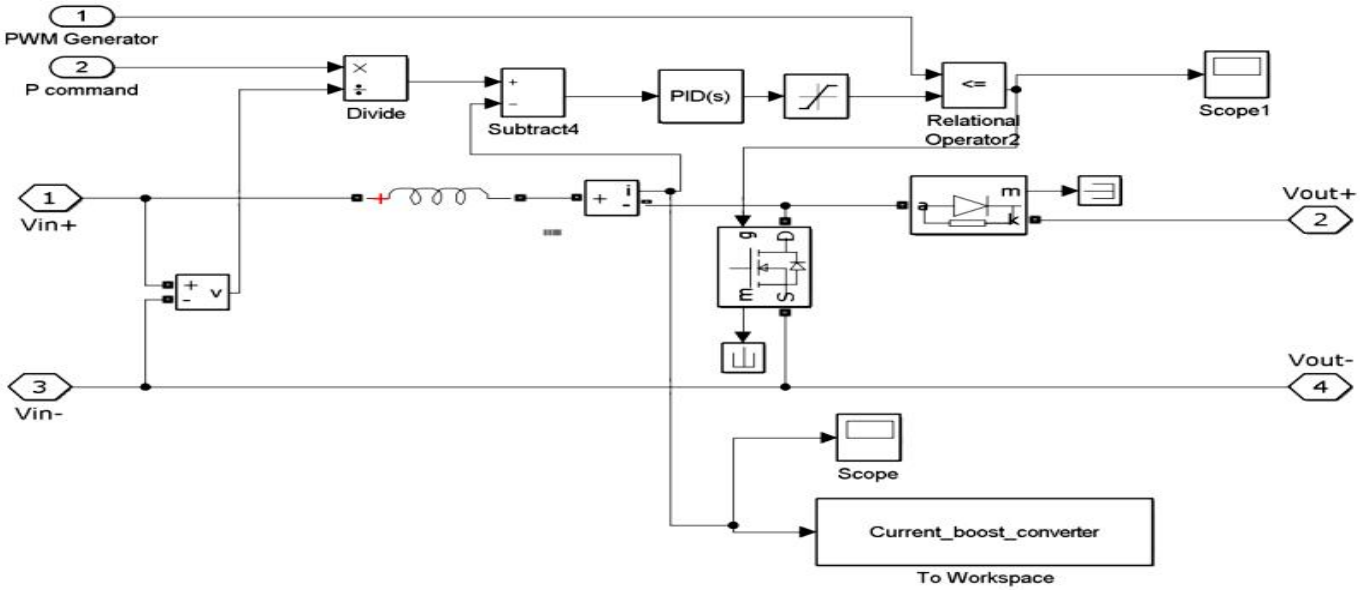

(a) Fuel cell with boost DC-DC converter

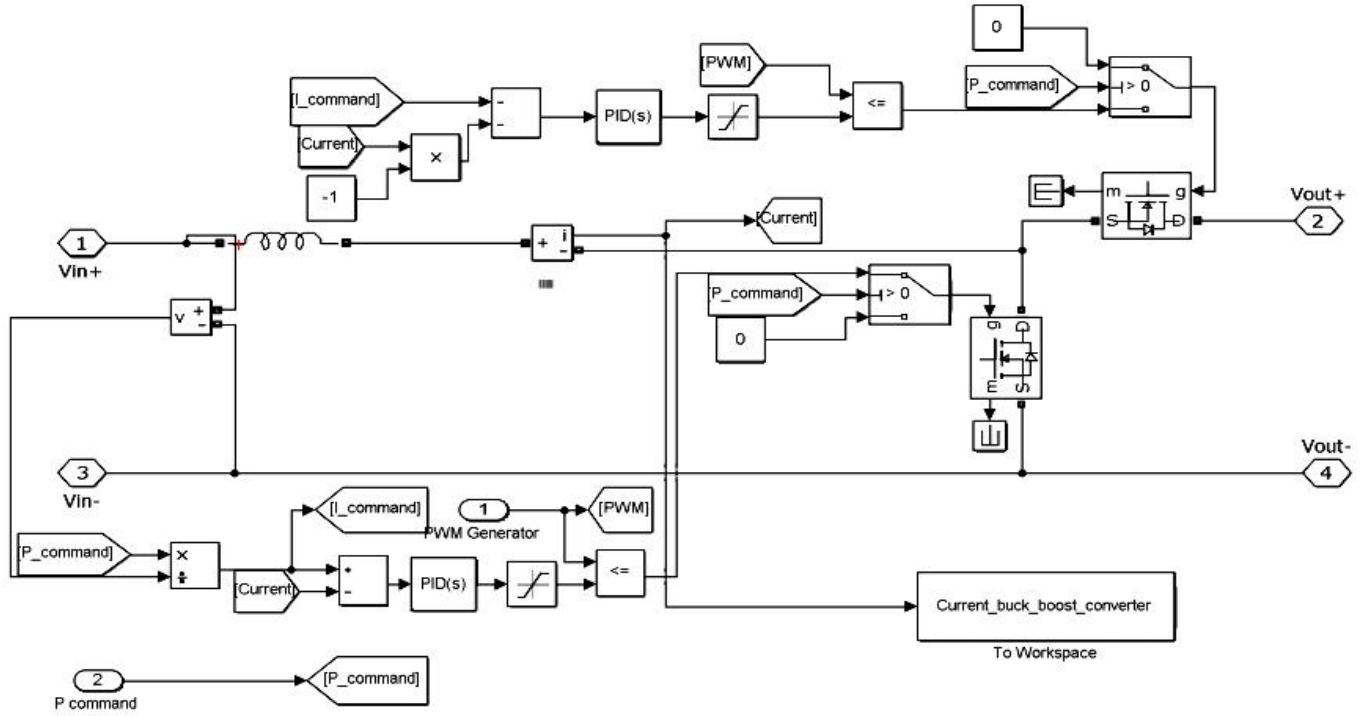

(b) Super-capacitor with buck-boost DC-DC converter

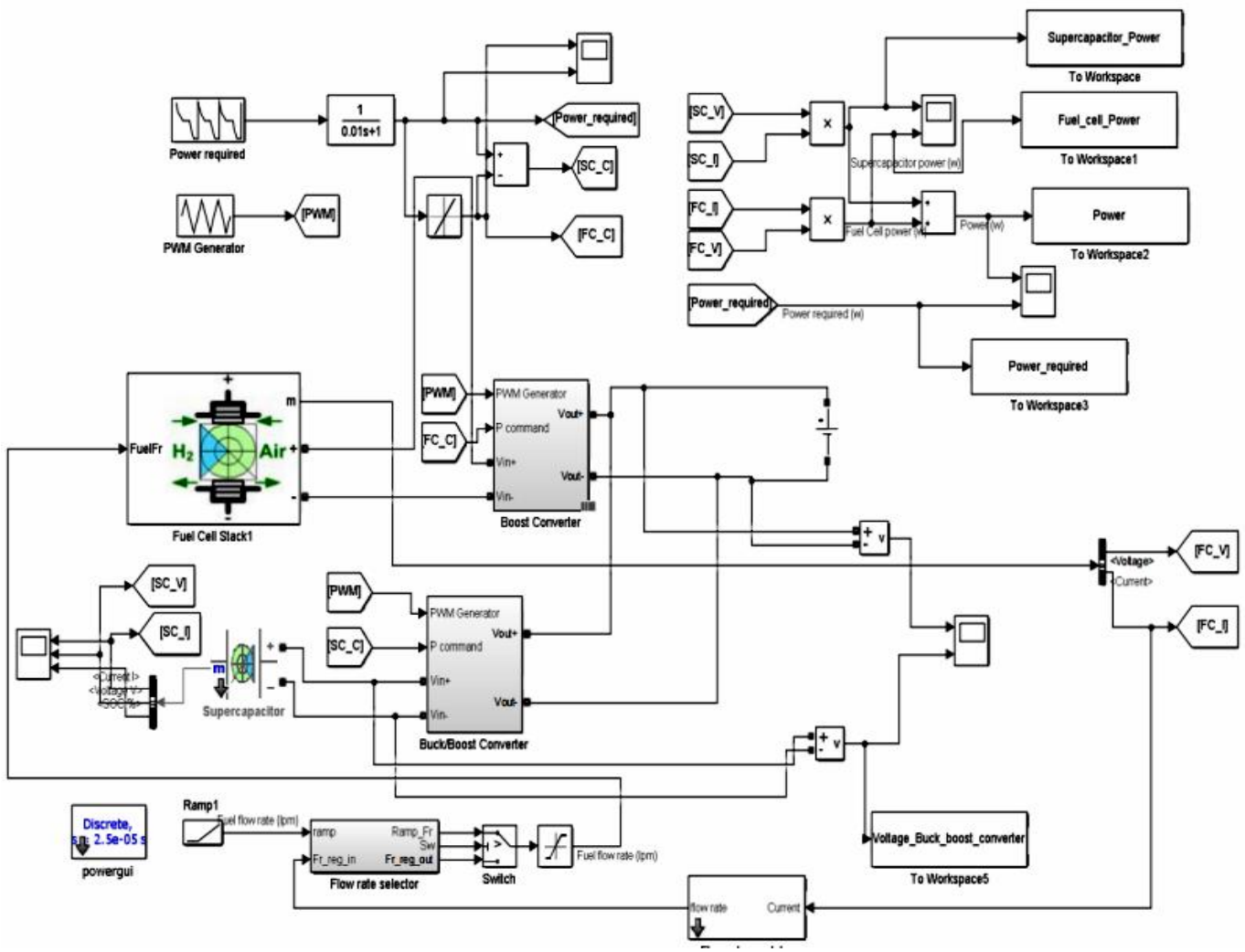

(c) Fuel cell and super-capacitor with boost and buck-boost DC-DC converters

Figure 2.42: Hybrid fuel cell and super-capacitor power System with respective boost and buck-boost DC-DC converters (adapted from Corcau *et al.*, 2019)

2.3.2.26 Current-fed Modular Multilevel Converter (CMMC) for Fuel Cell and PV Integration

Indicated in Abdelhakim and Blaabjerg (2020), is a CMMC single-stage solution to interface a low voltage photovoltaic and fuel cells DC power supplies to a higher voltage AC load and or grid. Usually, power conditioning stage (PCS) in the form of modular multilevel converters, have been used in various low to high voltage applications with good results. However, their two-stage configuration makes them bulky, hence the need for CMMC — whereby the boosting capability is integrated within the inversion, making it a single-stage DC-AC converter / inverter with additional redundancy and modularity. This enables it use in low voltage applications, where low voltage MOSFETs with low ON-state resistance can be used to increase the power conversion efficiency. A 10kW three-phase CMMC using PLECS, was simulated to verify its functionality. Figures 2.43a and 2.43b depict the traditional two-stage DC-AC using (a) a boost converter before the inversion and (b) a step-up transformer after the inversion. Figure 2.43c exemplifies the single-stage CMMC.

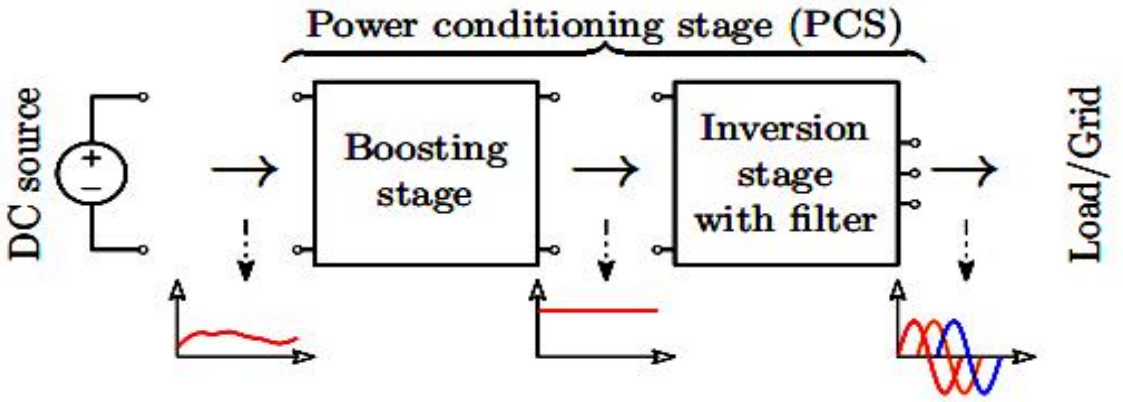

(a) Two-stage DC-AC with boost converter before the inversion

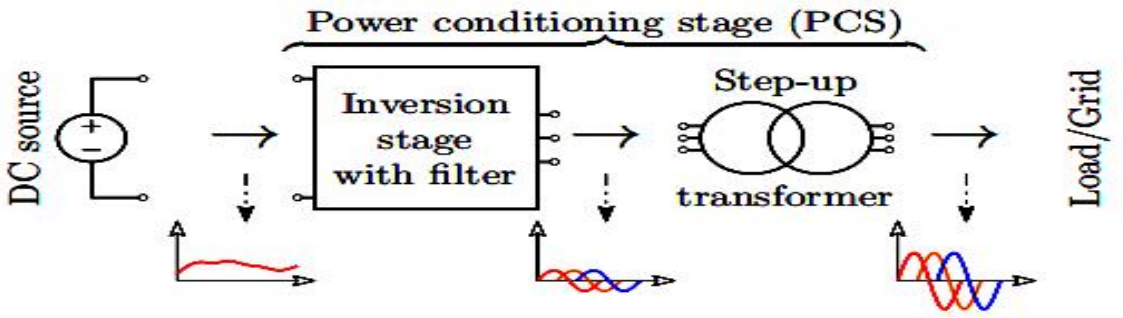

(b) Two-stage DC-AC with step-up transformer after the inversion

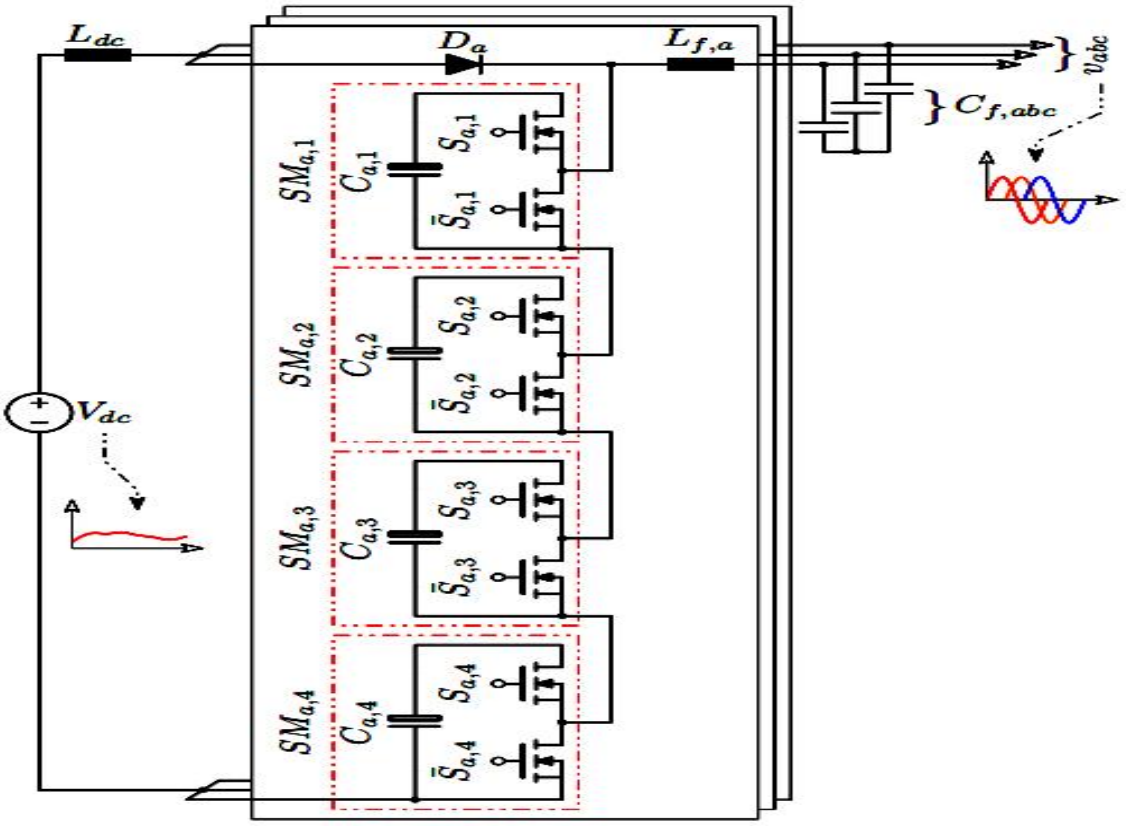

(c) Single-stage DC-AC three-phase CMMC with four sub-modules per phase

Figure 2.43: Two-stage traditional and single-stage CMMC DC-AC inverters (adapted from Abdelhakim & Blaabjerg, 2020)

2.3.2.27 Novel Four-Port DC–DC Converter for Interfacing Solar PV–Fuel Cell Hybrid Sources with Low-Voltage Bipolar DC Micro-grids

Presented in Prabhakaran and Agarwal (2020), is a bipolar DC micro-grid (BDCMG) power supply system based on a novel 4-port dual-input dual-output DC-DC converter to interface fuel cells, PV and wind power sources to a low voltage BDCMG. Usually, a BDCMG requires several traditional DC-DC power converters to supply power to the BDCMG poles; however, their researched model in addition to being reliable and efficient, is also compact and unidirectional. It can also function as a single-input dual-output converter as well as with two degrees of freedom using its two switches. Furthermore, the duty cycle changes has no effects on the converter dynamic model; thus, the converter can be controlled with just one controller in different modes, making it less complex. By deriving a small signal model for each operating mode, the converter control system was designed. MPPT was used to track the PV voltage and inductor current without needing an extra PV sensor. Its steady and dynamic states operations were validated using close and open loops results.

In-lined with both simulations and theoretical analyses, they observed that the 24V pole voltage and the photovoltaic power are maintained under different conditions (such as during solar irradiation fluctuations and transient load power demands); thus, validating the converter design performance and reliability. The converter was found to have a 93% peak efficiency and ~87% rated power efficiency. Figure 2.44a exemplifies the proposed BDCMG power scheme and Figure 2.44b depicts the converter topology whereas Figure 2.44c shows a different load configuration.

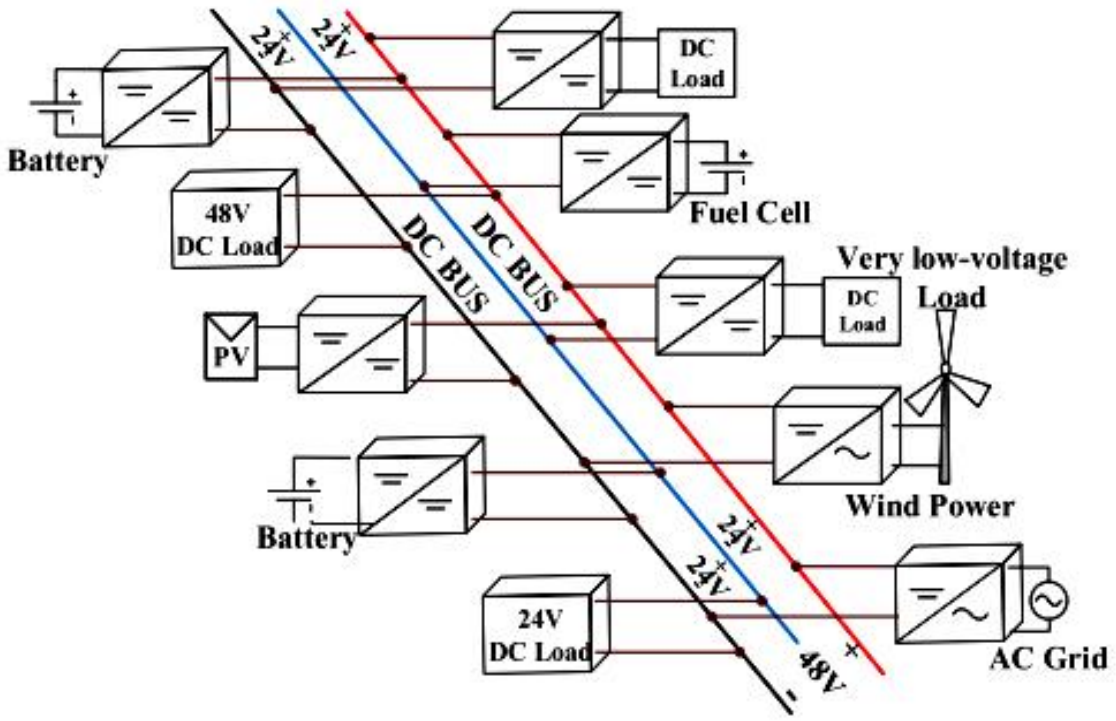

(a) Low-voltage (48V) BDCMG system.

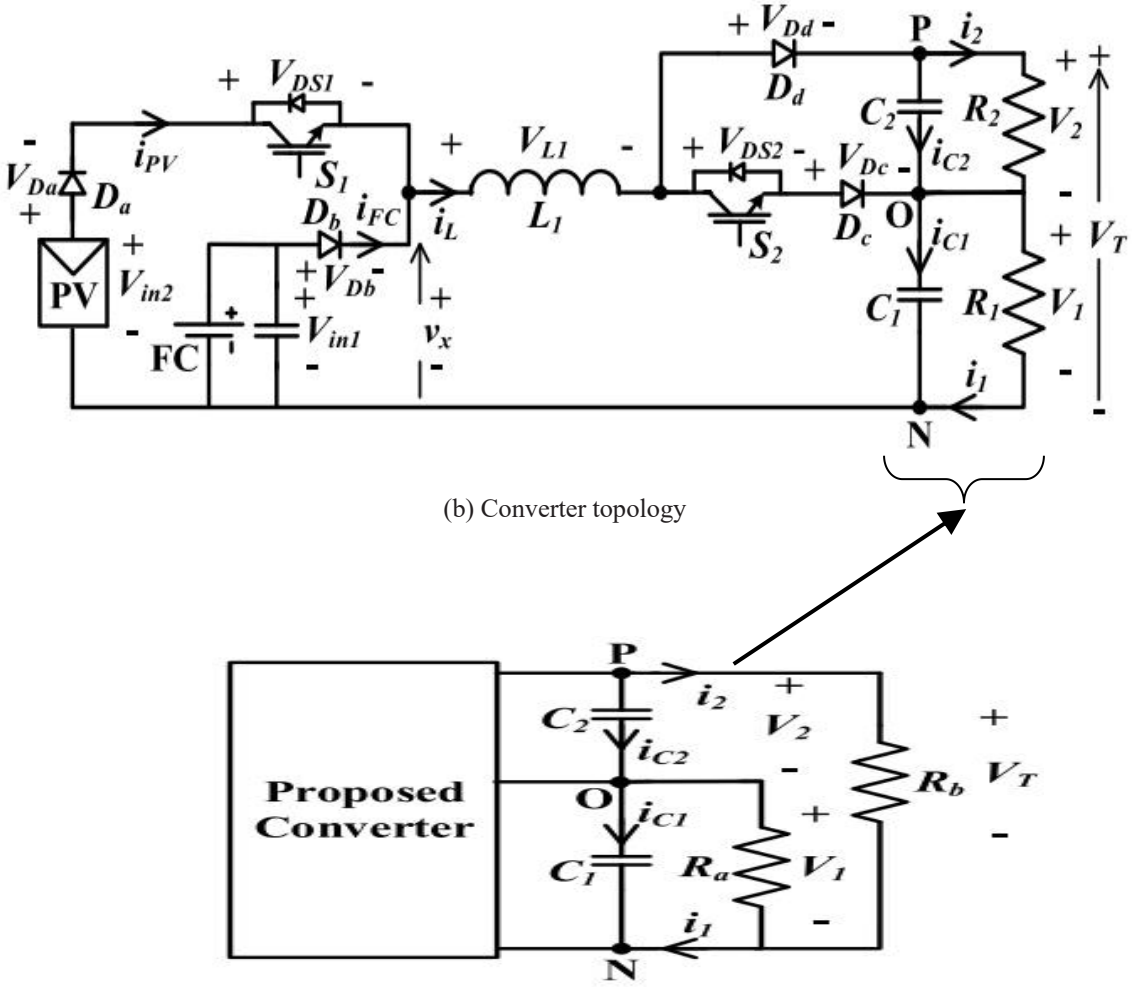

(b) Converter topology

(c) Converter topology with alternative load representation

Figure 2.44: BDCMG system and converter topologies (adapted from Prabhakaran & Agarwal, 2020)

2.3.2.28 Study on Boost Converters with High Power-Density for Hydrogen-FC Hybrid Railway System

Investigated in Youn *et al.* (2020) is a high power hybrid hydrogen fuel cell railway system portrayed in Figure 2.45a − with focus on designing an efficient and high power density DC-DC converter, since fuel cells are normally low DC power sources and can not supply the needed 1500V to drive the inverter input needed for the railway traction AC motors. Therefore, two DC-DC power converters, namely the interleaved boost converter shown in Figure 2.45b and the three-level boost converter depicted in Figure 2.45c, were researched to determine the most suitable DC-DC boost power converter architecture. Taking into considerations and also using optimal design methods were the boost inductor, output capacitor and power semiconductor devices performances with respect to the hybrid railway specifications. Both power converters designs were verified with a 600V input and 1200V / 20kW output setup and the results concluded that the three-level boost converter performed better in-terms of the efficiency, power density and dynamic current response. As a result, it was chosen as the most suitable topology for the hybrid hydrogen fuel cell rail system.

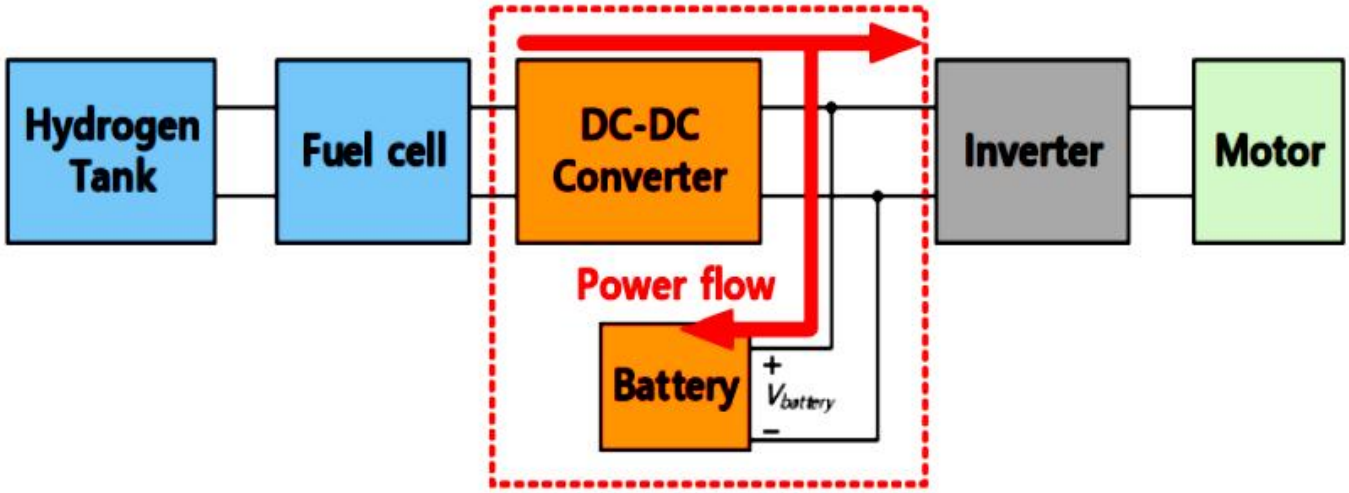

(a) Propulsion system for hybrid hydrogen-fuel-cell railway system

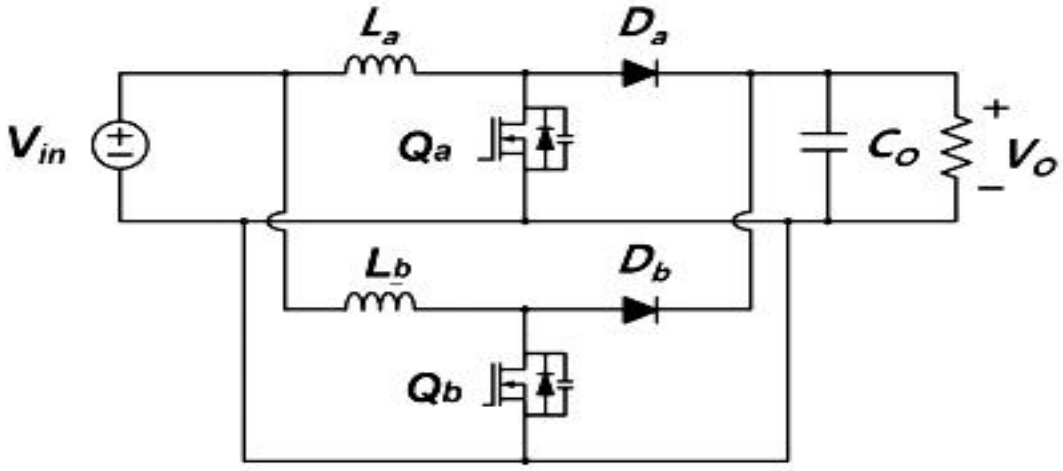

(b) High step-up DC-DC interleaved boost converter (IBC)

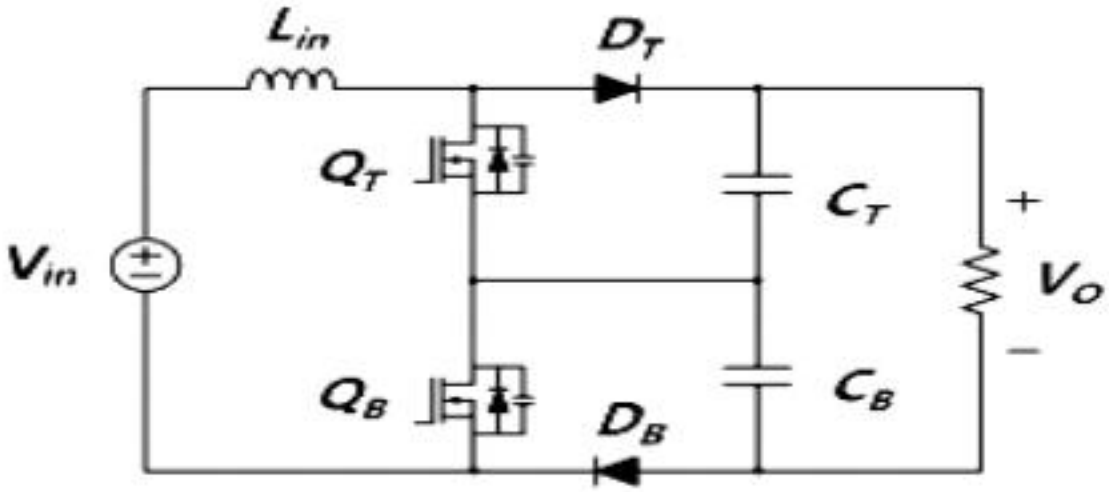

(c) High step-up DC-DC three-level boost converter

Figure 2.45: Concept design with high step-up DC-DC IBC and three-level boost converter (adapted from Youn *et al.*, 2020)

Table 2.6 summarizes the fuel cells power converters studies reviewed − in which the major highlights, advantages and disadvantages of each where applicable, are briefly recapitulated.

Table 2.6: Power converters studies examined summary (adapted from Bayendang *et al.*, 2020a / 2021a)

Power Converters	Highlights, Merits and Demerits
Study 2.3.2.1 (Kolli A. *et al.*, 2015)	Various FCs DC-DC power converters setups. Emphasis on different types of interleaved converters for high, medium and low power uses. FCs in parallel /series raise output power.
Study 2.3.2.2 (Kabalo M. *et al.*, 2010)	FC vehicles cutting edge DC-DC converters. High voltage ratio, compactness and efficiency with affordability, should be used to implement power converters. Presented different schemes.
Study 2.3.2.3 (Delshad M. & Farzanehfard H., 2011)	ZVS current fed push-pull DC-DC converter. When power is off, voltage surge across the switch is absorbed. This improve its efficiency and compactness to enable basic PWM control.
Study 2.3.2.4 (Bizon N., 2011) [15]	A new architecture of FC HPS for efficient functioning and better steadfastness. HPS with active MPPT and hysteretic current controls were used to minimize ripple current from FC.
Study 2.3.2.5 (Ahmed O.A. & Bleijs J.A.M., 2013)	For an UC in DC micro-grids, a bidirectional voltage-fed setup is preferred for quick dynamic response, though for a broad input voltage instability at the UC, there is greater circulating power flow and conduction losses.
Study 2.3.2.6 (Carvalho A. *et al.*, 2011)	Modeled a PEM FC using Matlab. Noted the preferred model must take control and optimise the FC operation points. Soft switching based on series resonant and SA was used, as it reduces switching losses and boost efficiency.
Study 2.3.2.7 (Mwaniki F.M., 2014)	Multi-phase tapped-coupled inductor suited for varying high power DC-DC converter uses. Showed minimal input & output power ripples.
Study 2.3.2.8 (Huangfu Y. *et al.*, 2015)	High power efficiency step-down converter for discrete wind power supply scheme, akin PV. Achieved a 2kW supply with 96% efficiency with step-down ZVS/LCD scheme with MPPT.
Study 2.3.2.9 (Seyezhai R. *et al.*, 2013)	Interleaved converters with switched capacitor are considered the suitable topology for FC systems, because of reduced ripple power in the input and output, quicker transient reaction, small EMI, enhanced efficiency and reliability.
Study 2.3.2.10 (Nymand M. & Andersen M.A.E., 2008)	A new low-leakage inductance low-resistance design approach to low-voltage high-power isolated boost converters. Poorest efficiency at minimum input voltage with maximum power was ~97%. The maximal efficiency was ~98%.
Study 2.3.2.11 (Eckardt B. *et al.*, 2005)	FC automotive power-train application using high current buck-boost DC-DC converter with digital control to render apt protection against over-current, over-voltage & over-temperature.
Study 2.3.2.12 (Kirubakaran A. *et al.,* 2009)	PEM FC setup with DC-DC step-up converter: Design, modeling and simulation. For instant load fluctuation from 0.6 – 1.1kW, the FC current and voltage took ~50 - 70ms (fuel starvation) to attain a new steady state. The altering voltage was tracked with PI controller.
Study 2.3.2.13 (Outeiro M.T. & Carvalho A., 2013)	A method to devise power converters for fuel cell rooted schemes using resonant technique. Independent voltage and PEMFC controllers. Enhanced FC efficiency by managing FC P_{out}.
Study 2.3.2.14 (Wang H., 2019)	Devise and management of a 6-phase IBC rooted in SiC with EIS functionality for FC HEV. IBC dynamic model with HIL real-time.
Study 2.3.2.15 (Fanjul L.M.P., 2006)	Design deliberations for DC-DC converters in FC schemes. Used analytical and experimental schemes to achieve a steady and efficient FC & power converter system. A modular FC stack and DC-DC converter were pioneered by dividing it into autonomous optimal sections.

Power Converters	Highlights, Merits and Demerits
Study 2.3.2.16 (Ravi D. *et al.*, 2018)	IBC and BDC were researched. IBC improves power ripples. The more the interleaving, the better the ripple reduction; though, the more costly. BDC can charge storage devices and furthermore, the isolated types offer galvanic protection in high power uses; however, their large size makes them unfit for portable uses.
Study 2.3.2.17 (Gao J. *et al.*, 2019)	FCs have various challenges and the best solution is one that is inclusive with various hardware and software solutions to optimize better FCs costs, performance and longevity.
Study 2.3.2.18 (Liu H. *et al.*, 2020)	Investigated a high power fuel cell system. Two test setups were used; a i) rated and ii) cycle working condition tests and found that fuel cell power engine reached 80kW at rated power with the peak power exceeding 100kW.
Study 2.3.2.19 (Miyazaki R. *et al.*, 2020)	A current-fed snubber-less ZCS FC high step-up DC-DC converter was studied. It achieved a greater voltage boost ratio and low power ripple, making it suitable for smart homes use.
Study 2.3.2.20 (Bhaskar M.S. *et al.*, 2020)	Reviewed extensively and comprehensively in theory and topologically, the different types of fuel cells with focus on the use of fuel cells in FCEV power-trains. Miscellaneous types of power converters were also assessed in details.
Study 2.3.2.21 (Rathode K.S. *et al.*, 2019)	Researched a hybrid PV and FC system. The power electronics used a DC-DC converter, a three phase DC-AC inverter for interfacing to the electrical grid and AC loads with P&O MPPT as well as reference frame theory and PLL to enable a reliable power supply system.
Study 2.3.2.22 (Kavyapriya S. & Kumar R.K., 2020)	Modeled and simulated four step-up power converters schemes. Found that the ZETA topology offers the best THD, followed by LUO, SEPIC and Boost with THD of 31.22%, 53.83 %, 65.38 % and 80.22 % respectively.
Study 2.3.2.23 (Bazin P. *et al.*, 2020)	Implemented a smart FC with built-in DC-DC power converter. The classic boost converter with 6-phase interleaving was chosen, as it fitted well, efficient & offered least parts used. The efficiency was >95% for a nominal output power of ~1.5kW and output voltage of 240V.
Study 2.3.2.24 (Gonnet A. *et al.*, 2019)	Studied power converter topology for FC battery voltage conditioning. The classic boost converter inductor was replaced with a LCL filter. Gave good performance at varying loads.
Study 2.3.2.25 (Corcau J. *et al.*, 2019)	Modeled & simulated a hybrid aerodrome FC power source consisting of a FC stack, a boost and buck-boost DC to DC converters as well as super-capacitor to provide clean, stable, peak power and energy dynamics during transients.
Study 2.3.2.26 (Abdelhakim A. & Blaabjerg F., 2020)	Proposed a CMMC single-stage solution to interface a low voltage PV and fuel cells DC power supplies to a higher voltage AC load or grid. This offers better performance and is less bulky, contrary to a two-stage boost converter.
Study 2.3.2.27 (Prabhakaran P. & Agarwal V., 2020)	Presented a BDCMG power supply system based on a novel 4-port dual-input dual-output DC-DC converter to interface fuel cells, PV and wind power sources to a low voltage BDCMG. The converter was reliable, compact, versatile and unidirectional with a 93% peak efficiency and a ~87% rated power efficiency.
Study 2.3.2.28 (Youn H.S. *et al.*, 2020)	Investigated a high power hybrid hydrogen FC railway system with focus on designing an efficient and high power density DC-DC converter. Two DC-DC power converters, namely the IBC and three-level boost converter were researched to determine the most suitable DC-DC boost power converter architecture. The three-level boost converter out performed the IBC in terms of efficiency, power density and dynamic current response and was chosen.

2.3.3 Energy Management Systems / Storage (EMSs)

As examined and summarised in Table 2.7, EMS simply deals with the partial or overall management / control of a device, a section or the entire system – that is, from when, where and how the energy / power is generated, used, processed, converted and or stored. Furthermore, some housekeeping such as thermal management is carried-out as well. The management performed could be i) on-demand (upon users requests or executions as per system dynamics dictates), ii) on-schedule (pre-programmed to do certain routine tasks at a particular time) and iii) artificial intelligence (based-on machine learning). Usually, a dedicated microcontroller and or power management chip or an adequate computing platform is used to optimally process and execute advanced control algorithms that i) manages power generation devices (fuel cells, solar-cells, wind-farms, TEGs, etc) and supporting systems (water pumps or fans), ii) manages power conversion switching devices (switch ON and Off or pulsing the power ICs or MOSFETs or IGBTs etc as required), iii) monitoring energy storage devices (batteries, super-capacitors / ultra-capacitors etc), iv) controlling the end user applications (e.g. HEV) and finally v) housekeeping (temperature monitoring, timestamp etc) and interacting with the system processes optimally to ensure the closed loop power generation / energy conversion and storage processes are efficient, affordable, quicker, safer and reliable. Examined in what follows are some case studies on power and energy conversions management schemes applicable to fuel cells and suitable for FC CCHP systems.

2.3.3.1 MIL, SIL and PIL Tests for MPPT Algorithm

Investigated by Motahhir *et al.* (2017), a boost converter is necessary to convert DC voltage to another DC voltage (DC-DC). In their research, solar energy was harvested by PV array and tracked for continuous power generation using model based MPPT technique. The converter contained a MOSFET as the converter switch, which is managed by PWM signal. Once the MOSFET switch is ON, the energy from the PV module is stored in the inductor and the reverse biased diode disengages the output from the PV generator while the output capacitor supplies current to the load. Conversely, when the MOSFET switch is OFF, the inductor is in a discharge state and forward biases the diode to engage the output to the PV generator. The PV panel voltage and inductor voltage (discharging state) combine to give the output voltage, which is always more than input voltage, hence boost conversion. The study was systematically performed in three stages as follows i) model-in-the-loop (MIL), ii) software-in-the-loop (SIL) and iii) processor-in-the-loop (PIL) as depicted in Figure 2.46 − whereby an algorithm with tailored variable step was modeled and connected to a simulated PV panel and a boost converter. The MPPT model was simulated first using Simulink and the process is called MIL as shown in Figure 2.46. The result acquired using MIL test under STC was asserted in the study and as presented in the steady state, the PV power is equal to 60.54W which is the highest power of the Solarex MSX-60 panel under STC (1,000W/m² and 25°C). The study first demonstrated the MIL test result when the irradiance was raised from 500 to 1000 W/m², then reduced to 800W/m² and finally to 600W/m² − the tailored algorithm gave quicker

response during irradiance changes and the steady-state oscillations were almost negligible. The algorithm was changed from MIL format to SIL and the same irradiance test pattern repeated again to test the MPPT tracking and the same result was achieved similar to that of MIL. Finally, the code was changed to PIL format and the same irradiance test pattern repeated again to test the MPPT tracking using hardware-in-the-loop as illustrated in Figure 2.46, which also gave the same result. This concludes that the implemented MPPT algorithm is accurate, as all the three algorithm formats gave the same outcomes. This approach can be applicable also to fuel cells.

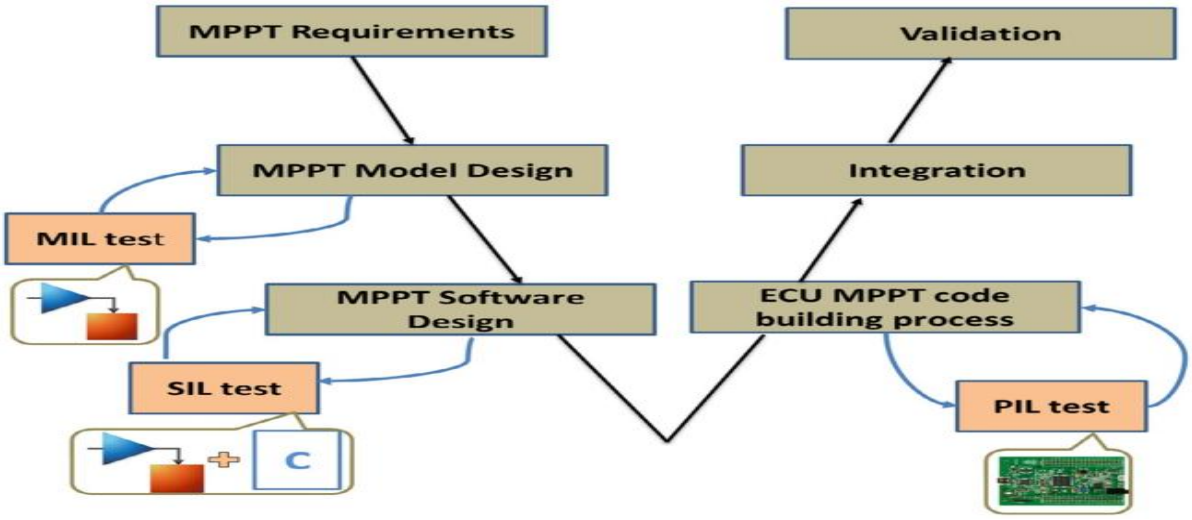

Figure 2.46: MIL, SIL and PIL Tests for MPPT algorithm (adapted from Motahhir *et al.*, 2017)

2.3.3.2 Review on EMS for FCs Hybrid Electric Vehicle: Issues and Challenges

According to Sulaiman *et al.* (2015), different ways of using a battery to supplement a fuel cell to reliably supply power without experiencing the fuel cell fuel starvation phenomenon were investigated. The basic rationale in the literature was to formulate various types of power converters and energy management systems / storage (EMS) governed by different control strategies − which include but not limited to the followings techniques a) fuzzy logic (Xiao & Wang, 2012), b) power frequency splitting (Ouddah, 2013), c) space dynamic equation, d) deterministic dynamic programming (Sundstrom & Stefanopoulou, 2006), e) neural network optimization algorithm (Xie, 2008), etc.

Furthermore in Sulaiman *et al.* (2015), super-capacitor (SC) instead of a battery, was used to supplement a fuel cell. Super-capacitors are known to have very high power density (relative to a battery or FC), enabling it to react fastest in transient conditions of brief high current demand. This method requires as well various topologies of power converters and EMS governed by different control techniques, which include but unlimited to the following methods a) differential flatness controls (Thounthong, 2010), b) polynomial control technique (Tani, 2013), c) wavelet-based load-sharing algorithm (Uzunoglu & Alam, 2008), d) fuzzy logic (Efstathiou *et al.*, 2012), e) wavelet adaptive linear neuron (WADALINE) (Ates *et al.*, 2009), f) adaptive optimal control algorithm (AOCA) (Zheng, 2013), etc. Though the EMSs focus on HEV herein, they can be applied for other applications.

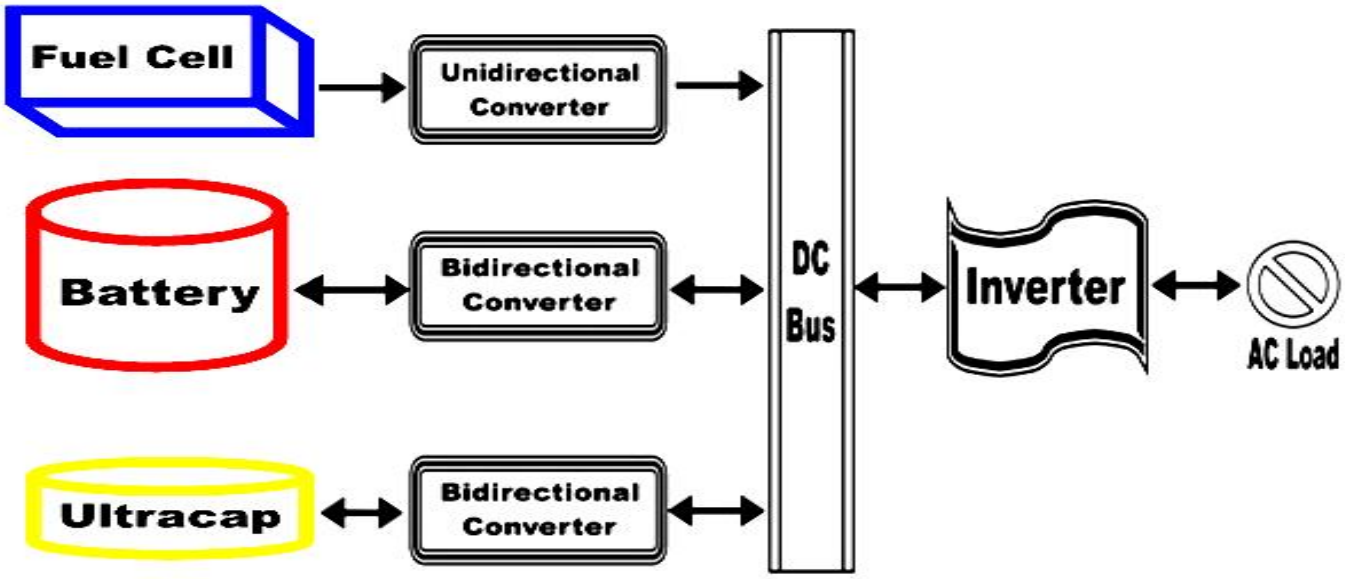

Figure 2.47: Fuel cell, battery and ultra-capacitor hybrid power system (redrawn from Sulaiman *et al.*, 2015)

Finally, the third setup as stated in Sulaiman *et al.* (2015), involves all three – the FC, battery and finally the super-capacitor all connected in parallel. This setup requires as well various topologies of power conversion and EMS governed by different control methods, which include but unlimited to the following approaches a) proportional integral (PI) regulator (Hannan, 2012), b) fuzzy logic (Martinez, 2011), c) various FC, battery and SC configurations (Schaltz, 2008), d) traction control method (Paladini, 2007), e) flatness control technique (Zandi, 2011), f) PWM control (Fathabadi, 2018), state machine strategy by Li (2016), PI and nonlinear sliding mode controllers (Kraa, 2015), etc. The fuel cell, battery and super-capacitor technique is the most effective and widely used, as it provides both high energy and high power densities, as well as storage when needed. Figure 2.47 summarises this technique.

2.3.3.3 A Comparative Study of EMS Schemes for a FC Hybrid Emergency Power System of More-Electric Aircraft (MEA)

Researched in Motapon *et al.* (2014), an articulation of assorted EMS for a fuel cell-based emergency power system of a More-electric aircraft was presented. Akin to Figure 2.47, the fuel cell hybrid system comprises of a FC, Li-ion battery and super-capacitor, together with DC-DC converters and DC-AC inverter as shown in Figure 2.48. The EMS techniques comparatively studied include those used in FC vehicle applications such as the proportional integral (PI), the state machine, the fuzzy logic /frequency decoupling, the equivalent consumption minimization and the rule-based fuzzy logic strategies. The main metrics used to compare the various EMS strategies performance are the i) the H_2 consumption, ii) state of charge of the batteries / super-capacitors and iii) general system efficiency. Lastly, a novel technique using the wavelet transform of their instantaneous power, was used to measure the tensions on each energy source to determine the impact on their life cycle. Simulation models as well as an experimental test setup were developed to simulate and practically verify their study.

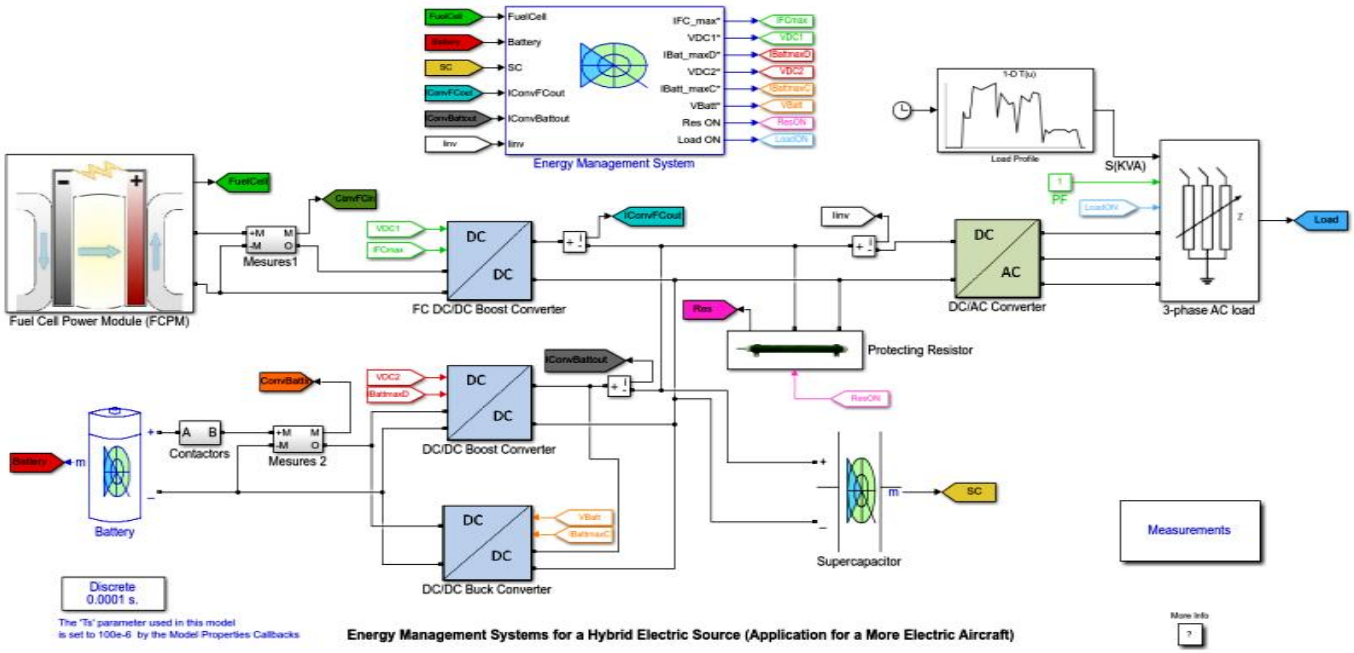

Figure 2.48: Hybrid fuel cell, battery and super-cap with EMS (adapted from Motapon *et al.*, 2014)

2.3.3.4 Model-Free Control of Multi-phase IBC for FC / Reformer Power Generation

Fuel cells require power converters to boost their low DC output voltage, as well as a control mechanism to optimize its operation. According to Mungporn *et al.* (2019), the regulation parameters are set using a linear method to assess the convergence problem; as a result, they developed further a model free control (MFC) to manage the fuel cell power for DC micro-grid applications. In their approach, a 2-phase interleaved boost converter was implemented to address the non-linear control problem. Relative to PI and flatness control techniques, a MFC is simple and don't need precise info of the DC micro-grid parameters, though MFC still needs to know the power converter inductances value. The simulated design was done using dSPACE MicroLabBox and practically tested using a 50V 2.5kW PEMFC with two 2.5kW converters connected in parallel to the FC output and both tests correlated with excellent performance. Figure 2.49a depicts the FC power plant overview and Figures 2.49b - 2.49c respectively represent the IBC architecture and a two-phase MFC technique.

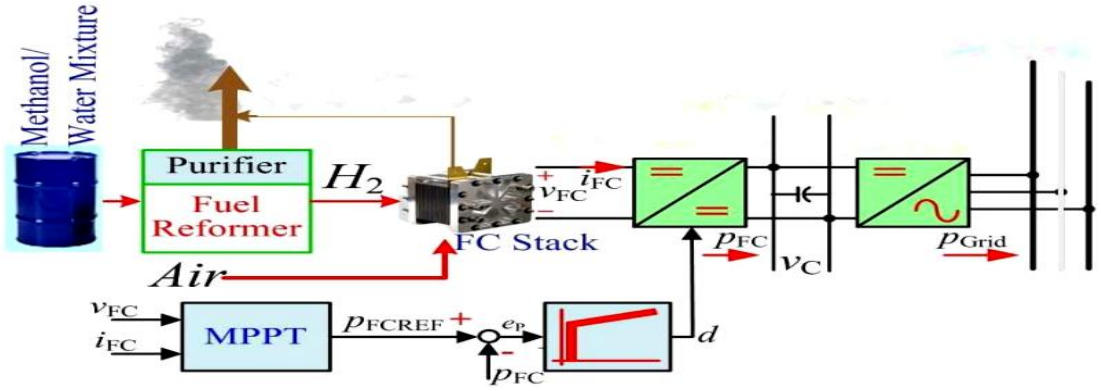

(a) FC / reformer power plant for grid connected applications

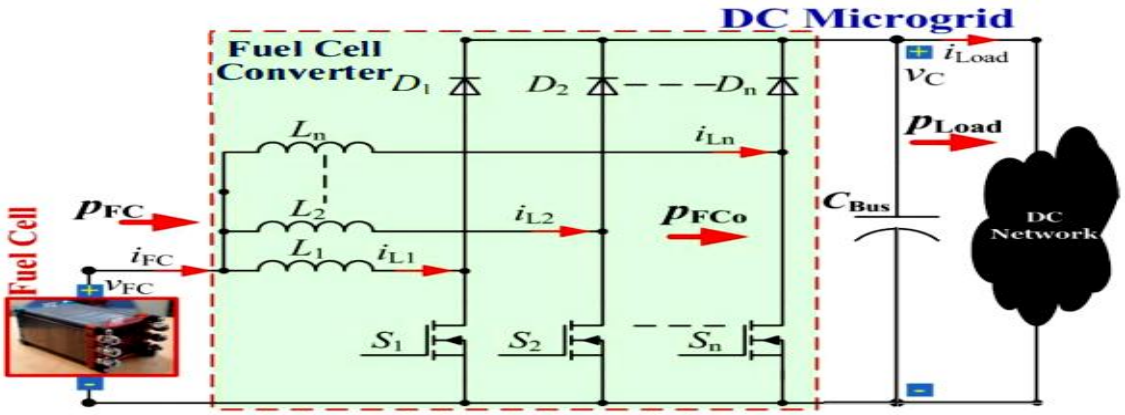

(b) Multi-phase parallel IBC for FC applications

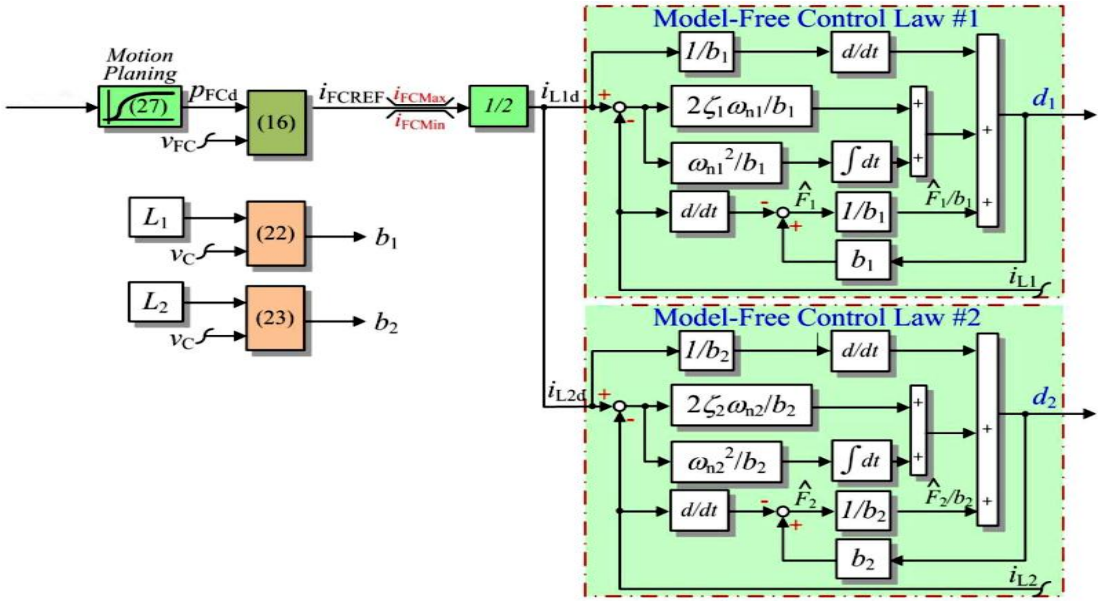

(c) Suggested MFC of the FC power for the multi-phase FC power converter

Figure 2.49: FC power plant, power converter and MFC (adapted from Mungporn *et al.*, 2019)

2.3.3.5 Control and Grid Connection of a FC Power System

As now known, FC is gaining traction in micro-grids and other applications due to their environmental friendliness. Studied in Suárez-Velázquez *et al.* (2020) is 900 cells (0.7V per cell) 625V PEMFC stack connected to a 3-phase electrical network using a 700V DC-DC conventional boost converter and a 420V voltage source converter (VSC) DC-AC inverter. PI linear controllers are used in the power converter to monitor the voltage /current and to regulate the electrical dynamics needed to reliably supply power to the grid. The VSC regulates autonomously the active and reactive powers injected to the grid, using two linear control loops PI(1) and PI(2) and a sinusoidal pulsed width modulation (SPWM) scheme. Matlab and Simulink were used to model and simulate the design and the PI controller could reach steady state within 50ms. The VSC inverter controller was able to reach steady state within 30ms when the active and reactive powers were doubled. Figure 2.50a illustrates the FC electrical network and Figures 2.50b and 2.50c, respectively denote the PI and VSC controllers strategy.

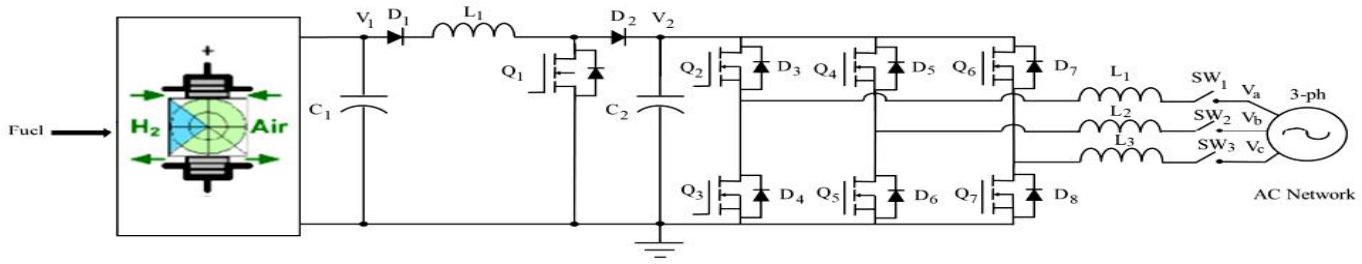

(a) The fuel cell stack, power converter and 3-phase grid

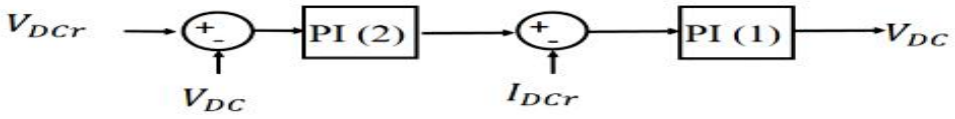

(b) The boost converter PI controller sketch

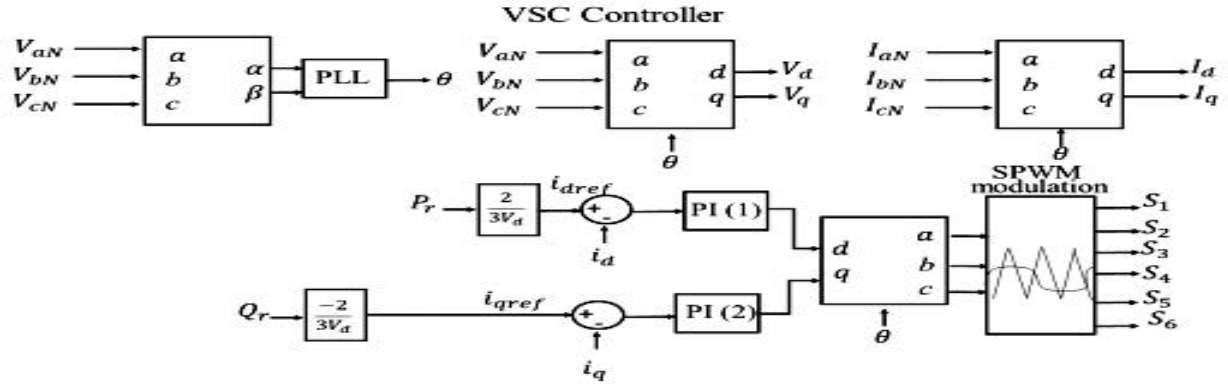

(c) The VSC control and modulation strategy

Figure 2.50: The FC, power converter and electrical grid with PI and VSC controllers schemes (adapted from Suárez-Velázquez *et al.*, 2020)

2.3.3.6 A Novel Control Scheme for High Efficiency FC Power Systems in Parallel Structure

Discussed in Jeong *et al.* (2019), is a basic control technique for greater efficiency power converters of a FC distributed generation (DG) system shown in Figures 2.51a − 2.51c. Usually, multiple FCs and power converters are connected in parallel to meet the power rating required for a FC DG systems. However, power systems have three main losses; namely core, switching and conduction losses − the switching and core losses are insensitive to load fluctuations, whereas the conduction loss is proportional to power output. Therefore, when power systems work under light-load conditions, the switching and the core losses can significantly contribute to the total losses, as the conduction loss will be small. As a result, the traditional paralleling approach entails the power system operates the same irrespective of the load size, making the power system in-efficient at light-load (small current) conditions, due to the predominantly switching and core losses. Therefore, the parallel system efficiency under light-load is enhanced by changing accordingly the quantity of parallel power units to meet just the light-load demand − doing so substantially reduce the switching and core losses, as less power units will be operating and more can be added under heavy-load. Three 300W units were paralleled to achieve a 900W FC DG efficient system.

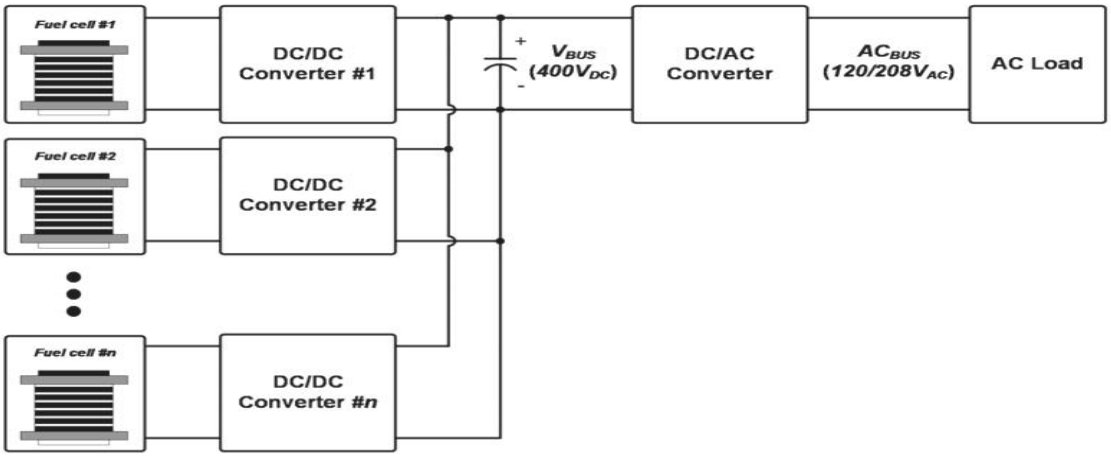

(a) Parallel FC DG system

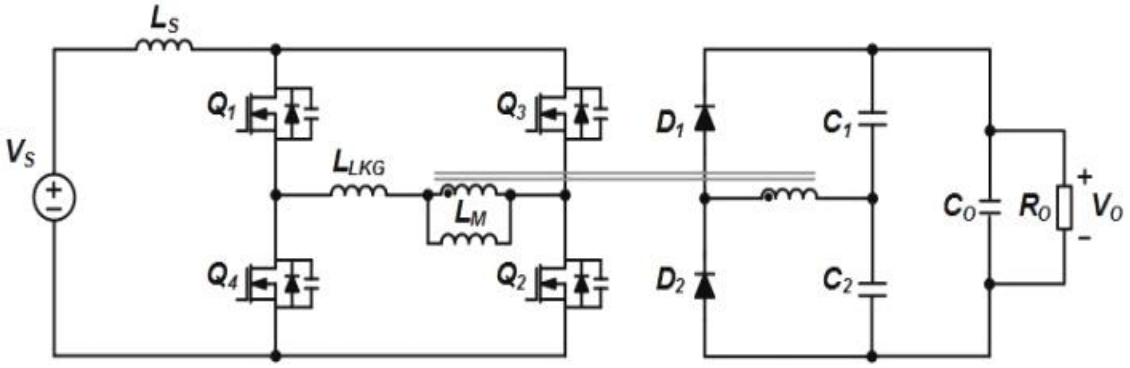

(b) Current-fed isolated full-bridge power converter

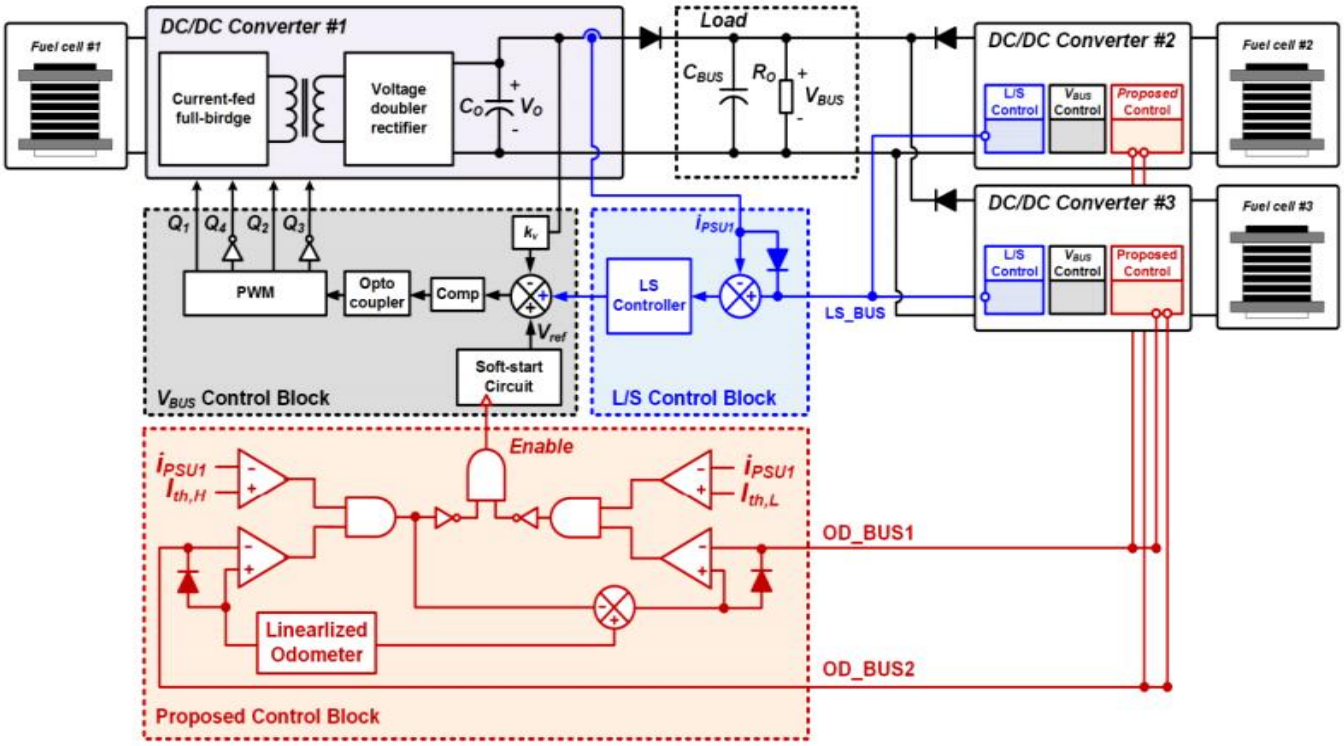

(c) Proposed control scheme block diagram

Figure 2.51: Their proposed FC system, power converter and controller scheme (Jeong *et al.*, 2019)

2.3.3.7 An EMS Strategy Based-on State Machine with Power Compensation for PV-PEMFC-Li-ion Battery Power System

Investigated in Zhang *et al.* (2019) is a hybrid power supply system constituting a PEMFC, PV and auxiliary Li-ion battery for electric vehicles as exemplified in Figure 2.52a. A conventional FC and solar cell DC-DC boost converters are used and for a Li-ion battery, a boost-buck power converter is employed. To efficiently coordinate the different power / energy sources and stabilize the DC bus voltage, a state machine EMS control technique with power compensation was employed. The rationale is to minimize the frequency of the PEM FC power output variations and ensuring the Li-ion battery charges and discharges within the ideal intervals. Figure 2.52b illustrates the state machine EMS used to adjust the FC voltage and Li-ion SoC to attain optimal results.

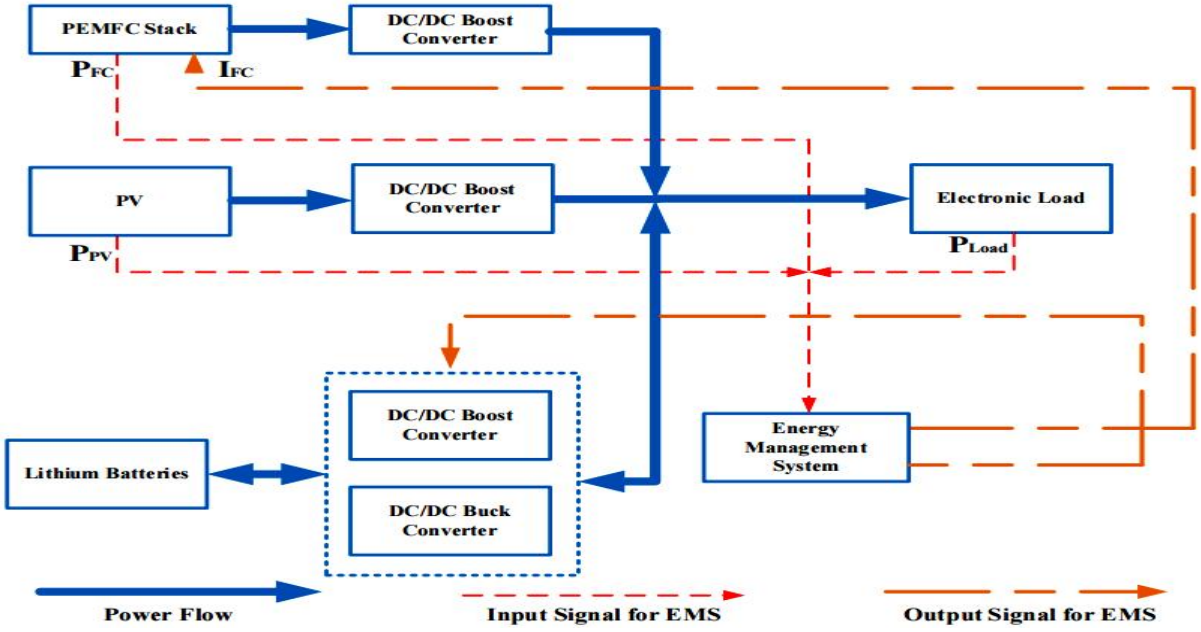

(a) FC, TV and Li-ion power system overview

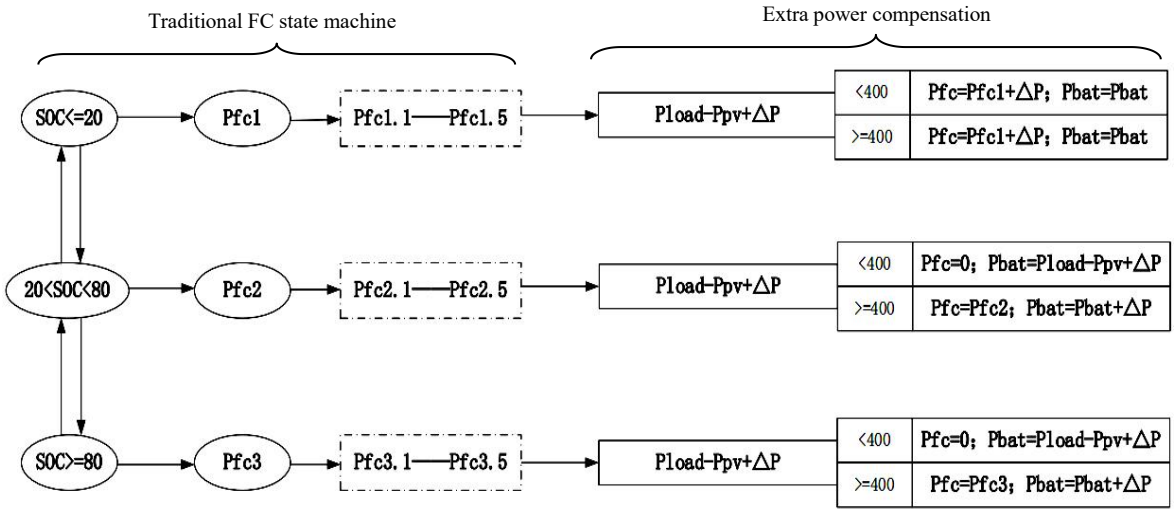

(b) Optimized FC state machine EMS with power compensation

Figure 2.52: Their postulated power system and state machine EMS (adapted from Zhang *et al.*, 2019)

2.3.3.8 Development of a Fuzzy-Logic-Based EMS for a Multi-port Multi-operation Mode Residential Smart Micro-grid

Demonstrated in Jafari *et al.* (2019) is an advanced grid-tied residential smart micro-grid composing of a fuel cell, solar cell and battery bank to supply the local loads using both electric and magnetic buses. Typically, an electric bus comprising of multiple converter based micro-grids is used; however, this setup is costly and bulky with numerous and large conversion stages. Thus, the addition of a common magnetic bus with multi-port converters circumvent these shortcomings and furthermore isolate the conversion ports. Their hybrid architecture with EMS translates to a centralized quicker and versatile system. The suggested micro-grid was capable of working in multiple grid-tied and off-grid modes using a fuzzy logic energy management unit (EMU) controller to choose the proper mode of operation − taking into cognizance short and long-term energy generation and usage. The micro-grid operation performance was enhanced using synchronized bus-voltage balance control technique. The executions of the micro-grid and EMU were experimentally tested for three different cases of the residential load in grid-connected and off-grid modes. The energy distribution and cost analyses for each case show the merits of the EMU for both the grid and the user. The various control schemes for each of the power converters/inverters is detailed in their full article. Figure 2.53 exemplifies and summarizes their research.

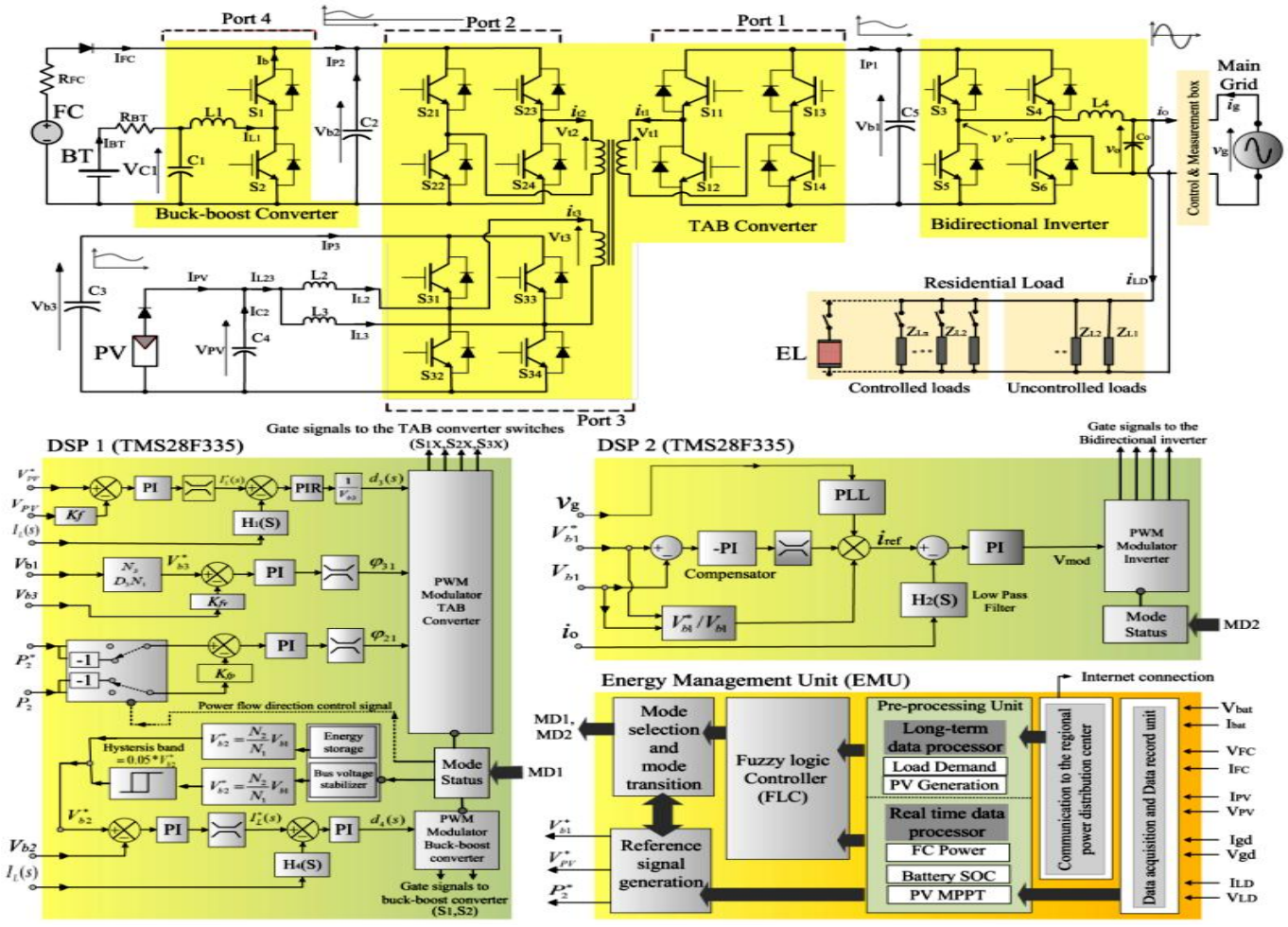

Figure 2.53: Smart micro-grid including converters, controllers and EMU (adapted from Jafari *et al.*, 2019)

2.3.3.9 Frequency Separation-based Power Management Strategy for a FC-Powered Drone

Studied in Boukoberine *et al.* (2020) is a hybrid FC and super-capacitor with a DC-DC boost converter power system for drones depicted in Figure 2.54a. The EMS control technique exploited is routed-in frequency separation-based technique whereby the required power is shared between the energy sources − in this case, the FC and super-capacitor. Depicted in Figures 2.54b and 2.54c, the drone flight load profile is divided into low and high frequency components, in which the FC connected to the DC-DC boost converter is controlled to handle the low frequency dynamics, whereas the supercapacitor handles the high frequency dynamics during peak power demands as expatiated in Figure 37c. The system was simulated using a real power profile from a small hexacopter experimental flight test and the results justify their EMS was capable of minimizing the fuel cell power variations with the supercapacitor handling all of the transient / peak power demands, consequently prolonging the FC lifetime and drone flight periods.

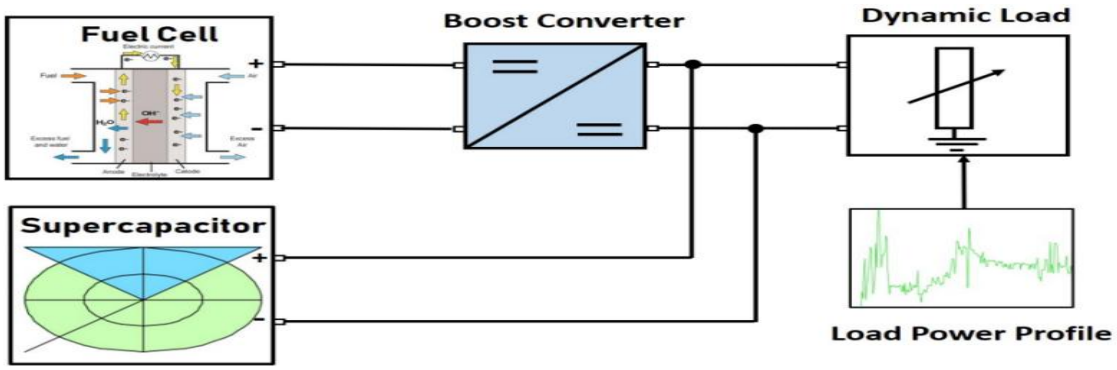

(a) Drone FC and super-capacitor power system overview

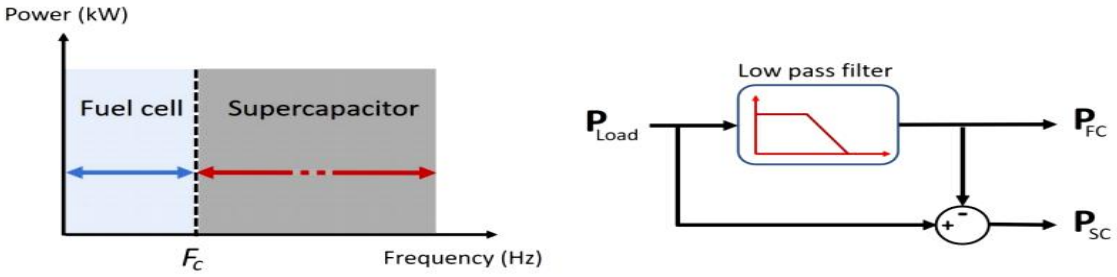

(b) Frequency power sharing concept

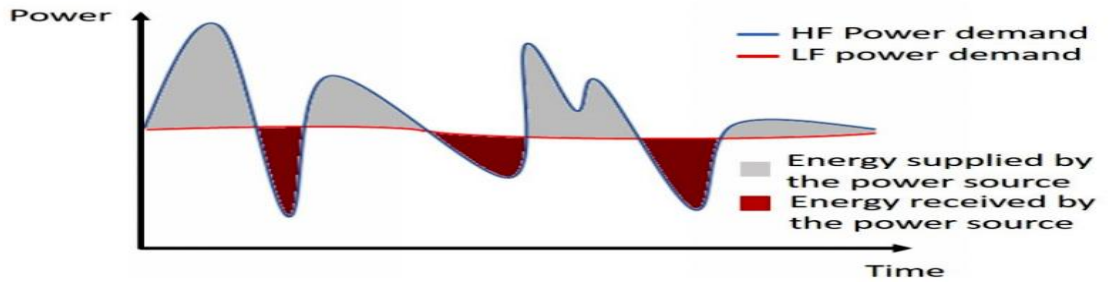

(c) Power frequency sharing

Figure 2.54: Drone hybrid power system and frequency separation EMS (adapted from Boukoberine *et al.*, 2020)

2.3.3.10 MPPT Control of an IBC for a PEM FC Applications

Stated in Barhoumi *et al.* (2020) is simply how FC power can be stepped-up using a four-phase IBC and controlled efficiently using a MPPT P&O EMS. The IBC further reduced the FC voltage and current ripples whereas the MPPT ensured maximum power is extracted from the fuel cell. Figures 2.55a-2.55c summarize the implementation.

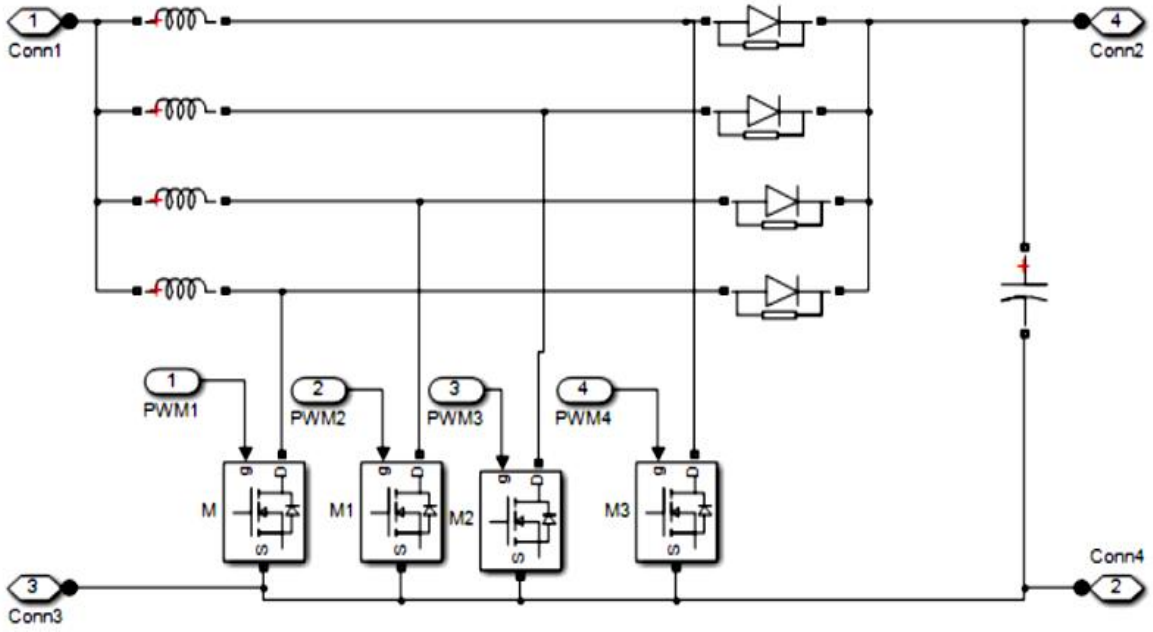

(a) Four-phase IBC Simulink model

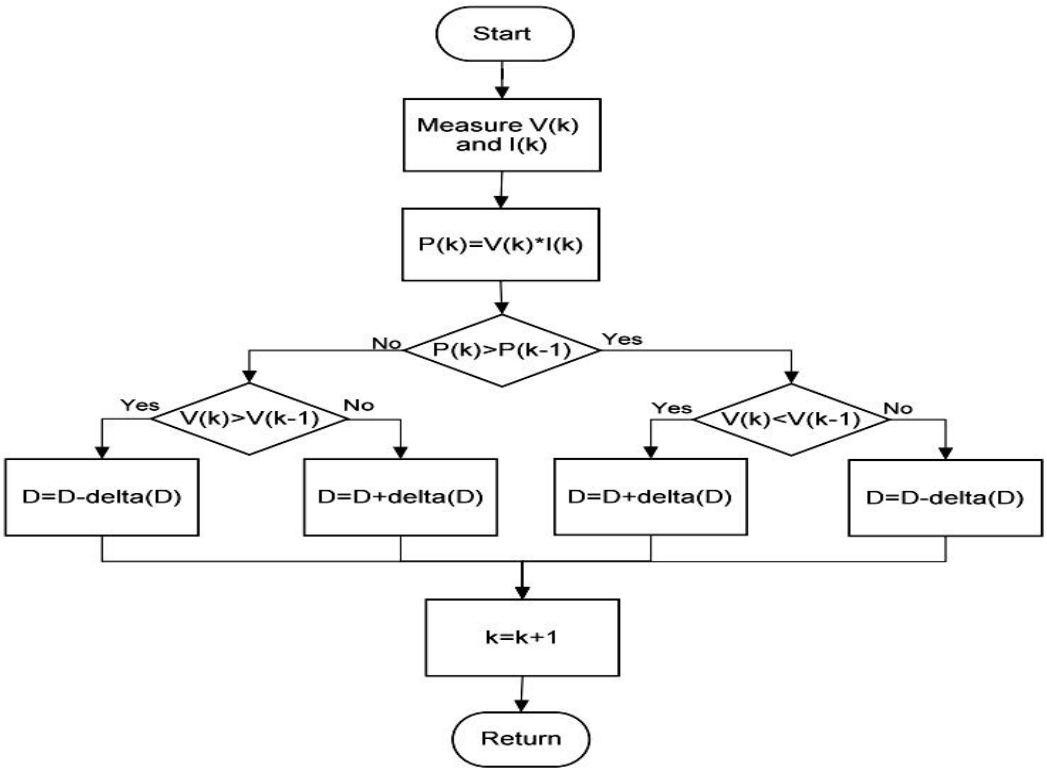

(b) Perturb and Observe MPPT

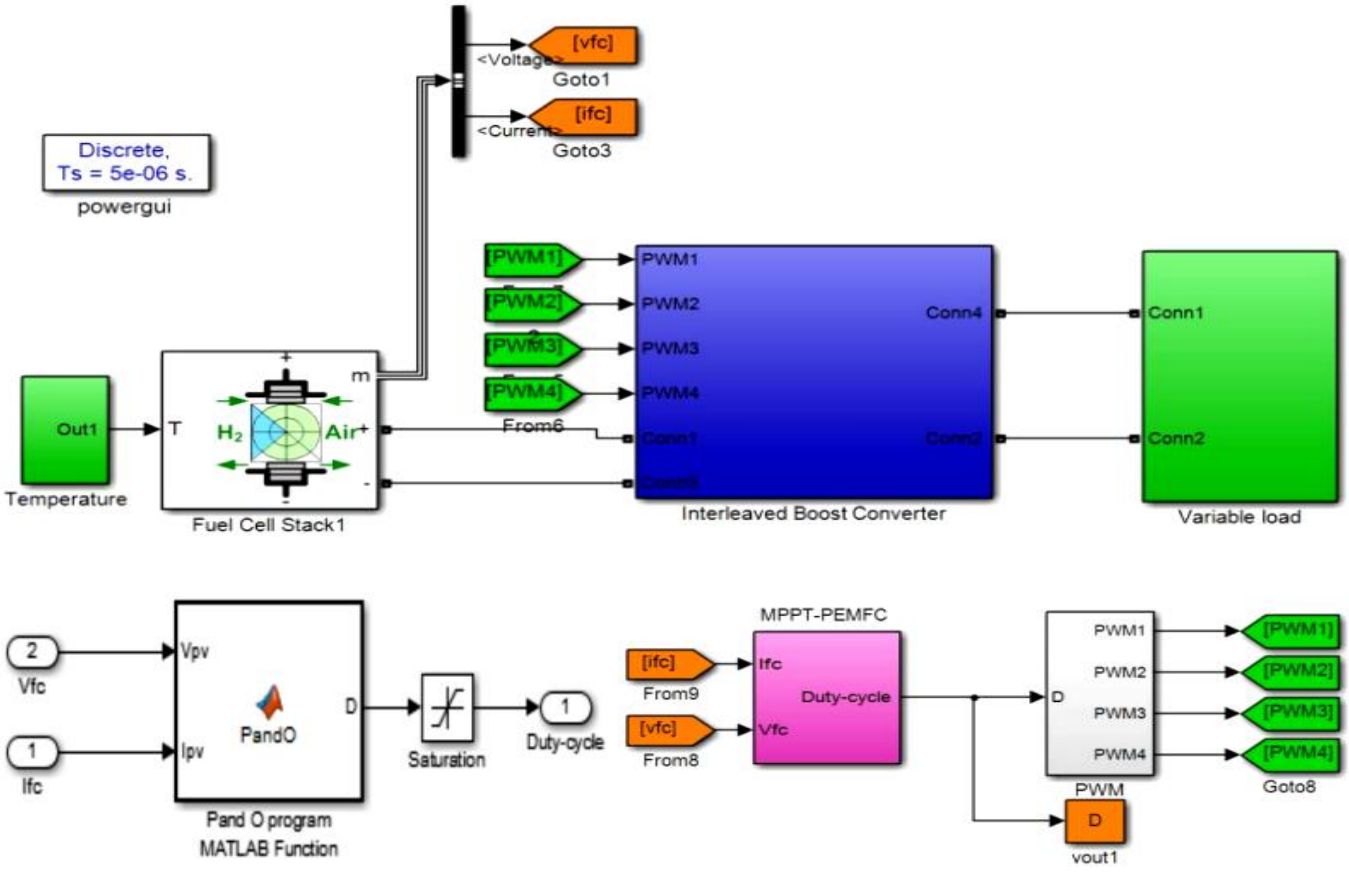

(c) IBC with MPPT Simulink model

Figure 2.55: FC and four-phase IBC with MPPT P&O EMS (adapted from Barhoumi *et al.*, 2020)

2.3.3.11 Power Flow Control via Differential Power Processing to Enhance Reliability in Hybrid Systems based on PEM FC

Presented in Artal-Sevil *et al.* (2020) is an interesting study on interconnecting fuel cells to obtain maximum output power. Two interconnection techniques; namely, the i) modular integrated converter (MIC) and ii) differential power processing (DPP) including their power converters (synchronous switching bidirectional buck-boost) and EMS technique (MPPT P&O / Hill Climbing (HC)) were modeled using Matlab and discussed in details. As depicted in Figure 2.56a, the MIC topology has each FC connected in parallel to its own separate converter and each converter is in turn connected in series. This allows several converter topologies and control schemes to be implemented independently. However, the main disadvantages are the number of converters used, the cost involved and poor conversion efficiency − as 100% of the power produced by each FC sub-module is processed. As displayed in Figure 2.56b, the DPP architecture simply has two FCs connected in parallel with a single buck-boost converter, thereby reducing the total number of power converters by one. Further advantages include simplicity, speed, affordability and improved efficiency − since only a fraction of the FC sub-module generated power is processed. However, the main disadvantage is the complexity in the control technique implementation, since the active balance needs to communicate with each fuel cell sub-module to apply MPPT.

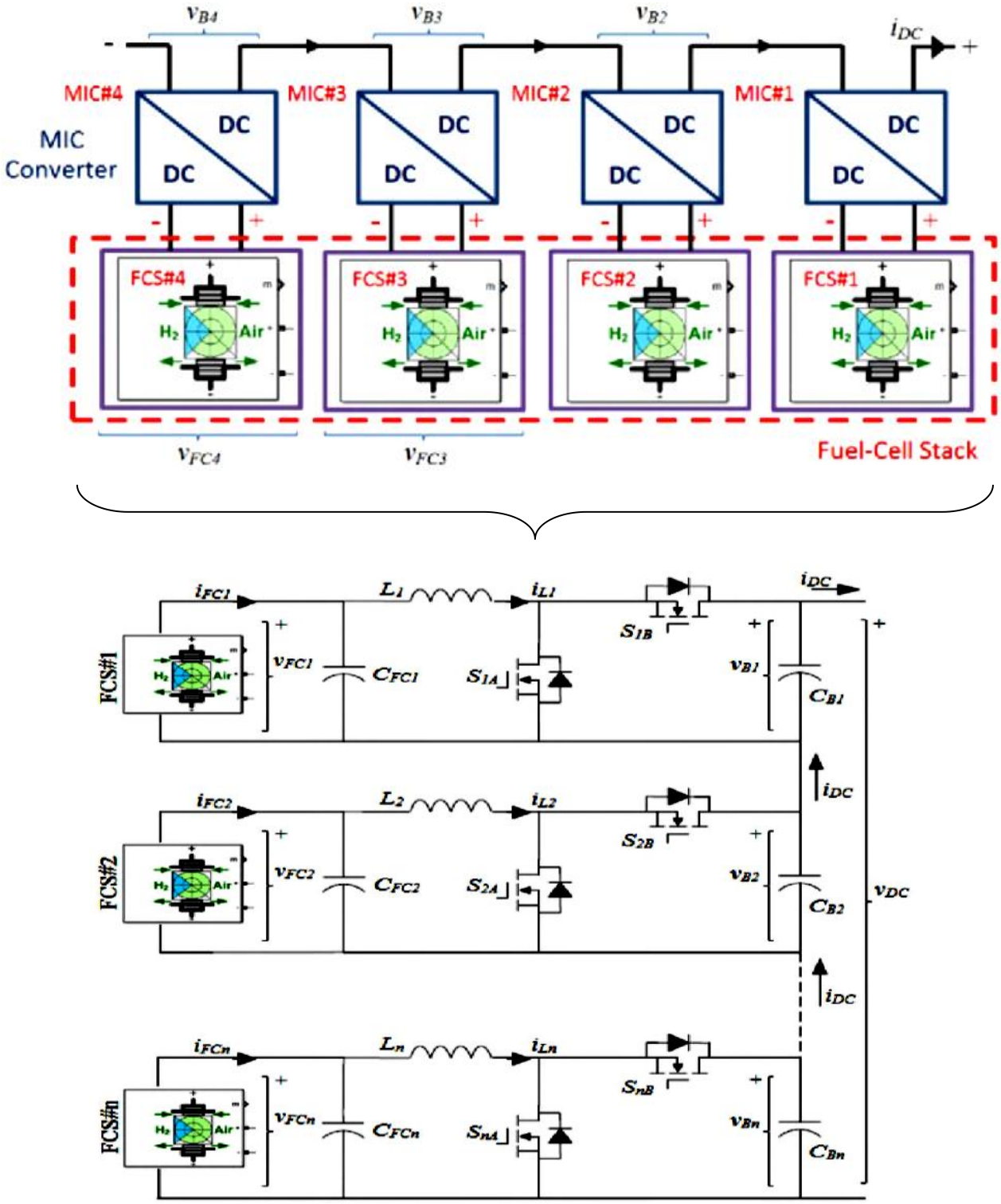

(a) MIC topology showing FCs and converters interconnections

Using Matlab and Simulink, MPPT P&O algorithm illustrated in Figure 2.56c was implemented on the DPP converter to achieve a fast control loop. Their simulation verified the merits of the DPP topology and the MPPT P&O algorithm convergence technique.

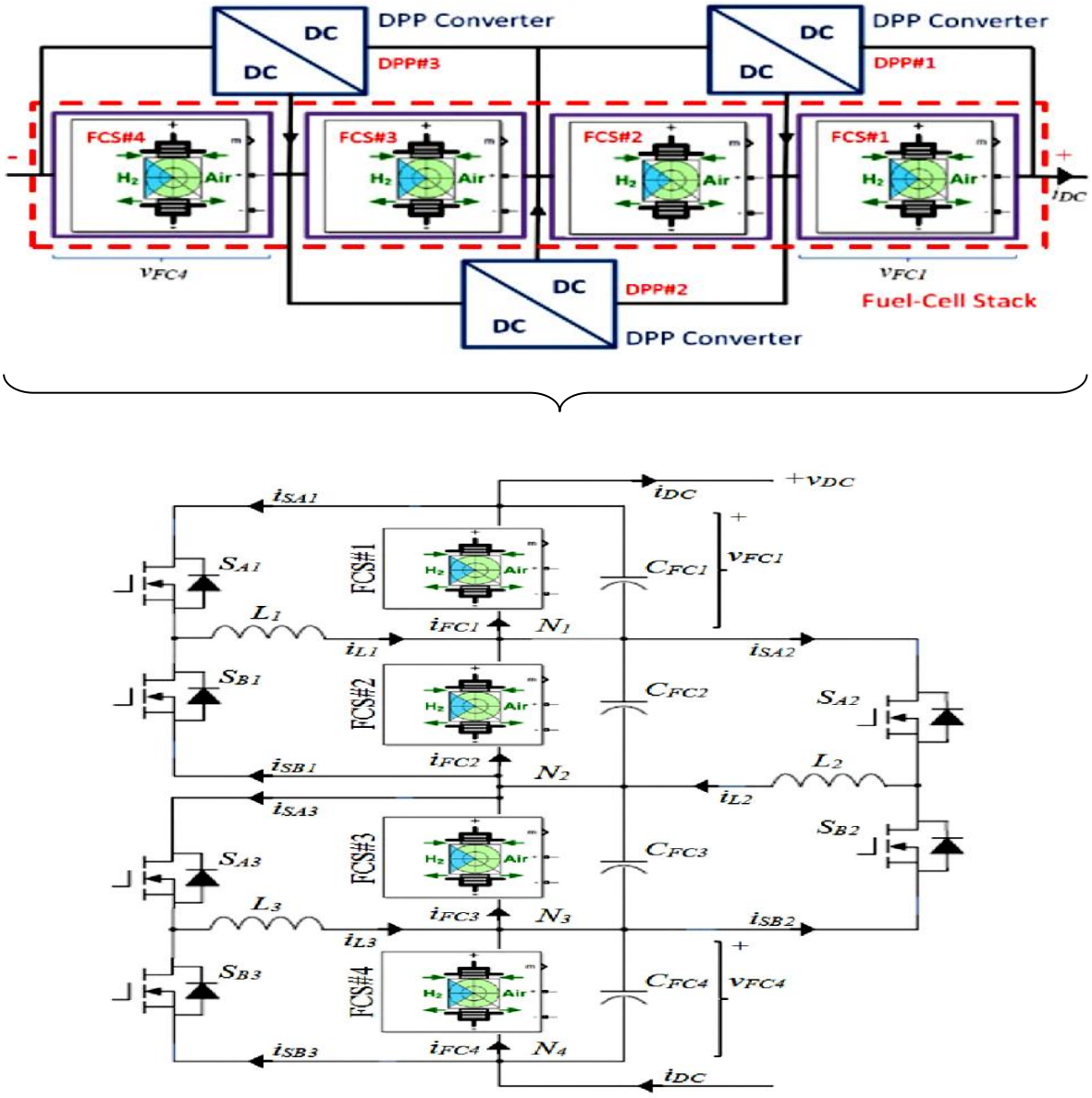

(b) DPP topology showing FCs and converters interconnections

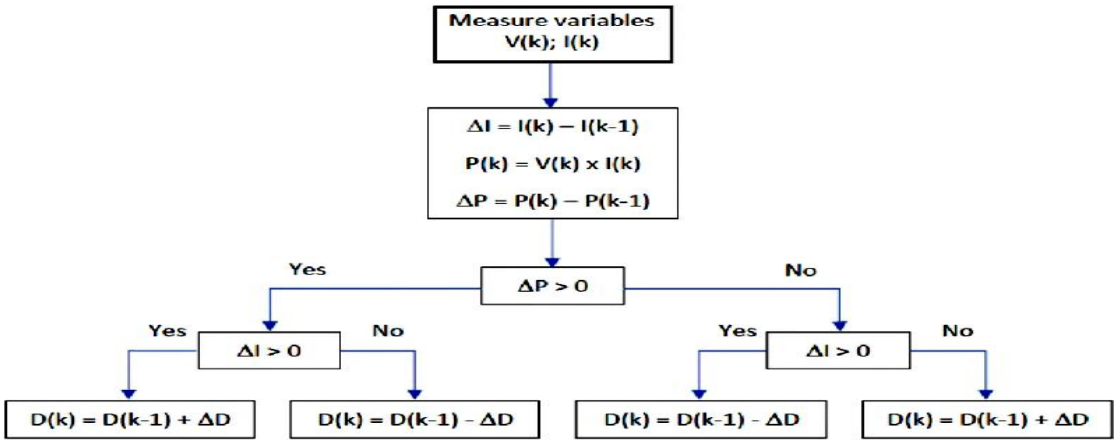

(c) HC / P&O MPPT control algorithm

Figure 2.56: MIC, DPP and MPPT P&O techniques (adapted from Artal-Sevil *et al.*, 2020)

2.3.3.12 EMS in a Multi-source System using Isolated DC-DC Resonant Converters

Described in Arazi *et al.* (2020), is a hybrid fuel cell and super-capacitor with PI controller power system. The research purpose was to develop a control mechanism for the fuel cell and super-capacitor DC-DC resonant power converters to share the system power according to their dynamic responses. Usually, the FC has a slower power dynamic relative to the super-capacitor; therefore, initially the super-capacitor will handle the instant peak power demands whereas the FC provides the bulk of the power during steady state. The isolated LLC resonant converter connects the fuel cell to the DC bus, whereas the super-capacitor connects to the DC bus via the bidirectional resonant converter which charges and discharges the super-capacitor. The modeling and simulations were done using Matlab / Simulink with PLECS and the findings affirm the merits of using resonant converters − which also offer isolation and reduced switching losses. Portrayed in Figure 2.57a is the FC and super-capacitor hybrid power system and Figures 2.57b and 2.57c respectively lucubrate FC and super-capacitor PI controllers.

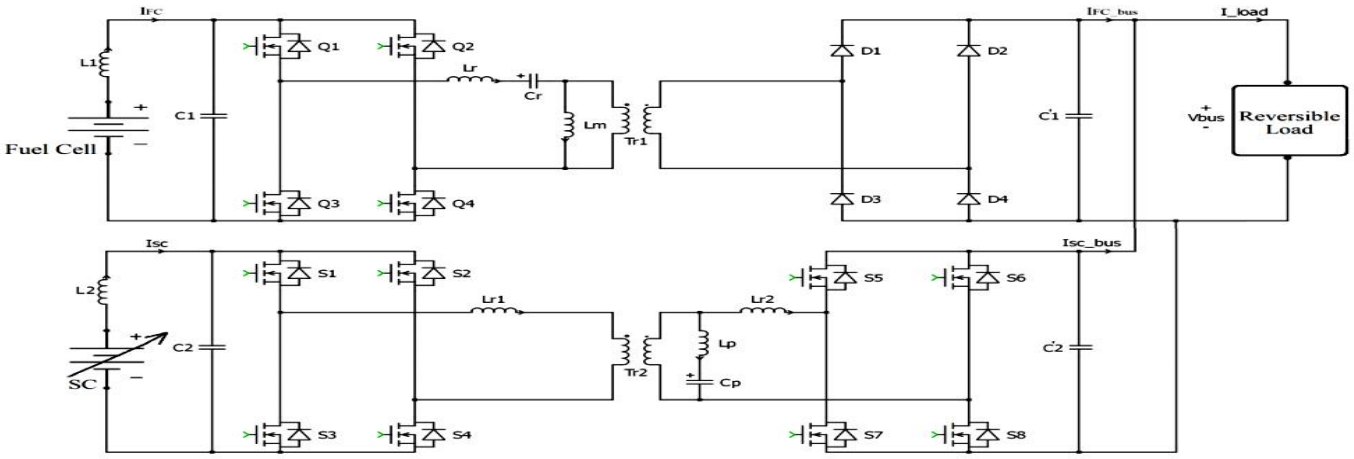

(a) FC and super-capacitor hybrid system

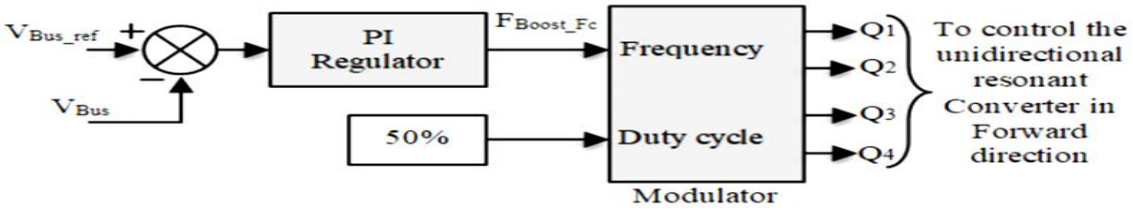

(b) Fuel cell voltage control loop

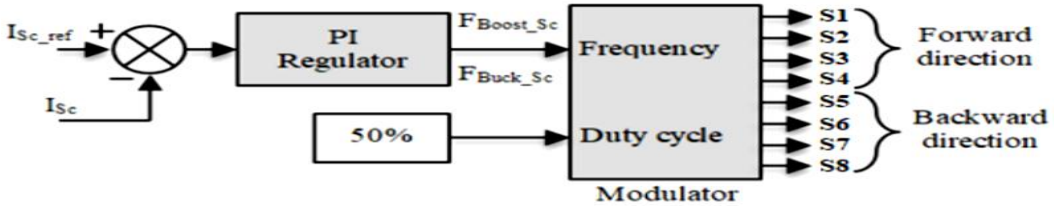

(c) Super-capacitor's bidirectional control loop

Figure 2.57: FC, Super-capacitor hybrid power system with PI controller (adapted from Arazi *et al.*, 2020)

2.3.3.13 EMS Optimization for a FC Hybrid Vehicle based on Power Losses Minimization

Indicated in Martin-Lozano *et al.* (2020), fuel cells hybrid vehicle is a suitable alternative to internal combustion engine vehicles, as they are environmentally friendly. Their research thus proposed an energy management optimization technique for the power distribution system, to increase the driving range of fuel cell hybrid vehicles. The hybrid energy system constitutes a FC connected to a power converter which in turns connects concurrently to a battery and a DC load as represented in Figure 2.58a. Their suggested control optimization algorithm is based on minimizing the energy losses in the system. Using Simulink / PSIM; the losses, costs, size and mass were evaluated, in which it was found that lower FC power and higher battery capacity offer low energy losses and low consumption; whereas maximum fuel cell power and lowest battery capacity provide minimum costs, mass and size. The results correlated other studies in the literature. Figures 2.58b and 2.58c depict the basic FC and battery models respectively and Figure 2.58d shows the optimization scheme high level overview.

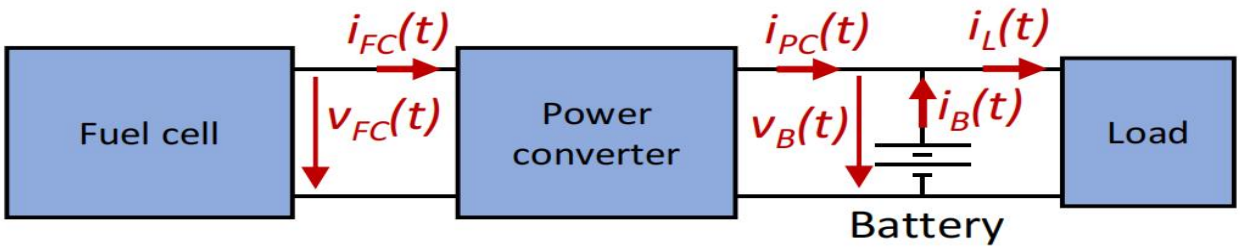

(a) Fuel cell, power converter and battery hybrid power overview

$$v_{FC}(t) = v_{FCoc} - R_{FCc} \cdot i_{FC}(t) - R_{FCv}(i_{FC}) \cdot i_{FC}(t) \tag{2.16}$$

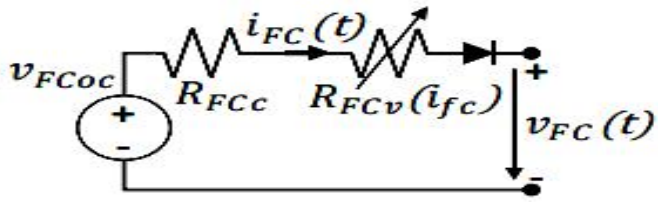

(b) Super-capacitor simplified model

$$v_B(t) = v_{Boc}(SoC) - R_B \cdot i_B(t) \tag{2.17}$$

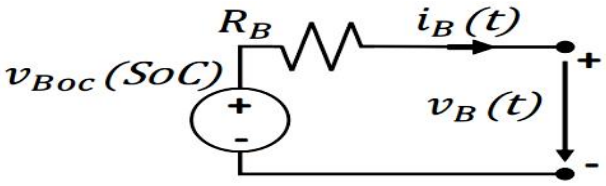

(c) Battery basic model

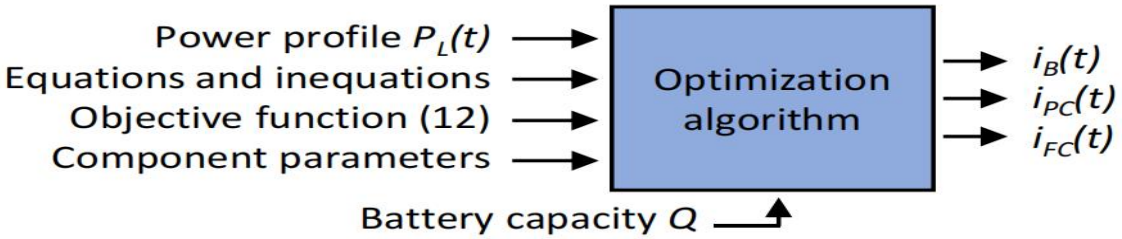

(d) Optimization algorithm input and output data

Figure 2.58: System overview, fuel cell and battery models and optimization algorithm overview (adapted from Martin-Lozano *et al.*, 2020)

2.3.3.14 Dynamic Modeling and Closed-loop Control of Hybrid Grid-connected Renewable Energy System with Multi-input Multi-output Controller

Proposed in Salimi *et al.* (2021) and summarized in Figure 2.59a, is the use of multi-input multi-output (MIMO) technique to dynamically model and closed-loop control a hybrid grid-tied renewable energy system. The system constitutes a solar cell and fuel cell each respectively connected to their boost converters which are in turn connected in parallel to a single-phase H-bridge inverter to supply an AC load. The system employed the traditional MPPT and PI control techniques compensated by the MIMO network detailed in Figure 2.59b. Using the system transfer functions frequency response, the MIMO controller gains are tuned. Matlab and Simulink were used to simulate and analyse the designed MIMO controller accuracy and effectiveness and from the results, MIMO is quick and stable at various functional points, having a negligible steady-state error as well as with a grid THD of ~1.48% in accordance with standards of distribution networks.

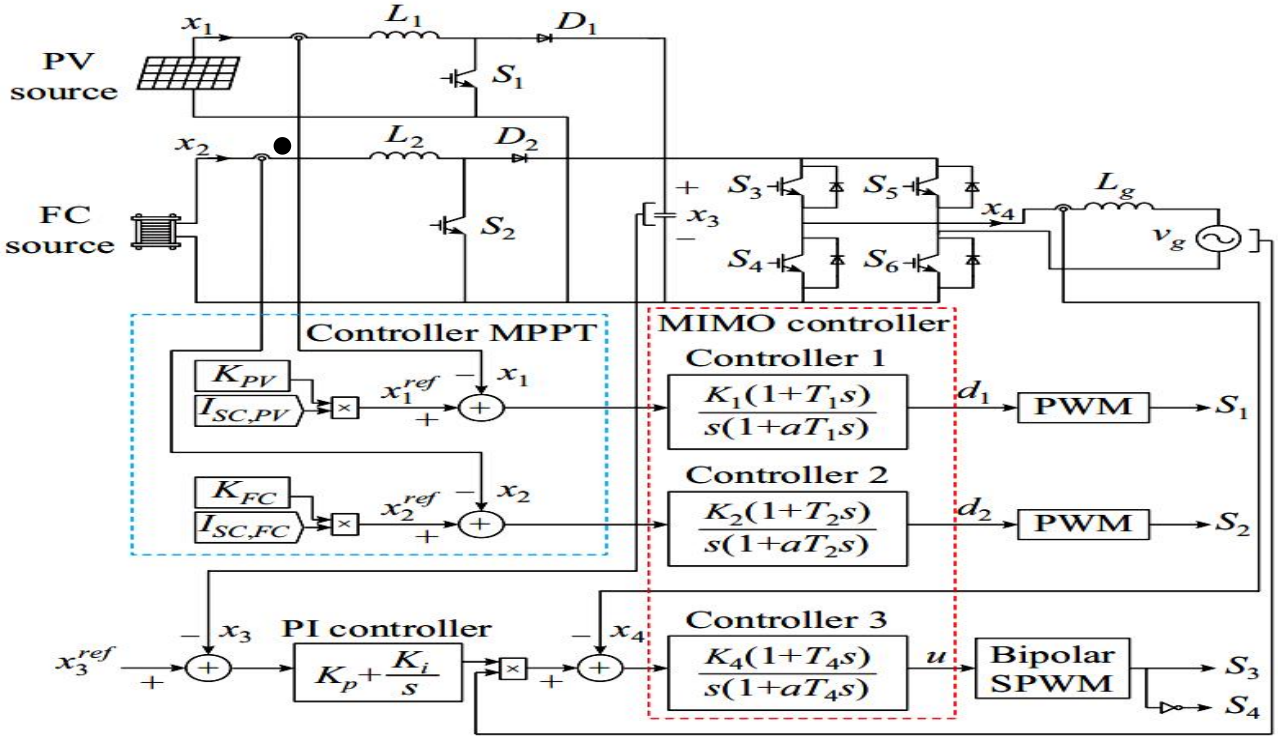

(a) Their suggested control structure for grid-connected PV/FC hybrid energy system

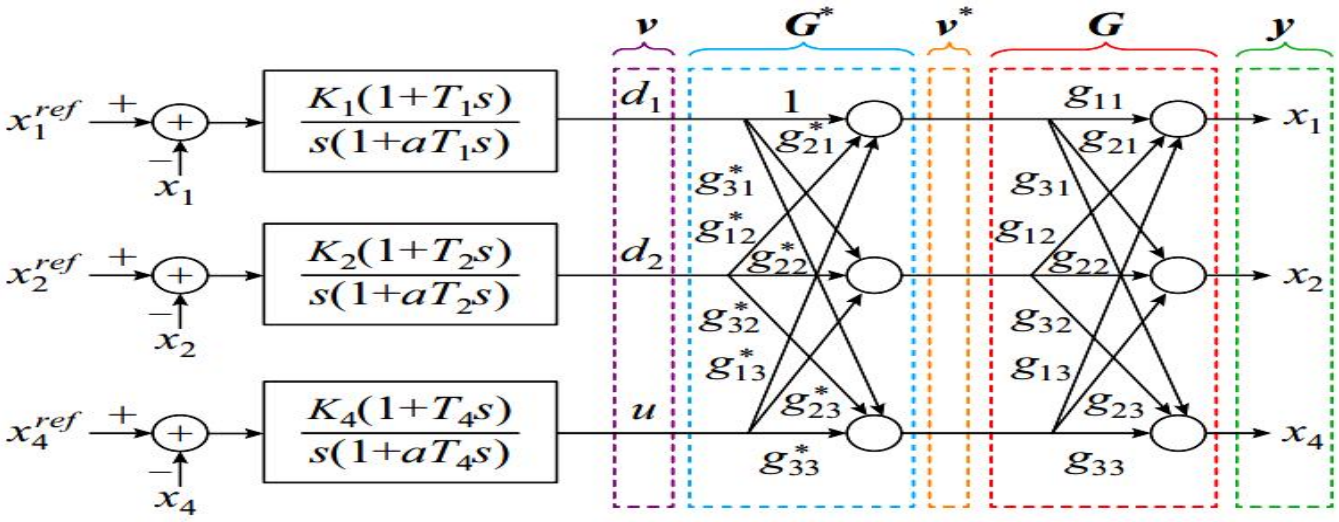

(b) Compensation network

Figure 2.59: FC and PV hybrid energy system and compensation network (adapted from Salimi *et al.*, 2021)

2.3.3.15 FCEVs — A Brief Review of Current Topologies and EMS Strategies

Articulated in Sorlei *et al.* (2021), advancement in technology and new international policies on electric / hybrid electric vehicles are becoming trendy. In light of this, their research focused on fuel cells and energy storage devices as well as power converters and EMS techniques to sustain hybrid electric vehicle dynamic power demands. Different fuel cell energy / power configurations and power converters topologies were assessed and the highlights are presented in Figures 2.60a and 2.60b − respectively a fuel cell with storage devices and dual-input high step-up isolated converter. Furthermore, miscellaneous EMS strategies were examined with focus on energy efficiency, usage of hydrogen and sub-systems decay involved. The pros and cons of rule-based, learning-based and optimisation-based EMS strategies were discussed and the conclusion is to hybridize modern and existing strategies to eliminate the uncertainties regarding EMS techniques robustness.

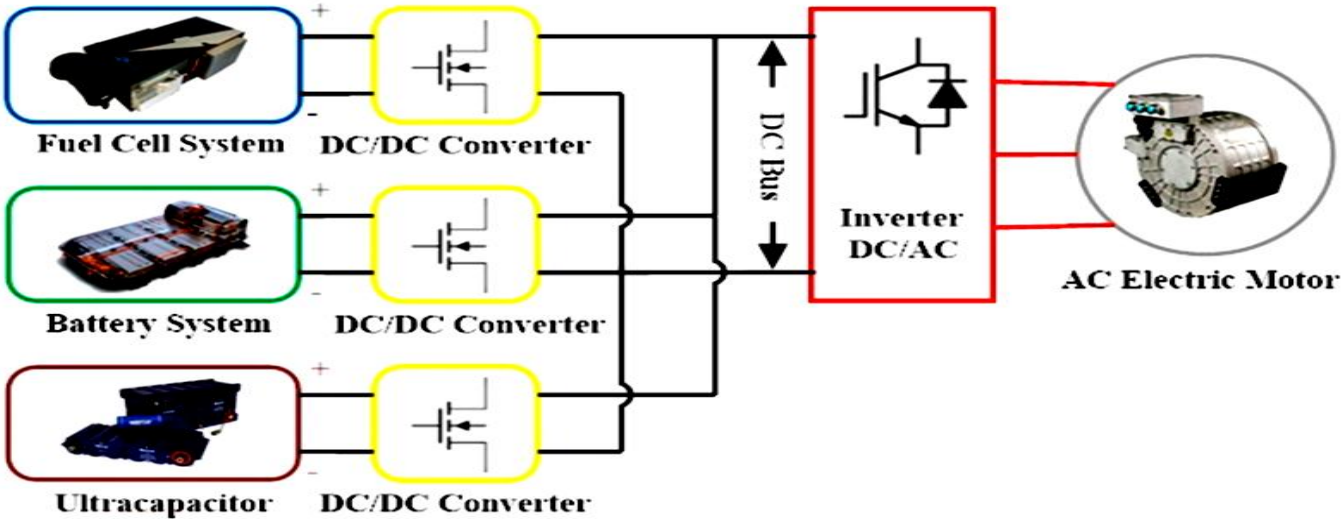

(a) FC, battery and ultra-capacitor hybrid electric vehicle configuration

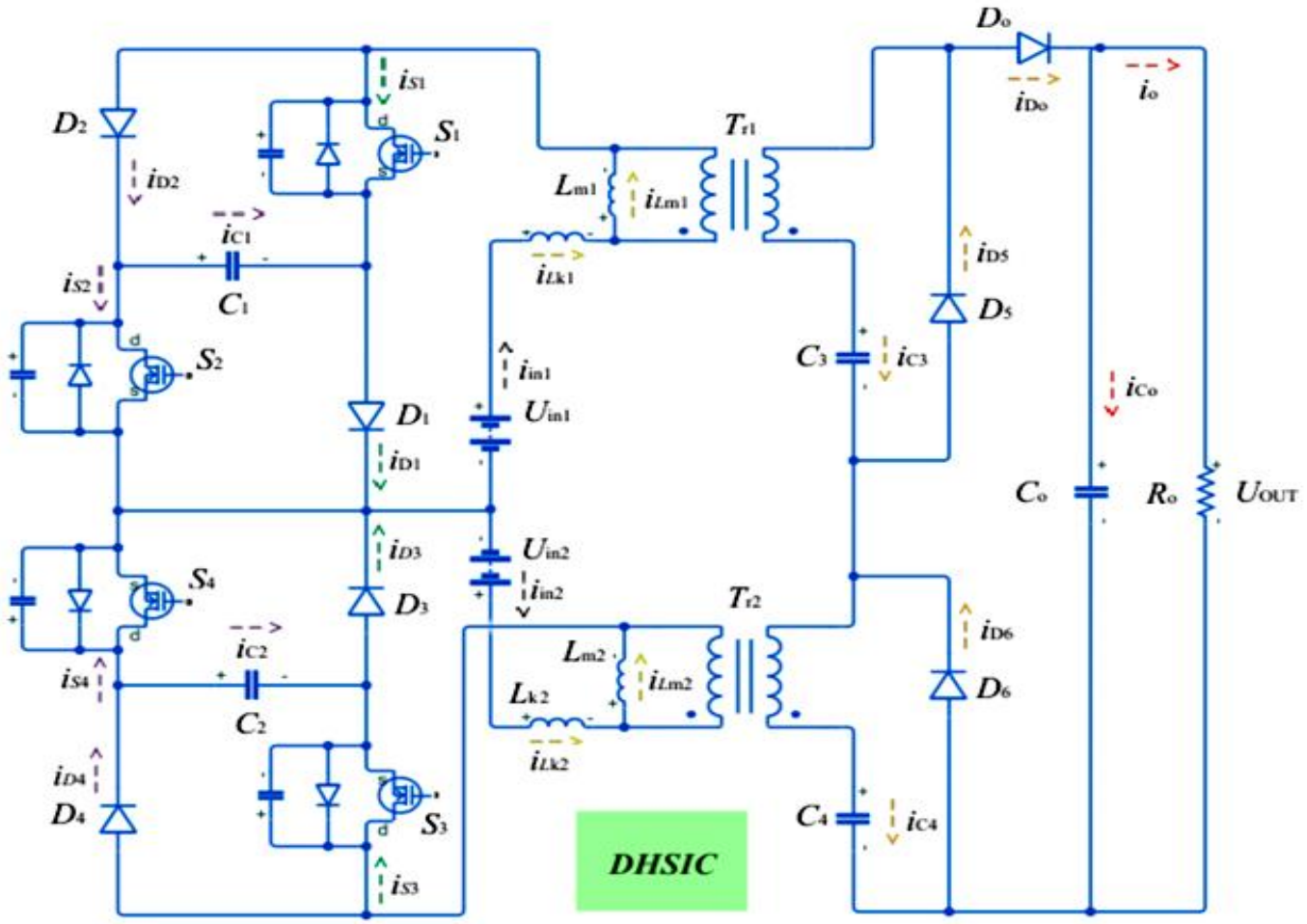

(b) Dual-Input high step-up isolated converter (DHSIC)

Figure 2.60: FC hybrid electric vehicle and DHSIC scheme (adapted from Sorlei *et al.*, 2021)

2.3.3.16 A Review and Research on FCEVs: Topologies, Power Electronic Converters, EMS Methods, Technical Challenges, Marketing and Future Aspects

Analyzed extensively in İnci *et al.* (2021), fuel cells are the future especially for FCEV as shown in Figure 2.61a. In this respect, a comprehensive study of types of FCs with electric motors are explained with focus on their areas of applications, diagnostic properties and working environments. Furthermore, power converters which boost the FC voltages to drive different motor topologies used in FCEVs, are elaborated based on their structural frequency of use, their architecture and difficulty. Summarized in Figure 2.61b, assorted FCEVs power converters EMS schemes and technical challenges were examined and the final closing remarks highlighted the present status and future prospects using significant number of marketing and target data. As stated earlier, even though the techniques apply herein to FCEV, it can also be applied to other FC applications.

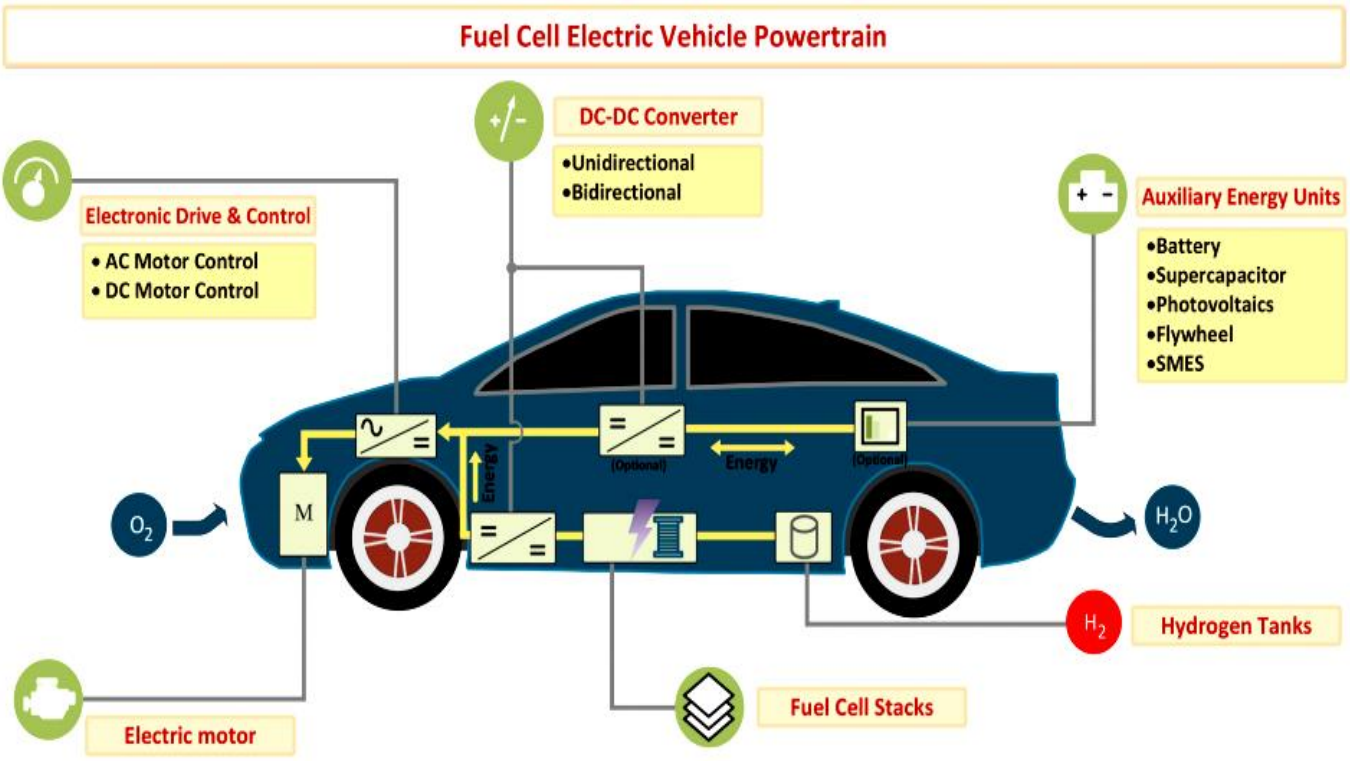

(a) FCEV power transmission system with auxiliary power supplies

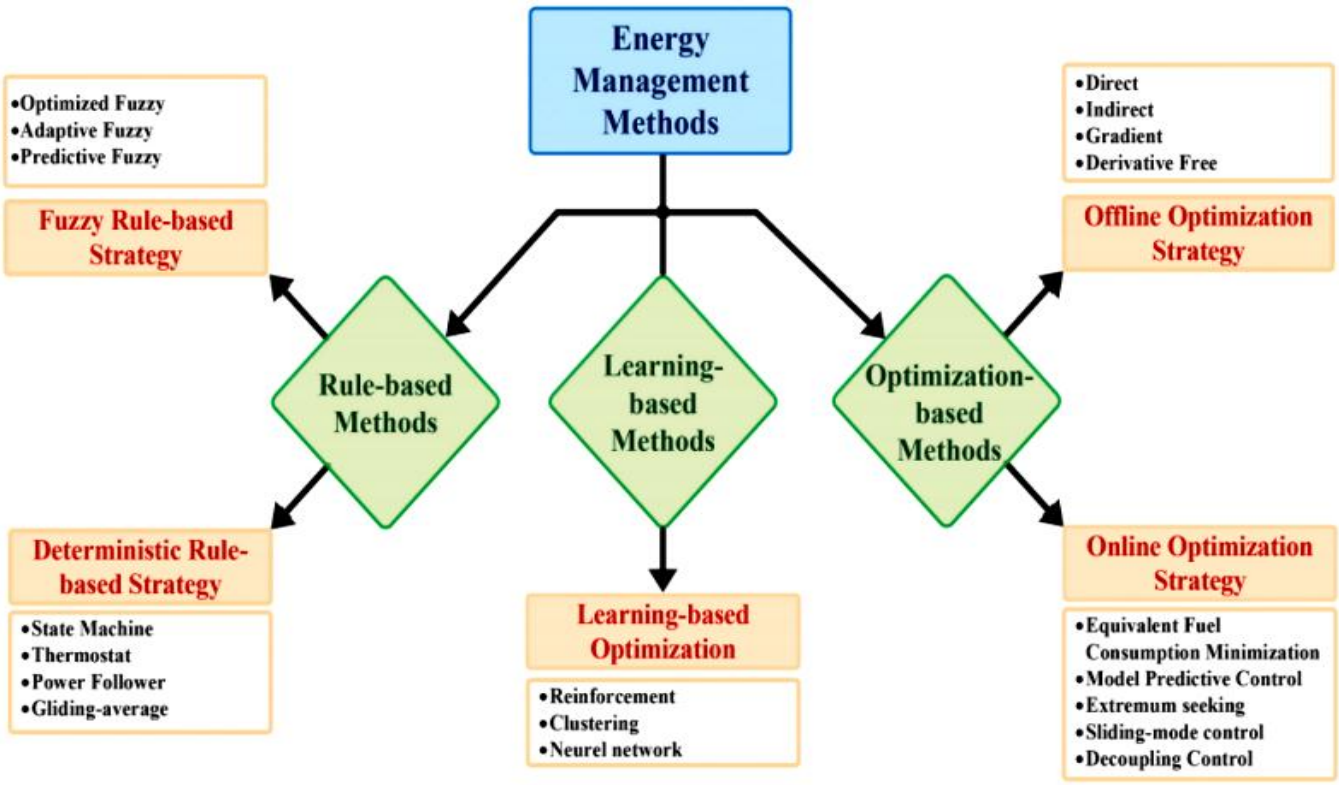

(b) FCEVs EMS classification of technical challenges and system problems

Figure 2.61: FCEV power transmission system and EMS schemes and challenges (adapted from İnci *et al.*, 2021)

Table 2.7: EMS case studies examined summary (adapted from Bayendang *et al.*, 2021a)

EMS Research	Highlights, Merits and Demerits
Study 2.3.3.1 (Motahhir S. *et al.*, 2017)	MIL, SIL and PIL tests for MPPT algorithm. Implemented MPPT algorithm on each and all three formats reasonably gave similar results.
Study 2.3.3.2 (Sulaiman N. *et al.*, 2015)	Extensive analysis on FC fuel starvation and EMS schemes for FC HEV: In-depth FC issues, challenges & solutions were presented.
Study 2.3.3.3 (Motapon S.N. *et al.*, 2014)	Implemented simulated and experimental test frameworks for relative analyses of various EMS methods for a FC hybrid power system.
Study 2.3.3.4 (Mungporn P. *et al.,* 2019)	Developed further a model free control (MFC) to manage the fuel cell power for DC micro-grid applications. In their approach, a 2-phase interleaved boost converter was implemented to address the non-linear control problem and the simulated and practical results correlated.
Study 2.3.3.5 (Suárez-Velázquez G.G. *et al.,* 2020)	Used VSC to autonomously regulate the active and reactive powers injected to the grid, via a sinusoidal SPWM strategy and two linear control loops PI(1) and PI(2). The VSC was able to reach steady state within 30ms when the active and reactive powers were doubled.
Study 2.3.3.6 (Jeong Y. *et al.,* 2019)	The efficiency of parallel FC systems under light-load is enhanced by changing accordingly the quantity of parallel power units to meet the light-load demand and substantially reduce the switching / core losses. Three 300W units were paralleled to achieve a 900W efficient system.
Study 2.3.3.7 (Zhang Y. *et al.,* 2019)	A state machine EMS control technique with power compensation was employed to curb the frequency of the PEM fuel cell power output variations and ensuring the Li-ion battery charges & discharges within the ideal periods.
Study 2.3.3.8 (Jafari M. *et al.,* 2019)	Demonstrated an advanced grid-tied household smart micro-grid consisting of a fuel cell, solar cell and battery bank to provide the local loads using both electric and magnetic buses. The magnetic bus with the multi-port converters augments the electric bus and further isolates the conversion ports. The EMU controller was tested for three distinct scenarios of the home load and the distribution of energy and cost analyses for each case, show the EMU merits.
Study 2.3.3.9 (Boukoberine M.N. *et al.,* 2020)	The EMS method used is routed-in frequency separation-based scheme, whereby the required power is shared between the energy sources.
Study 2.3.3.10 (Barhoumi E.M. *et al.*, 2020)	FC power can be stepped-up using a four-phase IBC and controlled efficiently using a MPPT EMS scheme to reduce power ripples.
Study 2.3.3.11 (Artal-Sevil K.S. *et al.*, 2020)	Presented MIC and DPP connections of FCs with power converters. MPPT was used on the DPP converter to achieve a fast control loop.
Study 2.3.3.12 (Arazi M. *et al.*, 2020)	Developed a mechanism for FCs and SCs DC-DC resonant power converters to share the system power using their dynamic responses.
Study 2.3.3.13 (Martin-Lozano A. *et al.*, 2020)	Proposed an EMS optimization technique for the power distribution system to increase the driving range of fuel cell hybrid vehicles. The results correlated other studies in the literature.
Study 2.3.3.14 (Salimi M. *et al.*, 2021)	Suggested the used of MIMO technique to dynamically model and closed-loop control a FC hybrid grid-tied renewable energy system.
Study 2.3.3.15 (Sorlei I.S. *et al.*, 2021)	Used FCs and energy storage devices as well as power converters and EMS techniques to sustain hybrid electric vehicle dynamic power.
Study 2.3.3.16 (İnci M. *et al.*, 2021)	Reviewed extensively FC types with electric motors with focus on their uses, diagnostic properties and finally working environments.

Table 2.7 summarizes the reviewed EMS FC applicable studies.

2.3.4 Summary

Energy insecurity and electrical energy in particular, is a progressive pressing societal crisis in South Africa and Africa. In this regard, this section articulated a structural review of forty four different power converters and EMS research case studies to reasonably choose and develop a suitable FC power converter and EMS scheme for a hybrid FC CCHP system for households / commercial applications. From the review, it was observed that the power converters based on IBC /variants and as well isolated boost converters were of interests. IBC are simple, more robust, good for ripples reduction and peak power applications. However, the fundamental IBC topology is not isolated and adding isolation transformers offers protection but increases the costs and size. Likewise, EMS techniques can be grouped under rule-based, learning-based and optimization-based but the most popular EMS strategy used with power converters are the MPPT and PI controller. Furthermore, FCs can also be modularized with each FC sub-module having its own power converters and EMS scheme to increase the system efficiency. In sum, there is no method that is flawless − choosing a particular approach and trading-off different features depend on the targeted applications and the research objectives; which could be whether to maximize efficiency, robustness, safety, performance etc and or minimize costs, size, noise, complexity etc. For my research project, power converters based-on IBC variants and BDC with EMS based on MPPT and or proportional−integral−derivative (PID) controller for use with fuel cell, Li-ion battery, ultra-capacitor and thermoelectric devices, are considered to investigate further the CCHP system postulated in Figure 2.62.

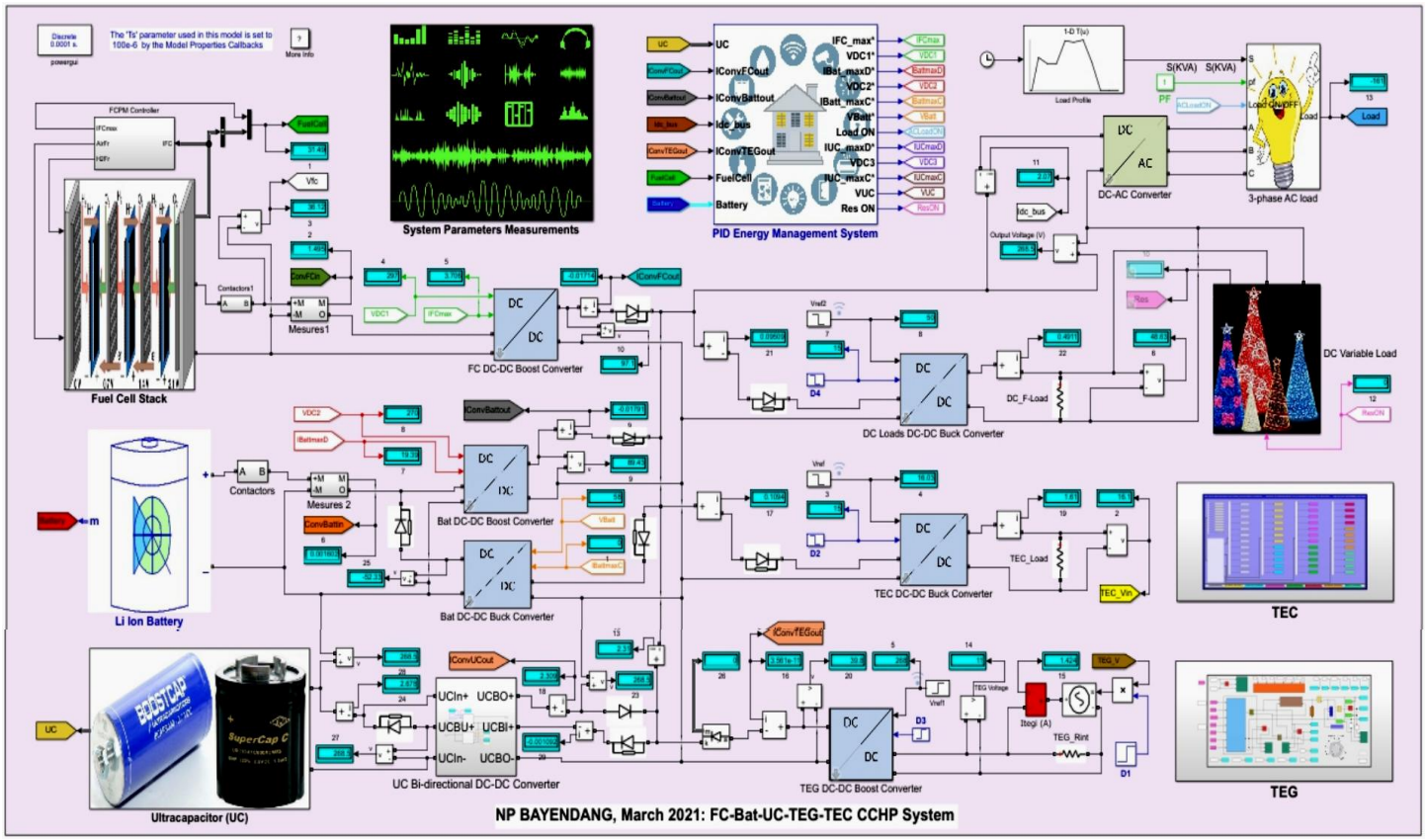

Figure 2.62: Proffered fuel cell CCHP system undergoing research

2.4 A Structural Review of Thermoelectricity for Fuel Cell CCHP Applications

This section starts by introducing the ongoing South Africa electricity crisis followed by thermoelectricity, in which eighteen miscellaneous applicable case studies are structurally analysed in detailed. The aim is to establish best practices for the R&D of an efficient thermoelectric (TE) and fuel cell (FC) CCHP system. The examined literature reviews, covered studies that focused on thermoelectricity principle, highlighting TE devices basic constructions, TEGs and TECs as well as some investigations on the applications of thermoelectricity with FCs, whereby thermoelectricity was applied to recover waste heat from FCs to boost the power generation capability by ~7 – 10%. Furthermore, non-stationary TEGs whose generated power can be increased by pulsing the DC-DC power converter, showed that an output power efficiency of 8.4% is achievable and that thicker TEGs with good area coverage can efficiently harvest waste heat energy better in dynamic applications. TEG and TEC exhibit duality and the higher the TEG temperature difference, the more the generated power – which can be stabilised using MPPT technique with a 1.1% tracking error. A comparison study of TEG and solar energy demonstrated that TEG generates more power compared to solar cells of the same size, though more expensively. TEG output power and efficiency in a thermal environment can be maximised simultaneously if its heat flux is stable but not the case if its temperature difference is stable. The review concluded with a TEC LT-PEM-FC hybrid CCHP system capable of generating 2.79kW of electricity, 3.04kW of heat and 26.8W of cooling with a total efficiency of ~77% and fuel saving of 43.25%. The presented findings are the contributions brought forward, as they heuristically highlights miscellaneous thermoelectricity studies and parameters of interest, which further established that practical applications of thermoelectricity is possible and can be innovatively applied together with fuel cells for efficient CCHP applications.

2.4.1 Introduction

In Bessarabov *et al.* (2017), South Africa and Africa in general is faced with ongoing electrical energy and power crises and this section broadly examines various research on thermoelectricity in order to determine, develop and apply best practices for the devise of an efficient TE fuel cell hybrid power energy system for home and commercial Combined Cooling, Heating and Power (CCHP) applications. Thermoelectricity as per the review summarised in Table 2.10, is a thermal and or electrical process, in which a material based on its thermal and or electrical properties, can either generates heat or cold depending on the voltage polarity across the material or this same material is capable of generating electricity from heat, when there is a temperature difference (ΔT) on the material (technically known as a thermocouple) surfaces. Furthermore, there are three effects governing thermoelectricity commonly called thermoelectric effects, which are i) the Seebeck effect (named after the discoverer, Thomas Seebeck) − which is the generation of electricity from

heat and the devices that enable such a process are popularly known as thermoelectric generators (TEG); ii) the Peltier effect, (named after the discoverer, Jean Peltier) − which is, depending on the applied voltage polarity, is the generation of cold from electricity or when the same applied voltage polarity is reversed, is the generation of heat from electricity and the devices that enable such a process are popularly known as thermoelectric coolers (TEC) and iii) the Thomson effect (named after the discoverer, William Thomson or popularly known as Lord Kelvin), is the generation or absorption of heat when voltage is applied across a uniform material that has a temperature difference along its length and depending on the flow of the electric current, the Thomson effect could be positive or negative. This Thomson effect is reversible and as a result, is different from Joule or Ohmic heating – which is an irreversible generation of heat when an electric current flows through an electrical conductor. Thomson effect is usually negligible in practise (cannot be harnessed to produce the desired practical effect) and as a result, practical thermoelectricity is normally focussed on the Seebeck and Peltier effects and therefore, thermoelectricity can be practically defined as a reversible two-way or triple display of the same thermo-electrical process, known as the Peltier-Seebeck effect. According to the literature, thermoelectricity can be practically applied to i) cogenerate electricity and or ii) provides thermal management (cooling and or heating). In Twaha *et al.* (2016), the electrical and thermal conductivities are related through the Wiedemann-Franz law by:

$$k_{ec} = L_o \sigma T \tag{2.18}$$

where k_{ec} is the thermal conductivity charge carrier contribution, L_o is a constant known as the Lorenz number (2.44×10^{-8} $W\Omega K^{-2}$), σ is the electrical conductivity and T is the absolute temperature in kelvin. Furthermore, the thermoelectric materials are categorised based on their dimensionless figure of merit, zT, defined by:

$$zT = \frac{S^2 \sigma T}{k} \tag{2.19}$$

where S is the Seebeck voltage per unit of temperature in kelvin, σ is the electrical conductivity, k is the thermal conductivity and T is the absolute temperature in kelvin (273.15 K) or 0°C.

The TE device maximum efficiency (η_{max}) determined by ZT (different from zT), is given by:

$$\eta_{max} = \eta \frac{\sqrt{1+Z\overline{T}}-1}{\sqrt{1+Z\overline{T}}+\frac{T_c}{T_h}} \quad \text{where } \eta = \frac{\Delta T}{T_h} \text{ is the Carnot Efficiency and } \overline{T} = \frac{T_h+T_c}{2} \tag{2.20}$$

where ZT is the TEG dimensionless figure of merit, ΔT is the temperature difference between T_h *and* T_c; $Z\overline{T}$ is the device dimensionless figure of merit at temperature $\overline{T}$ while T_h and T_c are respectively the device hot and cold sides temperature. When $ZT = zT$ the relationship becomes;

$$Z = z = \frac{S^2 \sigma}{k} \tag{2.21}$$

where $Z=z$ is the figure of merit in K^{-1} and $S^2\sigma$ is known as the TEG electrical power factor.

The TEG thermal/conversion efficiency (η_{TEG}) is defined by: $$\eta_{TEG} = \frac{TEG_{Pout}}{Q_h} \quad (2.22)$$

where TEG_{Pout} is the generated TEG output power and Q_h the heat absorbed on TEG hot side.

$$TEG_{Pout} = n\,[S\,I\,(T_h - T_c)] - (I^2R)] \quad (2.23)$$

$$Q_h = n\,[S\,T_h\,I - 0.5(I^2R) + K\,(T_h - T_c)] \quad (2.24)$$

where n is the TEG thermocouple p-n junction quantity, I the output current, r the TEG thermocouple p-n junction resistance and K the thermal conductance.

TEC coefficient of performance (CoP) is given by; $$TEC_{COP} = \frac{Thermal\ cooling\ power}{Electrical\ input\ power} \quad (2.25)$$

2.4.2 Thermoelectricity Case Studies of Interest

In the following sections, eighteen assorted thermoelectricity applicable case studies are examined to determine several factors that can be applied and developed to devise a novel CCHP system. NB: the eighteen thermoelectricity case studies analysed herein are those vital to my research objectives.

2.4.2.1 Thermoelectric Device as a Construct, TEG and TEC

Examined in Bell (2008) and Gao (2014), thermoelectric (TE) materials are solid-state energy converters whose combination of thermal, electrical and semiconducting properties; allow them to be used easily to convert waste heat into electricity or electrical power directly into cold and heat. The materials must be very good electrical conductor but poor thermal conductors; otherwise, the temperature difference that must be maintained between the hot and cold sides will produce large heat backflow. A TEG dimensionless figure of merit *ZT*, expresses the efficiency of the P-type and N-type materials that make up a TEG/TEC device at absolute temperature in kelvin (273.15 K). The TEG figure of merit Z in per kelvin, is the square of the Seebeck voltage per unit of temperature, multiplied by the electrical conductivity and divided by the thermal conductivity, where T is the absolute temperature. In today's best commercial TEG/TEC devices, *ZT* is about 1.0; however, various research has shown that *ZT* can be hugely improved, depending on the classic material treatment approaches; such as nanotechnology, reduce device dimensionality, doping to increase the band structure and using new materials with complex crystalline structure. Thermoelectric materials intensively studied include Bismuth and Bismuth-antimony, Lead Telluride and related compounds, Silicon-germanium alloys, skutterudites and clathrates, oxides as

well as some other types: Zinc antimonide, half-heusler compounds, metal silicides and Boron carbide. As stated in Gao (2014), there are three categories of TEGs: i) low-temperature (<200°C), ii) medium-temperature (200 - 600°C) and iii) high-temperature (600 - 1000°C). More efficient thermodynamic cycles and designs that reduce material costs are transcending into commercial production. Figure 2.63 depicts a thermoelectric device as, A) a Construct, B) a TEG and C) a TEC.

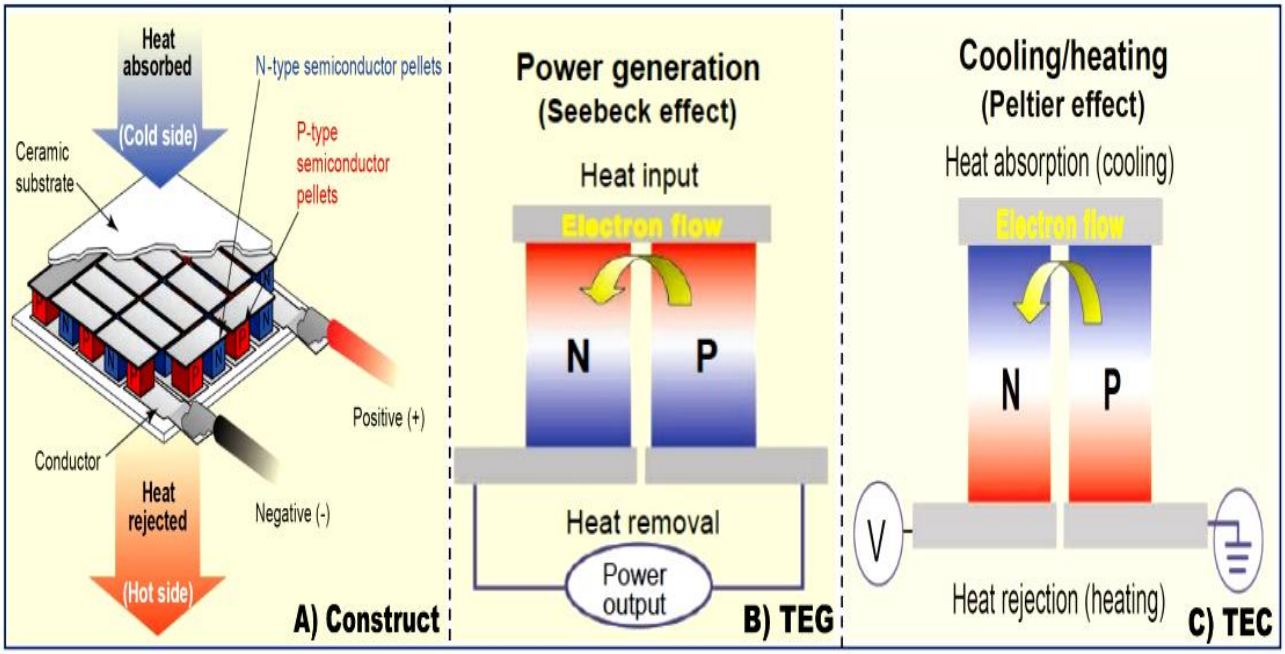

Figure 2.63: Thermoelectric device as A) Construct, B) TEG and C) TEC (adapted from Bell, 2008)

2.4.2.2 Harness Thermal Energy using TEGs in a HT-PEM FC Power System

Researched by Gao (2014), TE devices can be used to enhance the efficiency and the load following capability of a high temperature polymer electrolyte membrane fuel cell (HT-PEM FC). A heat recovery subsystem based on compact plate-fin heat exchangers and TEGs were designed to harvest the system hot exhaust gas for electricity. The maximum power point tracking (MPPT) power conditioning method was also systematically examined. TEGs were integrated into the methanol evaporator of the HT-PEM FC system to improve the entire system load-following capability. By reducing heat loss, the system power efficiency can be boosted. The TEG modules working modes were various and unique; as a result, were redefined as thermoelectric heat flux regulators (TERs). Three crucial parameters were determined and they are i) heat exchanger surface type, ii) its housing dimensions and iii) TEG power conditioning. In light of these, a practical TEG system was recommended to have four sub-systems as follows i) heat exchanger support structure, ii) TEG array (converts heat to DC voltage), iii) cooling and iv) electrical power converters to provide working DC and or AC voltages to the loads. Figure 2.64 depicts the researched scheme.

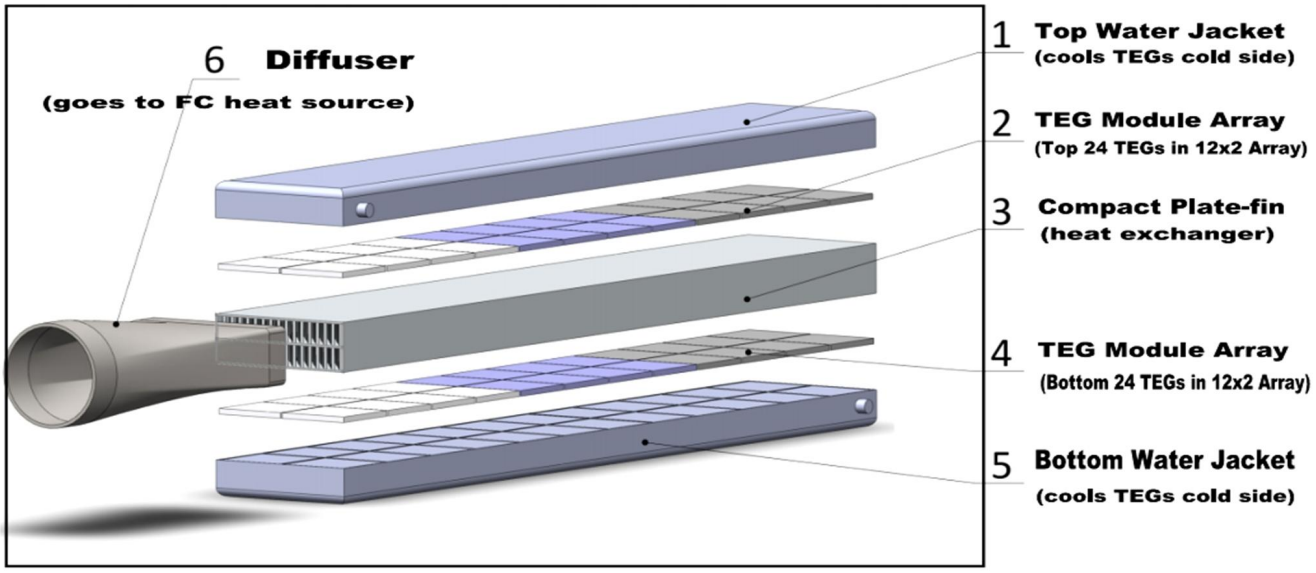

Figure 2.64: TEG and HT-PEM FC energy harvesting setup (adapted from Gao, 2014)

2.4.2.3 TEG and Fuel Cell Cogeneration

Studied in Huston *et al.* (2004), an electrical energy conversion efficiency of approximately 15 percent would be required to obtain an acceptable return on investment for thermoelectric devices. As a result, a feasibility study was performed to determine how, assuming 16% efficiency, thermoelectric devices could impact the US Department of Defence (DoD) power generation capabilities. Based on research indicating energy conversion efficiencies of 20%, thermoelectric devices were built and tested. Of the 27 thermoelectric devices supplied, only 8 were functional; of which each device produced only 1W of electrical power. Current manufacturing processes and design parameters were examined and recommendations made. In concluding the research, more than 40 specific applications (facility and non facility) for thermoelectric devices were investigated, in which it was realised that in all these applications, thermoelectric devices form factor was key, which enabled TEGs to be mounted on hot surfaces, in hot gas streams, along processes to absorb radiant heat or integrated in stacks or process insulation. This adaptability allows thermoelectric systems to be integrated within industrial processes with minimal impacts on the process. In Table 2.8, it was shown that thermoelectric devices have the potential to increase efficiency and when used with different types of fuel cells, their respective power generations were increased by ~7 to 10%. Furthermore shown in Table 2.9, TE devices generated 464 000 MWh of electricity each year when applied to low grade heat (LGH) generated from military processes, which translates yearly to greater than $34.5 million cost avoidance for the production of electricity and results in approximately 1.5 billion BTUs of energy production from normally discarded LGH. Additionally, this equates to 268 000 barrels of oil yearly equivalent.

Table 2.8: Efficiency improvement of FCs incorporating thermoelectric devices (adapted from Huston *et al.*, 2004)

Fuel Cell Type	Operating Temperature	Efficiency	Heat Percentage Waste	Power Generation Increase	Final Efficiency	Efficiency Improvement
LT – HT PEM FC	80 - 180°C	40%	60%	**9.6%**	49.6%	24%
Alkaline FC	65 - 220°C	60%	40%	**6.4%**	66.4%	11%
Phosphoric Acid FC	205°C	37 - 42%	60%	**9.6%**	49.6%	24%
Molten Carbonate FC	650°C	45%	55%	**8.8%**	53.8%	20%
Solid Oxide FC	600 - 1000°C	45 - 65%	45%	**7.2%**	62.2%	13%

Table 2.9: Potential annual benefits of thermoelectric device application (adapted from Huston *et al.*, 2004)

Sector	Electricity Generation (MWh)	Generation Capacity (MWe)	Cost Avoidance ($1M)	Oil Equivalent Saved (thousands of barrels)	Carbon Emissions Savings (metric kilotons)	Number of Potential Applications
Defense	464 000	53	34.5	268	21	43
Utility / non-utility generation (CTC & LTI 2001b)	603 000 000	68 000	45 000	355 000	41 200	57
US industries of the future (CTC & LTI 2001a)	74 000 000	8 400	5 500	43 000	5 000	101

2.4.2.4 Ionic Thermo-electric Super-capacitor (ITESC)

As stated in Zhao *et al.* (2016), temperature gradients are generated by the sun and a vast array of technologies, which can induce molecular concentration gradients in solutions via thermo-diffusion (Soret effect). In the case of ions, this leads to a thermo-voltage that is determined by the thermal gradient ΔT across the electrolyte, together with the ionic Seebeck coefficient (α_i). Due to a lack of strategy to harness the energy from the Soret effect, redox-free electrolytes have not been explored in thermoelectric applications. As a result, a new means to harvest energy from intermittent heat sources and converted into stored charge via the ionic Soret effect in an ionic thermoelectric super-capacitor (ITESC) was demonstrated – from which it was shown that, the stored electrical energy of the ITESC is proportional to $(\Delta T\alpha_i)^2$ and that its α_i reaches beyond 10mV/K. The resulting ITESC can convert and store several thousand times more energy as compared to a conventional TEG connected in series with a super-capacitor. According to Zhao *et al.* (2016), it was demonstrated for the first time that the Soret effect in a polymer electrolyte leads to significant ionic thermoelectric effect that could be used to charge a super-capacitor. The presented ITESC device requires a variation in the applied temperature gradient to function, which makes the concept suitable for intermittent heat sources, such as the sun. They explained potential

enhancements of the ITESC concept and forecasted the heat-to-electricity charging conversion efficiency to be able to improve if good thermoelectric electrolytes are designed with low specific heat capacitance, low thermal conductivity, large Seebeck coefficient and high ionic conductivity. Importantly, all materials (polymer and inorganic salts) consisting of the ITESC are fully compatible with industry processing. Contrary to a usual thermoelectric device constituting a semiconductor and two metal contacts, where a constant electrical power can be provided to an external load by imposing a temperature gradient along the metal-semiconductor-metal stack; however, the same harnessing principle is not directly applicable if the semiconductor is replaced by an electrolyte solution with ions as charge carriers. The reason for this is that the thermo-diffused ions are stopped at the surface of the metal electrode and cannot pass through the external circuit. Furthermore, akin to classic electronic materials, the efficiency will increase with higher ionic conductivity, Seebeck coefficient and lower thermal conductivity. However, for materials with the same zT value, the maximum efficiency from typical TEGs is greater than from ITESC. This is because the output power is not constant in ITESC, which instead decreases with time as illustrated in Figure 2.65a. In Figure 2.65b, is the summary that explains their research on ITESC.

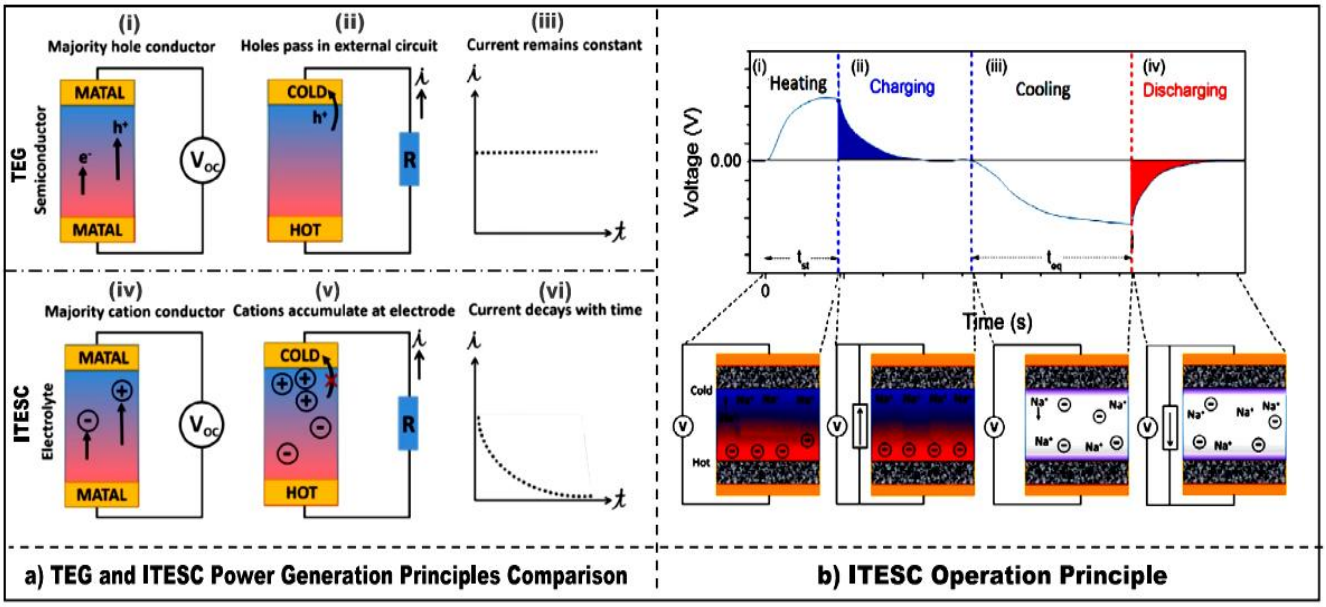

Figure 2.65: Ionic thermoelectric super-capacitor summary (adapted from Zhao *et al.*, 2016)

2.4.2.5 Small Modular TEG Power Generation Analysis

According to Mahmud *et al.* (2017), from the thermoelectric characterization, it can be concluded that to generate more voltage, TEGs must be connected in series and in parallel to generate more current. Furthermore, the voltage and current (power) increases when the TEG cold side is cooled – which was studied with a setup with and without a fan. Figures 2.66a − 2.66d summarise the

experiments. It should be noted that, TE device P-N thermocouples are inherently connected electrically in series and thermally in parallel (Yusop *et al.*, 2013) − the reason is to increase electrical conductivity and decrease thermal conductivity.

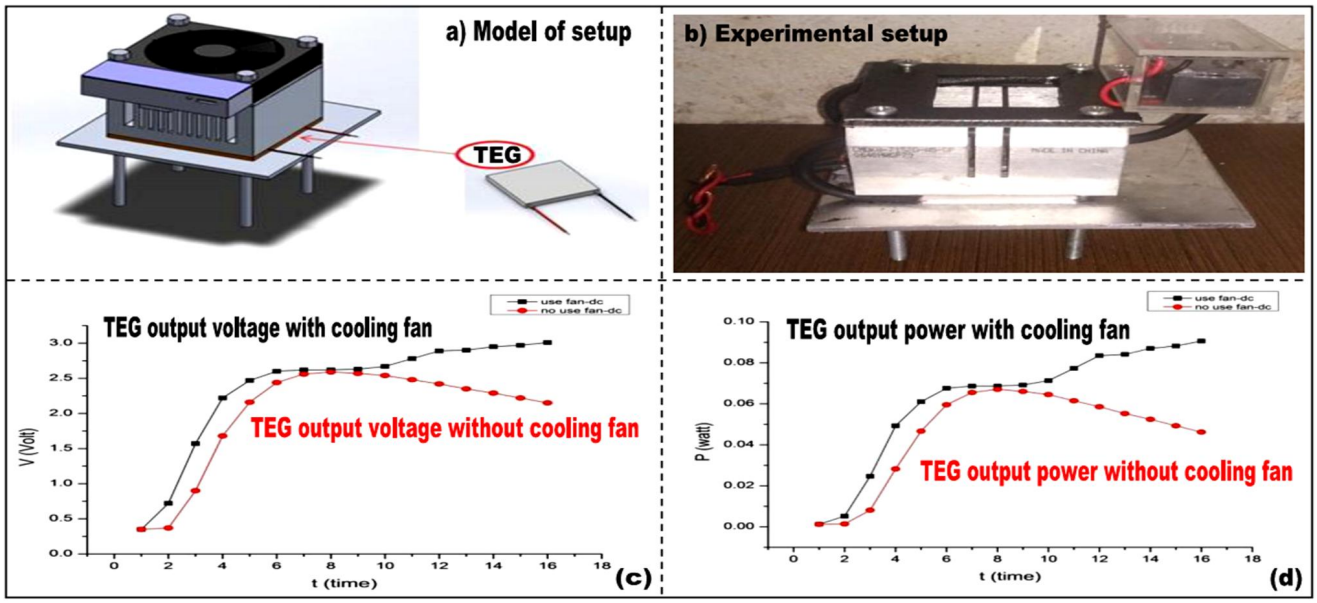

Figure 2.66: Modular TEG characterisation (adapted from Mahmud *et al.*, 2017)

2.4.2.6 TEG and Micro-turbine Combined Heat and Power (CHP) System

In Qu *et al.* (2018), a thermodynamic model was developed for the TEG and micro-turbine combined power generation system as shown in Figure 2.67. The numerical results showed that the addition of TE device can almost doubles the CHP output power generated. Also in an investigation in Huston (2004), TEG cogenerations are more efficient compared to other equivalent forms of CHP systems.

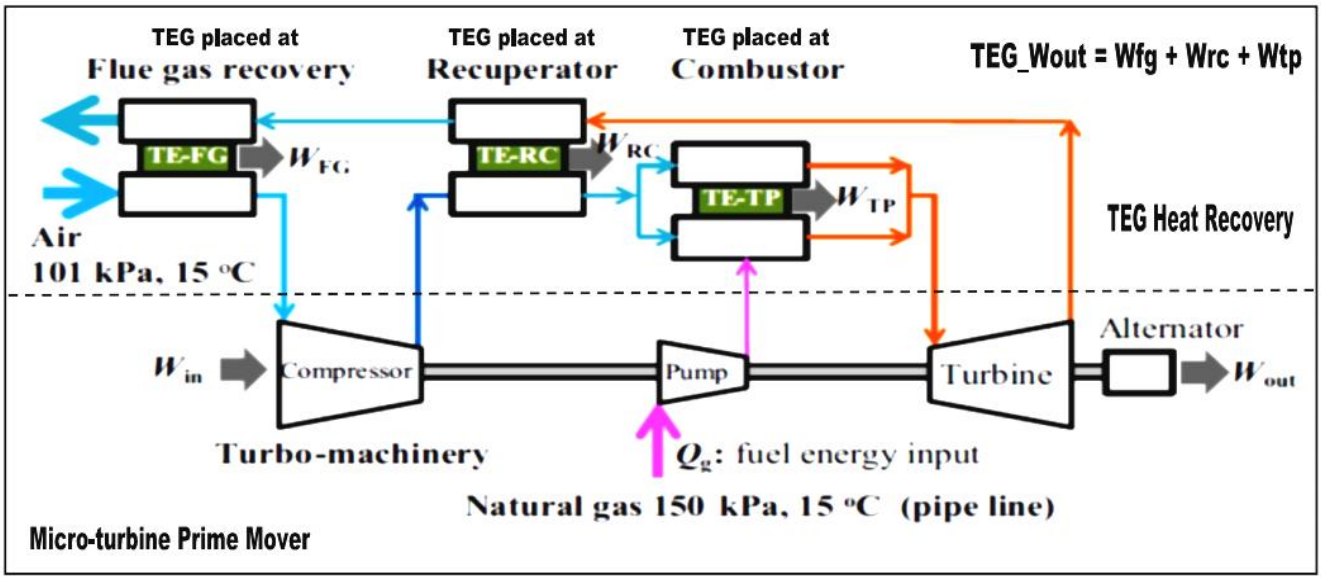

Figure 2.67: TEG and micro-turbine cogeneration (adapted from Qu *et al.*, 2018)

2.4.2.7 High Temperature TEG Module Characterisation System

Stated in Katkus (2015), Thermoelectric (TE) power generators (TEGs) are used to convert thermal energy directly into electrical energy; however, present TEGs have limited conversion efficiencies and lack the capacity to penetrate these highly important industry sectors, though successfully applied in niche fields; such as space applications, scientific equipment facilities and hot lasers. Most of research efforts concentrated on the development of novel TE materials, which would have higher figure of merit (zT) – a value that signifies how good/bad thermoelectric material is. It is a widely established fact that for practical considerations, the figure of merit for any given thermoelectric material, P-type or N-type, has to exceed unity. However, knowing the basic characteristics of a given thermoelectric material cannot be directly related to the conversion efficiency of a TEG. The manufacturing of a TEG includes selection of TE materials, electrodes, insulating plates, adhesives and module architecture. The complexity of this task is evident by the few number of research papers describing characterisation of thermoelectric modules. Furthermore, as claimed in Katkus (2015), in contrast to existing TE material characterisation systems, there are no commercial systems available that would allow accurate characterisation of fabricated TEGs. Hence, their research was undertaken to design and construct a comprehensive computer controlled characterisation system, which would allow efficient characterisation of in-house built TEG modules. This system incorporated all of the above mentioned features in a bench-top engineering solution integrating high power heating, liquid cooling, hydraulic compression, force and temperature sensing – all in a controllable atmosphere. The measurement system has been specifically designed to accommodate wide range of TEG modules suited for low to high temperature applications. The system accurately reproduced application conditions the TEG devices may be subjected to in a real world environment − which was tested with direct heat flux measurements using reference materials.

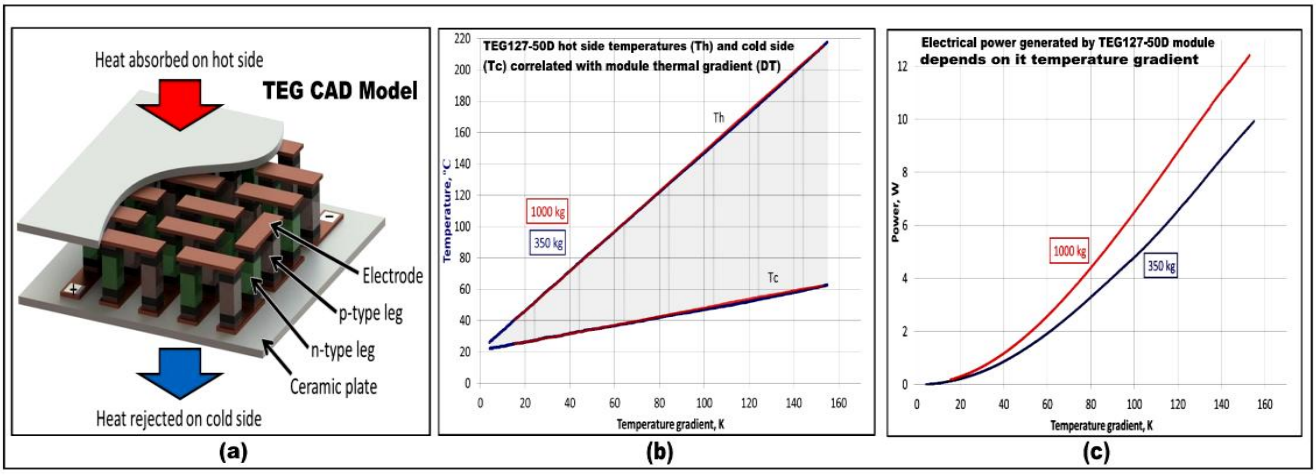

Figure 2.68: High temperature TEG characterisation (adapted from Katkus, 2015)

Bismuth telluride based Thermonamic TEHP-12656-0.3 and Everredtronics TEG 127-50D TEG modules were characterised. Their performance data were analysed and compared to the available manufacturer data. The measured data correlated with anticipated values, though some discrepancies were noticed due to overlooked inaccuracies in the traditional module resistance measurements. Figures 2.68a - 2.68c show some results of the study.

2.4.2.8 On-chip TECs and TEGs Model Based Design

As in Sullivan (2012), TE devices for the last decades have been used in many power generation or cooling applications; such as energy recovery in space and cooling of sensors located in heat-sinking missiles. This research focused on the possibility of embedding thermoelectric devices within electronic packaging for both hot spot TEC and TEG. The commercial CFD solver FLUENT and the analog electronic circuit simulator SPICE were used to study operations of single and arrayed TECs and TEGs integrated inside a FLUENT model based chip – which were arranged in a programmable 3x3 array to be up to 9 TECs and or TEGs depending on the tests configurations.

This array of nine TECs or TEGs as depicted in Figures 2.69a and 2.69b, provided vital results related to thermal coupling of adjacent TECs and transient pulse operation of TECs. Figure 2.69c showed the cooling currents and their effects to the TEC (at mid hotspot of 5, Figure 2.69b) at various levels (from steady-state of 3A to transient levels of 6, 8 and 10A. Figure 2.69d illustrates the cooling coupling among TECs, which is strongest when more TECs are turned ON and the cooling is also best in steady-state, whereas weakest with less TECs turned ON as well as worst in transient conditions (i.e. large current is involved). From the analyses of various pulse shapes portrayed in Figure 2.69e, the square root pulse shown in Figure 2.69f, was noticed to yield the best cooling considering all the important parameters – maximum cooling, temperature overshoot after current pulse is turned off, total energy used and settling time. As per Figure 2.69g, it was also established that the shortest duration of the transient pulse, positively affects the cooling, which degrades if left longer, as the longer the pulse switch ON current, the more Ohmic heating – as evident in the initial control results for random hotspots using the square root pulse. In all, frequent hotspots should be cooled with steady-state currents and infrequent hotspots may be cooled using square root transient pulses of least period. A thinner TIM and or bigger thermal conductivity enhances the cooling.

Similar analyses of the on-chip TEGs yielded vital and intuitive results. As shown in Figure 2.70a, the maximum power transfer (MPT) occurred at a load resistance bigger than the TEG device resistance, contrary to the established fact that MPT occurs when load and source resistances equal. This deviation was mainly due to the dependence of the generated power on the temperature

difference between the hot and cold junctions. This temperature difference is also dependent on the generated current and is inversely proportional to the load resistance. Hence, as depicted in Figure 2.70b, useful MPT occurs only when the load and TEGs resistances are i) equal and ii) the TEG temperature is constant. Also increasing the background heat flux, initially increased useful power (load power) linearly which later changed to a parabolic increment, as Power = I^2R. Figure 2.70c also showed that reducing the TIM thickness between the hot junction of the TEG and the surface of the chip, yielded improved power generation from the TEGs. The effect of transient to on-chip TEG is trivial, since a TEG is passive and there is dynamic change in on-chip heat flux. Finally, the result in Figure 2.70d, displayed a study done on various TEGs array (see Figure 2.70b for layout), to research the total useful power and average useful power per TEG in mW for five setups with varying number of on-chip TEGs as follows: (i) TEG 5 only (ii) TEGs 3, 5 and 7 (iii) TEGs 1, 3, 5, 7 and 9 (iv) all TEGs except 2 and 8 and (v) all TEGs 1-9. It was established that adding more on-chip TEGs always first increases the total useful power generated; however, on-chip TEG efficiency decays when more are added due to over-crowding.

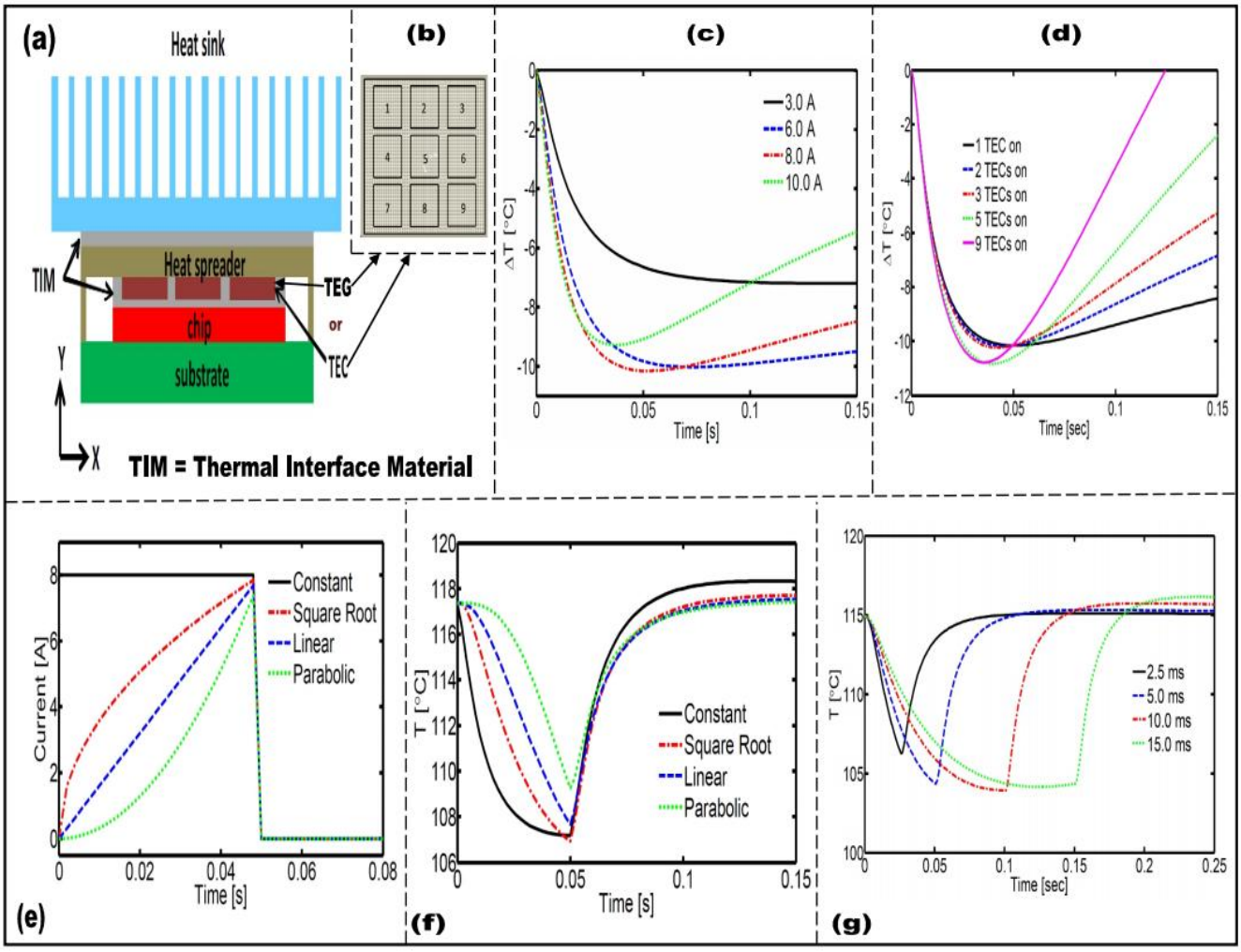

Figure 2.69: Simulation summary of the modeled on-chip TEC (adapted from Sullivan, 2012)

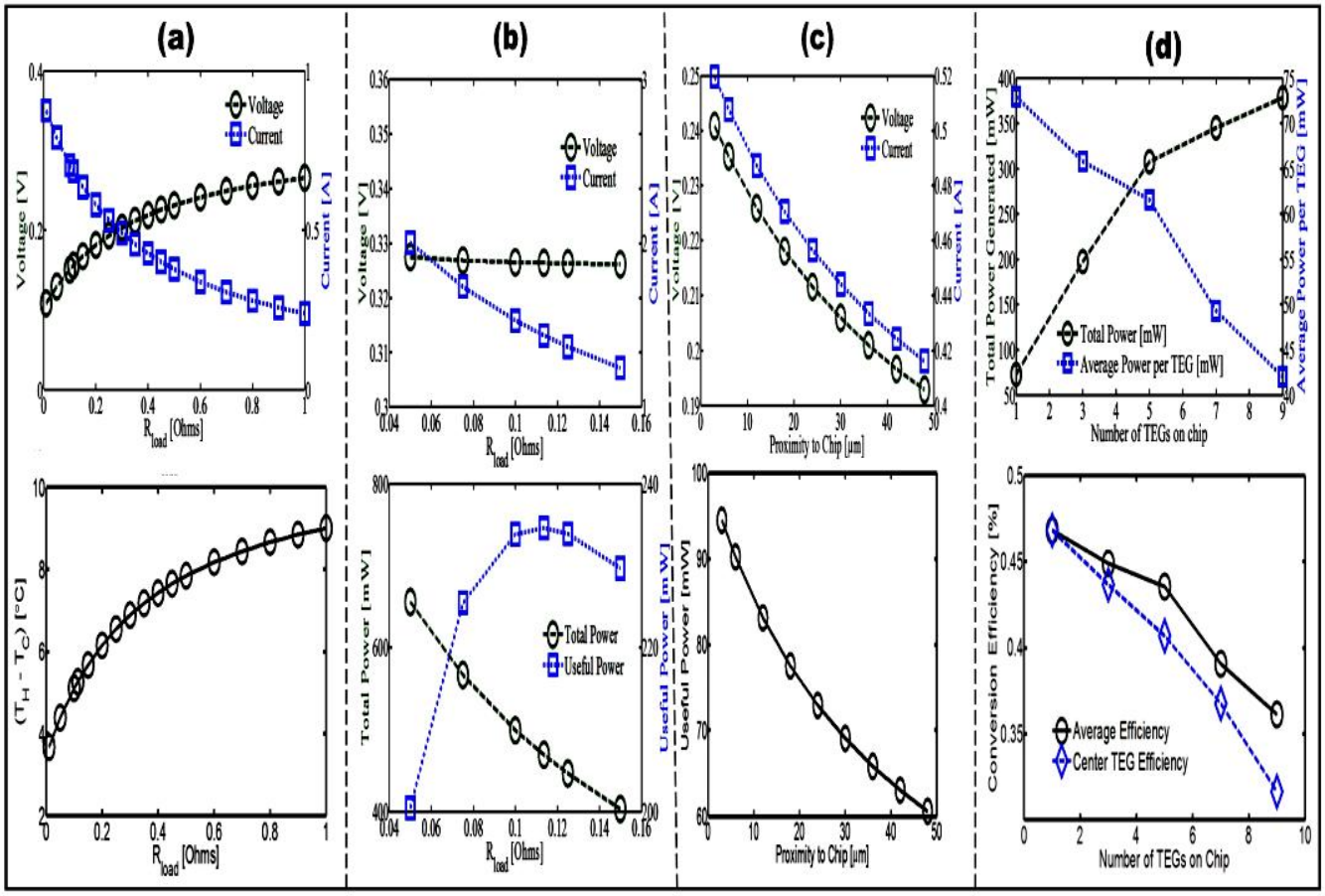

Figure 2.70: Simulation summary of the modeled on-chip TEG (adapted from Sullivan, 2012)

2.4.2.9 Hybrid TEC-TEG Modelling and Experimentation

According to Teffah *et al.* (2018), a new thermoelectric cooler–thermoelectric generator (TEC-TEG) module was simulated (Figure 2.71c) and experimentally (Figures 2.71d − 2.71e) studied using COMSOL Multi-physics modelling software as illustrated in Figures 2.71a − 2.71g. The researched module consisted of a TEC (Figure 2.71a), TEG (Figure 2.71b) and total system heat-sink (Figures 2.71c - 2.71e) all connected thermally in series. An input voltage (1 to 5V) was applied to the TEC where the electrons by means of Peltier effect, converted heat from the upper side of the module ($T_{cold\ TEC}$) to the lower side ($T_{hot\ TEC\text{-}TEG}$) creating temperature difference. The TEG acts as an intermediate heat-sink for the TEC by transferring this waste heat to the total system heat-sink and converting an amount of this heat into electricity by a phenomenon called Seebeck effect. The temperature contour of TEC-TEG and TEG's electric potential at different TEC's input voltage: (i) V = 0 and V = 1; (ii) V = 2 and V = 3; (iii) V = 4 and V = 5 were measured. Figure 2.71f shows the effect of the input voltage of TEC on the temperature difference (ΔT) across the cold and hot sides of TEG in both simulated and experimented results – where ΔT is directly proportional to the input voltages and directly proportional to the TEG output voltages as shown in Figure 2.71g correlated results.

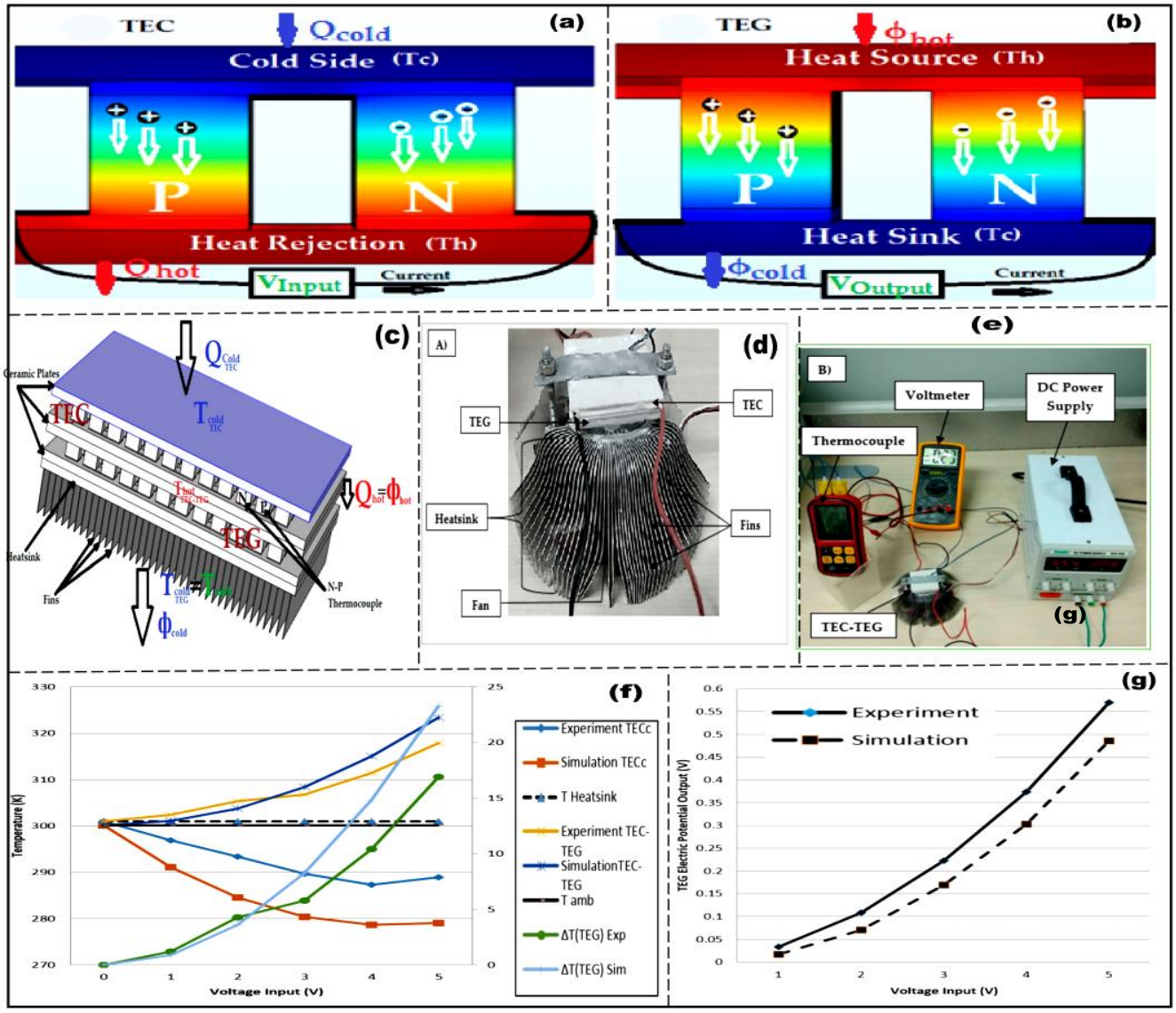

Figure 2.71: Summary of the simulated model and experimented TEC-TEG (adapted from Teffah *et al.*, 2018)

2.4.2.10 Non-stationary TEGs

In Stockholm *et al.* (2015a), Stockholm *et al.* (2015b) and Stockholm (2016), a review of theoretical publications on non-steady thermoelectrics were presented, in which different aspects of non-stationary and pulsed processes in thermoelectric materials and devices were examined. Theoretical analyses of dynamic behaviour of thermoelectric devices, including analyses of small and large signals of thermoelectric generator, are given and details of the principle of quasi-equilibrium thermoelectricity are discussed as well. Special attention was given to theoretical study of the non-routine regime of non-steady thermoelectricity – fast-time dependence of thermoelectric properties when TE material / device is well out of equilibrium. Theoretical results of fast-time dependence gave reason to think that it can increase the output electrical power of thermoelectric generator compared to stationary techniques of operations.

Experimental results acquired using first ever non-stationary thermoelectric generator prototype, which was designed for operation in fast-time dependence mode, was disclosed. There have been ongoing R&D to confirm that more electrical output power can be obtained in AC mode (AC frequency about hundreds of kHz) than in DC mode and TE parameters of interests include energy capacity, speed of response, response time improvement, temperature dependence of physical parameters and output characteristics; accounting for Peltier heat production, effectiveness of side surfaces of thermal insulation and thermal stabilization based on the model of finite length. In the early 90s, Aspen and Strachan filed a priority patent on thermoelectric energy conversion in high-frequency mode and later published results of development and demonstration tests of MHz thermoelectric generator, which became the first work on thermoelectric operating far from equilibrium. Strachan, who developed a vibrator with it to break kidney stones also noticed that his device could function as a heat pump (to produce ice) or with temperature difference between both sides, it could generate electrical power sufficient to operate a small fan. Jon Schroeder in 1994 announced a ring-shaped TEG pulsed at 60Hz and he published a paper about it in 1999 and built a prototype in 2004 but regrettably, it did not work.

Schroeder further designed a ring-shaped TE device called Schroeder ring. In which heat is produced in the centre by hot gases, which can be combustion gases from natural gas. The heat is transferred by convection and radiation to the radial blades. Non-stationary TEGs are TEGs with high values of capacitance in Farad range (akin to super-capacitors), which makes them pulse operable at more than 100 kHz. Apostol postulated that pulsing can improve TEG efficiency due to ultra-fast conduction as predicted. Nedelcu and Stockholm observed in 2001 that, when electrical current is pulsed at 50kHz, the electrical power was constant at $Rs > R_L$ – this demonstrated that small electrical resistance (impedance to be correct), should be taken into account to extract electrical power efficiently. Nedelcu later confirmed Apostol's work by building a TEG with four commercial TEGs connected electrically in parallel. Electrical current output was pulsed using MOSFETs at around 200kHz. The output current from the transformer is rectified. The load was 100W filament light bulb. The voltage measured was 210V and current 0.4A giving electrical output power of 84W. The total efficiency (including heat losses) was 8.4% deduced from the ~1kW heat source. This approach has about twice higher conversion efficiency to when operated in DC mode. Figure 2.72 illustrates how a TEG electrical output power is pulsed.

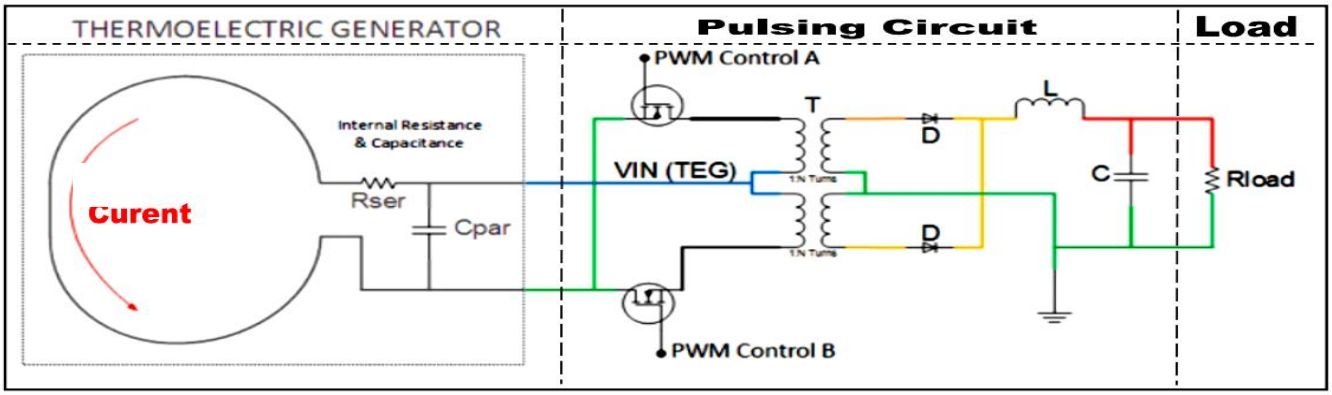

Figure 2.72: Pulsing TEG electrical output power using MOSFETs (adapted from Stockholm *et al.*, 2015b and Stockholm, 2016)

2.4.2.11 TEG Design in Dynamic Thermoelectric (TE) Energy Harvesting

Presented in Kiziroglou *et al.* (2016), is an analysis of TEG design for dynamic TE harvesting – which enables electricity generation from temperature fluctuations in an environment, such as a vehicle body or an industrial machine. Depicted in Figure 2.73, it employed a heat storage unit (HSU), with a phase change material (PCM) to increase heat storage, insulated from the environment and in thermal contact with a TEG. This available energy for a given temperature cycle is finite and determined by the HSU capacity. It was demonstrated by simulation and experimentally that, specific TEG designs can boost the energy output by optimizing the balance between heat leakage and dynamic response delay. A 3D printed double wall HSU was developed for the experiments. The output energy of 30J from 7.5g of phase change material from a temperature cycle between ± 22°C is shown – which is enough to supply typical duty-cycled wireless sensor platforms. The research showed that total maximum potential performance is achieved with thicker TEGs and choosing a specific surface coverage area. TEGs of various thicknesses were tested as shown in Figure 2.73. These outcomes may serve as guidelines for the design and fabrication of dynamic TE harvesters for applications requiring surroundings with moderate temperature (<50°C) variations.

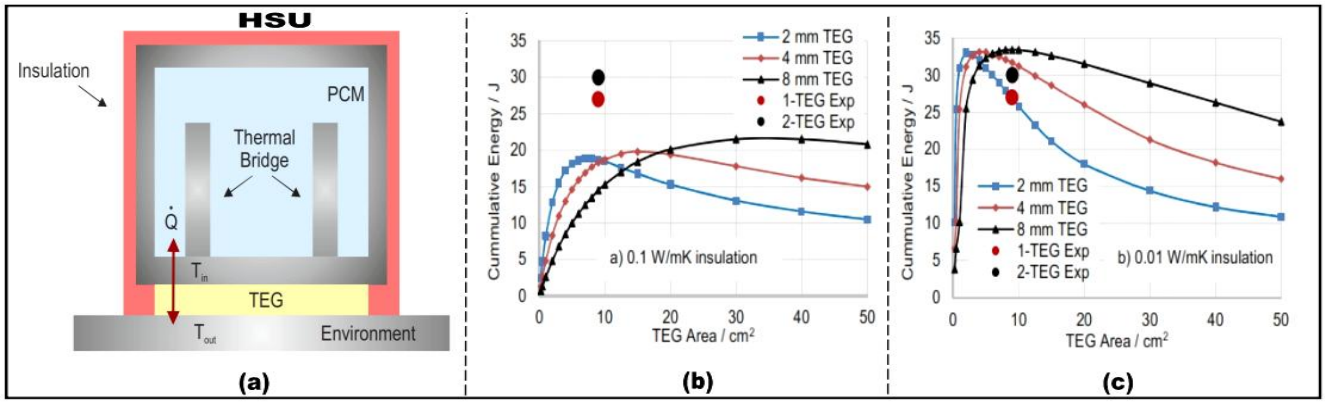

Figure 2.73: TEG design in dynamic TE energy harvesting (adapted from Kiziroglou *et al.* 2016)

2.4.2.12 TEG and 1kW Low Temperature (LT) PEM FC Waste Heat Recovery

In Sulaiman *et al.* (2017), fuel cell is a device that generates electricity through electrochemical reaction between Hydrogen and Oxygen. A major by-product of the exothermic reaction is waste heat. The recovery of this waste heat has been subjected to research in order to improve the overall energy utilisation. However, nearly all of the investigations focused on high temperature fuel cells using advanced thermodynamic cycles due to the high quality of waste heat. In this publication, the method, characteristics and challenges in harvesting waste heat from a low temperature fuel cell using a direct energy conversion device was studied. A heat recovery system for an open cathode 1kW LT-PEM FC was developed using a single unit of TEG attached to a heat pipe. Power output of the fuel cell was varied to obtain the performance of TEG at different stack temperatures. Natural and forced convection modes of cooling were applied to the TEG cold side. This was to simulate the conditions of a mini fuel cell vehicle at rest and in motion. The experimental results were analysed and a mathematical model based on the thermal circuit analogy was developed and compared. Forced convection mode resulted in higher temperature difference, output voltage and maximum power which are 3.3°C, 33.5 mV and 113.96mW respectively. The heat recovery system for a 1kW LT-PEM FC using single TEG was successfully established and improved the electricity production from the fuel cell. Moreover, the experimental results obtained correlated their theoretical results. Figure 2.74 depicts the theoretical and experimental setups and their test results.

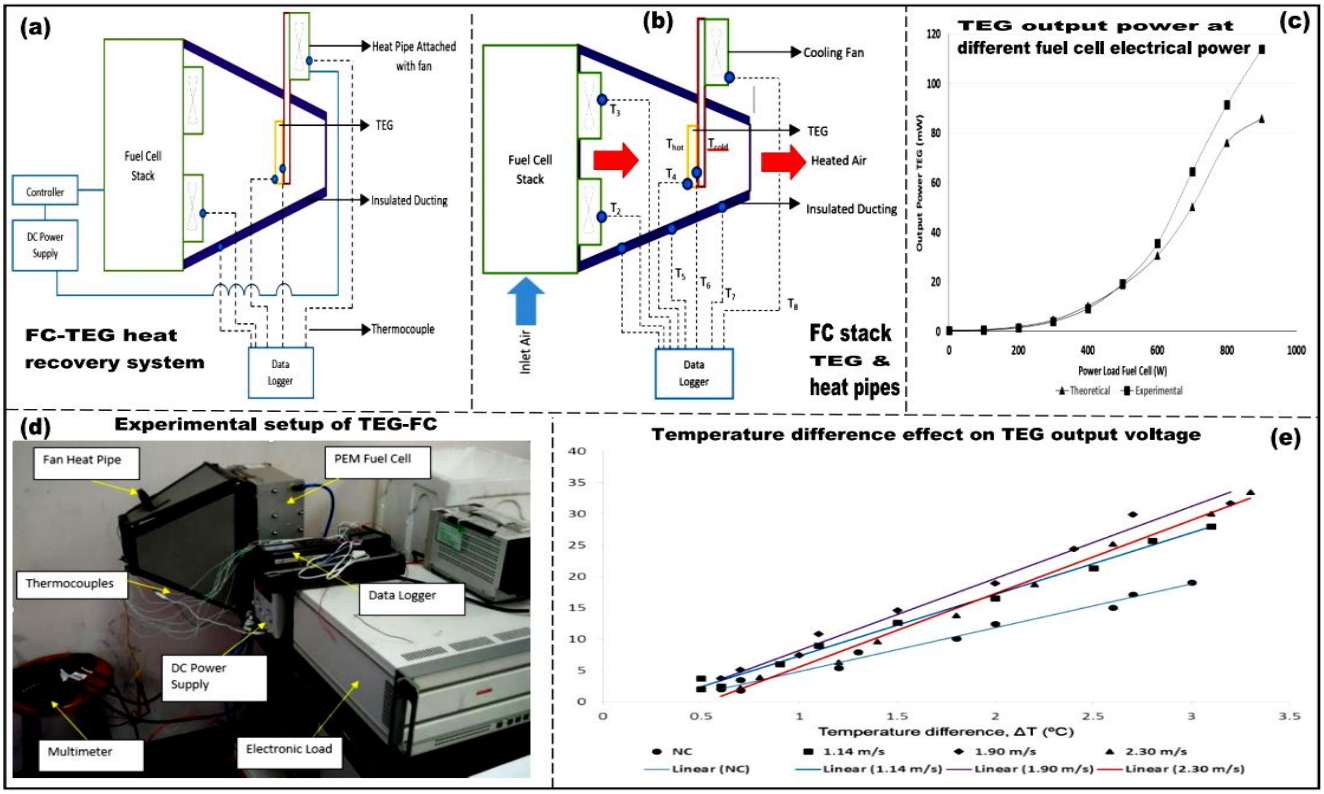

Figure 2.74: TEG and 1kW LT-PEM FC waste heat recovery system (adapted from Sulaiman *et al.*, 2017)

2.4.2.13 TECs as TEGs with 5kW LT-PEM FC CHP Waste Heat Recovery

Presented in Hasani and Rahbar (2015), is the experimental performance of TECs as TEGs (Figure 2.75b) in waste heat recovery system from a 5kW LT-PEM FC (Figure 2.75a). The system setup (Figure 2.75d) constituted a thermoelectric heat recovery system (THRS: see Figure 2.75e) consisting of a heat exchanger (Figure 2.75c), four TECs (Figure 2.75f) and a typical heat-sink (Figure 2.75e_1) attached on the cold sides of the TECs 2x2 array. Figures 2.75g - 2.75j display the various measured parameters as exemplified. The experiment outcomes showed that TECs as TEGs can be suitable to recover waste heat from a LT-PEM FC. The CHP system total efficiency decreased with increases in the outlet water temperatures due to low ΔTs; as a result, the TEG open circuit voltages decreased. Finally, to assess the useful output power, MPT occurred when the load resistance changed from 1-10Ω.

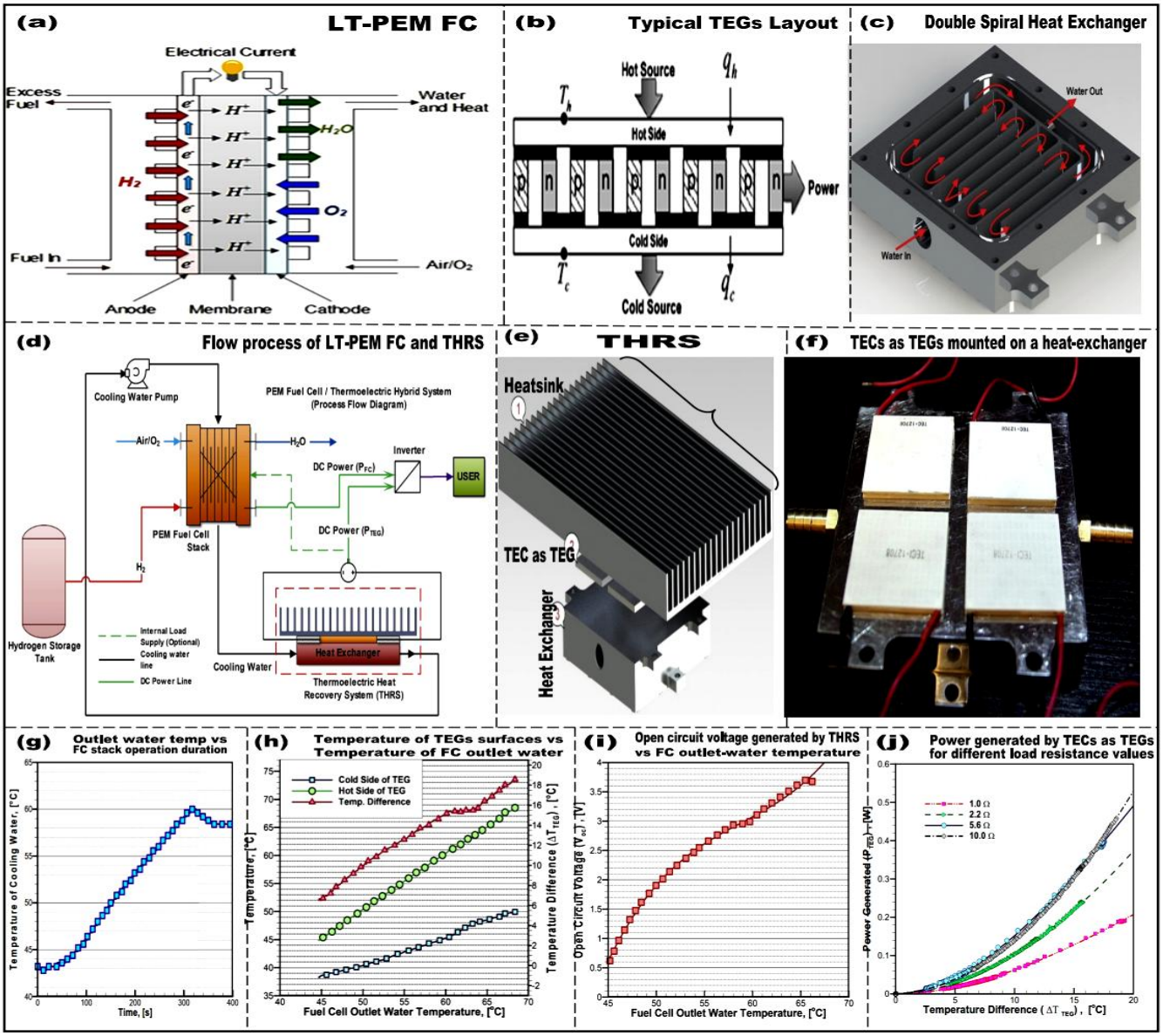

Figure 2.75: TECs as TEGs with 5kW LT-PEM FC waste heat recovery system (adapted from Hasani & Rahbar, 2015)

2.4.2.14 Uninterrupted TE Energy Harvesting with Temperature Sensor Based MPPT

Investigated in Park *et al.* (2014), is a thermoelectric generator energy harnessing system with a temperature sensor based maximum power point tracking (MPPT) scheme. The Perturb and Observe (P&O) technique is generally used in TEG applications but it responds poorly to a fast-changing power output. In addition, habitual MPPT algorithms for photovoltaic (PV) cells may not be appropriate for TEG power generation because an important amount of time is needed for TEG systems to reach a steady state. Furthermore, complexity and extra power consumption in conventional circuits and periodic disconnections of power source are not desirable for low-power energy harvesting applications. The researched scheme in Figures 2.76a, 2.76e - 2.76g; can track the fluctuating maximum power point (MPP) with an easy and inexpensive temperature-sensor-based circuit without instantaneous power measurement or TEG disconnections. This method used TEG's open circuit voltage (OCV) attributes with respect to temperature gradient to generate a proper reference voltage signal that is half of the TEG's OCV. The boost power converter controller maintained the TEG output voltage at the reference level so that the maximum power can be extracted for the given temperature condition. This feed forward MPPT approach is inherently stable and can be implemented without any complex microcontroller circuit. The investigated technique analytically and experimentally correlated and had a maximum power tracking error of 1.15%. Figure 2.76b is the TEG equivalent circuit. Figures 2.76c and 2.76d show the operational waveforms.

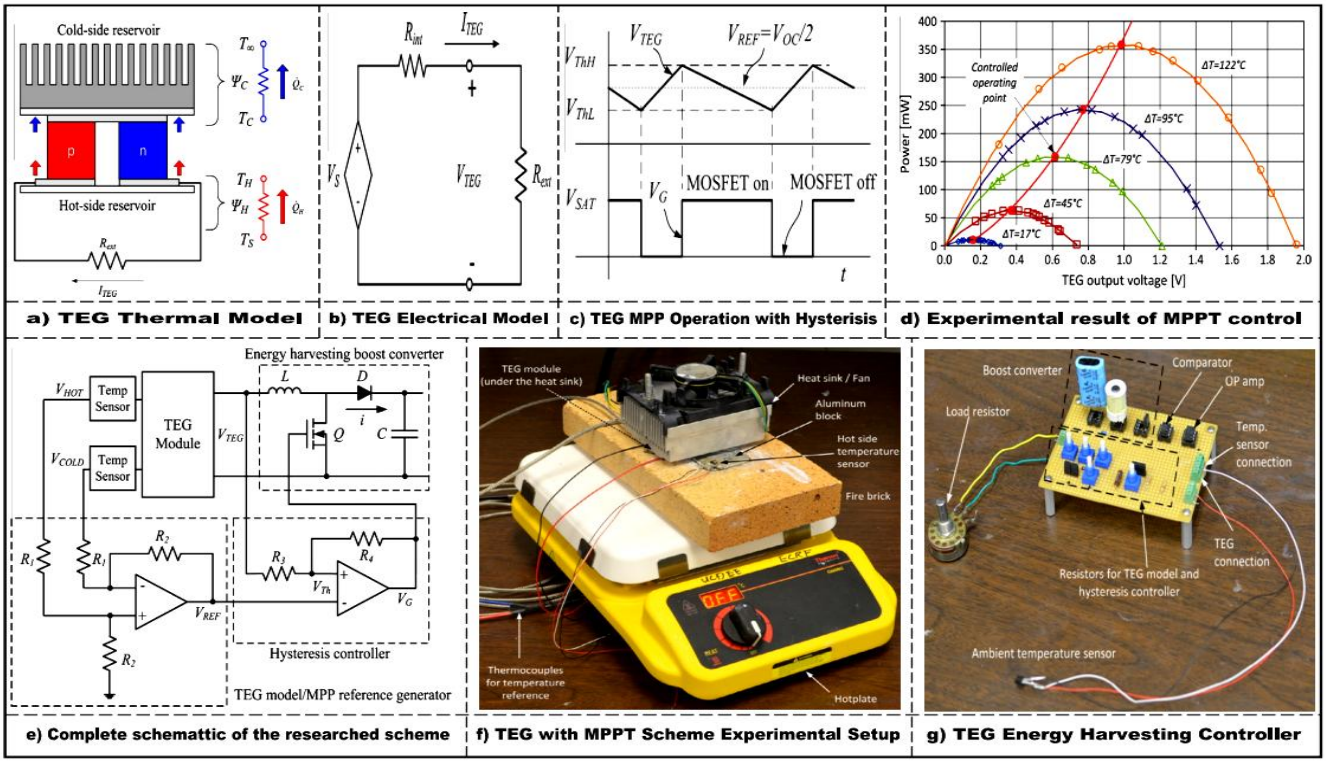

Figure 2.76: Uninterrupted TE energy harvesting with temperature sensor based MPPT (adapted from Park *et al.*, 2014)

2.4.2.15 TEG verse Solar Energy Generations Comparison

Examined in Yildiz *et al.* (2013), is a comparison study of TEG and solar energy as shown in Figure 2.77e. Figure 2.77a shows the TEG concept. Figure 2.77b depicts the output power based on TEG temperature differences on both sides. The tested TEG hot side temperature ranged from 50-300°C and cold side from 25 to 100°C. The bigger the ΔT, the more the output power from the TEG. The TEG generated ~20W with a 275°C temperature difference – hot side temperature of 300°C and cold side 25°C. Figures 2.77c and 2.77d show the TEG and solar tests setups. It was concluded that size wise, a TEG module can generate more power relative to a solar module; however, TEG are more costly to generate the same amount of power. Also, TEGs need large ΔT to generate reasonable power.

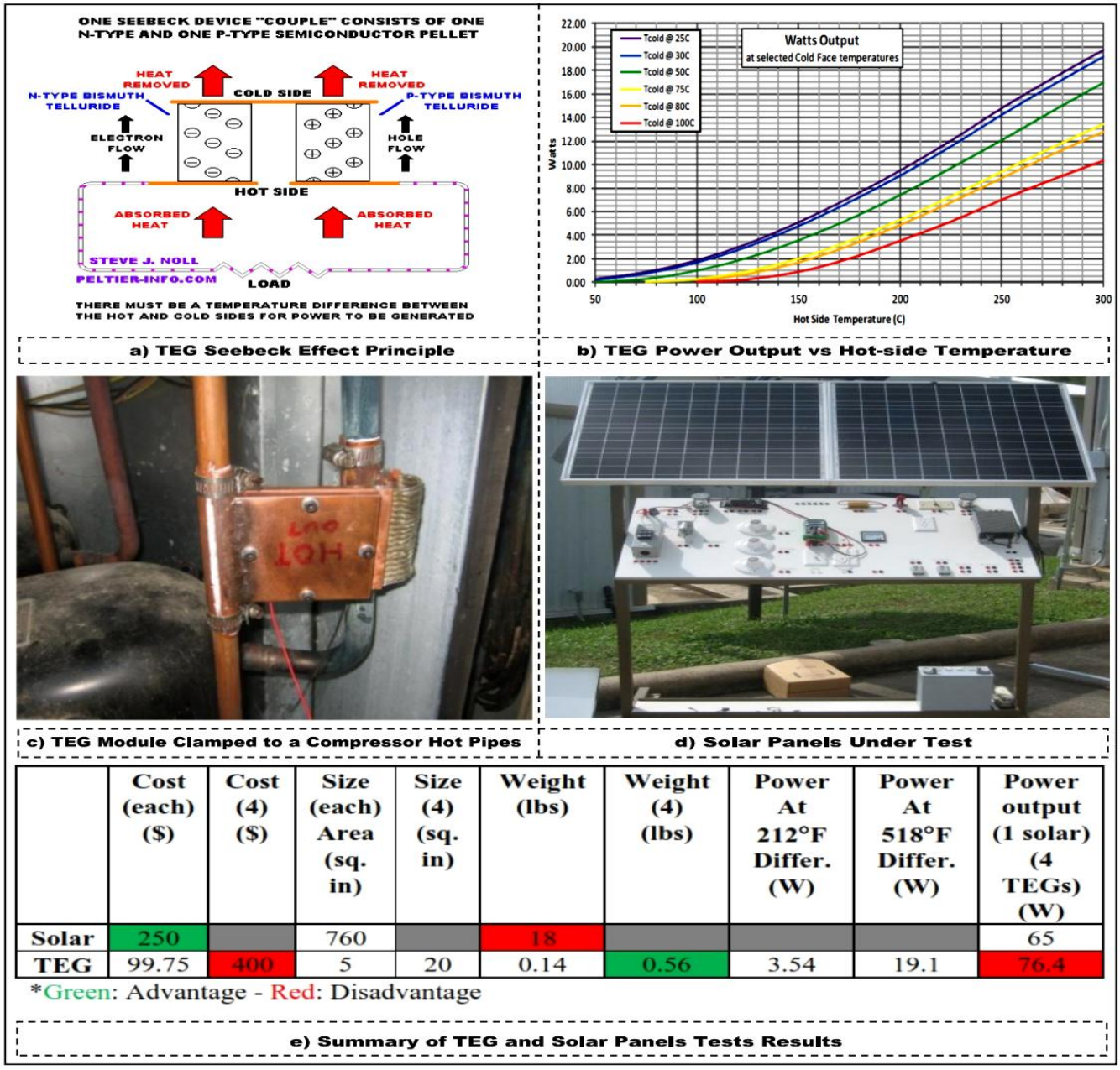

	Cost (each) ($)	Cost (4) ($)	Size (each) Area (sq. in)	Size (4) (sq. in)	Weight (lbs)	Weight (4) (lbs)	Power At 212°F Differ. (W)	Power At 518°F Differ. (W)	Power output (1 solar) (4 TEGs) (W)
Solar	250		760		18				65
TEG	99.75	400	5	20	0.14	0.56	3.54	19.1	76.4

*Green: Advantage - Red: Disadvantage

e) Summary of TEG and Solar Panels Tests Results

Figure 2.77: TEG verse solar energy generations comparison (adapted from Yildiz *et al.*, 2013)

2.4.2.16 Influence of Thermal Environment on Optimal Working Conditions of TEGs

As established in Apertet *et al.* (2014), a Thevenin (Figure 2.78a) and Norton (Figure 2.78b) TEG models were used to show that TEG output power and efficiency in a thermal environment, can be maximised simultaneously if its heat flux is constant but not the case if its ΔT is constant. Figures 2.78c and 2.78d respectively depict the TEG normalised output power as a function of maximization ratio and as a function of normalised efficiency for both TEGs (Figures 2.78a and 2.78b). The study concluded by suggesting a TEG power optimisation may be conducted in three steps: i) choosing a TEG device or material with best $Z\overline{T}$ or $z\overline{T}$, ii) use thermal impedance matching to determine the TEG dimension and iii) use electrical impedance matching to determine the TEG electrical load.

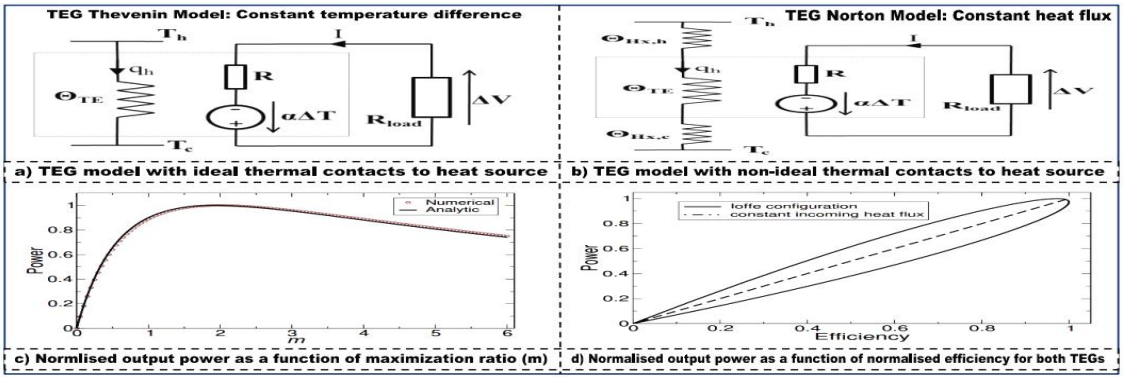

Figure 2.78: Influence of thermal environment on optimal working conditions of TEGs (adapted from Apertet *et al.*, 2014)

2.4.2.17 Thermoelectric Cooler (TEC) and LT PEM Fuel Cell CCHP System

According to Ebrahimi and Derakhshan (2018), the prime mover is a LT PEM FC. A low-quality heat of ~80°C and water condensate were recovered as the by-products. A thermoelectric cooler (TEC) was used as the cooling system. The mathematical models of the fuel cell and the thermoelectric cooler were implemented and the results of simulations were confirmed with published data in the literature. The results validated a new micro CCHP system. The results showed that the cycle is capable of producing 2.79kW of electricity, 3.04kW of heat and 26.8W of cooling with a total efficiency of the tri-generation cycle of 76.94% and fuel saving of 43.25%. Figure 2.79 summarises the scheme.

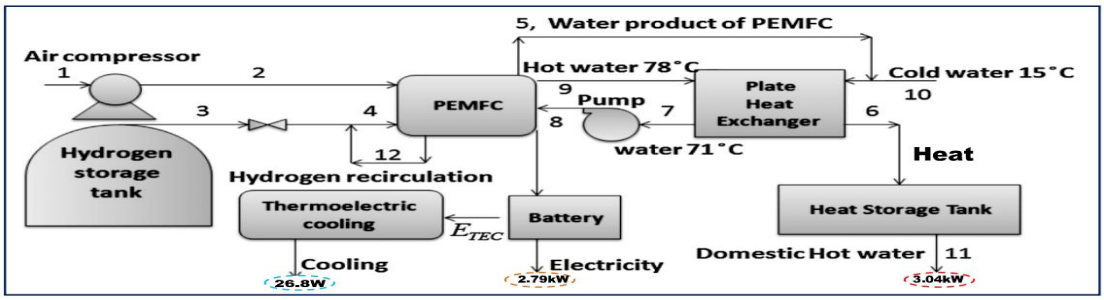

Figure 2.79: TEC and PEM fuel cell CCHP system (adapted from Ebrahimi & Derakhshan, 2018)

2.4.2.18 Modelling of TEG and P&O MPPT with Load and Temperature Variations

Investigated in Mamur and Çoban (2020), maximum power is attained when the load connected to a TEG, matches it internal resistance. However, impedance matching is not always practically guaranteed. As a result, in the setup as per Figure 2.80a, Matlab/Simulink was employed to model TEG and the implementation was based on a TEG manufacturer's datasheets. TEGs were connected to a boost converter without MPPT using different loads, from which up to 98% of the TEG power was transferred to the load when matched with ~7Ω but was not the case with other load values. In another run, P&O MPPT algorithms were employed in the boost converter and its output was connected again to different loads and the generated power of ~20W was constant to loads from 7 up to 70Ω as shown in Figure 2.80c. A similar setup was done with TEG hot side temperature (T_{hot}) variations using a fixed cold side temperature of 20°C and it was realised that the output power efficiency was <90% for T_{hot} <70°C. The proposed TEG, boost converter and P&O MPPT models were validated with an experimental TEG system setup as demonstrated in Figure 2.80b.

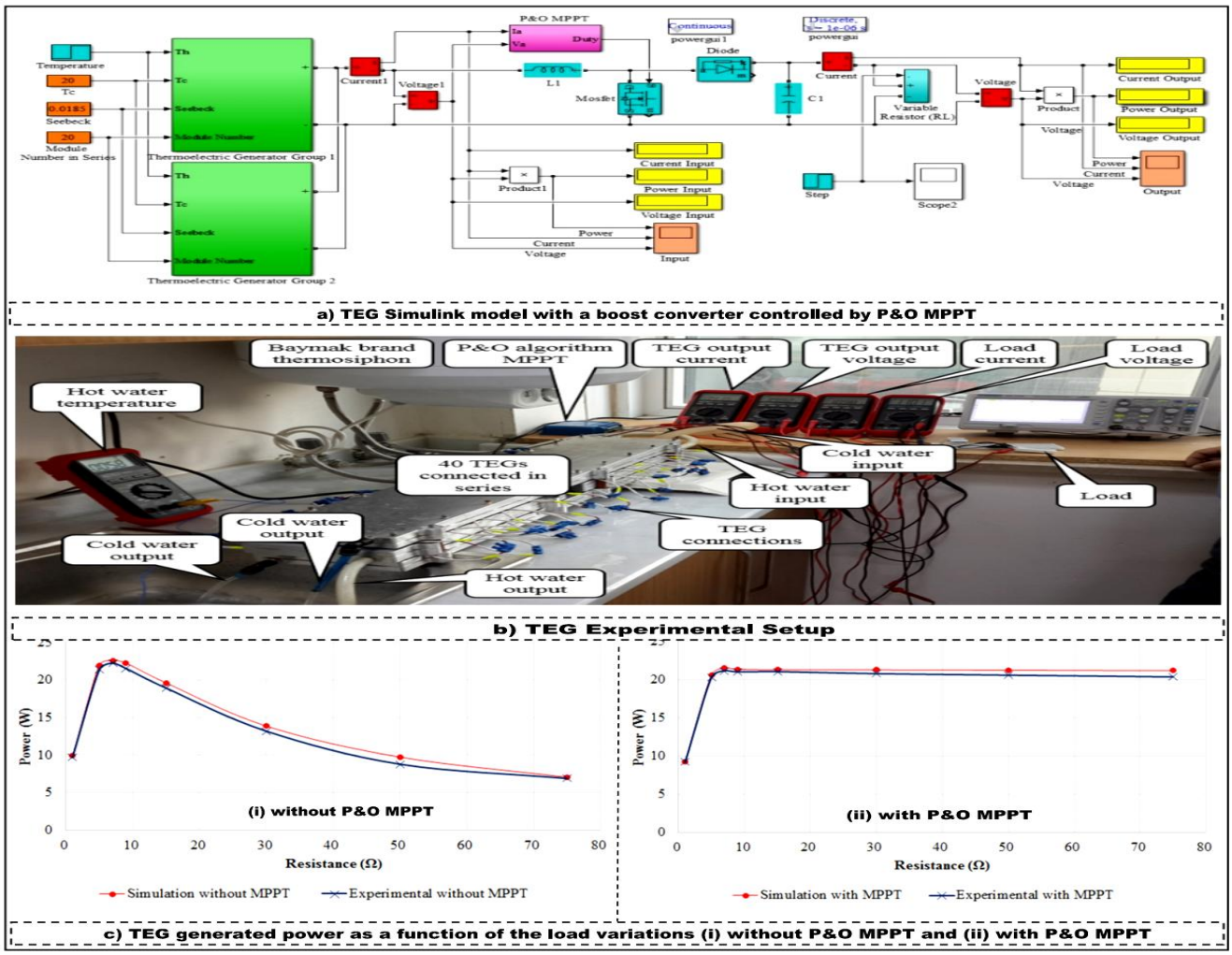

Figure 2.80: Simulated and experimental TEG, boost converter and P&O MPPT schemes (adapted from Mamur & Çoban, 2020)

2.4.3 Eighteen Thermoelectricity Case Studies Examined Summary

Table 2.10 presents the highlights of each case study as well as the pros and cons where applicable.

Table 2.10: Summary of the eighteen thermoelectricity case studies reviewed (Bayendang *et al.*, 2020b)

Case Studies Analysed	Highlights, Advantages and Disadvantages
Case Study 2.4.2.1 (Bell L.E., 2008)	- The principle of thermoelectricity: Construction, TEG and TEC. - ZT: TE device dimensionless figure of merit. More ZT, the better.
Case Study 2.4.2.2 (Gao X., 2014)	Showed that TEG can be used as TERs to harvest exhaust heat and boost HT PEM FC efficiency with emphasis on i) heat exchanger surface type, ii) its housing dimensions and iii) power conditioning.
Case Study 2.4.2.3 (Huston J. *et al.*, 2004)	- About 40 specific applications of TEG were researched and it was noticed that TEG form factor is key to enable mounting anywhere. - TEG was used with various FCs to boost output power by 7-10%.
Case Study 2.4.2.4 (Zhao D. *et al.*, 2016)	Showed how energy was harnessed from intermittent heat sources and converted into stored charge via the ionic Soret Effect in an ITESC. Max efficiency is very low compared to TEG of same ZT.
Case Study 2.4.2.5 (Mahmud K.H. *et al.*, 2017)	Demonstrated that TEGs connected in series and parallel, generate more voltage and current respectively, that also increases with Tc.
Case Study 2.4.2.6 (Qu Z. *et al.*, 2018)	Developed a thermodynamic model for the TEG and micro-turbine. Showed that TEG almost doubled the hybrid CHP output power.
Case Study 2.4.2.7 (Katkus T., 2015)	The manufacturing of a TEG involve choosing a TE material with good ZT (>1), electrodes insulating plate, adhesives and module architecture. A real system was built to characterise TEG modules.
Case Study 2.4.2.8 (Sullivan O.A., 2012)	Modeled TEGs and TECs on a chip. TECs are more efficient using more and better if operated at steady state for frequent hotspot. For infrequent hotspots, TECs maybe cooled with square root transient pulses of very short duration. TEG MPT occurred at greater load resistance. TEG useful power is firstly linear and later parabolically proportional to the heat flux. More TEGs increase output power but decrease later. Thinner TIM improves TECs and TEGs capabilities.
Case Study 2.4.2.9 (Teffah K. *et al.*, 2018)	- TEC was used as a TEG cooler in simulated and practical setups. - The ΔT was directly proportional to the TEC V_{in} and TEG V_{out}.
Case Study 2.4.2.10 (Stockholm J., 2016) (Stockholm J. *et al.*, 2015b)	Demonstrated that the output power from TEG when pulsed, doubles the conversion efficiency. An 8.4% increase was attained.
Case Study 2.4.2.11 (Kiziroglou M.E. *et al.*, 2016)	Proved that thicker TEGs with good area coverage can be used to harvest electricity from environment with fluctuating temperatures.
Case Study 2.4.2.12 (Sulaiman S.M. *et al.,* 2017)	Showed the use of a TEG with FC under simulated natural (static) and forced convection cooling (dynamic) to convert heat to power. However, very high ΔT is required to generate significant power.
Case Study 2.4.2.13 (Hasani M. & Rahbar N., 2015)	Demonstrated the duality of TECs as TEGs in a FC CHP using a THRS. Low ΔTs gave low V_{outs}. MPT occurred at R_{load} of 1 – 10Ω.
Case Study 2.4.2.14 (Park J. *et al.*, 2014)	Showed the use of a low-cost microcontroller and temperature sensor based circuit, to track TEG MPP with a 1.1% tracking error.
Case Study 2.4.2.15 (Yildiz F. *et al.*, 2013)	Compared TEG and Solar energy conversion. A TEG generates more power relative to solar module of same size but more costly.
Case Study 2.4.2.16 (Apertet Y. *et al.*, 2014)	Deduced that a TEG output power and efficiency in a thermal environment, can be simultaneously maximised if its heat flux is constant but not the case if its temperature difference is constant.
Case Study 2.4.2.17 (Ebrahimi M. & Derakhshan E., 2018)	Proved that a TEC LT-PEM FC hybrid CCHP system is capable of producing 2.79kW of electricity, 3.04kW of heat and 26.8W of cooling with a total efficiency of ~77% and fuel saving of 43.25%.
Case Study 2.4.2.18 (Mamur H. & Çoban Y., 2020)	TEGs have no moving parts, have long service life, operate quietly and are green. TEGs have low efficiency and are expensive. By using the manufacturer datasheets, TEGs were modeled, simulated, experimented and results correlated. Impedance matching with boost converter and P&O MPPT schemes gave 98.64% efficiency.

2.4.4 Summary

Energy security and electricity crisis in particular, is an ongoing pressing societal problem in South Africa. In view of this, this study embarked on a structural review and presented eighteen assorted thermoelectricity applicable studies, to be applied to best devise a hybrid CCHP system for domestic / commercial applications. In the study, diverse analyses on past research on thermoelectricity were examined, in which case studies related to co / tri-generation with fuel cells were of most interests. In these studies, thermoelectricity increased the power efficiency by converting waste heat into DC electricity using TEGs and converted DC electricity into cold using TECs. Also examined was how ionic thermoelectricity exhibits super-capacitor properties and in conclusion was a TEC and PEMFC hybrid CCHP system study, where the PEMFC was the prime mover and TEC was the cooler; capable of generating 2.79kW of electricity, 3.04kW of heat and 26.8W of cold − giving a total efficiency of ~77% and fuel saving of 43.25%. The relevant highlights, advantages and disadvantages of the eighteen case studies examined were summarised as the principal findings and the contributions realised. As a result, an alternative research model incorporating thermoelectricity for use with fuel cell in CCHP applications and to address the FC fuel starvation phenomenon is doable and shall be researched further.

2.5 Combined Cold, Heat & Power (CCHP) Systems & Fuel Cells for CCHP Applications: A Topological Review

This section commences by stating the prevailing electricity crisis in South Africa as basis for the study. Thirty four combined cold, heat and power (CCHP) systems including the internal combustion engine (ICE), the Stirling engine, biomass, micro-turbine, solar and biogas, photovoltaic (PV) and gas-turbine, wind turbine, photovoltaic and micro-turbine, solid oxide and phosphoric acid fuel cells (FCs), ICE and thermoelectric generator (TEG), low temperature (LT) polymer electrolyte membrane (PEM), inlet air throttling gas-turbine, ground source heat pump (GSHP) micro gas-turbine and PV, ICE and GSHP, ICE with dehumidification and refrigeration, 5kW PEM FC, thermoelectric cooler (TEC) and LT PEM FC, Stirling engine and molten carbonate fuel cell, organic Rankine cycle (ORC), solar thermal (ST), geothermal, integrated energy systems (IES), power and heat storage systems, energy conversion systems, thermodynamic and thermo-economic optimization strategies, working fluids based on Hydrogen, Helium as well as Ammonia, H_2O, CO_2 etc were investigated and from these CCHP system types reviewed, the fuel cells based CCHP systems were of most interests and particularly PEM FC. Consequently, FCs were further investigated whereby the popular six kinds of FCs were compared from which the PEM FC was preferred because of its practical popularity.

However, PEM FC like all FCs, are susceptible to fuel cells fuel starvation phenomenon and therefore, six fuel cells assisted schemes were examined, from which the fuel cell assisted with super-capacitor and battery technique is the most widely applied. In sum, the study significance entails assorted CCHP systems, fuel cells, their novelties and applications thereof to formulate a different research model of an innovative alternative energy efficient CCHP system based-on fuel cells, Li-ion battery, ultra-capacitor and thermoelectricity as well as energy management system using Matlab / Simulink.

2.5.1 Introduction

South Africa and like most African countries in general, is currently and constantly experiencing electrical energy and power crises, which are having huge adverse effects to the country's economy and livelihoods, since electricity is now very central to our daily activities. A variety of potential alternative energy / power initiatives are being exploited and commissioned in a bid to address the raging crises and to this effect, this study extended from Bayendang *et al.* (2020a), topologically examines in details, various research (summarized in Tables 2.11 - 2.13) on combined cooling, heating and power (CCHP) systems and fuel cells (FCs). This is to establish inventive techniques that can be developed and deployed for the design of an energy efficient FC hybrid power system for residential and commercial CCHP applications. As examined and summarized in Table 2.11, CCHP also known as tri-generation, is basically a parallel combined heating and power (CHP) energy system (co-generation) with extra cooling. As per Figure 2.81, it concisely comprises of a prime mover and energy conversion/ management processes, which wholly can produce power and heat as well as cold when fueled, allowing it to efficiently provide direct standalone energy utility to homes and businesses. According to Ming *et al.* (2015) and Zhang *et al.* (2018); CCHP systems especially those based-on FCs, are becoming trendy as a result of its energy-saving, environmentally friendly, cost saving and flexible features. However, fuel cells are prone to the intrinsic fuel cell fuel starvation – which is investigated further in this study. Presented next is the CCHP systems review, followed by fuel cells (FCs) with focus on kinds of FCs and the fuel cell fuel starvation phenomenon as well as the mitigation methods, proceeded by my proffered CCHP system model undergoing research and finally closing remarks are drawn to conclude the study.

2.5.2 CCHP Systems

CCHP systems produce simultaneously heat and power in the same process, with the cooling later obtained from the generated power and or from the heat, depending on the type of CCHP system implementation. With a properly designed CCHP system, the total energy efficiency could exceed 90%. Usually, CCHP prime movers comprise of diverse sources of energy as well as conversion techniques

and from the literature analysis and indicated in Badea *et al.* (2010) and Bozchalui and Sharma (2012); a particular CCHP system name is normally gotten from its prime mover or power generation unit (PGU). Miscellaneous CCHP systems were investigated and in what follows are thirty four case studies shown.

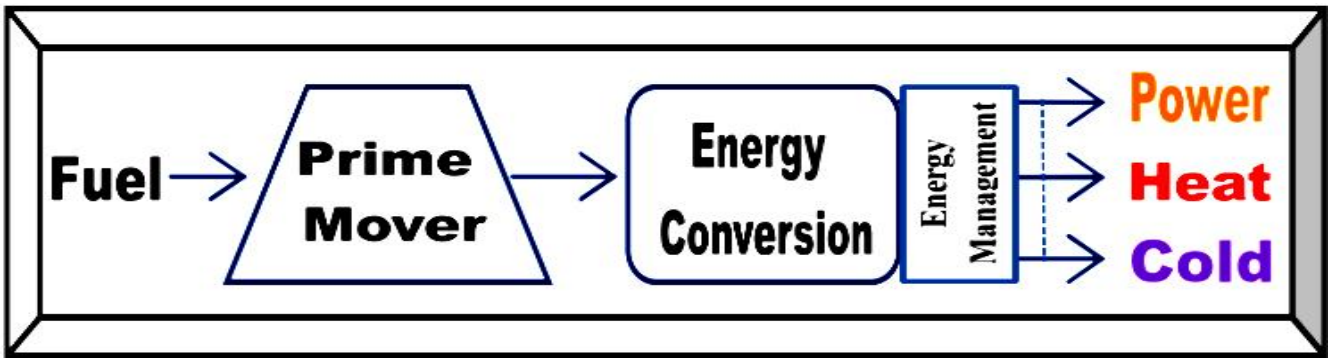

Figure 2.81: CCHP system overview

2.5.2.1 Natural Gas Internal Combustion Engine (ICE) CCHP System

Studied in Badea *et al.* (2010), ICEs infuse fuel and air into cylinders where combustion happens, causing the fuel and air mixture to have temperature/pressure variations to produce useful work. This process occurs in cycles making difficult the complete burning of the fuel, resulting to noise and pollution. Contrary to modern ICE CCHP systems, earlier ones were based on automotive engines transformed to work with natural gas; as a result, were unreliable and requires very high maintenance. According to Bozchalui and Sharma (2012), ICEs have matured with relatively low-cost, high efficiency and rapid start-up time and can be powered by natural gas (see Figure 2.82), petrol and gasoline fuels.

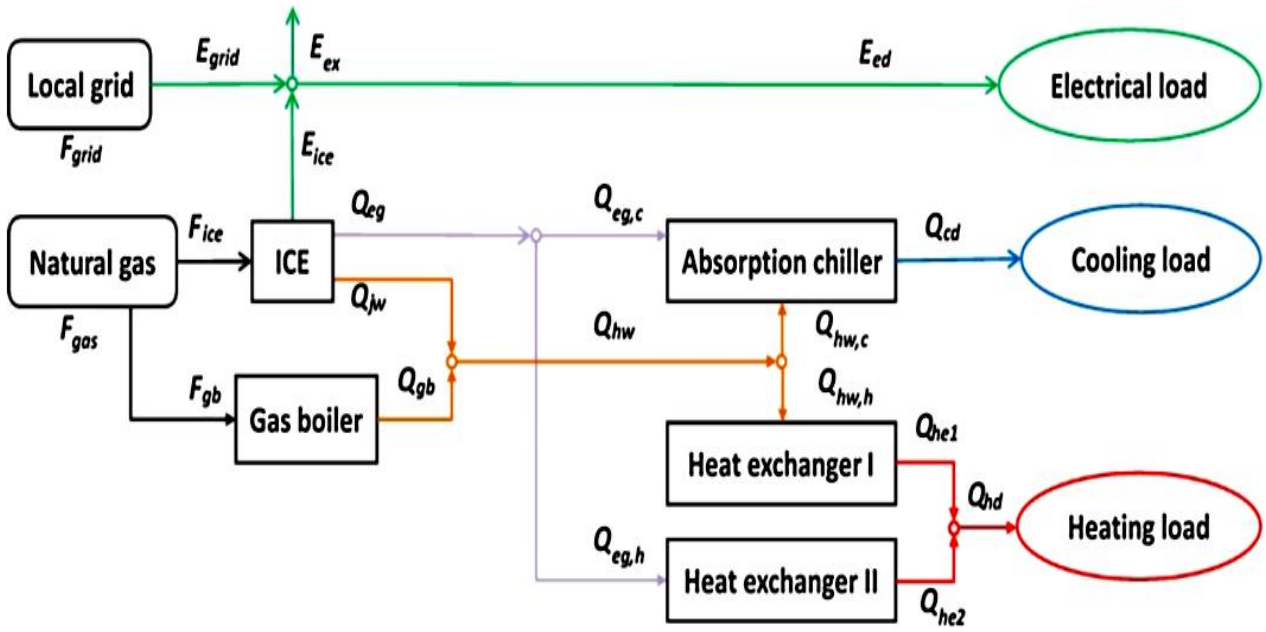

Figure 2.82: Natural gas (Fossil Fuel) ICE CCHP system (adapted from Badea *et al.*, 2010)

2.5.2.2 External Combustion Engine (ECE) or Stirling Engine CCHP System

Researched in Badea *et al.* (2010), the most popular micro-CHP systems are ECEs, as they are mostly apt to a static or continuously active utilization. A typical example is a Stirling engine, which employs an easy ambient pressure combustor, equivalent to a hot water heater or furnace, to generate a continuous heat source that is passed to a gas that enlarges to move a piston to do work. After work is completed by the gas, it's transferred through a regenerator (a heat exchanger) where any residual usable heat left is brought back to preheat the in-flowing gas, which is then recycled to and fro to always remain in the engine, making ECEs more efficient and environmentally friendly compared to ICEs. Figure 2.83 portrays a micro CCHP system rooted in Stirling engine.

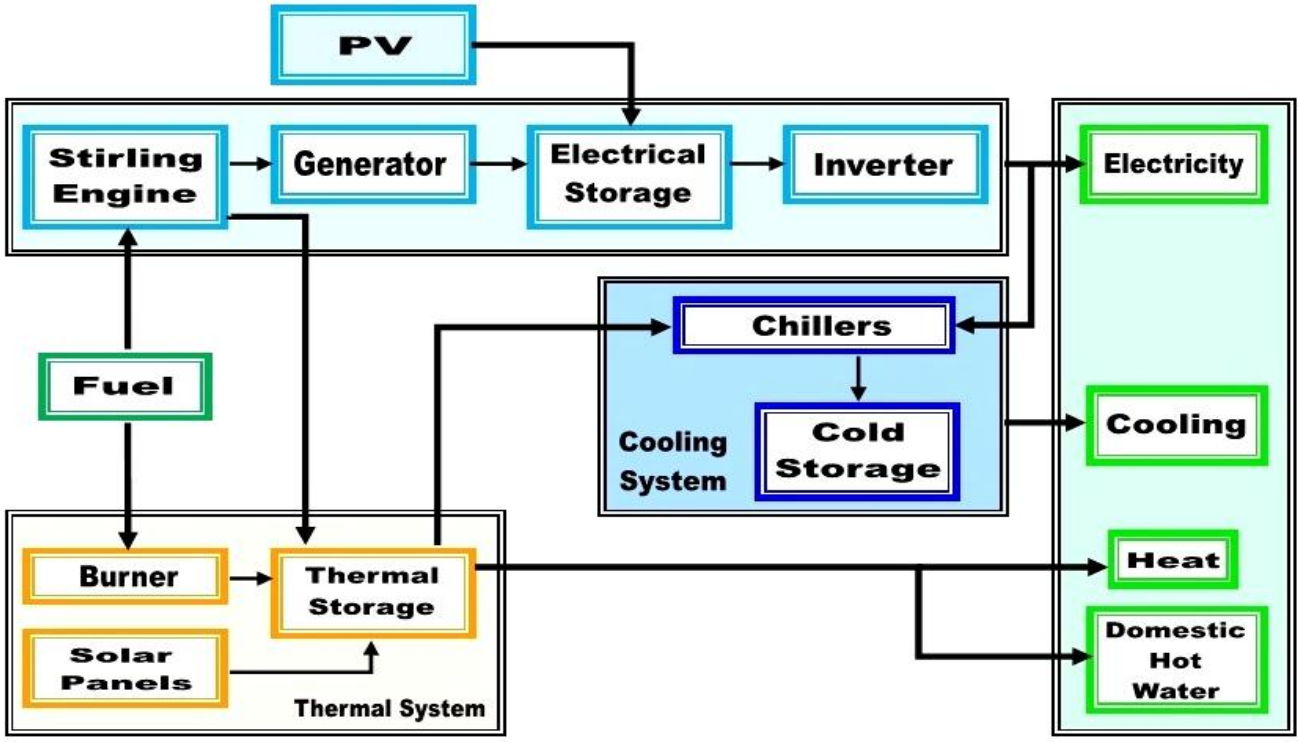

Figure 2.83: Stirling engine CCHP system (redrawn from Badea *et al.*, 2010)

2.5.2.3 Biomass CCHP System

As stated in Maraver *et al.* (2013), CCHP systems founded on biomass incineration have already established their worth in some functional settings. Nevertheless, their energy and ecological performances might also be poorer relative to traditional standalone power production systems. To make provisions for procedures concerning their environmental viability, a life cycle assessment methodology is employed to assess biomass CCHP systems. A thermodynamic model that takes into accounts the incorporation of various dimensions of cooling and co-generation units, were advanced to suitably characterize the life cycle inventory stage. Figure 2.84 shows the biomass CCHP system.

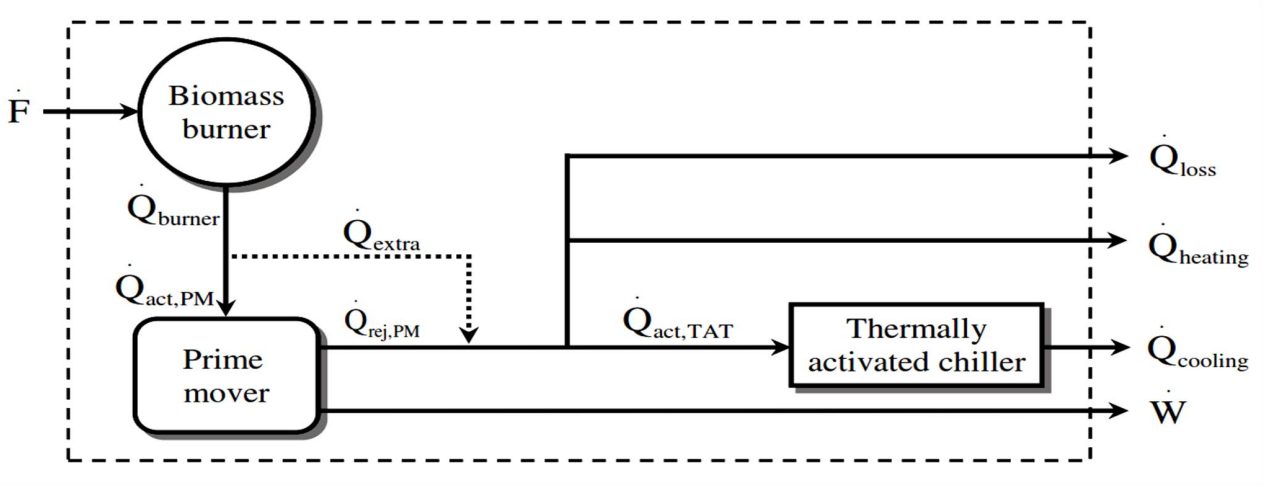

Figure 2.84: Biomass CCHP system (adapted from Maraver *et al.*, 2013)

2.5.2.4 Micro-turbine CCHP System

Akin to a usual gas turbine and according to Ming *et al.* (2011) and Xu *et al.* (2014), air is initially drawn into the compressor, where it is pressurized and pumped to the recuperator cold side to combine effectively with the exhaust heat to create cold with the absorption refrigerating machine as presented in Figure 2.85.

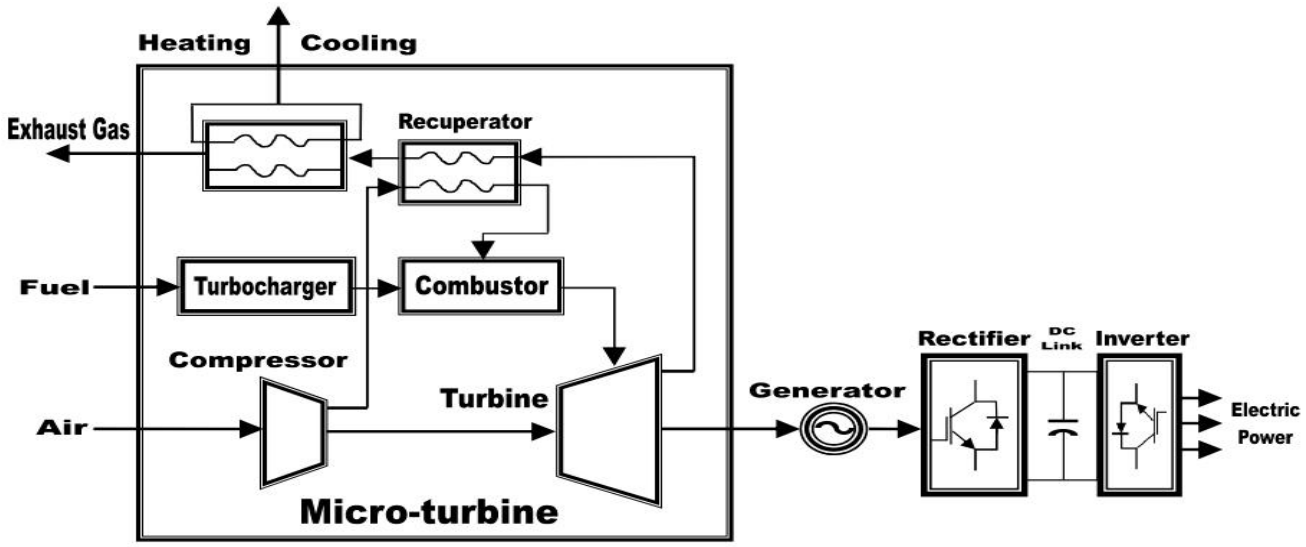

Figure 2.85: Micro-turbine CCHP system (redrawn from Xu *et al.*, 2014)

2.5.2.5 Solar and Biogas CCHP System

In Su *et al.* (2016), a photovoltaic (PV) and biomass CCHP system, comprising of a scaled down biogas PGU, solar cell, auxiliary boiler, absorption chiller, solar thermal collector (STC), etc is proposed − in which the model was implemented using genetic algorithm to obtain an optimum functional approach considering economic, environmental and energetic criteria as in Figure 2.86.

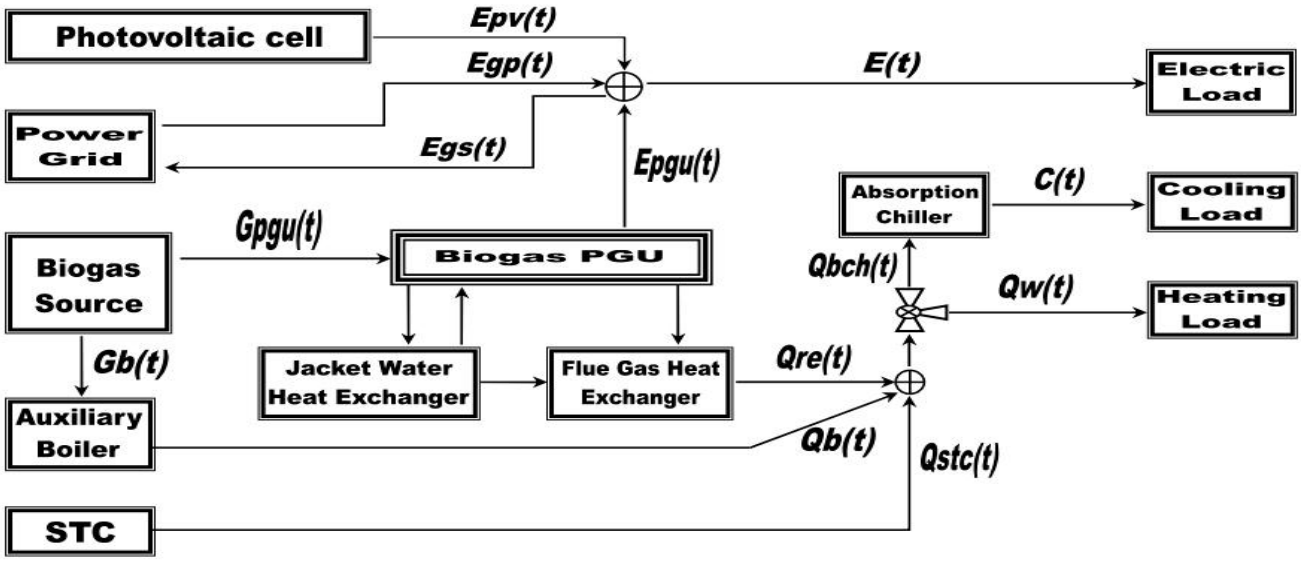

Figure 2.86: Biomass and solar CCHP system (redrawn from Su *et al.*, 2016)

2.5.2.6 Photovoltaic and Gas-turbine CCHP System

As per Wongvisanupong and Hoonchareon (2013), a proposal of an online economic optimum functioning PV and CCHP system is presented. Linear programming (LP) was used to formulate and model the system using Matlab. The simulation results showed that a hybrid CCHP and PV system under the projected optimum operation, obtained the least cost of operations. Figure 2.87 depicts the proposed CCHP system.

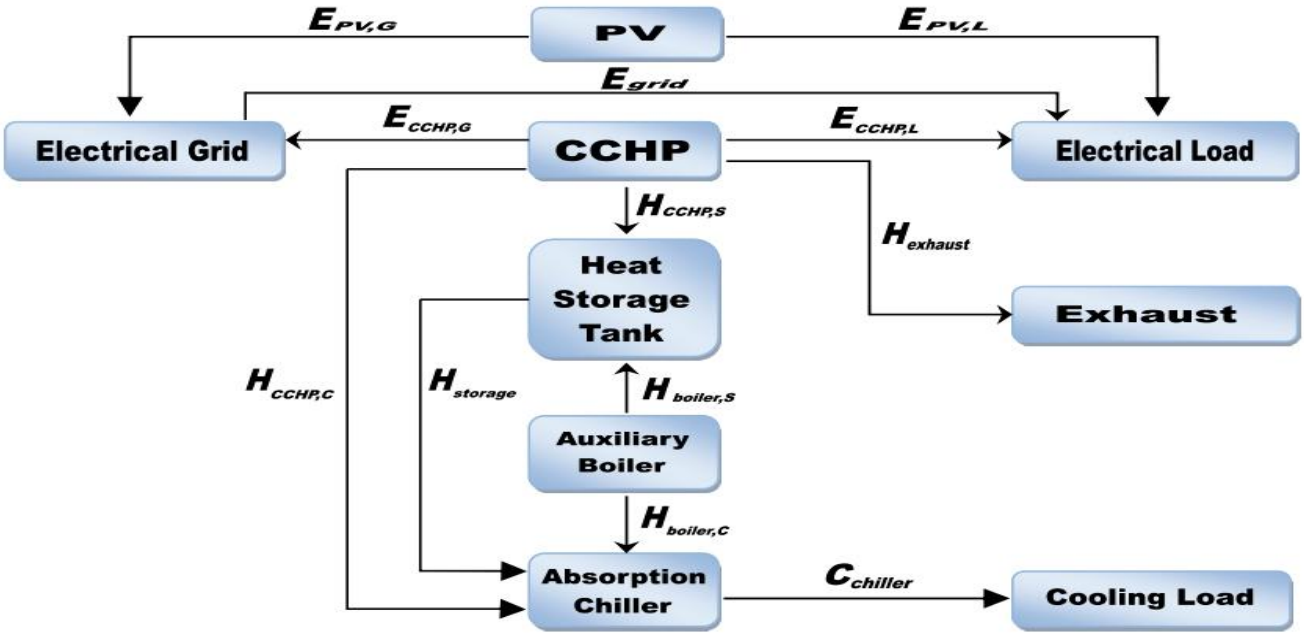

Figure 2.87: Gas-turbine and photovoltaic CCHP system (redrawn from Wongvisanupong & Hoonchareon, 2013)

2.5.2.7 Wind Turbine, PV and Micro-turbine CCHP System

In Zhao *et al.* (2018), a combination of wind and photovoltaic energy together with gas micro-turbine were used for generating power as well as supply of heat and cold as per Figure 2.88. They claimed it saves energy better without pollution effects. HOMER software was used to model an optimum economic functioning model of a micro-grid having the optimization objective being the net present cost.

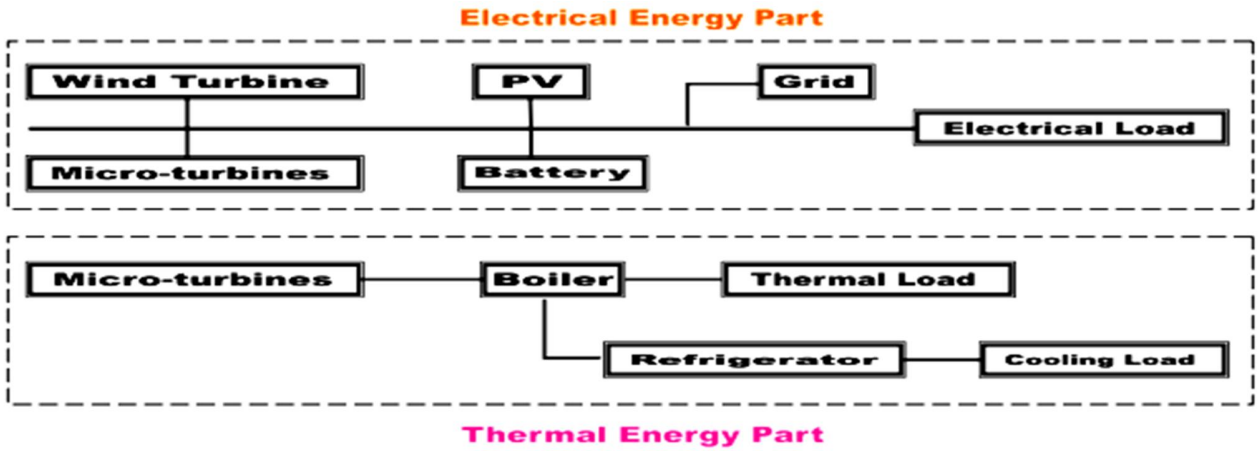

Figure 2.88: Wind turbine, photovoltaic and micro-turbine CCHP system (redrawn from Zhao *et al.*, 2018)

2.5.2.8 Solid Oxide FC (SOFC) and Phosphoric Acid FC (PAFC) CCHP System

According to Wang *et al.* (2018), there are several ongoing investigations on FC based CCHP systems though not much on electrolysis, that is hydrogen production from water using electricity – which their paper is based-on. Their evaluation system included PAFC and SOFC, thermal and technical economies including environmental protection factors. Figure 2.89 portrays their CCHP system.

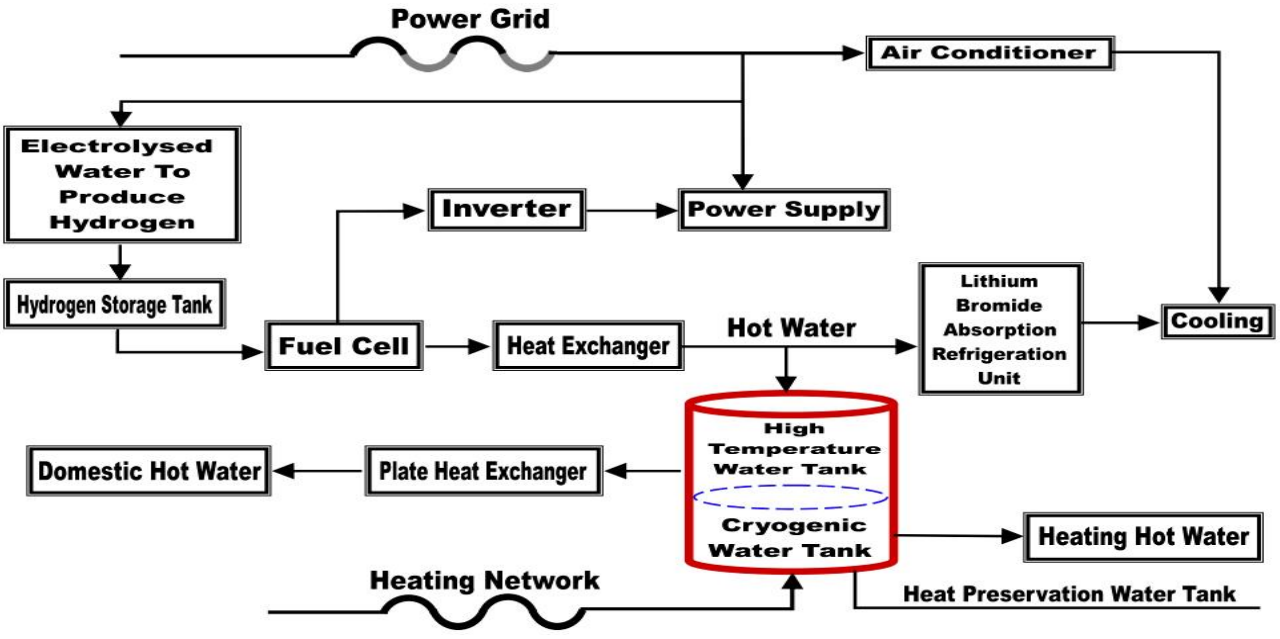

Figure 2.89: Hydrogen fuel cell CCHP system (redrawn from Wang *et al.*, 2018)

2.5.2.9 ICE and Thermoelectric Generator (TEG) CCHP System

As proposed by Wang *et al.* (2014), the CCHP system is based on ICE for electricity production, cooling and for heating household water; whereas the condensing heat exchanger and thermo-electric generator (TEG) are used to ably recuperate the waste heat of ICE exhaust gas. The scheme was devised using the concept of energy cascading utilization. Figure 2.90 depicts the CCHP system.

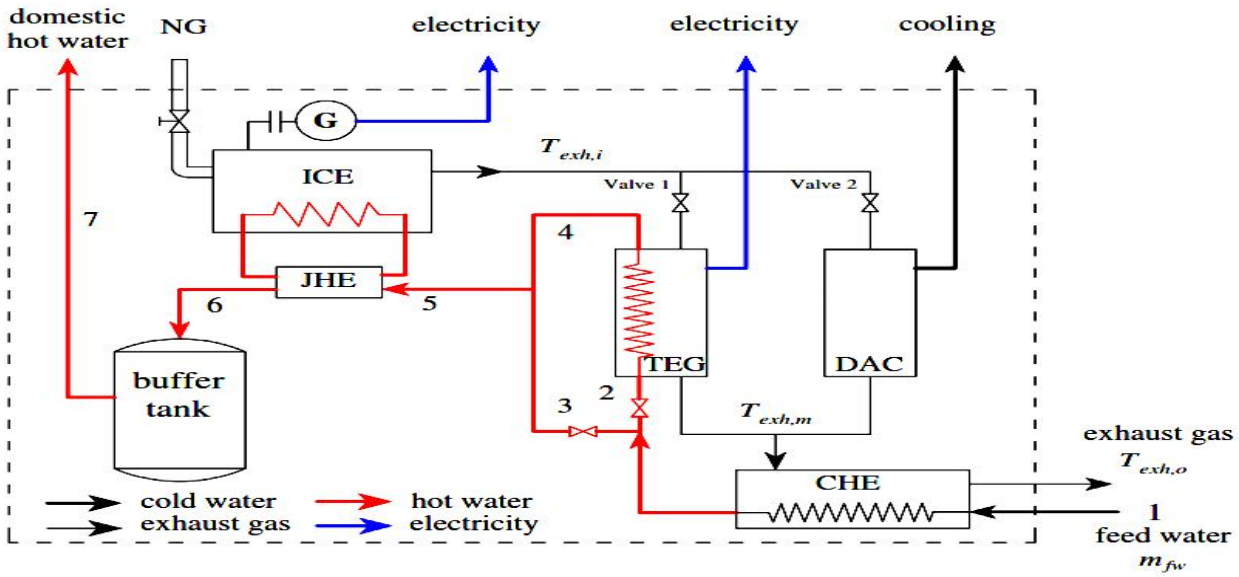

Figure 2.90: ICE and TEG CCHP system (adapted from Wang *et al.*, 2014)

2.5.2.10 Low Temperature Polymer Electrolyte Membrane FC (LT PEM FC) CCHP System

The aim of their research as per Cozzolino (2018), was to appraise the performances and the energetic viability of a unique domestic micro CCHP system using a LT-PEM FC power unit and half effect LiBr absorption chiller. The numerical outcomes displayed a good execution in terms of exergy and energy in the full tri-generation system functional field. Figure 2.91 represents their CCHP system.

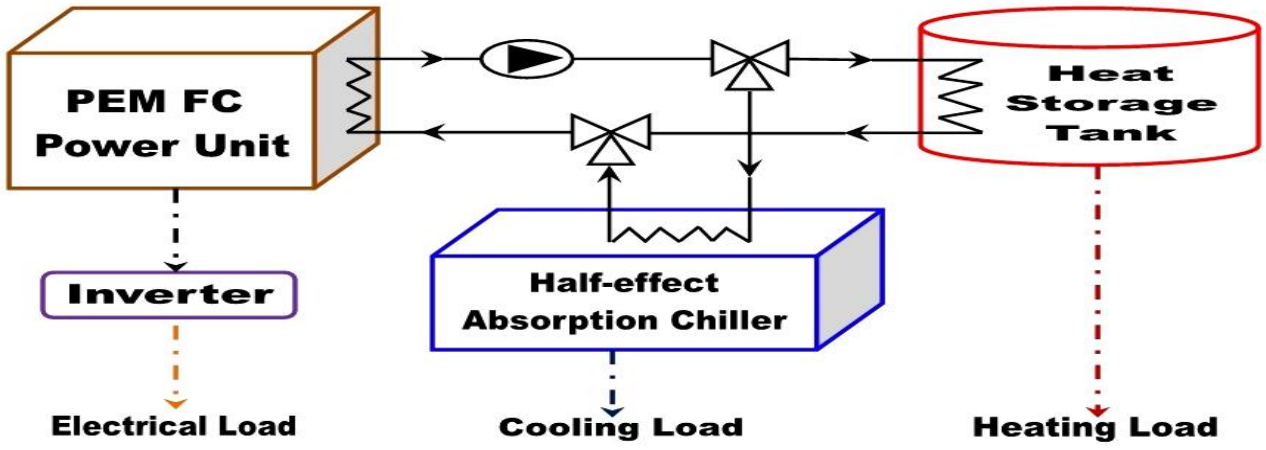

Figure 2.91: LT-PEM fuel cell CCHP system (redrawn from Cozzolino, 2018)

2.5.2.11 Inlet Air Throttling Gas-turbine CCHP System

In Wang *et al.* (2018), with reference to a CCHP system, the inlet air throttling (IAT) functioning schemes for gas turbine together with following the thermal load (FTL), following the electric load (FEL) and following the hybrid thermal-electric load (FHL) action techniques were used to assess the CO_2 emission (CDE), principal energy consumption (PEC) and operation costs. The similarities between the various working approaches and the energy requisite of the reference were analysed and the outcomes showed that the CCHP scheme is advanced to the individual scheme on yearly analysis, regardless of which working method was applied. Figure 2.92 depicts their CCHP system.

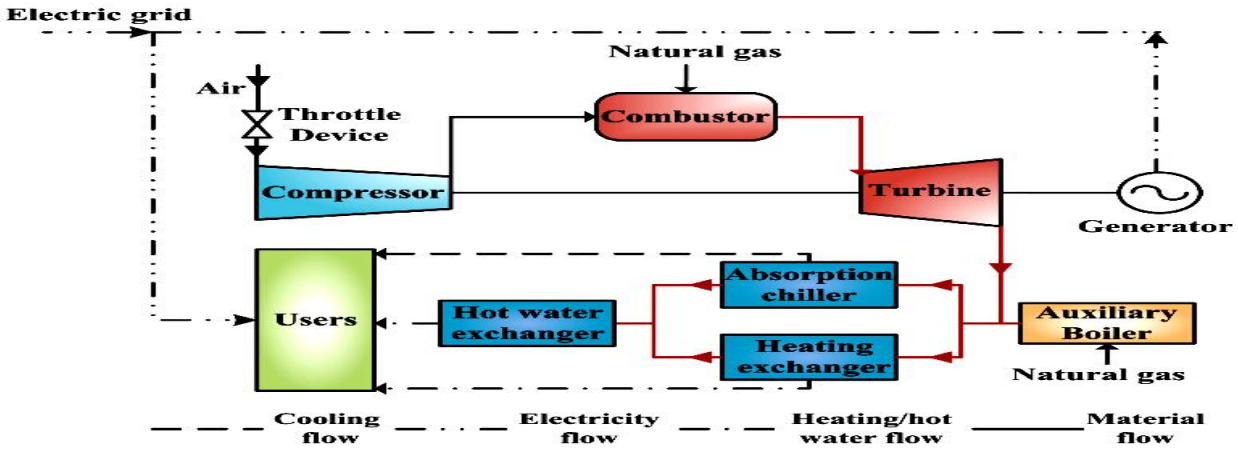

Figure 2.92: IAT gas-turbine CCHP system (adapted from Wang *et al.*, 2018)

2.5.2.12 Ground Source Heat Pump (GSHP) Micro Gas-turbine and Solar CCHP System

In Lu *et al.* (2018) as shown in Figure 2.93, is proposed a multi-energy local energy provision system with usual CCHP scheme central to it, as well as combined with GSHP and PV power productions. The research brought forth an efficient method for a joined CCHP multi-energy system design optimization and deduced an innovative approach for addressing related optimization problems.

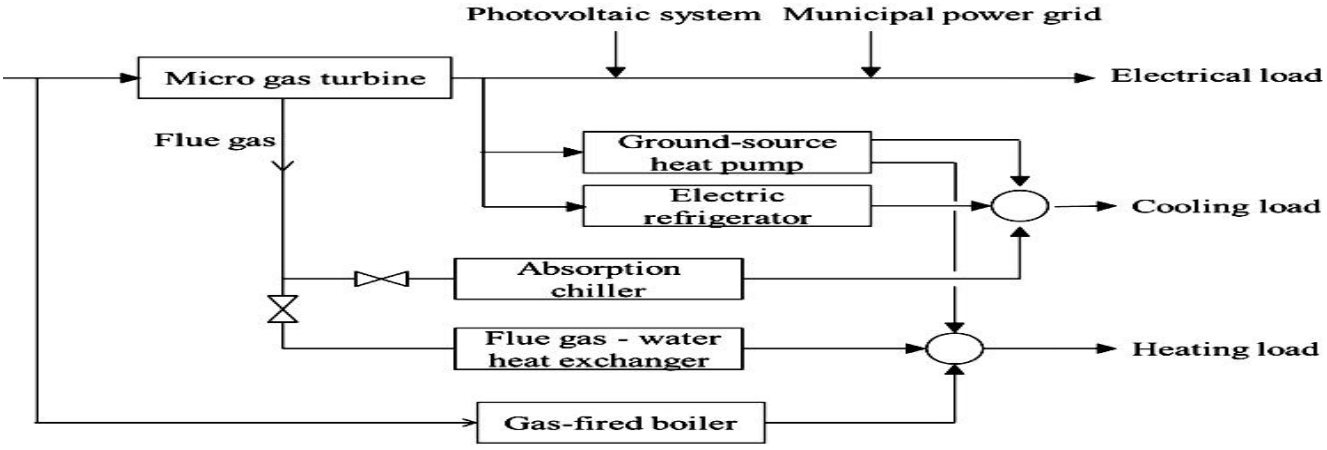

Figure 2.93: GSHP micro gas-turbine and photovoltaic CCHP system (adapted from Lu *et al.*, 2018)

2.5.2.13 ICE and GSHP CCHP System

According to Li *et al.* (2019), a GSHP coupling setup with heat exchanger was researched to improve the CCHP GSHP scheme execution and it out-performed the CCHP system with no heat exchanger. Figures 2.94a and 2.94b exemplify both CCHP GSHP systems that were used in their research.

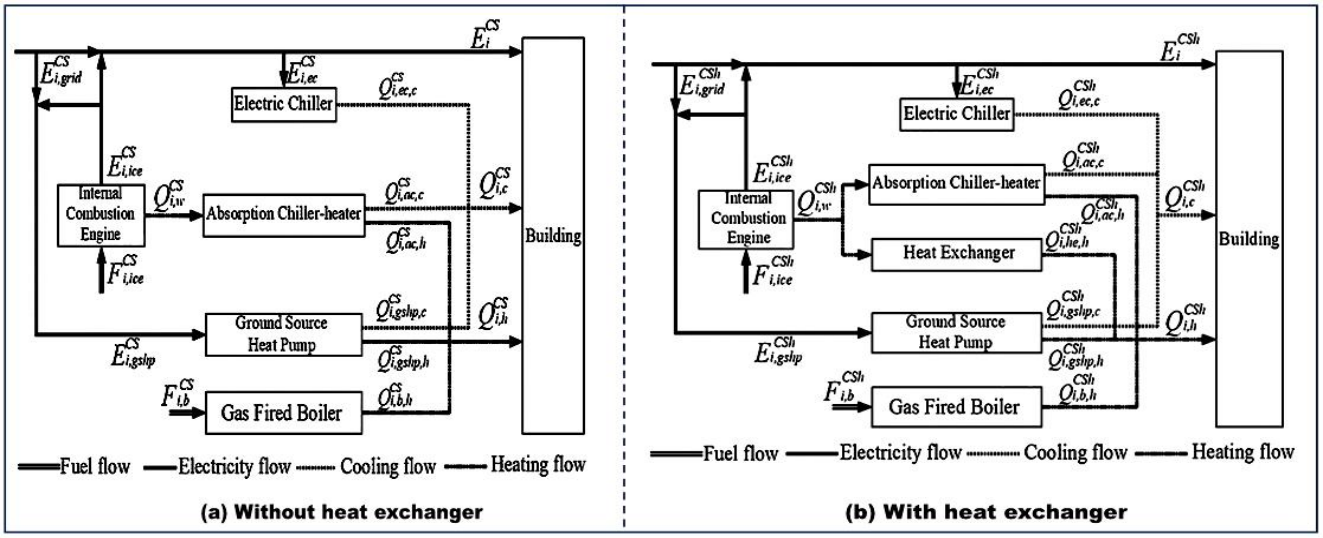

Figure 2.94: ICE and GSHP CCHP system without and with heat exchanger (adapted from Li *et al.*, 2019)

2.5.2.14 ICE with Refrigeration and Dehumidification CCHP System

In Jiang *et al.* (2017), postulated is a dehumidification and hybrid cooling CCHP system, in which ICE was used as the PGU. A "jacket water of ICE" was applied to enable the absorption dehumidifier to yield dehumidification. The hybrid cooling system consists of an electric compression cooler and absorption chiller. The design and functioning technique of the system was optimized using a constrained non-linear programming (NLP) solution and a thermo-economic model of the CCHP scheme was instituted. Figure 2.95 illustrates the CCHP system.

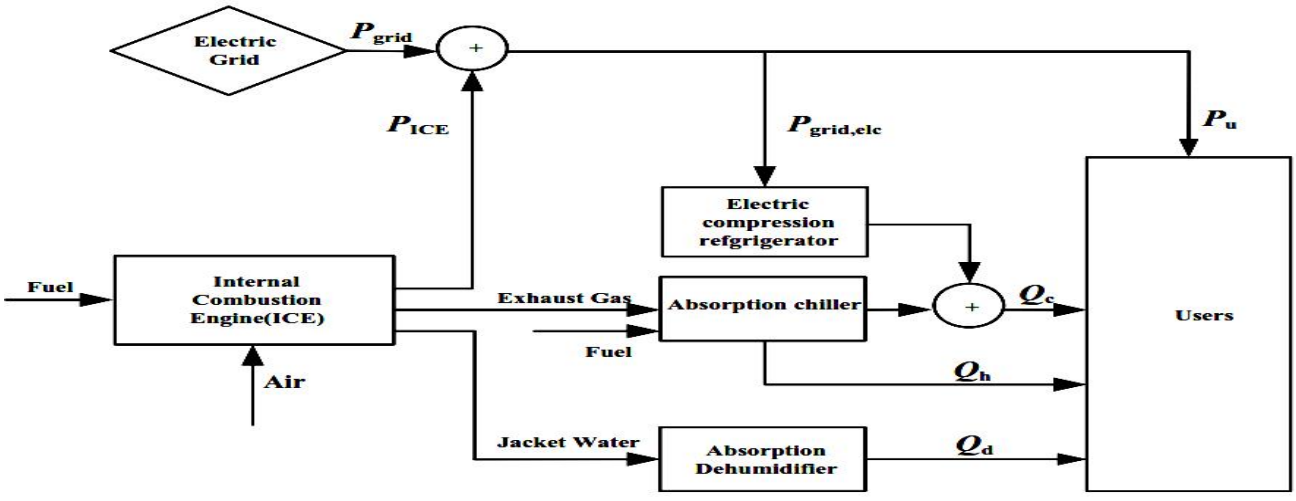

Figure 2.95: ICE with dehumidification and refrigeration CCHP system (adapted from Jiang *et al.*, 2017

2.5.2.15 5kW PEM FC CCHP System

As per Chen *et al.* (2018), a multi-criteria research was done on a 5kW PEM FC based residential CCHP system as portrayed in Figure 2.96. The CCHP system thermodynamic model was partly proven, whereby a parametric analysis scheme was applied to assess the system executions, including exergy and energy efficiencies, pollutant emission reduction and yearly cost. The system was optimized using evolution algorithm to obtain 3D Pareto solutions and optimum functional set of parameters. The outcomes indicated that more relative humidity, small operating temperature and more inlet gases pressure are vital for enhancing system emission, effectiveness and exergy.

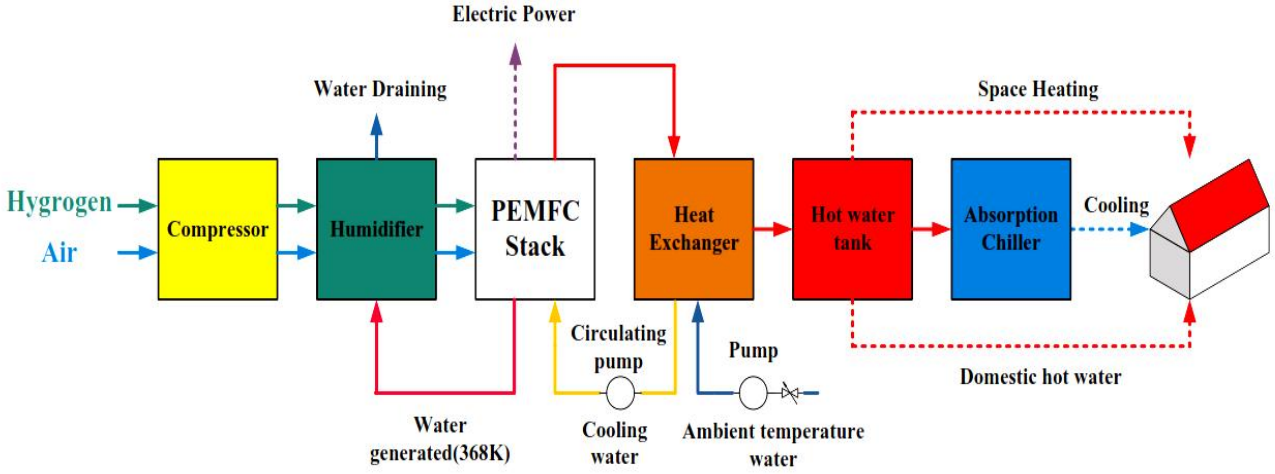

Figure 2.96: 5kW PEM fuel cell CCHP system (adapted from Chen *et al.*, 2018)

2.5.2.16 LT PEM FC and Thermoelectric Cooler (TEC) CCHP System

Articulated in Ebrahimi and Derakhshan (2018), the PGU is a LT PEM FC and a TEC was utilized as the refrigerating system. Water condensate and low-grade heat of ~80°C were convalesced as the by-products. The FC and the TEC mathematical models were realized and the simulations outcomes were in consistence with existing scholarly publications − validating their micro CCHP scheme as novel and proficient to generate 26.8W of cold, 2.79kW of power and 3.04kW of heat, having an overall efficiency of 76.94% and 43.25% fuel savings. Figure 2.97 portrays their tri-generation technique.

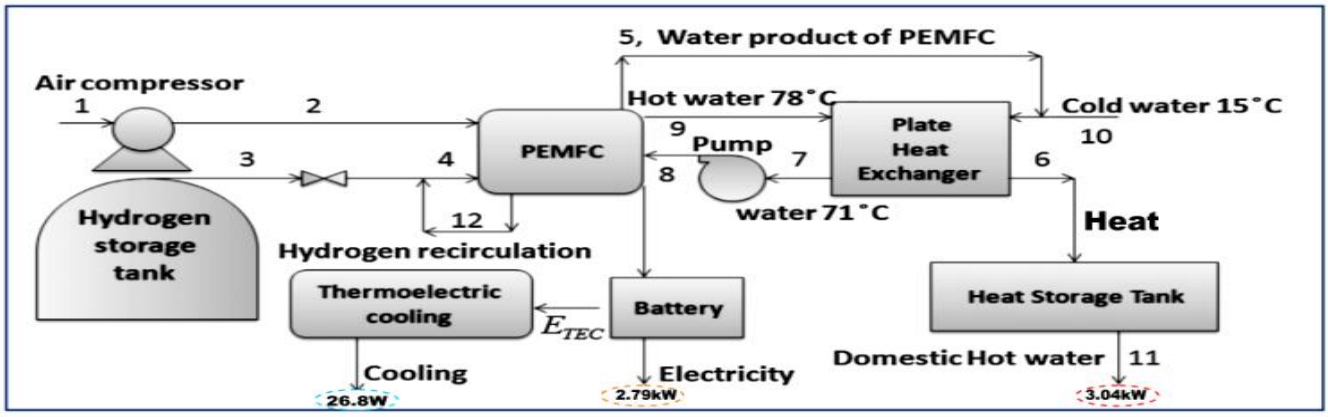

Figure 2.97: PEM FC and TEC CCHP system (adapted from Ebrahimi & Derakhshan, 2018)

2.5.2.17 Molten Carbonate FC (MCFC) and Stirling Engine CCHP System

Indicated in Mehrpooya *et al.* (2017), Stirling engine, MCFC and a double effect LiBr/H_2O absorption chiller CCHP system is suggested. MCFC is the prime mover and its exhaust heat is utilized as heat source to the Stirling engine that subsequently supplies heat to the generator of the absorption chiller. The electricity, heat and cold that were generated are respectively 6482kW, 2137kW and 1372kW. Figures 2.98a and 2.98b respectively sum up their CCHP system diagram and as well the flow process.

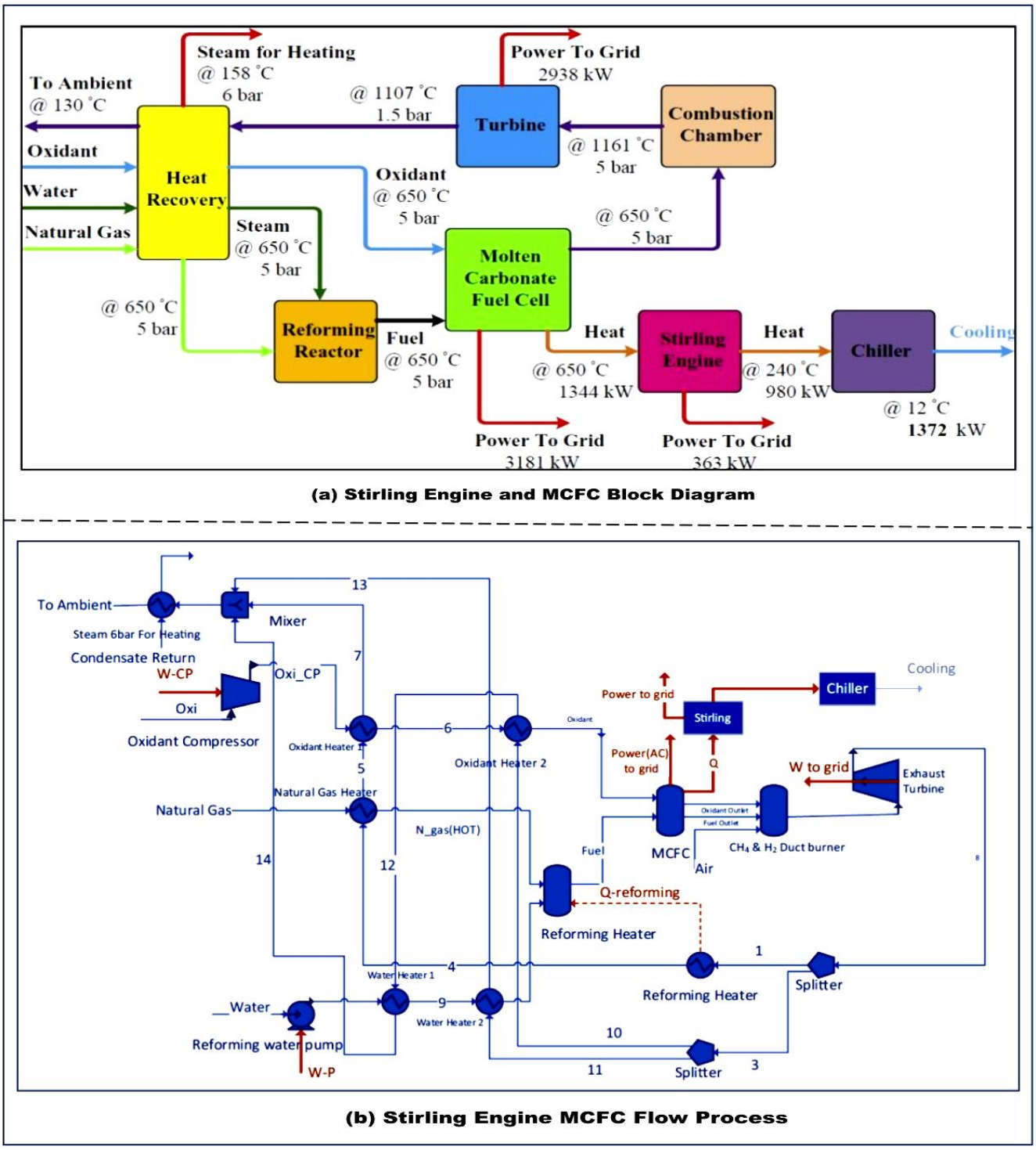

Figure 2.98: Stirling engine and MCFC CCHP system (adapted from Mehrpooya *et al.*, 2017)

2.5.2.18 CCHP System Integrated ORC and Solar Thermal Utilization

Researched in Wu *et al.* (2019) is a new solar thermal (ST) organic Rankine cycle (ORC) CCHP integrated system shown in Figure 2.99. Unlike conventional CCHP and CCHP-ST systems, the CCHP-ST-ORC system harmonizes fossil fuel with renewable energy and its performance was assessed based on thermodynamics. Their findings revealed that their CCHP-ST-ORC system i) could produce an extra 5.1kW electricity relative to the other two systems, ii) has a higher energy ratio of 22.6% more than ordinary CCHP system, iii) consumes 12.4% less energy than CCHP-ST system, iv) with a PLR of 100%, can generate up to 108kW of electricity and heat, v) can meet the heat requirements without gas boilers but by using the solar collectors and ICE and vi) has similar exergy efficiency of 40% compared to the traditional CCHP and CCHP-ST systems. Their results lend itself to coupling CCHP system design, development, functioning and applications.

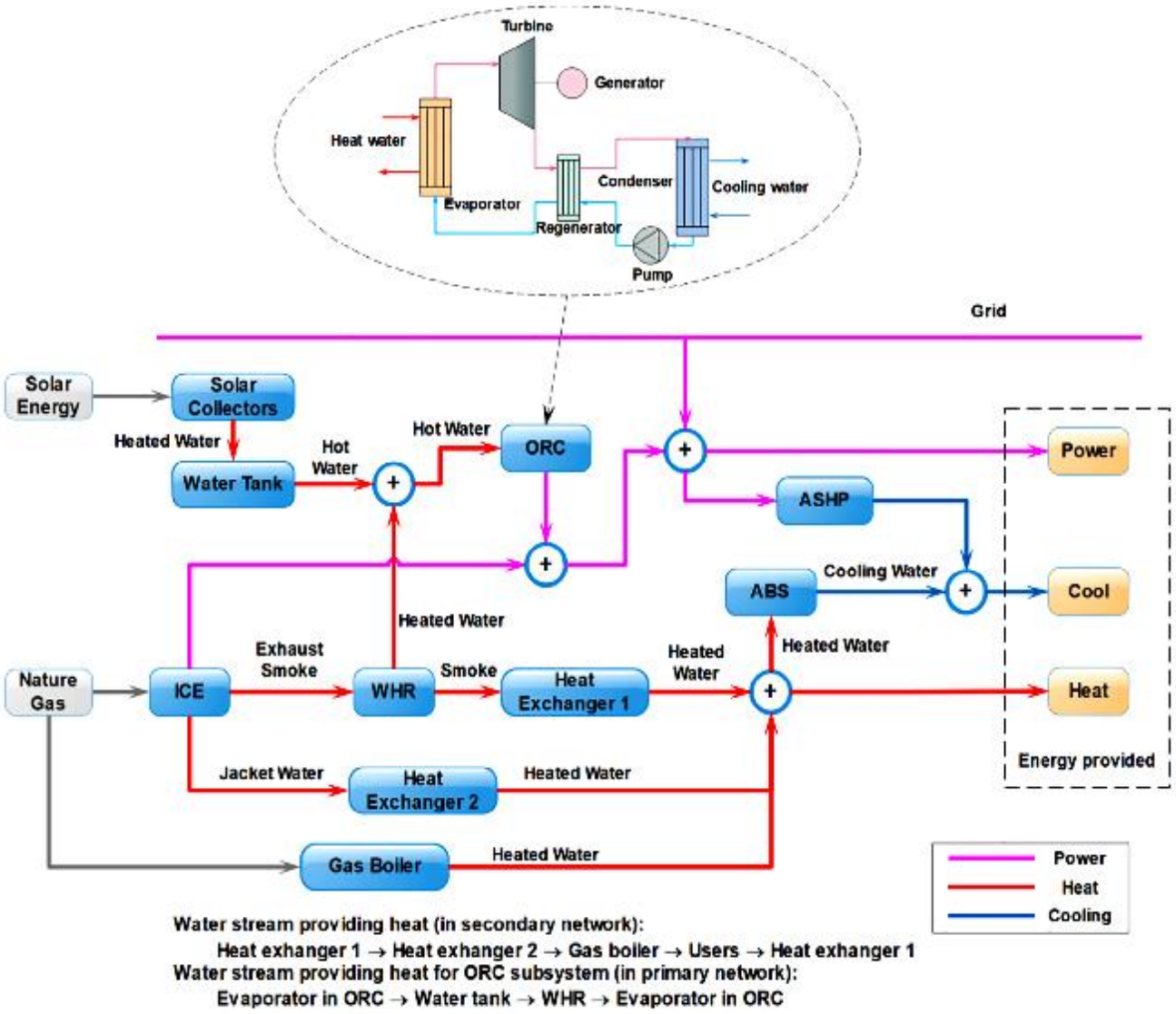

Figure 2.99: CCHP system integrated ORC and ST utilization (adapted from Wu *et al.*, 2019)

2.5.2.19 CCHP System Integrated with PV / Thermal Panels and Thermal Energy Storage

According to Mao *et al.* (2020), CCHP is becoming promising technology to provide cascaded efficient energy and the system performance can be enhanced by integrating PV / thermal panels as well as energy storage controlled by an effective strategy of operation to manage the system energy flow. They formulated a mathematical model of their postulated system and they determined the optimal size of the main components using particle swarm optimization (PSO) technique. Their system was tested in a domestic area in Beijing using four setups and the relative results showed the scheme has better cost and primary energy savings of 17.6%. Figure 2.100 shows their system.

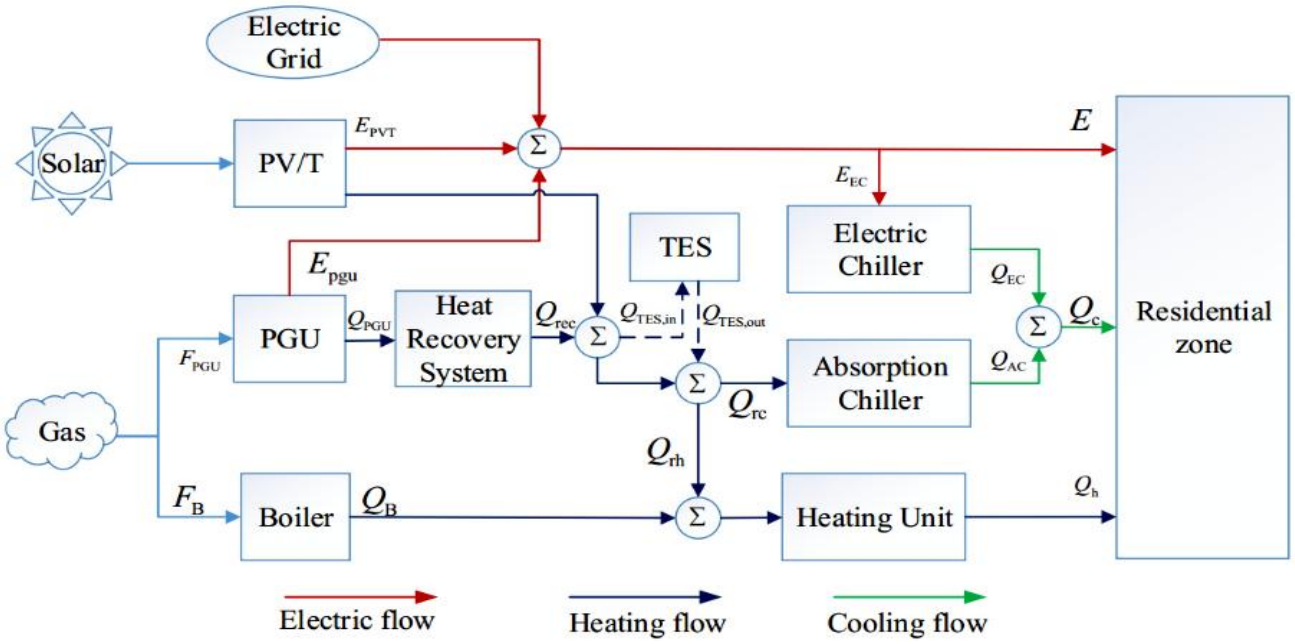

Figure 2.100: CCHP system integrated with PV / thermal panels & thermal energy storage (adapted from Mao *et al.*, 2020)

2.5.2.20 Multi-energy Oriented CCHP System: Energy Flow Optimization Method

Studied in Lingmin *et al.* (2020) and shown in Figure 2.101, is a CCHP multi-energy system integrating gas, PV and wind energy as well as power storage controlled by PSO method. By defining the reliability index for the supply of a particular energy form, an index for heat and power losses probability were constructed, also taking into considerations the cost of investment, CO_2 emission and primary energy consumption. The renewable energy is prioritized for power generation under FEL, during which it can reach above 50% in peak load period or when windy at night and the demand is low. As a result of this fluctuations, the fossil fuel PSU is on standby to track the load power demands. This method improves renewable energy production and reliable energy supply.

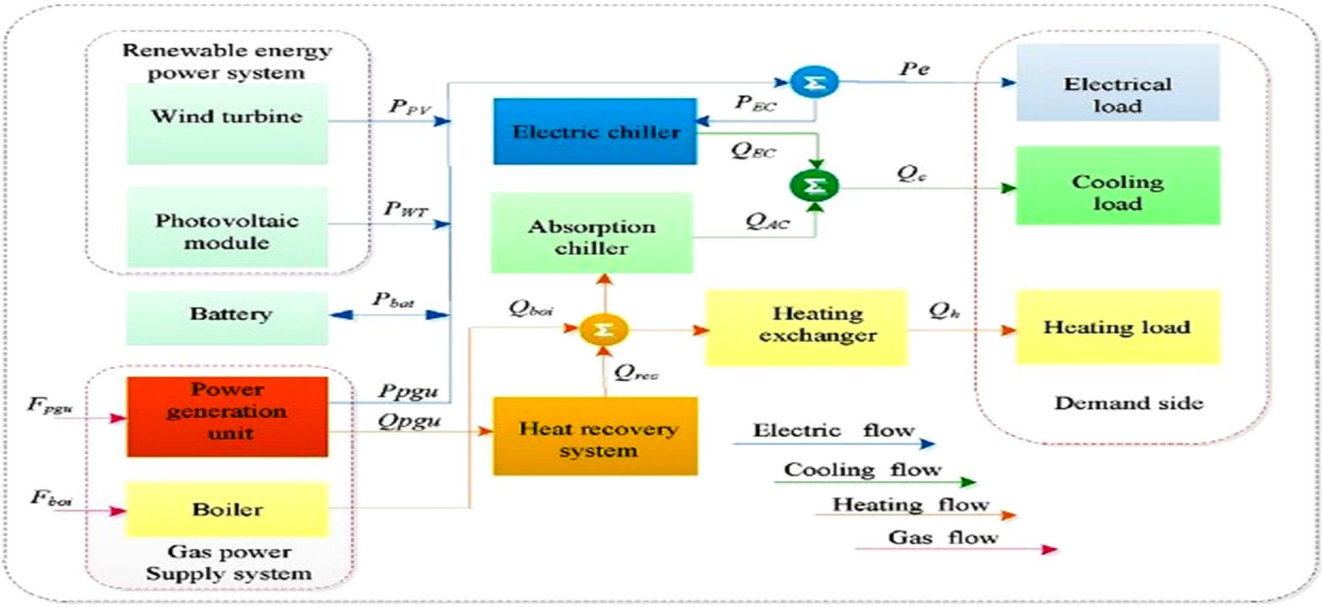

Figure 2.101: Multi-energy oriented CCHP system (adapted from Lingmin *et al.*, 2020)

2.5.2.21 Improved CCHP System based-on Developed Owl Search Algorithm

Examined in Cao *et al.* (2020) and shown in Figure 2.102 is an enhanced CCHP system routed in a developed owl search technique and Levy flight mechanism, in which the energy flow for a CCHP system to reduce the main electricity usage in Kerman area in Iran is suggested. In the proposed system, wasted heat from hot gases is recycled while at the same time producing power, enabling a system energy efficiency above 85%. The system is analyzed and optimized with respect to the cost of operation and emission reductions as well as energy utilization. Their simulation revealed that with the use of optimal parameters, the system main components efficiency can be enhanced.

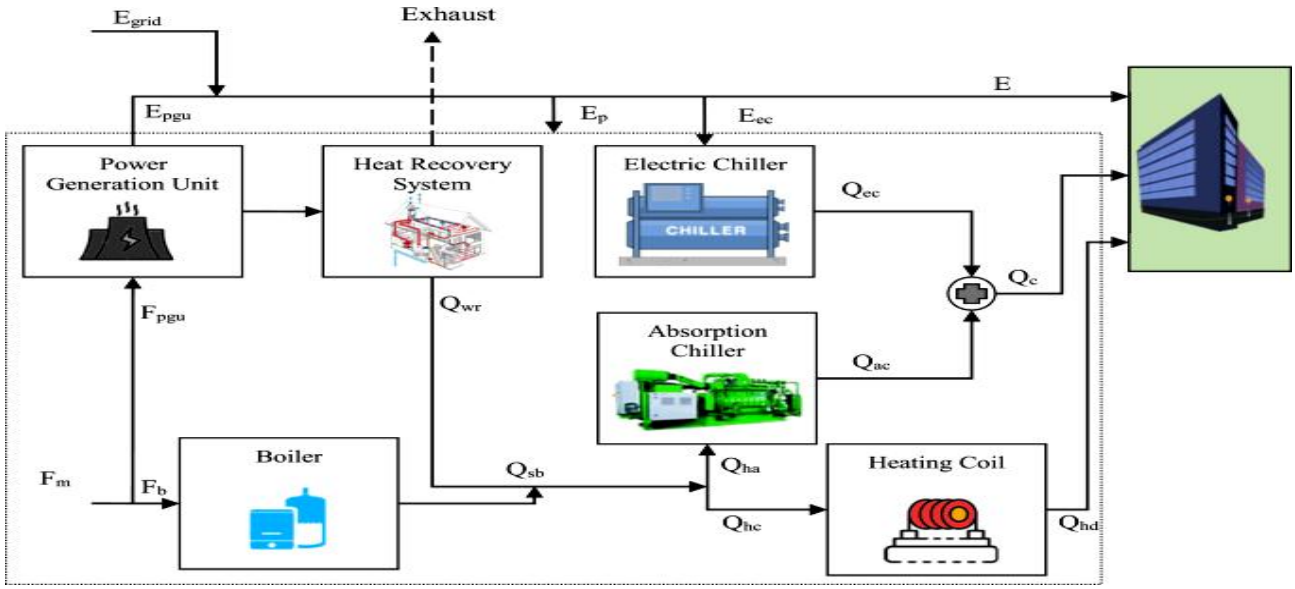

Figure 2.102: Improved CCHP system based-on developed Owl search algorithm (adapted from Cao *et al.*, 2020)

2.5.2.22 Residential Building Smart Energy Management System Fitted with CCHP System

Postulated in Farmani *et al.* (2018) and exemplified in Figure 2.103, is a smart energy management system concept of a micro grid CCHP system for buildings, to control the schedules of its energy storage and renewable systems. The building energy operation cost is minimized for stochastic and deterministic scenarios and the effectiveness and applicability of the suggested concept was tested using the 24 h-ahead optimum energy planning. The conclusion drawn is the use of CCHP system fitted with a smart controller, could significantly lowers a building energy operating cost.

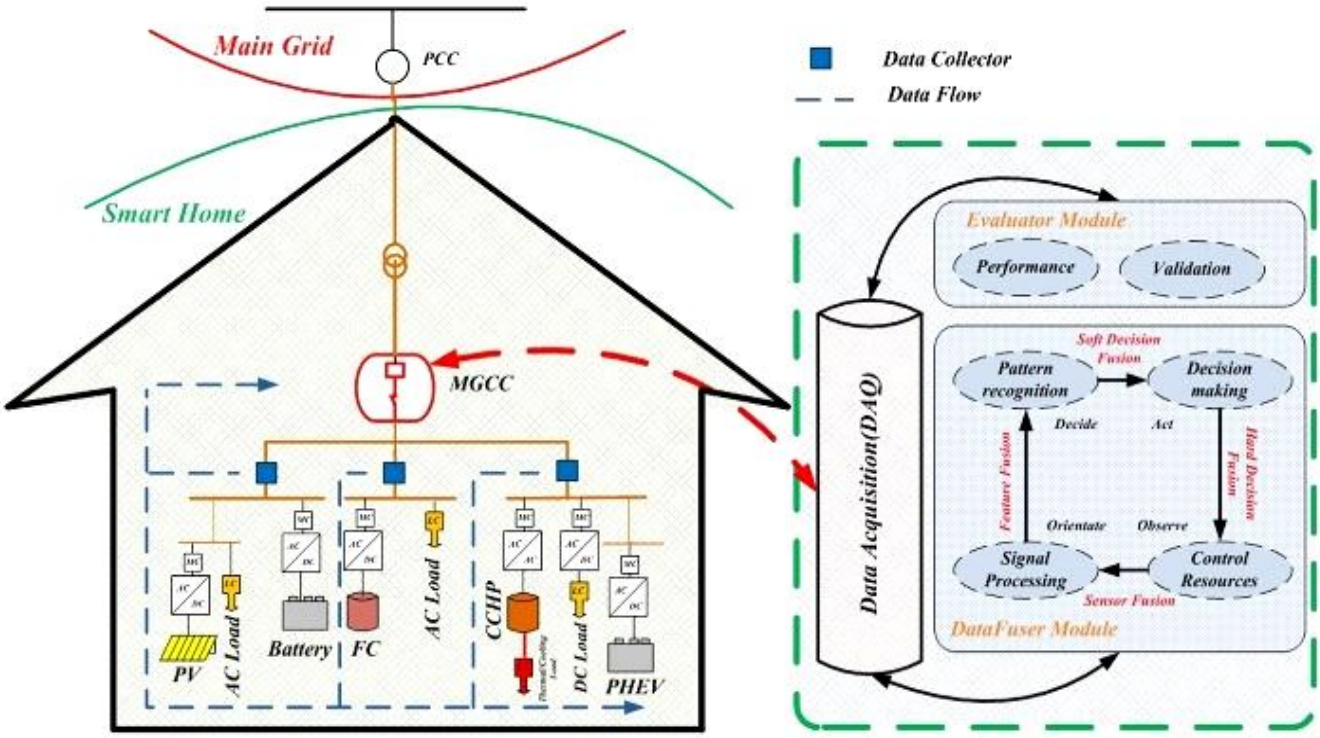

Figure 2.103: Residential building smart EMS fitted with CCHP system (adapted from Farmani *et al.*, 2018)

2.5.2.23 Geothermal Driven CCHP Systems Integrating Ejector Trans-critical CO2 (TRCC) & Rankine Cycles

According to Zare and Takleh (2020), CCHP systems benefits are becoming remarkable due to inclusion of efficient thermodynamics cycles and renewable energy. In their proposed model shown in Figure 2.104a is a geothermal CCHP system with the ejector TRCC fitted with a traditional Rankine cycle and in Figure 2.104b, the gas cooler is substituted with an internal heat exchanger (IHE). Parametric analysis and thermodynamics modeling were performed to study the design variable influences. Their findings noted that replacing the gas cooler resulted to 30.9% exergy efficiency, 49.1% net power output and 75.8% cooling output increments, although losing the heating output by 39.1%.

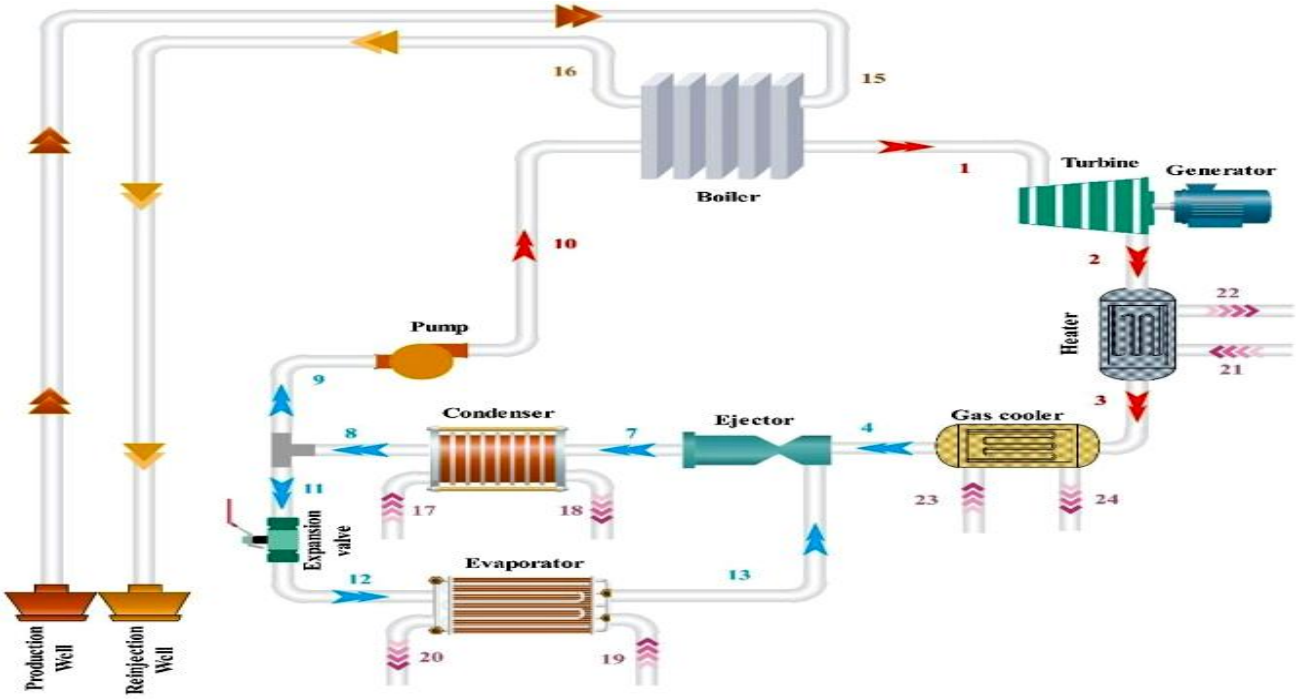

(a)

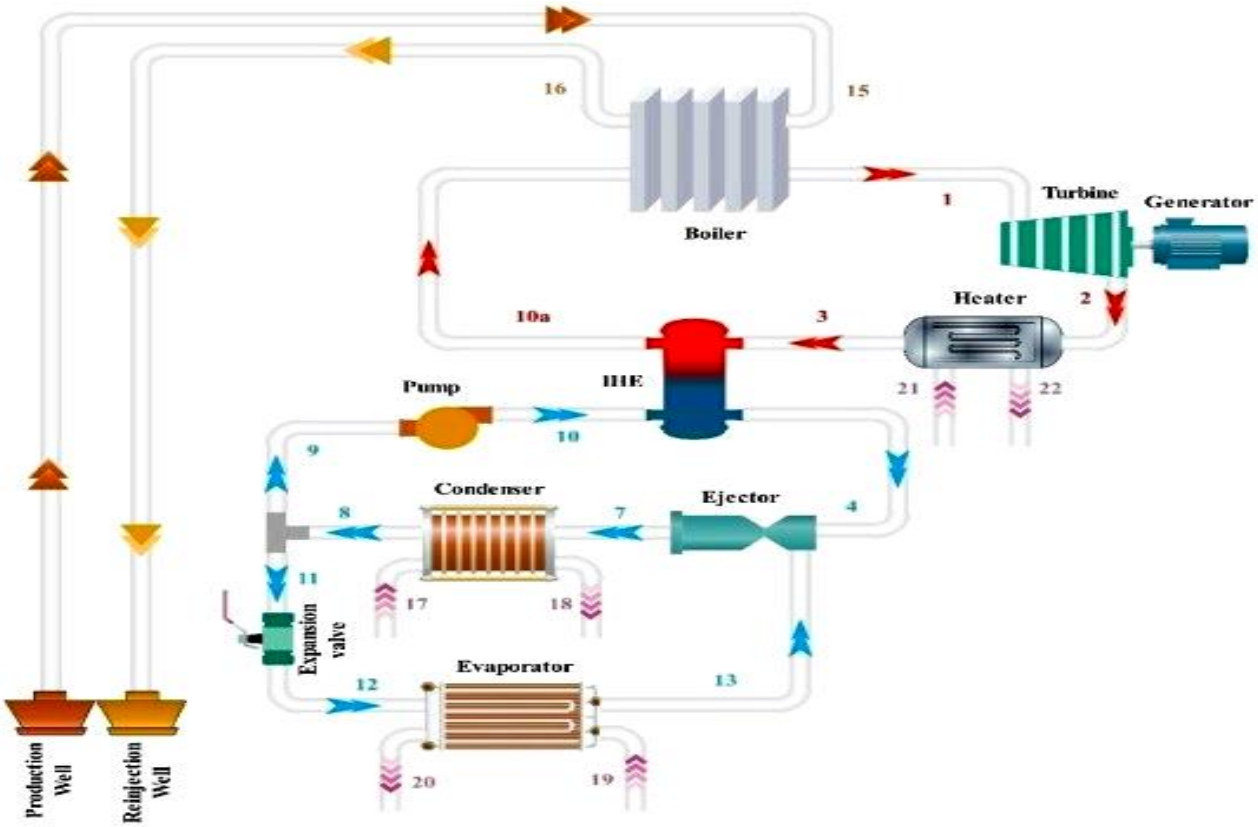

(b)

Figure 2.104: Postulated CCHP systems based on (a) TRCC cycle and (b) TRCC with an IHE (adapted from Zare & Takleh, 2020)

2.5.2.24 Thermodynamic and Economic Analysis of Different Co-generation and Tri-generation Systems Based-on CO_2 Vapor Compression and Refrigeration Systems

Investigated in Mohammadi and Powell (2020), are miscellaneous new integrated co-generation and tri-generation systems configurations which were suggested using a CO_2 parallel compression economization-vapor compression refrigeration cycle with a 1MW capacity and evaporator temperatures between -35 to 45°C. Their research main contribution was an in-depth techno-economic assessment of numerous possible variations for these systems for assorted practical uses. Depicted in Figure 2.105a is a tri-generation system for refrigeration, air conditioning and hot water production and in Figure 2.105b is a tri-generation system for refrigeration, air conditioning and power. A parametric study was further conducted to establish the impact of the various modalities and critical design dynamics as well as the functioning parameters performances on the suggested systems. The indicated waste energy recovery from the compressor outlet reduces the carbon footprint, due to a reasonable decline in the energy requirement for producing various important energy demands.

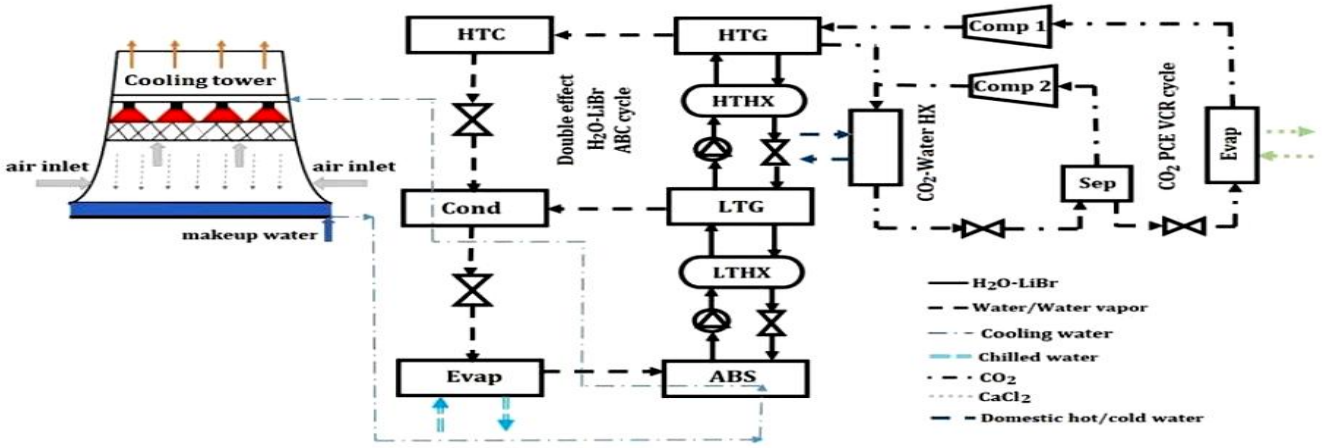

(a)

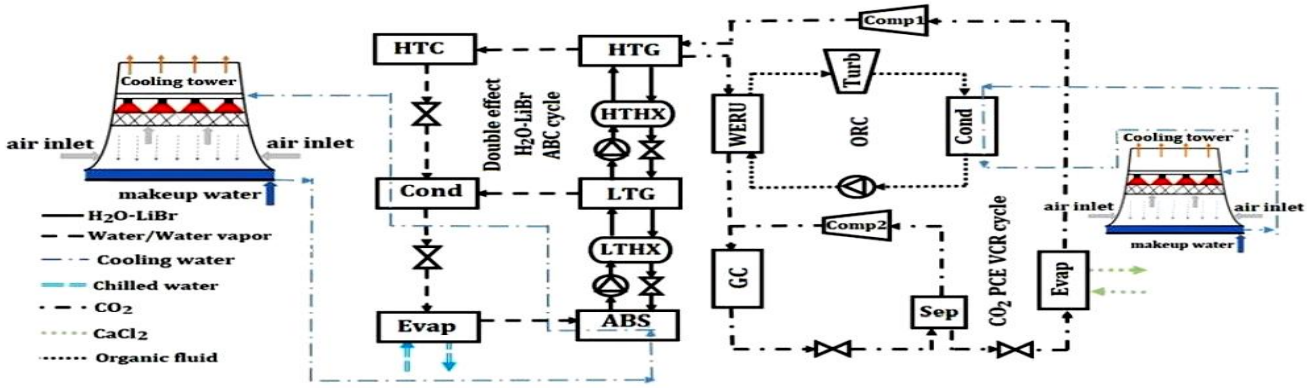

(b)

Figure 2.105: Tri-generation systems for (a) refrigeration, air conditioning and hot water production with heat exchanger and (b) refrigeration, air conditioning and power production with ORC (adapted from Mohammadi & Powell, 2020)

2.5.2.25 Energy, Environmental and Economic Evaluations of a CCHP System Driven by Stirling Engine with Hydrogen and Helium as Working Gases

Researched in Chahartaghi and Sheykhi (2019), and summarily portrayed in Figure 2.106, is a dual Stirling engine CCHP system with Hydrogen and Helium as the functioning gases. The engine was assessed with a non-ideal idiabatic model and the absorption chiller energy assessment was articulated using the engine waste heat. The Stirling engine vital specifications effects such as the heater temperature, re-generator length, CCHP efficiency, absorption chiller working gases coefficient of performance (CoP), CCHP primary energy saving, CO_2 emission reduction, operation cost reduction and engine rotational speed compared to traditional energy systems were investigated. The power, cold and heat productions, CCHP efficiency and CoP results using Hydrogen were respectively 15.24 kW, 19.65 kW, 12.65 kW, 70% and 64.4% and the power production, cold production, heat production, CCHP efficiency and CoP results using Helium were respectively 22.52 kW, 21.65 kW, 14.43 kW, 72.29% and 66.7%. As can be seen, Helium offered better results.

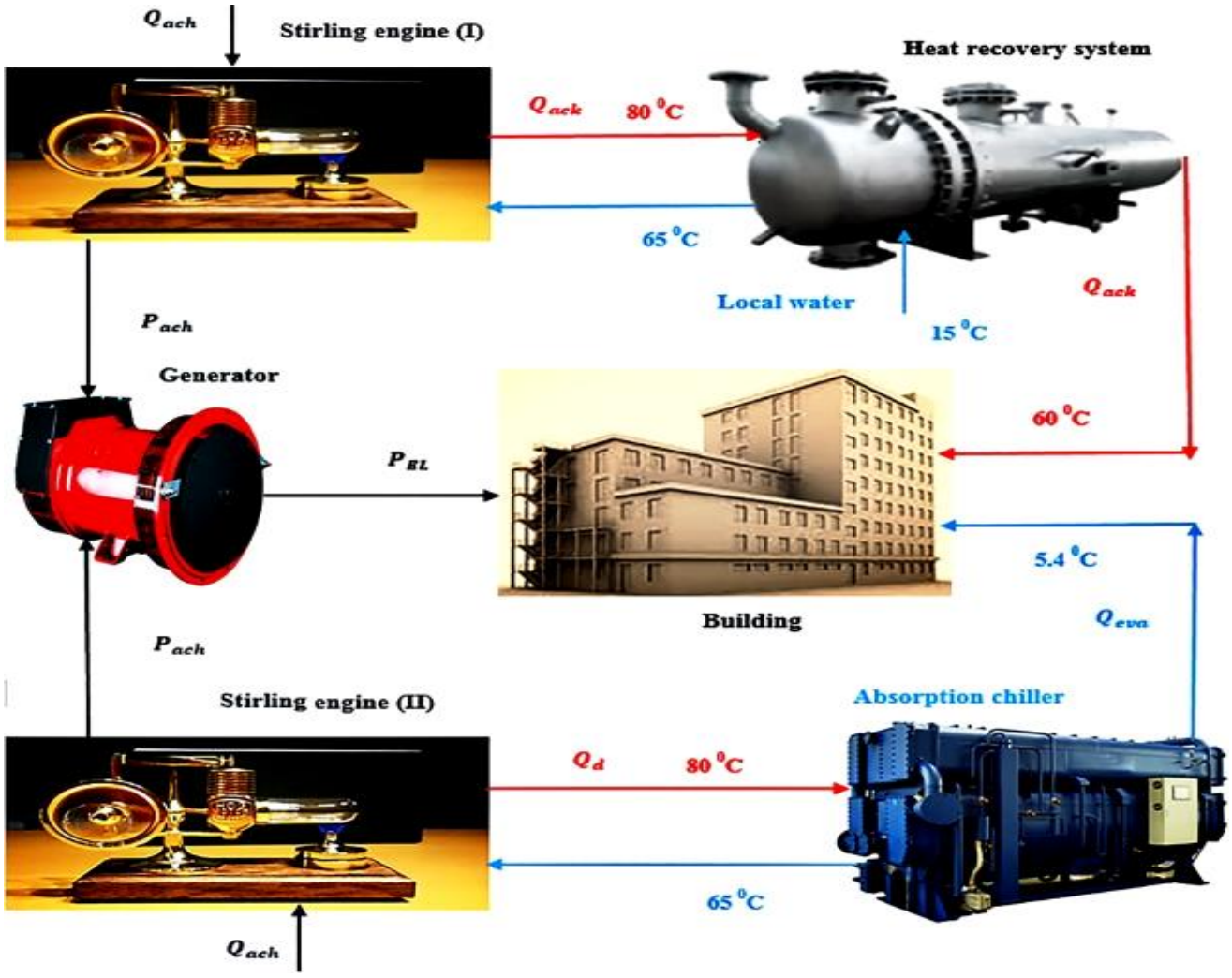

Figure 2.106: Researched CCHP system overview (adapted from Chahartaghi & Sheykhi, 2019)

2.5.2.26 Thermodynamic and Thermo-economic Analysis of Ammonia-Water Mixture Cycle

Proposed in Parikhani *et al.* (2020) and illustrated in Figure 2.107, is a novel ammonia-water mixture CCHP system driven by a low temperature heat source (LTHS) − which is a tailored version of a Kalina cycle. Thermodynamics and thermo-economics balance equations for performance analysis of the thermal system were used to investigate the viability of the recommended system. The energy and exergy efficiencies were respectively calculated to be 49.83% and 27.68%. The electrical, cooling and heating capacities were respectively 0.253 MW, 1.610 MW and 1.972 MW. More energy efficiency can be acquired by raising the evaporation temperature and basic ammonia concentration or by reducing the separators pressure, heating unit temperature and the terminal temperature difference of the vapour generator.

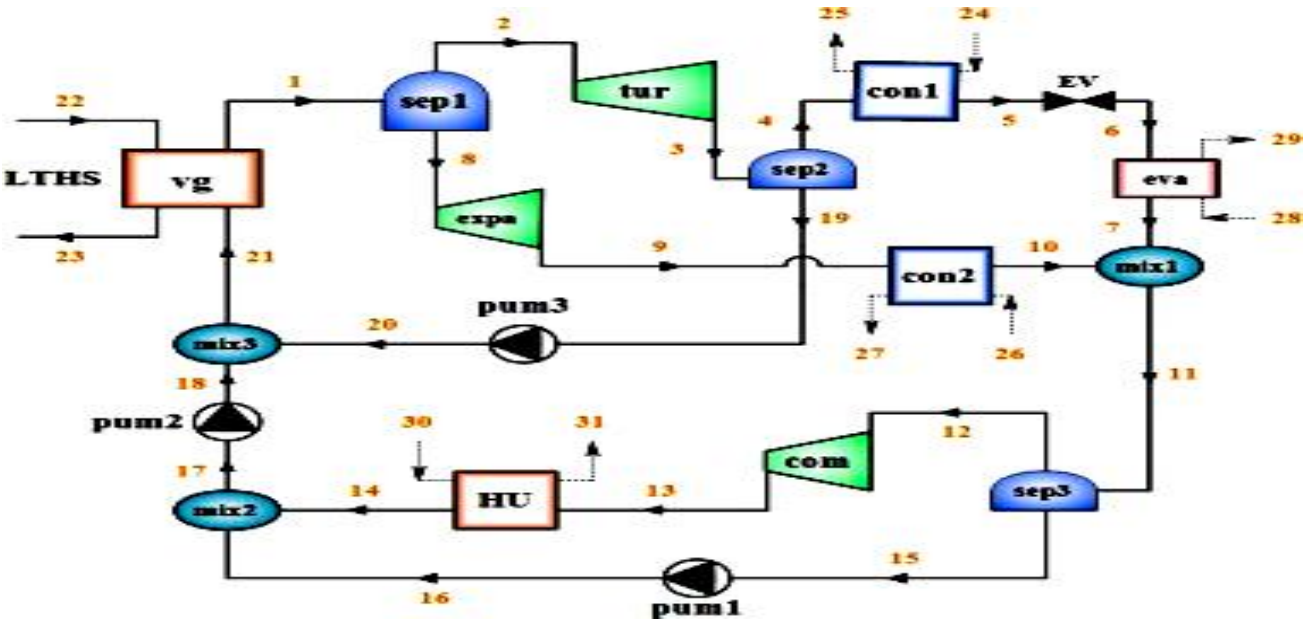

Figure 2.107: LTHS CCHP system overview (adapted from Parikhani *et al.*, 2020)

2.5.2.27 A Configuration Optimization Framework for Renewable Energy Systems Integrating with Electric-heating Energy Storage in a Remote Tourist Area

Studied in Lingmin *et al.* (2021) and pictured in Figure 2.108 is a wind, solar and natural gas CCHP system for a remote tourist area. Taking into account the complexity of the system, a CHP energy hub was put in place to concentrate and dispense power and heat. An integrated optimization framework that reduces yearly economic, maintenance and fuel costs by inserting the constraints of energy supply reliability and renewable energy penetration indices was constructed and it can inform the reliability of power, heat and cold supplies. The PGU supply the bulk of the power during wind and solar outages and the heat and power storage devices also assist in these regards to reduce wastage and to enhance the system performance, though at the expense of the system complexity.

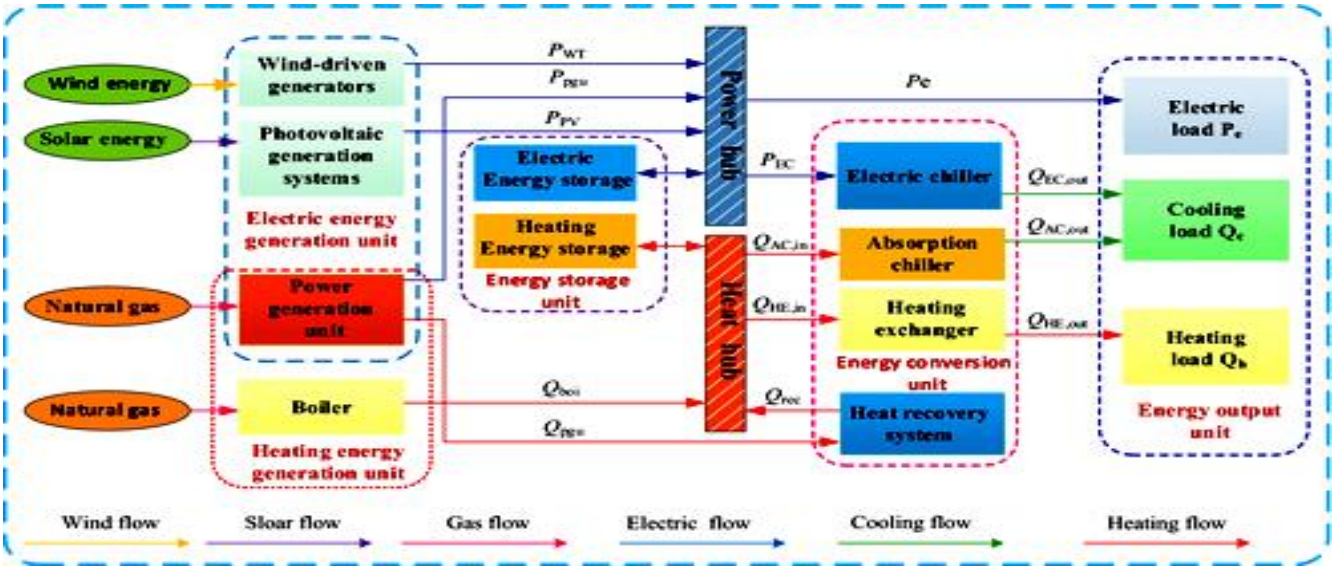

Figure 2.108: Researched CCHP system overview (adapted from Lingmin *et al.*, 2021)

2.5.2.28 ORC Co-generator and Adsorption Chiller CCHP Experimental Prototype

Examined in Lombardo *et al.* (2020) and summarized in Figure 2.109, is a CCHP system based on PV, micro-ORC plant and an adsorption chiller with built-in real bio-climatic nearly zero energy building (NZEB) modeled with TRNSYS software and the analyses performed included energy, economic and environmental. It was realized that the system effectiveness is affected by the solar irradiance and weather condition. The system was analyzed hourly and sensitivity result showed that locations have an impact on the system. The system was operated for 100 days in a year and the efficiency was between 32 and 42%. The system was proven to be apt for home ventilation use.

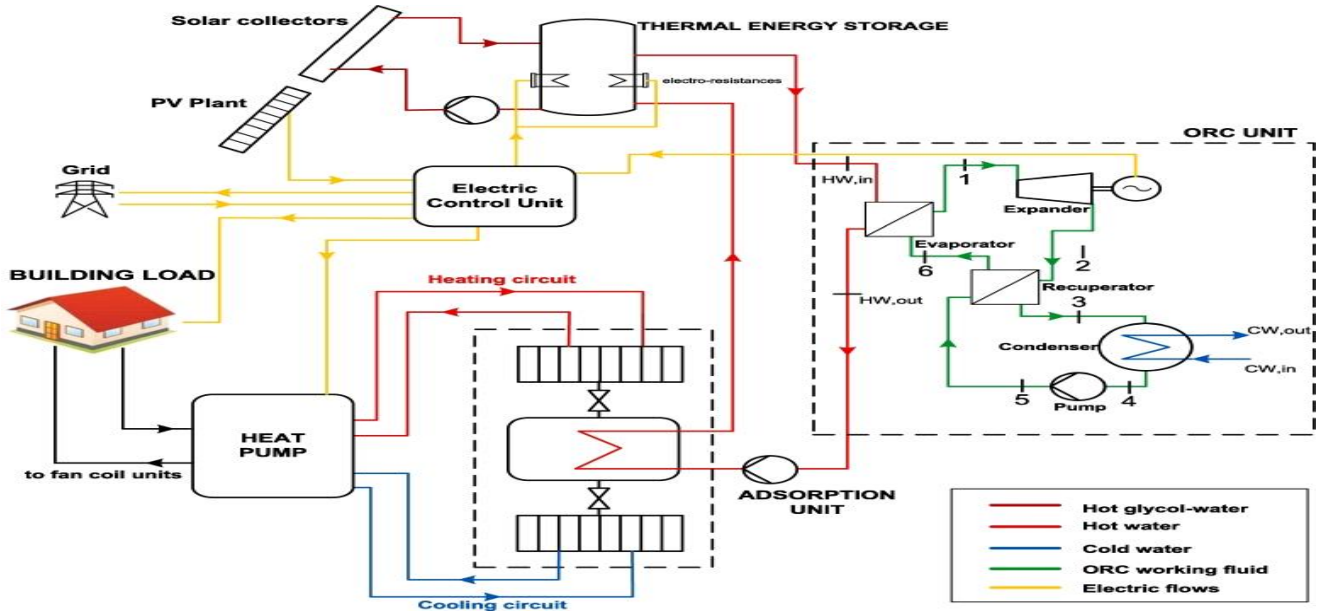

(a)

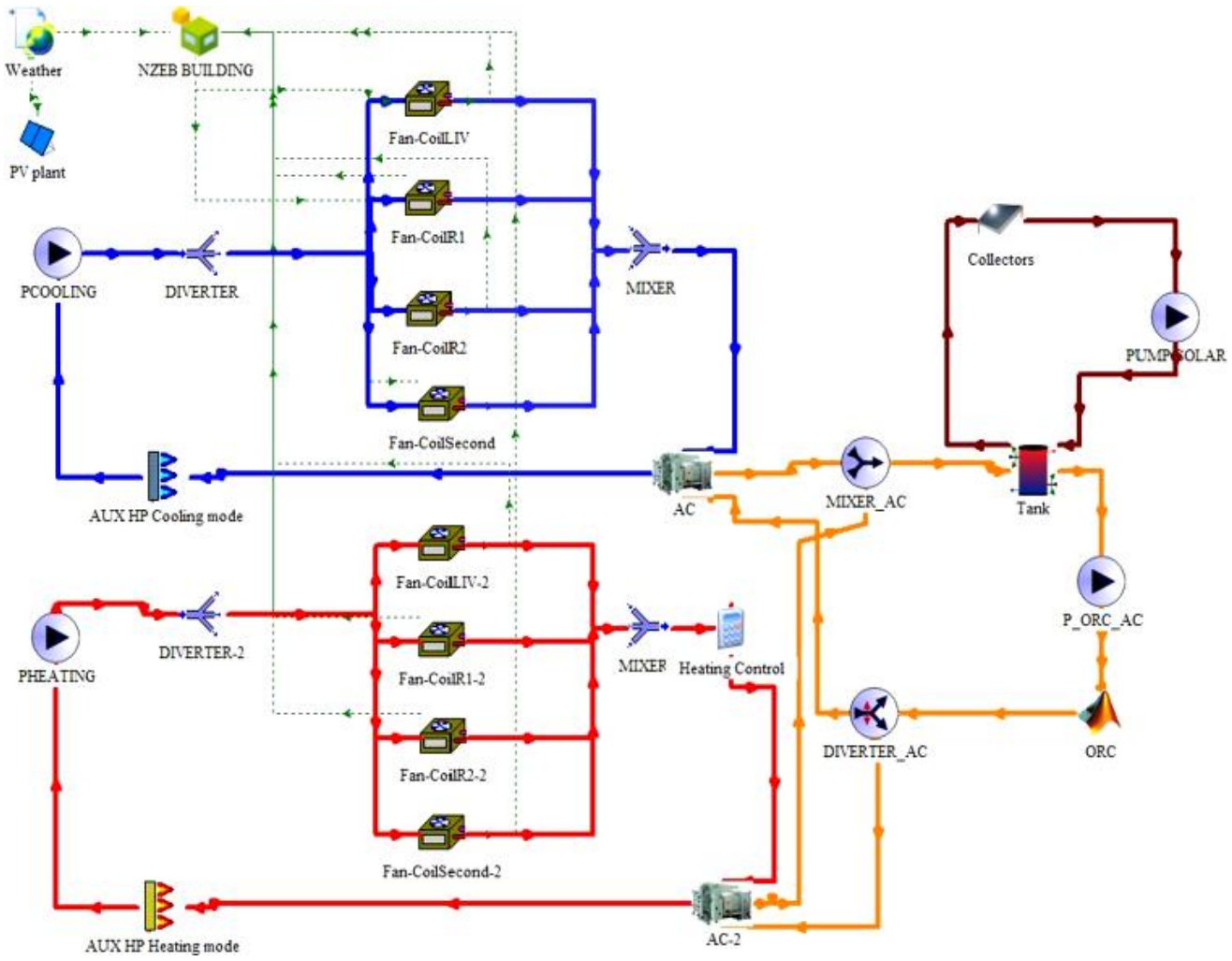

(b)

Figure 2.109: Researched CCHP system a) overview and b) TRNSYS model (adapted from Lombardo *et al.*, 2020)

2.5.2.29 Comparative Study of Optimization Method and Optimal Operation Strategy for Multi-scenario Integrated Energy System (IES)

Articulated in Wu *et al.* (2021) and captured in Figure 2.110, is an integrated multi-scenario CCHP system theoretical model. A novel self-adaption technique based on exhaustive search algorithm was suggested for a minimum per hour operation cost. Using various operation methods for remote and connected cases, the optimal capacity and operation parameters were ascertained. It was found that using self-adaption technique, the remote scenario provided the minimum annual system costs of \$23.6/m^2 and \$19.39/m^2 respectively for commercial and office buildings. A synergised optimization approach that harmonizes genetic algorithm and the orthogonal experimental strategy were initiated to establish multiple decision variables and the results revealed it can reduce the annualized cost by 0.67% relative to non-collaborative optimization.

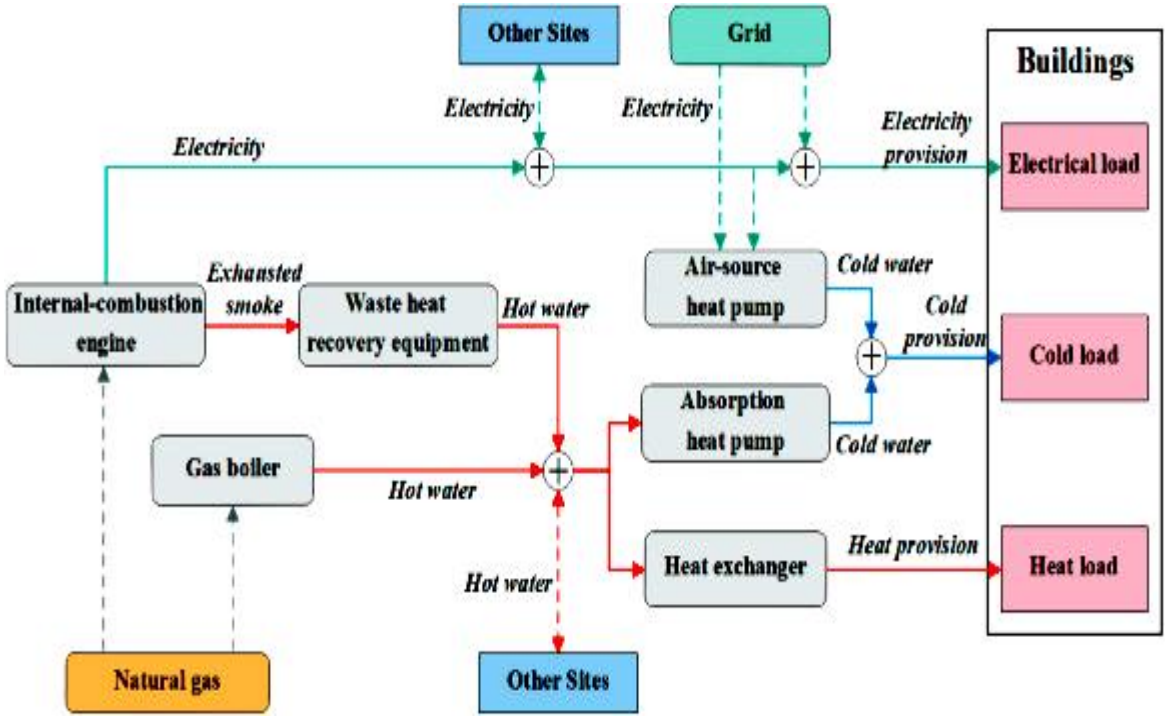

Figure 2.110: Multi-scenario integrated CCHP system (adapted from Wu *et al.*, 2021)

2.5.2.30 A Shopping Mall CCHP-ORC Distributed Energy System Operation Simulation

Presented in Ma *et al.* (2020), is a CCHP-ORC system to stabilize irregular power and heat demands as well as enhance the versatility and changeability of the heat to power ratio on the source side. By using the TRNSYS software, a simulation model for the functioning of the CCHP-ORC system was developed based on system configuration coupling analysis and the thermodynamics parameters. A commercial building was used as an example. Figure 2.111 summarized the study.

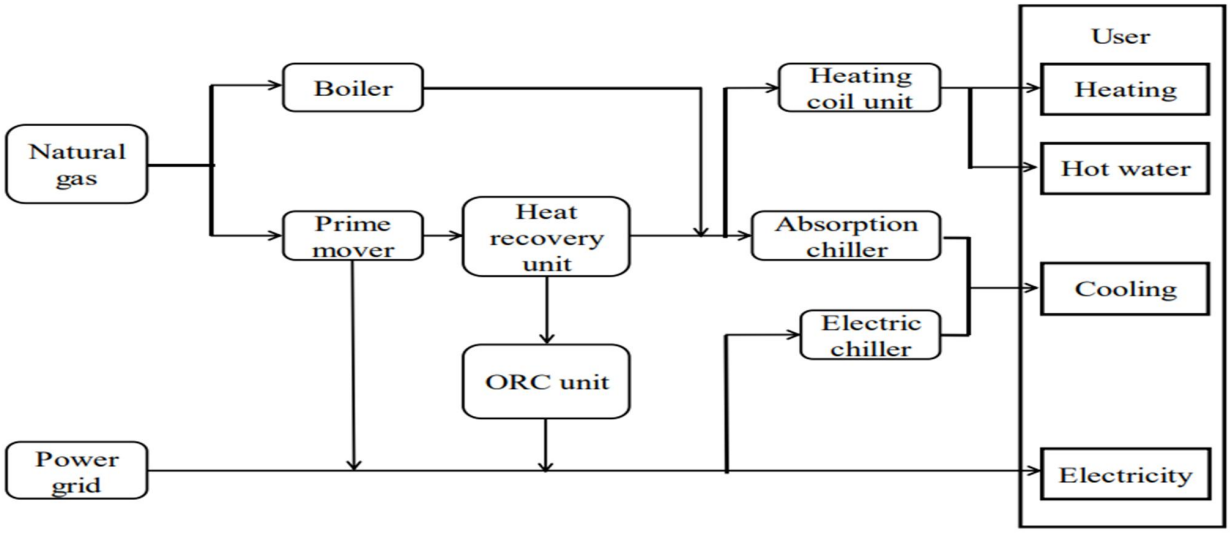

Figure 2.111: A Shopping mall CCHP-ORC distributed energy system operation simulation (adapted from Ma *et al.*, 2020)

2.5.2.31 CCHP System Capacity Configuration Research Ideas

According to Miao *et al.* (2020), a cascaded CCHP system reduces emissions, though its provisions makes it complex and therefore a challenge for optimal configuration and performance assessment. As a result, analysis is required and two operating modes namely "fixing power based on heat" and "fixing heat based on power" were assessed with the latter being the better with a lower annual cost. Numerical results revealed that the system energy utilization rate is at best when the adsorption chiller and gas turbine models are similar. Figure 2.112 summarized the investigation.

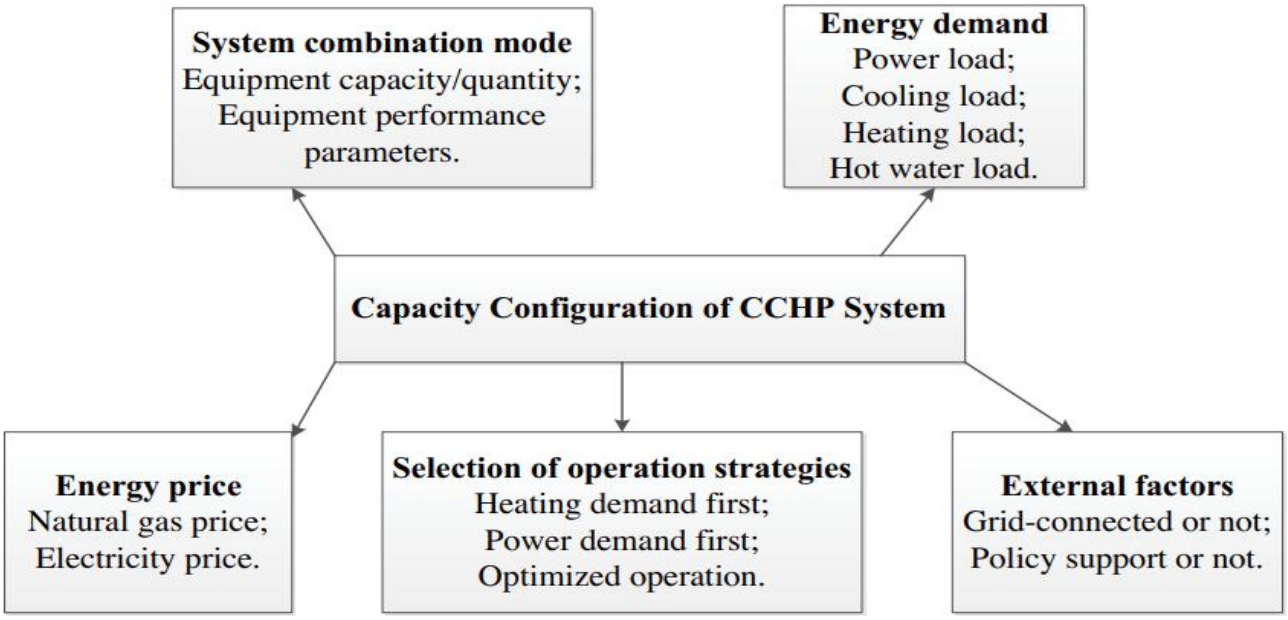

Figure 2.112: CCHP system capacity configuration research ideas (adapted from Miao *et al.*, 2020)

2.5.2.32 CCHP System Integrated with an ORC and Hybrid Energy Storage System Design & Optimization

Demonstrated in Ji *et al.* (2020) and exemplified in Figure 2.113, is a novel CCHP system with in-built hybrid energy storage system and ORC, with the research goal to evaluate its performance. The hybrid energy storage system function is to improve the entire CCHP system supply and operations, whereas the ORC role is to convert the LTHS to power. Modeling / simulation and practical optimization studies were performed to evaluate the system performance. Different load profiles were used and the results which include the load consumed energy, power supplied and efficiency enhancement; indicated that the performance is load dependent and the efficiency is attributed to the large amount of waste heat recovered. In their case study one, the efficiency varied between 35.70% and 42.70% with the efficiency improvement above 40% relative to traditional CCHP systems, with 3.61 kWh and 1.86 kWh energy savings in summer and winter respectively. In their case study two, the overall efficiency for the six scenarios ranged from 33.49% to 56.53%.

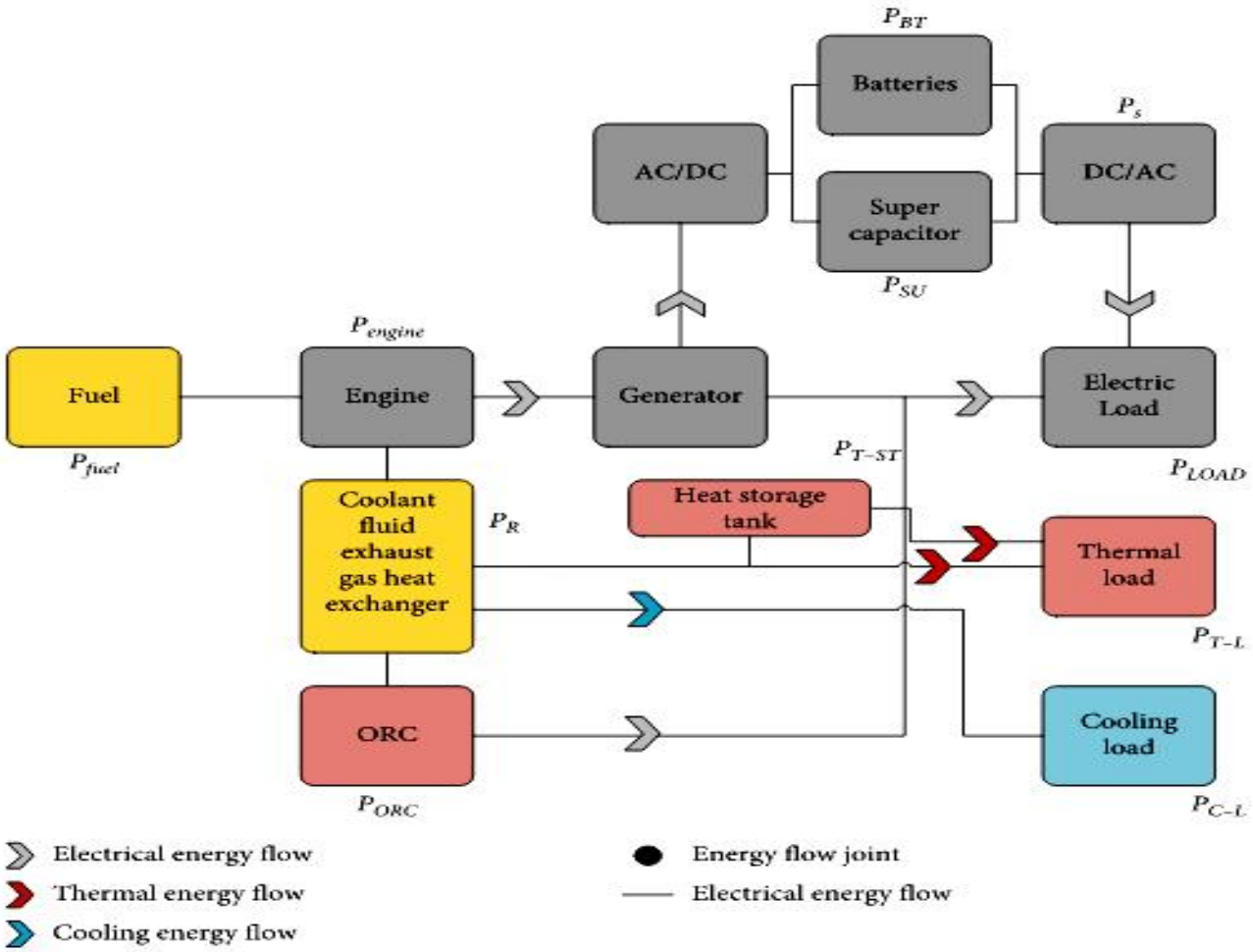

Figure 2.113: CCHP system integrated with an ORC and a hybrid energy storage system (adapted from Ji *et al.*, 2020)

2.5.2.33 CCHP System Thermodynamic Performance Analyses Coupled with ORC and Solar Thermal Utilization

Asserted in Jia *et al.* (2021) and exposit in Figure 2.114, a CCHP system with integrated ORC and solar thermal (ST) was studied and had better thermodynamic performance, as they are versatile with more power production capability, more energy and more waste heat efficient. Their proposed system ORC is driven by solar energy and exhaust heat. The system energy efficiency and economy were improved taking into cognizance the functioning technique and system configuration optimization. Using the collaborative optimization approach, the researched system was applied to office and commercial buildings. With the aid of parametric analysis with focus on the effects of ICE rated capacity and ORC temperature of evaporation; the test results revealed that the typical cost per unit supply area of the CCHP-ORC-ST of commercial and office buildings were respectively 25.9 \$/m^2 and 19.8\$/m^2. Relative to conventional CCHP systems, this translates to a yearly cost saving increase of 15.0% in commercial buildings and 27.0% in office buildings.

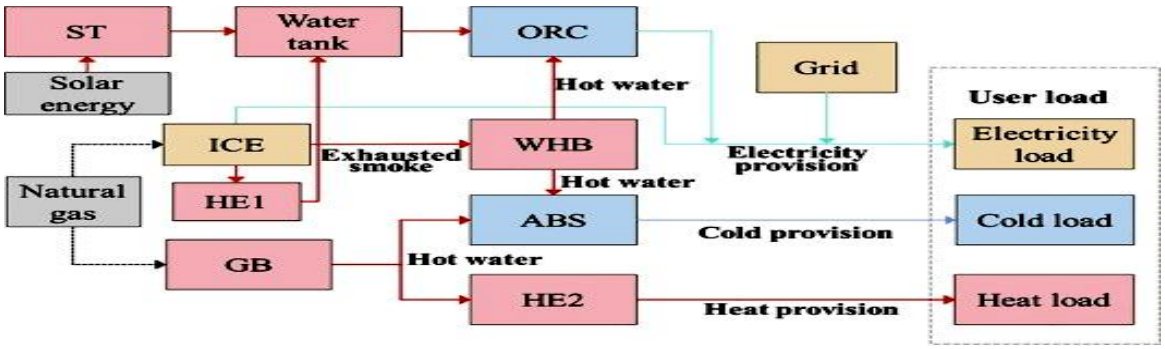

Figure 2.114: CCHP-ORC-ST system under a novel operation strategy (adapted from Jia *et al.*, 2021)

2.5.2.34 Operation Optimization of IES in a Renewable Energy Dominated Future Prospect Considering both Independence and Benefit

Reviewed in Li *et al.* (2021) and summarized in Figure 2.115, is an assessment of traditional CCHP systems based on fossil fuels and modern types based on integrated energy systems (IES) with renewable energy − which are less controllable and more versatile. Taking a standalone IES into account, optimum techniques with emphasis on an independent and integrated perspectives were analyzed by initially considering the holistic optimization process based on the flow of energy and optimization strategies to manage supply-demand and to achieve maximum benefits. Uncertainty modeling methods such as data-driven uncertainty and multistage functioning methods to ensure accuracy of the techniques and decrease unfavourable circumferences on the upper grid were assessed. The hybrid timescale such as gas–electricity IES, heat–electricity IES and as well heat–gas–electricity IES of the various attributes of the various flows of energy were looked into and game theory was considered to heighten the execution versatility of the IES. Furthermore, the various energy coordination is analyzed to decrease the entire unfavourable conditions as a unit. In summary, renewable energy CCHP systems are gradually replacing fossil fuel CCHP systems; however, unlike fossil fuel, renewable energy is unstable due to outages which may affect the energy security; therefore, an IES approach is paramount to coordinate and maximize the different energy flows in both an independent and isolated CCHP systems setup.

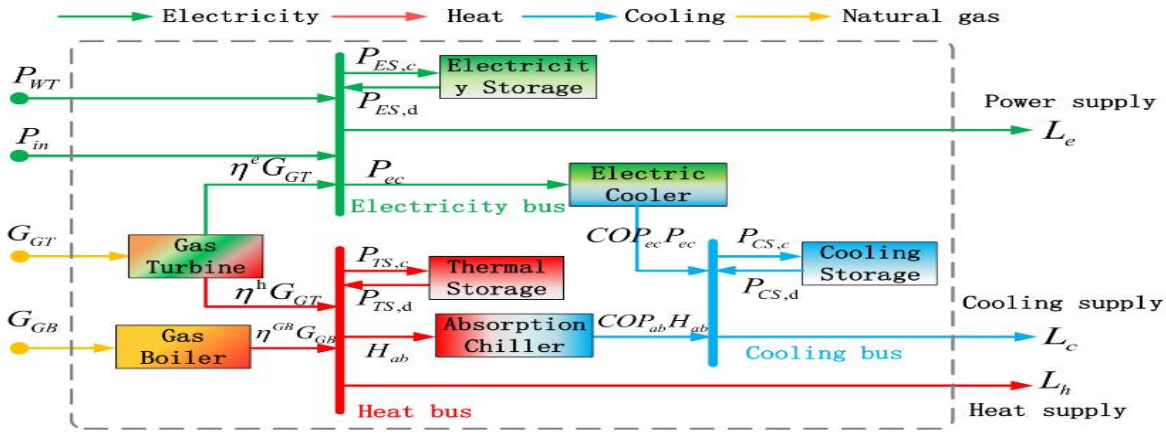

Figure 2.115: Reviewed CCHP IES system (adapted from Li *et al.*, 2021)

Table 2.11 summarizes the CCHP systems reviewed with highlights on each case study main contributions as well as their advantages and disadvantages where applicable. From the reviewed case studies, fuel cells CCHP systems are of curiosity, as they can i) simultaneously provide power and heat, ii) are trendy, iii) environmentally friendly and iv) can be applied in different niche applications.

Table 2.11: Reviewed CCHP systems case studies summary (adapted from Bayendang *et al.*, 2020a)

CCHP Research Reviewed	Highlights, Advantages and Disadvantages	CCHP Research Reviewed	Highlights, Advantages and Disadvantages
Case Study 2.5.2.1 (Bozchalui M.C. & Sharma R., 2012)	ICEs CCHP system: Has advanced with comparatively fast start-up time, high efficiency and affordability. Fuels can be petrol, natural gas and gasoline. However, it is noisy, noxious & need high servicing.	Case Study 2.5.2.10 (Cozzolino R. 2018)	LT PEM FC CCHP: The results revealed better execution based on exergy and energy in the overall functional field of the CCHP (tri-generation) scheme. However, LT PEMFC requires expensive Pt catalyst.
Case Study 2.5.2.2 (Badea N. *et al.*, 2010)	Stirling Engine CCHP: Green and more efficient. Suitable mostly for motionless or non-stop working applications. Works by re-using the fuel (gas) back and forth.	Case Study 2.5.2.11 (Wang Z. *et al.,* 2018)	Inlet Air Throttling Gas-turbine CCHP: Findings showed that the CCHP scheme is better than the discrete scheme on yearly review, regardless of the working system that is employed. Needs high temperature.
Case Study 2.5.2.3 (Maraver D. *et al.*, 2013)	Biomass CCHP: A thermodynamic model that takes into account various sizes of CHP and cooling units was advanced. It however needs lots of space to implement.	Case Study 2.5.2.12 (Lu S. *et al.*, 2018)	PV CCHP and GSHP Micro Gas-turbine: A multi-energy regional energy supply system optimization was accomplished. It is nonetheless very expensive to install.
Case Study 2.5.2.4 (Xu A.D. *et al.*, 2014)	Micro-turbine CCHP system: By means of pressure, air is then pumped to the recuperator cold side to ably combine with heat for cold production. It requires high temperature to produce more power.	Case Study 2.5.2.13 (Li B. *et al.*, 2019)	GSHP and ICE CCHP: The hybrid scheme execution having heat exchanger was superior to the same system not having heat exchanger. It is environmentally not friendly – high temperature, noisy & large.
Case Study 2.5.2.5 (Su Z. *et al.*, 2016)	Biomass & solar CCHP: Utilized genetic algorithm to realize a model to acquire an optimum operation technique; considering energetic criteria, the environment and economics. It dismally requires sunlight.	Case Study 2.5.2.14 (Jiang R. *et al.*, 2017)	ICE with cooling and dehumidification CCHP system: A thermo-economic model was instituted and a constrained NLP resolve was employed to maximize the system blueprint and functioning strategy.
Case Study 2.5.2.6 (Wongvisanupong K. & Hoonchareon N., 2013)	Gas-turbine and Photovoltaic CCHP: Optimum execution having smallest cost modeled as a LP based-on Matlab. An online economic optimum functioning was simulated. Needs sunlight to function.	Case Study 2.5.2.15 (Chen X. *et al.*, 2018)	A 5kW PEM FC CCHP: The outcomes revealed that inlet gases small working temperature, more pressure and relative humidity are paramount for enhancing system competence, exergy and emission. It was optimized with evolution algorithm.
Case Study 2.5.2.7 (Zhao H. *et al.*, 2018)	Micro-turbine, PV and wind turbine CCHP system: Used HOMER to model an optimum economic operation model of a micro-grid having net current cost as the optimization purpose. It has a reasonable energy saving and contamination effects.	Case Study 2.5.2.16 (Ebrahimi M. & Derakhshan E., 2018)	LT-PEM FC TEC hybrid CCHP scheme is proficient in producing 26.8W of cold, 3.04kW of heat and 2.79kW of power with an overall efficiency of ~77% and 43.25% fuel saving. Has water management issues and requires costly catalyst because of LT.
Case Study 2.5.2.8 (Wang R. *et al.*, 2018)	PAFC and SOFC CCHP system: Thermal, electrolysis and technical economies as well as including factors that protect the environment were investigated. PAFC produces less power relative to other fuel cells of the same size and weight. SOFC has high CHP efficiency but needs high temperature that slows the start-up time.	Case Study 2.5.2.17 (Mehrpooya M. *et al.*, 2017)	Stirling Engine and MCFC CCHP system: MCFC is the primary source of power and its exhaust heat was utilized to provide the Stirling engine, from which it delivers heat to the cold generator absorption chiller. The combined cold, heat and power that were generated are respectively 1372kW, 2137kW and 6482kW. Usually very high temperature involved. No catalyst needed.
Case Study 2.5.2.9 (Wang J.L. *et al.*, 2014)	ICE & TEG CCHP system: Utilized ICE to produce power, cold and heat – which is stored in hot water. The heat exchanger and TEG were employed to effectively recuperate the ICE's exhaust gas emitted heat. It is power efficient due to TEG incorporation; however, may have environmental issues because of ICE usage.		

Table 2.11: Reviewed CCHP systems case studies summary continued

CCHP Research Reviewed	Highlights, Advantages and Disadvantages	CCHP Research Reviewed	Highlights, Advantages and Disadvantages
Case Study 2.5.2.18 (Wu D. *et al.*, 2019)	CCHP-ST-ORC system harmonizes fossil fuel with renewable energy and its performance was assessed based on thermodynamics. Their findings revealed that their CCHP-ST-ORC system could produce an extra 5.1kW electricity. CCHP-ST-ORC has similar exergy efficiency of 40% compared to the traditional CCHP and CCHP-ST systems.	Case Study 2.5.2.27 (Lingmin C. *et al.*, 2021)	A wind, solar and natural gas CCHP system for a remote tourist area with energy hub for electric power and heat with cold from the chillers. The PGU supply the bulk of the power during wind and solar outages and the heat and power storage devices as well assisted in these regards to reduce wastage and to enhance the system performance. Complex system.
Case Study 2.5.2.19 (Mao Y. *et al.*, 2020)	CHP is becoming promising technology to provide cascaded efficient energy and the system performance can be enhanced by integrating PV / thermal panels as well as energy storage. Their system has better cost and primary energy savings of ~17%.	Case Study 2.5.2.28 (Lombardo W. *et al.,* 2020)	A CCHP system based on PV, micro-ORC plant and an adsorption chiller with built in real bioclimatic NZEB, modeled with TRNSYS. The system effectiveness is affected by weather condition. The system yearly efficiency ranged from 32 to 42%.
Case Study 2.5.2.20 (Lingmin C. *et al.*, 2020)	CCHP multi-energy system incorporating gas, solar and wind energy as well as power storage controlled by PSO method. Power generation under FEL can reach above 50% during peak load periods.	Case Study 2.5.2.29 (Wu D. *et al.*, 2021)	Integrated multi-scenario CCHP system theoretical model. A novel self-adaption technique based on exhaustive search algorithm was suggested for a least / hour operation cost, reduced yearly by 0.67%.
Case Study 2.5.2.21 (Cao Y. *et al.*, 2020)	CCHP system routed in a developed owl search technique. In the proposed system, wasted heat from hot gases is recycled while at the same time producing power, enabling > 85% system energy efficiency.	Case Study 2.5.2.30 (Ma H. *et al.*, 2020)	CCHP-ORC system to stabilize irregular power and heat demands and enhance the versatility and changeability of the heat to power ratio on the source side. Used TRNSYS to develop a simulation model.
Case Study 2.5.2.22 (Farmani F. *et al.*, 2018)	A smart EMS concept of a micro grid CCHP system for buildings, to control the schedules of its energy storage and renewable systems. The conclusion drawn is the use of CCHP system fitted with a smart controller, could significantly lowers a building energy operating cost.	Case Study 2.5.2.31 (Miao N. & *et al.*, 2020)	Cascaded CCHP systems reduce emission, but their provisions are challenging for optimal setup. Thus, analysis is required and two operating modes namely "fixing power based on heat" and "fixing heat based on power" were assessed with the latter the better having a lower yearly cost.
Case Study 2.5.2.23 (Zare V. & Takleh H.R., 2020)	A geothermal CCHP system with the ejector TRCC fitted with a traditional Rankine cycle. The findings noted that replacing the gas cooler resulted to 30.9% exergy efficiency, 49.1% net power output and 75.8% cooling output rise, but with a 39.1% loss in the heating output.	Case Study 2.5.2.32 (Ji J. *et al.*, 2020)	A novel CCHP system with in-built hybrid energy storage system and ORC, with the research goal to evaluate its performance. In one of the case studies, the efficiency varied between 35.70% and 42.70% with the efficiency improvement above 40% relative to the traditional CCHP systems, having 3.61 kWh and 1.86 kWh energy savings in summer & winter respectively.
Case Study 2.5.2.24 (Mohammadi K. & Powell K., 2020)	New integrated co-generation and tri-generation systems configurations using a CO_2 parallel compression economization-vapor compression refrigeration cycle with a 1MW capacity. Their research main contribution is an in-depth techno-economic assessment of the numerous possible variations for these systems.	Case Study 2.5.2.33 (Jia J. *et al.*, 2021)	A CCHP-ORC-ST system was studied and had better thermodynamic performance, as they are versatile with greater power production capability, more energy and more waste heat efficient. Relative to conventional CCHP systems, the yearly cost saving increase was 15.0% in commercial and 27.0% in office buildings.
Case Study 2.5.2.25 (Chahartaghi M. & Sheykhi M., 2019)	Dual Stirling engine CCHP system with H_2 and Helium as the functioning gases. The power, cold, heat productions, CCHP efficiency and CoP results using H_2 were respectively 15.24 kW, 19.65 kW, 12.65 kW, 70% and 64.4% and Helium 22.52 kW, 21.65 kW, 14.43 kW, 72.29% and 66.7%. Helium offered better results.	Case Study 2.5.2.34 (Li J. *et al.*, 2021)	Assessment of traditional CCHP systems based on fossil fuels and modern types based on IES with renewable energy. However, unlike fossil fuel, renewable energy is unstable due to outages and may affect the energy security; as a result, an IES approach is paramount to coordinate and maximize the various energy flows.
Case Study 2.5.2.26 (Parikhani T. *et al.*, 2020)	A novel ammonia-water mixture CCHP system driven by a low temperature heat source (LTHS) − which is a tailored version of a Kalina cycle. Thermodynamics and thermo-economics balance equations for performance analysis of the thermal system were used to investigate the viability of the recommended system. The energy and exergy efficiencies were respectively calculated to be 49.83%, 27.68%. The electrical, cooling and heating optimum capacities were respectively 0.253 MW, 1.610 MW and 1.972 MW.		

2.5.3 Fuel Cells (FCs)

Fuel cells are further assessed, as CCHP systems rooted in fuel cells are of interests as deduced from the CCHP systems review. According to Thomas (1999) and Hoogers (2002); in 1839, William Grove brought to light FC concept and coined it "gaseous voltaic battery" and in 1842 notified Michael Faraday. From the review summarised in Table 2.13, FCs are electrochemical devices that can constantly produce electricity from chemical energy and in the process give by-products of water and heat, provided they are always furnished with fuel (H_2) and reactant gas (O_2) in the case of PEM FC. This process is portrayed in Figure 2.116 and is chemically represented by the following electrochemical equation (Thounthong & Sethakul, 2007) in (2.26).

$$4H_2 + 2O_2 \longrightarrow \text{Electricity} + 4H_2O + \text{Heat} \qquad (2.26)$$

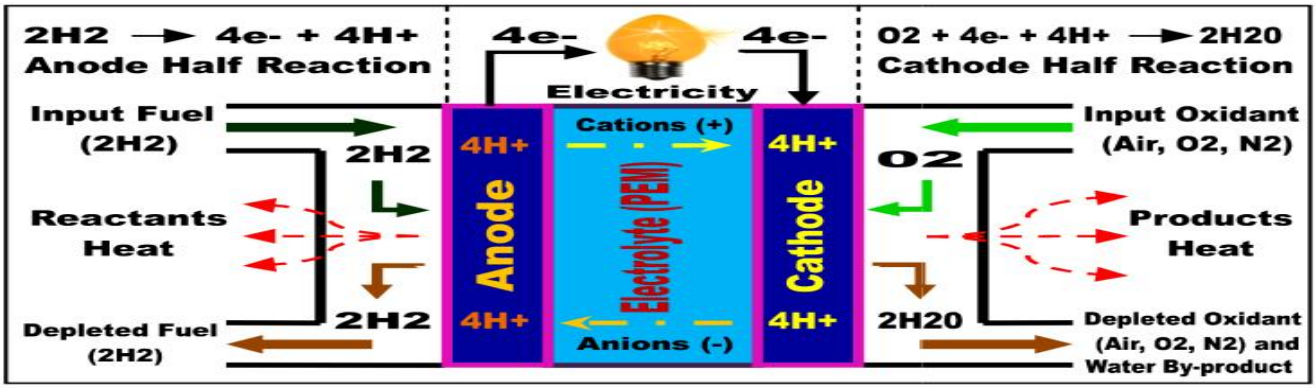

Figure 2.116: PEM fuel cell operation principle overview

As per Thounthong and Sethakul (2007) and Chandan *et al.* (2013), Hydrogen FCs (based-on polymer electrolyte membrane (PEM)), are clean and renewable energy sources, that are slowly becoming alternative energy sources with assorted applications. Nonetheless, as elaborated in Thounthong and Sethakul (2007) and portrayed in Figure 2.117, fuel cells (FC) are usually vulnerable to a phenomenon called "fuel starvation" – the delay or lack of H_2 and or O_2 flow, leading to FCs having difficulties coping with transient current demand when loaded, thus dropping the FC voltage. As researched in Taniguchi (2004), fuel (H_2) / O_2 starvation, must not even occur momentarily, as it will cause severe and durable destruction to the FC electro-catalyst and furthermore lowering its power / energy supply reliability, capability, durability and efficiency.

Researched by Sulaiman *et al.* (2015), a FC has low power density but high energy density; therefore, a FC is unable to i) provide the high electric power initially needed to immediately switch-on a load (e.g. when a hybrid electric vehicle (HEV) starts up, ii) rapidly react should there be an abrupt variation in the load current (e.g. when a HEV accelerates Boettner *et al.,* (2002) and Khaligh & Li, (2010)) and iii) absorb the regenerative power (e.g. when a HEV decelerates or brakes). As a result, an additional device

that stores energy (e.g. a rechargeable battery) and or a source of power with faster dynamic response (e.g. an ultra-capacitor bank), combined with power and energy conversion devices as well as energy management systems (EMS), are required to assist the FC. Consequently, various research endeavours to tackle this crucial fuel cell fuel starvation phenomenon issue as summarised in Table 2.12, have been undertaken over a period of time and stated in the following is a precis of some techniques which constitute but unlimited to the six noted schemes as follows: 1) FC assisted with fuel flow-rate control, 2) FC assisted with a battery, 3) FC assisted with ultra / super-capacitor (UC / SC), 4) FC assisted with a battery and SC / UC, 5) FC assisted with CombiLit and 6) FC assisted with PV and SC /UC.

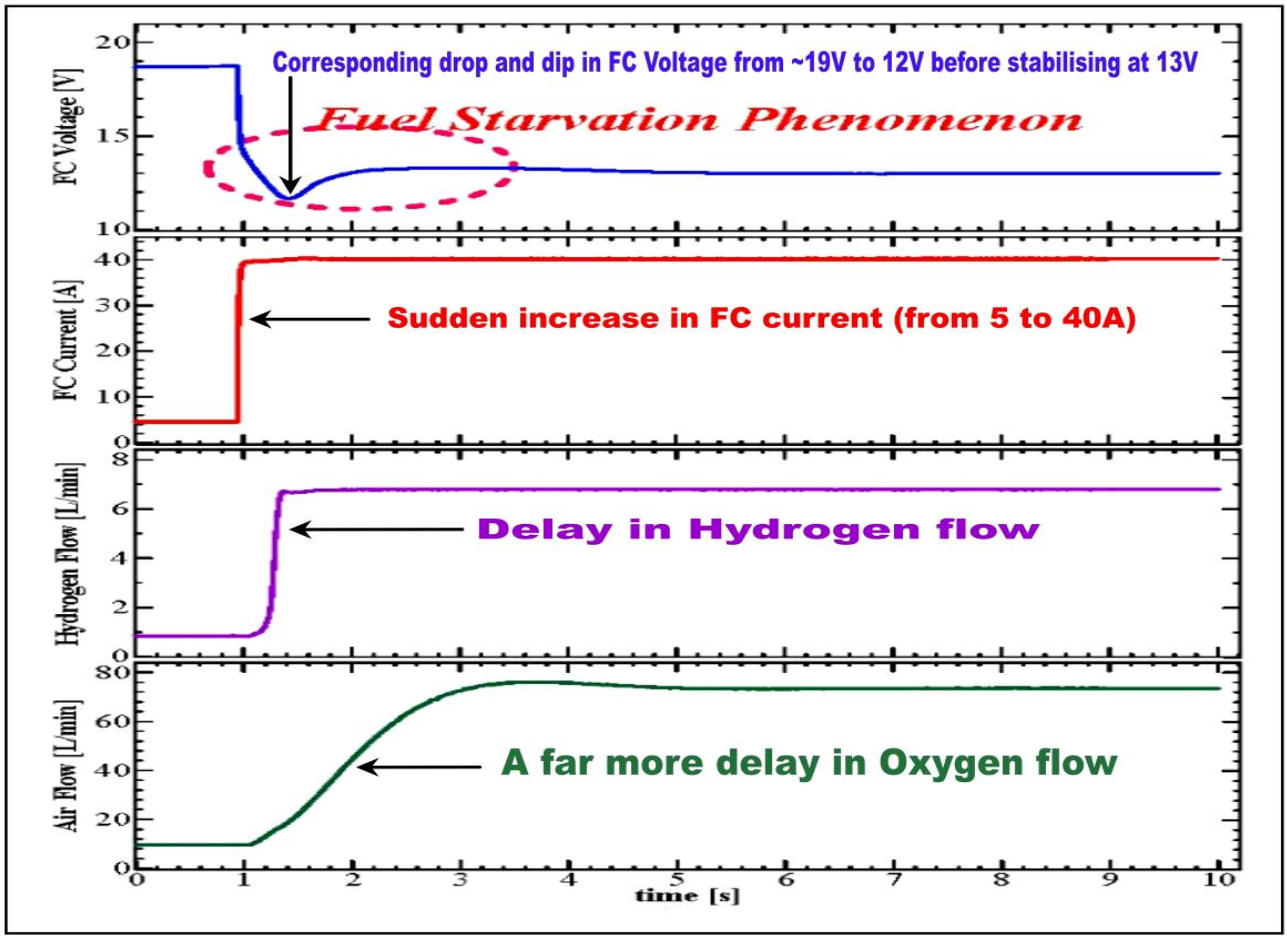

Figure 2.117: Fuel cell fuel starvation phenomenon (adapted from Thounthong & Sethakul, 2007)

2.5.3.1 Fuel Cell Assisted with Fuel Flow-rate Control

This approach as presented in Thounthong and Sethakul (2007) and Thounthong *et al.* (2008), entails the flow-rate of the fuel Hydrogen (H_2) and reactant gas Oxygen (O_2) are continuously controlled to track the FC current variations, by controlling the current gradient of the fuel cell or by sustaining a regular fuel flow-rate to make sure the fuel cell constantly has an adequate fuel flow. This approach is nonetheless inefficient, as the fuel flow is habitually invariable at the highest value. Figure 2.118 exemplifies this method.

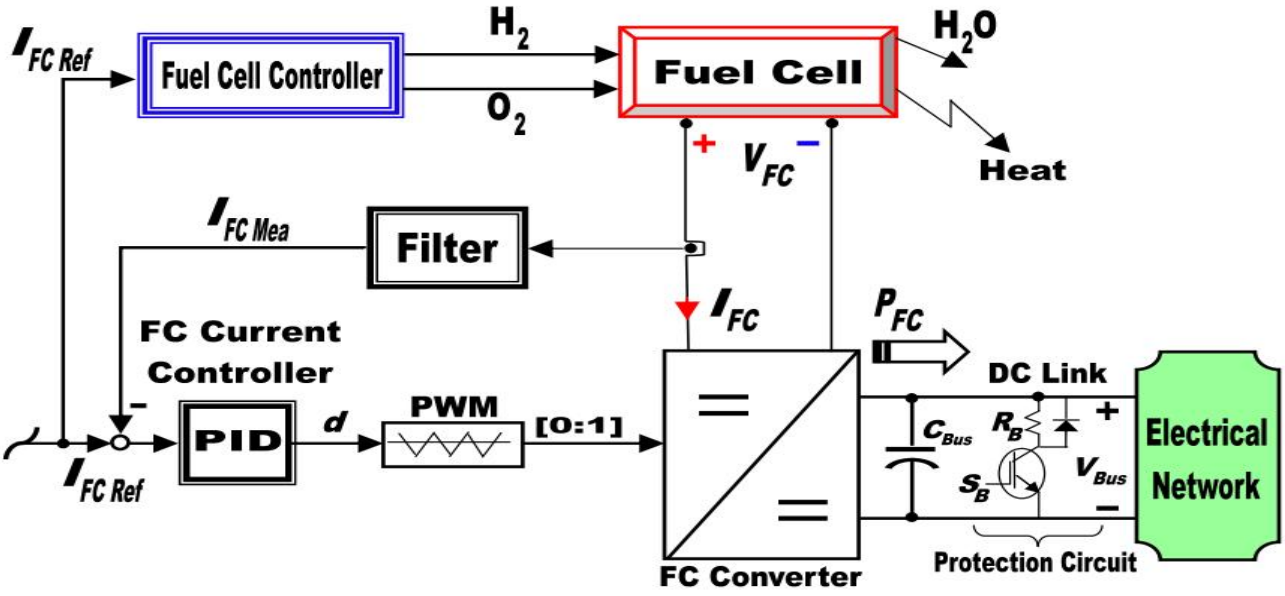

Figure 2.118: Fuel cell assisted with fuel flow-rate control (adapted from Thounthong & Sethakul, 2007)

2.5.3.2 Fuel Cell Assisted with Battery

Usually, a battery (be it of type Lithium Ion (Li-ion), Nickel Metal Hydride (NiMH), lead acid etc) has a higher power density Sulaiman *et al.* (2015) relative to a FC. As a result, it quickly reacts and provides peak power should there be a high transient current demand by the load, thereby assisting the FC from its sluggishness due to "fuel starvation". In addition, a FC can only provide electrical energy but cannot stores it. As a result, a battery furthermore offers storage during regenerative braking Livint *et al.* (2011). However, batteries take long to charge and their lifetime depends on their state of charge (SOC) and their depth of discharge (DoD) Sulaiman *et al.* (2015) – the faster the rate of charge and discharge, the likely the shorter the longevity of the battery's life. Figure 2.119 depicts this assisting technique.

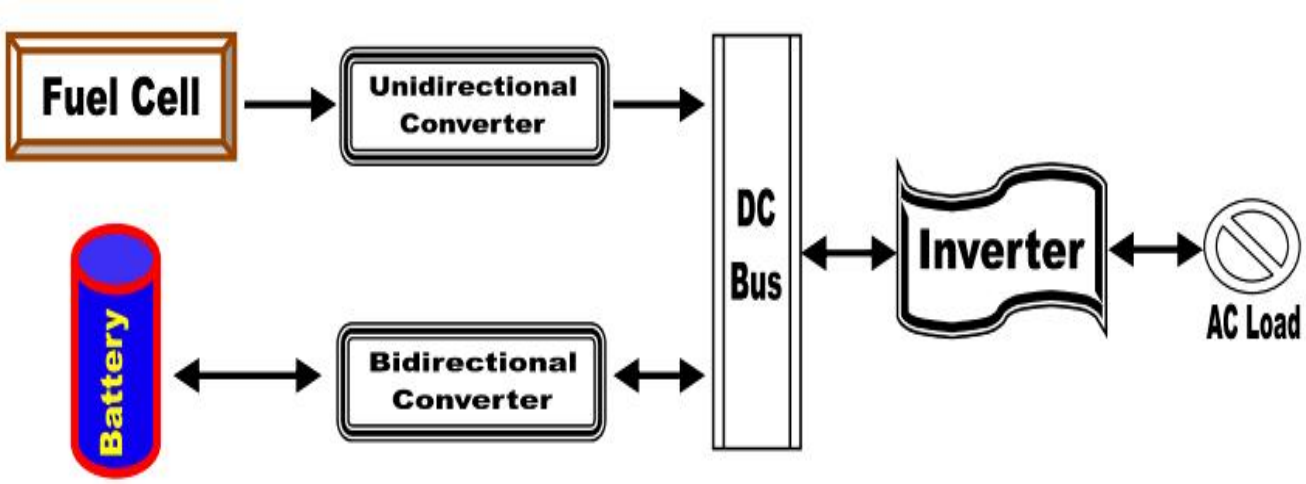

Figure 2.119: Fuel cell assisted with battery

2.5.3.3 Fuel Cell Assisted with Ultra-capacitor (UC) or Super-capacitor (SC)

Super-capacitor or Ultra-capacitor has the utmost power density and best transient response compared to fuel cells and batteries. According to Yu *et al.* (2013), they are thus the preferred energy storage devices for high current applications, as they can be rapidly dis/charged in short period of time. This SC or UC very fast transient response, makes them the most suitable device to assist fuel cells circumvent the inertia "fuel starvation" phenomenon Sulaiman *et al.* (2015). This method is shown in Figure 2.120.

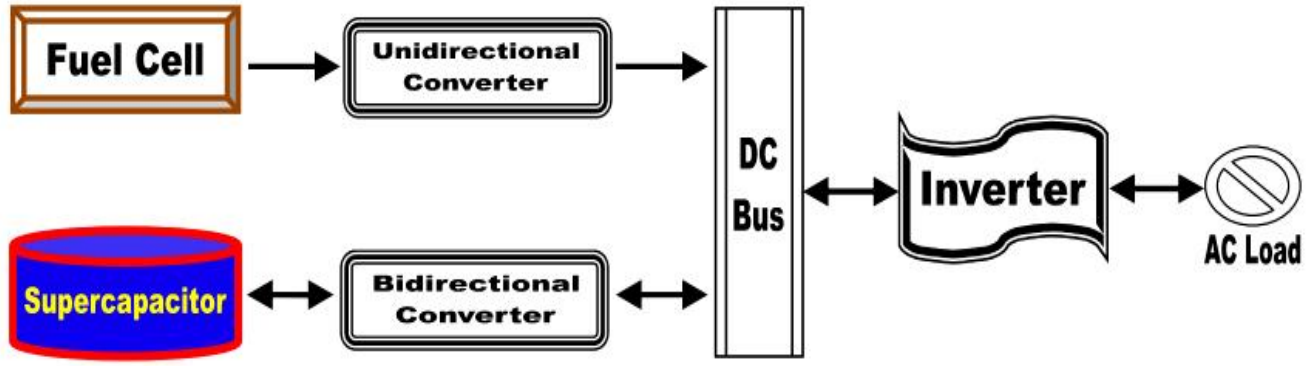

Figure 2.120: Fuel cell assisted with super-capacitor or ultra-capacitor

2.5.3.4 Fuel Cell Assisted with Battery and Super-capacitor or Ultra-capacitor

In this approach, the battery and UC or SC are used to supply power for small intervals of peak power needs, for instance during acceleration in the case of HEV – in which reliable acceleration demands both high energy and high power densities Livint *et al.* (2011). As shown in Figure 2.121, having both UC or SC and battery is crucial, because relatively, the UC or SC has the least energy density but the highest power density, whereas the battery has moderate energy and power densities Hannan *et al.* (2014); therefore, using both schemes assist the FC when simultaneous peak power and energy are needed.

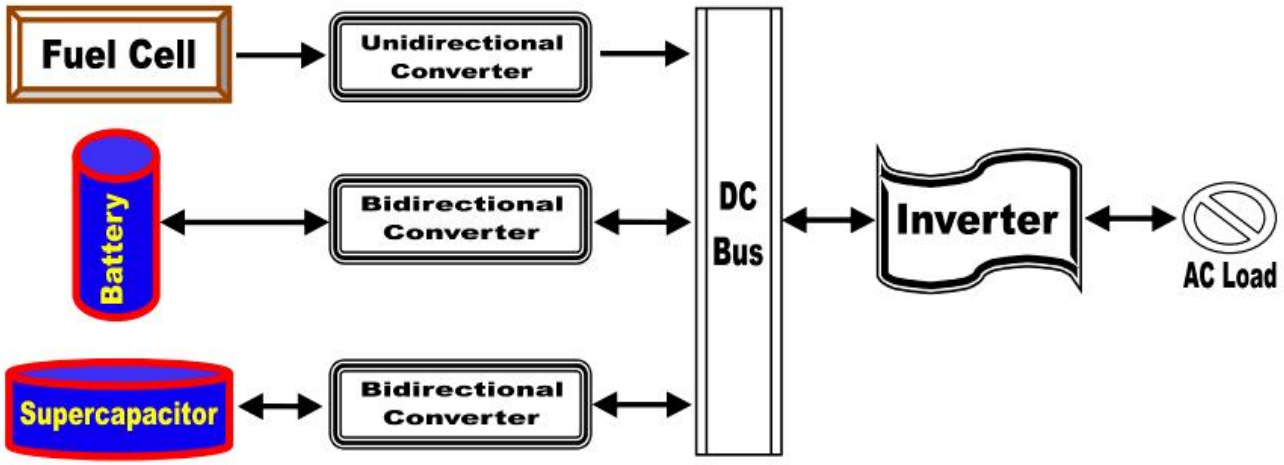

Figure 2.121: Fuel cell assisted with battery and super-capacitor or ultra-capacitor

2.5.3.5 Fuel Cell Assisted with CombiLit

According to Pollet *et al.* (2014), CombiLit is a composite device that stores energy by coalescing in a cell the electrodes of a peak power density super-capacitor with a lofty energy density Li-ion battery. This setup together with a FC, can be adapted to give changing levels of peak power discharge, increase in energy storage, lengthy cycle life and low-costs. The idea is similar to Figure 2.121.

2.5.3.6 Fuel Cell Assisted with Solar Cell and Super-capacitor

In Thounthong *et al.* (2011), a solar cell (photovoltaic array) replaces the battery energy source. The energy sources (fuel cells and solar cells) have high energy densities, whereas the power source (UC or SC) has high power density. The power source provides the high current during transient conditions and is recharged from the core energy source(s) when the demand is less. The drawback with this scheme is that solar cells can only provide energy when there is sunlight. Figures 2.122a and 2.122b respectively display the setup and dynamic responses of the FC, PV and super-capacitor.

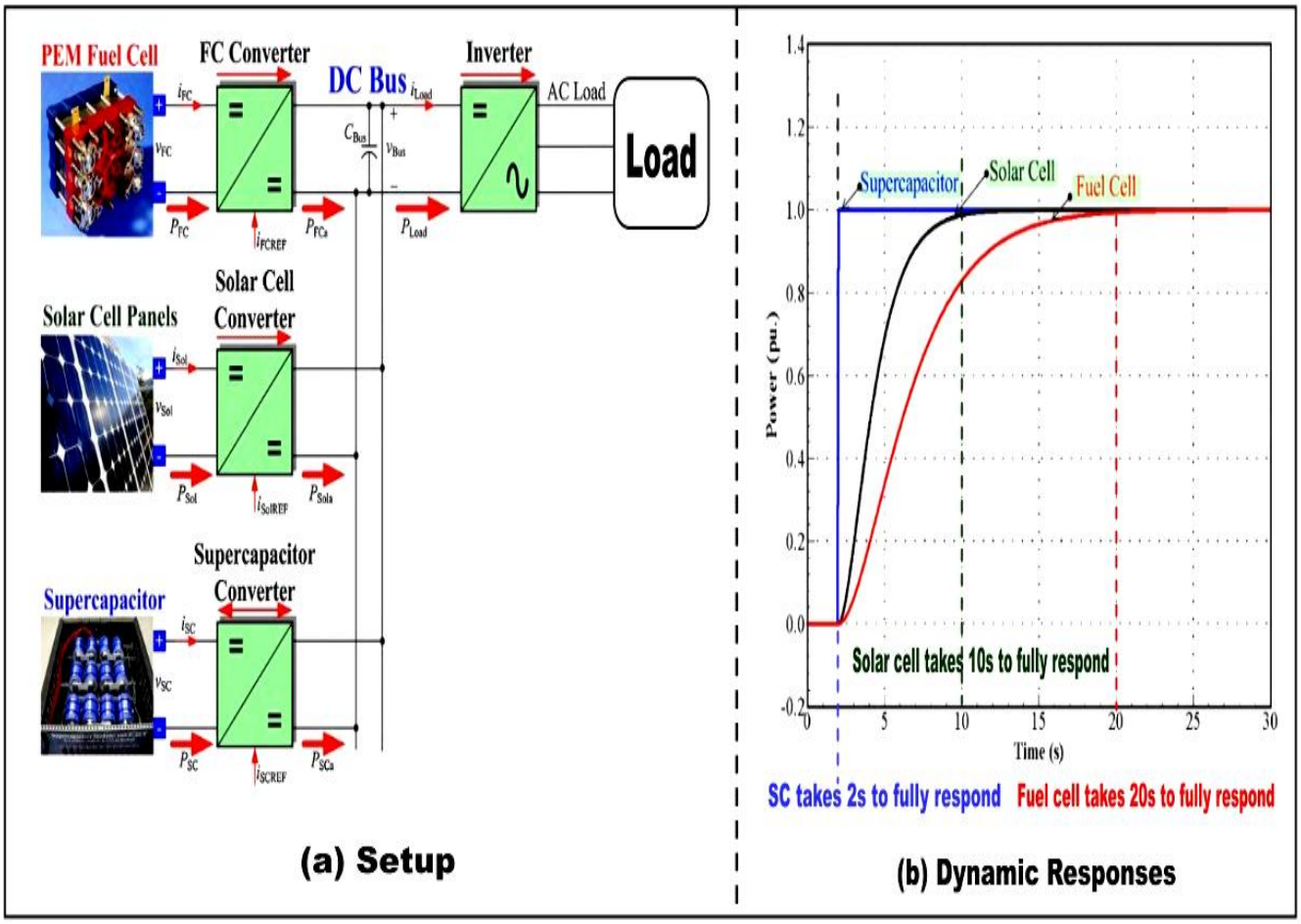

Figure 2.122: Fuel cell assisted with solar cell and super-capacitor a) setup and b) dynamic responses (adapted from Thounthong *et al.*, 2011)

Table 2.12: Fuel cells assisted techniques comparison summary (adapted from Bayendang *et al.*, 2020a)

Fuel Cells Assisted Schemes	Highlights, Advantages and Disadvantages
Section 2.5.3.1 Fuel Flow-rate Control	H_2 and O_2 are continually controlled to track the FC current variations, by noticing the FC current slope and by sustaining a steady flow-rate of the fuel to make sure the FC at all times has sufficient fuel flow. Although this method ensures the fuel cell is not deprived of H_2 and O_2, it is nevertheless not efficient, because the fuel flow is usually stable particularly at the highest value.
Section 2.5.3.2 Battery (e.g. Li-ion)	Battery has a higher specific power relative to FCs, thus retorts swiftly & provides the peak power should there be a transient current. Batteries unlike FCs, store energy. Conversely, battery needs time to charge and will degrade if discharge and charge faster and frequently in high current uses.
Section 2.5.3.3 Ultra-capacitor (UC) or Super-capacitor (SC)	SCs / UCs have the fastest transient response and highest power density compared to batteries and FCs; hence, they're the most ideal energy storage devices for peak current uses, since they charge rapidly & helps circumvent FC slowness but they've the least energy density (discharges fastest).
Section 2.5.3.4 Battery and SC or UC	The most suitable FC assisted technique is this, as using both aids the FC when peak power and utmost energy are needed at the same time. Drawback is it's a bit costly due to more components.
Section 2.5.3.5 CombiLit	CombiLit is a composite device that stores energy, by merging in same cell, the electrodes of a lofty energy density Li-ion battery and a peak power density SC. Need costly repairs when faulty.
Section 2.5.3.6 Solar Cell and SC	Solar cell has max energy density and SC has peak power density that assists the FC during transients. However, constant sunlight is required and the response performance depends on SC.

In Table 2.12 is a summary of the various fuel cells fuel starvation assisted techniques presented.

2.5.3.7 Fuel Cell Types and Comparisons

From reviewing Thomas (1999), Hoogers (2002), Moqsud *et al.* (2014) and Kabutey *et al.* (2019); fuel cells can be summarised under commonly six types (apart from Direct Methanol (DM) FC – since it is practically a PEMFC, besides it directly uses methanol as fuel, though its electrolyte is still PEM) as shown in Table 2.13 − which compares this six most commonly used FCs and their characteristics.

Table 2.13: Fuel cell types and comparisons (adapted from Bayendang *et al.*, 2020a)

FC Types	Electrolyte	Reactions	Advantages	Disadvantages
Polymer Electrolyte Membrane (PEM) FC	Solid organic polymer poly-perfluorosulfonic acid. LT: [50 – 100°C] Polybenzimidazole (PBI) HTPEM: [100 – 200°C]	Anode: $4H_2 \rightarrow 8H^+ + 8e^-$ Cathode: $2O_2 + 8H^+ + 8e^- \rightarrow 4H_2O$ Cell: $4H_2 + 2O_2 \rightarrow 4H_2O$	• Solid electrolyte lowers decay & servicing. • Low – mid temperature. • Rapid startup (LT-PEM) • Trivial or no effluence. • Power efficiency 45%.	• Low temperature needs costly catalysts (Pt). • High reaction to fuel contaminants such as CO. • HT-PEM not durable. • LT-PEM water deluge.
Alkaline FC (AFC)	Aqueous solution of KOH drenched in a matrix Temp: [60 – 200°C]	Anode: $2H_2 + 4(OH)^- \rightarrow 4H_2O + 4e^-$ Cathode: $O_2 + 2H_2O + 4e^- \rightarrow 4(OH)^-$ Cell: $2H_2+O_2 \rightarrow 2H_2O$	Cathode reaction faster in alkaline electrolyte; therefore, high execution. >55% power efficiency.	Very costly CO_2 extraction from the fuel requiring air streams, thus prone to CO_2 emission. Requires pure H_2.
Phosphoric Acid FC (PAFC)	Liquid Phosphoric Acid doused in a matrix Temp: [175 – 200°C]	Anode: $2H_2 \rightarrow 4H^+ + 4e^-$ Cathode: $O_2 + 4H^+ + 4e^- \rightarrow 2H_2O$ Cell: $2H_2 + O_2 \rightarrow 2H_2O$	• Approx 85% efficiency if use CHP systems. • ~40% power efficiency • Use impure H_2 fuel.	• Needs pricey Pt catalyst. • Low power & current. • Bulky size and weight. • Aggressive electrolyte.
Molten Carbonate FC (MCFC)	Liquid solution of Lithium or Sodium or Potassium Carbonates drenched in a matrix Temp: [600 – 1000°C]	Anode: $H_2 + CO_3^{2-} \rightarrow H_2O + CO_2 + 2e^-$ Cathode: $0.5O_2+CO_2+2e^- \rightarrow CO_3^{2-}$ Cell: $H_2 + 0.5O_2 + CO_2 \rightarrow H_2O + CO_2$ (CO_2 is made at the anode and used at the cathode)	High temperature, thus no need for over-priced catalysts. Flexibility to use other fuels. Power efficiency is >50%.	High temperature speeds rust and degradation of FC components. Long start-up time. Expensive thermal management.
Solid Oxide FC (SOFC)	Solid Zirconium Oxide with added small Ytrria (Y_2O_3) amount Temp: [600 – 1000°C]	Anode: $H_2+O^{2-} \rightarrow H_2O +2e^-$ Cathode: $1/2O_2+2e^- \rightarrow O^{2-}$ Cell: $H_2 + 1/2O_2 \rightarrow H_2O$	Can use contaminated fuels. Akin to PEM, has solid electrolyte merits. Power efficiency >50%.	High temperature enhances decay and destruction of FC parts. Sluggish starting up. Poor capability at ~ 600°C.
Plant Microbial	Different soil types, wetland sediments, rhizo-deposits, microbes, compose Ambient Temp (±20°C)	Anode: $(CH_2O)_6 + 6H_2O \rightarrow 6CO_2 + 24H^+ + 24e^-$ Cathode: $6O_2 + 24e^- + 24H^+ \rightarrow 12H_2O$ Cell: $6H_2O + 6CO_2 \rightarrow 6O_2 + (CH_2O)_6$	Eco-friendly, organic (B N_2, NH_4 etc) removal in wastewater treatments, plant bio-sensing, used in wetlands / agricultural lands to generate power.	Bioelectricity generation is relatively very low, regular maintenance to replace plants, natural operational conditions need observing, photosynthesis dependent.

2.5.4 Postulated CCHP System Model Under Research

Best practices established from the literature reviews were applied to formulate a CCHP system based-on PEM FC, Li-ion battery, ultra-capacitor, thermoelectricity (thermoelectric generator and cooler), power converters with proportional integral derivative (PID), energy management and storage. Figure 2.123a exemplifies the proffered system under research with Matlab/Simulink. In the presented CCHP system, the FC (HT PEM) is the prime mover. The Li-ion battery and the ultra-capacitor bank serve as the storage devices and also aid the FC during peak power demands. The TEG is use to convert waste heat produced by the FC to DC power, thereby increasing the power output / efficiency. The TEC provides cooling (can also provides heating by reversing the current flow or voltage polarity). The power converters convert and maintain the required levels of DC and or AC voltages and the PID EMS controls the entire tri-generation scheme accordingly. Figure 2.123b depicts the operational dynamics.

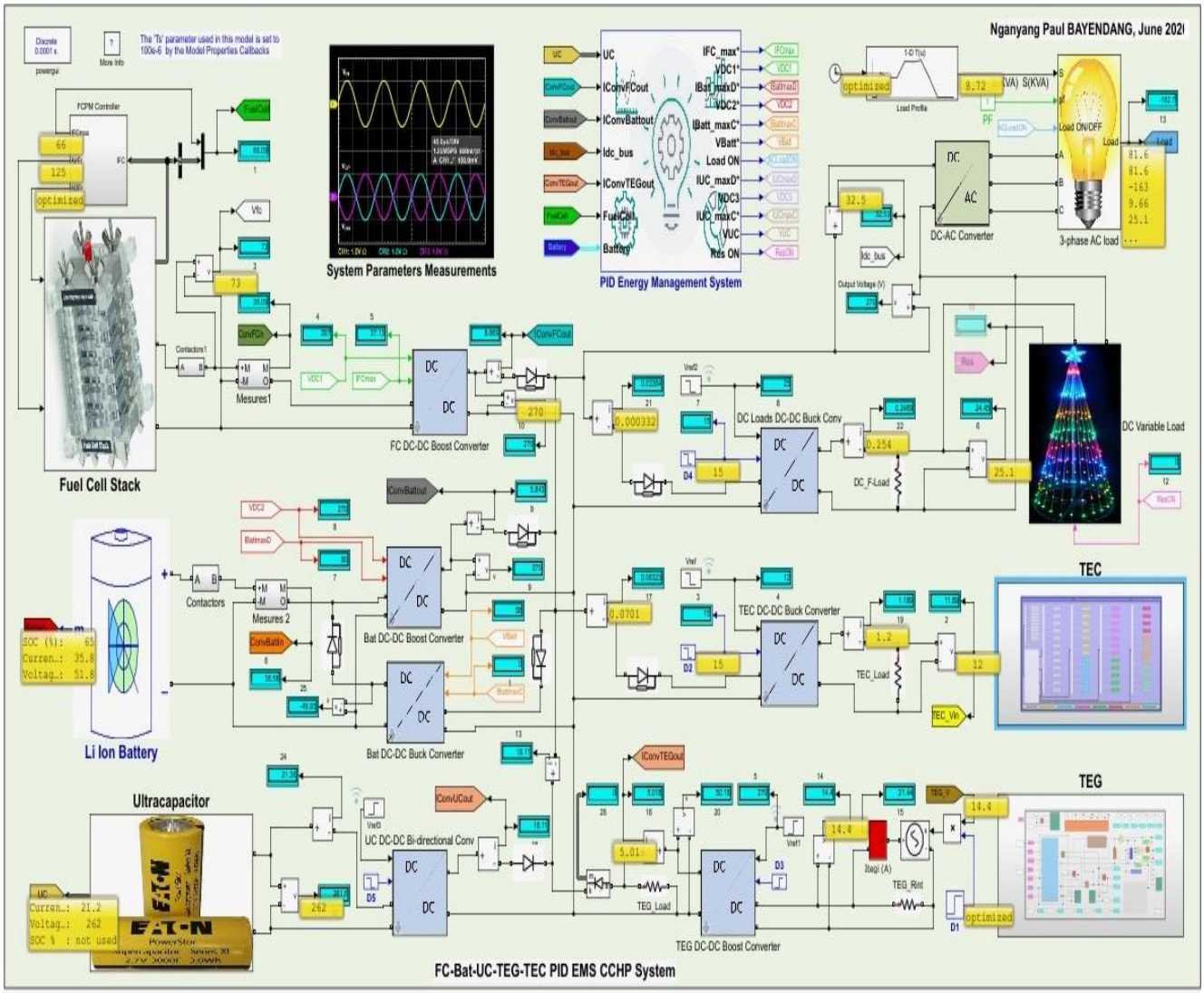

(a) Postulated CCHP systems under research

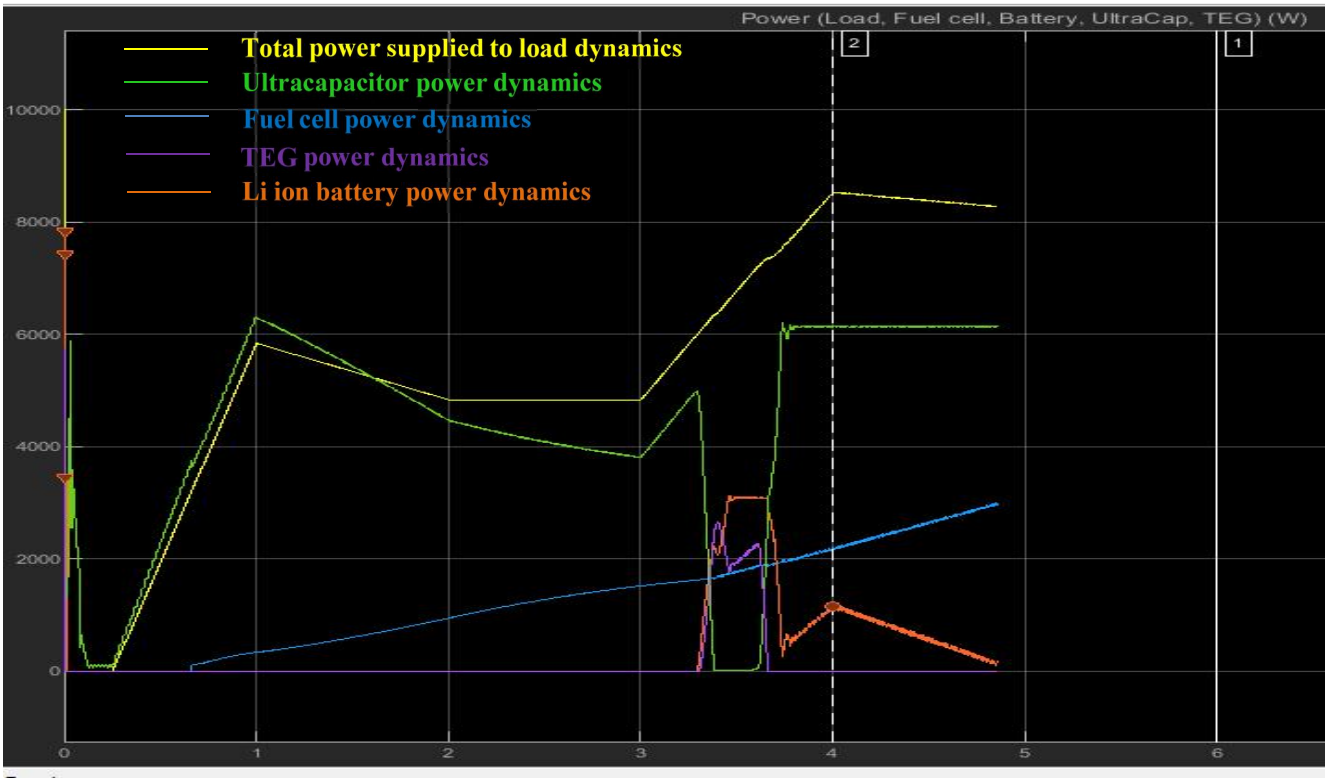

(b) Postulated CCHP systems operation dynamics

Figure 2.123: PEM fuel cell, battery, UC, TEG, TEC and PID EMS CCHP system research model

2.5.5 Summary

Energy insecurity and in particular electricity crisis, is a continuous serious national concern in South Africa and by extension in Africa. Various approaches are being sought after and as my contribution to this quest, this study presented a topological review of thirty four assorted CCHP systems as well as fuel cells research, in order to prudently develop a hybrid FC CCHP system for commercial and residential applications. CCHP systems provide cold, heat and power in one and these three forms of energy are fundamentally a necessity in most households and businesses. The rationale is, with an energy efficient system, the dire energy and electricity crises could be reasonably managed and the objective is therefore to institute an innovative energy efficient CCHP system. To attain this, miscellaneous analyses on past studies on CCHP systems and FCs were examined, in which FCs based CCHP systems were more meritorious, especially PEM FCs. As a result, FCs were investigated further with emphasis on the FC fuel starvation phenomenon as well as FC types. It was realized that the FCs aided with battery and super-capacitor technique was the most suitable. In light of these highlighted findings, an alternative HT-PEM FC CCHP system model constituting Li-ion battery, ultra-capacitor, thermoelectricity (TEG and TEC), power converters and EMS that are clean / energy efficient and can uniquely address the FC fuel starvation phenomenon assisted with a TEG, is postulated and is currently undergoing research.

CHAPTER 3

TEG and TEC Modelings and Simulations: Design, Results, Validation and Discussions

3.1 Overview

South Africa has been experiencing intermittent national electricity supply crisis. Many efforts have been made to alleviate the problem and one of which is commissioning renewable energy sources to augment the national grid and as well for private use. A detailed literature review was conducted on various hybrid energy power technologies and in-line with these developments, the unique case for thermoelectricity was mainly modeled to primarily institute a theoretical framework that can be used to simulate thermoelectricity parameters to have a better theoretical understanding of their properties and functional capabilities. Thermoelectricity is a dual electro-thermal process that enables DC power generation from heat using thermoelectric generators (TEGs) in a process called the Seebeck effect, whereas the reverse process called the Peltier effect, enables generating from electricity, cold and or heat depending on the voltage polarity (current flow direction) using thermoelectric coolers (TECs). In practice, a TEC device can be reversibly used as a TEG device, especially at temperatures up to 200℃.

In accordance with the research problem which resonates around inefficient energy conversion, thermoelectricity is central to the postulated CCHP system being researched, whereby TEG devices will be used to harness and convert waste heat to DC power and TEC devices will be used to provide cooling as well as heating. In addition, the efficiencies of the TEG and TEC are also investigated, since thermoelectricity is a linear and non-linear process which must be applied within strict operational limits to enable optimal / efficient operations. Therefore, it's paramount to first theoretically understand thermoelectricity before embarking on a practical implementation; if not, it would just be a matter of trial and error, because with TE, more inputs doesn't necessarily translates to more output performance.

This chapter therefore focuses on popular thermoelectricity parameters mathematics, the modelings and finally the simulations using Matlab and Simulink. This section presentation is adapted from my two original publications as listed below, in which the first article focuses on TEG and the second on TEC.

- Bayendang, N.P., Kahn, M.T., Balyan, V., Draganov, I. & Pasupathi, S. 2020. A comprehensive thermoelectric generator (TEG) modelling. *AIUE Congress 2020: Energy and Human Habitat Conference*, Cape Town, South Africa, 1-7. http://doi.org/10.5281/zenodo.4289574.

- Bayendang, N.P., Kahn, M.T., Balyan, V., Draganov, I. & Pasupathi, S. 2020. A comprehensive thermoelectric cooler (TEC) modelling. *AIUE Congress 2020: International Conference on Use of Energy*, Cape Town, South Africa, 1-7. http://dx.doi.org/10.2139/ssrn.3735378.

3.2 A Comprehensive Thermoelectric Generator (TEG) Modelling

Confronted with the ongoing electricity and energy crises in South Africa and Africa in general, this section articulates a comprehensive modelling of thermoelectric generator (TEG), in an effort to devise an innovative renewable energy source that can be applied in conjunction with a heat source, to serve as an efficient hybrid DC power source, whereby generated heat from various sources can be converted to DC power, thereby increasing the total DC power production and efficiency. The novel findings brought about is a simulated TEG model in Matlab / Simulink that can be easily configured with respect to an electrical load, to simulate and determine TEGs optimal parameters for an increase in the output power (P_o) generation and also to better the TEG thermal / electrical / conversion efficiency (η).

3.2.1 Introduction

According to Eberhard *et al*. (2017), energy and electricity crises are progressively becoming serious problems in Sub-Saharan Africa. In South Africa, various alternative electrical energy sources are being explored with keen focus on renewable energy sources − which include but unlimited to solar, wind energy, hydro energy, fuel cells, ocean energy, geothermal energy, bio-energy and waste heat (Abolhosseini *et al.,* 2014; Naveen *et al.,* 2020). Waste heat can be divided into three grades i) high grade heat >650°C, ii) medium grade heat between 277°C and 650°C and iii) low grade heat <277°C – which accounts for 66% of waste heat as stated in Haddad *et al.* (2014). Low grade waste heat is thus, reasonably available and can therefore be harvested from various heat sources such as human habitats, industrial processes, FCs, appliances heat, vehicles exhaust − to name a few. In light of this, this study focuses on the theoretical modeling, harnessing and conversion of waste heat to DC electrical power based on thermoelectricity using TEG. Thermoelectricity as examined extensively in Bayendang *et al.* (2020a) to (2022b), is basically a Seebeck-Peltier reversible triple display of the same thermo-electrical process, in which heat is converted to DC power using TEG or by using TEC, DC power is converted to heat and or cold depending on the supply voltage polarity (i.e. the current flow direction).

Numerous scholarly publications have been done on thermoelectricity; however, most failed to extensively convey the mathematics governing the physics models. The goal of this study is to logically express the mathematics that represent various thermoelectricity key parameters with focus on TEG and how they are applied to comprehensively model TEG(s) using Matlab / Simulink. The rationale is to ascertain a comprehensive TEG model, which can be used to understand, develop, simulate and design a theoretical TEG system that is energy efficient and innovative. Proceeding the introduction is the TEG mathematical analysis, followed by the TEG modelling after which the results are analysed and finally concluding remarks are drawn preceded by the research scientific contributions.

3.2.2 TEG Steady-state Mathematical Analysis

There are several technical parameters that enable a thermoelectric (TE) device to generate DC electricity when subjected to a heat source. The general thermoelectricity parameters are highlighted with emphasis on the crucial parameters that determine the performance of TEGs. The mathematics is detailed in Goldsmid (1995), Lee (2016) and Twaha *et al.* (2016), from which developed and presented next are what is applicable to my research.

3.2.2.1 Thermoelectric Conductivities

The Wiedemann-Franz law relates the thermal and electrical conductivities as:

$$k_E = \sigma L_o T \quad \text{(W/mK)} \tag{3.1}$$

where k_E is the thermal conductivity electrons charge carrier contribution (W/mK), σ is the electrical conductivity (Siemens/m), L_o is a constant known as the Lorenz number (2.44×10^{-8} WΩK^{-2}) and T is the absolute temperature in kelvin (273.15K) or (zero degree Celsius).

3.2.2.2 Seebeck Coefficient (*S*)

In honour of the TEG discoverer Thomas Seebeck, S defines the ratio between the electromotive force (V_{emf}) and the TEG temperature difference (ΔT) expressed as:

$$S = \frac{V_{emf}}{\Delta T} = \frac{V_{emf}}{T_h - T_c} \quad \text{(V/K)} \tag{3.2}$$

where T_h and T_c are respectively the TE device hot and cold sides junction temperature in kelvin.

3.2.2.3 Thermoelectricity Figure of Merits (*Z* and *z*)

The TE device and material figure of merits are respectively denoted as (Z) and (z) and expressed as:

$$Z = z = \frac{S^2\sigma}{k} = \frac{S^2}{\rho k} \quad \text{(K}^{-1}\text{)} \tag{3.3}$$

where $S^2\sigma$ is the TEG electrical power factor and k is the TEG thermal conductivity (W/mK) and ρ is the TEG electrical resistivity ($\rho = \sigma^{-1}$) in Ω m.

3.2.2.4 TE Dimensionless Figure of Merits (*ZT* and *zT*)

The TE device and material dimensionless figure of merits are respectively denoted as (ZT) and (zT) and expressed as:

$$ZT = zT = \frac{S^2\sigma T}{k} = \frac{S^2}{L_0} = \frac{S^2 T}{\rho k} \tag{3.4}$$

3.2.2.5 TE Mean Dimensionless Figure of Merits ($Z\overline{T}$ and $z\overline{T}$)

The TE device and material average dimensionless figure of merits are respectively denoted as ($Z\overline{T}$) and ($z\overline{T}$) and expressed as:

$$Z\overline{T} = z\overline{T} = \frac{S^2\sigma\overline{T}}{k} = \frac{S^2\overline{T}}{\rho k} \tag{3.5}$$

where the average temperature $\overline{T} = 0.5\,(T_h + T_c)$ in K.

3.2.2.6 TE Device P-N Junction Thermocouple Unit Resistance (*r*)

The TEG internal p-n junction thermocouples combined ($r = r_p + r_n$) resistance (r) in ohm is calculated using:

$$r = \frac{\rho L}{A} \qquad (\Omega) \tag{3.6}$$

where L is the TEG p-n junction thermocouple combined length in meter (m) and A is the TEG p-n junction thermocouples combined area ($A = A_p + A_n$) in m^2.

3.2.2.7 TE Device P-N Junction Thermocouple Resistivity (ρ)

TEG internal p-n junction thermocouples combined electrical resistivity (ρ) in ohm meter (Ωm) is given by:

$$\rho = \frac{rA}{L} \qquad (\Omega m) \tag{3.7}$$

3.2.2.8 TE Device P-N Junction Thermocouple Conductance (*K*)

TEG internal p-n junction thermocouple combined thermal conductance (K) in (W/K) is computed as:

$$K = \frac{kA}{L} = \frac{k\rho}{r} = \frac{S^2}{Zr} \qquad (W/K) \tag{3.8}$$

NB: take special note of the difference between the various notations of K, K and k where used in this study.

3.2.2.9 TEG Module Unit Resistance (*R*)

TEG module resistance (R) in ohm, is deduced as:

$$R = nr \qquad (\Omega) \tag{3.9}$$

where n (which varies in quantity depending on the manufactured TE device capability) is the total quantity of p-n thermocouples used during the TEG manufacturing.

3.2.2.10 TEG Temperature Difference (Δ*T*)

TEG ΔT is the temperature difference between the TEG hot and cold sides temperature, calculated as:

$$\Delta T = T_h - T_c \qquad (°C) \text{ or } (K) \tag{3.10}$$

where T_h and T_c are respectively the TEG hot and cold sides temperature in °C or K.

3.2.2.11 TEG Module Output Voltage (V_o)

A TEG module generated voltage in volt is given as:

$$V_o = n[S\,(T_h - T_c)] - IR \qquad (V) \tag{3.11}$$

where I is the output current from the TEG.

3.2.2.12 TEG Module Output Current (*I*)

A TEG module output current in ampere is defined as:

$$I = \frac{nS\Delta T}{R+R_L} \quad \text{(A)} \tag{3.12}$$

where R_L is the load resistance connected to the TEG. The flow of I causes the internal Joule or Ohmic heating.

3.2.2.13 Heat Absorbed on TEG Module Hot-side (Q_h)

For TEG to generate power, TEG hot-side must be at a temperature T_h to create a constant heat flux (Q_h) in (W).

$$Q_h = n\,[(SIT_h) + (K\Delta T)] - 0.5I^2R \quad \text{(W)} \tag{3.13}$$

3.2.2.14 Heat Emitted on TEG Module Cold-side (Q_c)

For TEG to generate power, TEG cold-side must be at a lower temperature T_c to dissipate the heat Q_c in watt.

$$Q_c = n\,[(SIT_c) + (K\Delta T)] + 0.5I^2R \quad \text{(W)} \tag{3.14}$$

3.2.2.15 TEG Module Generated Power (P_o)

TEG output power in watt, is the difference between Q_h and Q_c.

$$P_o = Q_h - Q_c \quad \text{(W)} \tag{3.15}$$

or

$$P_o = IV_o = n\,[(SI\Delta T)] - I^2R \quad \text{(W)} \tag{3.16}$$

3.2.2.16 TEG Carnot Efficiency (η_c)

Efficiency determine based-on the TEG temperatures.

$$\eta_c = \frac{\Delta T}{T_h} = \frac{T_h - T_c}{T_h} = 1 - \frac{T_c}{T_h} \tag{3.17}$$

3.2.2.17 TEG Thermal / Electrical / Conversion Efficiency (η)

This is the ratio of TEG output power and heat absorbed on TEG hot-side. It's a performance parameter.

$$\eta = P_o / Q_h \tag{3.18}$$

3.2.2.18 TEG Conversion Efficiency Expression (η_e)

This efficiency is the same as η. It is simply the raw expression when P_o and Q_h equations are used in (3.18).

$$\eta_e = \eta_c \frac{(nR_L/R)}{[(1+nR_L/R) - 0.5\eta_c + ((1/(2Z\overline{T}))(1+nR_L/R)^2(1+T_c/T_h))]} \tag{3.19}$$

3.2.2.19 TEG Maximum Conversion Efficiency (η_m)

This is TEG's efficiency when $R / R_L = \sqrt{1 + Z\overline{T}}$ and the expression for η_m is:

$$\eta_m = \eta_c\left[\frac{(\sqrt{1+Z\overline{T}})-1)}{(\sqrt{1+Z\overline{T}}+(T_c / T_h))}\right] \tag{3.20}$$

3.2.2.20 TEG Maximum Power Conversion Efficiency (η_{mp})

This is TEG's efficiency at maximum P_o (i.e. $R = R_L$).

$$\eta_{mp} = \eta_c / (2 - 0.5\eta_c + (2/Z\overline{T})\ (1+T_c/T_h)) \tag{3.21}$$

The efficiency parameters define the TEG effectiveness.

3.2.2.21 TEG Maximum Output Power (Po_{max})

Maximum power transfer theoretically occurs when TEG's $R = R_L$.

$$Po_{max} = (nS\Delta T)^2(R_L/R) / (R(1+(R_L/R))^2) \quad \text{(W)} \tag{3.22}$$

3.2.2.22 TEG Maximum Output Voltage (Vo_{max})

TEG maximum output voltage occurs at open circuit – i.e. when R_L = infinity or unconnected, I = 0A.

$$Vo_{max} = nS(T_h - T_c) = nS\Delta T \quad \text{(V)} \tag{3.23}$$

3.2.2.23 TEG Maximum Output Current (I_{max})

TEG maximum current occurs at short circuit – that is, when R_L = 0Ω. This means R is the only resistance.

$$I_{max} = nS(T_h - T_c)/R_t = nS\Delta T / R \quad \text{(A)} \tag{3.24}$$

The maximum parameters define the TEG useful limits.

3.2.2.24 TEG Normalized Output Current (I_n)

This is the normalised TEG output current between $0 \le I_n \le 1$. At maximum power transfer ($R = R_L$), I_n = 0.5. I_n is the TEG output current divided by the maximum current the TEG can generate, expressed as:

$$I_n = \frac{I}{I_{max}} = \frac{R}{R + R_L} \tag{3.25}$$

3.2.2.25 TEG Normalized Output Voltage (V_n)

This is the normalised TEG output voltage between $0 \le V_n \le 1$. At maximum power transfer ($R = R_L$), V_n = 0.5. V_n is the TEG output voltage divided by the maximum voltage the TEG can generate, expressed as:

$$V_n = \frac{V_o}{Vo_{max}} = \frac{R_L}{R_L + R} \tag{3.26}$$

3.2.2.26 TEG Normalized Output Power (P_n)

This is the normalised TEG output power between $0 \leq P_n \leq 1$. At maximum power transfer ($R = R_L$), $P_n = 1$. P_n is the TEG output power divided by the maximum power the TEG can generate, expressed as:

$$P_n = \frac{P_o}{Po_{max}} = \frac{4(R_L/R)}{[(R_L/R)+1]^2} \tag{3.27}$$

3.2.2.27 TEG Normalized Conversion Efficiency (η_n)

This is the normalised TEG conversion efficiency between $0 \leq \eta_n \leq 1$. η_n is determined by R / R_L, T_c / T_h *and* $Z\overline{T}$. η_n is the ratio of the TEG conversion efficiency and the TEG maximum conversion efficiency, expressed as:

$$\eta_n = \eta / \eta_m \tag{3.28}$$

3.2.2.28 TEG Effective Seebeck Coefficient (S_e)

S_e is the TEG effective Seebeck coefficient in volt per kelvin.

$$S_e = 4Po_{max} / [n\, I_{max}\Delta T] \quad \text{(V/K)} \tag{3.29}$$

3.2.2.29 TEG Effective Electrical Resistivity (ρ_e)

ρ_e is the TEG effective electrical resistivity in ohm meter.

$$\rho_e = 4[(A/L)Po_{max}] / nI_{max}^2 \quad (\Omega\ \text{m}) \tag{3.30}$$

3.2.2.30 TEG Effective Figure of Merit (Z_e)

Z_e is the TEG material effective figure of merit in per kelvin.

$$Z_e=[(2/\overline{T})(1+(T_c/T_h))]/[\eta_c((1/\eta_{mp})+0.5)-2] \quad (K^{-1}) \tag{3.31}$$

3.2.2.31 TEG Effective Thermal Conductivity (k_e)

k_e is the TEG effective thermal conductivity in W/mK.

$$k_e = S_e^2 /\rho_e\, Z_e \quad \text{(W/mK)} \tag{3.32}$$

The effective parameters assist system designers bridge the gap between measured and theoretical specifications, by using maximum parameters to factor in TEG system losses.

3.2.2.32 TEG Heat Flux Density (*HFD*)

HFD is the TEG amount of heat absorbed per its hot side surface area.

$$HFD = Q_h / TEG\ Surface\ Area \quad (W/cm^2) \tag{3.33}$$

The more the heat flux density and absorption with little or no thermal resistance, the more the TEG output power.

This concludes the theoretical TEG steady-state mathematical analysis.

3.2.3 TEG Modelling

TEG has been modeled variously; however, these models lack the applicable mathematics to complement the implemented physics models and as well some of these models are rigid, basic, unclear and also lack certain parameters and features to heuristically simulate TEGs. Modelling of TEG in Tsai and Lin (2010), Yusop *et al.* (2013), Lee (2016), Twaha *et al.* (2016), Chen *et al.* (2017) and Mamur and Çoban (2020); were examined as the bases, from which i developed further to realize the TEG implementations in Figures 3.1 and 3.2 using Matlab / Simulink. What is mostly unique and advanced in both my theoretical modelings are the following implemented improvements and novelties:

- The mathematical analysis in Section 3.2.2 is included.
- Any number of TEG quantities can be simulated.
- Different TEGs configurations can be simulated.
- R_L can be changed while the simulation is running.
- Power loss due to r, R and R_L can be seen on the fly.
- Various TEGs characteristics curves are generated.
- More TEG parameters are added, tested and shown.
- The practical limitations of TEG(s) are observable.
- The user interface is clearer, better and informational.
- A better and bigger TEG(s) module can be simulated.

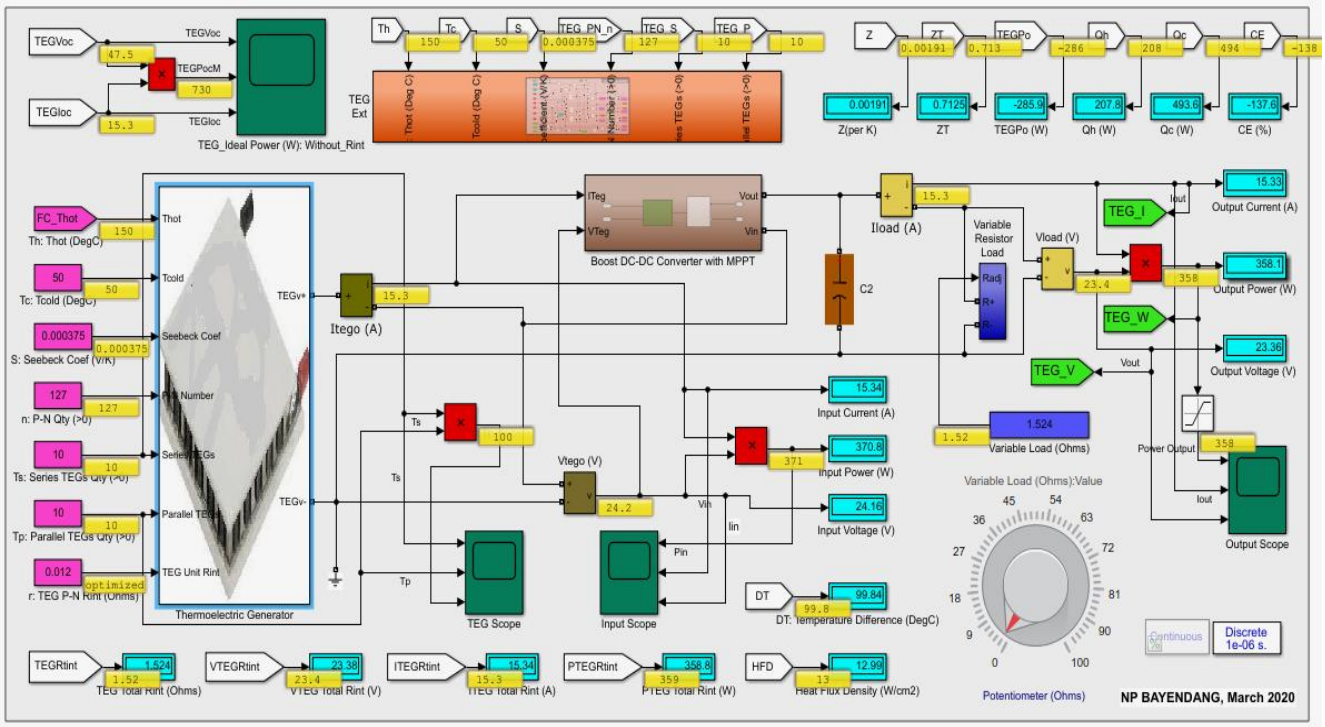

Figure 3.1: TEG model developed by application of Section 3.2.2 presented maths

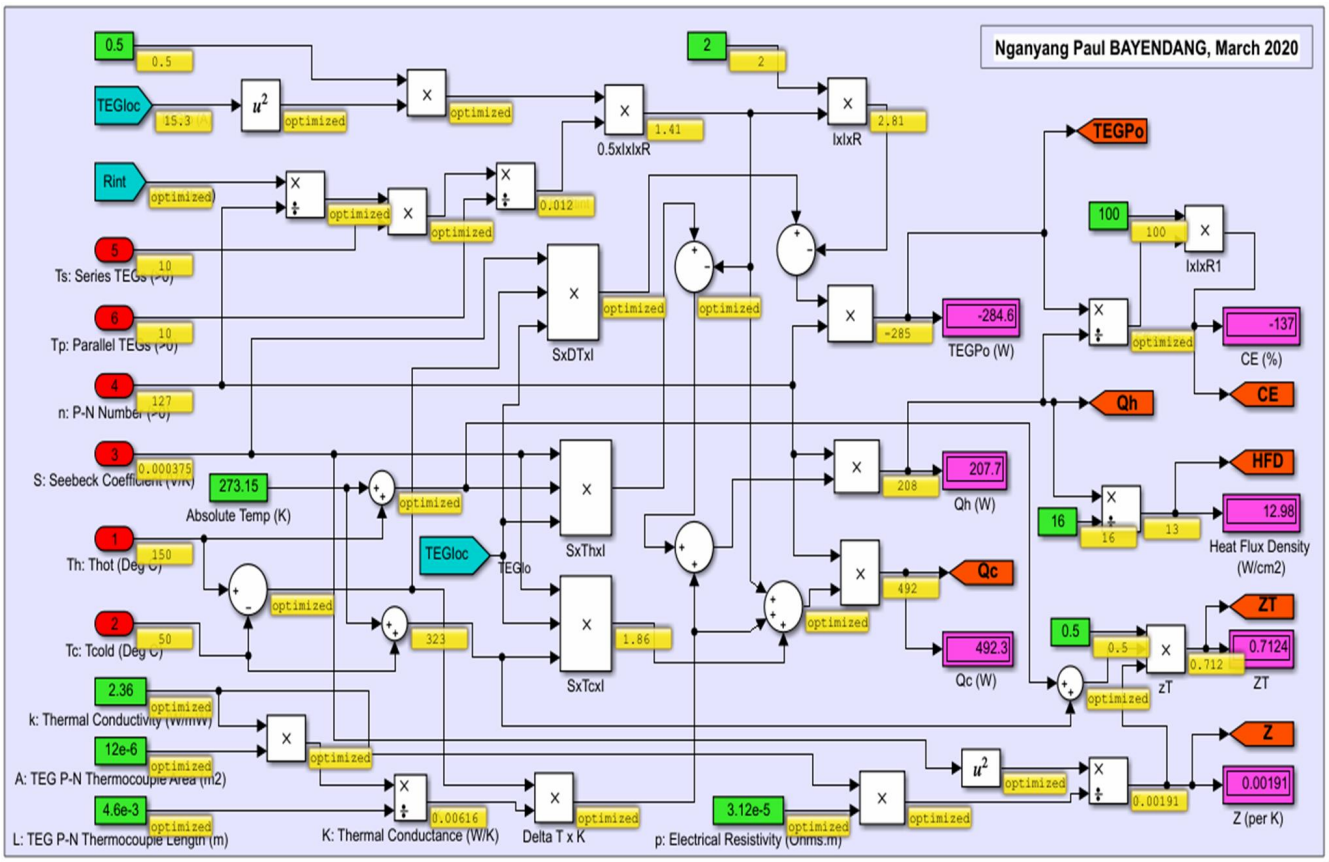

Figure 3.2: TEG model novel implementation details snippet

3.2.4 TEG Modelling Results and Analyses

The modeled TEG(s) was simulated using realistic datasets and specs from TEG(s) manufacturers datasheets, research articles and scholarly publications including Goldsmid (1995), Tsai and Lin (2010), Yusop *et al.* (2013), Lee (2016), Twaha *et al.* (2016), Chen *et al.* (2017) and Mamur and Çoban (2020). As indicated earlier, Figure 3.1 depicts the user interface where a TEG input parameters of interest (e.g. Seebeck coefficient, hot and cold side temperatures, p-n thermocouples count, electrical load resistance etc) can be entered, changed on the fly and the results variously displayed as well as plotted as pictured in Figures 3.3, 3.5 – 3.6. In Figure 3.4 is the TEG (η, P_o) *vs I* in Mathcad from Lee (2016) − it was used to compare and validate my Matlab TEG model (P, η) *vs I* as depicted in Figures 3.5 and 3.6.

TEG P_o is proportional to ΔT and I as shown in Figure 3.3; however, I above a certain value (midpoint) as clearly evident in Figure 3.5, starts to decrease P_o which is due to Joule or Ohmic heating in the TEG caused by more I. The P_o, ΔT and I optimal result is highlighted in green in Figure 3.3. In sum, TEG output power is linear (with less output current) and becomes non-linear (with more output current). The more I increases the temperature on the TEG cold side, which consequently decreases ΔT, P_o and η.

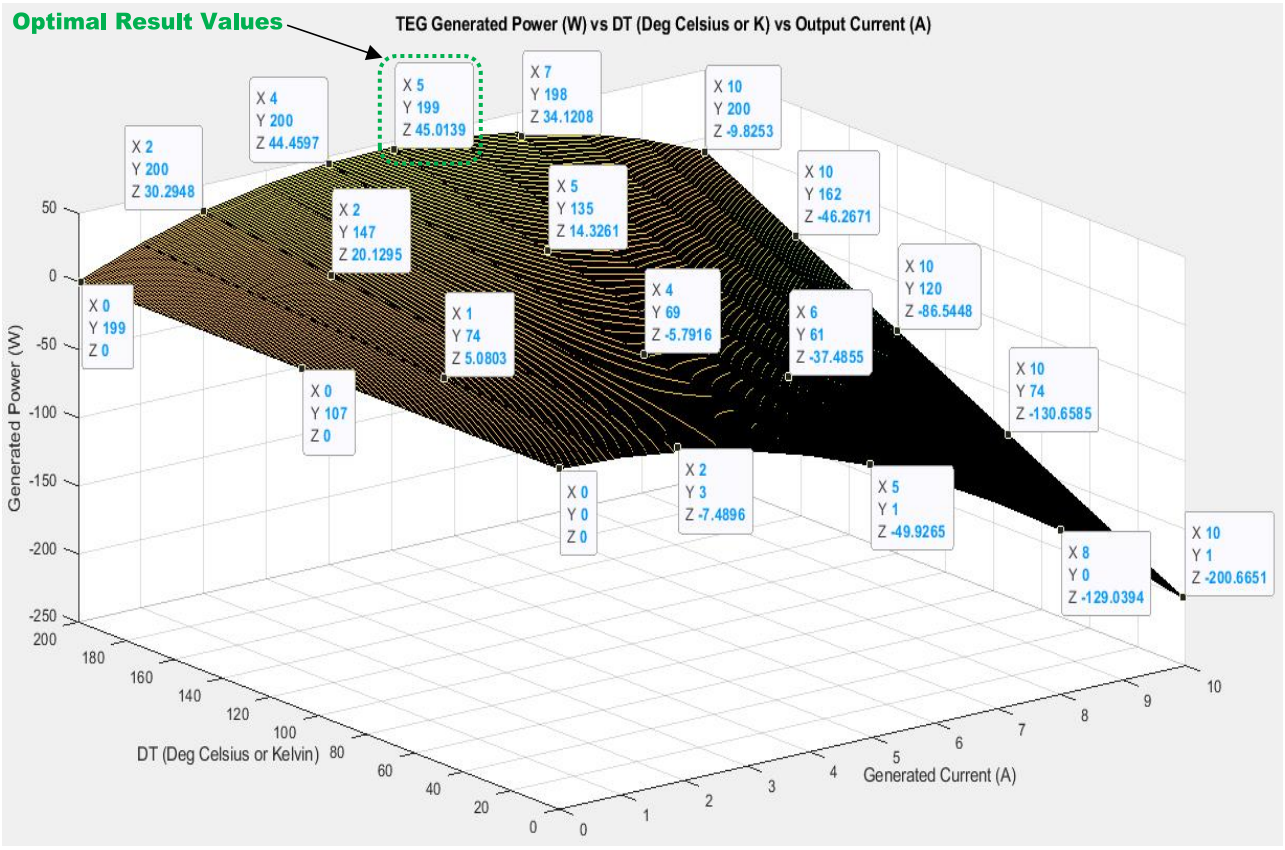

Figure 3.3: TEG output power (W) vs ΔT (°C) vs output current (A)

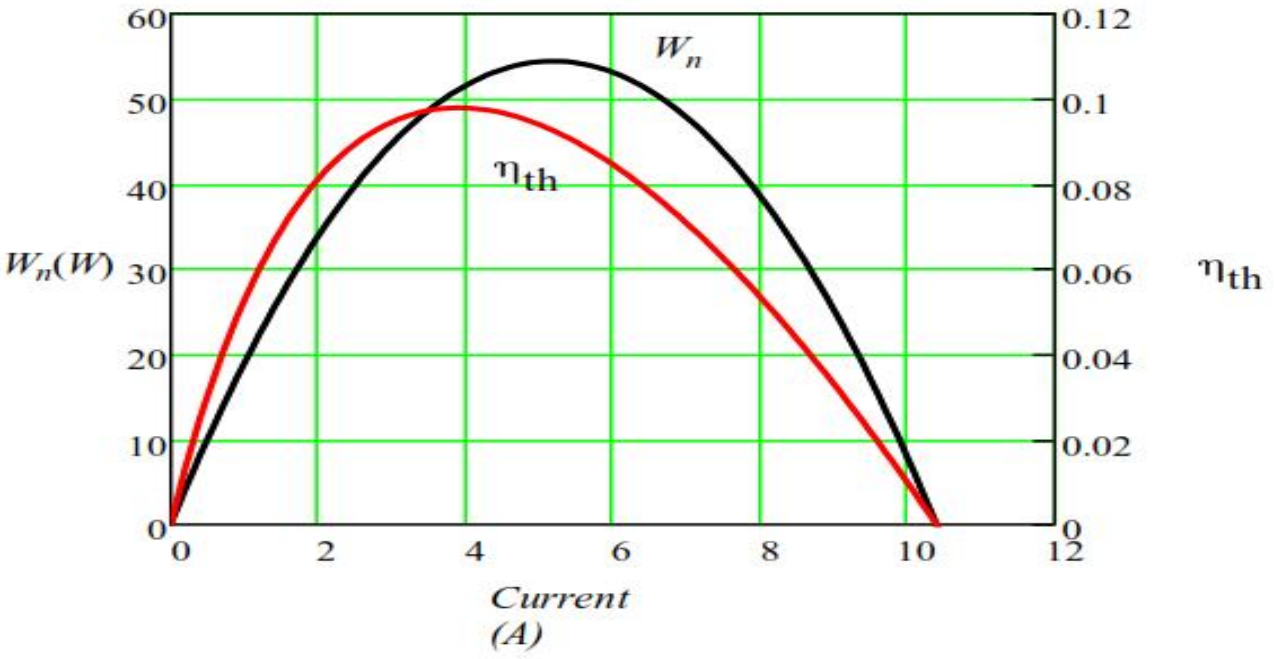

Figure 3.4: Mathcad TEG (η , P_o) vs I (A) (adapted from Lee, 2016)

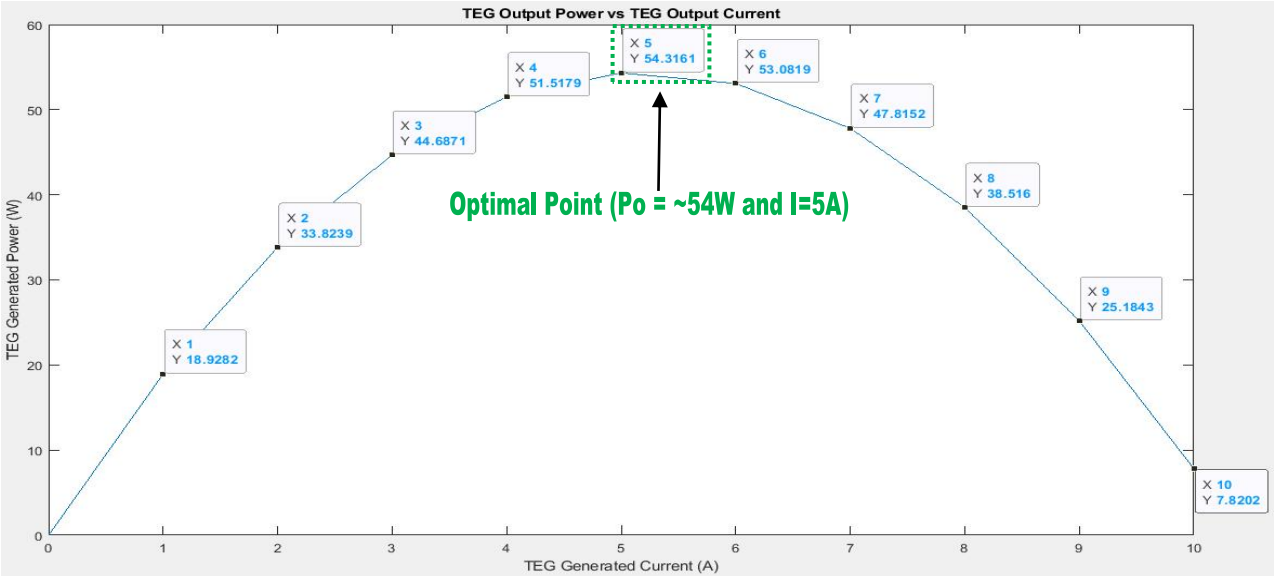

Figure 3.5: TEG output power P_o (W) vs output current I (A)

Akin to Figure 3.5, TEG η is directly proportional to I up to 5A max, hereafter η decreases henceforth as depicted in Figure 3.6 and highlighted in green is the optimal result. NB: Ohmic heating is proportional to current; as a result, it increases the cold side temperature which reduces ΔT, P_o and subsequently the conversion efficiency η; hence the bell-shaped curves as expounded.

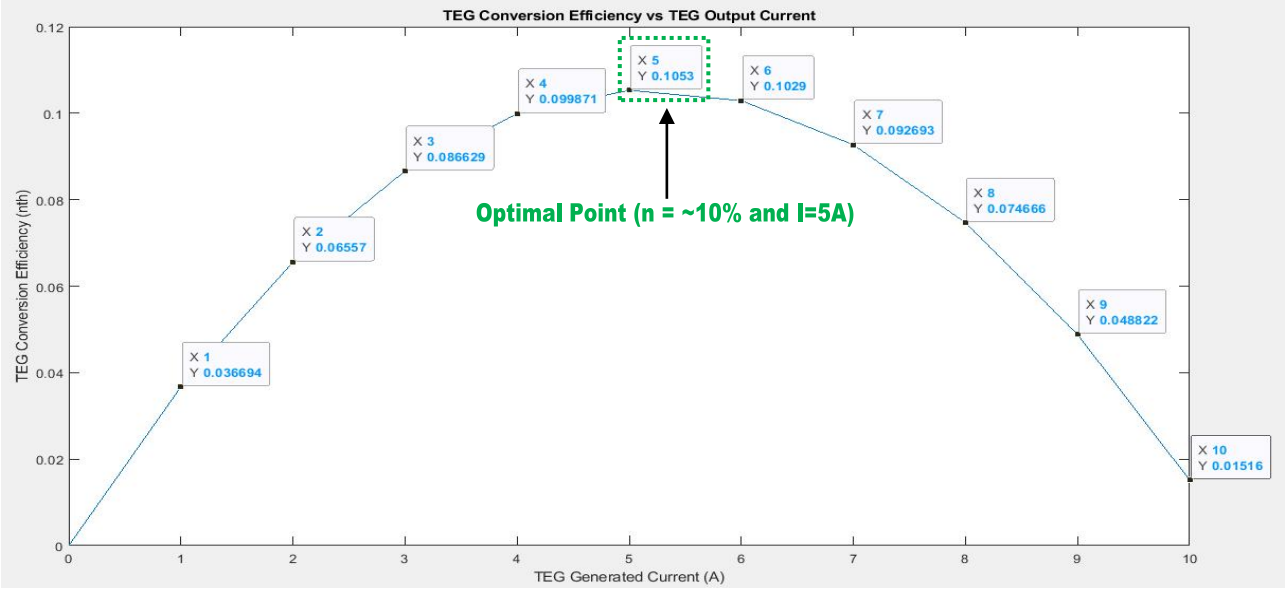

Figure 3.6: TEG conversion efficiency η vs output current I (A)

3.2.5 Research Scientific Contributions

This research is herein summarised and its significance additionally to the findings already established in Section 3.2.3 are highlighted and advanced below as the study scientific contributions:

- A comprehensive / extensive TEG steady-state maths is exhibited.
- A clear comprehensive TEG(s) model is instituted.
- An advanced TEG simulator is uniquely developed.
- Multiple TEGs can be simulated in various patterns.
- An efficient practical TEG(s) system can be devised.

However, the researched TEG model and mathematics have the following limitations:

- Practical realities were not factored-in, as the model focused only on theoretical TEG at unit and module levels and not at system level where other coupling factors and dynamics exist. Some of these practicalities include thermal / contact resistance heat losses when TEGs are used with heat exchangers / heat-sinks / pipes. NB: TEGs in practice require heat exchangers / heat-sinks for thermal management in order to maintain an acceptable ΔT to ensure proper and reliable operations.
- The researched simulated model has to be practically tested to correlate the mathematics and simulated analyses.

3.2.6 Summary

This section started by briefly introducing the ongoing electricity crisis in South Africa followed by the assorted renewable energy and power sources provisions as the innovative solutions being sought after, with keen focus on waste heat and in particular low grade waste heat which is abundantly produced in various settings and notably in domestic, commercial, industrial and vehicular processes. This low grade waste heat energy sources make them suitable for use with TEG – a thermoelectric device that converts heat to DC electricity based-on Seebeck effect. The mathematical analysis of thermoelectricity with emphasis on TEG was examined, developed and elaborately presented to determine how much power can be generated and from what optimal TEG parameters. A unique TEG model in Matlab / Simulink was developed incorporating these improvements and the advance implementation was also simulated with practical TEG specifications from different manufacturers data and the generated results confirmed that, to get max output power (P_o) and η from TEGs, ΔT must be highest, which will initially increase I until it has no confirmatory effect on η. These outcomes were analysed in conformity with information reported in scholarly TEGs publications and datasheets. The research highlights were asserted as the scientific contributions to conclude the study. The recommendation is to practically implement the research findings to correlate the TEG mathematical and simulated analyses, whereby the TEG(s) shall be used with fuel cells and other potentially available heat sources to efficiently convert waste heat to DC power in a larger combined cooling, heating and power (CCHP) system.

3.3 A Comprehensive Thermoelectric Cooler (TEC) Modelling

Faced with the ongoing energy and electricity crises in South Africa and by extension Africa, this section presents a comprehensive model of thermoelectric cooler (TEC), in a bid to devise an innovative renewable energy cooler to serve as an efficient heat pump, in which a low DC power source can be applied to it to generate cold, thereby decreasing the total power consumption. The novelty brought forward is an original simulated TEC model in Matlab / Simulink that can easily be configured with respect to a given DC source and thermal load, to simulate and determine a TEC optimal operational parameters to increase its heat absorption (cooling power Q_c) capacity and as well its coefficient of performance (*CoP*).

3.3.1 Introduction

According to Eberhard *et al.* (2017), energy and electricity crises are becoming serious problems in the entire Sub-Saharan Africa. In South Africa, diverse alternative electrical energy sources are being commissioned with interests on renewable energy sources − which include but not limited to solar energy, bio-energy, wind energy, wave energy, fuel cells, geothermal energy and waste heat (Abolhosseini *et al.,* 2014). However, these alternative energy sources are aptly good for light duty applications, hence necessitates a cooling device (e.g. heat pump, refrigerator, air conditioner etc) that is energy efficient. Cold energy is simply the absence of heat or thermal energy. Cold can be generated using various means or devices; some of which include passive, absorption, compression, magnetic, laser and TEC as per Brown and Domanski (2014). However, the latter (TEC) as per Zhao and Tan (2014), is becoming trendy because of its size, flexibility (can generate cold, heat and power) and environmental friendliness. Thus, this study focuses on theoretically generating cold from DC electrical power based-on thermoelectricity using TEC. Thermoelectricity as covered in detail in Bayendang *et al.* (2020a) to (2022b), is simply a Seebeck-Peltier reversible triple display of the same thermo-electrical process, in which DC power is converted to cold and or heat depending on the supply current direction.

Several scholarly publications have been done on thermoelectricity, though most absconded to extensively express the mathematics governing the physics models. The aim of this study is therefore to reasonably articulate the mathematics that embody various thermoelectricity key parameters with focus on TEC and how they are applied to comprehensively model TEC(s) using Matlab/Simulink. The rationale is to establish a theoretical TEC model, which can be used to understand, develop, simulate and design a comprehensive TEC system that is innovative and energy efficient. Proceeding the introduction is the TEC mathematical analysis, followed by the TEC modelling after which the results are analysed and finally concluding remarks are drawn preceded by the research scientific contributions.

3.3.2 TEC Steady-state Mathematical Analysis

There are numerous technical parameters that enable a thermoelectric (TE) device to generate cold / heat when subjected to a power source. The main thermoelectricity parameters are herein highlighted with emphasis on the crucial parameters that determine the performance of TECs. The mathematics is detailed in Goldsmid (1995), Tritt (2002), Terasaki (2011), Meseguer *et al.* (2012), Lee (2016), Mani (2016) and Twaha (2016), from which evaluated systematically next are what's relevant to my research.

3.3.2.1 Thermoelectric Conductivities

The Wiedemann-Franz law connects the electrical and thermal conductivities as:

$$k_E = \sigma T L_o \quad \text{(W/mK)} \tag{3.34}$$

where k_E is the thermal conductivity electrons charge carrier contribution (W/mK), σ is the electrical conductivity (Siemens/m), T is the absolute temperature in kelvin (273.15K) or (0°Celsius) and L_o is a constant known as the Lorenz number (~2.45x10^{-8} V^{2}K^{-2}).

3.3.2.2 Peltier Coefficient (Π)

In honor of the TEC discoverer Jean Peltier, Π defines the product between the Seebeck coefficient S and the absolute temperature T in kelvin or the ratio between the thermal current (Q_t) and the TEC electrical current (I_e) expressed as:

$$\Pi = ST = \frac{Q_t}{I_e} \qquad \text{(V)} \tag{3.35}$$

3.3.2.3 Thermoelectricity Figure of Merits (Z and z)

The TE device and material figure of merits are respectively denoted as (Z) and (z) and expressed as:

$$Z = \ z = \frac{S^2\sigma}{k} = \ \frac{S^2}{\rho k} \qquad \text{(K}^{-1}\text{)} \tag{3.36}$$

where $S^2\sigma$ is the TEC electrical power factor and k is the TEC thermal conductivity (W/mK) and ρ is the TEC electrical resistivity ($\rho = \sigma^{-1}$) in Ω m.

3.3.2.4 TE Dimensionless Figure of Merits (ZT and zT)

The TE device and material dimensionless figure of merits are respectively denoted as (ZT) and (zT) and expressed as:

$$ZT = \ zT = \frac{S^2\sigma T}{k} = \frac{S^2}{L_0} = \ \frac{S^2 T}{\rho k} \tag{3.37}$$

3.3.2.5 TE Mean Dimensionless Figure of Merits ($Z\overline{T}$ and $z\overline{T}$)

The TE device and material average dimensionless figure of merits are respectively denoted as ($Z\overline{T}$) and ($z\overline{T}$) and expressed as:

$$Z\overline{T} = \ z\overline{T} = \frac{S^2\sigma\overline{T}}{k} = \ \frac{S^2\overline{T}}{\rho k} \tag{3.38}$$

where the average temperature $\overline{T} = 0.5\ (T_h + T_c)$ in K.

3.3.2.6 TE Device P-N Junction Thermocouple Unit Resistance (*r*)

The TEC internal p-n junction thermocouples combined ($r = r_p + r_n$) resistance (r) in ohm is calculated using:

$$r = \frac{\rho L}{A} \qquad (\Omega) \tag{3.39}$$

where L is the TEC p-n junction thermocouples combined length in meter (m) and A is the TEC p-n junction thermocouples combined area ($A = A_p + A_n$) in m^2.

3.3.2.7 TE Device P-N Junction Thermocouple Resistivity (ρ)

TEC internal p-n junction thermocouples combined electrical resistivity (ρ) in ohm meter (Ωm) is given by:

$$\rho = \frac{rA}{L} \qquad (\Omega m) \tag{3.40}$$

3.3.2.8 TE Device P-N Junction Thermocouple Conductance (*K*)

TEC internal p-n junction thermocouple combined thermal conductance (K) in (W/K) is computed as:

$$K = \frac{kA}{L} = \frac{k\rho}{r} = \frac{S^2}{Zr} \qquad (W/K) \tag{3.41}$$

NB: take special note of the difference between the various notations of K, K and k where used in this study.

3.3.2.9 TEC Module Unit Resistance (*R*)

TEC module resistance (R) in (Ω) is construed as:

$$R = nr \qquad (\Omega) \tag{3.42}$$

where n (which varies in amount depending on the capability of the manufactured TE device) is the total quantity of p-n thermocouples used during the TEC manufacturing.

3.3.2.10 TEC Temperature Difference (ΔT)

TEC ΔT is the temperature difference between the TEC hot and cold sides temperature, calculated as:

$$\Delta T = T_h - T_c \qquad (°C) \text{ or } (K) \tag{3.43}$$

where T_h and T_c are respectively the TEC hot and cold sides temperature in K or °C.

3.3.2.11 TEC Module Input Voltage (V_{in})

A TEC module input voltage in volt is given as:

$$V_{in} = n[S\,(T_h - T_c)] + IR \qquad (V) \tag{3.44}$$

where I is the input current to the TEC.

3.3.2.12 TEC Module Input Current (*I*)

A TEC module input current in ampere is defined as:

$$I = \frac{nS\Delta T}{R_s - R} \qquad \text{(A)} \tag{3.45}$$

where R_s is the source resistance connected to the TEC. The flow of I causes the internal Ohmic or Joule heating.

3.3.2.13 Heat Absorbed on TEC Module Cold-side (Q_c)

For TEC to generate cold, TEC cold-side must be at temperature T_c to create a stable cooling power (Q_c) in W.

$$Q_c = n\,[(SIT_c) - (K\Delta T)] - 0.5I^2R \qquad \text{(W)} \tag{3.46}$$

3.3.2.14 Heat Emitted on TEC Module Hot-side (Q_h)

For TEC to generate cold, TEC hot-side must be at a higher temperature T_h to dissipate the heat Q_h in watt.

$$Q_h = n\,[(SIT_h) - (K\Delta T)] + 0.5I^2R \qquad \text{(W)} \tag{3.47}$$

3.3.2.15 TEC Module Input Power (P_{in})

TEC input power in watt is the difference between Q_h and Q_c.

$$P_{in} = Q_h - Q_c = n\,[(SI\Delta T)] + I^2R \qquad \text{(W)} \tag{3.48}$$

Or $$P_{in} = IV_{in} \qquad \text{(W)} \tag{3.49}$$

3.3.2.16 TEC Carnot Efficiency (η_c)

$$\eta_c = \frac{\Delta T}{T_h} = \frac{T_h - T_c}{T_h} = 1 - \frac{T_c}{T_h} \tag{3.50}$$

3.3.2.17 TEC Coefficient of Performance (*CoP*)

CoP is the TEC cooling power and input power ratio.

$$CoP = Q_c / P_{in} \tag{3.51}$$

3.3.2.18 TEC CoP Expression (CoP_e)

CoP_e is the same as *CoP*. It is simply the final raw expression when P_{in} and Q_c equations are put in (3.51).

$$CoP_e = \frac{[(SIT_c) - (K\Delta T) - (0.5I^2R/n)]}{[(SI\Delta T) + (I^2R/n)]} \tag{3.52}$$

3.3.2.19 TEC Current to Yield CoP (I_{cop})

$$I_{cop} = \frac{nS\Delta T}{R[\left(\sqrt{1+Z\overline{T}}\right) - 1]} \qquad \text{(A)} \tag{3.53}$$

3.3.2.20 TEC Maximum CoP (CoP_{max})

$$CoP_{max} = \frac{[T_c/\Delta T]\left((\sqrt{1+Z\overline{T}}) - \frac{T_h}{T_c}\right)}{((\sqrt{1+Z\overline{T}})+1)} \tag{3.54}$$

3.3.2.21 TEC Maximum Cooling Power Current (Icp_{max})

$$Icp_{max} = nST_c / R \qquad \text{(A)} \tag{3.55}$$

3.3.2.22 TEC I_{cop} Maximum Cooling Power (Qcp_{max})

$$Qcp_{max} = n[(SI_{cop}T_c) - (K\Delta T)] - 0.5I_{cop}^2R \qquad \text{(W)} \tag{3.56}$$

3.3.2.23 TEC Maximum Temperature Difference (ΔT_{max})

TEC ΔT_{max} occurs when Q_c = 0W and I is at maximum.

$$\Delta T_{max} = \left(T_h + \frac{1}{Z}\right) - \sqrt{(T_h + \frac{1}{Z})^2 - {T_h}^2} \qquad \text{(K)} \tag{3.57}$$

3.3.2.24 TEC Maximum Input Current (I_{max})

TEC maximum input current occurs when Q_c = 0W.

$$I_{max} = nS(T_h - \Delta T_{max}) / R = nS\Delta T / R \qquad \text{(A)} \tag{3.58}$$

3.3.2.25 TEC Maximum Input Voltage (Vin_{max})

Vin_{max} yields maximum ΔT_{max} when $I = I_{max}$.

$$Vin_{max} = nST_h \qquad \text{(V)} \tag{3.59}$$

3.3.2.26 TEC Maximum Cooling Power (Qc_{max})

Qc_{max} is the max thermal load at ΔT = 0℃ and $I = I_{max}$.

$$Qc_{max} = (n\ S)^2(T_h^2 - \Delta T_{max}^2) / 2R \qquad \text{(W)} \tag{3.60}$$

3.3.2.27 TEC Normalized Input Current (I_n)

TEC I_n is the ratio of I_{cop} and I_{max}.

$$I_n = I_{cop} / I_{max} \tag{3.61}$$

3.3.2.28 TEC Normalized Input Voltage (Vin_n)

TEC V_{in} is the ratio of V_{in} and Vin_{max}.

$$Vin_n = V_{in} / Vin_{max} \tag{3.62}$$

3.3.2.29 TEC Normalized Cooling Power (Qc_n)

TEC Qc_n is the ratio of Q_c and Qc_{max}.

$$Qc_n = Q_c / Qc_{max} \tag{3.63}$$

3.3.2.30 TEC Normalized CoP (CoP_n)

TEC CoP_n is the ratio of CoP and CoP_{max}.

$$CoP_n = CoP / CoP_{max} \tag{3.64}$$

3.3.2.31 TEC Effective Seebeck Coefficient (S_e)

$$S_e = 2Qc_{max} / nI_{max} (T_h + \Delta T_{max}) \quad \text{(V/K)} \tag{3.65}$$

3.3.2.32 TEC Effective Electrical Resistivity (ρ_e)

$$\rho_e = AS_e (T_h - \Delta T_{max}) / LI_{max} \quad (\Omega \text{ m}) \tag{3.66}$$

3.3.2.33 TEC Effective Figure of Merit (Z_e)

$$Z_e = 2\Delta T_{max} / (T_h - \Delta T_{max})^2 \quad (\text{K}^{-1}) \tag{3.67}$$

3.3.2.34 TEC Effective Thermal Conductivity (k_e)

$$k_e = S_e^2 / \rho_e Z_e \quad \text{(W/mK)} \tag{3.68}$$

The effective parameters enable system designers bridge the gap between theoretical and measured specifications, by using manufactured maximum TEC parameters to factor in system losses (Lee, 2016).

3.3.2.35 TEC Midpoint Current (I_{mid})

$$I_{mid} = 0.5 (I_{mp} + I_{cop}) \quad \text{(A)} \tag{3.69}$$

3.3.2.36 TEC Midpoint Cooling Power (Q_{Cmid})

$$Q_{Cmid} = n [(SI_{mid}T_c) - (K\Delta T)] - 0.5I_{mid}^2R \quad \text{(W)} \tag{3.70}$$

3.3.2.37 TEC Midpoint Input Power (Pin_{mid})

$$Pin_{mid} = n [(SI_{mid}\Delta T)] + I_{mid}^2R \quad \text{(W)} \tag{3.71}$$

3.3.2.38 TEC Midpoint CoP (CoP_{mid})

$$CoP_{mid} = Q_{Cmid} / Pin_{mid} \tag{3.72}$$

TEC midpoint parameters ensure a safe optimal design.

3.3.2.39 TEC Cold Flux Density (CFD)

$$CFD = Qc / TEC\ Surface\ Area \quad (\text{W/cm}^2) \tag{3.73}$$

3.3.3 TEC Modelling

TEC has been sparsely modeled in the literature; as a result, there is little or inadequate research publications on TEC models, especially using Matlab / Simulink, let alone accompanied by the relevant mathematics to supplement the TEC implemented models. TEC models that are common are in ready-made packages based-on computational fluid dynamics such as Ansys Fluent, COMSOL Multiphysics and also Mathcad as well others including Simscape in Matlab − which is even very basic. TEC models in these modelling and simulation packages, especially when published, do not expand on the various parameters and the maths governing them and some of these models are basic, rigid, vague and also lack certain parameters and features to heuristically simulate TECs. Therefore to bridge this gap between thermoelectricity with focus on the TEC maths and the implemented TEC models, I employed Matlab / Simulink to model and simulate TEC(s) from first principle, to institute an easy original TEC simulator as portrayed in Figure 3.7. The mathematical equations were modeled using Matlab, from which they were later ported to Simulink using Embedded Matlab Function, followed by designing the user interface further in Simulink. The layout is simple, in which parameters of interests are entered and shown and the results displayed accordingly. The inputs values can be easily changed while the simulation is in progress. The input parameters are TEC manufacturers and TEC modules specific. These input parameters are use to simulate the actual TEC performance before practically designing it. The only input values the user can optimize here are the T_h, T_c, T_s and T_p parameters and to some extent V_{in}; the rest input parameters are intrinsic in the TEC and can only be changed during manufacturing. However, all the input values can be changed in the simulation in order to have a practical feel of how the TEC would have performed − if it was manufactured based on the chosen hypothetical input values. The output operational, commercial, performance and maximum parameters; are those sometimes indicated in a TEC manufacturer's datasheets or technical information. Colour coding was utilised to reasonably group and differentiate all the various TEC parameters accordingly. In all, what is mostly unique and advanced in Figure 3.7 are the following implemented TEC parameters and novelties:

- The mathematical analysis in Section 3.3.2 is modeled.
- Multiple TEC modules can be furthermore simulated.
- V_{in} can be changed while the simulation is running.
- Various TECs characteristics curves are generated.
- More TEC parameters can be easily added / tested.
- The practical limitations of TEC(s) are noticeable.
- Friendly user interface – simple and informational.
- A better and bigger TEC(s) module can be simulated.

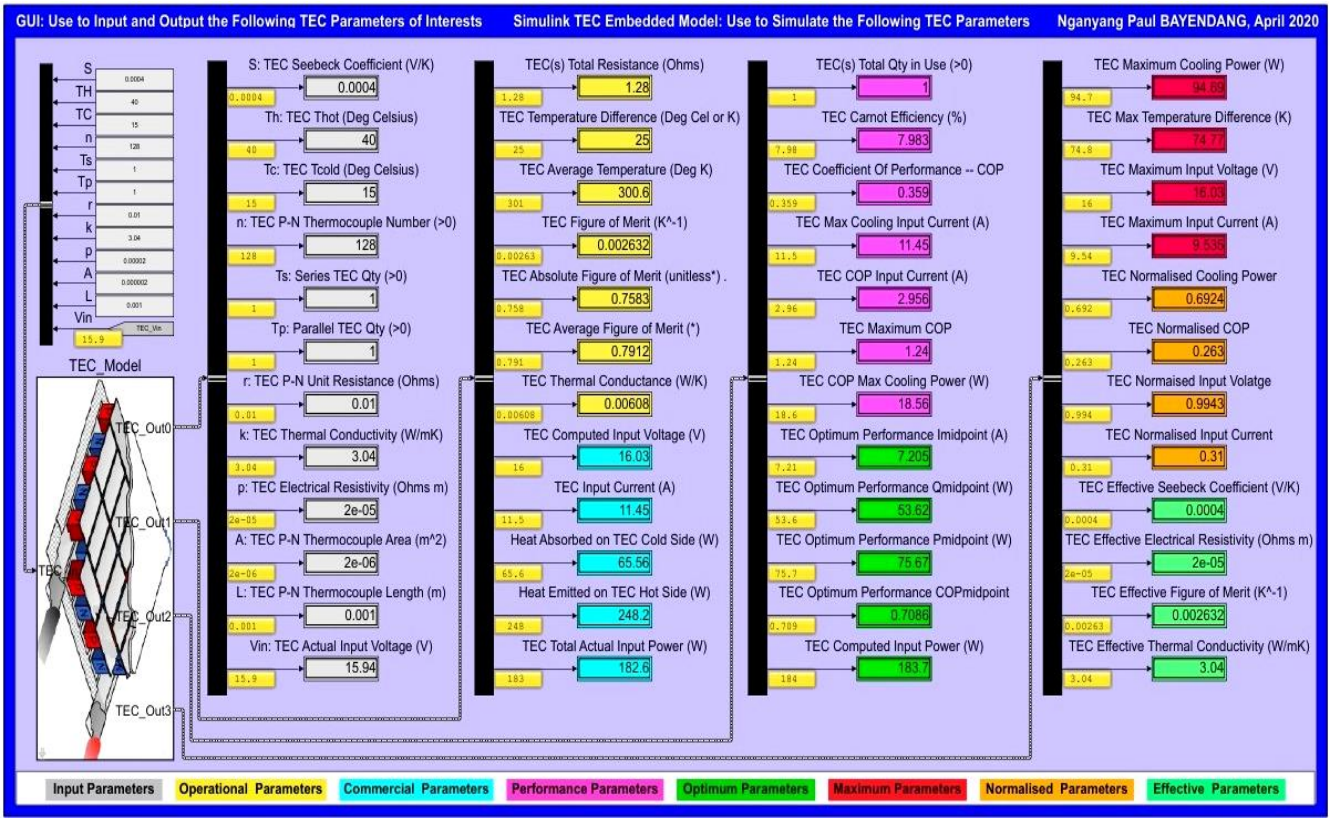

Figure 3.7: TEC original model based on Matlab / Simulink

3.3.4 TEC Modelling Results and Analyses

The modeled TEC was simulated using realistic data and specifications from TEC(s) manufacturers datasheets, books, miscellaneous research articles and scholarly publications found in Goldsmid (1995), Tritt (2002), Terasaki (2011), Meseguer *et al.* (2012), Lee (2016), Mani (2016) and Twaha (2016).

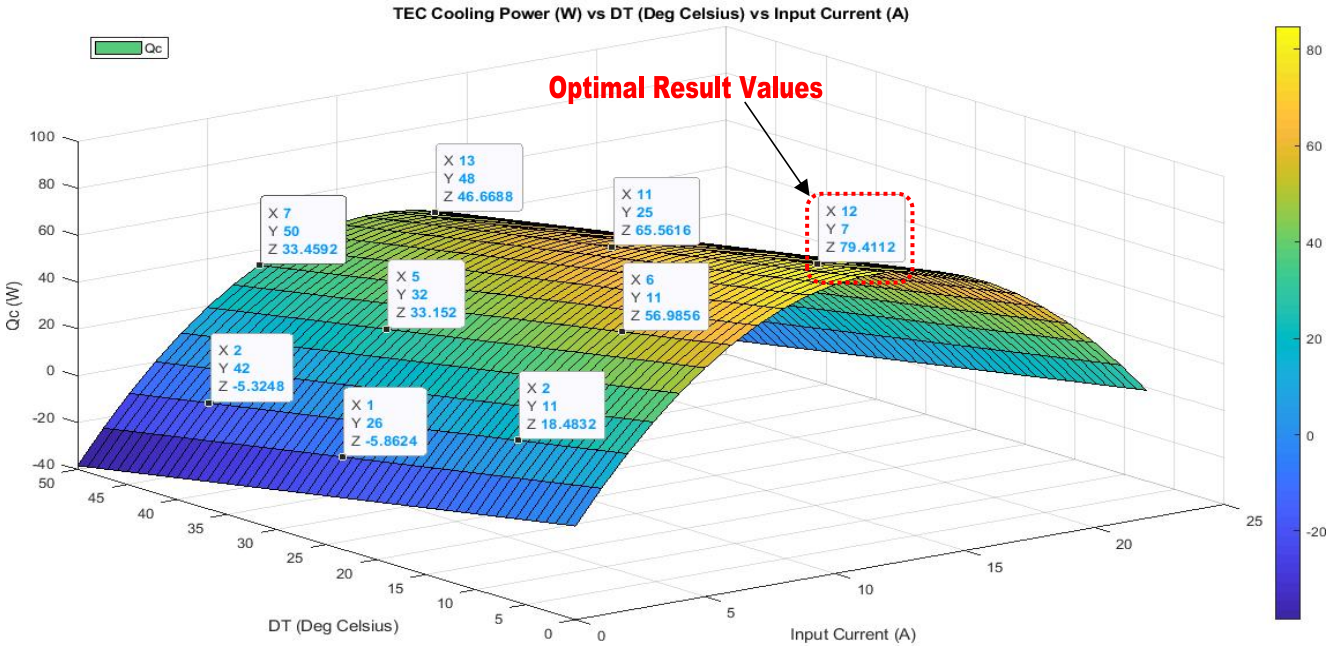

Figure 3.8: TEC cooling power (W) vs ΔT (°C) vs *I* (A)

Figures 3.8 and 3.9 revealed that Q_c is inversely proportional to ΔT but directly proportional to I up to 11A, after which Q_c drops. In Figures 3.8 and 3.9, the reason is due to Joule heating and also the Second Law of Thermodynamics. The $Q_c, \Delta T$ and I optimal results point are highlighted in red.

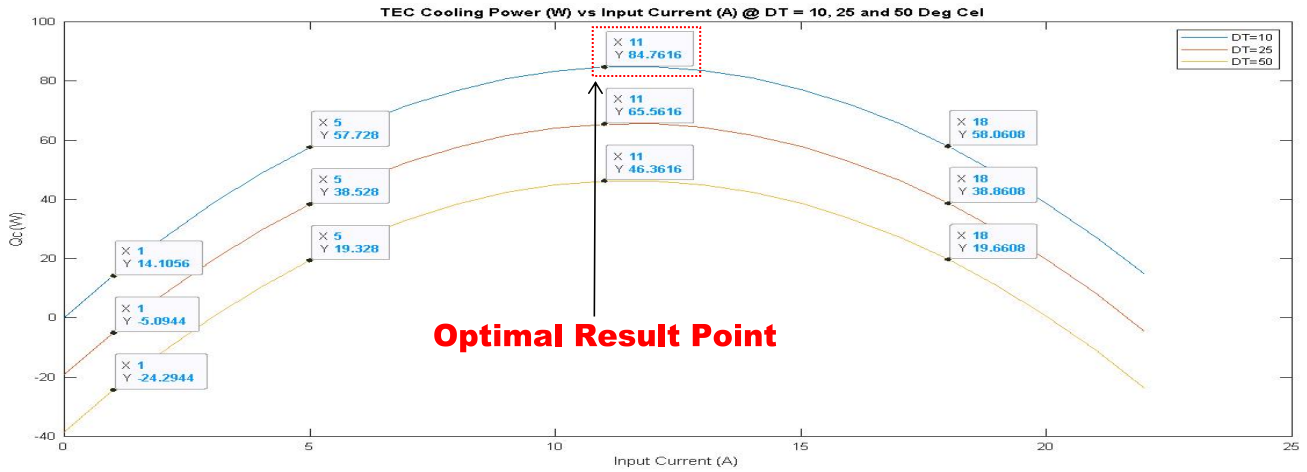

Figure 3.9: TEC Q_c (W) vs I (A) @ ΔT = 10, 25 and 50°C

Figures 3.8 and 3.10 depict that Q_c is inversely proportional to ΔT at various values of input current I. As can be seen, the cooling power or heat absorbed on TEC cold side Q_c, is maximum at 81.1W when ΔT is minimum @ 5°C and at maximum I of 11.53A. Q_c increases with I up to optimally at ~11.53A.

Akin to Figures 3.8 and 3.9, the reason is also due to Joule heating and as well the Second Law of Thermodynamics (entropy). The Q_c and ΔT optimal results point are highlighted in red as shown.

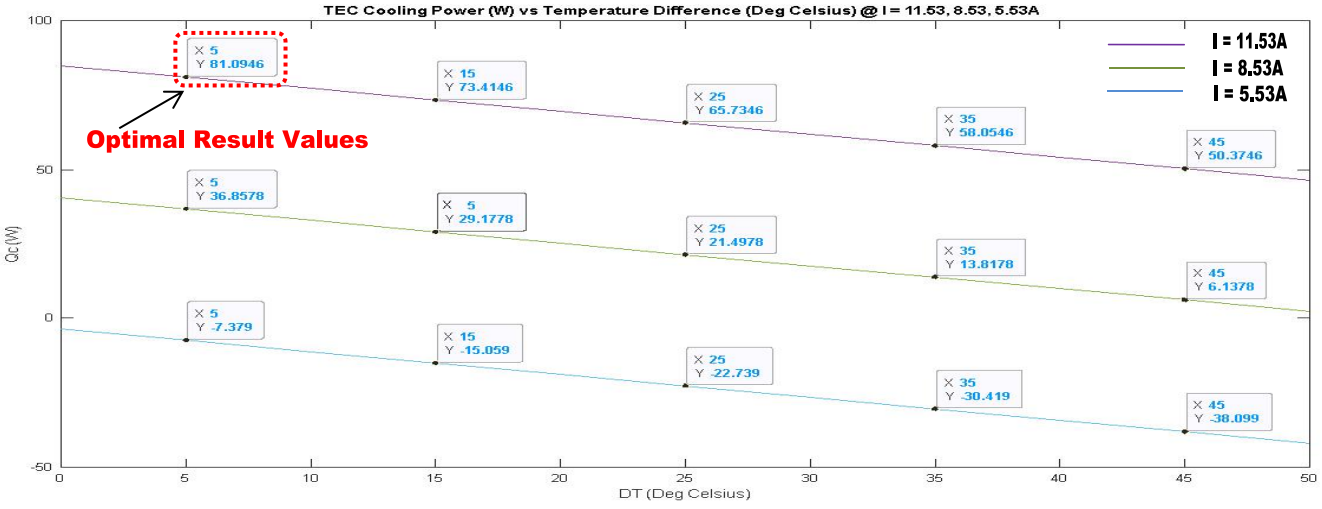

Figure 3.10: TEC Q_c (W) vs ΔT °C @ I = 11.53, 8.53 and 5.53A

Figure 3.11 demonstrates how *CoP* like Q_c; increases with decreasing ΔT and with increasing I up to 2A @ ΔT = 20°C and starts to decrease as I increases henceforth until Q_c hits 0W. The optimal result is highlighted in red. The reason is akin to Figures 3.8 and 3.10 – that is, because of Ohmic heating and as well the Second Law of Thermodynamics − simply put, heat flows from a hotter to a colder surface.

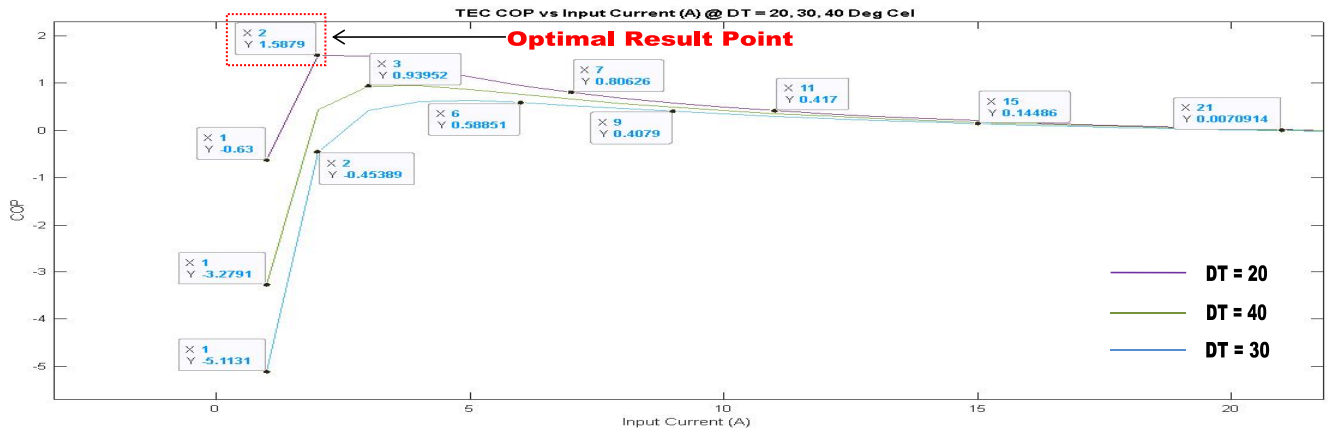

Figure 3.11: TEC *CoP* vs *I* (A) @ ΔT = 20, 30 and 40°C

Figures 3.9 – 3.11 are respectively compared with Figures 3.12a – 3.12c to validate the TEC modelling and as evident, the respective results of each figure correlated that of Figure 3.12.

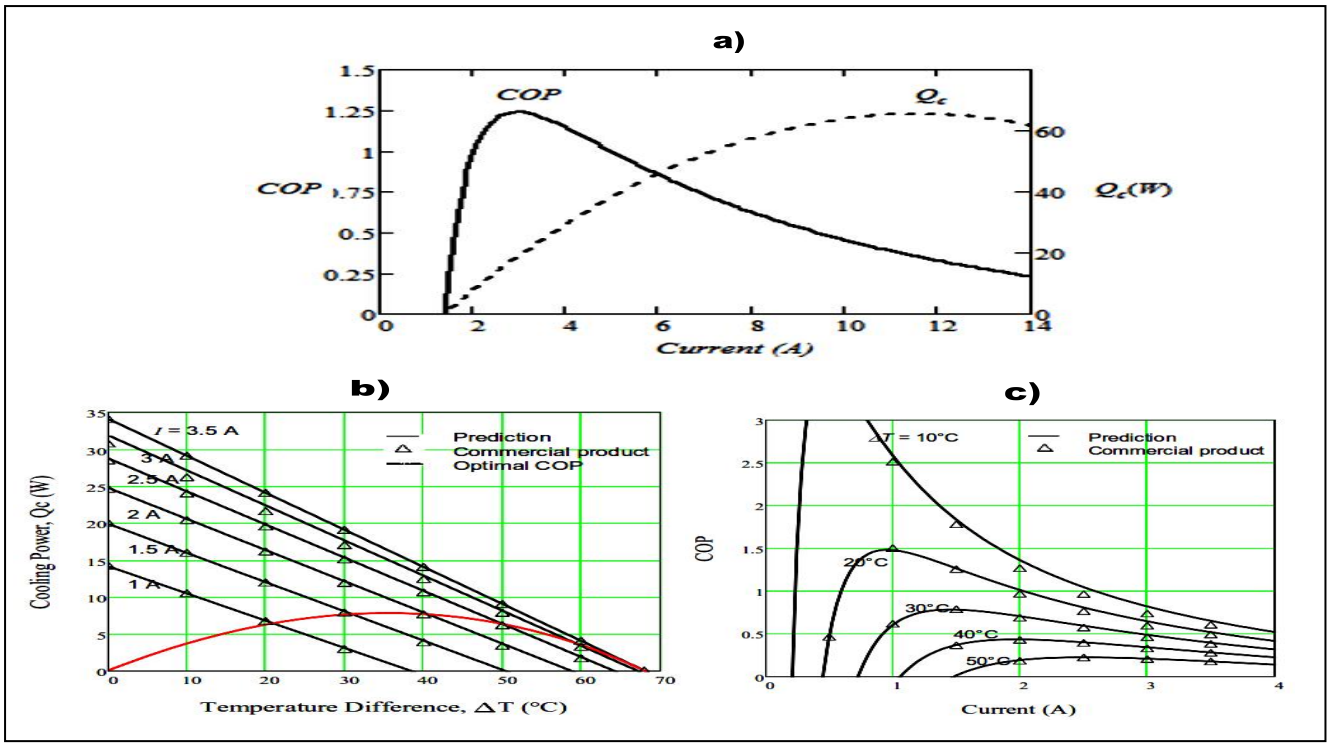

Figure 3.12: Mathcad TEC results a) Q_c/*CoP* vs *I*; b) Q_c vs ΔT & c) *CoP* vs *I* (adapted from Lee, 2016) used to validate my Matlab TEC

In summary, to get maximum cooling power (Q_c) and maximum *CoP* from a TEC, ΔT must be minimum and *I* should be increased until it has no positive effect on Q_c and the *CoP*. Represented in Figures 3.7 and 3.8 are summarily this particular research scientific contributions.

3.3.5 Research Scientific Contributions

The research is abridged here and its importance in addition to the findings already pictured in Section 3.3.3 are herein highlighted and advanced as the study scientific contributions:

- An extensive TEC steady-state maths is showcased.
- A clear comprehensive TEC(s) model is established.
- The TEC simulator is unique based on first principle.
- Multiple TECs can be simulated in various patterns.
- An efficient practical TEC(s) system can be devised.

However, the researched TEC model and mathematics have the following limitations:

- Practical realities were not factored-in, as the model focused only on theoretical TEC at unit and module levels and not at system level where other coupling factors and dynamics exist. Some of these practicalities include thermal / contact resistance heat losses when TECs are used with heat exchangers / heat-sinks / pipes. NB: TECs in practice require heat exchangers / heat-sinks for thermal management to maintain an acceptable ΔT to ensure proper and reliable operations.
- The researched simulated model has to be practically tested to correlate the mathematics and simulated analyses.

3.3.6 Summary

This section began by briefly introducing the ongoing electricity crisis in South Africa followed by the diverse renewable energy / power sources being commissioned as potential solutions. However, some of these energy/power sources are not apt for heavy loads, one of which is heat pumps – it is therefore prudent to devise energy efficient coolers and of interest is TEC – a thermoelectric device that converts DC power to cold based-on the Peltier effect. This low power DC load makes its many cooling applications suitable for use with renewable power. The mathematical analysis of thermoelectricity with emphasis on TEC(s) was investigated, developed and extensively expressed to determine how much heat absorption (Q_c) and CoP can be produced and from what optimal TEC parameters. A novel TEC model in Matlab / Simulink was implemented incorporating these advancements and the original TEC implementation was simulated by using practical TEC specifications from various TECs manufacturers and the generated results affirmed that, to get maximum cooling power (Q_c) and CoP from TECs, ΔT must be lowest and I should be increased until it has no affirmative effect on Q_c. These results were analysed in consistency with information published in diverse scholarly TECs articles, books and datasheets. Highlights of the study were asserted as the scientific contributions to conclude the research. The recommendation is to practically implement the research findings to correlate the TEC simulated and mathematical analyses, whereby the TEC(s) shall be used with FCs to efficiently generate cold from DC power in a larger combined cooling, heating and power (CCHP) system.

CHAPTER 4

TEG and TEC with Heatsinks Modelings and Simulations: Design, Results and Interpretation

4.1 Overview

In Chapter 3, I advanced thermoelectricity as an alternative energy option in a bid to alleviate the ongoing South Africa electrical energy crisis and with respect to the research problem of inefficient energy conversion. The focus in Chapter 3 was to establish a theoretical foundation to easily study thermoelectricity parameters and their operations using simulated models done with Matlab / Simulink. However, in practice, thermoelectricity can not function well without heatsinks / heat exchangers − which are required to dissipate excessive heat and also to maintain a safe temperature difference across the TEG and TEC. Moreover, adding heatsinks / heat-exchangers add thermal resistance which further decrease the TEG and TEC efficiencies as well the output / cooling powers, instead of increasing them. This issue must be addressed; therefore, this chapter develops further the theoretical models, taking now into considerations a physical implementation of TEG and TEC including the addition of heatsinks.

With respect to the research problem which revolves around inefficient energy conversion, thermoelectricity as indicated earlier, is an electrical and thermal effects, therefore both the electrical and thermal aspects must be examined to better its efficiency which is related to its output power. While the simulated models in Chapter 3 focused on its electrical theoretical operations, Chapter 4 focuses on the practical electrical and thermal operations when heatsinks are added on both sides of a TEG/TEC − when TEG devices are applied to harvest and convert waste heat to DC power and TEC devices to provide cooling as well as heating. However, the added heatsinks unfortunately add thermal resistances on both sides of the TEG and TEC, which resist the rate of heat absorption on the TEG hot side and TEC cold side, as well as resist the rate of heat release on the TEG cold side and TEC hot side.

Various techniques have been used to address this issue and this chapter develops the technique based on dimensional analysis and is mathematically developed, modeled and finally simulated using Matlab and Simulink. This section presentation is adapted from my two unique articles listed below − in which the first article focuses on TEG with heatsinks and the second article focuses on TEC with heatsinks.

- Bayendang, N.P., Kahn, M.T. & Balyan, V. 2021. Simplified thermoelectric generator (TEG) with heatsinks modeling and simulation using Matlab and Simulink based-on dimensional analysis. *AIMS Energy*, 9(6): 1213-1240. http://dx.doi.org/10.3934/energy.2021056.

- Bayendang, N.P., Kahn, M.T. & Balyan, V. 2021. Simplified thermoelectric cooler (TEC) with heatsinks modeling and simulation using Matlab and Simulink based-on dimensional analysis. *AIUE Conference 2021: 2nd Energy and Human Habitat Conference*, Cape Town, South Africa, 1-8. http://dx.doi.org/10.2139/ssrn.3900757.

4.2 Simplified Thermoelectric Generator (TEG) with Heatsinks Modeling and Simulation using Matlab and Simulink based-on Dimensional Analysis

Energy sustainability is becoming paramount today, with South Africa by and large Africa being no exceptions, considering the rampant electricity outages. This section dwells on clean alternative energy rooted in thermoelectricity with focus on TEG with heatsinks. While theoretically a modeled TEG functions without heatsinks, in practice, a TEG needs heat-exchangers or heatsinks to properly work but heatsinks present another problem − thermal resistance, which affects a TEG power output and efficiency and thus, must be addressed. Consequently, a TEG with heatsinks model based-on dimensional analysis using Matlab and Simulink is investigated. My research unique contributions are i) analytical formulas derivation for the TEG dimensionless hot and cold sides temperature and by introducing and applying a new dimensionless parameter, the temperature difference (DT_s) ii) further simplifications of these novel TEG dimensionless hot and cold sides temperature analytical formulas to obtain new, optimal, simpler and simplest forms and iii) a TEG with heatsinks Matlab / Simulink theoretical model that employs the simplified dimensional analysis. With this model, a TEG with heatsinks parameters of interest can be simply simulated to variously determine the analytical, numerical and graphical results with optimal options, before executing a practical implementation.

4.2.1 Introduction

Indicated in Van der Walt (2017), South Africa has pledged its commitments to become a carbon reduced and green economy system, by considering a mixture of energy sources to secure energy sustainability. Upon ratifying the Paris agreement on climate change, renewable energy and energy efficiency consolidations as well as the regulatory policies are developed and continuously fine-tuned taking into cognizance the current energy dynamics − the intermittent electrical blackouts as a result of more pressure on the national grid due to increase demands that the Eskom utility is struggling to sustain because of incompetent power stations that can not handle the full load demands. In this regard, there is necessity and increasing demand for renewable energy to supplement and stabilize the unstable national grid, as well as for private use. These circumstances, warrant my research for an alternative energy rooted in thermoelectricity, focusing on basic home/commercial energy sources and energy efficient loads. TEGs convert heat to DC power, whereas their dual TECs, reversibly converts DC power to cold and heat. If TEGs and TECs are properly designed, both can be relatively energy efficient and helpful for essential domestic energy use such as low-voltage DC power, lighting, heating and cooling. Theoretical frameworks for both TEG and TEC were comprehensively presented in Bayendang *et al.* (2020c) and Bayendang *et al.* (2020d) respectively; notwithstanding, both fell short of practical aspects − which this study articulates next and as well in Bayendang *et al.* (2021c).

In Lee (2013), Lineykin *et al.* (2014) and Melnikov *et al.* (2017), thermoelectricity or thermoelectric (TE) devices (TEGs and TECs), require heatsinks or heat-exchangers to physically and reliably function and maintain a working temperature difference on the TEG and TEC hot and cold sides and most significantly to discharge the internal heat resulting from Joule heating cause by the current flowing through the TEG / TEC. This heating will become excessive if not properly managed and will consequently cause inefficiency (change in entropy − heat flow will change direction) and can as well damage the TEG and TEC as a result of over-heating − which will melt the thermoelectric devices p-n thermocouples solder joints. The inclusion of heatsinks as a solution to alleviate this over-heating practical limitations in thermoelectric devices, unfortunately as well add / increase the TEGs and TECs hot and cold sides thermal resistances which then oppose the heat flow, hence making the TE devices inefficient.

To circumvent this thermal resistance problem resulting from adding heatsinks / heat-exchangers, various approaches have been investigated; including Lee (2013) − whereby thermal resistance was converted to convection conductance using dimensional analysis, Lineykin *et al.* (2014) − in which a TEG with heatsink for waste energy harvesting was analysed and optimised as a Thevenin equivalent circuit, Melnikov *et al.* (2017) − whereby dimensionless model of a TEC functioning at real heat transfer state was investigated, Li *et al.* (2015) − in which multi-physics simulations were conducted to examine the thermal and electric performance of a TEG module sand-witched between hot and cold blocks, Casano and Piva (2012) − whereby a parametric thermal analysis of TEG performance was done using dimensional analysis, Dos Santos Guzella (2021) − numerical simulation and performance analysis of a TEC based-on the lattice Boltzmann method was researched, Hao *et al.* (2021) − multi-parameters analysis and optimization of a typical TEC with dimensional analysis was studied, Lu *et al.* (2018) − thermal resistance matching for TEC systems was investigated, Chen *et al.* (2000) − herein an optimal design of a multi-couple TEG was examined, Lineykin and Ben-Yaakov (2006) − a graphical approach was employed to design TEC systems, Hubbard *et al.* (2020) − demonstrated electron-transparent TEC using nano-particles and condensation thermometry, He *et al.* (2016) − researched optimal heat-exchanger in different automobile exhaust temperatures for TEG system using dimensional analysis and Bayendang *et al*. (2021b) − simplified TEC with heatsinks based-on dimensional analysis using Matlab / Simulink with derivation of novel analytical formulas. From the reviewed studies, the dimensional analysis technique, especially the unique and practical approach presented in Lee (2013) to improve TE devices efficiency when used with heatsinks, is of interest and this study with keen focus on TEG as exemplified in Figure 4.1, applies and further develops the dimensional analysis, by now employing a simplified Matlab and Simulink implementation.

Articulated next is the TEG with heatsinks applicable maths with emphasis on the novel analytical TEG hot and cold sides dimensionless temperatures formulas I derived, as well as the optimal simplifications relative to the shortcomings of the TEG hot and cold sides dimensionless temperatures closed-form formulas presented in Lee (2013). This is then proceeded with the TEG with heatsinks simulator easy user interface modeled with Matlab / Simulink and thereafter the research results are presented, followed by the results discussions as well as validations to conclude the study.

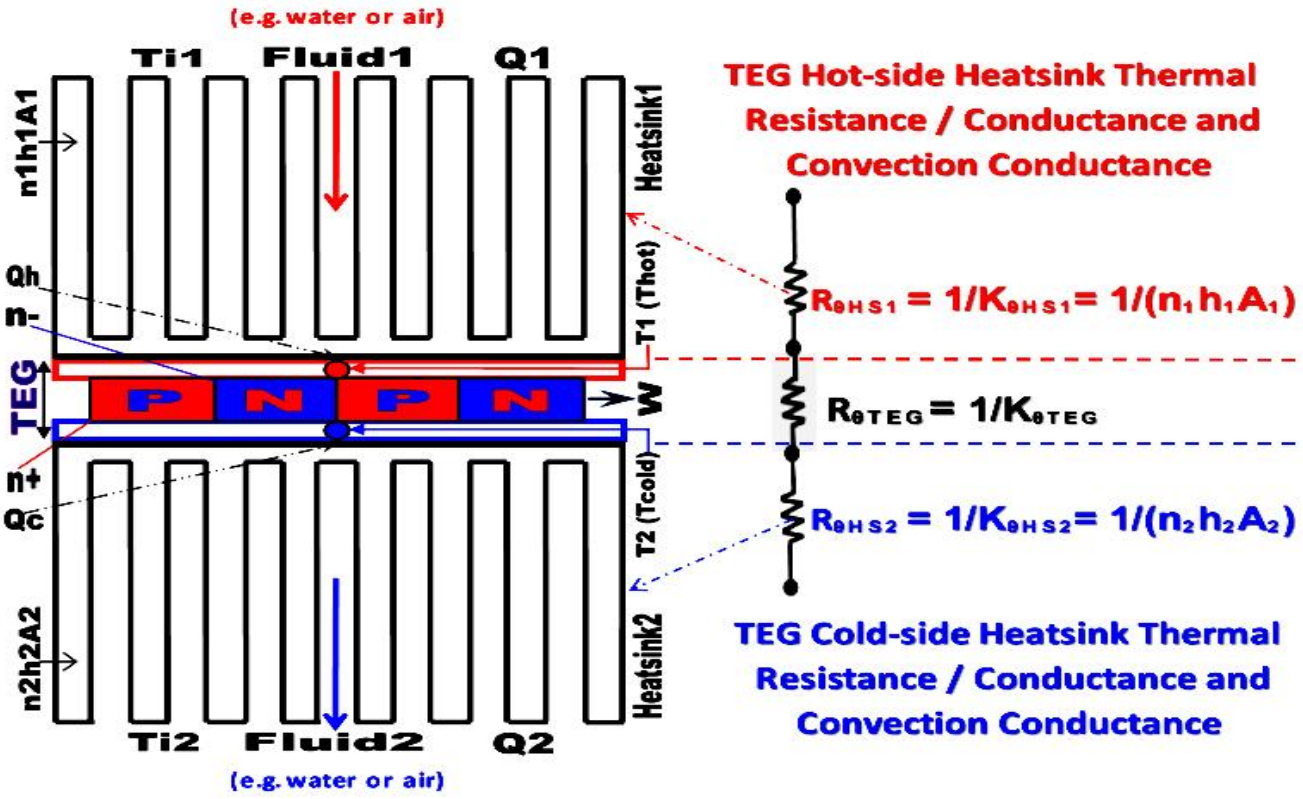

Figure 4.1: TEG with heatsinks on its hot and cold sides (adapted from Lee, 2013)

4.2.2 TEG with Heatsinks Applicable Mathematics

The relevant mathematics for a TEG with heatsinks is expressed herein and then, I introduce the new dimensionless temperature difference (DT_s) − which is employed to simplify the apt approach presented by Lee (2013). Dimensional analysis is simply a technique that enables parameters with the same unit to be normalized within a minimum and maximum value, thus making them dimensionless and easier to work with, without worrying about their dimensions or unit of measurement. Nonetheless, novel in Lee (2013) is the conversion of TEG heatsinks thermal resistance to their convection conductance − this optimization technique gets rid of the TEG heatsinks thermal resistance which are harder to work with, in place of the TEG heatsinks fluid convection conductance which are related to the TEG heatsinks fluid temperature and physically simpler to work with. This approach is pragmatic and its implicit mathematical analysis is articulated in details in what follows.

4.2.2.1 TEG with Heatsinks General Heat Flow Equations

Herein, the TEG heat equations, the heatsinks thermal resistance, their corresponding thermal conductance and convection conductance links are constituted as follows:

$$Q_1 = K_1(T_{i1} - T_1) \quad \text{(W)} \tag{4.1}$$

$$Q_2 = K_2(T_2 - Ti_2) \quad \text{(W)} \tag{4.2}$$

with Q_1 and Q_2 being respectively the heat flow rates on the TEG heatsinks hot and cold sides, K_1 and K_2 are respectively the TEG hot and cold sides heatsinks thermal conductance, T_{i1} and T_{i2} are respectively the temperatures of the heatsinks fluid on the TEG hot and cold sides and lastly T_1 and T_2 are respectively the TEG hot and cold sides p-n junction temperature. It is worthy of note that thermal resistance is the reciprocal of thermal conductance (K) − which corresponds to the convection conductance (ΠhA) and thus, equations (4.1) and (4.2) in respect of the convection conductance, can be re-written as:

$$Q_1 = \Pi_1 h_1 A_1(T_{i1} - T_1) \quad \text{(W)} \tag{4.3}$$

$$Q_2 = \Pi_2 h_2 A_2(T_2 - T_{i2}) \quad \text{(W)} \tag{4.4}$$

with Π_1 being the fin efficiency of heatsink1 (on the TEG hot-side), h_1 is the convection coefficient of heatsink1 and A_1 is the total surface area of heatsink1. Similarly, Π_2 is the fin efficiency of heatsink2 (on the TEG cold-side), h_2 is the convection coefficient of heatsink2 and lastly A_2 is the total surface area of heatsink2. The TEG standard ideal heat flow equations are defined as:

$$Q_h = n[(SIT_1) + (K\Delta T)] - 0.5I^2R \quad \text{(W)} \tag{4.5}$$

$$Q_c = n[(SIT_2) + (K\Delta T)] + 0.5I^2R \quad \text{(W)} \tag{4.6}$$

where Q_h is the heat absorbed on the TEG hot side, n is the number of p-n junction thermocouples used in the TEG, S being the Seebeck coefficient, I being the output current from the TEG, K is the thermal conductance (computed as ak/L, with a being the area of the TEG p-n junction thermocouple, k is the TEG thermocouple p-n junction thermal conductivity and L is the TEG thermocouple p-n junction length), $\Delta T=T_1-T_2$ is the temperature difference between the TEG hot and cold sides, $R=nr$ is the TEG module resistance, with r being the resistance of the TEG thermocouple p-n junction and Q_c is the heat released on the TEG cold side. The three terms on the right side of equations (4.5) and (4.6) are the Seebeck, Fourier and Ohmic terms respectively with S, K and R considered as temperature invariant. Now, taking into account the energy balance of the TEG with heatsinks system, equations (4.1), (4.3) and (4.5) are respectively equivalent now to equations (4.2), (4.4) and (4.6) − which boils down to (with parameters T_1, T_2 and I being the unknowns):

$$Q_1 = Q_h = K_1(T_{i1} - T_1) = \eta_1 h_1 A_1 (T_{i1} - T_1) = n[(SIT_1) + (K\Delta T)] - 0.5I^2R \quad \text{(W)} \quad (4.7)$$

$$Q_2 = Q_c = K_2(T_2 - T_{i2}) = \eta_2 h_2 A_2 (T_2 - T_{i2}) = n[(SIT_2) + (K\Delta T)] + 0.5I^2R \quad \text{(W)} \quad (4.8)$$

In accordance with Lee (2013), TEG with heatsinks (HS) is optimised by defining in what follows, the dimensionless parameters with regards to fluid 2 (water or air on the TEG cold side of heatsink2) and because the optimization is rendered dimensionless relative to fluid 2, fluid 2 temperature (T_{i2}) and convection conductance must be given initially.

4.2.2.2 TEG-HS Dimensionless Thermal Conductance (N_k)

This is the ratio of the thermal conductance K and the convection conductance ηhA in fluid 2, deduced as:

$$N_k = K / \eta hA = (ak/l) / \eta_2 h_2 A_2 \quad (4.9)$$

4.2.2.3 TEG-HS Dimensionless Convection (N_h)

This is the ratio of fluid 1 and fluid 2 convection conductances, denoted as:

$$N_h = \eta_1 h_1 A_1 / \eta_2 h_2 A_2 \quad (4.10)$$

4.2.2.4 TEG-HS Dimensionless Current (N_i)

$$N_i = SI / K = SI / (ak/l) = ZT_{i2}(T_{s1} - T_{s2})/(R_r + 1) \quad (4.11)$$

4.2.2.5 TEG Dimensionless Temperatures (T_{s1}, T_{s2}, T_i and DT_s)

TEG dimensionless temperatures are presented as:

T_1 dimensionless temperature: $T_{s1} = T_1 / T_{i2}$ (4.12)

T_2 dimensionless temperature: $T_{s2} = T_2 / T_{i2}$ (4.13)

Fluids dimensionless temperature: $T_i\ (T_{is}) = T_{i1} / T_{i2}$ (4.14)

Dimensionless temperature difference $DT_s = T_{s1} - T_{s2} = \Delta T / T_{i2}$ (4.15)

4.2.2.6 TEG-HS Dimensionless Heat Absorbed (Q_{s1})

$$Q_{s1} = Q_1 / \eta_2 h_2 A_2 T_{i2} \quad (4.16)$$

4.2.2.7 TEG-HS Dimensionless Heat Released (Q_{s2})

$$Q_{s2} = Q_2 / \eta_2 h_2 A_2 T_{i2} \quad (4.17)$$

4.2.2.8 TEG Dimensionless Output Power (P_{out*} or P_{os})

$$P_{out*} = P_{out} / \eta_2 h_2 A_2 T_{i2} \quad (4.18)$$

$$P_{os} = P_{out*} = Q_{s1} - Q_{s2} \quad (4.19)$$

where P_{out} is the TEG output power (i.e. power delivered to the electrical load).

4.2.2.9 TEG Dimensionless Output Voltage (V_{os} or N_v)

$$N_v = V / nST_{i2} \tag{4.20}$$

$$N_v = V_{os} = P_{os} / N_i N_k \tag{4.21}$$

4.2.2.10 TEG Dimensionless Conversion Efficiency (Eff^*)

$$Eff^* = P_{os} / Q_{s1} \tag{4.22}$$

NB: TEG conversion efficiency by default is dimensionless. The mentioned of dimensionless here in front conversion efficiency is just for emphasis with respect to the dimensionless technique applied.

4.2.2.11 TEG-HS Dimensionless Heat Absorbed (Q_{s1}) in terms of T_{s1}

$$Q_{s1} = N_h (T_i - T_{s1}) \tag{4.23}$$

4.2.2.12 TEG-HS Dimensionless Heat Released (Q_{s2}) in terms of T_{s2}

$$Q_{s2} = T_{s2} - 1 \tag{4.24}$$

4.2.2.13 TEG-HS Dimensionless Internal Electrical Resistance (R_r)

$$R_r = R_L / R_t \tag{4.25}$$

where R_L is the electrical load connected to the TEG output and R_t is the TEG module internal electrical resistance. NB: R_r is denoted as *rr* in the simulator in Figure 4.2.

4.2.2.14 TEG Dimensionless Temperatures (T_{s1} and T_{s2}) Formula

Using the dimensionless formulas of (4.9) - (4.14); equations (4.3) - (4.6) reduce to the following two expressions of (4.26) and (4.27) having five unknowns that must be found for T_{s1} and T_{s2} in terms of five independent dimensionless parameters of ZT_{i2} (dimensionless merit figure at T_{i2}), T_i, N_h, N_k and R_r.

$$N_h(T_i - T_{s1})/N_k = ((ZT_{i2}(T_{s1} - T_{s2})T_{s1}) / (R_r+1)) - (((ZT_{i2}(T_{s1} - T_{s2})^2)) / (2(R_r+1)^2)) + (T_{s1} - T_{s2}) \tag{4.26}$$

$$(T_{s2} - 1)/N_k = ((ZT_{i2}(T_{s1} - T_{s2})T_{s2}) / (R_r+1)) + (((ZT_{i2}(T_{s1} - T_{s2})^2)) / (2(R_r+1)^2)) + (T_{s1} - T_{s2}) \tag{4.27}$$

As seen, equations (4.26) and (4.27) are clumsy and unsolved further in Lee (2013) in terms of T_{s1} and T_{s2}; thus, there are no exact analytical equations to directly compute T_{s1} and T_{s2}. Equations (4.26) and (4.27) are awkward expressions of T_{s1} and T_{s2}, which can only be solved by using numerical analysis; as a result, a numerical method using iterations, tables, graphs and approximations were employed by Lee (2013), as well as using a computer programme (NEDO) was further recommended. Consequently, because expressions (4.26) and (4.27) could not be simplified further by Lee (2013), T_{s1} and T_{s2} could only be expressed as in (4.28) and (4.29) as functions of ZT_{i2}, T_i, N_h, N_k and R_r for solving numerically.

This entire numerical process is cumbersome to determine T_{s1} and T_{s2}; thus, this limitation motivated my research to seek for an analytical and better solution which is asserted next.

$$T_{s1} = f\,(ZT_{i2},\ T_i,\ N_h,\ N_k,\ R_r) \tag{4.28}$$

$$T_{s2} = f\,(\ ZT_{i2},\ T_i,\ N_h,\ N_k,\ R_r) \tag{4.29}$$

I now introduce equation (4.15) − the dimensionless temperature difference DT_s and is used to replace $T_{s1}-T_{s2}$ in equations (4.26) and (4.27) to give now formulas (4.30) and (4.31) as:

$$N_h(T_i-T_{s1})/N_k = ((ZT_{i2}(DT_s)T_{s1}) / (R_r+1)) - ((((ZT_{i2}(DT_s)^2)) / (2(R_r+1)^2)) + (DT_s) \tag{4.30}$$

$$(T_{s2}-1)/N_k = ((ZT_{i2}(DT_s)T_{s2}) / (R_r+1)) + ((((ZT_{i2}(DT_s)^2)) / (2(R_r+1)^2)) + (DT_s) \tag{4.31}$$

As instantly seen, formulas (4.30) and (4.31) can respectively and directly be solved for T_{s1} and T_{s2} independently in terms of the five dimensionless parameters ZT_{i2}, T_i, N_h, N_k and R_r. Now, making T_{s1} and T_{s2} subjects of their respective formulas (4.30) and (4.31), I derived new analytical equations for T_{s1} and T_{s2} as given in formulas (4.32) and (4.33) as:

$$T_{s1} = (N_kZT_{i2}DT_s^2 - 2N_kDT_sR_r^2 - 4N_kDT_sR_r - 2N_kDT_s + 2N_hT_iR_r^2 + 4N_hT_iR_r + 2N_hT_i) / (2(R_r + 1)(N_h + N_hR_r + DT_sZT_{i2}N_k)) \tag{4.32}$$

$$T_{s2} = (N_kZT_{i2}DT_s^2 + 2N_kDT_sR_r^2 + 4N_kDT_sR_r + 2N_kDT_s + 2R_r^2 + 4R_r + 2) / (2(R_r + 1)(R_r - DT_sN_kZT_{i2} + 1)) \tag{4.33}$$

Furthermore, by adding formulas (4.26) and (4.27) or formulas (4.30) and (4.31); we can easily get rid of the non-linear quadratic terms and by re-arranging and solving for T_{s1} and T_{s2}, I further derived a simpler novel analytical formula for T_{s1} and T_{s2} as follows:

$$N_h(T_i-T_{s1})/N_k + (T_{s2}-1)/N_k = (ZT_{i2}DT_sT_{s1}) / (R_r+1) + (ZT_{i2}DT_sT_{s2}) / (R_r+1) + DT_s + DT_s \tag{4.34}$$

$$N_h(T_i-T_{s1})/N_k - ((ZT_{i2}DT_sT_{s1}) / (R_r+1)) - DT_s = ((ZT_{i2}DT_sT_{s2}) / (R_r+1)) + (T_{s2}-1)/N_k + DT_s \tag{4.35}$$

Now, re-arranging equation (4.34) gives equation (4.35), such that the left hand side (LHS) of equation (4.35) constitutes T_{s1} without term T_{s2} and the right hand side (RHS) of equation (4.35) constitutes T_{s2} without term T_{s1}. Finally, the LHS and RHS can both be solved independently by equating each to zero, to easily obtain T_{s1} in terms of ZT_{i2}, T_i, N_h, N_k, R_r and DT_s and similarly obtain T_{s2} in terms of ZT_{i2}, N_k, R_r and DT_s to give now simpler formulas (4.36) and (4.37) as follows:

$$T_{s1} = (N_hT_i - DT_sN_k)(R_r + 1) / (N_h + N_hR_r + DT_sN_kZT_{i2}) \tag{4.36}$$

$$T_{s2} = (DT_sN_k + 1)(R_r + 1) / (R_r - DT_sN_kZT_{i2} + 1) \tag{4.37}$$

As noticeable, T_i and N_h are absent in equations (4.33) and (4.37), meaning these two dimensionless parameters don't affect T_{s2} directly but only through DTs and T_{s1}; thus, making this approach insightful.

Finally, I furthermore obtained the simplest optimal analytical relationship to calculate T_{s1} and T_{s2} by utilizing a set of optimal numerical values from Lee (2013) as; $ZT_{i2}=1$, $T_i=2.6$, $N_h=1$, $N_k=0.3$, $R_r=1.7$ and $DT_s = 0.8$ and substituting in equation (4.35) and solving to get equations (4.38) and (4.39) as:

$$T_{s1} = 41T_{s2} / 49 + (36/35) \tag{4.38}$$

$$T_{s2} = 49(T_{s1} - (36/35)) / 41 \tag{4.39}$$

It should be noted that, the $ZT_{i2}=1$, $T_i=2.6$, $N_h=1$, at $N_k=0.3$, $R_r=1.7$ and now $DT_s = 0.8$ optimal values are not arbitrarily chosen but specifically deduced optimal values, that are inter-linked to each other and obtained under the same specified operating conditions. Furthermore, parameters ZT_{i2}, T_i and N_h are initially provided or can be calculated from a chosen TEG-HS operating parameters and finally the optimal combinations of N_k, R_r and now DT_s, can all be found from the above specified dimensionless equations. NB: other optimal values set can be put in (4.35) to get new (4.38) & (4.39).

Now, as validation, I put the same set of optimal values of $ZT_{i2}=1$, $T_i=2.6$, $N_h=1$, $N_k=0.3$, $R_r=1.7$ and $DT_s=0.8$ to finally determine, compare and verify the T_{s1} and T_{s2} values, using my newly introduced and now called simple, simpler and simplest analytical T_{s1} and T_{s2} formulas − respectively using equations (4.32) and (4.33), equations (4.36) and (4.37) and equations (4.38) and (4.39) as follows:

Using the simple formulas /equations (4.32) and (4.33), T_{s1} and T_{s2} are optimally directly computed as:

$$T_{s1} = 2.1794$$
$$T_{s2} = 1.3754$$

Using the simpler formulas/equations (4.36) and (4.37), T_{s1} and T_{s2} are optimally directly computed as:

$$T_{s1} = 2.1673$$
$$T_{s2} = 1.3610$$

As clearly evident, both these simple and simpler optimal solutions are approximately the same. We can then also easily verify both using equations (4.38) and (4.39) to get the simplest solution, by substituting T_{s2} to calculate T_{s1} or vice versa. As apparent, I've now introduced three novel analytical sets of formulas to easily find T_{s1} and T_{s2} without going through the cumbersome numerical process. With T_{s1} and T_{s2} now deduced, the other dimensionless parameters and ultimately all their physical dimensional parameters can be worked out as presented in the formulas above obtained from Lee, 2013.

4.2.3 TEG with Heatsinks Simulated Model

The relevant TEG with heatsinks mathematics based on dimensional analysis was articulated in Section 4.2.2 and the formulas for T_{s1} and T_{s2} were developed and expressed analytically in respect of the now six independent parameters ZT_{i2}, T_i, N_k, N_h, R_r and DT_s. T_{s1} and T_{s2} were furthermore optimally simplified and validated in terms of T_{s1} and T_{s2} using equations (4.38) and (4.39). As apparent, the entire numerical as well as analytical procedures could be very tedious and as well subject to errors if manually done. In view of this, a Matlab and Simulink TEG model with heatsinks on both the TEG hot and cold sides, was then implemented using the formulas asserted in Section 4.2.2. Enclosed in the simulated TEG with heatsinks model, are the followings: the i) TEG parameters analysed in Section 4.2.2 which includes; S the Seebeck coefficient, 273.15 the absolute temperature in kelvin, T_{i1} fluid temperature of heatsink1, T_{i2} fluid temperature of heatsink2, if required the TEG configuration in series T_s and or in parallel T_p, r the TEG thermocouple p-n junction resistance, k the TEG thermocouple p-n junction thermal conductivity, ρ the TEG thermocouple p-n junction electrical resistivity, a the TEG thermocouple p-n junction area, L the TEG thermocouple p-n junction length and P_{req} the TEG total output power required, and ii) heatsinks parameters, which includes; Ab the heatsink base area, n_1 fins efficiency of heatsink1, h_1 convection coefficient of heatsink1 fluid, A_1 total area of heatsink1 with fins sides, n_2 fins efficiency of heatsink2, h_2 convection coefficient of heatsink2 fluid and A_2 total area of heatsink2 with fins sides. All these parameters can easily be input and the TEG optimal parameters value computed as pictured in Figure 4.2.

Additionally, the TEG dimensionless parameters such as; N_i the dimensionless output current, N_k the dimensionless thermal conductance, Eff^* (n_{th}) the conversion efficiency, P_{os} (W_{s1}) the dimensionless output power, T_{s1} the TEG hot-side dimensionless temperature, T_{s2} the TEG cold-side dimensionless temperature and N_v the dimensionless output voltage, can all be either manually entered (as depicted in Figure 4.2 on the left side of the TEG with heatsinks model) or computed automatically and used to finally calculate the TEG practical parameters values in SI units (as shown in Figure 4.2 on the right side of the TEG with heatsinks model). Some of the TEG physical parameters of interest that are computed include; Z the TEG figure of merit, n the TEG amount of p-n junction thermocouples, Q_h (Q_1) the TEG hot side heat absorbed, Q_c (Q_2) the TEG cold side heat released, P_o the TEG output power, T_1 (T_h) the TEG hot side temperature, T_2 (T_c) the TEG cold side temperature, R_R (R_t) the TEG internal resistance, V_o the TEG output voltage, I the TEG output current, N the total amount of TEG modules required, DT or ΔT the TEG temperature difference, QPD the TEG with heatsinks heat flux density, nhA the dimensionless convection conductance of heatsinks 1 or 2 fluid, T_{i1} and T_{i2} are fluids 1 and 2 hot and cold temperatures respectively, T_i the dimensionless fluid temperature, N_h the dimensionless

convection conductance, ZT_{i2} the dimensionless figure of merit at T_{i2}, ZTA the TEG dimensionless figure of merit at TA and V_{oc} is the TEG ideal open circuit voltage. The TEG with heatsinks normalised, maximum and effective parameters are also computed.

In terms of the aesthetics, the TEG-HS output and inputs parameters were sorted together based on their commonalities, as well as labeled and colour coded accordingly to make the TEG with heatsinks model simple to comprehend and as well user friendly.

Finally, in addition to the TEG with heatsinks numeric model computations, miscellaneous characteristics curves of some of the TEG crucial parameters of interest such as Q_{s1}, Q_{s2}, P_{os}, Eff*, T_{s1} and T_{s2}; were plotted against N_k, R_r and DT_s to graphically calculate Q_{s1}, Q_{s2}, P_{os}, Eff*, T_{s1} and T_{s2} different optimal values for i) ZT_{i2}=1, N_h=1, T_i =2.6, N_k=0.3, R_r=1.7 and DT_S = 0.8 and ii) ZT_{i2}=1, N_h=1, T_i =2.6, N_k=0.1-0.4, R_r=0.5-2 and DT_S = 0.1-1. These graphical results are in details, variously portrayed next in Figures 4.3 to 4.9.

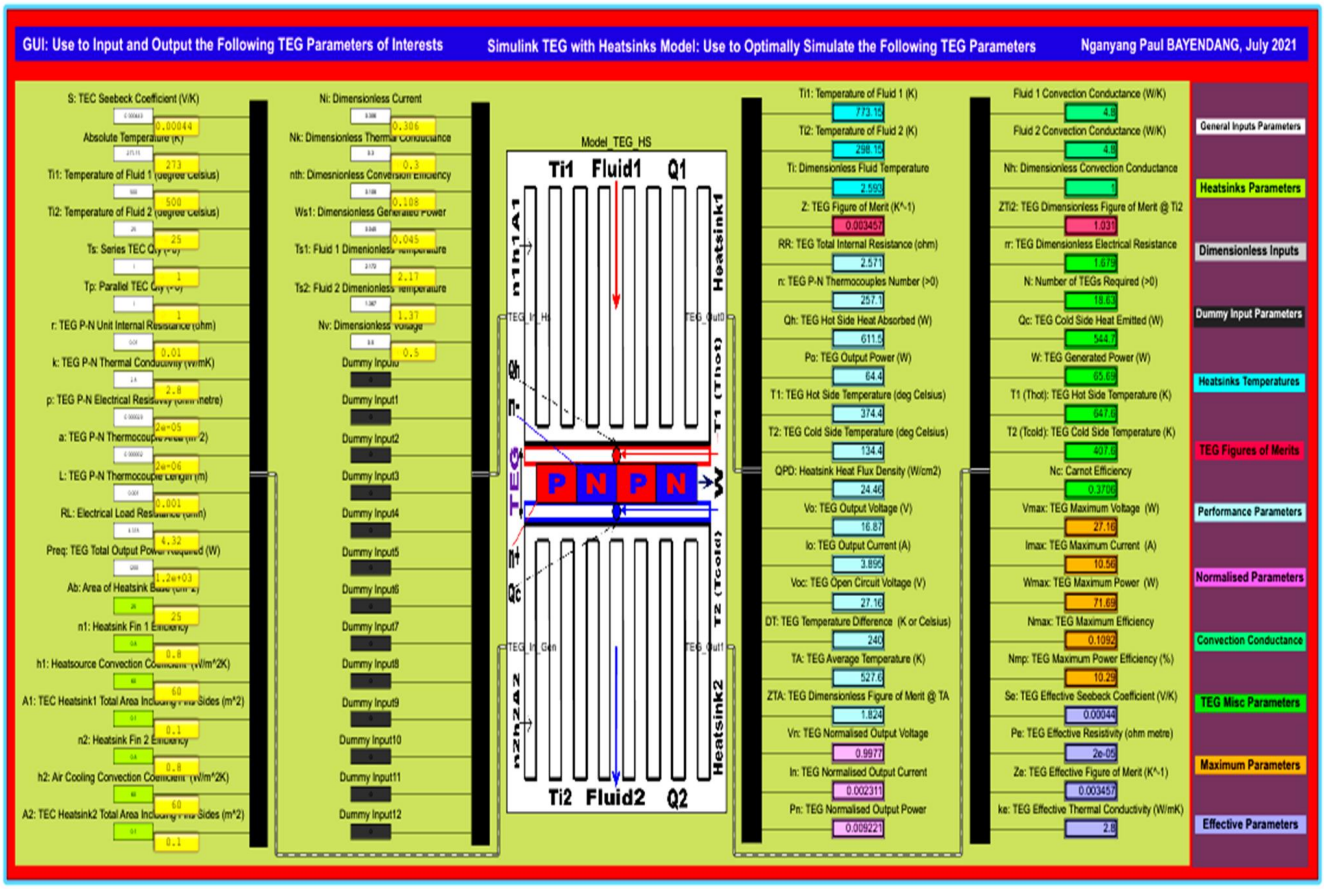

Figure 4.2: TEG with heatsinks model simulator with numeric results

4.2.4 TEG with Heatsinks Simulation Results

In Section 4.2.3, the TEG with heatsinks simulated model was presented with highlights on its various parameters and the numeric results, as summarised in Figure 4.2. These results as well as the numerous graphical results displayed extensively in what follows, are based on the novel analytical T_{s1} and T_{s2} formulas derived in Section 4.2.2. These are engaged next and various comparisons of Q_{s1}, Q_{s2}, P_{os}, T_{s1}, T_{s2} and Eff^* with different combinations of ZT_{i2}, N_h, T_i, N_k, R_r and DT_S using equations (4.32) and (4.33) as well as (4.36) and (4.37) are shown and organised as follows: i) all the figures on the left are based on using simple equations (4.32) and (4.33) T_{s1} and T_{s2} values, whereas all the figures on the right are based on using simpler equations (4.36) and (4.37) T_{s1} and T_{s2} values; ii) Figure 4.3 graphs depict Q_{s1}, Q_{s2}, P_{os}, T_{s1}, T_{s2} and Eff^* results using ZT_{i2}=1, N_h=1, T_i =2.6, N_k=0.3, R_r=0-6 and DT_S = 0.8; iii) Figure 4.4 graphs depict Q_{s1}, Q_{s2}, P_{os}, T_{s1}, T_{s2} and Eff^* results using ZT_{i2}=1, N_h=1, T_i =2.6, N_k=0.1-0.4, R_r=0-6 and DT_S = 0.8; iv) Figure 4.5 graphs depict Q_{s1}, Q_{s2}, P_{os}, T_{s1}, T_{s2} and Eff^* results using ZT_{i2}=1, N_h=1, T_i =2.6, N_k=0.05-0.5, R_r=1.7 and DT_S = 0.8; v) Figure 4.6 graphs depict Q_{s1}, Q_{s2}, P_{os}, T_{s1}, T_{s2} and Eff^* results using ZT_{i2}=1, N_h=1, T_i =2.6, N_k=0.05-0.5, R_r=0.5-2 and DT_S = 0.8; Figure 4.7 graphs depict in 3D Q_{s1}, Q_{s2}, P_{os}, T_{s1}, T_{s2} and Eff^* results using ZT_{i2}=1, N_h=1, T_i =2.6, N_k=0.05-0.5, R_r=0.2-3.2 and DT_S = 0.8; Figure 4.8 graphs depict in 3D Q_{s1}, Q_{s2}, P_{os}, T_{s1}, T_{s2} and Eff^* results with ZT_{i2}=1, N_h=1, T_i =2.6, N_k=0.3, R_r=0.2-3.2 and DT_S = 0.1-1 and Figure 4.9 graphs depict in 3D Q_{s1}, Q_{s2}, P_{os}, T_{s1}, T_{s2} and Eff^* results using ZT_{i2}=1, N_h=1, T_i =2.6, N_k=0.05-0.5, R_r=1.7 and DT_S = 0.1-1. Table 4.1 summarises the correlation of equations (4.32) and (4.33) and (4.36) and (4.37) results. Table 4.2 validates Figure 4.2.

Table 4.1: Summary of the study comparing the "simple" and "simpler" equations results

	R_r	N_k	DT_S	T_{s1}-T_{s2}	Q_{s1}	Q_{s2}	P_{os}	Eff^*	T_{s1}	T_{s2}
Using "Simple" Equations (4.32) and (4.33)	2	0.3	0.8	0.83564	0.404938	0.35942	0.045518	0.112407	2.19506	1.35942
	1.7	0.3	0.8	0.80401	0.420599	0.375429	0.0451302	0.10731	2.17944	1.37543
	1.1	0.3	0.8	0.7129	0.462515	0.424578	0.0379377	0.0820247	2.13748	1.42458
	1	0.3	0.8	0.69221	0.471429	0.436364	0.0350649	0.0743802	2.12857	1.43636
	0.5	0.3	0.8	0.54428	0.528736	0.526984	0.00175151	0.00331263	2.07126	1.52698
Using "Simpler" Equations (4.36) and (4.37)	2	0.3	0.8	0.83736	0.414815	0.347826	0.0669887	0.161491	2.18519	1.34783
	1.7	0.3	0.8	0.80637	0.432653	0.360976	0.0716775	0.16567	2.16735	1.36098
	1.1	0.3	0.8	0.71795	0.482051	0.4	0.0820513	0.170213	2.11795	1.4
	1	0.3	0.8	0.69805	0.492857	0.409091	0.0837662	0.16996	2.10714	1.40909
	0.5	0.3	0.8	0.55829	0.565517	0.47619	0.0893268	0.157956	2.03448	1.47619

Table 4.2: TEG input & output dimensionless & actual results adapted from (Lee H, 2013) to validate Figure 4.2

Compare values with values in Figure 4.2

Inputs	Dimensionless ($W^*_{n,opt}$)	Actual ($W_{n,opt}$)
$T_{\infty 1}$ = 500 °C, $T_{\infty 2}$ = 25 °C, $\Delta T_{\infty 1}$ = 475 °C	N_k = 0.3	n = 254
A = 2 mm², L = 1 mm	N_h = 1	$\eta_1 h_1 A_1$ = 4.8 W/K
η_2 = 0.8, h_2 = 60 W/m²K, A_2 = 1000 cm²	R_r = 1.7	R_L = 1.7 x n x R = 4.32 Ω
$\eta_2 h_2 A_2$ = 4.8 W/K	T^*_{∞} = 2.6	$T_{\infty 1}$ = 500 °C
Base area A_b of module = 5 cm x 5 cm	$ZT_{\infty 2}$ = 1.0	$ZT_{\infty 2}$ = 1.0
α_p = -α_n = 220 μV/K	T^*_1 = 2.172	T_1 = 374 °C
ρ_p = ρ_n = 1.0 x 10⁻³ Ωcm	T^*_2 = 1.367	T_2 = 137 °C
k_p = k_n = 1.4 x 10⁻² W/cmK	W^*_n = 0.045	W_n = 65 W
(Z = 3.457 x 10⁻³ K⁻¹)	η_{th} = 0.108	η_{th} = 0.108
(R = 0.01 Ω per thermocouple)	N_I = 0.306	I = 3.9 A
(η_1 = 0.8, h_1 = 60 W/m²K, A_1 = 1000 cm²)	N_v = 0.5	V = 16.7 V
(Power Density P_d = W_n/A_b W/cm²)	—	P_d = 2.6 W/cm²

Check colour coding with the markings on Figure 4.10

Compare values with values in Figure 4.2

Figure 4.3 graphs depict Q_{s1}, Q_{s2}, P_{os}, T_{s1}, T_{s2} and *Eff** results with ZT_{i2}=1, N_h=1, T_i =2.6, N_k=0.3, R_r=0-6 and DT_S = 0.8. It also compares the simple vs simpler equations results.

N_k=0.3: Using "simple" equations (4.32) and (4.33)

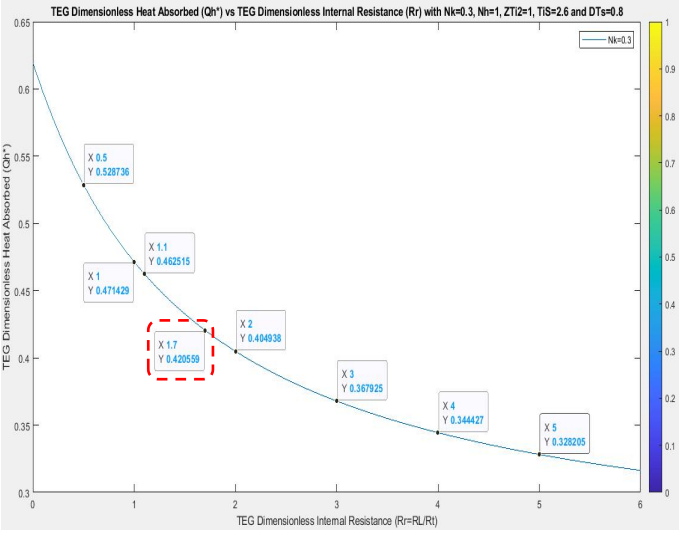

(a)

N_k=0.3: Using "simpler" equations (4.36) and (4.37)

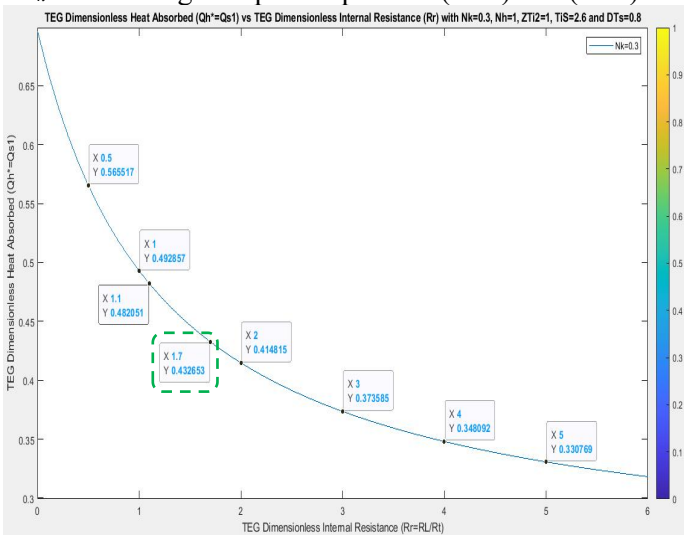

(g)

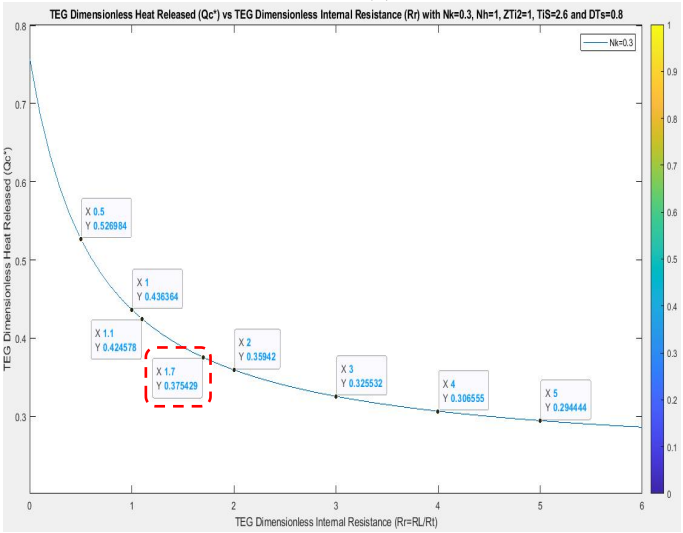

(b)

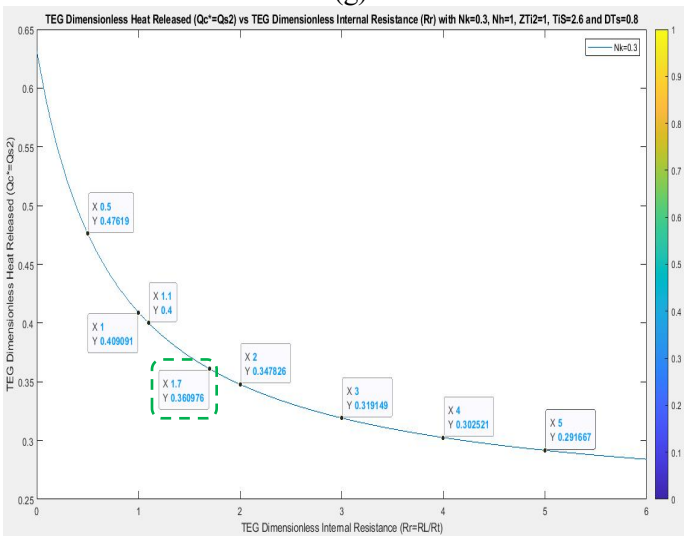

(h)

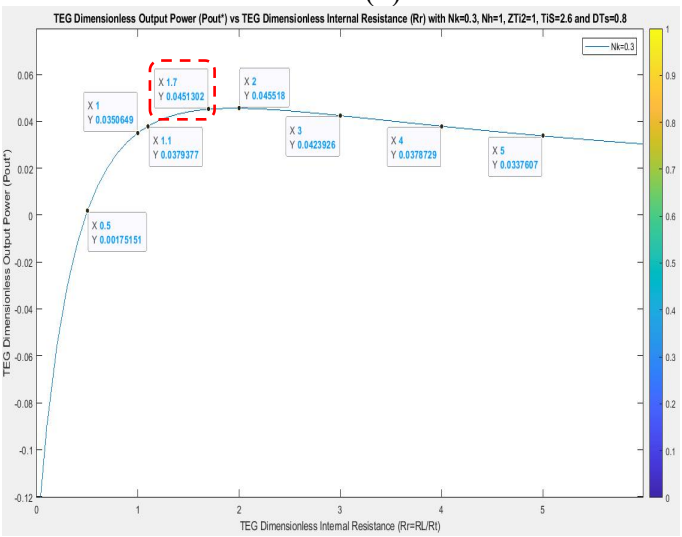

(c)

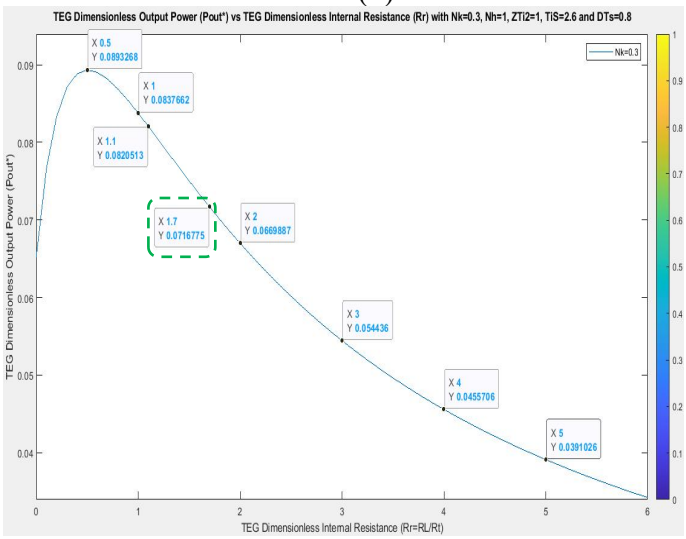

(i)

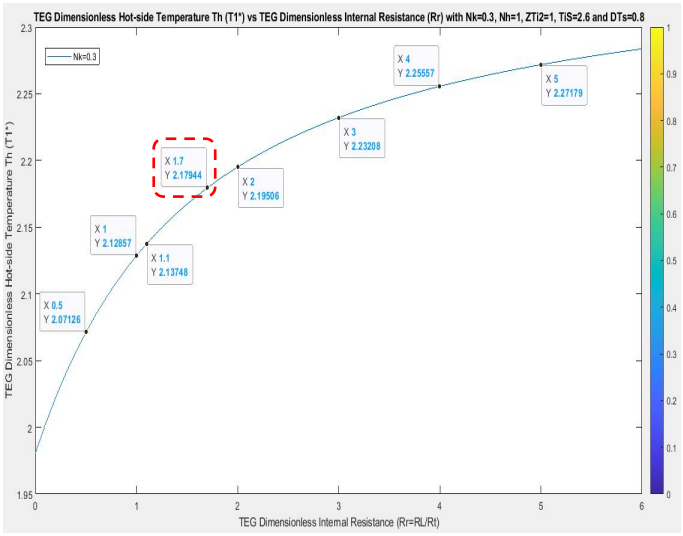

(d)

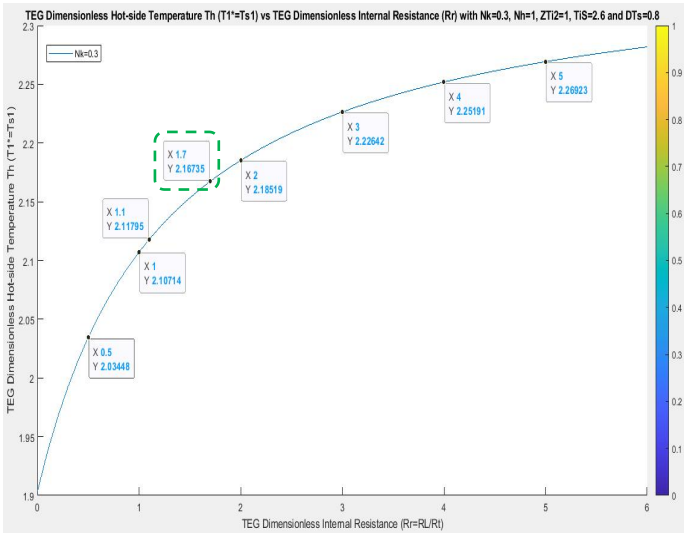

(j)

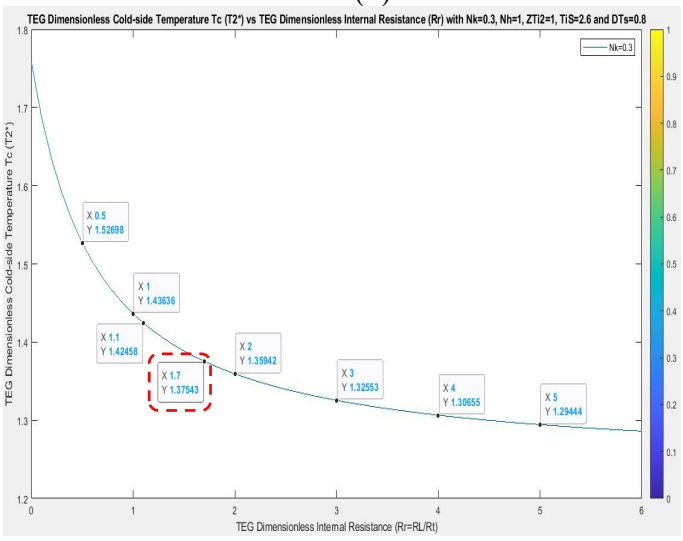

(e)

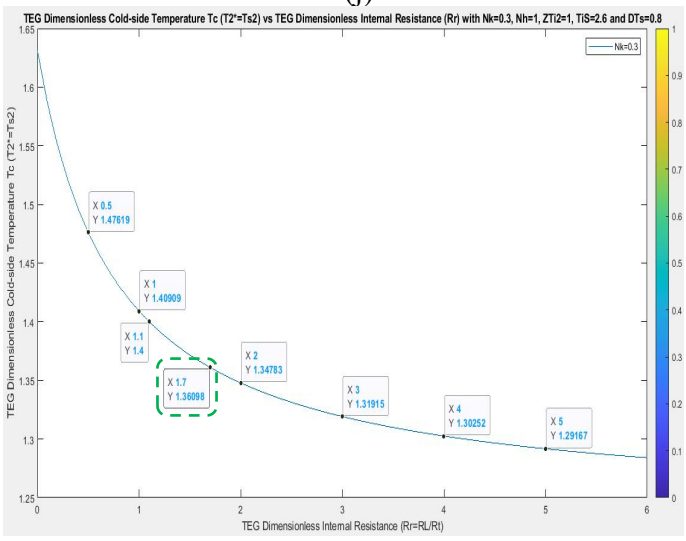

(k)

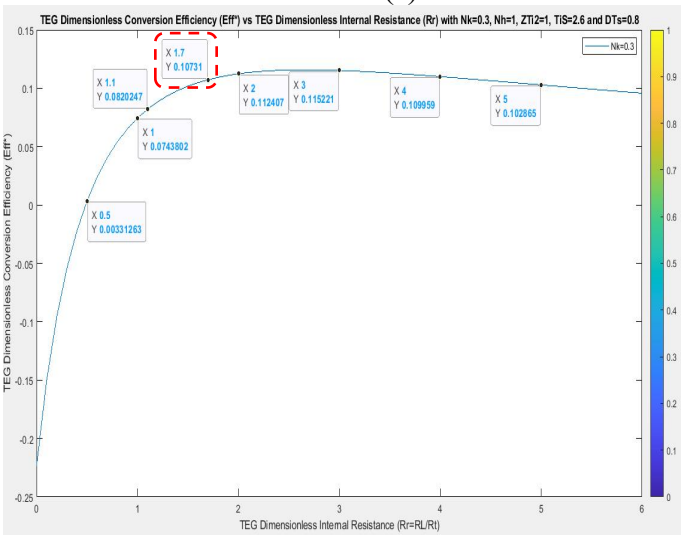

(f)

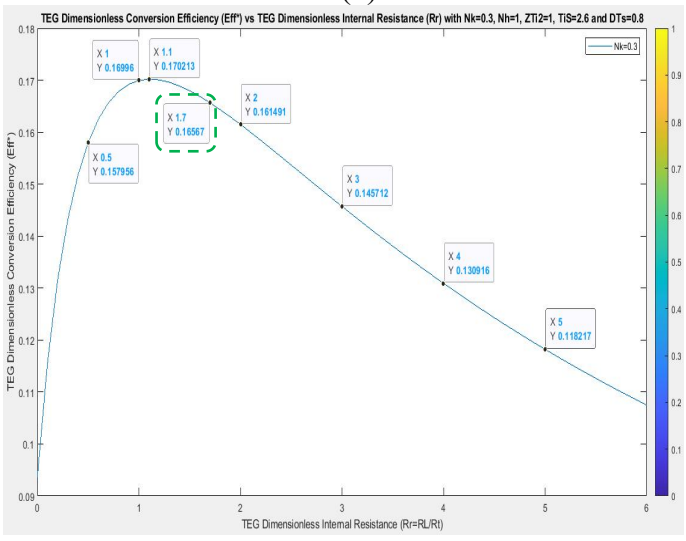

(l)

Figure 4.3: Performance and comparison plots of the: i) simple equations (4.32) and (4.33); **(a)** Q_{s1} vs R_r @N_k=0.3; **(b)** Q_{s2} vs R_r @N_k=0.3; **(c)** P_{os} vs R_r @N_k=0.3; **(d)** T_{s1} vs R_r @N_k=0.3; **(e)** T_{s2} vs R_r @N_k=0.3; **(f)** *Eff** vs R_r @N_k=0.3; versus ii) simpler equations (4.36) and (4.37); **(g)** Q_{s1} vs R_r @N_k=0.3; **(h)** Q_{s2} vs R_r @N_k=0.3; **(i)** P_{os} vs R_r @N_k=0.3; **(j)** T_{s1} vs R_r @N_k=0.3; **(k)** T_{s2} vs R_r @N_k=0.3; **(l)** *Eff** vs R_r @N_k=0.3.

Figure 4.4 graphs depict Q_{s1}, Q_{s2}, P_{os}, T_{s1}, T_{s2} and *Eff** results using ZT_{i2}=1, N_h=1, T_i =2.6, N_k=0.1-0.4, R_r=0-6 and DT_S = 0.8. It also compares the simple vs simpler equations results.

N_k=0.1-0.4: Using "simple" equations (4.32) and (4.33)

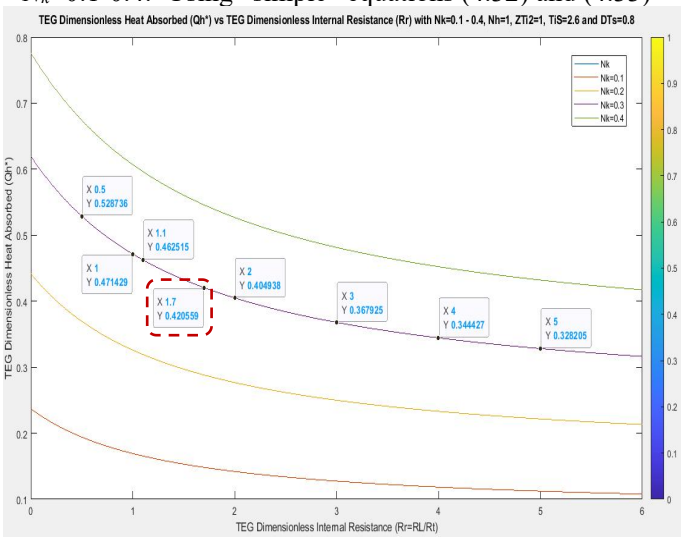

(a)

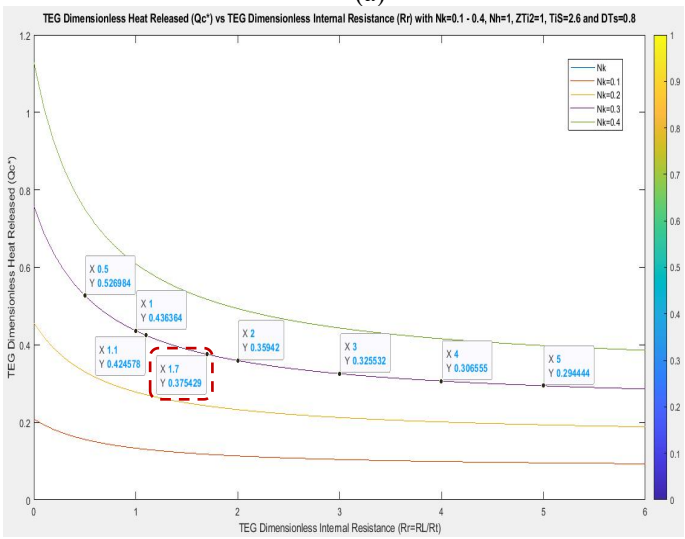

(b)

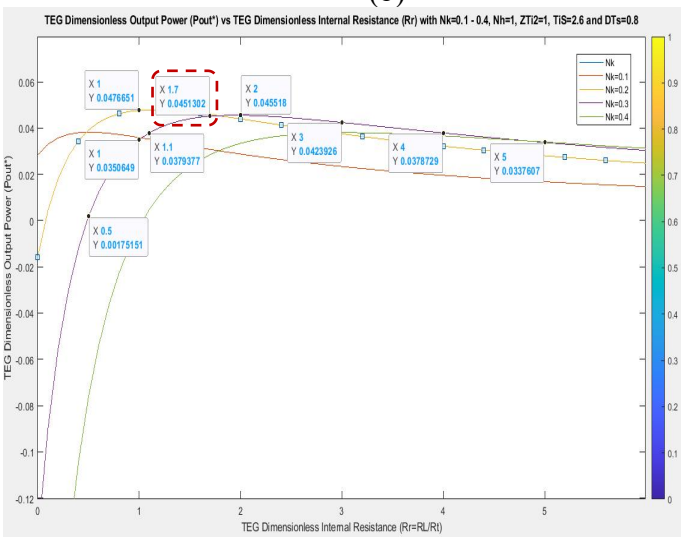

(c)

N_k=0.1-0.4: Using "simpler" equations (4.36) and (4.37)

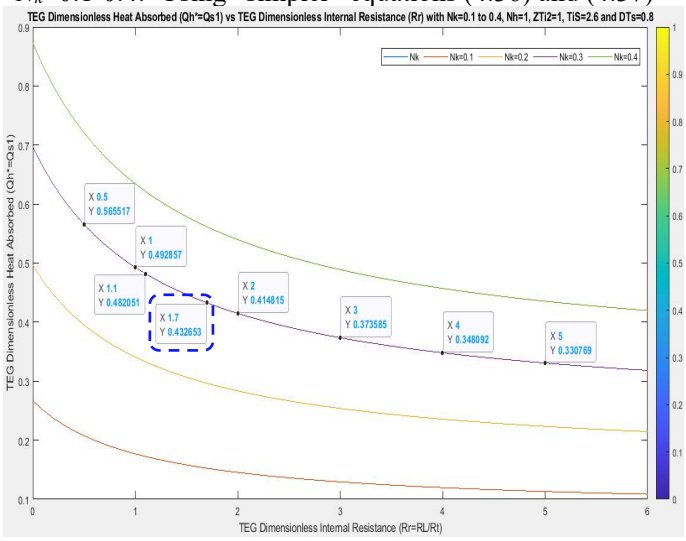

(g)

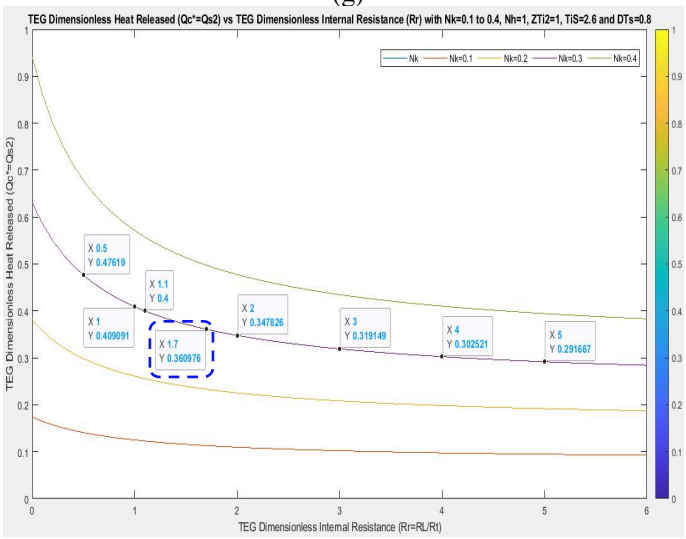

(h)

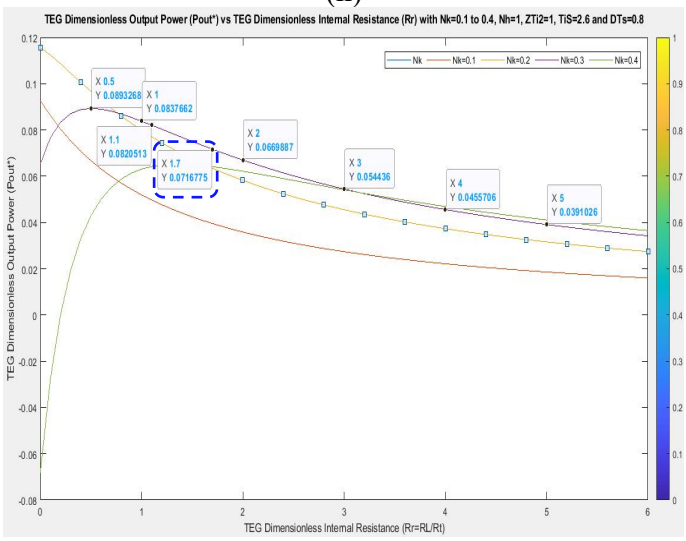

(i)

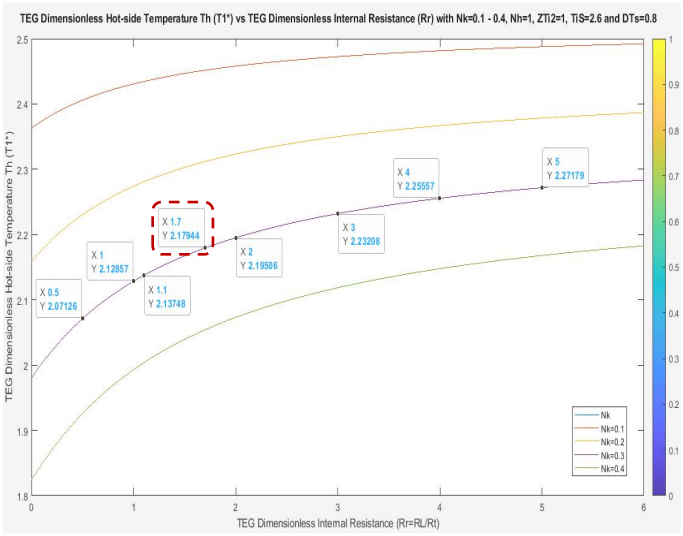

(d)

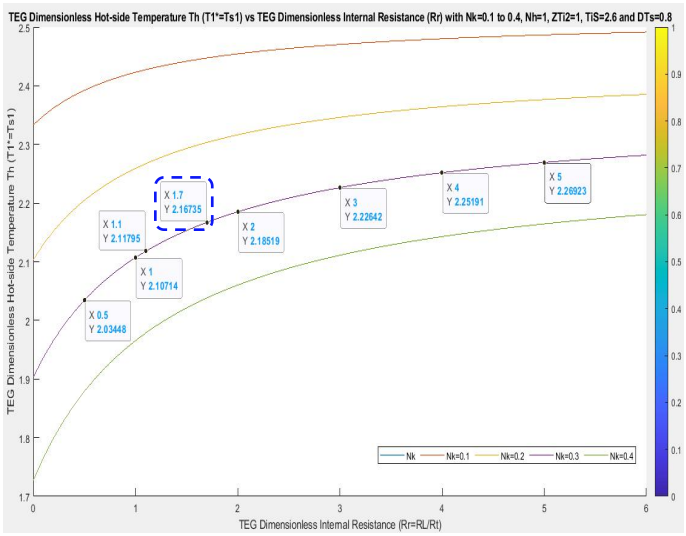

(j)

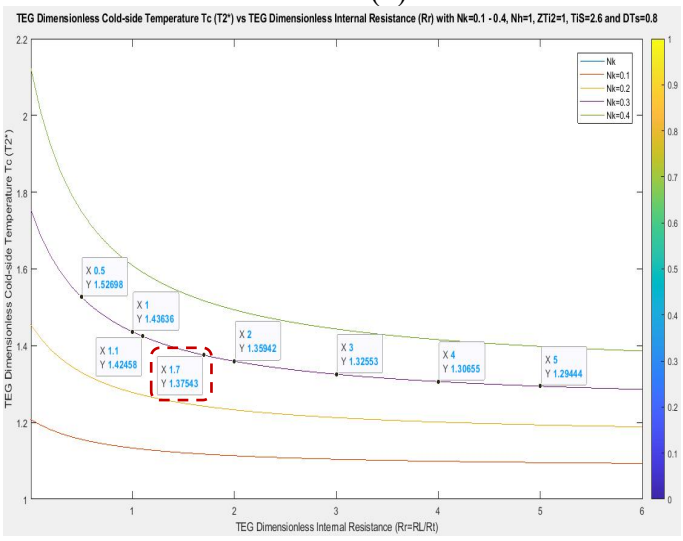

(e)

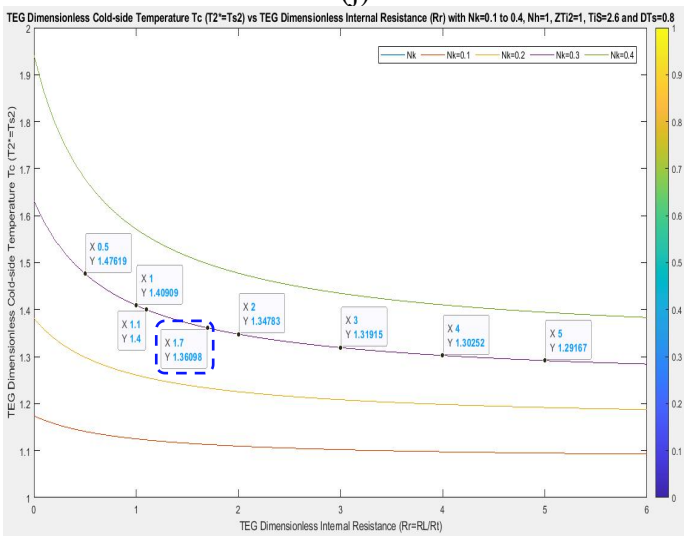

(k)

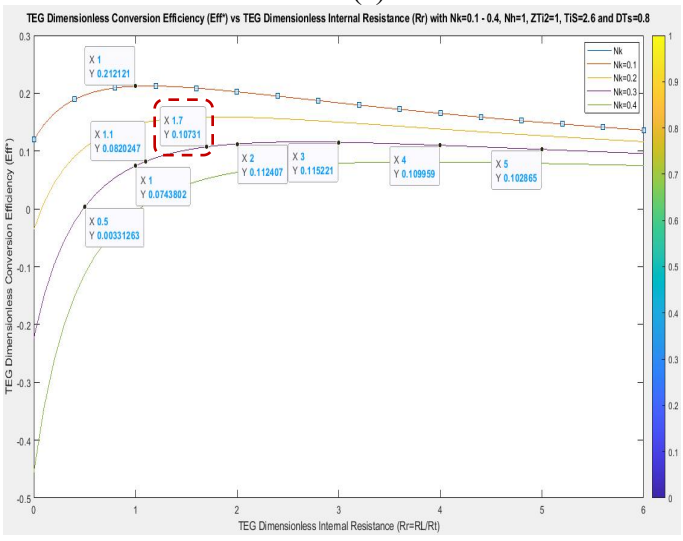

(f)

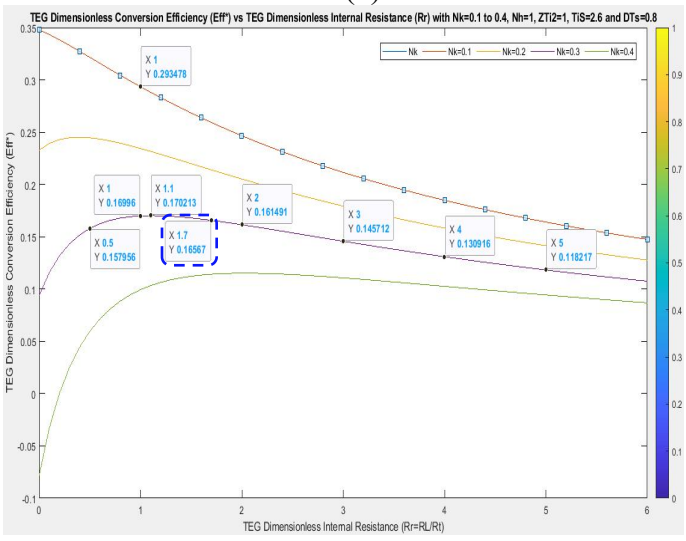

(l)

Figure 4.4: Performance and comparison plots of the: i) simple equations (4.32) and (4.33); **(a)** Q_{s1} vs R_r @N_k=0.1-0.4; **(b)** Q_{s2} vs R_r @N_k=0.1-0.4; **(c)** P_{os} vs R_r @N_k=0.1-0.4; **(d)** T_{s1} vs R_r @N_k=0.1-0.4; **(e)** T_{s2} vs R_r @N_k=0.1-0.4; **(f)** *Eff** vs R_r @N_k=0.1-0.4; ii) versus simpler equations (4.36) and (4.37); **(g)** Q_{s1} vs R_r @N_k=0.1-0.4; **(h)** Q_{s2} vs R_r @N_k=0.1-0.4; **(i)** P_{os} vs R_r @N_k=0.1-0.4; **(j)** T_{s1} vs R_r @N_k=0.1-0.4; **(k)** T_{s2} vs R_r @N_k=0.3; **(l)** *Eff** vs R_r @N_k=0.1-0.4.

Figure 4.5 graphs depict Q_{s1}, Q_{s2}, P_{os}, T_{s1}, T_{s2} and *Eff** results with ZT_{i2}=1, N_h=1, T_i =2.6, N_k=0.05-0.5, R_r=1.7 and DT_S=0.8. It also compares the simple vs simpler equations results.

R_r=1.7: Using "simple" equations (4.32) and (4.33)

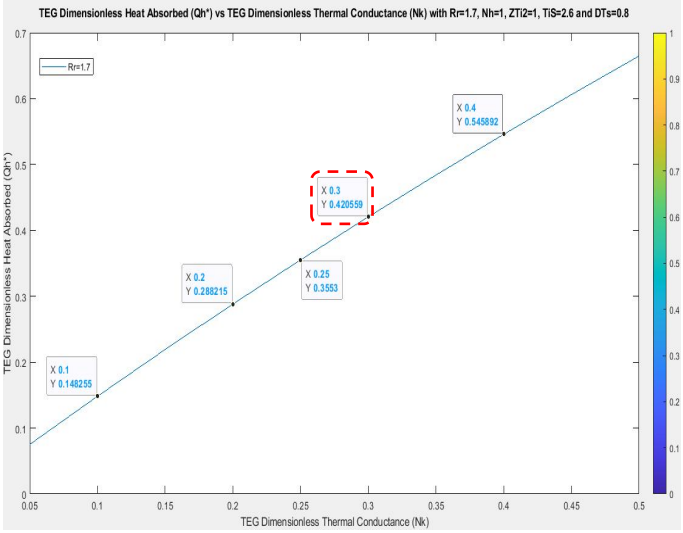

(a)

R_r=1.7: Using "simpler" equations (4.36) and (4.37)

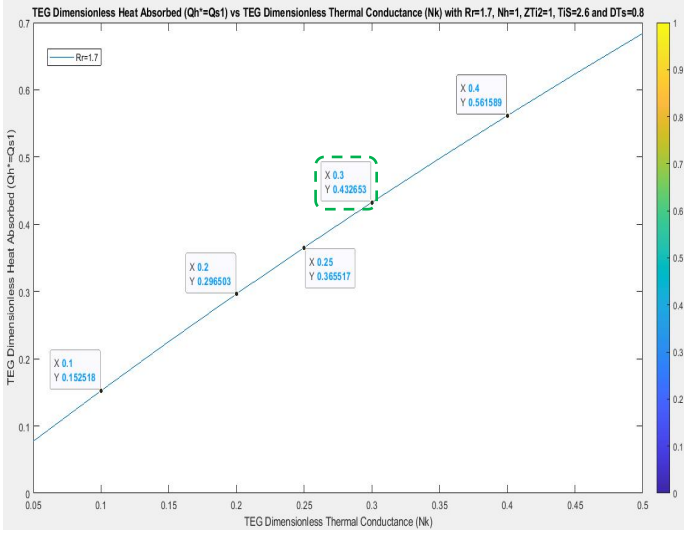

(g)

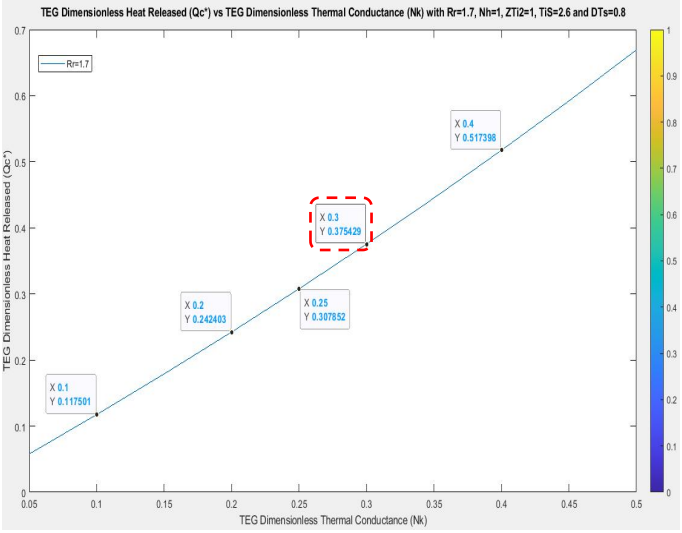

(b)

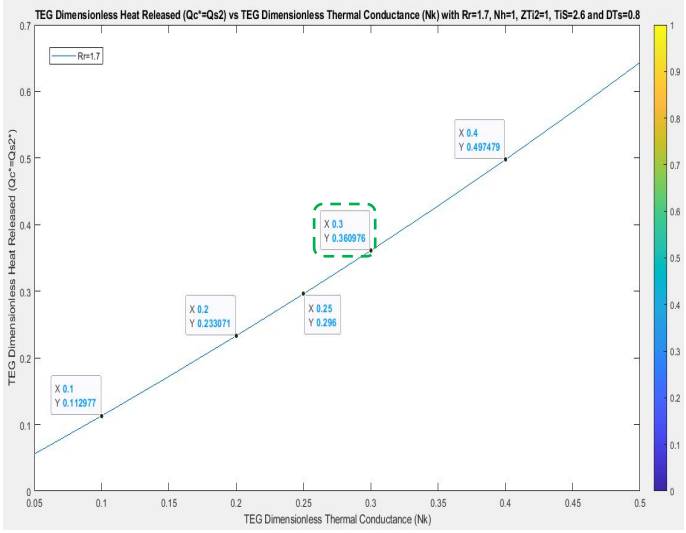

(h)

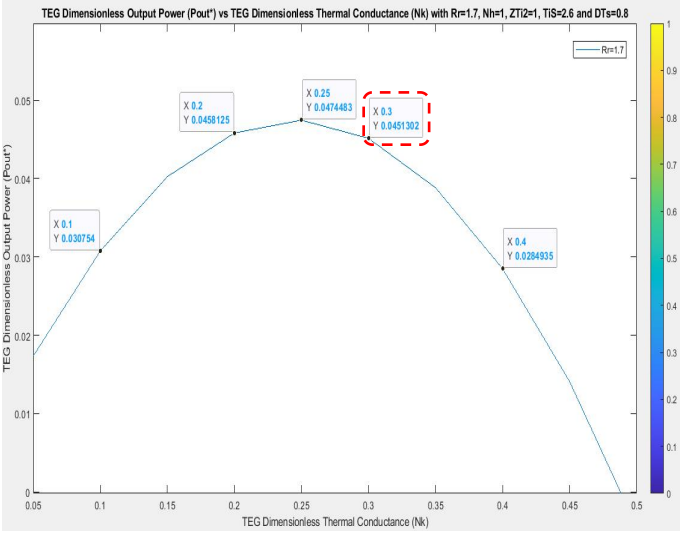

(c)

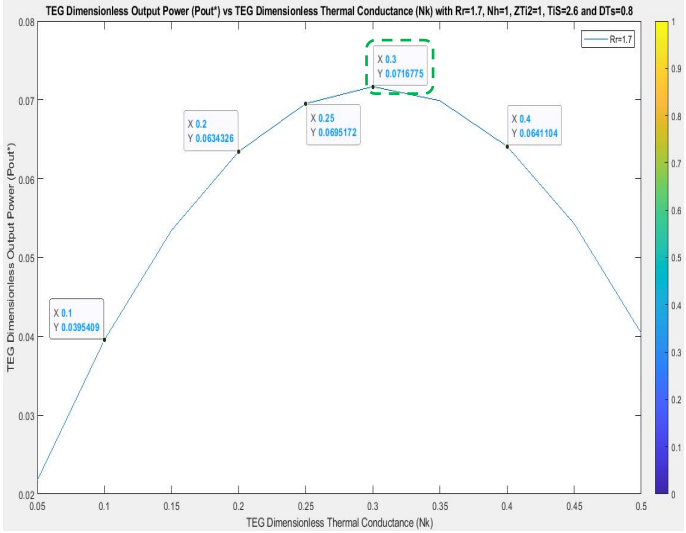

(i)

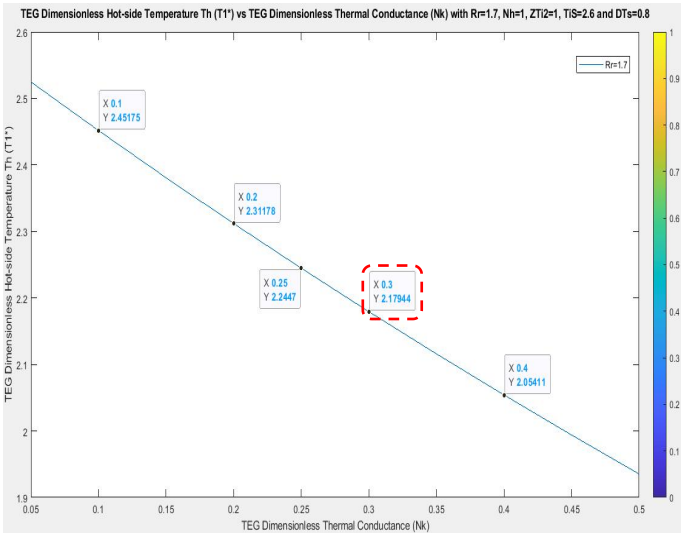

(d)

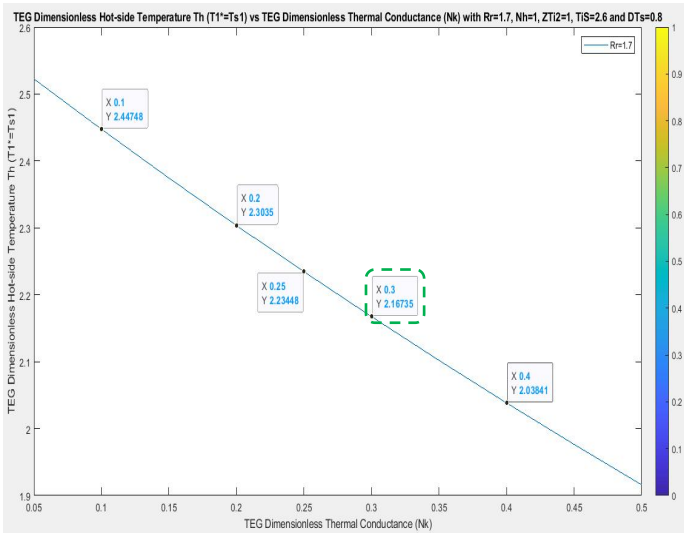

(j)

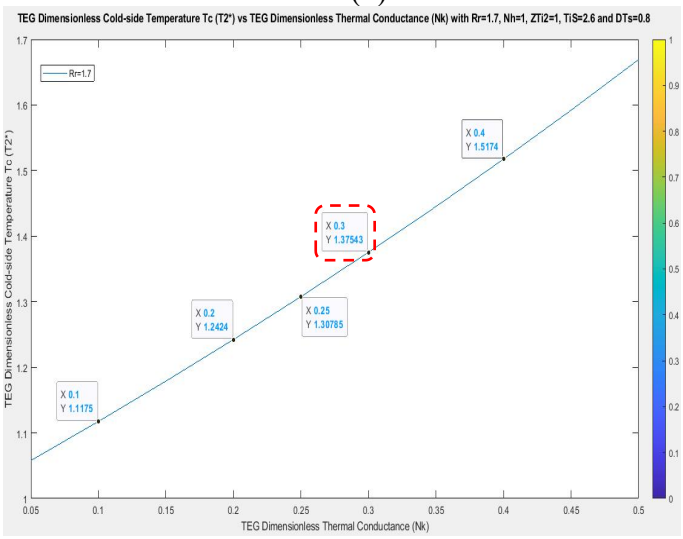

(e)

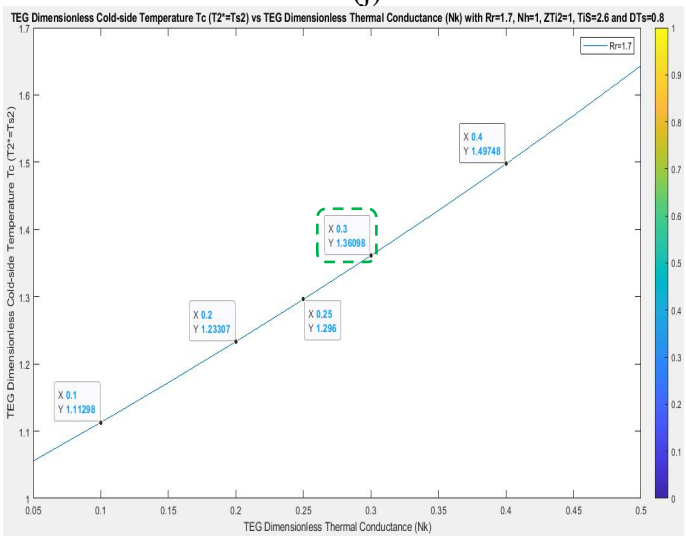

(k)

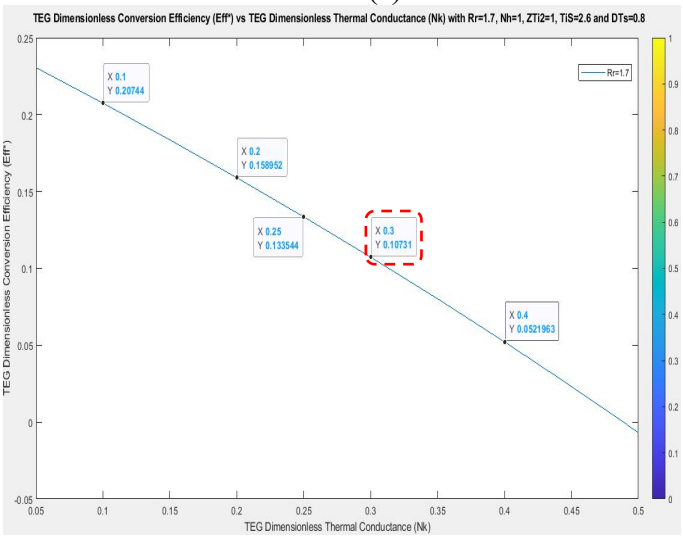

(f)

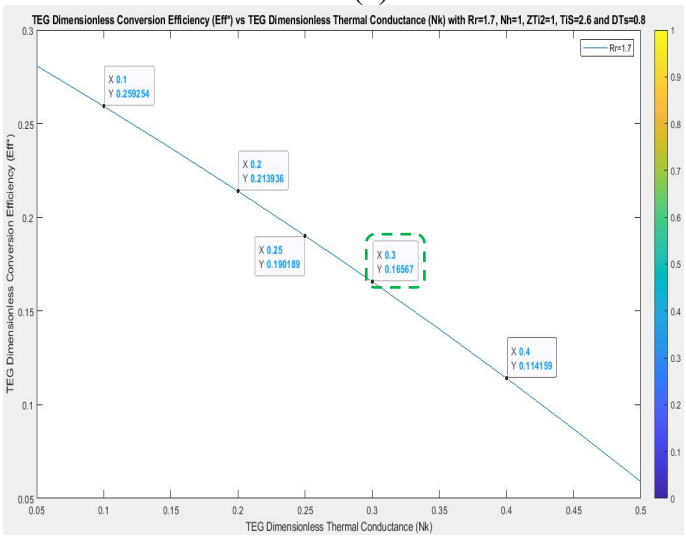

(l)

Figure 4.5: Performance and comparison plots of the: i) simple equations (4.32) and (4.33); **(a)** Q_{s1} vs N_k @R_r=1.7; **(b)** Q_{s2} vs N_k @R_r=1.7; **(c)** P_{os} vs N_k @R_r=1.7; **(d)** T_{s1} vs N_k @R_r=1.7; **(e)** T_{s2} vs N_k @R_r=1.7; **(f)** *Eff** vs N_k @R_r=1.7; versus ii) simpler equations (4.36) and (4.37); **(g)** Q_{s1} vs N_k @R_r=1.7; **(h)** Q_{s2} vs N_k @R_r=1.7; **(i)** P_{os} vs N_k @R_r=1.7; **(j)** T_{s1} vs N_k @R_r=1.7; **(k)** T_{s2} vs N_k @R_r=1.7; **(l)** *Eff** vs N_k @R_r=1.7.

Figure 4.6 graphs show Q_{s1}, Q_{s2}, P_{os}, T_{s1}, T_{s2} and Eff* results with ZT_{i2}=1, N_h=1, T_i =2.6, N_k=0.05-0.5, R_r=0.5-2 and DT_S=0.8. It also compares the simple vs simpler equations results.

R_r=0.5-2: Using "simple" equations (4.32) and (4.33)

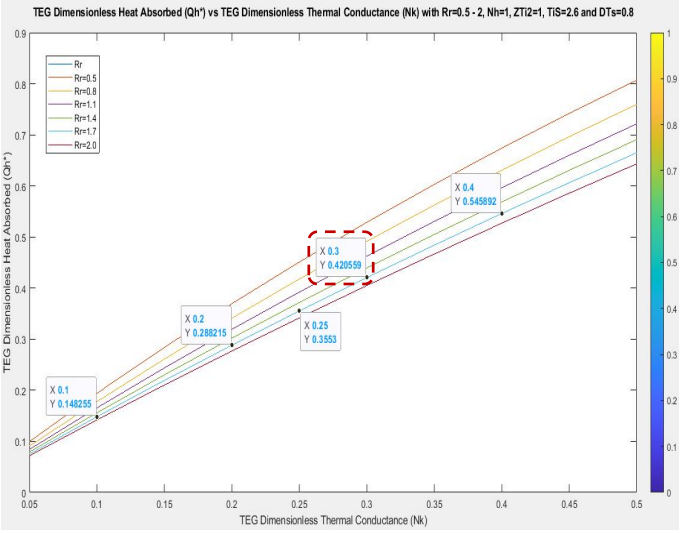

(a)

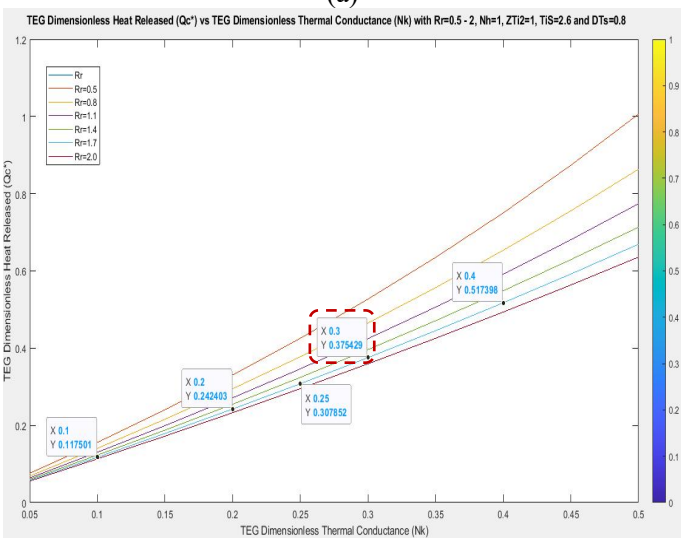

(b)

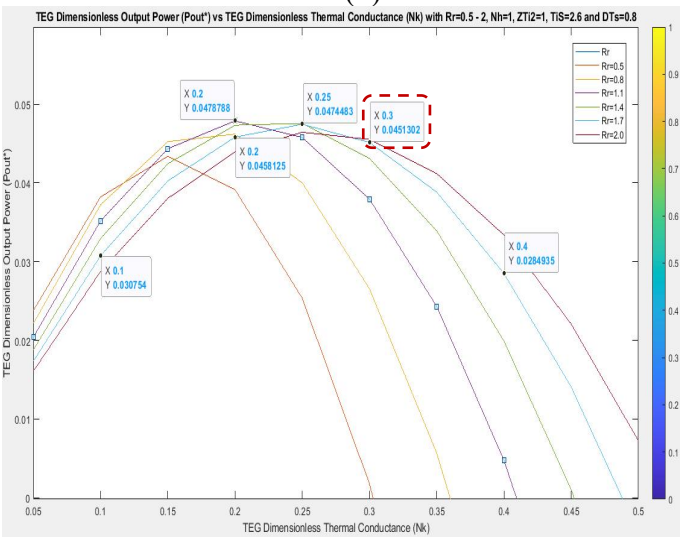

(c)

R_r=0.5-2: Using "simpler" equations (4.36) and (4.37)

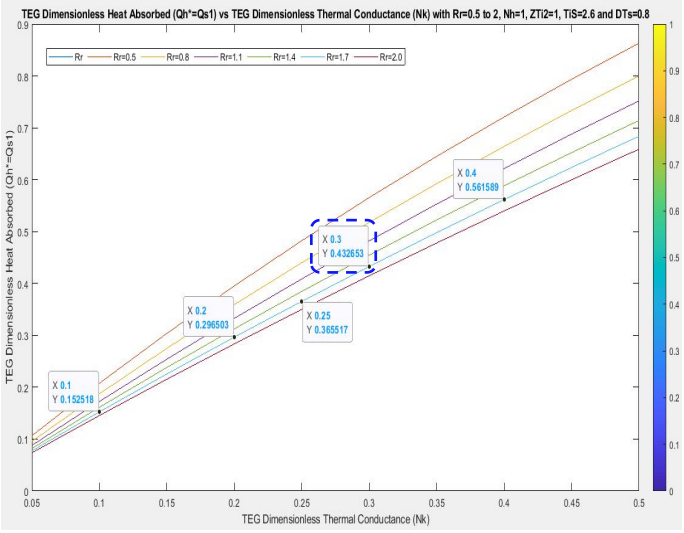

(g)

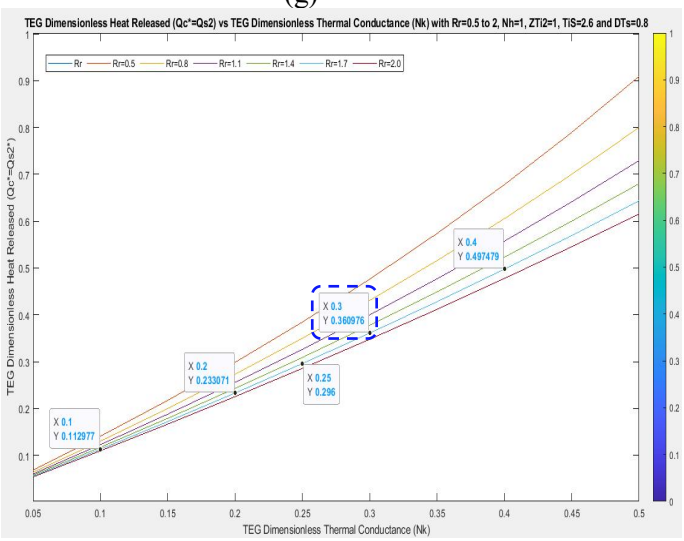

(h)

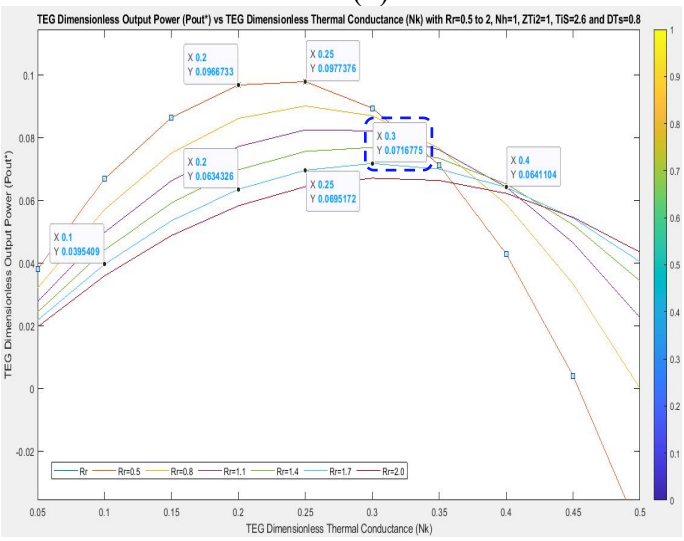

(i)

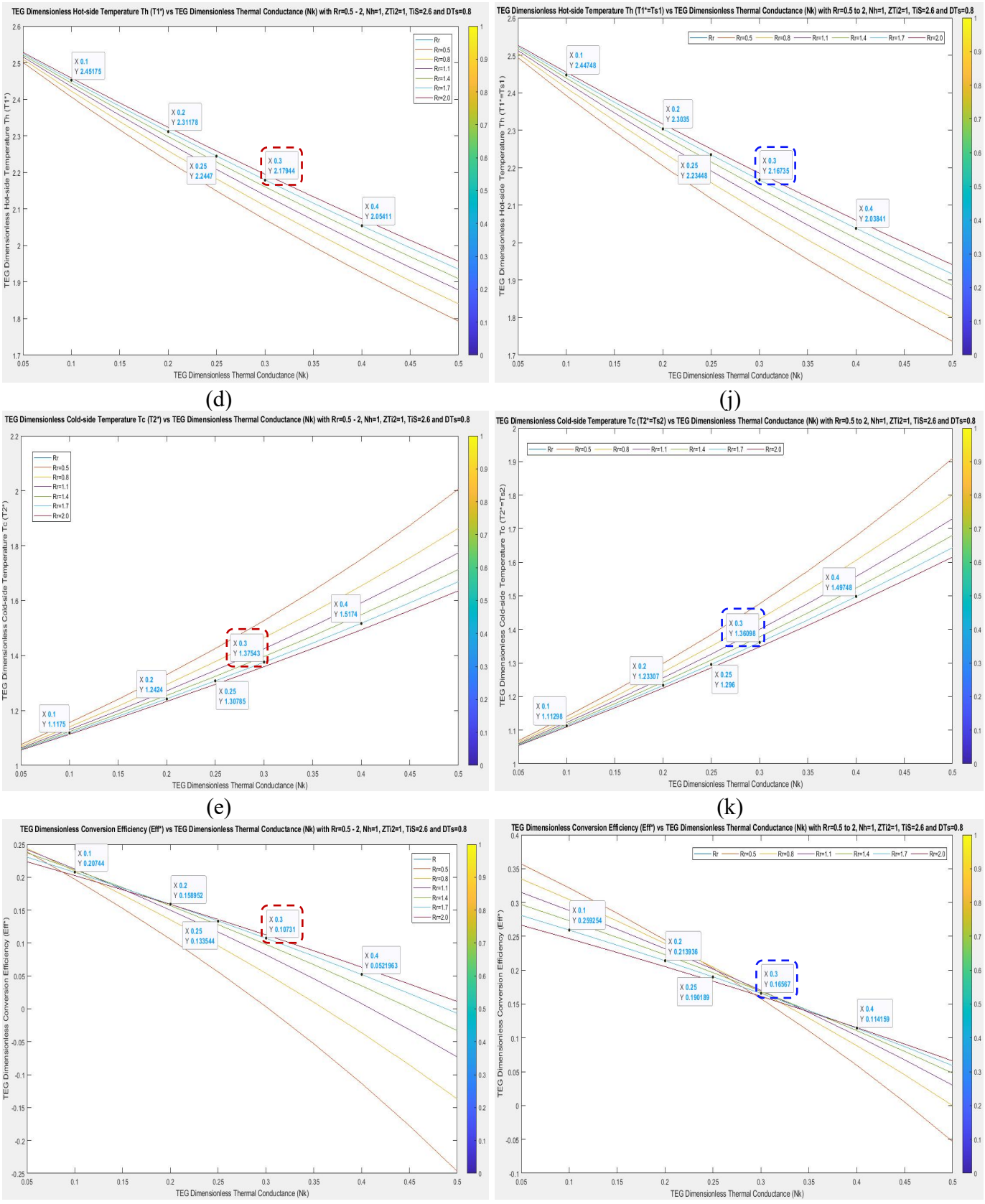

Figure 4.6: Performance and comparison plots of the: i) simple equations (4.32) and (4.33); **(a)** Q_{s1} vs N_k @R_r=0.5-2; **(b)** Q_{s2} vs N_k @R_r=0.5-2; **(c)** P_{os} vs N_k @R_r=0.5-2; **(d)** T_{s1} vs N_k @R_r=0.5-2; **(e)** T_{s2} vs N_k @R_r=0.5-2; **(f)** *Eff** vs N_k @R_r=0.5-2; versus ii) simpler equations (4.36) and (4.37); **(g)** Q_{s1} vs N_k @R_r=0.5-2; **(h)** Q_{s2} vs N_k @R_r=0.5-2; **(i)** P_{os} vs N_k @R_r=0.5-2; **(j)** T_{s1} vs N_k @R_r=0.5-2; **(k)** T_{s2} vs N_k @R_r=0.5-2; **(l)** *Eff** vs N_k @R_r=0.5-2.

Figure 4.7 graphs depict in 3D Q_{s1}, Q_{s2}, P_{os}, T_{s1}, T_{s2} and Eff^* results with ZT_{i2}=1, N_h=1, T_i =2.6, N_k=0.05-0.5, R_r=0.2-3.2 and DT_S=0.8. The simple vs simpler equations results are also compared.

R_r *vs* N_k: Using "simple" equations (4.32) and (4.33)

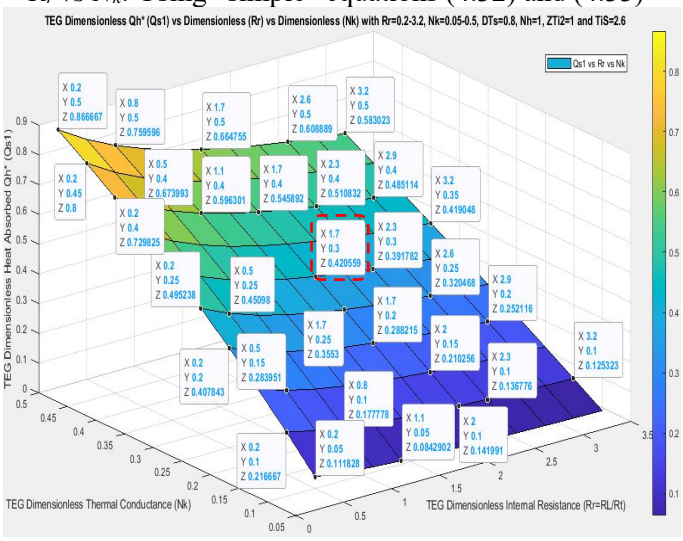

(a)

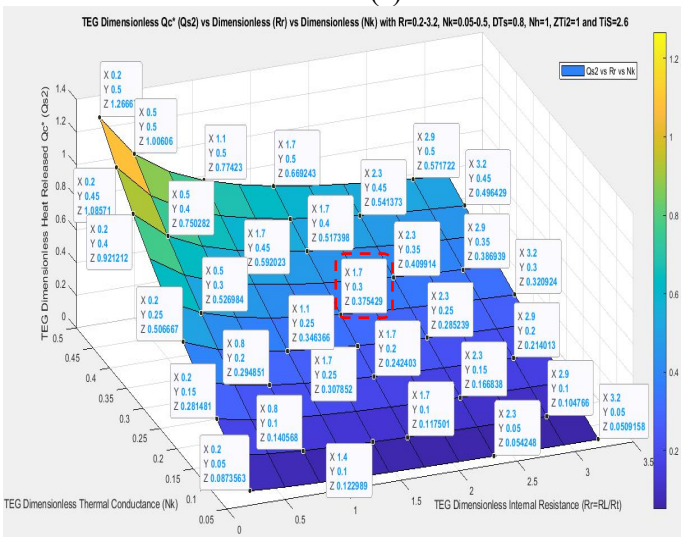

(b)

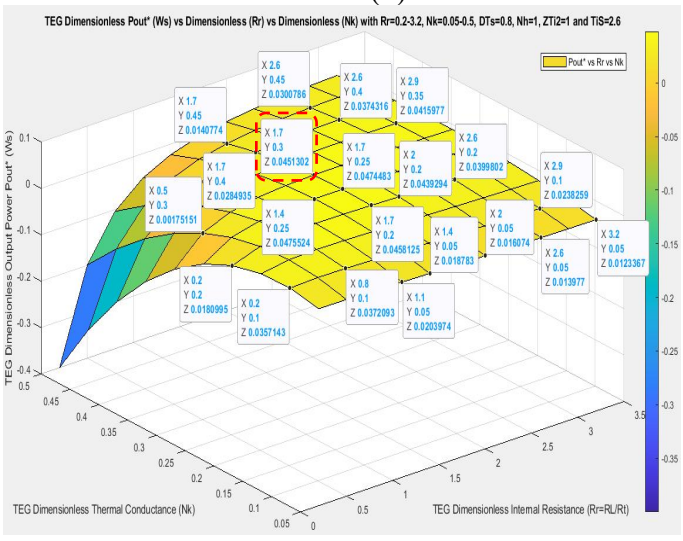

(c)

R_r *vs* N_k: Using "simpler" equations (4.36) and (4.37)

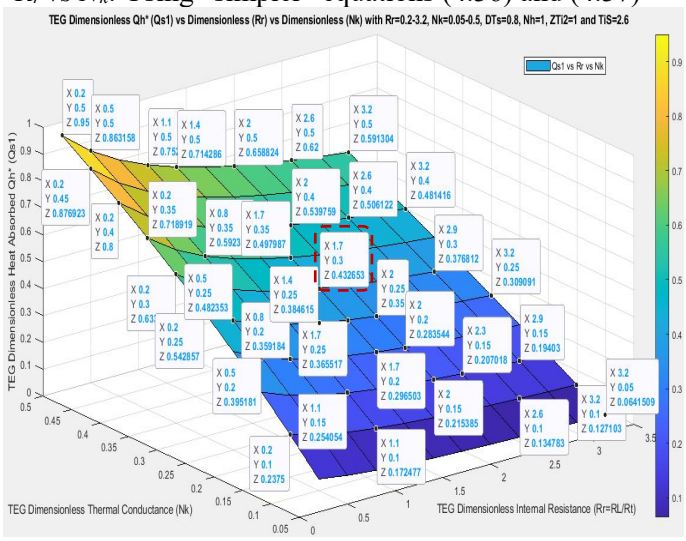

(g)

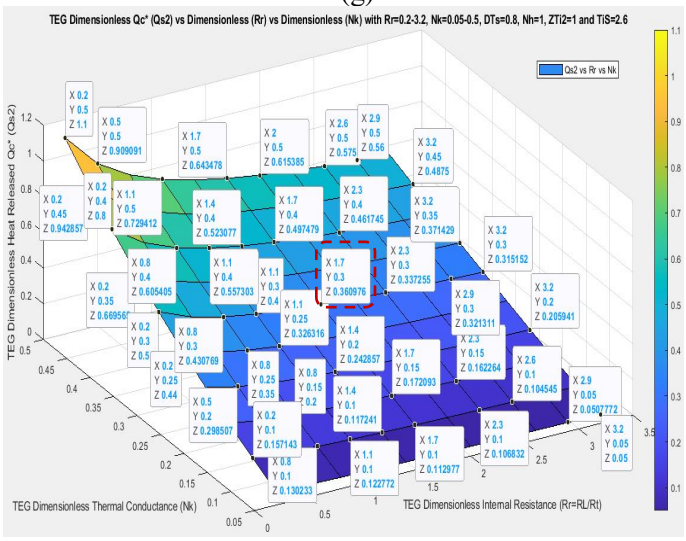

(h)

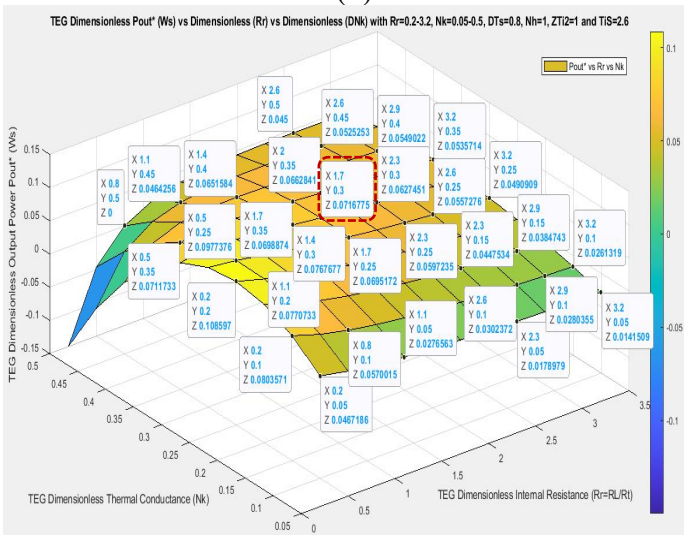

(i)

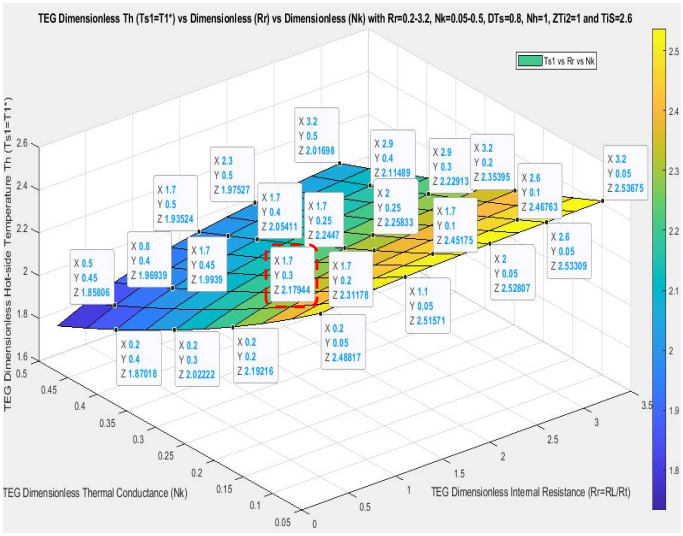

(d)

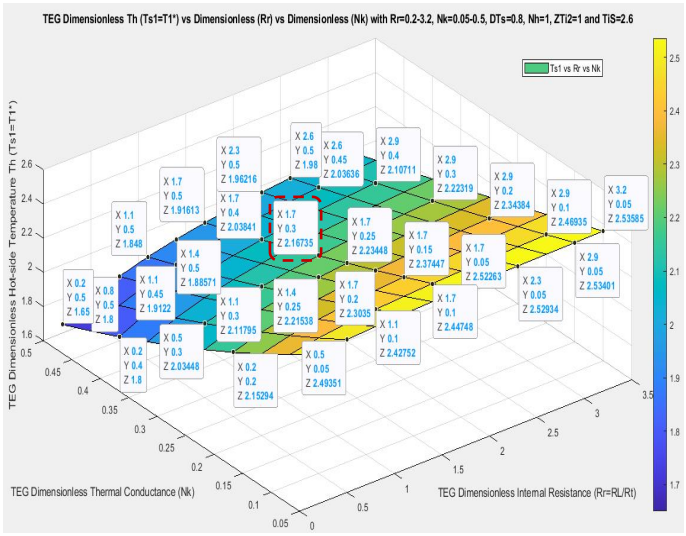

(j)

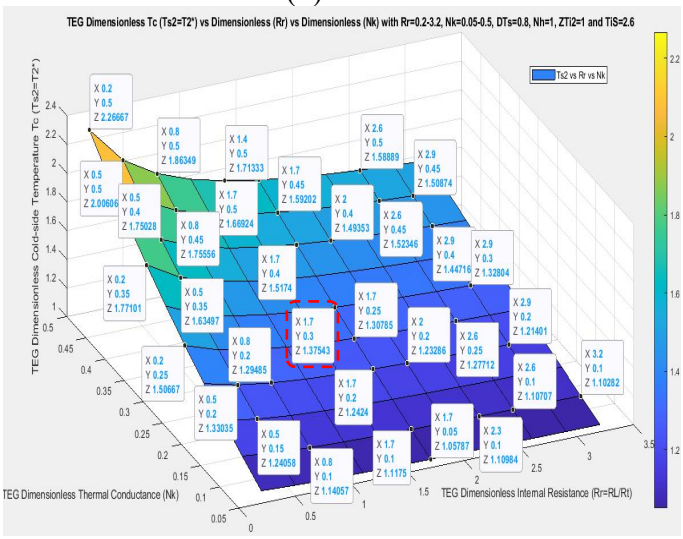

(e)

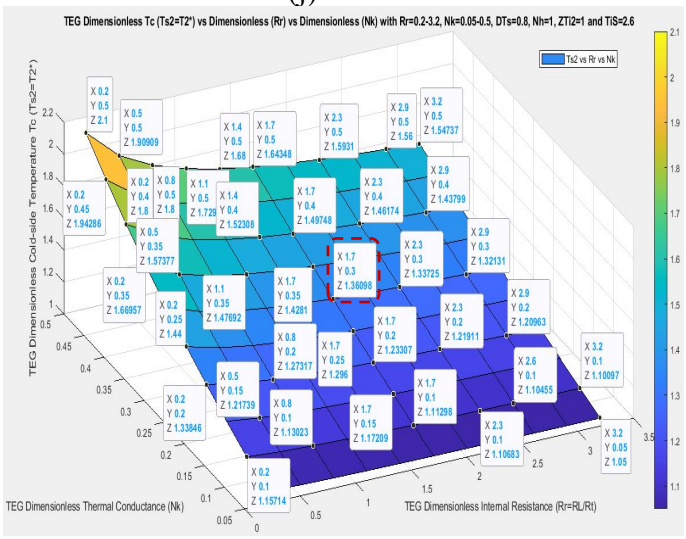

(k)

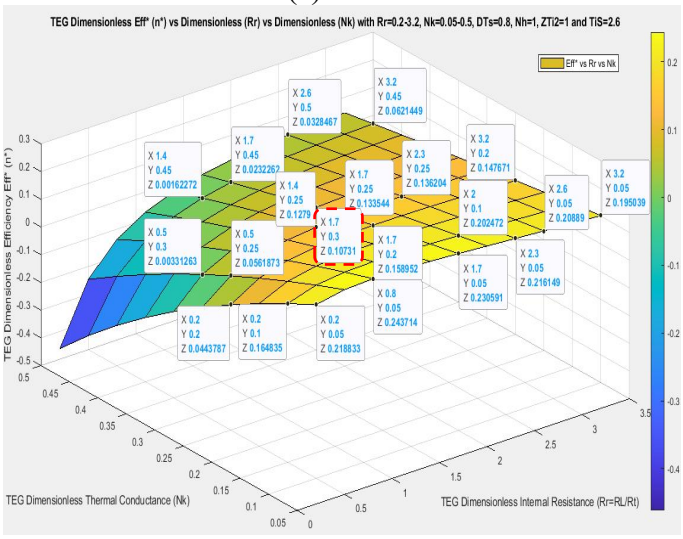

(f)

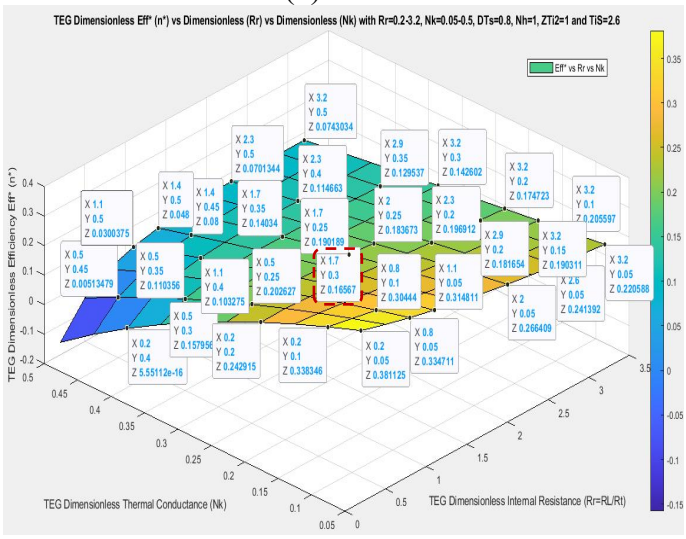

(l)

Figure 4.7: Performance and comparison plots of the: i) simple equations (4.32) and (4.33); **(a)** Q_{s1} vs R_r vs N_k; **(b)** Q_{s2} vs R_r vs N_k; **(c)** P_{os} vs R_r vs N_k; **(d)** T_{s1} vs R_r vs N_k; **(e)** T_{s2} vs R_r vs N_k; **(f)** *Eff** vs R_r vs N_k; versus ii) simpler equations (4.36) and (4.37); **(g)** Q_{s1} vs R_r vs N_k; **(h)** Q_{s2} vs R_r vs N_k; **(i)** P_{os} vs R_r vs N_k; **(j)** T_{s1} vs R_r vs N_k; **(k)** T_{s2} vs R_r vs N_k; **(l)** *Eff** vs R_r vs N_k.

Figure 4.8 graphs depict in 3D Q_{s1}, Q_{s2}, P_{os}, T_{s1}, T_{s2} and Eff^* results with ZT_{i2}=1, N_h=1, T_i =2.6, N_k=0.3, R_r=0.2-3.2 and DT_S=0.1-1. The simple vs simpler equations results are also compared.

R_r *vs* DT_s: Using "simple" equations (4.32) and (4.33)

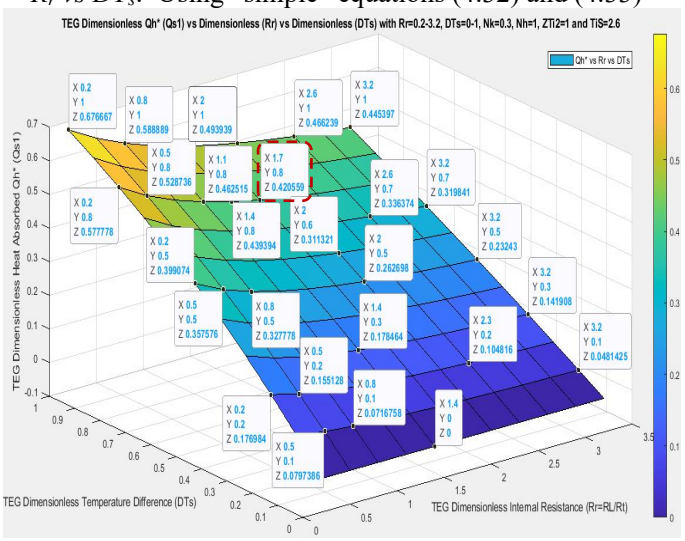

(a)

R_r *vs* DT_s: Using "simpler" equations (4.36) and (4.37)

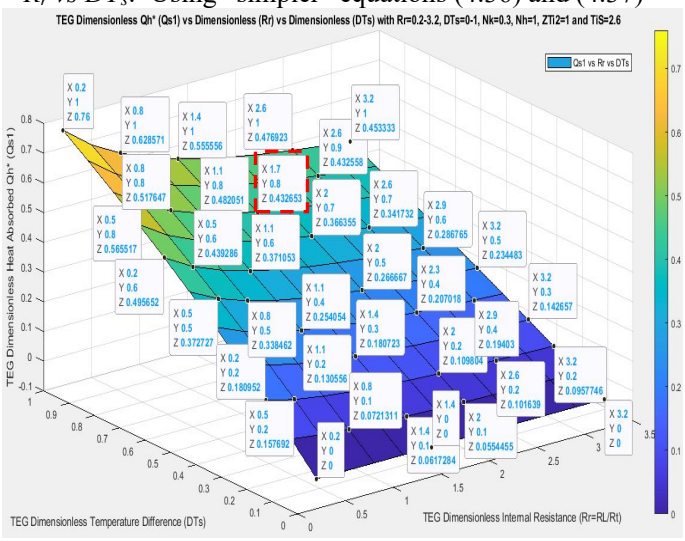

(g)

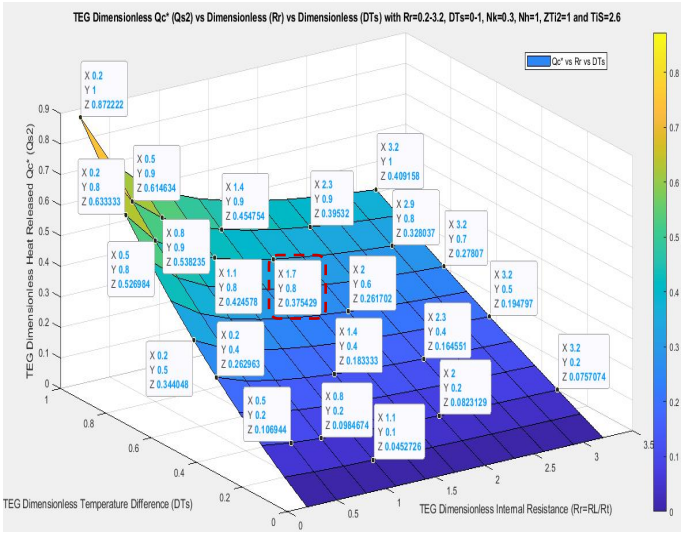

(b)

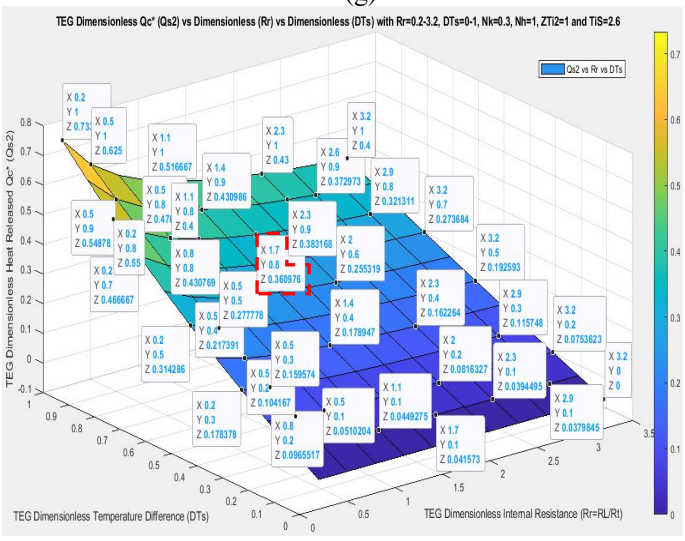

(h)

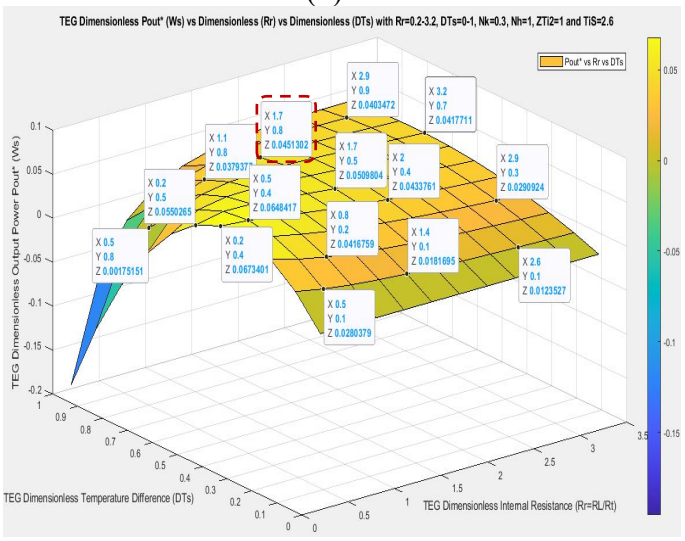

(c)

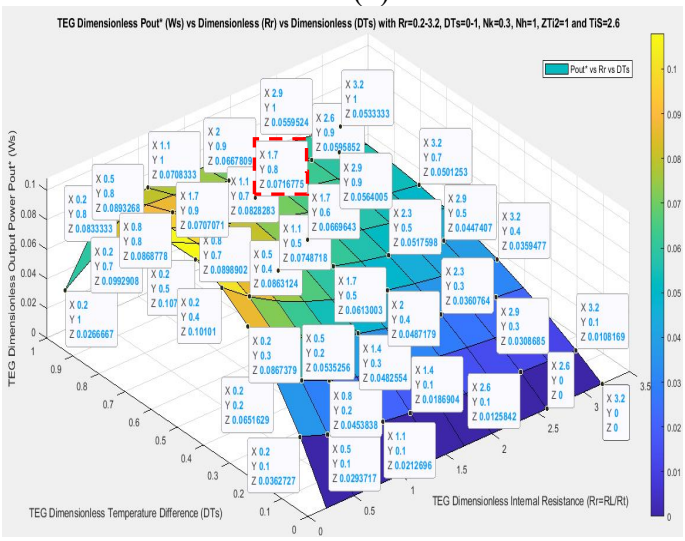

(i)

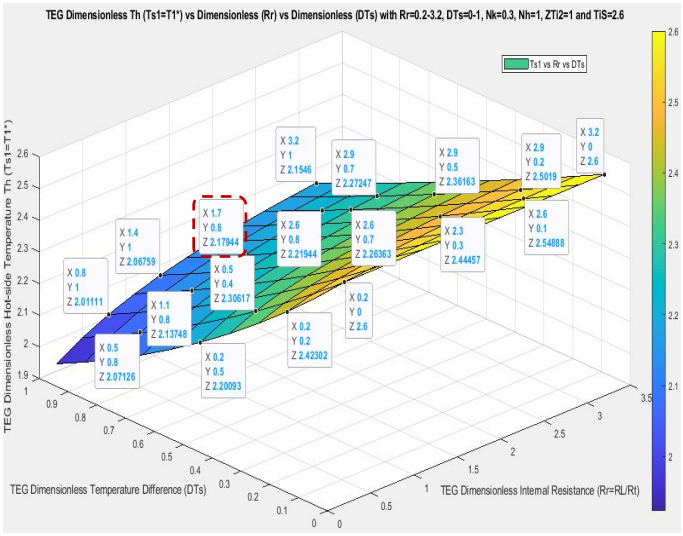

(d)

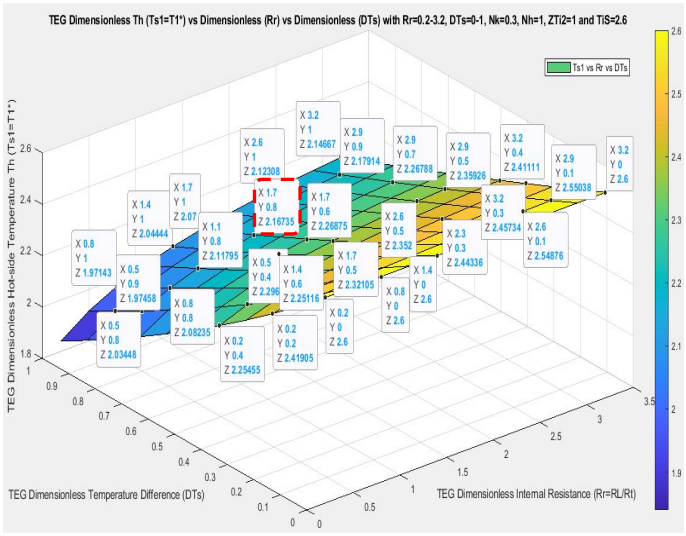

(j)

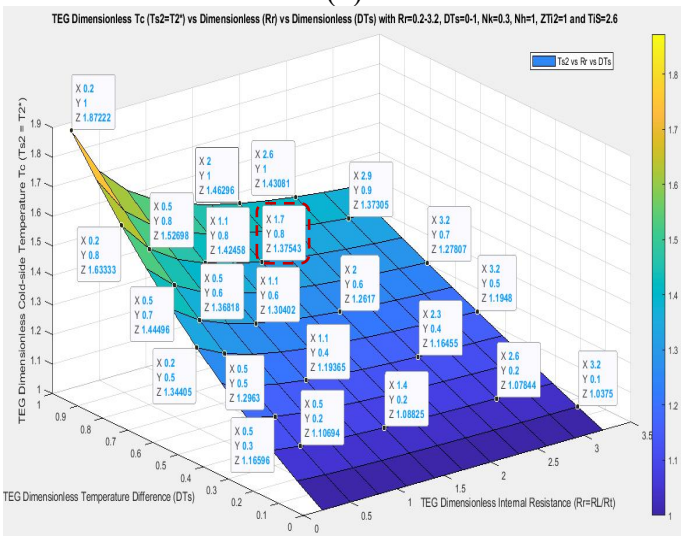

(e)

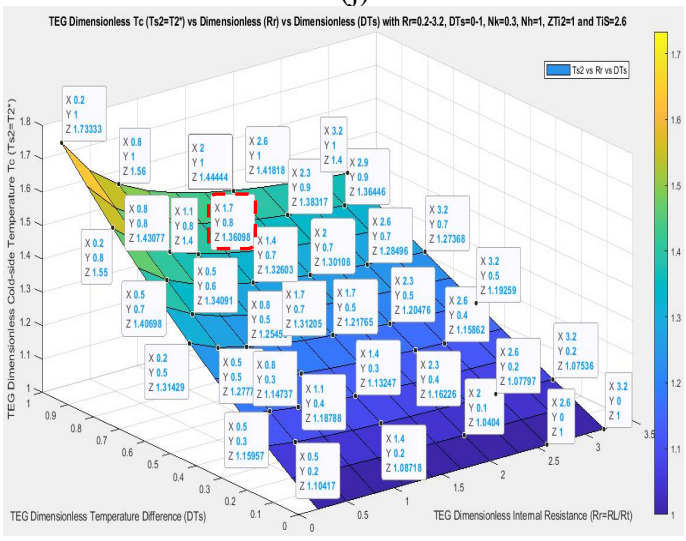

(k)

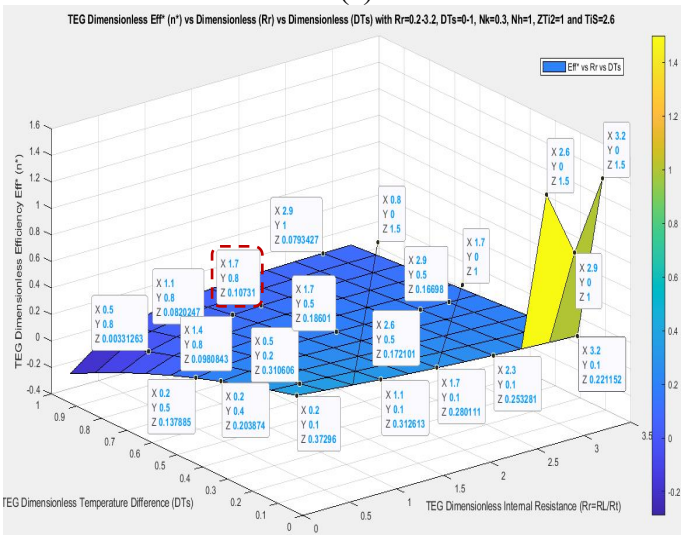

(f)

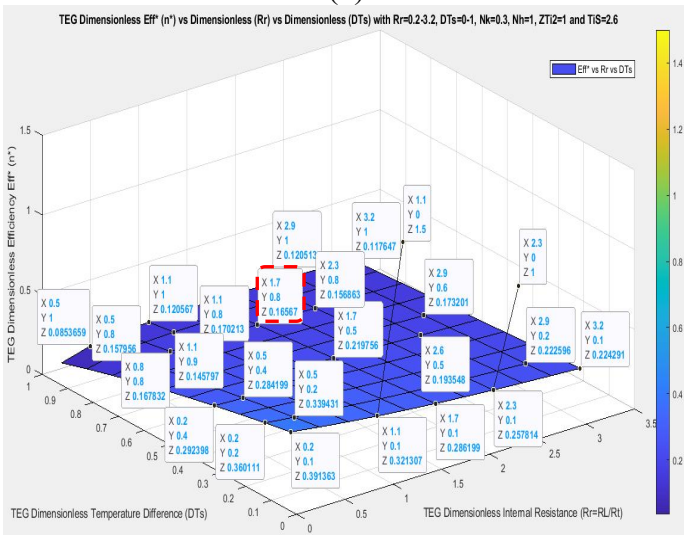

(l)

Figure 4.8: Performance and comparison plots of the: i) simple equations (4.32) and (4.33); **(a)** Q_{s1} vs R_r vs DT_s; **(b)** Q_{s2} vs R_r vs DT_s ; **(c)** P_{os} vs R_r vs DT_s ; **(d)** T_{s1} vs R_r vs DT_s ; **(e)** T_{s2} vs R_r vs DT_s ; **(f)** *Eff** vs R_r vs DT_s ; versus ii) simpler equations (4.36) and (4.37); **(g)** Q_{s1} vs R_r vs DT_s ; **(h)** Q_{s2} vs R_r vs DT_s ; **(i)** P_{os} vs R_r vs DT_s ; **(j)**T_{s1} vs R_r vs DT_s ; **(k)** T_{s2} vs R_r vs DT_s ; **(l)** *Eff** vs R_r vs DT_s.

Figure 4.9 graphs depict in 3D Q_{s1}, Q_{s2}, P_{os}, T_{s1}, T_{s2} and Eff^* results using ZT_{i2}=1, N_h=1, T_i = 2.6, N_k=0.05-0.5, R_r=1.7 and DT_S=0.1-1. The simple vs simpler equations results are also compared.

N_k *vs* DT_s: Using "simple" equations (4.32) and (4.33)

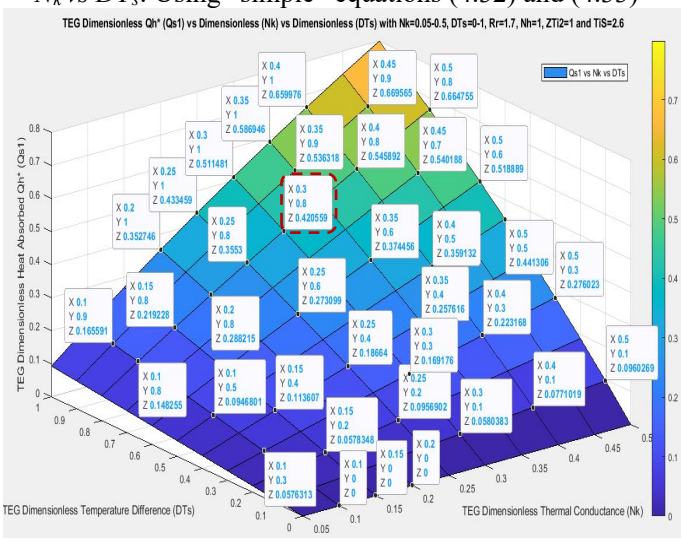

(a)

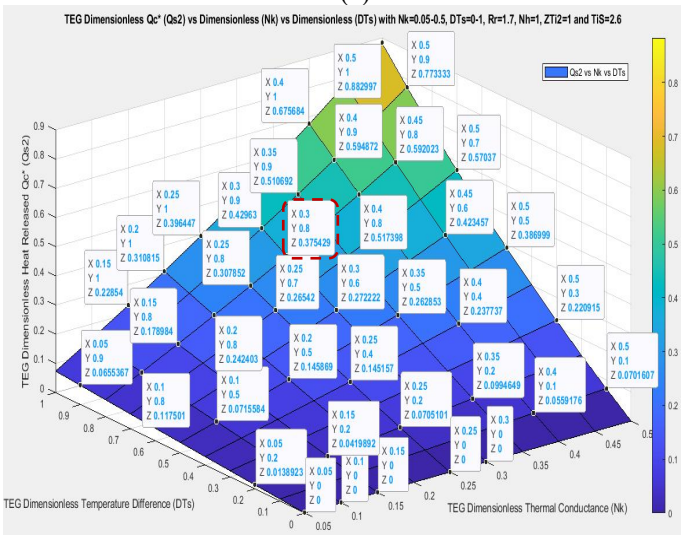

(b)

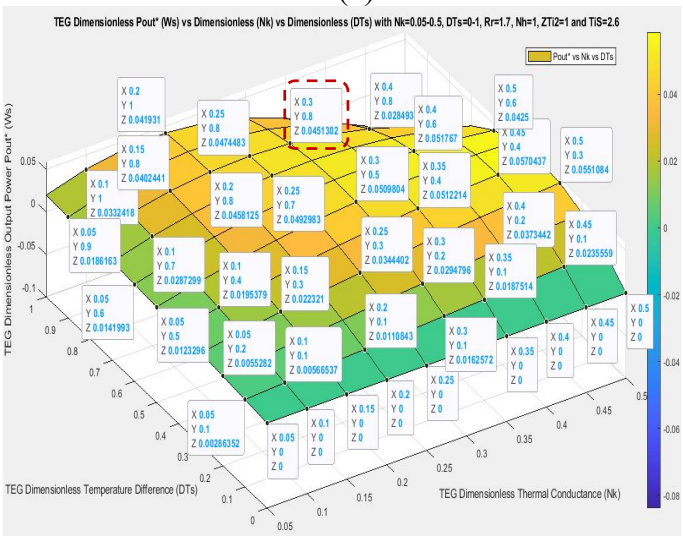

(c)

N_k *vs* DT_s: Using "simpler" equations (4.36) and (4.37)

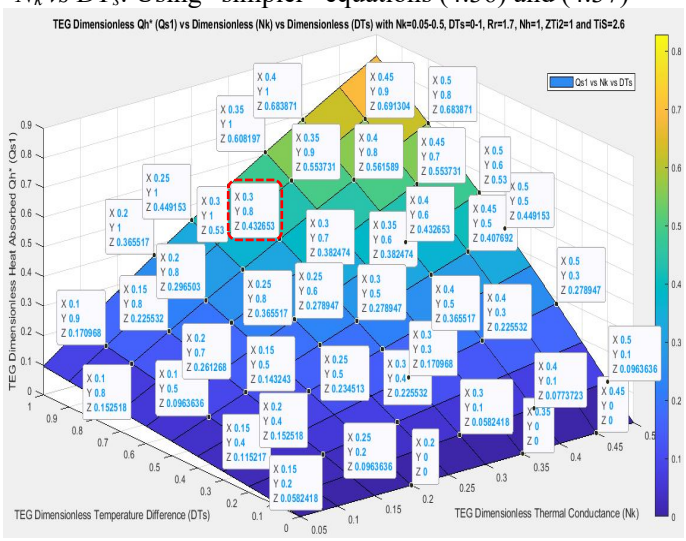

(g)

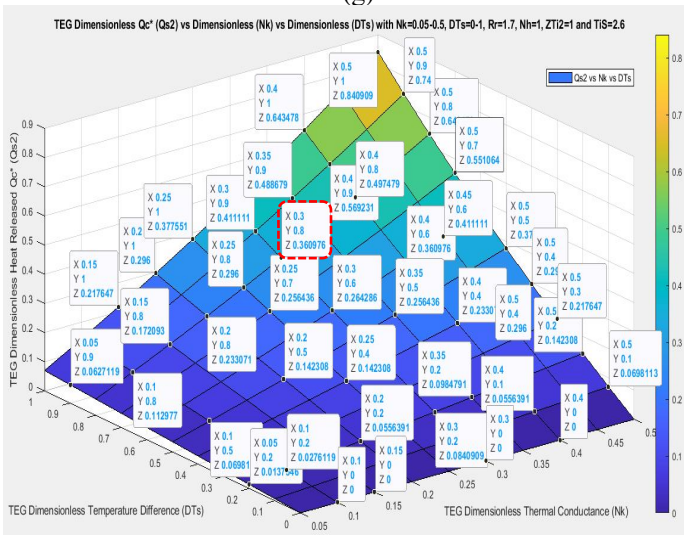

(h)

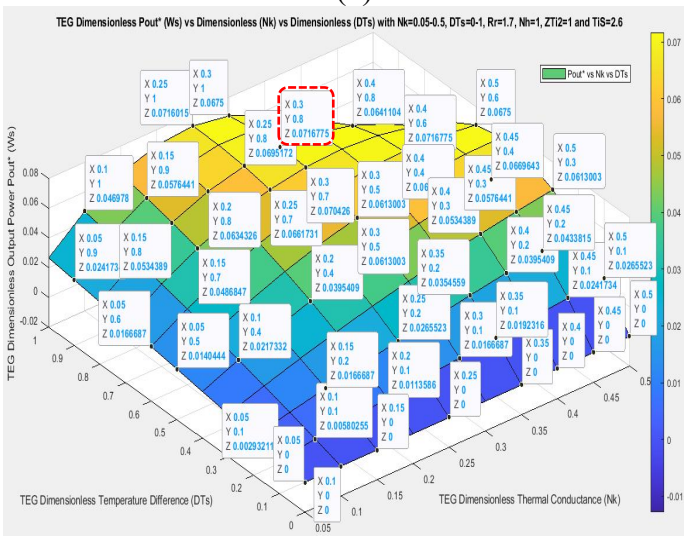

(i)

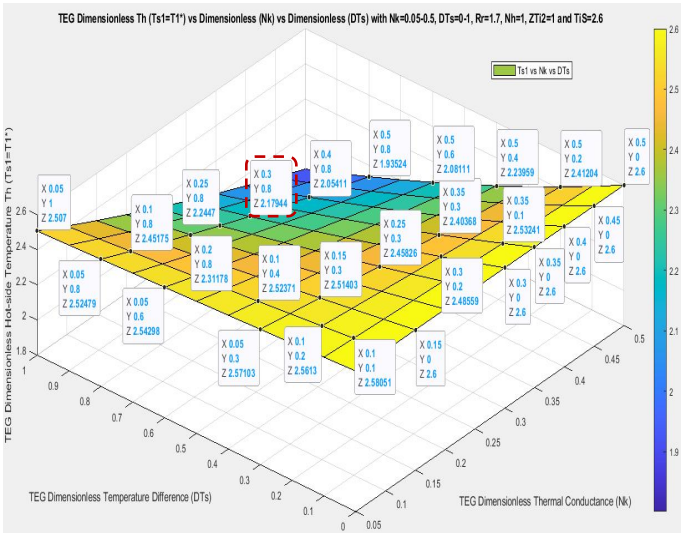

(d)

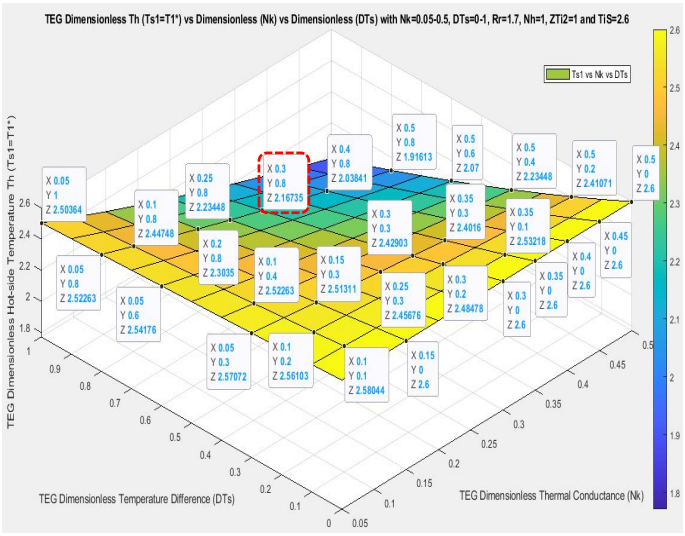

(j)

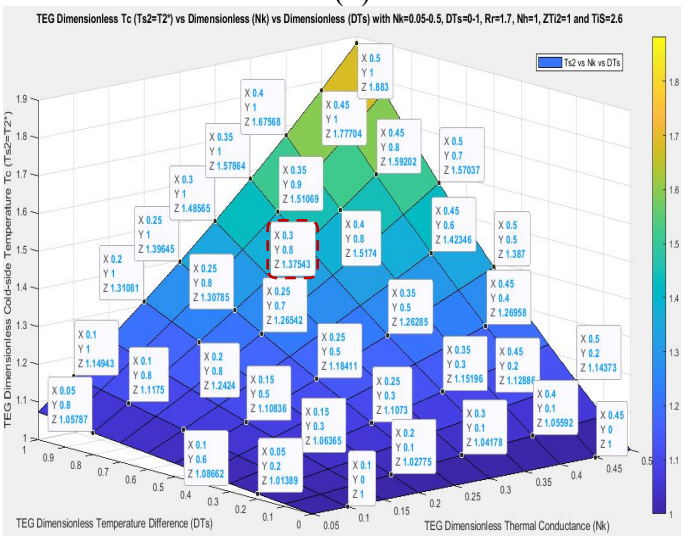

(e)

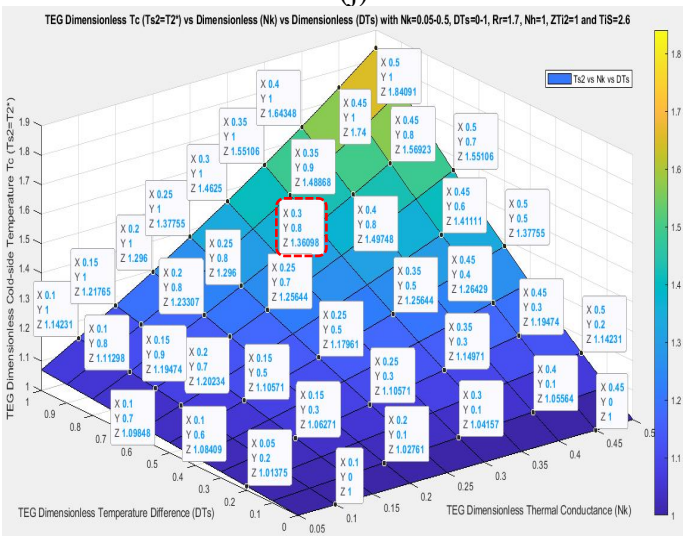

(k)

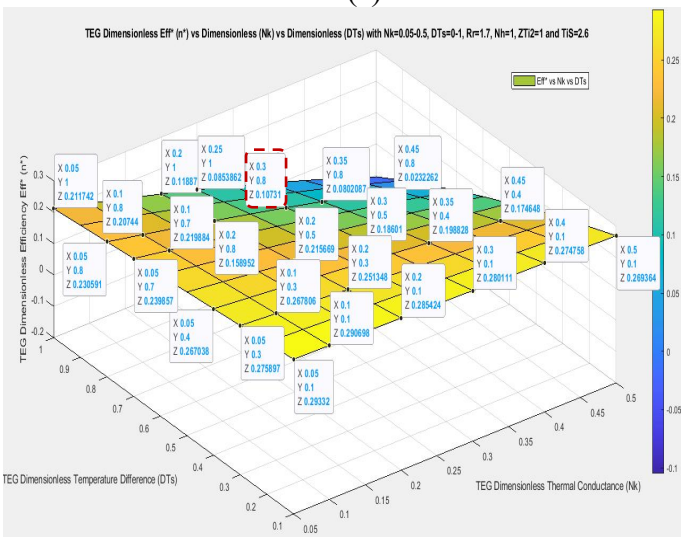

(f)

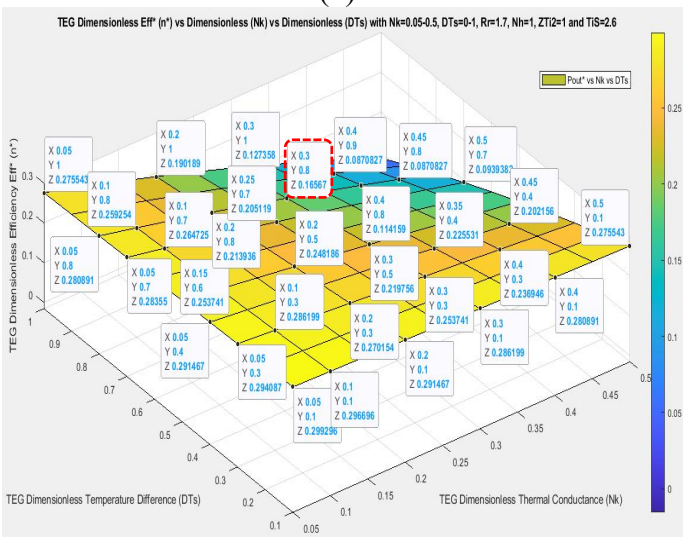

(l)

Figure 4.9: Performance and comparison plots of the: i) simple equations (4.32) and (4.33); **(a)** Q_{s1} vs N_k vs DT_s; **(b)** Q_{s2} vs N_k vs DT_s ; **(c)** P_{os} vs N_k vs DT_s ; **(d)** T_{s1} vs N_k vs DT_s ; **(e)** T_{s2} vs N_k vs DT_s ; **(f)** Eff^* vs N_k vs DT_s ; versus ii) simpler equations (4.36) and (4.37); **(g)** Q_{s1} vs N_k vs DT_s ; **(h)** Q_{s2} vs N_k vs DT_s ; **(i)** P_{os} vs N_k vs DT_s ; **(j)** T_{s1} vs N_k vs DT_s ; **(k)** T_{s2} vs N_k vs DT_s ; **(l)** Eff^* vs N_k vs DT_s .

4.2.5 TEG with Heatsinks Simulation Results Discussions and Validations

In Section 4.2.4, the study results were variously and extensively displayed, revealing what combinations of R_r vs N_k vs DT_s values that will give optimal Q_{s1}, Q_{s2}, P_{os}, T_{s1}, T_{s2} and Eff^* outcomes; by employing my newly introduced analytical equations (4.32) and (4.33) which are termed the "simple equations" and comparing with the further simplified versions, equations (4.36) and (4.37) which as well are termed the "simpler equations". It should be noted that each set of figures results, validate each other set of figures results. Furthermore, the figures on the left results (based on equations (4.32) and (4.33) exclusively) validate the figures on the right results (based on equations (4.36) and (4.37) exclusively). In what follows, the highlights of my presented findings are herein discussed and validated where applicable with reference to the original results presented in Lee (2013).

Beginning with Figure 4.3, parameters Q_{s1}, Q_{s2}, P_{os}, T_{s1}, T_{s2} and Eff^* are plotted against R_r with N_k =0.3 and DT_s=0.8 as well as ZT_{i2}=1, N_h=1, T_i=2.6 − which were fixed throughout my entire study and therefore have no relevance in my results and discussions. As evident, Q_{s1}, Q_{s2} and T_{s2} are inversely proportional to R_r with N_k=0.3 and DT_s=0.8. T_{s1} is directly proportional to R_r whereas P_{os} and Eff^* are initially directly proportional to R_r, until P_{os} and Eff^* reach their respective maximum value and then becomes inversely proportional to R_r and also with the rates of P_{os} and Eff^* incline and decline, being faster using the "simpler" equations (4.36) and (4.37). With the "simple" equations, my optimal values for P_{os} is 0.045518 and for Eff^* is 0.112407 and both occur at approximately R_r=2 and not at exactly R_r=1.7 as reported in Lee (2013); however, at R_r=1.7, my P_{os} and Eff^* values of 0.0451302 and 0.10731 respectively, are exactly the same as those reported in Lee (2013). With the "simpler" equations, my optimal values for P_{os} is 0.0893268 and for Eff^* is 0.170213 and both occur at different R_r values − at R_r=0.5 for P_{os} and at R_r=1.1 for Eff^*; however, at R_r=1.7, both the P_{os} and Eff^* values are respectively 0.0716775 and 0.16567, as well as respectively 0.0669887 and 0.161491 at R_r=2. The rest parameters Q_{s1}, Q_{s2}, T_{s1} and T_{s2} values are closely the same using either the "simple" or "simpler" analytical equations.

Figure 4.4 is similar to Figure 4.3, with the only difference being N_k =0.1-0.4 instead of just N_k =0.3 − this is to see the effects of different N_k values on Q_{s1}, Q_{s2}, P_{os}, T_{s1}, T_{s2} and Eff^* at also different R_r values. As observable, the results dynamics are the same; however, the following interesting aspects are evident i) Q_{s1}, Q_{s2} and T_{s2} values increase with increasing N_k values; however, they decrease with increasing R_r values as noticed and explained already; ii) T_{s1} values increase with decreasing N_k values; as well as increase with decreasing R_r values as noticed and already explained, iii) Eff^* values also increases with decreasing N_k values with the increase being more significant at lower values of R_r, especially at R_r values below 1 and finally iv) P_{os} values are interesting, as the dynamics are irregular

with different N_k values, with P_{os} values sharply increasing initially with decreasing N_k values and at very low R_r values and once after their respective optimal points, P_{os} values again increase but with now increasing N_k values and at high R_r values.

In Figure 4.5, parameters Q_{s1}, Q_{s2}, P_{os}, T_{s1}, T_{s2} and *Eff** are plotted against N_k with R_r=1.7 and DT_s=0.8 as well as ZT_{i2}=1, N_h=1, T_i=2.6 − which were fixed throughout the study. As can be seen, Q_{s1}, Q_{s2} and T_{s2} values are directly proportional to N_k. However, T_{s1} and *Eff** values are inversely proportional to N_k values. P_{os} initially increases proportionally to N_k till it reaches optimal point at N_k=0.25 in Figure 4.5c (simple equation) and N_k=0.3 in Figure 4.5i (simpler equation); thereafter, P_{os} values becomes inversely proportional to N_k.

Figure 4.6 is similar to Figure 4.5, with the only difference being R_r=0.5-2 instead of only R_r =1.7 − this is to see the effects of different R_r values on Q_{s1}, Q_{s2}, P_{os}, T_{s1}, T_{s2} and *Eff** at also over different N_k values. As noticeable, Q_{s1}, Q_{s2} and T_{s2} values are inversely proportional to R_r values, though directly proportional to N_k values as indicated earlier. Nevertheless, T_{s1} is directly proportional to R_r values but indirectly proportional to N_k. Initially, with increasing N_k, P_{os} increases more with less R_r at mostly low N_k values till maximum P_{os} is attained and thereafter, P_{os} decreases more with less R_r at high N_k values. The optimal P_{os} of 0.0478788 using my simple equation occurs at R_r=1.1 with N_k=0.2, whereas at R_r=1.7, the optimal P_{os}=0.0474483 with N_k=0.25 − slightly contrary to Lee (2013) which reported an optimal P_{os} of 0.045 at R_r=1.7 with N_k=0.3 − which we also have exactly the same result of P_{os}=0.0451302 at R_r=1.7 with N_k=0.3; however, this particular result values was not the exact optimal outcome in my case as reported above. Using my simpler equation, I have at R_r=0.5, two P_{os} optimal values of 0.0966733 and 0.0977376 at respectively N_k=0.2 and N_k=0.25. Initially *Eff** with increasing N_k, decreases more with more R_r at mostly low N_k values till optimal *Eff** is attained and thereafter, *Eff** decreases more with less R_r at high N_k values. This *Eff** dynamics is mostly and clearly noticeable in Figure 4.6l using my simpler equation.

Figure 4.7 is simply a 3D result representations of Figures 4.3 - 4.6 results. It enables better visualizations and interpretations of parameters Q_{s1}, Q_{s2}, P_{os}, T_{s1}, T_{s2} and *Eff** with both R_r and N_k varying respectively between 0.2-3.2 and 0.05-0.5 with DT_s fixed at 0.8.

Figure 4.8 is another 3D plot of Q_{s1}, Q_{s2}, P_{os}, T_{s1}, T_{s2} and *Eff** parameters against R_r=0.2-3.2 but with now DT_s=0-1 and N_k fixed at 0.3. The results summarily reveal that P_{os} and *Eff** increase proportionally with increasing DT_s, reach maximum and decrease, especially at lower R_r values but at higher R_r; P_{os} and *Eff** increase linearly with DT_s. Also, Q_{s1}, Q_{s2}, T_{s1} and T_s parameters exhibit comparable dynamics to those of Figure 4.7 results.

Figure 4.9 is another 3D plot of Q_{s1}, Q_{s2}, P_{os}, T_{s1}, T_{s2} and *Eff** parameters against N_k=0.05-0.5 but now with DT_s=0-1 and R_r fixed at 1.7. As apparent, Q_{s1}, Q_{s2} and T_{s2} have similar dynamics as already noted and discussed earlier in the previous figures. The only difference now is, these dynamics happen across different values of DT_s. The same dynamics applies to T_{s1} and *Eff**. P_{os} generally increases proportionally to DT_s at especially lower N_k values but at higher N_k values, P_{os} decreases with DT_s as revealed.

Generally, with the various dynamics, it is up to system designers to check and choose optimal values that will give the best outcomes depending on the aim, system constraints and the available resources.

Finally, Figure 4.10 shows the result adapted from Lee (2013) used to validate my findings − as asserted in Figures 4.2 - 4.9 and Table 4.1 where relevant. In sum, validating with Figure 4.10 results affirms i) exactly my simple equations results and ii) approximately my simpler equations results.

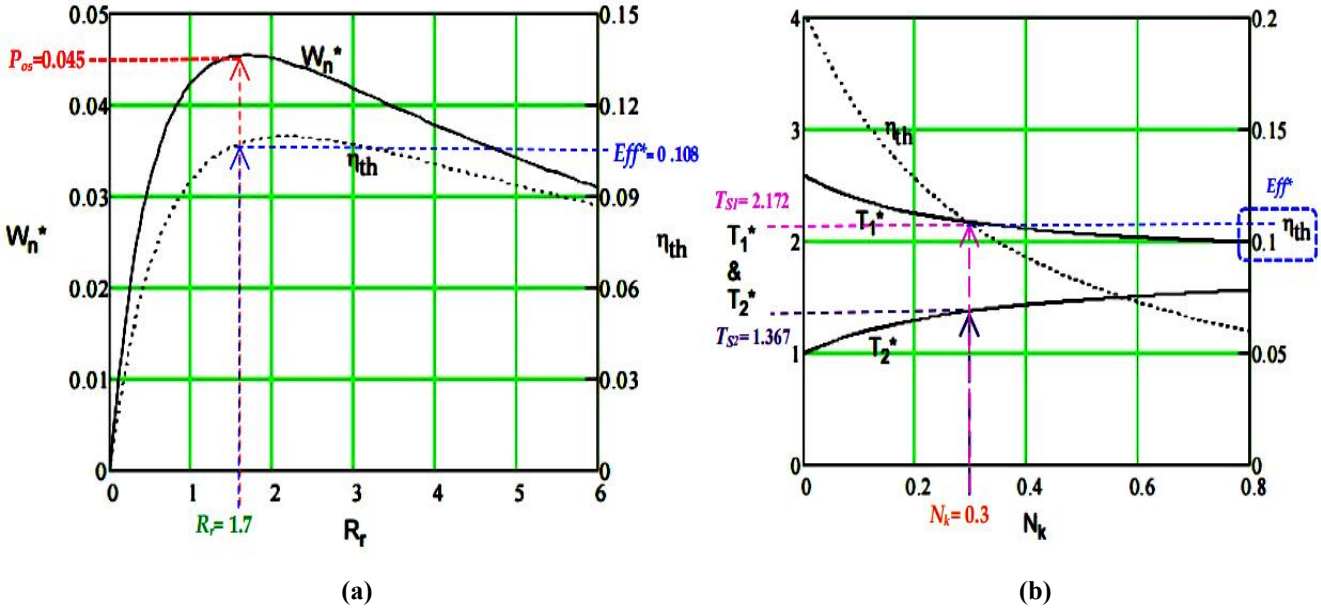

Figure 4.10: Results validation adapted from Lee (2013) (a) P_{os} (W_n*) and *Eff* *(n_{th}) vs R_r; (b) T_1*, T_2* and n_{th} vs N_k

4.2.6 Summary

South Africa has been facing unreliable electrical power supply which is becoming unbearable. Sustainable energy is transcending to be the future and to complement the national grid and for private use. As a result, I researched thermoelectricity as an alternative energy source (TEG) for household applications requiring low DC power and lighting. However, practical TEG use requires heatsinks to work efficiently and reliably but regrettably adding heatsinks add thermal resistances, which consequently degrades the TEG efficiency as well as its output power. I investigated various techniques, especially dimensional analysis and shortlisted the approach by Lee (2013) − which

converts thermal resistance to convection conductance, making it easier for practical use. However, the presentation in Lee (2013) falls short of the exact analytical formulas to directly calculate T_{s1} and T_{s2}; as a result, numerical analysis (a bit cumbersome) was used, which I developed further by introducing DT_s to simplify and derive novel simple accurate analytical formulas that can be applied to compute T_{s1} and T_{s2} directly. Furthermore, these simple formulas were further simplified to obtain simpler analytical equations for T_{s1} and T_{s2}. Finally, my simplest T_{s1} and T_{s2} formulas and their optimal relationship was established. These formulas were all verified with chosen optimal values and all gave approximate results that correlated each other. I further used these newly introduced formulas to model, numerically simulate and plotted various characteristics curves of Q_{s1}, Q_{s2}, P_{os}, T_{s1}, T_{s2} and Eff^* against R_r vs N_k vs DT_s using Matlab and Simulink. These results were articulated variously in both 2 and 3D plots and finally the outcomes were comparatively discussed and validated amongst each other and as well with results asserted in Lee (2013). In Lee (2013), P_{os} of 0.045 is optimal with N_k=0.3 at R_r=1.7, contrary to my study which gave optimal P_{os} of 0.0474483 at N_k=0.25 using my simple equations; however, using my simpler equations, it gave optimal P_{os} of 0.0716775 at N_k=0.3. Notwithstanding, my simple equations gave P_{os} of 0.0451302 at N_k=0.3 (though less optimal in my case) which corresponds exactly to optimal P_{os} value of 0.045 with N_k=0.3 as in Lee (2013). In addition, the magnitude of P_{os} and Eff^* are more (almost doubled) using my simpler equations (4.36) and (4.37), compared to using my simple equations (4.32) and (4.33). Furthermore, the optimal values of P_{os} and Eff^* using both my "simple" and "simpler" equations, respectively occurred at different values of R_r. In sum, Eff^* is best at very low N_k values. The highlights of this study are marked in the various figures and also summarized in Table 4.1 and it's worth mentioning that, DT_s=0.8 for this set of optimal values, is only rightly equal to T_{s1} - T_{s2} = ~0.8 only at R_r=1.7 and N_k=0.3 as optimally established and not at any other values when used in both my simple and simpler equations. Finally, in as much as my newly introduced simpler analytical formulas didn't give P_{os} and Eff^* results correlating those in i) Lee (2013) and ii) my newly introduced analytical simple equations (that gave accurate results the same as in Lee, 2013), I proffer my simpler equations can always be used as a first approximation to quickly find T_{s1} and T_{s2} values and then further find also Q_{s1} and Q_{s2} values which have been validated to be similar when using the new simple and simpler equations for T_{s1} and T_{s2}. In sum, T_{s1} and T_{s2} are the most vital parameters, as they are those that are easily practically manipulated to achieve the other values; however, first ascertaining the electrical load or R_r value is most paramount to achieve optimal results, as a TEG as well TEC, are non-linear devices whose dynamics must be well understood before embarking on a practical design − which is the next phase of my research, to validate and refine the study practically and then design a 1kW domestic power supply.

4.3 Simplified Thermoelectric Cooler (TEC) with Heatsinks Modeling and Simulation using Matlab and Simulink based-on Dimensional Analysis

Energy sustainability is becoming central nowadays, especially in South Africa due to electricity blackouts. This section embarks on clean alternative energy based-on thermoelectricity with focus now on TEC with heatsinks. Contrary to the theoretical TEC model, in practice, using a TEC do requires heatsinks or heat-exchangers to function properly but heatsinks also introduce thermal resistance which affects its cooling power and efficiency − which must be addressed. As a result, a TEC with heatsinks model based-on dimensional analysis using Matlab / Simulink is examined herein. My study novel contributions are i) derivation of analytical forms for the TEC dimensionless cold and hot sides temperature and ii) Simulink TEC with heatsinks theoretical model based-on a simplified dimensional analysis, whereby a TEC with heatsinks parameters of interest can be easily simulated to ascertain analytically, numerically and graphically its optimal performance before implementing physically.

4.3.1 Introduction

According to Van der Walt (2017), South Africa is being committed towards its fight for a low carbon and green economy with focus on energy mix to ensure energy security. As per ratification of the Paris agreement, renewable energy and energy efficiency integration, as well as the policies and regulatory developments are progressively refined with respect to the present framework − which is hampered by ongoing electrical power-cuts due to high pressure on the national grid from increase demands (especially during winter) that the Eskom supply cannot sustain because of inadequate infrastructure that's failing from time to time. As a result, there is need for renewable energy to sustain the unstable national grid and also for private use. These developments necessitate my research for an alternative energy based on thermoelectricity with focus on basic households and commercial energy supply and energy efficient loads. Simply, thermoelectric generators (TEGs) cleanly convert low grade heat to DC electricity, whereas TECs enable clean production of cold and heat from DC electricity. Both TEGs and TECs if designed properly, can be fairly energy efficient and very handy for primary households and commercial energy needs such as DC lighting, cooling and heating that are basic necessities. An ideal theoretical framework for TEGs and TECs were respectively comprehensively presented in Bayendang *et al.* (2020c) and Bayendang *et al.* (2020d); however, both lack practical considerations which this study seeks to bring forth and is thus, engaged next; as well as in Bayendang *et al.* (2021b).

4.3.2 Background

Thermoelectricity or thermoelectric (TE) devices in the forms of TEGs and TECs, cannot practically and reliably function without heatsinks or some sorts of proper heat-exchangers to maintain a safe temperature difference on the TEG and TEC sides and most importantly to dissipate the internal heat

cause by Ohmic heating as a result of the current flowing through the TEG / TEC. This heat if not handled properly and becomes excessive, will not only cause inefficiency but can damage the TEG and TEC due to over heating, which will cause the solder joints binding the thermoelectric devices p-n thermocouples to melt. However, the addition of heatsinks in this case to address the thermoelectric devices practical limitations, also adds / increases the thermal resistance on the TEGs and TECs sides as depicted in Figure 4.11, thus making the thermoelectric devices inefficient.

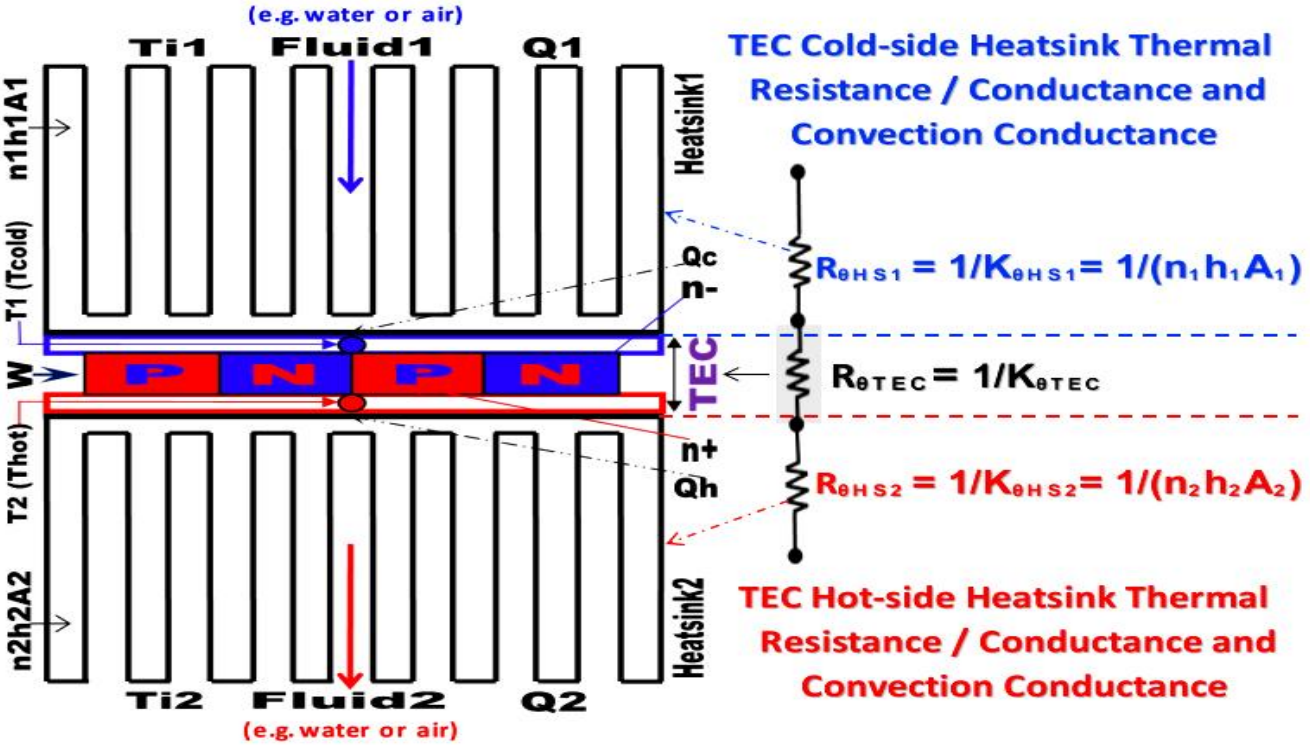

Figure 4.11: TEC with heatsinks on its hot and cold sides (adapted from Lee, 2013)

Asserted in Lineykin and Ben-Yaakov (2006), Casano and Piva (2012), Lee (2013), Flores-Niño (2015), Melnikov *et al.* (2017), Lu *et al.* (2018), Hao *et al.* (2020), Hubbard *et al.* (2020) and Dos Santos Guzella (2021), is a technique called dimensional analysis and can be used to improve TE devices efficiency when used with heatsinks. This study with focus on TEC, applies and developed further the apt approach in Lee (2013); by using now a simplified Matlab / Simulink implementation. Presented next is the applicable mathematics that applies to the heatsinks when used with a TEC and the newly derived analytical formulas as well as the extra equivalent numerical simplifications I contributed, considering the prior analytical methods limitation. This is then proceeded with the depiction of the simulator friendly user interface for the implemented TEC model using Matlab / Simulink, followed by the results and results interpretations as well as validations and finally, concluding remarks are drawn.

4.3.3 TEC with Heatsinks Applicable Mathematics

The applicable mathematics for a TEC when used with heatsinks is expressed and then followed by my additional simplification to the excellent approach presented by Lee (2013). Dimensional analysis basically enables same unit parameters to be normalised between their minimum and maximum values, hence making them dimensionless and easy to work with. However, unique in Lee (2013) is the conversion of TEC heatsink thermal resistances to their convection conductance − this optimization method eliminates the TEC heatsink thermal resistances which are difficult to work with, in favour of the TEC fluid convection conductance which are relatable to the TEC heatsinks fluid temperature and are practically easier to work with. The mathematical analysis is presented thus:

4.3.3.1 TEC with Heatsinks General Heat Flow Equations

The following heat equations are expressed and their thermal resistance, thermal conductance and convection conductance relationships are established as follows:

$$Q_1 = K_1(T_{i1} - T_1) \quad \text{(W)} \tag{4.40}$$

$$Q_2 = K_2(T_2 - Ti_2) \quad \text{(W)} \tag{4.41}$$

where Q_1 and Q_2 are respectively the heat flows on the heatsinks on the TEC cold-side and hot-side, K_1 and K_2 are the respective thermal conductance of the heatsinks on the TEC cold-side and hot-side, T_{i1} and T_{i2} are the respective temperatures of the heatsinks fluid on the TEC cold and hot sides and finally T_1 and T_2 are the respective cold and hot p-n junction temperatures on the TEC sides.

It should be noted that thermal resistance is the inverse of thermal conductance which is equivalent to convection conductance and therefore equations (4.40) and (4.41) in terms of the convection conductance (ηhA), can be written as:

$$Q_1 = \eta_1 h_1 A_1(T_{i1} - T_1) \quad \text{(W)} \tag{4.42}$$

$$Q_2 = \eta_2 h_2 A_2(T_2 - T_{i2}) \quad \text{(W)} \tag{4.43}$$

where η_1 is heatsink1 (on TEC cold-side) fin efficiency, h_1 is heatsink1 convection coefficient and A_1 is heatsink1 total surface area. Likewise, η_2 is heatsink2 (on TEC hot-side) fin efficiency, h_2 is heatsink2 convection coefficient and finally A_2 is heatsink2 total surface area.

TEC standard theoretical heat equations are given as:

$$Q_C = n[(SIT_1) - (K\Delta T)] - 0.5I^2R \quad \text{(W)} \tag{4.44}$$

$$Q_h = n[(SIT_2) - (K\Delta T)] + 0.5I^2R \quad \text{(W)} \tag{4.45}$$

where Q_c is the cooling power or heat absorbed on TEC cold-side, n quantity of thermocouples used in the TEC, S is the Seebeck coefficient, I the input current to the TEC, K is the thermal conductance (calculated as ak/l, where a is the area of the TEC p-n junction thermocouple, k the p-n junction thermocouple thermal conductivity and l the length of the TEC p-n junction thermocouple), ΔT is the temperature difference $T_2 - T_1$ across the TEC, $R=nr$ is the TEC module resistance, where r is the resistance of the TEC p-n junction thermocouple and Q_h is the heat emitted on TEC hot-side. It should be noted that the three terms on the right side of equations (4.44) and (4.45) are respectively the Seebeck / Peltier, Fourier / Heat and Ohmic / Joule terms with S, K and R considered as temperature independent. Considering the energy balance of the TEC with heatsinks system, equations (4.40), (4.42) and (4.44) are now respectively equivalent to equations (4.41), (4.43) and (4.45) which reduce to (with the unknown parameters being only T_1, T_2 and I):

$$Q_1=Q_C=K_1(T_{i1}-T_1)=\eta_1 h_1 A_1(T_{i1}-T_1) = n[(SIT_1)-(K\Delta T)]-0.5I^2R \quad \text{(W)} \quad (4.46)$$

$$Q_2=Q_h=K_2(T_2-T_{i2})=\eta_2 h_2 A_2(T_2-T_{i2}) = n[(SIT_2)-(K\Delta T)]+0.5I^2R \quad \text{(W)} \quad (4.47)$$

Now, according to Lee (2013), to optimize the TEC with heatsinks (HS), the following dimensionless parameters are defined with respect to fluid 2 (air or water on TEC hot-side heatsink2) and since the optimization is made dimensionless with respect to fluid 2, fluid 2 convection conductance and temperature (T_{i2}) are initially provided.

4.3.3.2 TEC-HS Dimensionless Thermal Conductance (N_k)

This is the thermal conductance K divided by the convection conductance ηhA in fluid 2, expressed as:

$$N_k = K / \eta hA = (ak/l) / \eta_2 h_2 A_2 \quad (4.48)$$

4.3.3.3 TEC-HS Dimensionless Convection (N_h)

This is fluid 1 convection conductance divided by fluid 2 convection conductance, expressed as.

$$N_h = \eta_1 h_1 A_1 / \eta_2 h_2 A_2 \quad (4.49)$$

4.3.3.4 TEC-HS Dimensionless Current (N_i)

$$N_i = SI / K = SI / (ak/l) \quad (4.50)$$

4.3.3.5 TEC Dimensionless Temperatures (T_{s1}, T_{s2} and T_i)

The dimensionless temperatures are given as:

$$T_1 \text{ dimensionless temperature: } T_{s1} = T_1 / T_{i2} \quad (4.51)$$

$$T_2 \text{ dimensionless temperature: } T_{s2} = T_2 / T_{i2} \quad (4.52)$$

$$\text{Fluids dimensionless temperature: } T_i = T_{i1} / T_{i2} \quad (4.53)$$

4.3.3.6 TEC-HS Dimensionless Cooling Power (Q_{s1})

$$Q_{s1} = Q_1 / \Pi_2 h_2 A_2\ T_{i2} \tag{4.54}$$

4.3.3.7 TEC-HS Dimensionless Heating Power (Q_{s2})

$$Q_{s2} = Q_2 / \Pi_2 h_2 A_2\ T_{i2} \tag{4.55}$$

NB: Q_{s2} is also known as the dimensionless heat released by the heatsink on the TEC hot-side.

4.3.3.8 TEC Dimensionless Input Power (P_{ins} or W_s)

$$P_{ins} = P_{in} / \Pi_2 h_2 A_2\ T_{i2} \tag{4.56}$$

$$W_s = P_{ins} = Q_{s2} - Q_{s1} \tag{4.57}$$

4.3.3.9 TEC Dimensionless Input Voltage (V_{ins})

$$V_{ins} = V / nST_{i2} \tag{4.58}$$

$$V_{ins} = P_{ins} / N_k N_i \tag{4.59}$$

4.3.3.10 TEC Coefficient of Performance (CoP)

NB: CoP is already dimensionless.

$$CoP = Q_{s1} / W_s \tag{4.60}$$

4.3.3.11 TEC-HS Dimensionless Cooling Power (Q_{s1}) in terms of T_{s1}

$$Q_{s1} = N_h (T_i - T_{s1}) \tag{4.61}$$

4.3.3.12 TEC-HS Dimensionless Heating Power (Q_{s2}) in terms of T_{s2}

$$Q_{s2} = T_{s2} - 1 \tag{4.62}$$

According to Lee (2013), by using the dimensionless equations (4.48) - (4.53); equations (4.42) - (4.45) boils down to the following two equations (4.63) and (4.64) with five unknowns which must be solved for T_{s1} and T_{s2} in terms of five independent dimensionless parameters of N_k, N_h, N_i, T_i and ZT_{i2}.

$$N_h(T_i - T_{s1}) / N_k = N_i T_{s1} - ((Ni^2) / (2ZT_{i2})) + (T_{s1} - T_{s2}) \tag{4.63}$$

$$(T_{s2} - 1) / N_k = N_i T_{s2} + ((Ni^2) / (2ZT_{i2})) + (T_{s1} - T_{s2}) \tag{4.64}$$

These two expressions (i.e. equations (4.63) and (4.64)) and the whole process is very cumbersome to determine T_{s1} and T_{s2}; as a result, it was not analytically solved further in Lee (2013) due to the inept closed-form expressions and were further expressed as functions shown in equations (4.65) and (4.66). A numerical method using tables / graphs / approximations were employed by Lee (2013) and also a simulation option using Mathcad was recommended.

$$T_{s1} = f(N_k, N_h, N_i, T_i, ZT_{i2}) \quad (4.65)$$

$$T_{s2} = f(N_k, N_h, N_i, T_i, ZT_{i2}) \quad (4.66)$$

However, I analytically simplify equations (4.63) and (4.64) further and expressed T_{s1} and T_{s2} directly in terms of the five independent dimensionless parameters N_k, N_h, N_i, T_i and ZT_{i2}. I developed the numeric approximation method further to clearly prove and calculate the exact values for T_{s1} and T_{s2} by using the now newly introduced analytical formulas for T_{s1} and T_{s2}. These new equations are not found anywhere in the available literature to the best of my knowledge. In the next section, my analytical approach is developed further from equations (4.63) and (4.64) to solve for T_{s1} and T_{s2} directly.

4.3.3.13 TEC Dimensionless Temperatures (T_{s1} and T_{s2}) Formula

Subtracting equation (4.63) from (4.64) and simplifying further gives equation (4.67) as expressed below:

$$(T_{s2} - 1) / N_k - (N_h (T_i - T_{s1})) / N_k \quad = \quad N_i T_{s2} - N_i T_{s1} + N_i^2 / ZT_{i2} \quad (4.67)$$

Solving for T_{s1} and T_{s2}, yield equations (4.68) and (4.69).

$$T_{s1} = (2N_k ZT_{i2} + Ni^2 N_k + 2N_i^2 N_k^2 - N_i^3 N_k^2 + 2N_h T_i ZT_{i2} + 2N_h N_k T_i ZT_{i2} - 2N_h N_i N_k T_i ZT_{i2}) / (2ZT_{i2}(N_h + N_k - N_i^2 N_k^2 + N_h N_k + N_i N_k - N_h N_i N_k)) \quad (4.68)$$

$$T_{s2} = (2N_h ZT_{i2} + 2N_k ZT_{i2} + 2N_i^2 N_k^2 + N_i^3 N_k^2 + 2N_i N_k ZT_{i2} + N_h N_i^2 N_k + 2N_h N_k T_i ZT_{i2}) / (2ZT_{i2}(N_h + N_k - N_i^2 N_k^2 + N_h N_k + N_i N_k - N_h N_i N_k)) \quad (4.69)$$

As can be seen, equations (4.68) and (4.69) can be used to directly calculate T_{s1} and T_{s2}. These are novel analytical T_{s1} and T_{s2} formulas derived in terms of N_k, N_h, N_i, T_i and ZT_{i2}; which together with formula (4.67) can now be easily solved further, given the N_k, N_h, N_i, T_i and ZT_{i2} values as follows.

Let ZT_{i2}=1 and N_h=1; equations (4.67) to (4.69) reduce to:

$$(T_{s2} - 1)/N_k - (T_i - T_{s1})/N_k = N_i T_{s2} - N_i T_{s1} + N_i^2 \quad (4.70)$$

$$T_{s1} = (2N_k + 2T_i + 2N_k T_i + N_i^2 N_k + 2N_i^2 N_k^2 - N_i^3 N_k^2 - 2N_i N_k T_i) / (-2N_i^2 N_k^2 + 4N_k + 2) \quad (4.71)$$

$$T_{s2} = (2N_k + 2N_k T_i + N_i^2 N_k + 2N_i^2 N_k^2 + N_i^3 N_k^2 + 2N_i N_k + 2) / (-2N_i^2 N_k^2 + 4N_k + 2) \quad (4.72)$$

Let ZT_{i2}=1, N_h=1 and T_i=0.97; equations (4.67) to (4.69) become:

$$(T_{s2}\text{-}1)/N_k + (T_{s1}\text{-}97/100)/N_k = N_i T_{s2} - N_i T_{s1} + N_i^2 \quad (4.73)$$

$$T_{s1} = (-N_i^3 N_k^2 + 2N_i^2 N_k^2 + N_i^2 N_k - (97N_i N_k)/50 + (197N_k)/50 + 97/50) / (-2N_i^2 N_k^2 + 4N_k + 2) \quad (4.74)$$

$$T_{s2} = (N_i^3 N_k^2 + 2N_i^2 N_k^2 + N_i^2 N_k + 2N_i N_k + (197N_k)/50 + 2) / (-2N_i^2 N_k^2 + 4N_k + 2) \quad (4.75)$$

Let ZT_{i2}=1, N_h=1, T_i=0.97 and N_k=0.3; equations (4.67) to (4.69) boil down to:

$$(10T_{s1})/3+(10T_{s2})/3 \ - \ 197/30 = N_iT_{s2} \ - N_iT_{s1}+N_i^2 \tag{4.76}$$

$$T_{s1} = ((9N_i^3)/100 \ - \ (12N_i^2)/25+(291N_i)/500 \ - \ 1561/500) \ / \ ((9N_i^2)/50 \ - \ 16/5) \tag{4.77}$$

$$T_{s2} = \ - \ ((9N_i^3)/100 + (12N_i^2)/25 + (3N_i)/5 + 1591/500) \ / \ ((9N_i^2)/50 \ - \ 16/5) \tag{4.78}$$

Finally, let ZT_{i2}=1, N_h=1, T_i=0.97, N_k=0.3 and Ni=0.5; equations (4.67) to (4.69) give the final optimum solutions as:

$$T_{s1} = 409 \ / \ 230 \ - \ (17T_{s2}) \ / \ 23 \tag{4.79}$$

$$T_{s2} = 23((409 \ / \ 230) \ - T_{s1}) \ / \ 17 \tag{4.80}$$

$$T_{s1} = \ 0.9318$$

$$T_{s2} = 1.1452$$

Equations (4.79) and (4.80) are the simplest optimal relationships between T_{s1} and T_{s2} and both can be substituted in equations (4.61) and (4.62) to compute Q_{s1}, Q_{s2} and as well compute W_s using equation (4.57). We can then further calculate the other parameters such as CoP, V_{ins}, V, P_{in}, Q_2, Q_1, T_2, T_1 and I.

4.3.4 TEC with Heatsinks Modeling

The applicable TEC heatsinks mathematics based on dimensional analysis was presented in Section 4.3.3 and the equations for T_{s1} and T_{s2} were developed and analytically expressed in terms of the five independent parameters N_k, N_h, N_i, T_i and ZT_{i2} and furthermore optimally simplified and validated in terms of T_{s1} and T_{s2} using equations (4.79) and (4.80). As evident, the whole analytical and numerical processes could be very cumbersome as well as erroneous if done manually. In light of this, a TEC model with heatsinks on both the TEC cold and hot sides, was designed based on the equations presented in Section 4.3.3 and modeled using Matlab and Simulink. Included in the simulated TEC with heatsinks model, are some of the i) TEC parameters analysed in Section 4.3.3 including: the Seebeck coefficient S, the absolute temperature in kelvin 273.15, heatsink1 fluid temperature T_{i1}, heatsink2 fluid temperature T_{i2}, if need be infinite TECs in series T_s and or parallel T_p, TEC p-n thermocouple resistance r, thermal conductivity k, electrical resistivity P, p-n thermocouple area a, p-n thermocouple length l and the TEC total cooling power required $Qreq$, and ii) heatsinks parameters such as the area of heatsink base Ab, heatsink1 fins efficiency n_1, heatsink1 fluid convection coefficient h_1, heatsink1 total area A_1 including fins sides, heatsink2 fins efficiency n_2, heatsink2 fluid convection coefficient h_2 and heatsink2 total area A_2 including fins sides. All these parameters can simply be

entered and the TEC optimal parameters value calculated as portrayed in Figure 4.12. Optionally, the TEC dimensionless parameters such as dimensionless current N_i, dimensionless thermal conductance N_k, the coefficient of performance CoP, the dimensionless cooling power Q_{s1}, TEC cold-side dimensionless temperature T_{s1}, TEC hot-side dimensionless temperature T_{s2} and the dimensionless voltage N_v as well as the TEC half dimensionless optimal parameters not discussed (which are simply half the value of the dimensionless parameters discussed, to ensure safer design margins), can be either input manually (as shown on the left side of the TEC with heatsinks in Figure 4.12) or automatically calculated and used to finally compute the actual physical parameters values in SI units, as depicted on the right side of the TEC with heatsinks in Figure 4.12. Some of the TEC physical parameters of interest auto calculated include the TEC figure of merit Z, the TEC number of p-n thermocouples n, the TEC cooling power Q_1, the TEC input power W_n or P_{in}, the TEC cold-side temperature T_1, the TEC hot-side temperature T_2, the TEC input voltage V_{in}, the TEC input current I, the total number of TEC modules required N, TEC total power consumption W_t, the TEC total internal source resistance R, the TEC temperature difference DT or ΔT, the TEC maximum CoP (CoP_{max}), the input current I_{cop} needed to give CoP, the TEC with heatsinks cooling power density QPD, fluids 1 and 2 dimensionless convection conductance (nhA) and as well the TEC corresponding half optimal values for the mentioned parameters. The input and output parameters were grouped together based on their similarities, named and colour coded accordingly to make the TEC with heatsinks model easy to understand and also user friendly.

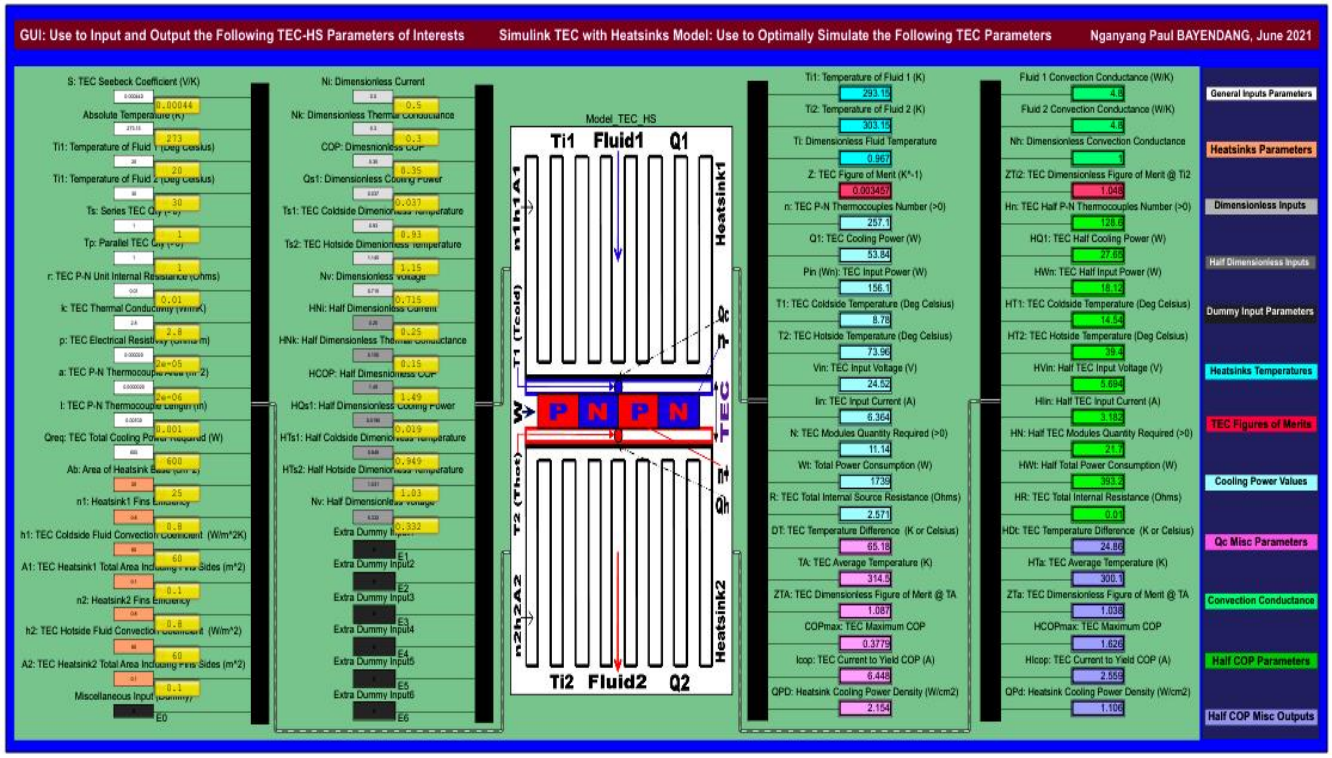

Figure 4.12: Novel Matlab / Simulink TEC with heatsinks model − simulated numerical results

In addition to the TEC with heatsinks numeric model calculations, characteristics curves of some of the crucial parameters such as the TEC dimensionless cooling power Q_{s1}, the TEC dimensionless heating power Q_{s2}, the TEC dimensionless input power P_{ins} or W_s, the TEC CoP and the TEC dimensionless temperatures T_{s1} and T_{s2}; were plotted against the TEC dimensionless input current N_i and the TEC dimensionless thermal conductance N_k to graphically calculate Q_{s1}, Q_{s2}, P_{ins}, CoP, T_{s1} and T_{s2} optimal values for i) ZT_{i2}=1, N_h=1, T_i =0.97, N_k=0.1-1 and N_i=0-1 and ii) for ZT_{i2}=1, N_h=1, T_i =0.97, N_k=0-1 and N_i =0.1-1. These graphical results are displayed next in Figures 4.13 to 4.24.

4.3.5 TEC with Heatsinks Graphical Results

The following characteristic curves were plotted.

4.3.5.1 With ZT_{i2}=1, N_h=1, T_i=0.97, N_k=0.1-1 and N_i=0-1

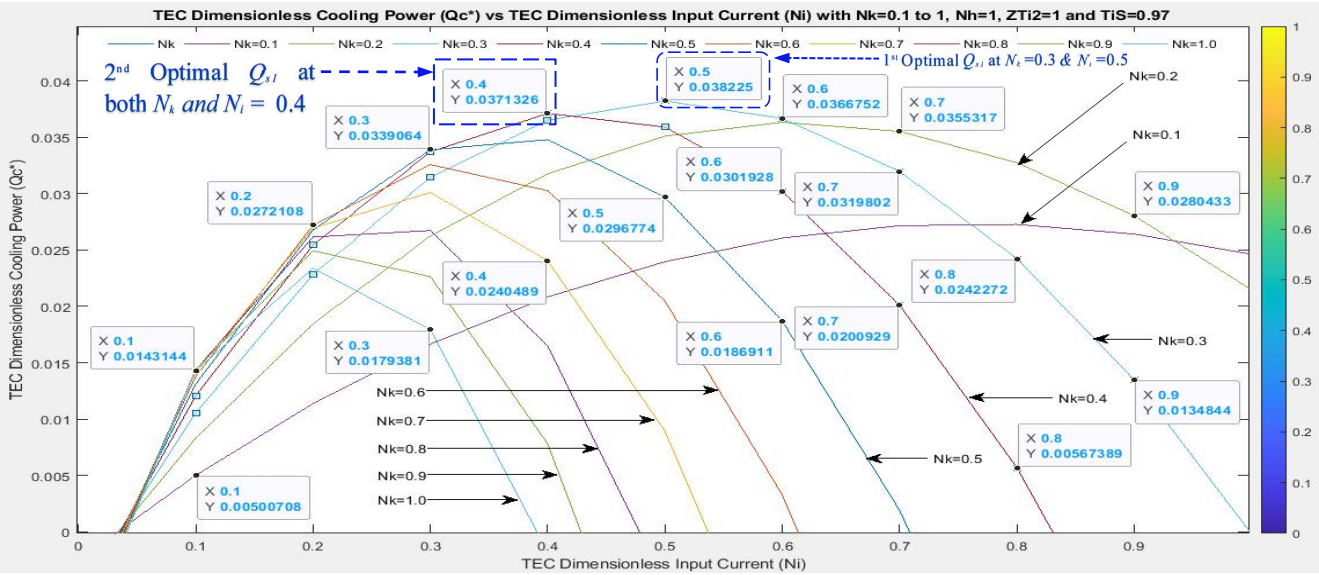

Figure 4.13: Dimensionless cooling power Q_{s1} *vs* dimensionless input current N_i

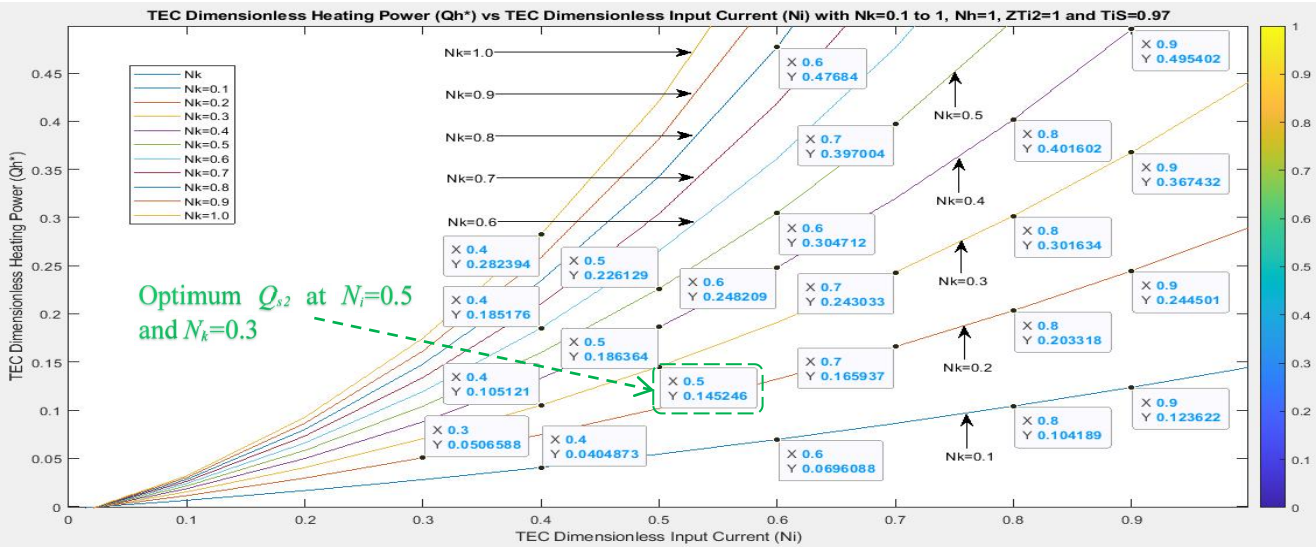

Figure 4.14: Dimensionless heating power Q_{s2} *vs* dimensionless input current N_i

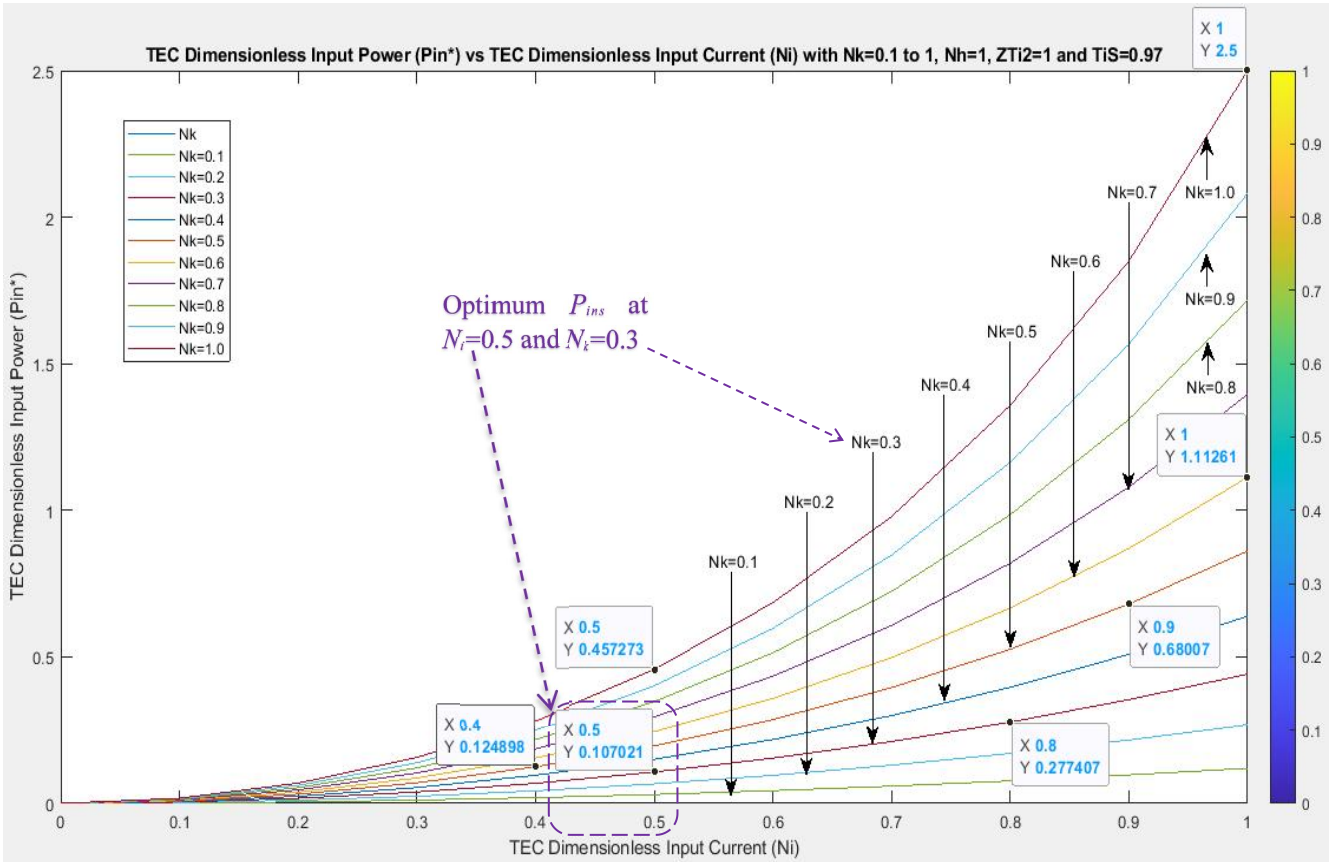

Figure 4.15: Dimensionless input power P_{ins} *vs* dimensionless input current N_i

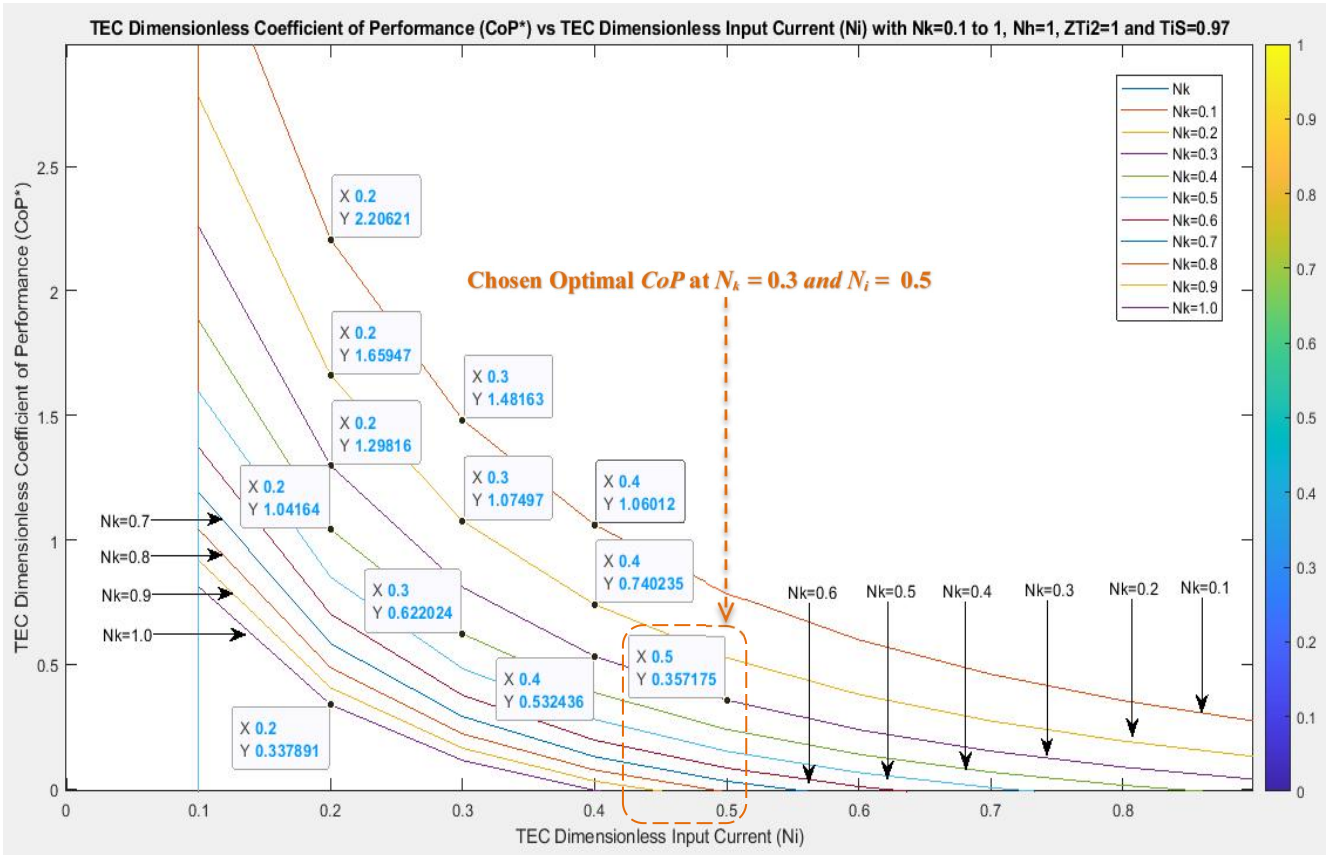

Figure 4.16: Dimensionless *CoP vs* dimensionless input current N_i

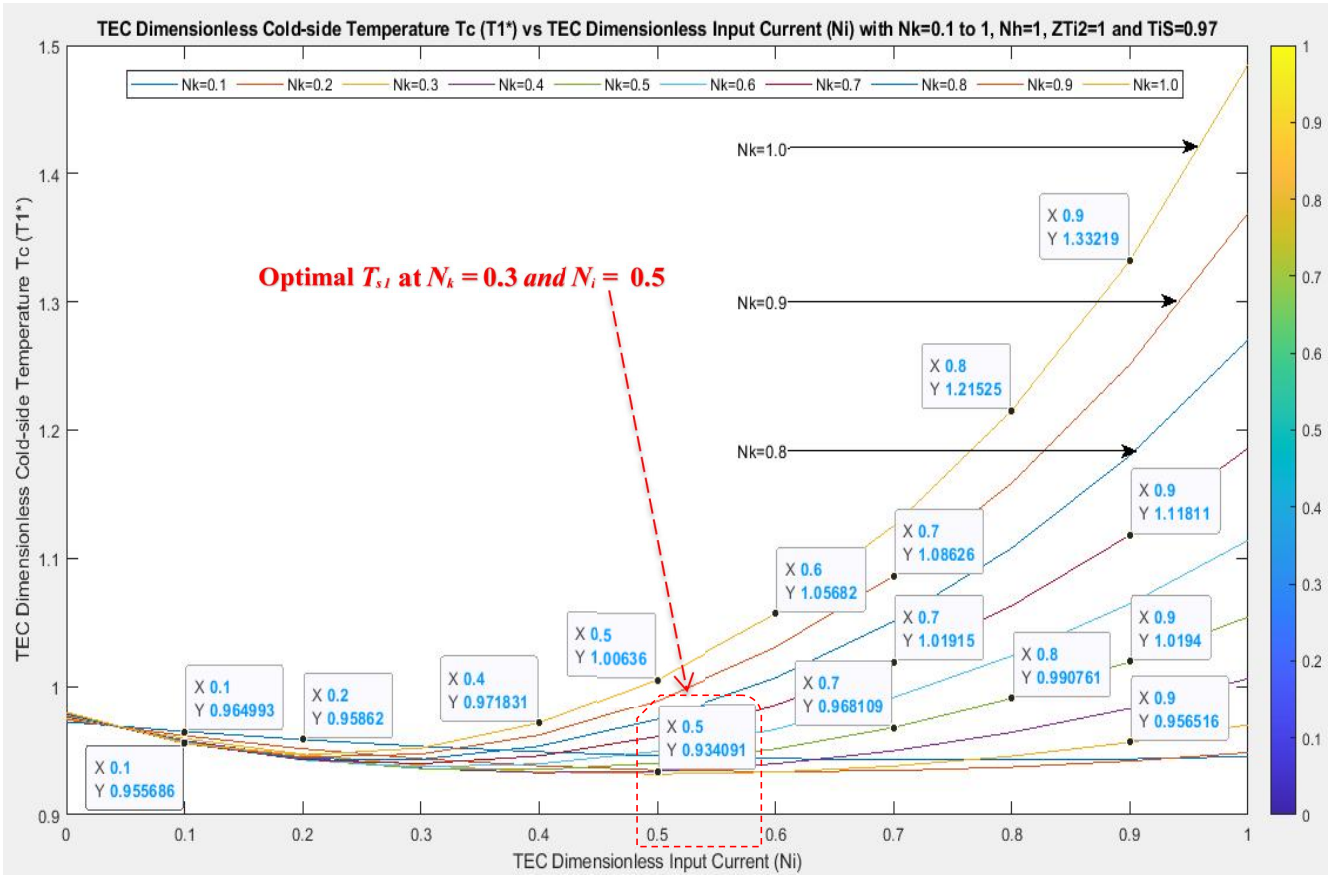

Figure 4.17: Dimensionless TEC cold-side T_{s1} *vs* dimensionless input current N_i

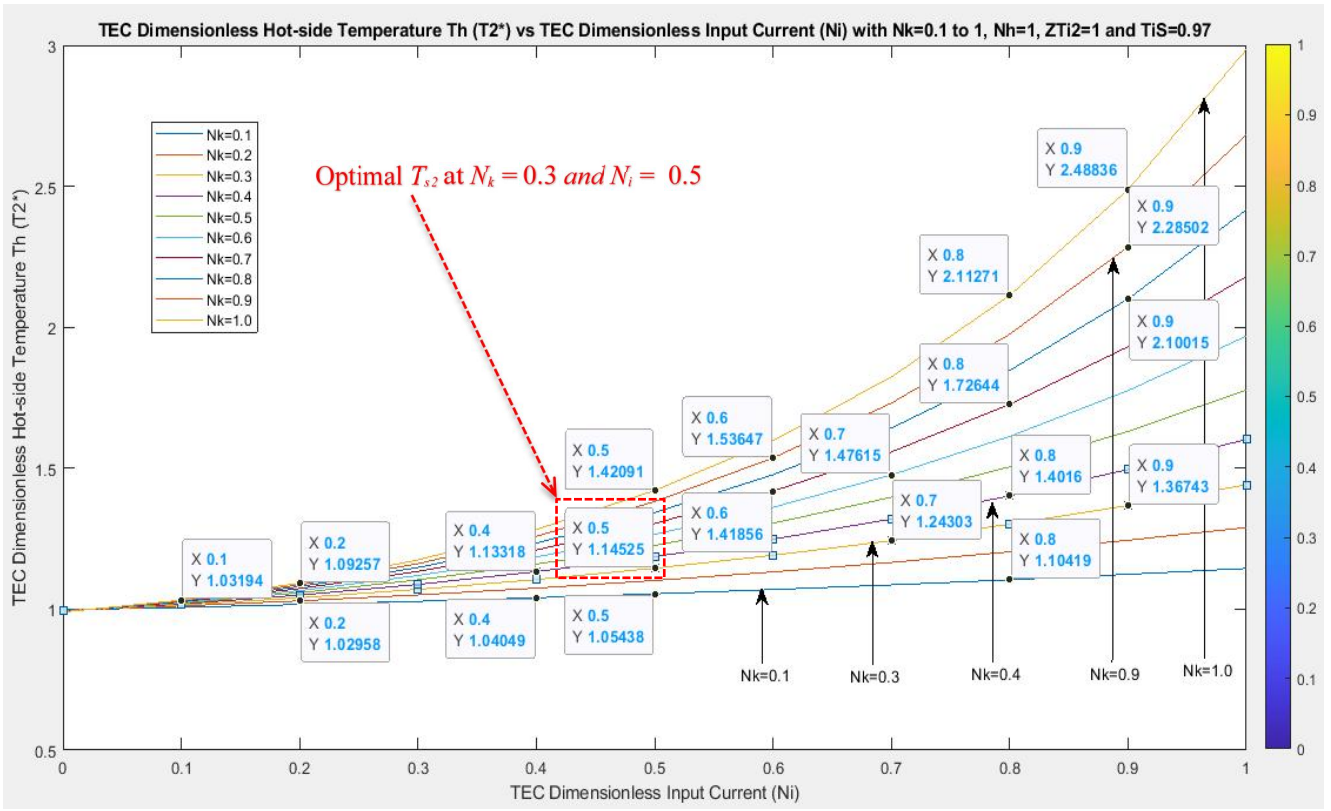

Figure 4.18: Dimensionless TEC hot-side T_{s2} *vs* dimensionless input current N_i

4.3.5.2 With ZT_{i2}=1, N_h=1, T_i=0.97, N_i=0.1-1 and N_k=0-1

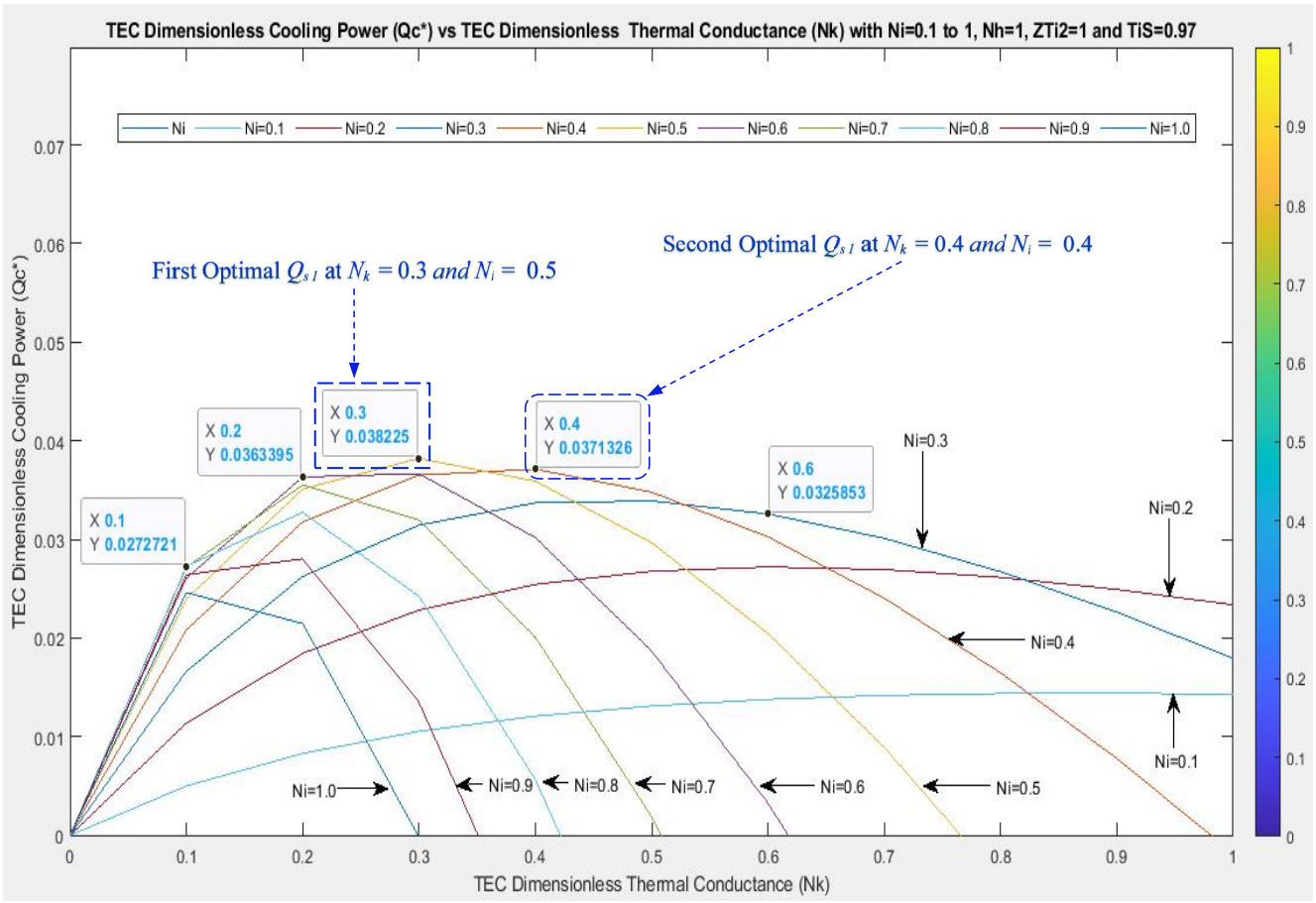

Figure 4.19: Dimensionless cooling power Q_{s1} *vs* dimensionless thermal conductance N_k

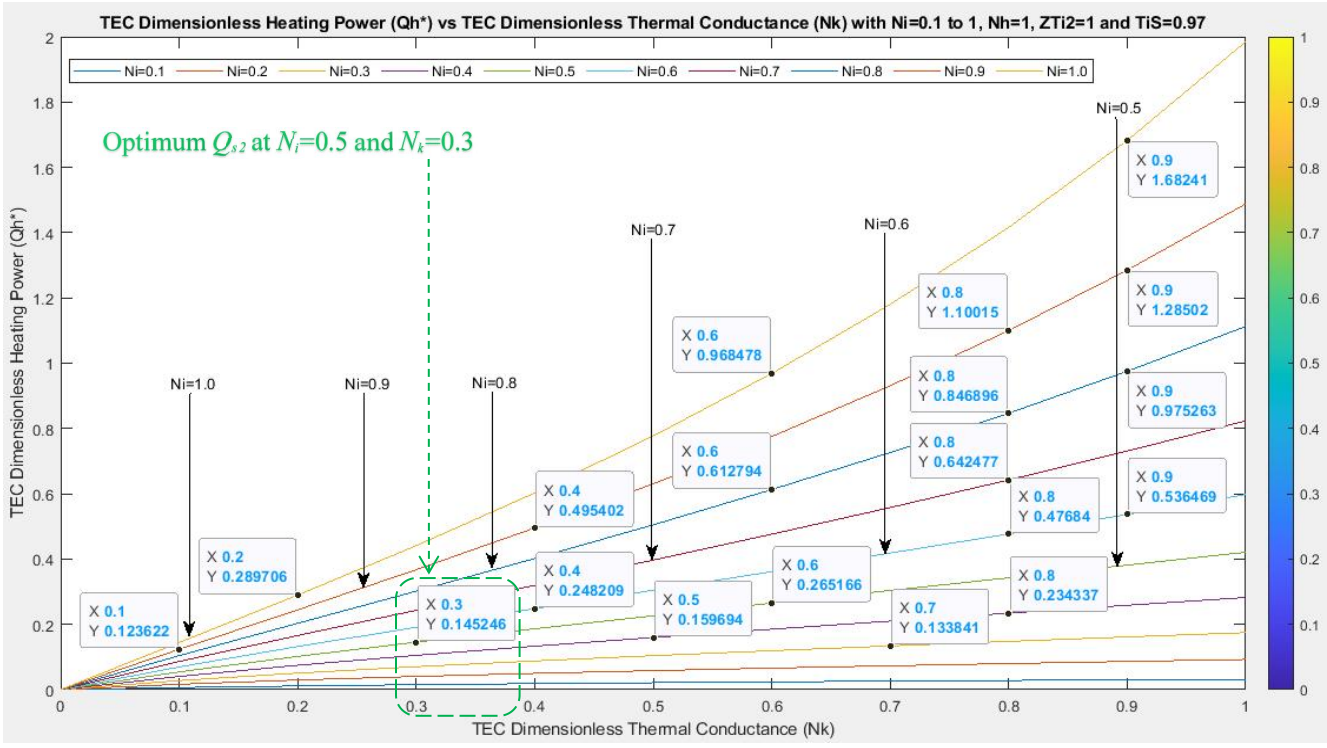

Figure 4.20: Dimensionless heating power Q_{s2} *vs* dimensionless thermal conductance N_k

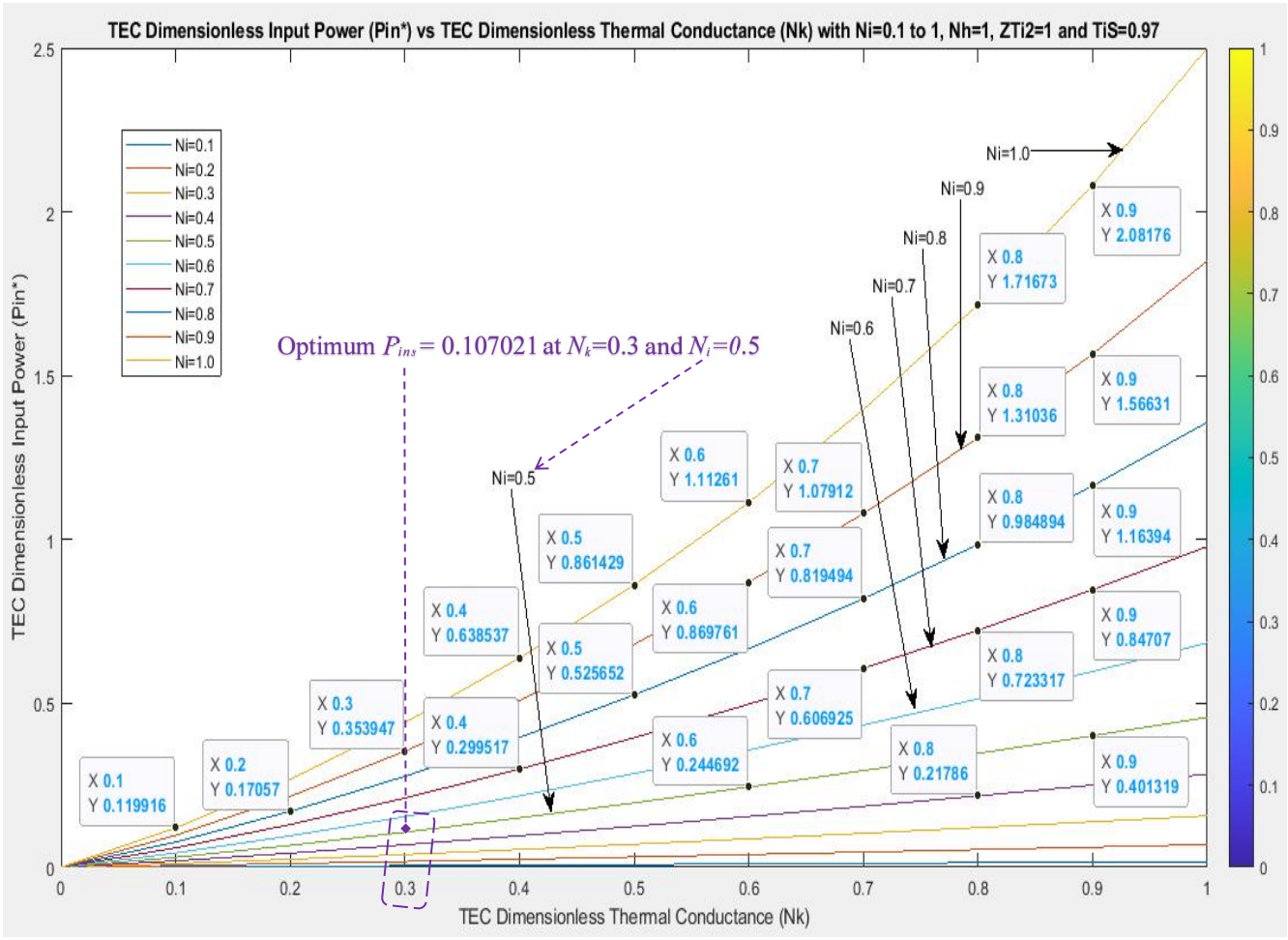

Figure 4.21: Dimensionless input power P_{ins} *vs* dimensionless thermal conductance N_k

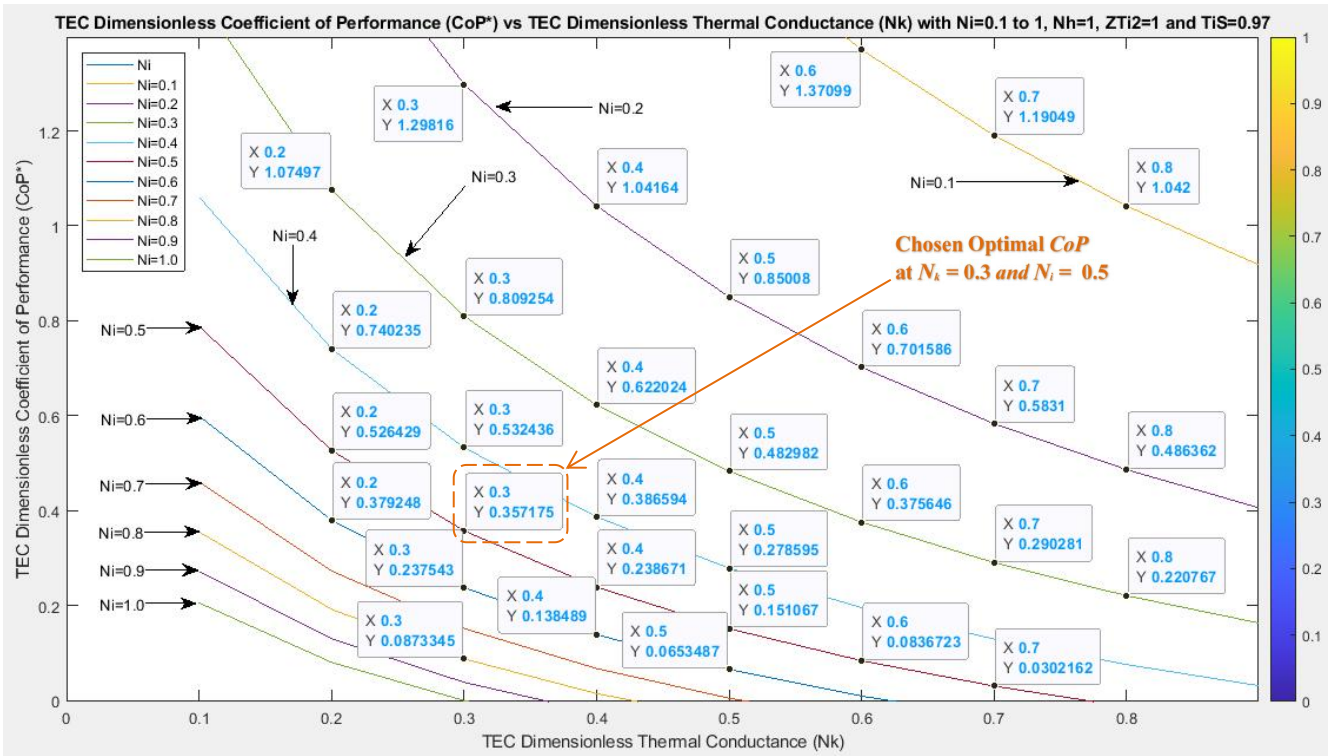

Figure 4.22: Dimensionless *CoP* *vs* dimensionless thermal conductance N_k

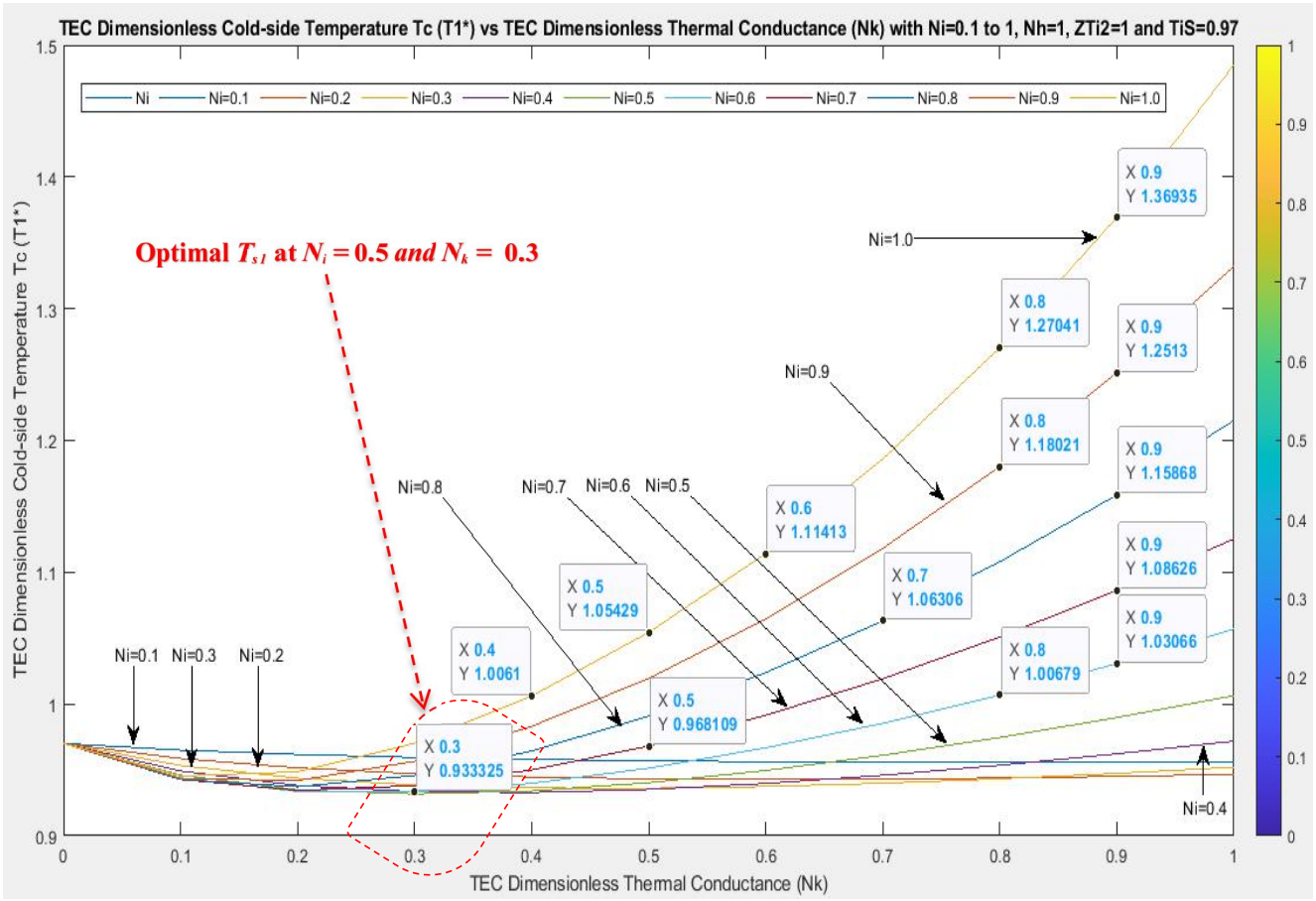

Figure 4.23: TEC dimensionless cold-side T_{s1} *vs* dimensional thermal conductance N_k

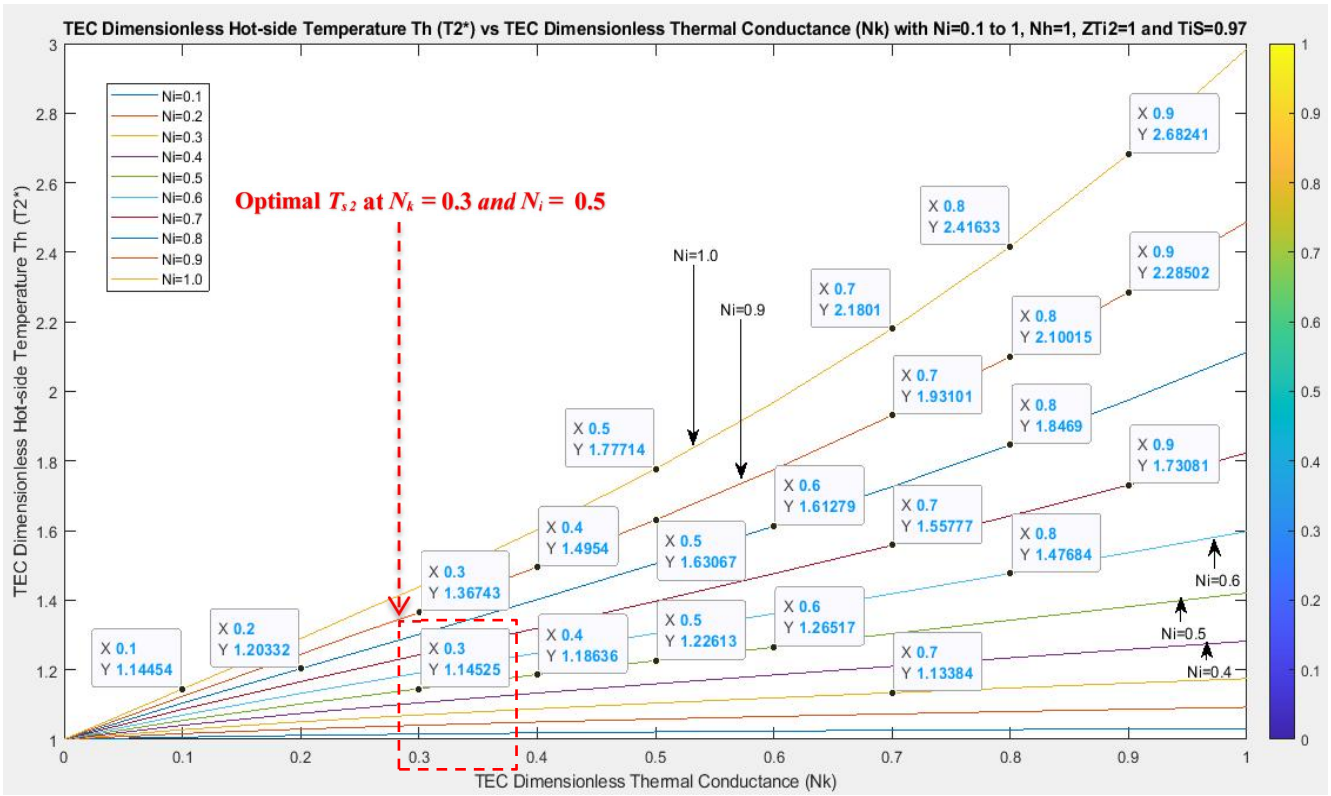

Figure 4.24: TEC dimensionless hot-side T_{s2} *vs* dimensionless thermal conductance N_k

4.3.6 Results Interpretation and Validation

In Section 4.3.3, the analytical formulas for T_{s1} and T_{s2} were derived and were used to calculate T_{s1} and T_{s2} optimal values and in Section 4.3.4, TEC with heatsinks simulated model was implemented and was employed to determine numerically its optimal results and as well graphically as portrayed in Section 4.3.5. These results are discussed and validated herein with the results presented in Lee (2013). Figure 4.12 simulated results are validated with Table 4.3 input and output values. For example, highlighted in red in Table 4.3, the TEC T_{s1} and T_{s2} values are valid and approximately the same as analytically, numerically and graphically demonstrated in Figures 4.12, 4.17, 4.18, 4.23 and 4.24. The practical relevance of T_{s1} and T_{s2} results are that, they enable an optimal design by easily manipulating the temperatures of the heatsinks fluid if known and at optimal performance, T_{s1} and T_{s2} are minimal for N_i and N_k values from $0.3 - 0.5$ and are depicted and validated with Figure 4.25 shown highlighted in red.

Table 4.3: TEC with HS optimal results validator (adapted from Lee, 2013)

Input	$Q^*_{1,opt}$ (dimensionless)	$Q_{1,opt}$ (Actual)	$COP_{1/2opt}$ (dimensionless)	$COP_{1/2opt}$ (Actual)
$T_{\infty 1} = 20°C$, $T_{\infty 2} = 30°C$	$N_k = 0.3$	$n = 257$	$N_k = 0.15$	$n = 128$
$A = 2$ mm^2, $L = 1$ mm	$N_h = 1$	$\eta_1 h_1 A_1 =$ 4.8 W/K	$N_h = 1$	$\eta_1 h_1 A_1 = 4.8$ W/K
$\eta_2 = 0.8$, $h_2 = 60$ W/m^{2}K,	$N_I = 0.5$	$I = 6.36$ A	$N_I = 0.25$	$I = 3.18$ A
$A_2 = 1000$ cm^2	$T^*_\infty = 0.967$	$T_{\infty 1} = 20°C$	$T^*_\infty = 0.967$	$T_{\infty 1} = 20°C$
Base area $A_b = 5$ cm × 5 cm	$ZT_{\infty 2} = 1.0$	$ZT_{\infty 2} = 1.0$	$ZT_{\infty 2} = 1.0$	$ZT_{\infty 2} = 1.0$
$\alpha_p = -\alpha_n = 220$ μV/K	$T^*_1 = 0.930$	$T_1 = 8.7°C$	$T^*_1 = 0.949$	$T_1 = 14.4°C$
$\rho_p = \rho_n = 1.0 \times 10^{-3}$ Ωcm	$T^*_2 = 1.145$	$T_2 = 73.9°C$	$T^*_2 = 1.031$	$T_2 = 39.4°C$
$k_p = k_n = 1.4 \times 10^{-2}$ W/cmK	$Q^*_1 = 0.037$	$Q_1 = 54.4$ W	$Q^*_1 = 0.019$	$Q_1 = 26.9$ W
($Z = 3.457 \times 10^{-3}$ K^{-1})	$COP = 0.35$		$COP = 1.49$	
($R = 0.01\Omega$ per thermocouple)	$N_V = 0.715$	$V_n = 24.5$ V	$N_V = 0.332$	$V_n = 5.7$ V
	$T^*_{\infty,\max} = 1.2$	$T_{\infty 1,max} =$ 91.3°C	$T^*_{\infty,\max} = 1.06$	$T_{\infty 1,max} =$ 49.7°C
	$T^*_{\infty,\min} = 0.83$	$T_{\infty 1,min} =$ −21.8°C	$T^*_{\infty,\min} = 0.84$	$T_{\infty 1,min} =$ −19.2°C
(Cooling Power Density $P_d = Q_1/A_b$)	-	$P_d = 2.18$ W/cm^2	-	$P_d = 1.08$ W/cm^2

Figures 4.13 and 4.19 depict the TEC optimal $Q_{s1} = 0.038$; respectively at N_i and N_k values of 0.5 and 0.3. This is validated with Figures 4.25 - 4.27 as shown highlighted in blue. However, at both N_i and N_k values of 0.4 in Figures 4.13 and 4.19, I reckon there also exists an optimal value of $Q_{s1} = \sim 0.037$; since it's considered optimum if also a suitable Q_{s1} is found with less N_i and more N_k. So, depending on the aim, available resources / system design constraints, two optimum Q_{s1} points exist that can be used.

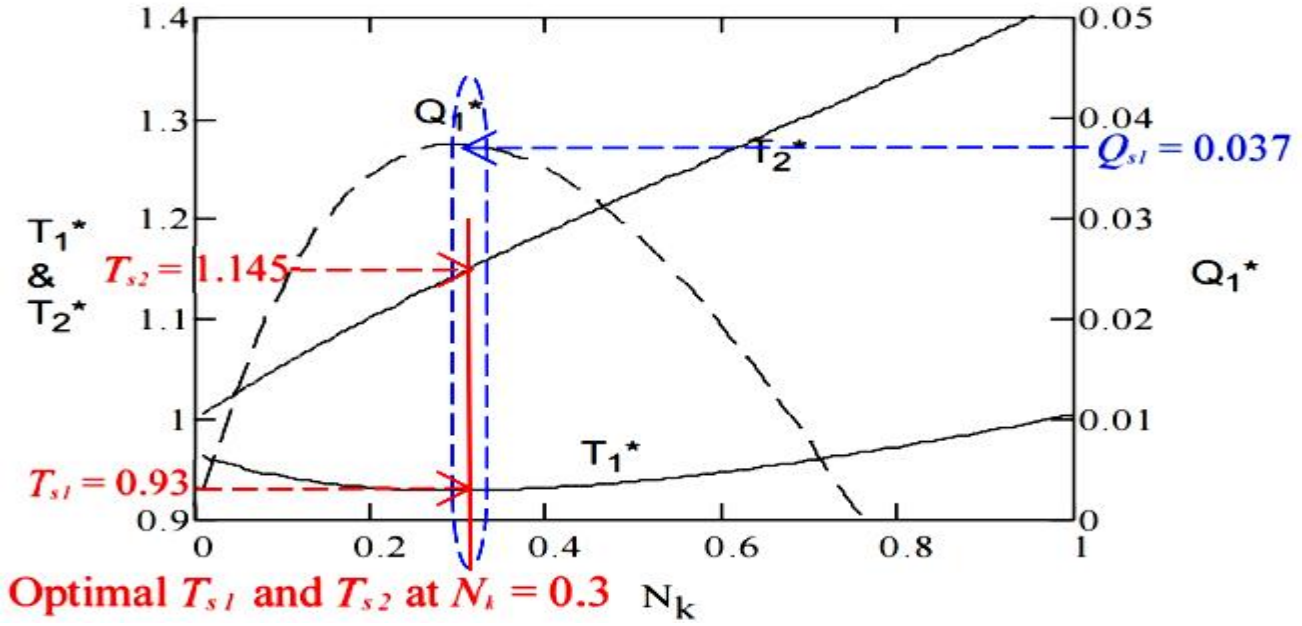

Figure 4.25: TEC with HS Q_{s1}, T_{s1} and T_{s2} optimal results validator (adapted from Lee, 2013)

In Figures 4.14 and 4.20, optimum value of Q_{s2} = 0.145246 is found when N_i = 0.5 and N_k=0.3 as highlighted in green. However, increasing N_k, gives more Q_{s2} at the same N_i =0.5. The practical relevance of this is it enables opting between operating the TEC as a cooler or a heater by adjusting N_k.

Figures 4.15 and 4.21 show P_{ins}, which is directly pro rata to N_i and N_k. Purple highlighted is optimal P_{ins} = 0.107021 at N_k = 0.3 and N_i = 0.5. This is also validated using Figure 4.26 as illustrated.

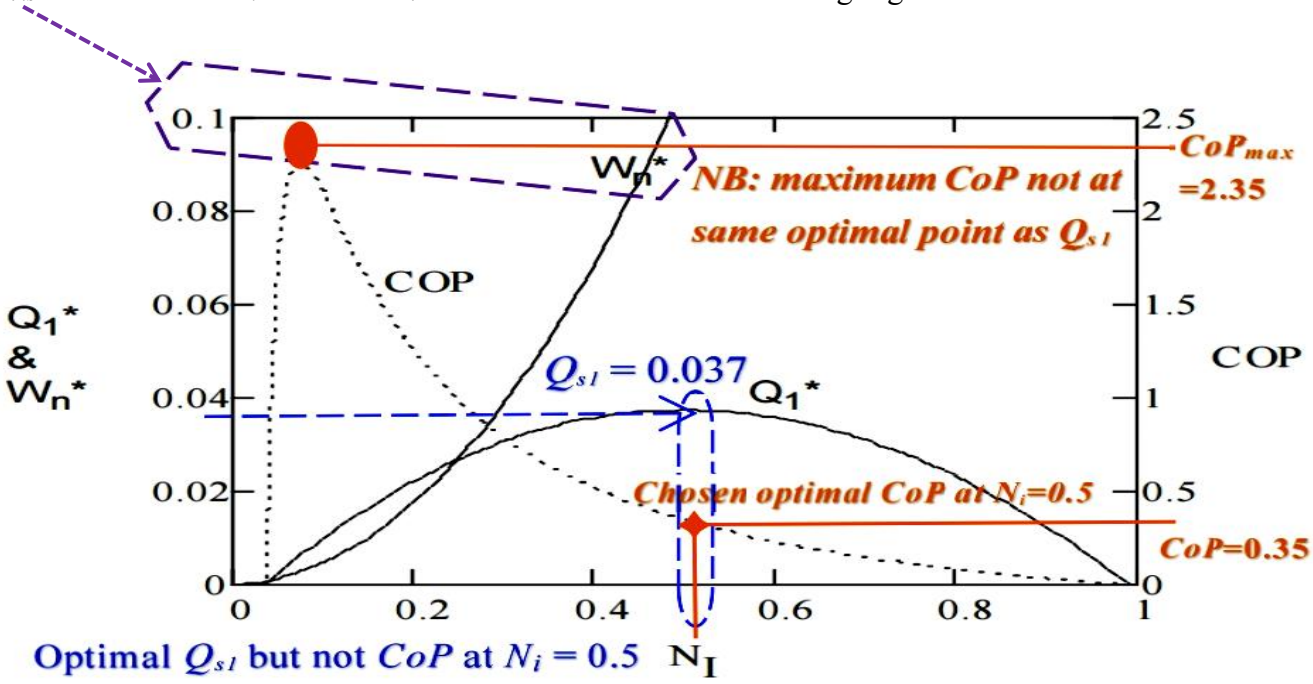

Figure 4.26: TEC-HS W_s, Q_{s1} and *CoP* optimal results validator (adapted from Lee, 2013)

Finally, the dimensionless *CoP* (NB: *CoP* is by default dimensionless, the dimensionless attribute here is just for emphasis with respect to the technique) is shown in Table 4.3 and Figure 4.22; but optimal *CoP* as seen in Figures 4.16, 4.22, 4.26 and 4.27, is not found at the optimal Q_{s1} using the dimensional analysis shown. As a result, the optimal *CoP* of 0.35 is manually chosen at optimal N_i=0.5 and N_k=0.3 and is orange highlighted in Figures 4.16 and 4.22 and validated with Table 4.3, Figures 4.26 and 4.27.

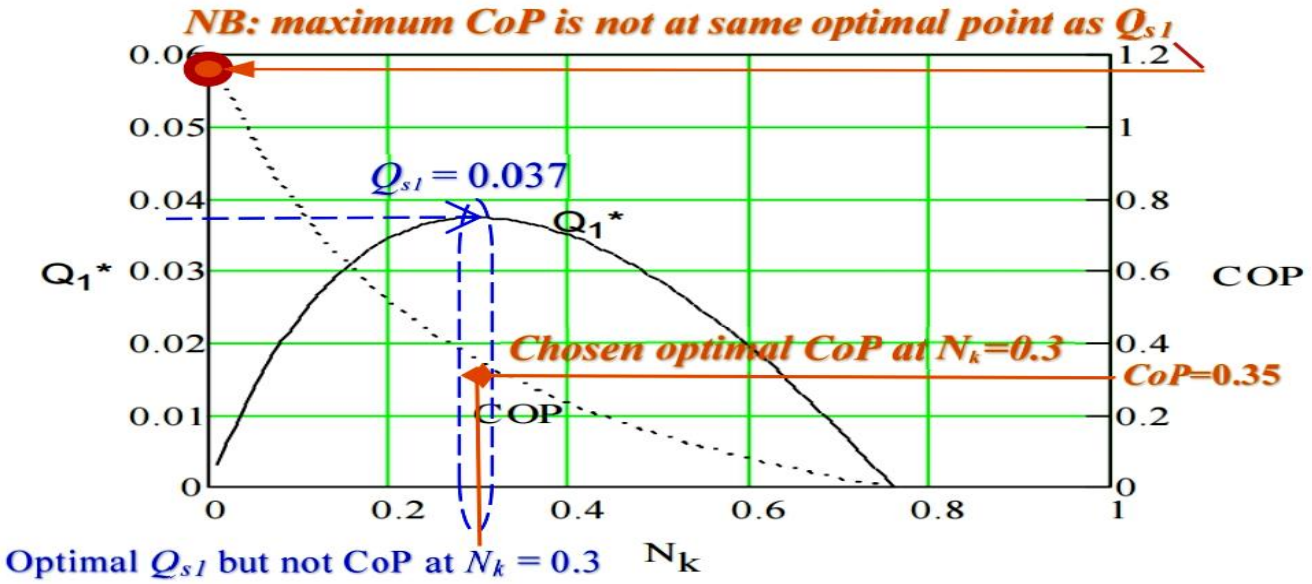

Figure 4.27: TEC with HS Q_{s1} and *CoP* optimal results validator (adapted from Lee, 2013)

4.3.7 Summary

This section began by briefly highlighting the ongoing South Africa energy crisis and the need for renewable energy / power sources and as well energy efficient loads. Alternative energy based on thermoelectricity and with focus on TEC was investigated to determine optimal TEC design with heatsinks when considering a good practical implementation. However, heatsinks introduce thermal resistances which negatively affect the TEC performance. Dimensional analysis, in particular one that easily converts the TEC thermal conductance to convection conductance was researched as the optimisation tact to facilitate an optimal practical design. I developed this approach and derived new analytical formulas to easily compute the TEC optimal dimensionless cold and hot sides temperatures. These new formulas were verified using analytical, numerical and graphical solutions with the aid of an easy TEC with heatsinks model I also implemented using Matlab and Simulink. The formulas optimal results were validated with the original research result done by Lee (2013) − using TEC manufacturers typical parameters value used in the industry. These outcomes define the research impacts, from which a physical design can be done and the new TEC model benchmark with for further use, to henceforth devise and implement a clean energy efficient cooling / heating device for households and businesses.

CHAPTER 5

TEGs and TECs Optimal Operation and Configurations: Results and Discussions

5.1 Overview

In Chapter 4, the focus was to develop the thermoelectricity theoretical model established in Chapter 3 but now with the addition of heatsinks considering a practical implementation. In both chapters, TEG and TEC were examined at module / unit level; however, in practice, more than one TEG and TEC have to be connected together to increase the output power (for TEG) and cooling power (for TEC). Furthermore, both TEG and TEC optimal operation points and configurations have to be determined to ensure maximum power is transferred between the source and the load for better efficiency. Connecting more than one TEG and TEC modules in series and or in parallel means the devices electrical resistance will be affected and as a result, their outputs and efficiencies will be affected as well; therefore, in this chapter, TEGs (more than one TEG module) and TECs (more than one TEC module) are investigated to study their optimal operation points and their electrical dynamics and performances.

Inline with the research problem of inefficient energy conversion, understanding TEGs and TECs configurations and optimal operation points are paramount to ensure maximal power and efficiency are derived from both devices. Though physical configuration plays an important role when implementing TEGs and TECs in practice by taking into considerations the nature (size, shape and surface) of where the TEGs and TECs will be used, the focus herein is on the electrical configurations and optimal setups.

In view of this, Chapter 5 thus focuses on the mathematical formulations (developed from Chapter 3), the modeling and simulation of TEGs and TECs using Matlab and Simulink. The simulated models allow more than one TEG and TEC modules of any amount and electrical configurations (series and or in parallel) to be theoretically simulated to determine their optimal electrical configuration and also their optimal operation points. This section presentation is adapted from my two original PhD articles as listed below – the first article focuses on the TEGs and TECs optimal operation points investigation and the second focuses on the TEGs optimum electrical configurations and performance determination.

- Bayendang, N.P., Kahn, M.T. & Balyan, V. 2022. Thermoelectric generators (TEGs) and thermoelectric coolers (TECs) modeling and optimal operation points investigation. *Adv. Sci. Technol. Eng. Syst. J.* 7(1): 60-78. http://dx.doi.org/10.25046/aj070107.

- Bayendang, N.P., Kahn, M.T. & Balyan, V. 2022. Thermoelectric generators (TEGs) modules – Optimum electrical configurations and performance determination. *Undergoing publication production.* [Accepted: March 9, 2022]. *AIMS Energy*.

5.2 Thermoelectric Generators (TEGs) and Thermoelectric Coolers (TECs) Modeling and Optimal Operation Points Investigation

Sustainable energy is gradually becoming the norm in South Africa due to ongoing national electricity supply outages. The quests for different renewable energy sources such as photovoltaic cells as well as energy efficient electrical appliances are becoming popular. Therefore, this section explores the alternative energy case for thermoelectricity with focus on the mathematics, modeling and simulation of multiple TEGs and TECs modules to study their dynamics and to establish their optimal operation points using Matlab and Simulink. The research affirms that the output current from TEGs or input current to TECs, initially respectively increases the output power of TEGs and the cooling power of TECs, until the current reaches a certain maximum optimal point, after which any further increase in the current, decreases the TEGs' and or TECs' respective output and cooling powers as well as efficiencies, due to Ohmic heating and or entropy change caused by the increasing current. The research outcome is an elaborate easy to use TEGs / TECs theoretical models that can be applied further to investigate an infinite quantity of TEG and TEC modules connections and be it in series and or in parallel, in an effort to assist system designers grasp better both TEGs/TECs theoretical operations and their limits, when designing waste heat recovery (using TEGs) and cooling (using TECs) systems, as well as energy efficient devices for industrial, residential, commercial and vehicular applications.

5.2.1 Introduction

South Africa akin most African nations, is suffering from an unreliable national electrical power generation and distribution as indicated in Eberhard *et al.* (2017); as a result, the demands for renewable and alternative energy sources such as solar and fuel cells, as well as energy efficient loads are on the rise in an effort to sustaining the national grid. In this regards, thermoelectricity is advanced as a potential alternative energy for sustainable energy source and loads – that is, as a clean DC power source for low energy lighting applications and as well to provide clean cooling / heating in various human habitats. Thermoelectricity as reviewed in Bayendang *et al.* (2020b), practically focuses on the Seebeck and Peltier effects. Seebeck effect is basically converting heat to electricity and the device that does this is a thermoelectric generator (TEG), whereas the reversed phenomenon is a Peltier effect – which is basically the production of cold from electricity and if the current flow direction changes (voltage is reversed), heat is also produced and the device that does this is called a thermoelectric cooler (TEC). Therefore, by efficiently applying thermoelectricity, clean alternative energy source for low power DC applications using TEGs and or energy efficient loads in the forms of heat pumps, air conditioners, refrigeration etc using TECs; can be passably implemented to help relieve South Africa households and businesses basic energy consumption such as lighting, cooling and heating. As already

examined in Bayendang *et al.* (2020b), thermoelectricity lends itself to various applications with focus on how TEG and TEC can be used respectively as a power source and as a load, which furthermore includes energy harvesting for field sensors as studied in Charris *et al.* (2019) and Noh *et al.* (2021); solar energy harvesting as indicated in Singh *et al.* (2016); re-configurable TEG as researched in Wan *et al.* (2016); electronic cooling as investigated in Chein and Huang (2004); a thermoelectric cooler in cascade as examined in Belovski and Aleksandrov (2019); in Lee (2016) extensive mathematical analyses were articulated for TEG and TEC; in Mamur and Çoban (2020), a TEG model was developed but lacks the detailed maths and the parallel TEG combinations was limited to 2; in Bayendang *et al.* (2020c) a comprehensive TEG model detailing the maths was presented accompanying the TEG model; in Bayendang *et al.* (2020d), a comprehensive TEC model as well as with detailed maths to complement the TEC model was presented; in Felgner *et al.* (2013), a modeling of TEG using Modelica is shown but lacks the comprehensive maths, especially considering modeling infinite multiple TEGs and as well TECs modules − which were not presented and in Luo *et al.* (2020) a parametric ANSYS study of TEG and TEC was presented but lacks also the detailed maths and for the case for infinite TEG and TEC modules. These are just a few noted studies; however, lacking in the TEG / TEC literature are comprehensive details on their maths, modeling and operations when connected in series and also in parallel to increase the output power (in the case of TEG) and the cooling power (in the case of TEC). This section therefore, expands on i) deriving and expressing further the theoretical maths covering the infinite TEGs and TECs parameters / modules – rooted in their total internal resistance, ii) the modeling of the multiple TEGs and TECs modules focusing on their limiting parameters and finally iii) the static and dynamic simulations and the optimal operation points investigation as well as the interpretations. The results are validated and closing remarks drawn.

5.2.2 TEGs and TECs Steady-state Mathematical Analyses and Modeling

In Lee (2016), Bayendang *et al.* (2020c) and Bayendang *et al.* (2020d), the standard mathematics defining various TEG and TEC parameters as well as their modeling are demonstrated. I now theoretically developed further and present in the following sections: i) the multiple TEGs and TECs maths and ii) the implemented models (based on their maths) using Matlab / Simulink and as well the simulation of infinite amount of TEG /TEC modules and be it in any series and in any parallel connection.

5.2.2.1 TEGs and TECs Steady-state Mathematical Analyses

The derivations thus far of the TEG and TEC parameters have been based-on the p-n thermoelement resistance at the thermocouple level and by extension at the module level as indicated in Lee (2016), Bayendang *et al*. (2020c) and Bayendang *et al.* (2020d). However, in practice, more than one TEG and TEC modules will be needed for more power production and this will take the form of series and or

parallel connections; as a result, their internal resistances will often change. This section re-defines it in a general multi TEG modules and multi TEC modules hypotheses and articulated next are the formulations.

5.2.2.1.1 TEGs Steady-state Mathematical Analysis

The following TEG parameters mathematics are developed and presented step-wise for multiple TEGs case as follows:

5.2.2.1.1.1 The Thermoelectric (TE) Device P-N Thermocouple Resistance (*r*)

The TE device p-n thermocouple resistance *r* in ohm is:

$$r = \rho L/A \qquad (\Omega) \tag{5.1}$$

with ρ being the TEG / TEC electrical resistivity in Ω.m, L is the length in metre (m) of the TEG / TEC p-n thermocouple and the TEG / TEC p-n thermocouple area is A in metre squared (m^2).

5.2.2.1.1.2 TE Device (TEG and TEC) Module Resistance (*R*)

The resistance in (Ω) of a TEG / TEC module is computed as:

$$R = nr \qquad (\Omega) \tag{5.2}$$

where n (which differs, could be 100, 127, 199, 255 etc) is a TEG / TEC manufacturer p-n thermocouples amount used in a TEG /TEC. The more the n, the more powerful is the TEG /TEC.

5.2.2.1.1.3 TEG / TEC Module(s) Total Resistance (R_t)

The total resistance R_t in (Ω) of a TEG / TEC module(s) is calculated as:

$$R_t = n\frac{T_s}{T_p}r \; = \; R\frac{T_s}{T_p} \qquad (\Omega) \tag{5.3}$$

with T_p being the TEGs / TECs (TEG / TEC modules) amount in parallel and T_s the TEGs / TECs (TEG / TEC modules) amount in series. NB: all the TEGs / TECs used in equation (5.3) must be identical model to make sure the individual TEG modules unit R is not different from each other.

5.2.2.1.1.4 TEG(s) Output Voltage (V_o)

The TEG(s) voltage generated in volt, is derived as:

$$V_o = nS\Delta T - IR_t \qquad (V) \tag{5.4}$$

with S being the TE device Seebeck coefficient in V/K, $\Delta T = T_h - T_c$ the TEG(s) temperature difference in kelvin or °C and the output current of the TEG(s) is I in ampere.

5.2.2.1.1.5 TEG(s) Output Current (*I*)

The TEG(s) generated current *I* in ampere is deduced as:

$$I = \frac{nS\Delta T}{R_L + R_t} \qquad \text{(A)} \qquad (5.5)$$

with R_L being the resistance of the electrical load connected to the TEG(s) output. NB: the higher the *I*, the higher the TEG(s) Joule heating (temperature increase) which negatively affects the TEGs efficiency.

5.2.2.1.1.6 TEG(s) Hot-side Heat Absorbed (Q_h)

TEG(s) produce DC power when their hot-side is at a high temperature T_h, during which the TEG(s) becomes hotter and the heat absorbed in watt is Q_h, given as:

$$Q_h = n[(SIT_h) + (K\Delta T)] - 0.5I^2R_t \qquad \text{(W)} \qquad (5.6)$$

with *K* being the TEG(s) thermal conductance in W/K.

5.2.2.1.1.7 TEG(s) Cold-side Heat Emitted (Q_c)

TEG(s) produce DC power when the cold-side of the TEG(s) is at a low temperature T_c releasing the heat Q_c in watt.

$$Q_c = n[(SIT_c) + (K\Delta T)] + 0.5I^2R_t \qquad \text{(W)} \qquad (5.7)$$

5.2.2.1.1.8 TEG(s) Output Power (P_o)

The TEG(s) modules generated power P_o in watt, is found variously as follows:

$$P_o = Q_h - Q_c \qquad \text{(W)} \qquad (5.8)$$

$$P_o = IV_o = n\,[(SI\Delta T)] - I^2R_t \qquad \text{(W)} \qquad (5.9)$$

5.2.2.1.1.9 TEG(s) Electrical / Conversion / Thermal Efficiency (η)

η is the TEG(s) power output P_o divided by the TEG(s) hot-side heat absorbed Q_h. η being a performance parameter, is obtained as:

$$\eta = P_o / Q_h \qquad (5.10)$$

5.2.2.1.1.10 TEG(s) / TEC(s) Carnot's Efficiency (η_c)

TEGs / TECs Carnot efficiency is the efficiency determined based-on their temperatures T_h and T_c.

$$\eta_c = \frac{\Delta T}{T_h} = \frac{T_h - T_c}{T_h} = 1 - \frac{T_c}{T_h} \qquad (5.11)$$

5.2.2.1.1.11 TEG(s) Conversion Efficiency Expression (η_e)

Simply, η_e is the raw expression of η. That is, when equations of Q_h and P_o (equations (5.6) and (5.8) or (5.9) respectively) are both substituted in equation (5.10).

$$\eta_e = \eta_c \frac{(nR_L/R_t)}{[(1+nR_L/R_t)-0.5\eta_c+((1/(2Z\overline{T}))(1+nR_L/R_t)^2(1+T_c/T_h))]} \tag{5.12}$$

with $Z\overline{T}$ being the TE device average dimensionless figure of merit. NB: Z is the TE device figure of merit in per K (K^{-1}) and $\overline{T} = (T_h + T_c) / 2$, is the TE device average temperature in K.

5.2.2.1.1.12 TEG(s) Maximum Conversion Efficiency (η_m)

η_m is the efficiency of the TEG(s) at $R_t / R_L = \sqrt{1 + Z\overline{T}}$. The η_m expression as a function of TEGs temperatures and Z is:

$$\eta_m = \eta_c[\frac{(\sqrt{1+Z\overline{T}}) - 1)}{(\sqrt{1+Z\overline{T}} + (T_c/T_h))}] \tag{5.13}$$

5.2.2.1.1.13 TEGs Maximum Power Conversion Efficiency (η_{mp})

As a function of temperatures and Z, η_{mp} is the efficiency of the TEG at its maximum output power P_o – that is at $R_t = R_L$.

$$\eta_{mp} = \eta_c / [2 - 0.5\eta_c + (2/Z\overline{T})\ (1+T_c/T_h)] \tag{5.14}$$

5.2.2.1.1.14 TEG(s) Maximum Power Output (Po_{max})

The TEG(s) maximum transfer of power theoretically happens at $R_t = R_L$. NB: in practice, this will hardly ever be the case.

$$Po_{max} = (nS\Delta T)^2(R_L/R_t) / R(1+(R_L/R_t))^2 \quad \text{(W)} \tag{5.15}$$

5.2.2.1.1.15 TEG(s) Maximum Voltage Output (Vo_{max})

TEG(s) Vo_{max} happens at open circuit, that is when R_L is not connected or R_L is infinity (extremely large), $I = 0$A.

$$Vo_{max} = nS(T_h - T_c) = nS\Delta T \quad \text{(V)} \tag{5.16}$$

5.2.2.1.1.16 TEG(s) Maximum Current Output (I_{Max})

TEG(s) I_{Max} happens at short circuit – meaning, when the load R_L is 0Ω. NB: R_t will therefore be the sole resistance.

$$I_{Max} = nS\Delta T / R_t = nS(T_h - T_c) / R_t \quad \text{(A)} \tag{5.17}$$

5.2.2.1.1.17 TEG(s) Generated Current Normalized (I_n)

I_n is the normalized current of the TEG(s) in the range $0 \leq I_n \leq 1$. At the TEG(s) maximum transfer of power ($R_t = R_L$), $I_n = 0.5$. Simply, I_n is the TEG(s) generated current divided by the TEG(s) maximum current output. It's calculated as:

$$I_n = \frac{I}{I_{Max}} = \frac{R_t}{R_t + R_L} \tag{5.18}$$

5.2.2.1.1.18 TEG(s) Generated Voltage Normalized (V_n)

V_n is the normalized voltage of the TEG(s) ranging from $0 \leq V_n \leq 1$. At the TEG(s) maximum transfer of power (R_L=R_t), $V_n = 1/2$. V_n is the TEG(s) voltage generated divided by the TEG(s) maximum (ideal) voltage generated. It's given as:

$$V_n = \frac{V_o}{Vo_{max}} = \frac{R_L}{R_L + R_t} \tag{5.19}$$

5.2.2.1.1.19 TEG(s) Output Power Normalized (P_n)

P_n is the normalised TEG(s) power bounded between $0 \leq P_n \leq 1$. $P_n = 1$ at the TEG(s) maximum transfer of power (R_L=R_t). P_n is the TEG(s) power generated divided by the TEG(s) maximum output power. It is expressed as:

$$P_n = \frac{P_o}{Po_{max}} = \frac{4(R_L/R_t)}{[(R_L/R_t)+1]^2} \tag{5.20}$$

5.2.2.1.1.20 TEG(s) Conversion Efficiency Normalized (η_n)

η_n is the conversion efficiency of the TEG(s) in the region $0 \leq \eta_n \leq 1$. η_n depends on R_t/R_L, T_c/T_h and $Z\overline{T}$. η_n is the conversion efficiency of the TEG(s) divided by the maximum conversion efficiency of the TEG(s), deduced as:

$$\eta_n = \eta / \eta_m \tag{5.21}$$

5.2.2.1.1.21 TEG(s) Effective Seebeck Coefficient (S_e)

S_e measured in volt / kelvin, is expressed as:

$$S_e = 4Po_{max} / (nI_{max}\Delta T) \qquad \text{(V/K)} \tag{5.22}$$

5.2.2.1.1.22 TEG(s) Effective Electrical Resistivity (ρ_e)

ρ_e measured in ohm metre, is expressed as:

$$\rho_e = 4[(A/L)Po_{max}] / nI_{max}^2 \qquad (\Omega.\text{m}) \tag{5.23}$$

5.2.2.1.1.23 TEG(s) Effective Figure of Merit (Z_e)

Z_e measured in per kelvin, is expressed as:

$$Z_e = [(2/\overline{T})(1+(T_c/T_h))] / [\eta_c((1/\eta_{mp})+0.5)-2] \quad (K^{-1}) \quad (5.24)$$

5.2.2.1.1.24 TEG(s) / TEC(s) Effective Thermal Conductivity (k_e)

k_e measured in watt per metre kelvin, is expressed as:

$$k_e = S_e^2 / (\rho_e Z_e) \quad (W/mK) \quad (5.25)$$

TEGs / TECs effective parameters enable researchers to factor in TEGs / TECs system losses using maximum parameters to bridge the theoretical and measured specifications differences (Lee, 2016).

5.2.2.1.1.25 TEG(s) Heat Flux Density (*HFD*)

HFD is the amount of heat absorbed per TEGs hot-side surface area (*TEGsa*) in watt per centimetre square.

$$HFD = Q_h / TEG_{sa} \quad (W/cm^2) \quad (5.26)$$

This concludes the TEG(s) modules steady-state mathematical analysis.

5.2.2.1.2 TECs Steady-state Mathematical Analysis

The following TEC parameters mathematics are examined and developed step-wise for multiple TECs case as follows:

5.2.2.1.2.1 TEC(s) Voltage Input (V_{in})

The TEC(s) applied voltage in volt, is expressed as:

$$V_{in} = n[S(T_h - T_c)] + I_{in}R_t \quad (V) \quad (5.27)$$

where I_{in} is the TECs input current from the power supply.

5.2.2.1.2.2 TEC(s) Input Current (I_{in})

The TECs input current in ampere is derived as:

$$I_{in} = \frac{nS\Delta T}{R_s - R_t} \quad (A) \quad (5.28)$$

where R_s is the internal or source electrical resistance of the power supply connected to the TECs. NB: as stated earlier, the higher the I_{in}, the higher the TEC(s) Joule heating (temperature will increase) which negatively affects the TECs efficiency, as the TECs internal temperature will increase and cause entropy.

5.2.2.1.2.3 TEC(s) Cold-side Heat Absorbed (Q_c)

TECs create cold when their cold-side is at a low temperature T_c to absorb heat and supply a steady cooling power Q_c in W.

$$Q_c = n[(SI_{in}T_c) - (K\Delta T)] - 0.5I_{in}^2R_t \quad \text{(W)} \tag{5.29}$$

5.2.2.1.2.4 TEC(s) Hot-side Heat Emitted (Q_h)

TECs produce cold when their hot-side is at a high temperature T_h emitting the heat Q_h in watt.

$$Q_h = n[(SI_{in}T_h) - (K\Delta T)] + 0.5I_{in}^2R_t \quad \text{(W)} \tag{5.30}$$

5.2.2.1.2.5 TEC(s) Power Input (P_{in})

The applied power P_{in} in watt required to power the TECs is calculated variously as follows:

$$P_{in} = Q_h - Q_c = n[(SI_{in}\Delta T)] + I_{in}^2R_t \quad \text{(W)} \tag{5.31}$$

$$P_{in} = I_{in}V_{in} \quad \text{(W)} \tag{5.32}$$

5.2.2.1.2.6 TEC(s) Coefficient of Performance (CoP)

This is TECs cooling power Q_c divided by its input power P_{in}.

$$CoP = Q_c / P_{in} \tag{5.33}$$

5.2.2.1.2.7 TEC(s) CoP Expression (CoP_e)

CoP_e is the raw expression of CoP when the equations of Q_c and P_{in} (equations (5.29) and (5.31) or (5.32)) are put in (5.33).

$$CoP_e = \frac{[(SI_{in}T_c) - (K\Delta T) - (0.5{I_{in}}^2R_t/n)]}{[(SI_{in}\Delta T) + ({I_{in}}^2R_t/n)]} \tag{5.34}$$

5.2.2.1.2.8 TEC(s) Current to Yield CoP (I_{cop})

I_{cop} is the TECs input current in (A) required to achieve CoP.

$$I_{cop} = \frac{nS\Delta T}{R_t[\left(\sqrt{1+Z\overline{T}}\right)-1]} \quad \text{(A)} \tag{5.35}$$

5.2.2.1.2.9 TECs Maximum CoP (CoP_{max})

CoP_{max} is the TECs maximum CoP that can be achieved.

$$CoP_{\max} = \frac{[T_c/\Delta T]\left((\sqrt{1+Z\overline{T}}) - \frac{T_h}{T_c}\right)}{((\sqrt{1+Z\overline{T}})+1)} \tag{5.36}$$

5.2.2.1.2.10 TEC(s) Maximum Cooling Power Current (Icp_{max})

Icp_{max} is TECs current in ampere needed to realise maximum Q_c.

$$Icp_{max} = nST_c / R_t \quad \text{(A)} \tag{5.37}$$

5.2.2.1.2.11 TEC(s) Icop Maximum Cooling Power (Qcp_{max})

Qcp_{max} in watt, is TECs maximum Q_c achieved based-on I_{cop}.

$$Qcp_{max} = n[(SI_{cop}T_c) - (K\Delta T)] - 0.5I_{cop}^2R_t \quad \text{(W)} \tag{5.38}$$

5.2.2.1.2.12 TEC(s) Maximum Temperature Difference (ΔT_{max})

TEC(s) ΔT_{max} in (K), occurs at maximum I_{in} and at $Q_c = 0$W.

$$\Delta T_{max} = \left(T_h + \frac{1}{Z}\right) - \sqrt{(T_h + \frac{1}{Z})^2 - {T_h}^2} \quad \text{(K)} \tag{5.39}$$

5.2.2.1.2.13 TEC(s) Maximum Input Current (I_{max})

I_{max} is TEC(s) maximum input current in ampere at $Q_c = 0$W.

$$I_{max} = nS(T_h - \Delta T_{max}) / R_t \quad \text{(A)} \tag{5.40}$$

5.2.2.1.2.14 TEC(s) Maximum Input Voltage (Vin_{max})

Vin_{max} is the maximum V_{in} in volt, that produces maximum ΔT_{max} when $I_{in} = I_{max}$, R_t=0, $T_c = 0$, $Q_c = 0$ and T_h is maximum.

$$Vin_{max} = nST_h \quad \text{(V)} \tag{5.41}$$

5.2.2.1.2.15 TEC(s) Maximum Cooling Power (Qc_{max})

Qc_{max} is the maximum absorbable heat or cooling power in watt, at $I_{in} = I_{max}$ and $\Delta T = 0$°C.

$$Qc_{max} = (nS)^2(T_h^2 - \Delta T_{max}^2) / 2R_t \quad \text{(W)} \tag{5.42}$$

5.2.2.1.2.16 TEC(s) Input Current Normalized (Iin_n)

TEC(s) Iin_n is I_{cop} divided by I_{max}.

$$Iin_n = I_{cop} / I_{max} \tag{5.43}$$

5.2.2.1.2.17 TEC(s) Input Voltage Normalized (Vin_n)

TEC(s) Vin_n is V_{in} divided by Vin_{max}.

$$Vin_n = V_{in} / Vin_{max} \tag{5.44}$$

5.2.2.1.2.18 TEC(s) Cooling Power Normalized (Qc_n)

TEC(s) Qc_n is Q_c divided by Qc_{max}.

$$Qc_n = Q_c / Qc_{max} \tag{5.45}$$

5.2.2.1.2.19 TEC(s) CoP Normalized (CoP_n)

TEC(s) CoP_n is CoP divided by CoP_{max}.

$$CoP_n = CoP / CoP_{max} \tag{5.46}$$

5.2.2.1.2.20 TEC(s) Normalised Temperature Difference (ΔT_n)

TECs ΔT_n, is ΔT divided by ΔT_{max} and it is expressed as:

$$\Delta T_n = \Delta T / \Delta T_{max} \tag{5.47}$$

Normalized parameters give dimensionless parameters.

5.2.2.1.2.21 TEC(s) Effective Seebeck Coefficient (S_e)

TECs S_e measured in VK^{-1}, is defined as:

$$S_e = 2Qc_{max} / [nI_{max} (T_h + \Delta T_{max})] \quad (V/K) \tag{5.48}$$

5.2.2.1.2.22 TEC(s) Effective Electrical Resistivity (ρ_e)

TECs ρ_e measured in ohm metre, is written as:

$$\rho_e = AS_e(T_h - \Delta T_{max}) / LI_{max} \quad (\Omega.m) \tag{5.49}$$

5.2.2.1.2.23 TEC(s) Effective Figure of Merit (Z_e)

TECs Z_e measured in per kelvin, is given as:

$$Z_e = 2\Delta T_{max} / (T_h - \Delta T_{max})^2 \quad (K^{-1}) \tag{5.50}$$

5.2.2.1.2.24 TEC(s) Midpoint Current (I_{mid})

I_{mid} measured in ampere, is the mean of Icp_{max} and I_{cop}.

$$I_{mid} = 0.5(Icp_{max} + I_{cop}) \quad (A) \tag{5.51}$$

5.2.2.1.2.25 TEC(s) Midpoint Cooling Power (Qc_{mid})

Qc_{mid} measured in watt, is expressed as:

$$Qc_{mid} = n[(SI_{mid}T_c) - (K\Delta T)] - 0.5I_{mid}^2R_t \quad (W) \tag{5.52}$$

5.2.2.1.2.26 TEC(s) Midpoint Input Power (Pin_{mid})

Pin_{mid} measured in watt, is deduced as:

$$Pin_{mid} = n[(SI_{mid}\Delta T)] + I_{mid}^2 R_t \quad \text{(W)} \tag{5.53}$$

5.2.2.1.2.27 TEC(s) Midpoint CoP (CoP_{mid})

CoP_{mid} is computed as:

$$CoP_{mid} = Qc_{mid} / Pin_{mid} \tag{5.54}$$

5.2.2.1.2.28 TEC(s) Cold Flux Density (*CFD*)

CFD is the cold amount produced (heat absorbed) per TECs cold-side surface area (*TECsa*) in W/cm^2. It is computed as:

$$CFD = Q_c / TECsa \quad \text{(W/cm}^2\text{)} \tag{5.55}$$

This concludes the TEC(s) modules steady-state mathematical analysis.

5.2.2.2 TEGs and TECs Static and Dynamic Modelings and Simulations

Covered in Section 5.2.2.1, TEGs and TECs parameters of interests were extensively expressed mathematically in steady-states with emphasis / basis on the total internal resistance R_t − which was derived and the regular TEG / TEC equations re-expressed based-on it to now cover TEG(s) / TEC(s). These equations are further modeled in Matlab and Simulink to institute the TEGs and TECs static and dynamic models that can be utilised to simulate and investigate optimal infinite TEGs and TECs performances. The detailed modeling is beyond the scope of this study; however, the building blocks and the Matlab constructs used are shown. Exemplified in Figures 5.1a and 5.1b, are the TEGs static and dynamic simulated model GUIs, from which the TEGs parameters expressed in Section 5.2.2.1.1, can all be statically and dynamically configured for an infinite amount of TEGs connections and then simulated to obtain the TEG(s) optimum operation points. Figures 5.1c and 5.1d zoom-in on the TEGs internal modeling. Figure 5.1e expands on the TEGs R_t modeling − this must be matched to the load resistance R_L − which can be changed before or while the simulation is running to match the TEGs R_t for maximum power transfer simulation. Figure 5.2 exemplifies the TECs simulator user interface. Also, multiple TECs combinations in T_s and T_p and the various parameters presented in Section 5.2.2.1.2, can be simulated. Likewise, maximum power will be transferred from the power supply to the TECs by matching R_s to R_t.

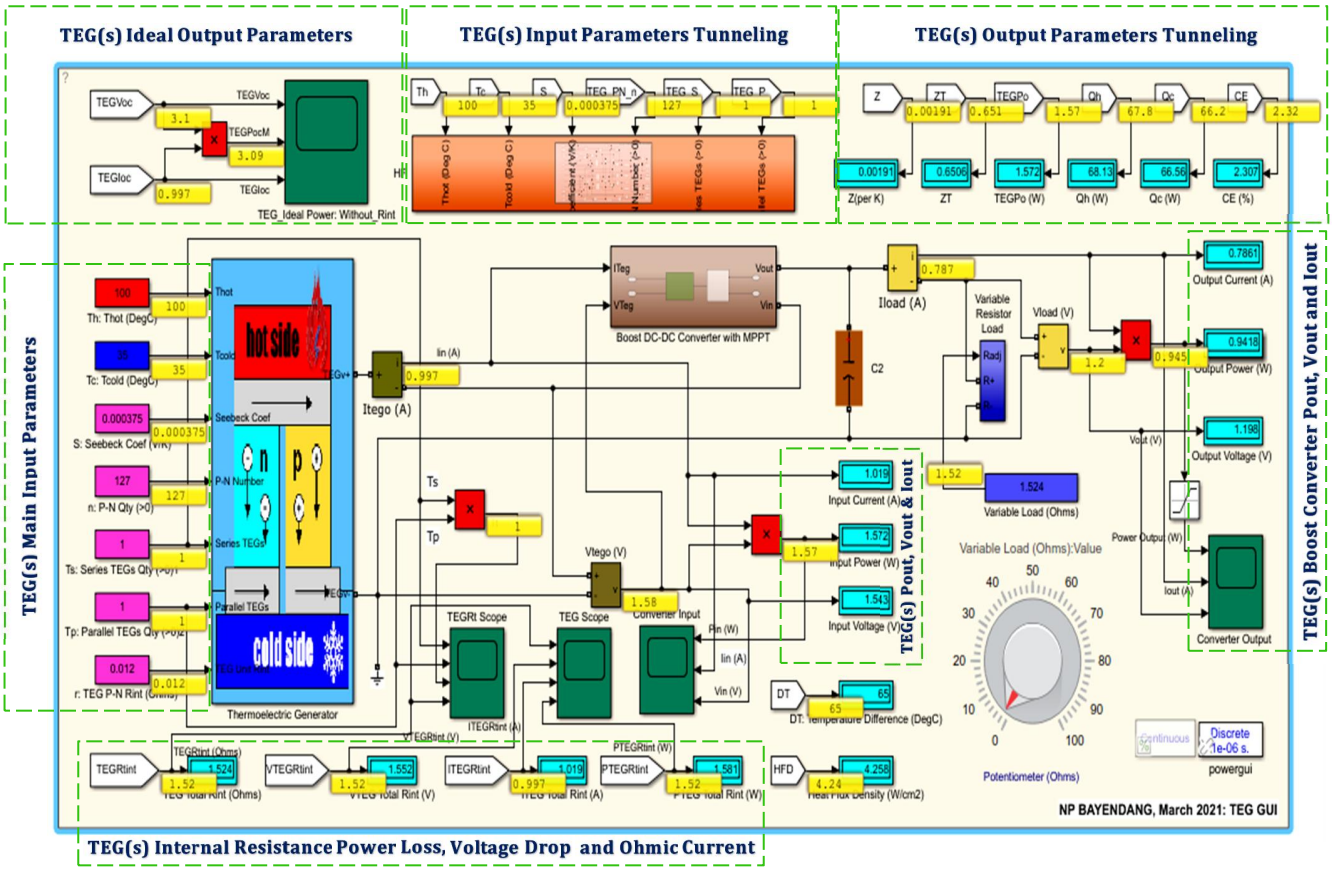

(a) TEG(s) static simulator user's interface: shows the steady-state simulation with all the input parameters fixed (though can change) over time

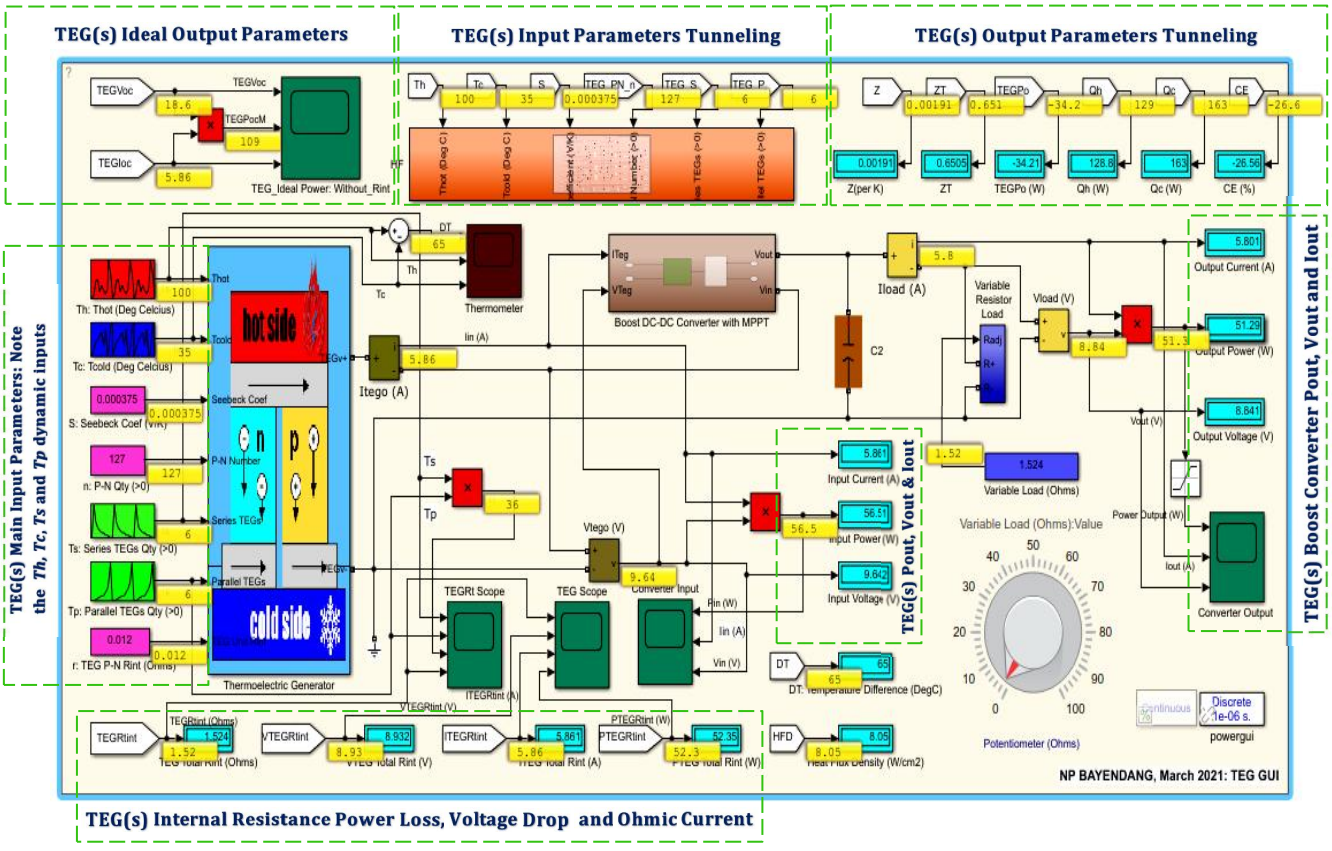

(b) TEG(s) dynamic simulator user's interface: shows the transient simulation with the T_h, T_c, T_s *and* T_p input parameters auto changing with time

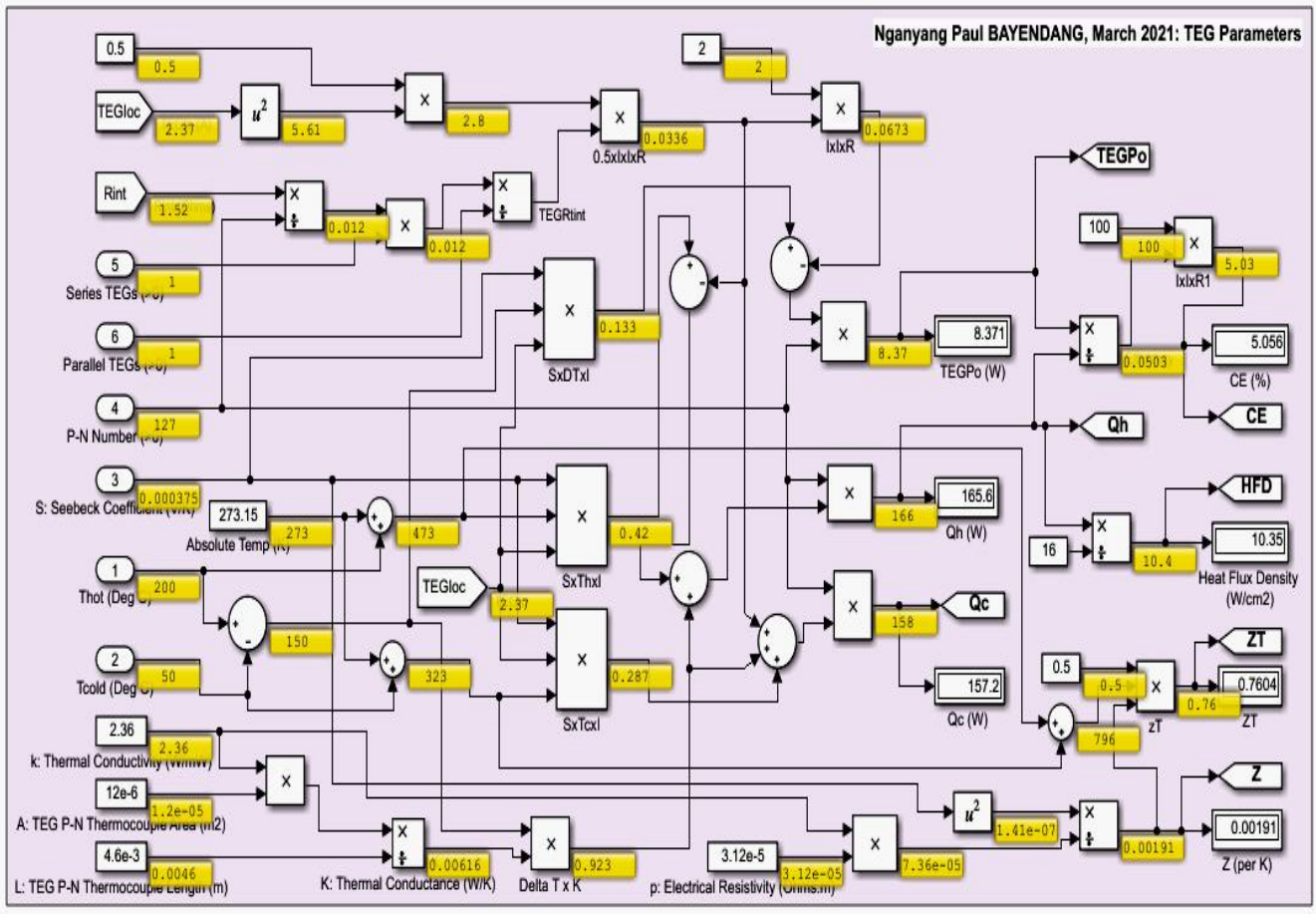

(c) TEG(s) modeling and simulation: TEG(s) parameters

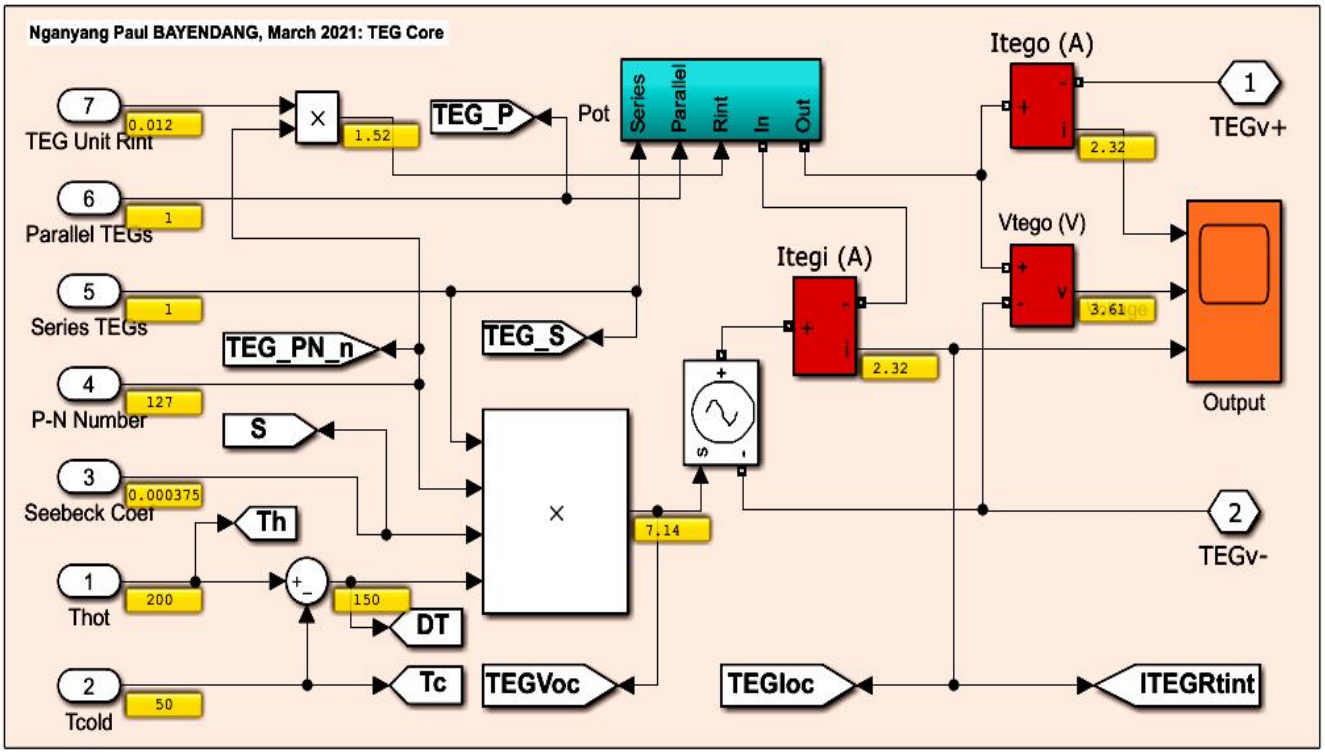

(d) TEG(s) engine

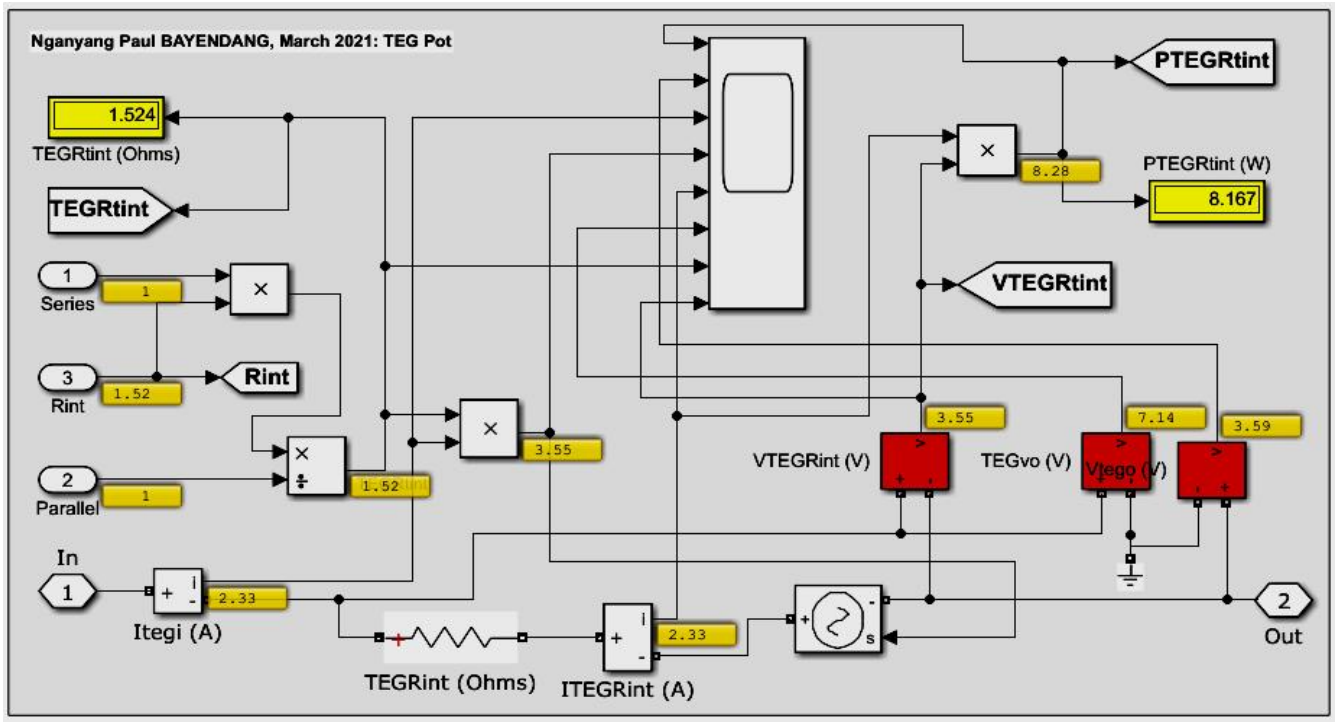

(e) TEG(s) automatic internal source total electrical resistance R_t

Figure 5.1: TEG(s) modeling and simulation

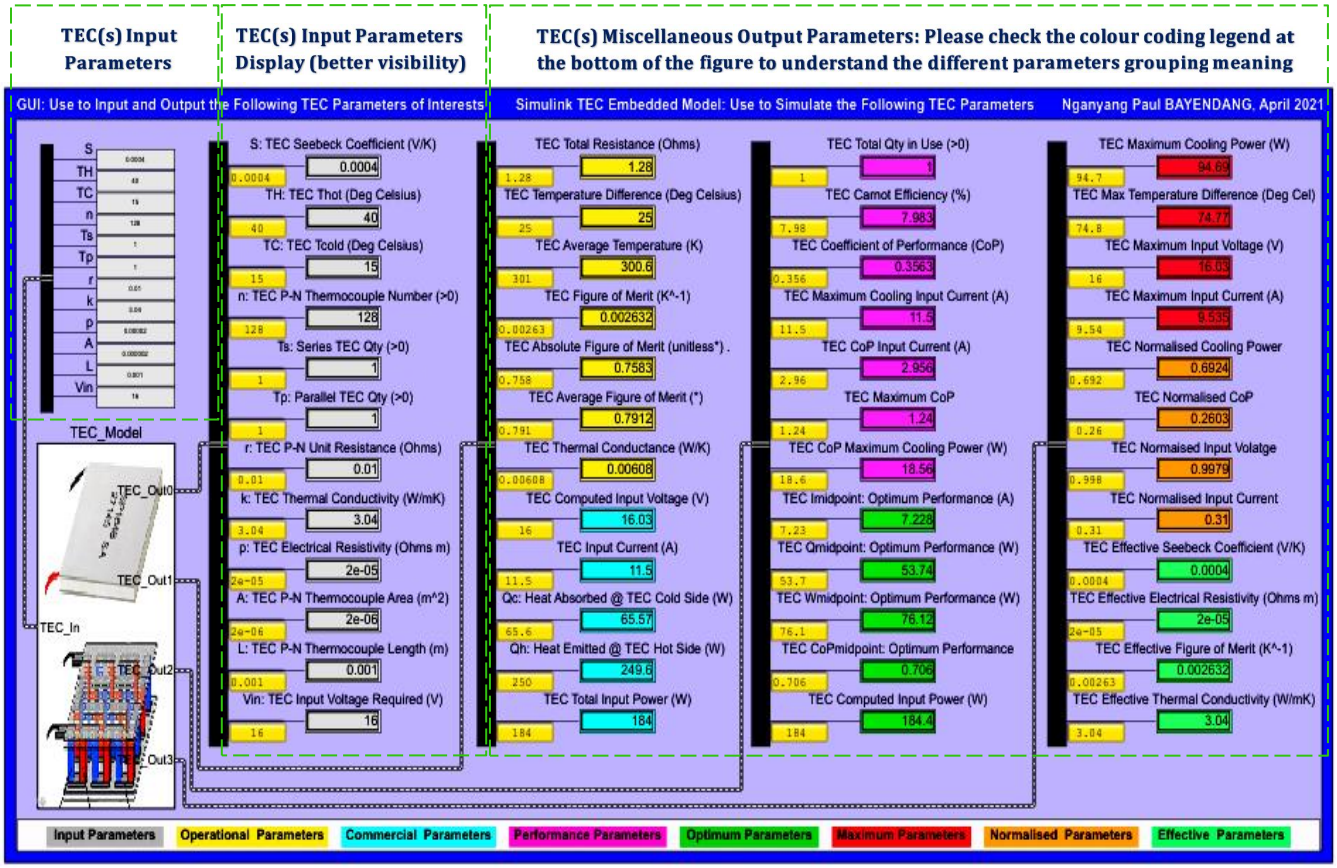

Figure 5.2: TEC(s) simulator: simulates TECs various parameters by inputting a TEC specific datasheet parameters and calculates its theoretical outputs

5.2.3 TEGs and TECs Static and Dynamic Simulations Results

The TEGs and TECs simulations results are presented in three parts as follows, the i) TEGs and ii) TECs parameters steady-state and iii) TEGs dynamics simulations, results. Understanding these dynamics are very paramount; otherwise, doing the physical design would just be a matter of taking chances and hoping for the best − which is likely the case, as most designers / users have reported very bad results, surely because the various operational dynamics were poorly understood. The results from investigating the TEG(s) and TEC(s) parameters optimal operation points/dynamics are later discussed in Section 5.2.4.

5.2.3.1 TEGs Parameters Steady-state (Static) Simulation Results

Figures 5.3 − 5.6 expound the TEGs parameters statically simulated to determine their optimal operation points shown marked in green.

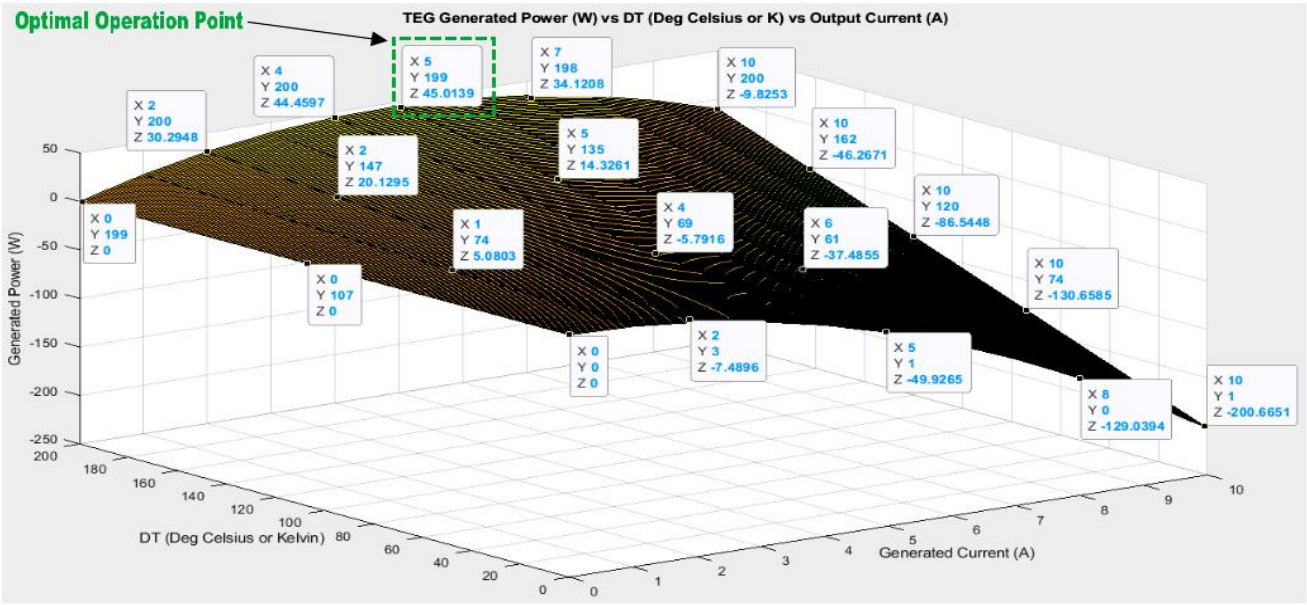

Figure 5.3: TEG power output P_o (W) vs temperature difference ΔT (°C) vs current output I (A)

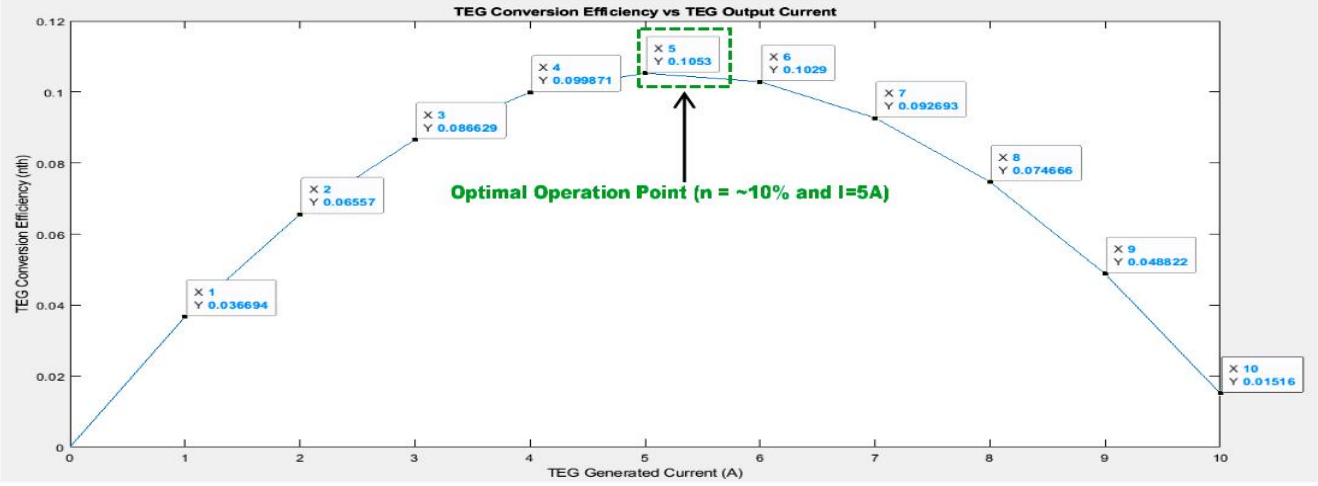

Figure 5.4: TEG conversion efficiency η vs current output I (A)

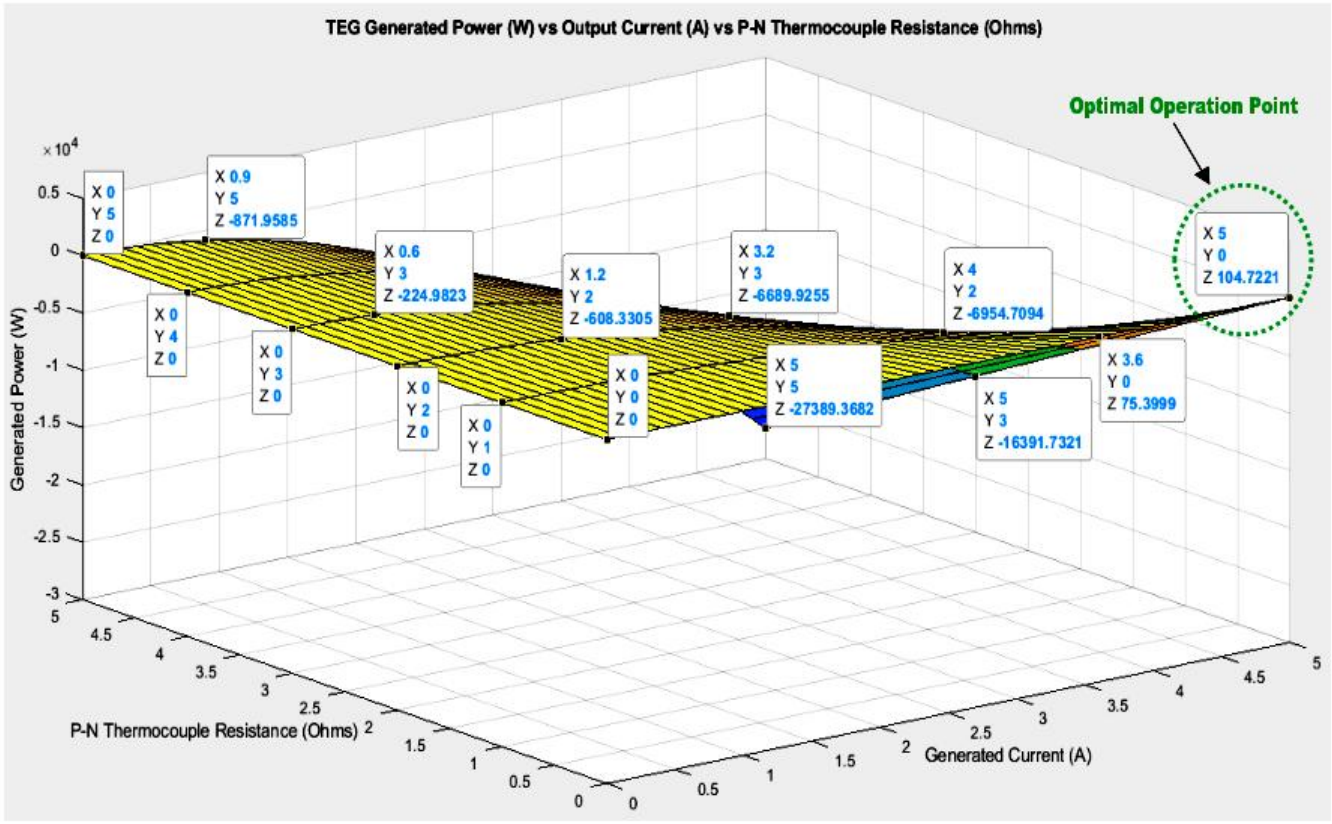

Figure 5.5: TEG power output P_o (W) vs r or R or R_t (Ω) vs current output I (A)

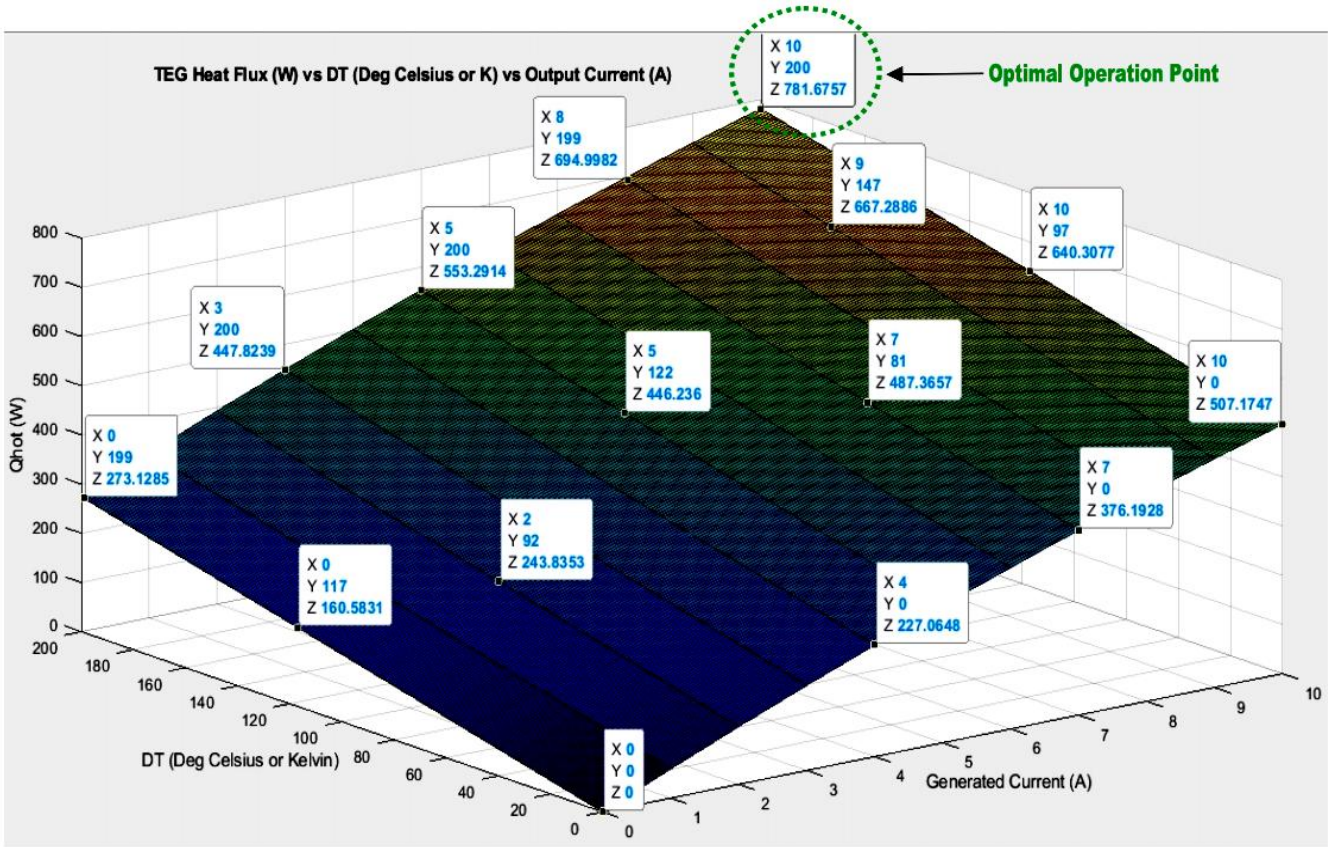

Figure 5.6: TEG heat absorbed Q_h (W) vs temperature difference ΔT (°C) vs output current I (A)

5.2.3.2 TECs Parameters Steady-state (Static) Simulation Results

TECs parameters are statically simulated to determine their possible various optimal operation points and the optimal results are shown highlighted in red in Figures 5.7 − 5.10.

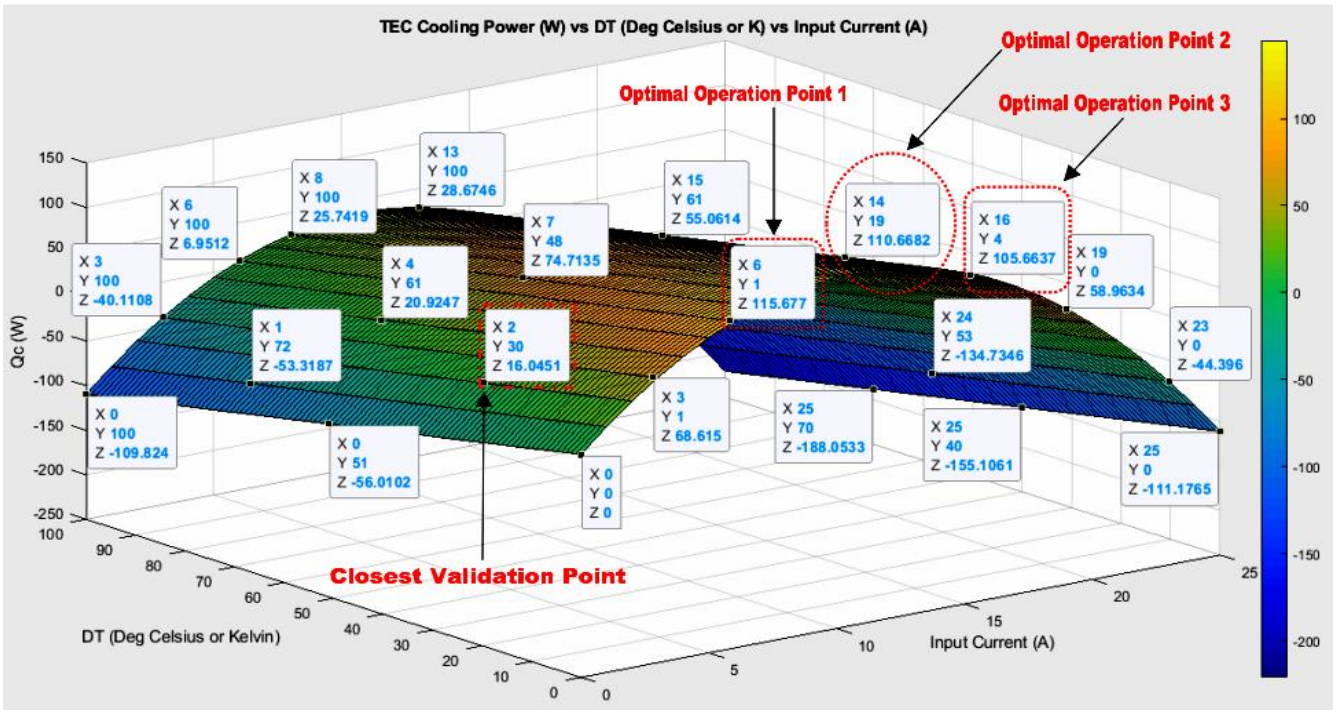

Figure 5.7: TEC cooling power or heat absorbed Q_c (W) vs temperature difference ΔT (°C) vs input current I_{in} (A)

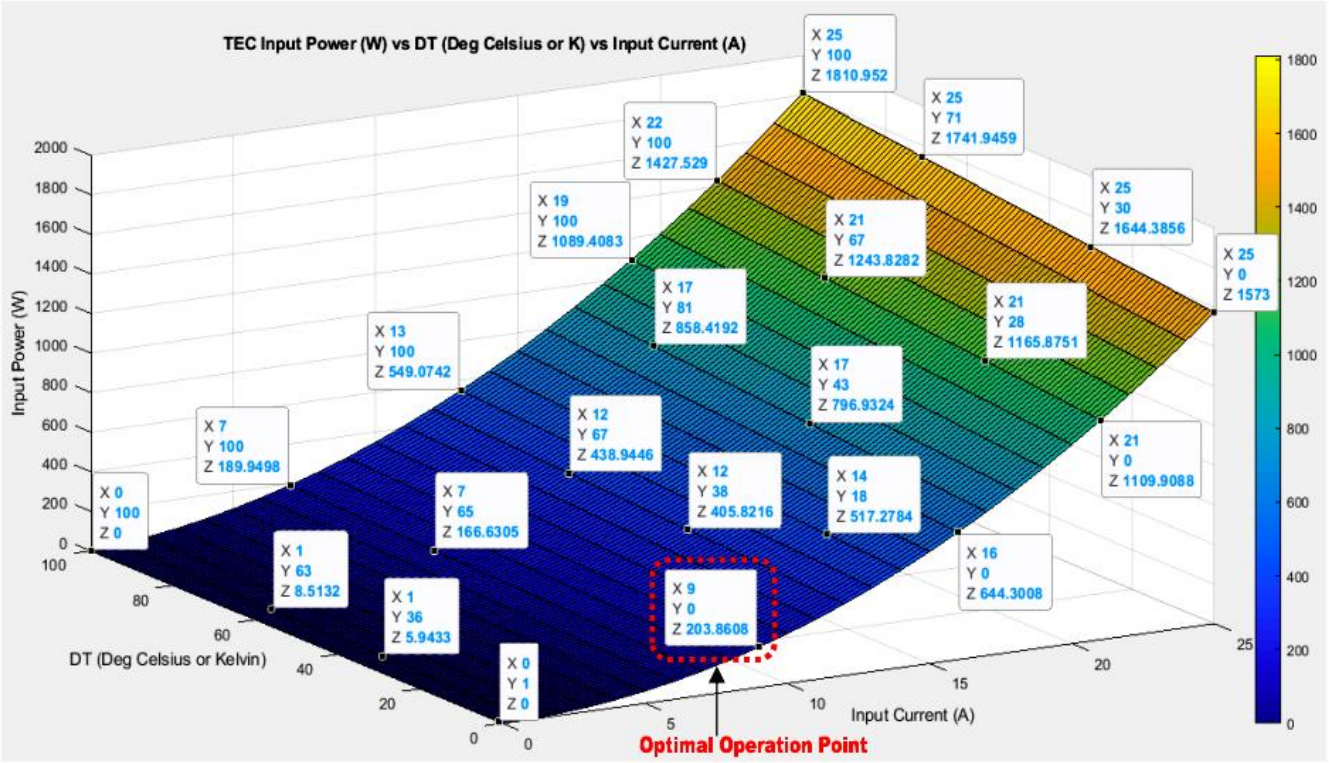

Figure 5.8: TEC input power P_{in} (W) vs temperature difference ΔT (°C) vs input current I_{in} (A)

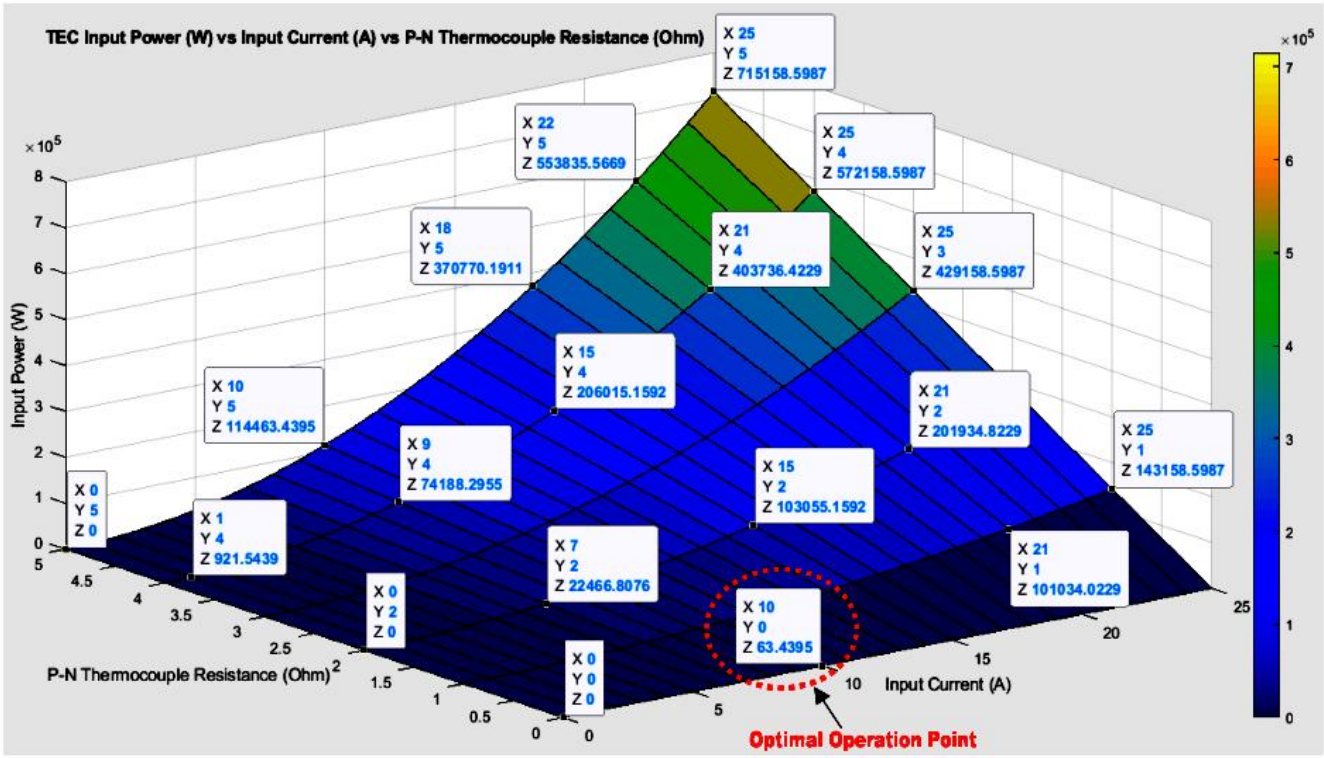

Figure 5.9: TEC input power P_{in} (W) vs internal resistance r or R or R_t (Ω) vs input current I_{in} (A)

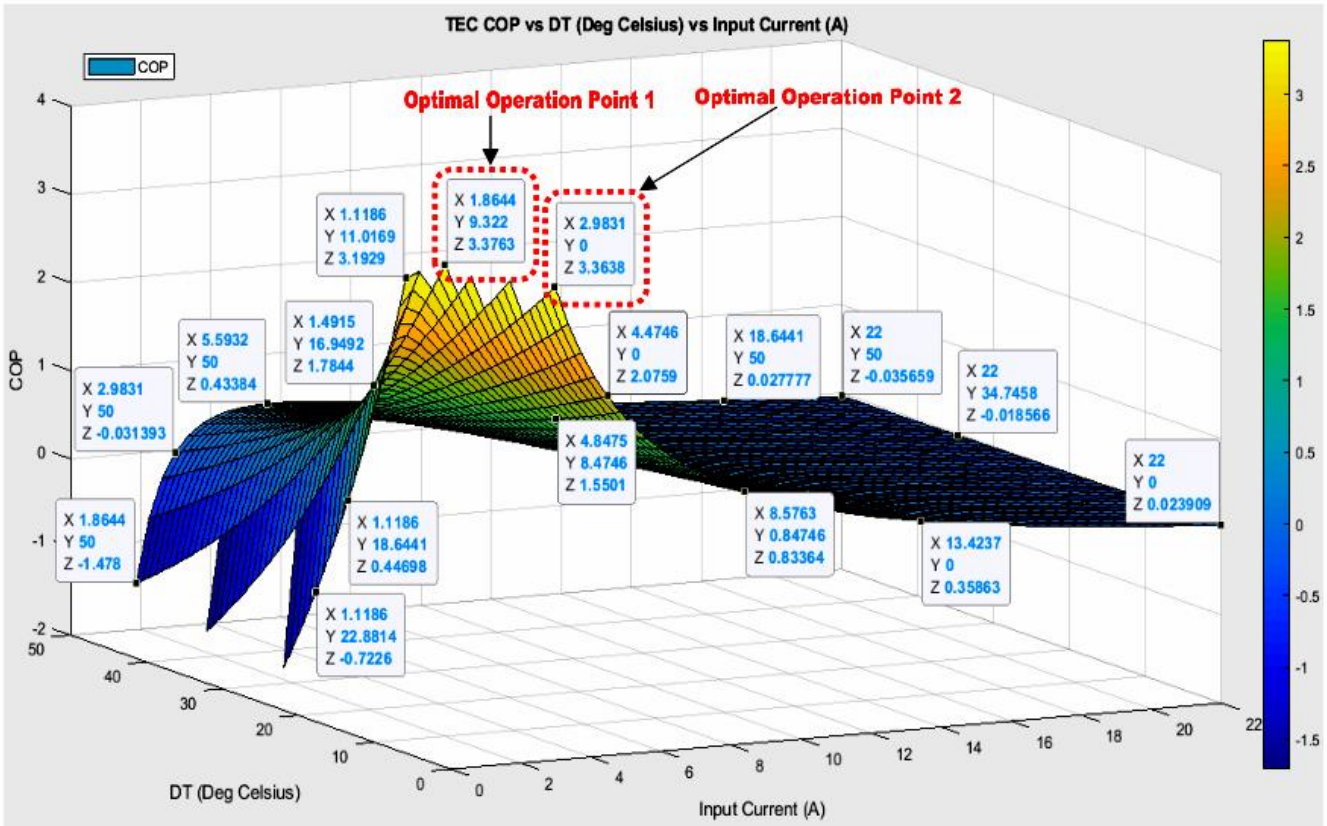

Figure 5.10: TEC coefficient of performance CoP (%) vs temperature difference ΔT (°C) vs input current I_{in} (A)

5.2.3.3 TEGs Parameters Dynamic (Transients) Simulation Results

Using time-series inputs, the TEG modules temperatures, its series and parallel connections dynamics are simulated and inputs and output dynamic results are captured and displayed in Figures 5.11a−5.11f.

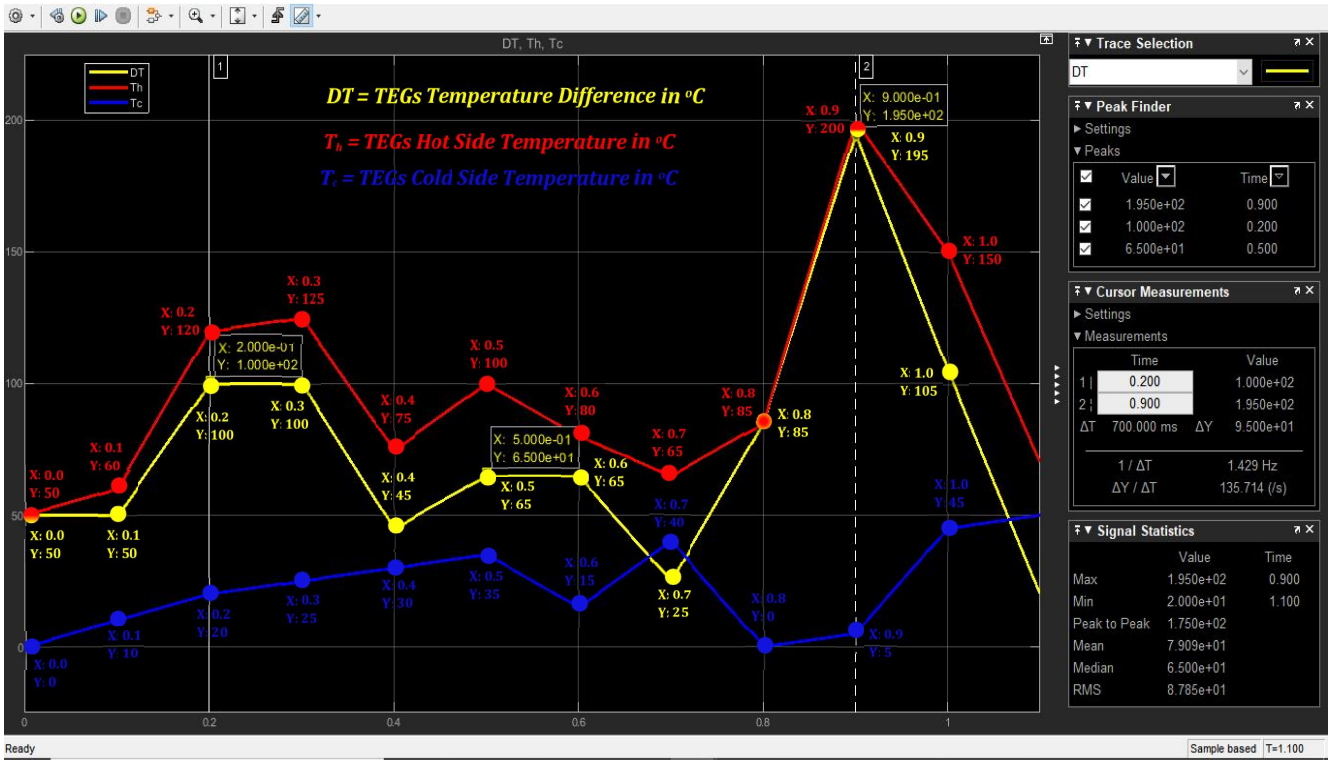

(a) 36 TEGs hot (T_h) and cold (T_c) temperatures as well as temperature difference (DT) dynamics: temperature changes as simulation progresses

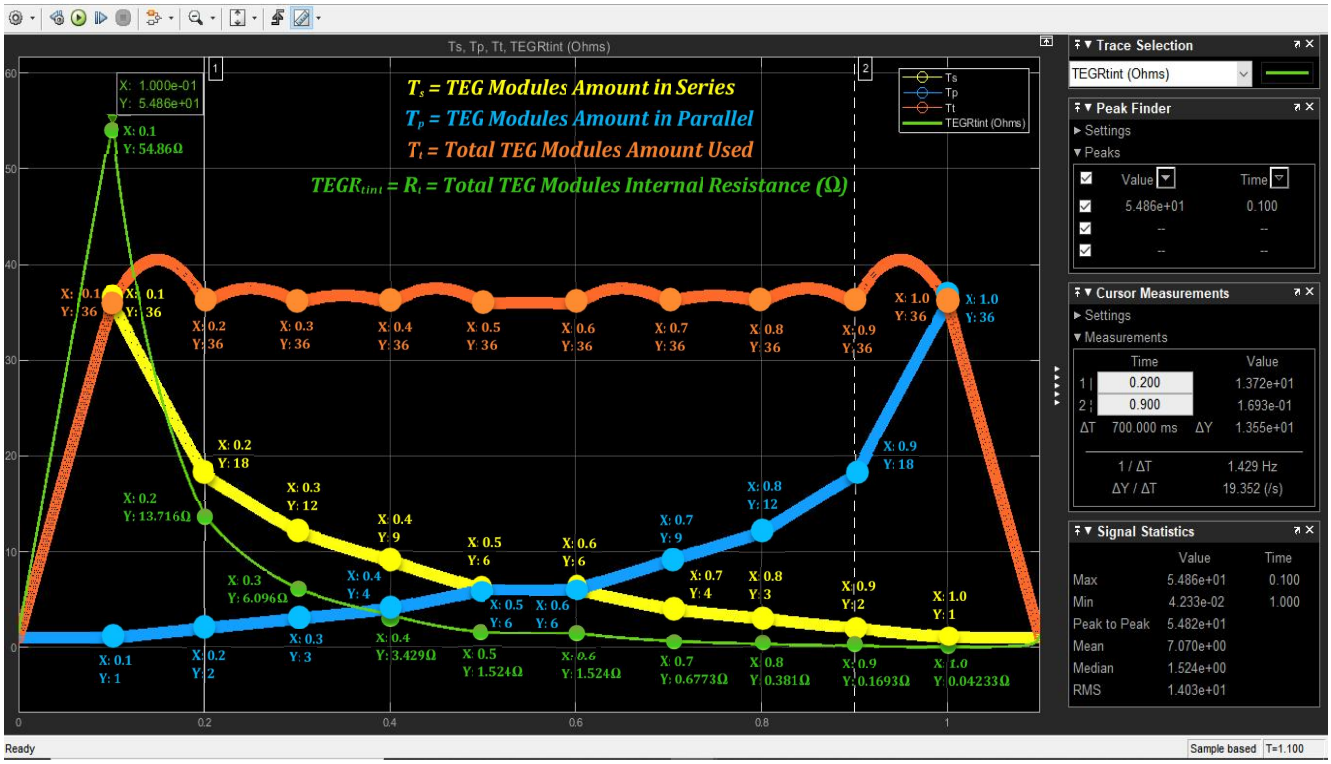

(b) TEGs in series (T_s), parallel (T_p) and total internal resistance (R_t) dynamics: 36 TEG modules simulated in 10 different auto reconfiguration

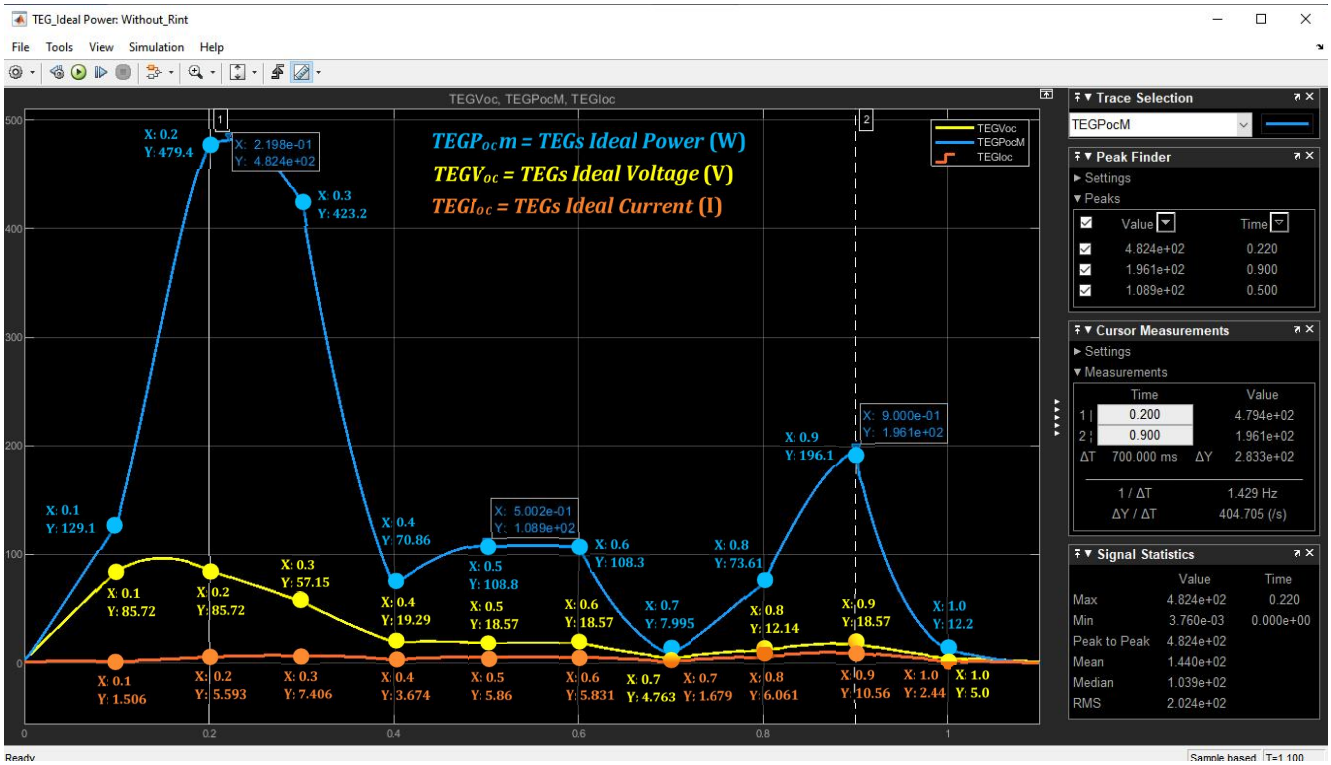

(c) 36 TEGs ideal output power, voltage and current dynamics; as TEGs temperatures and its 10 configurations change as simulation progresses

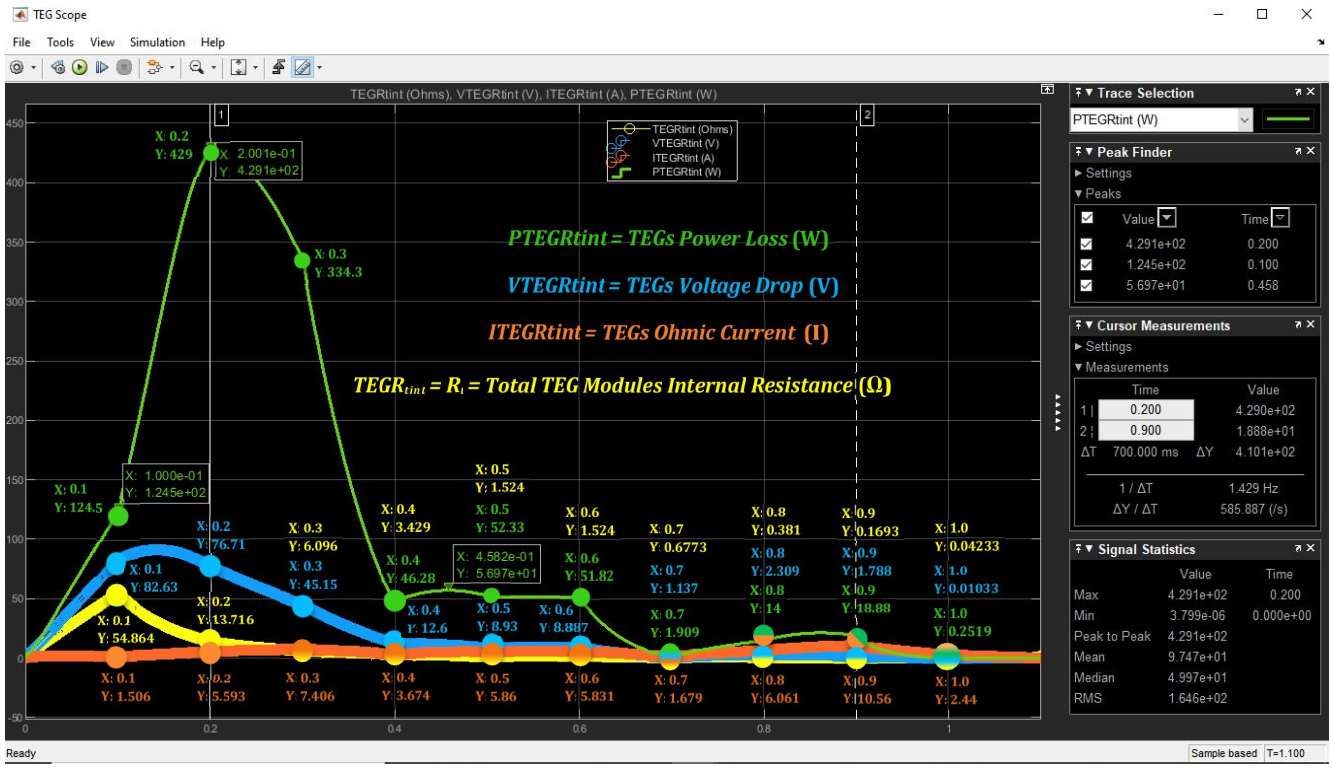

(d) 36 TEGs total internal resistance current, voltage and power losses dynamics; as the TEGs 10 configurations and temperatures auto change

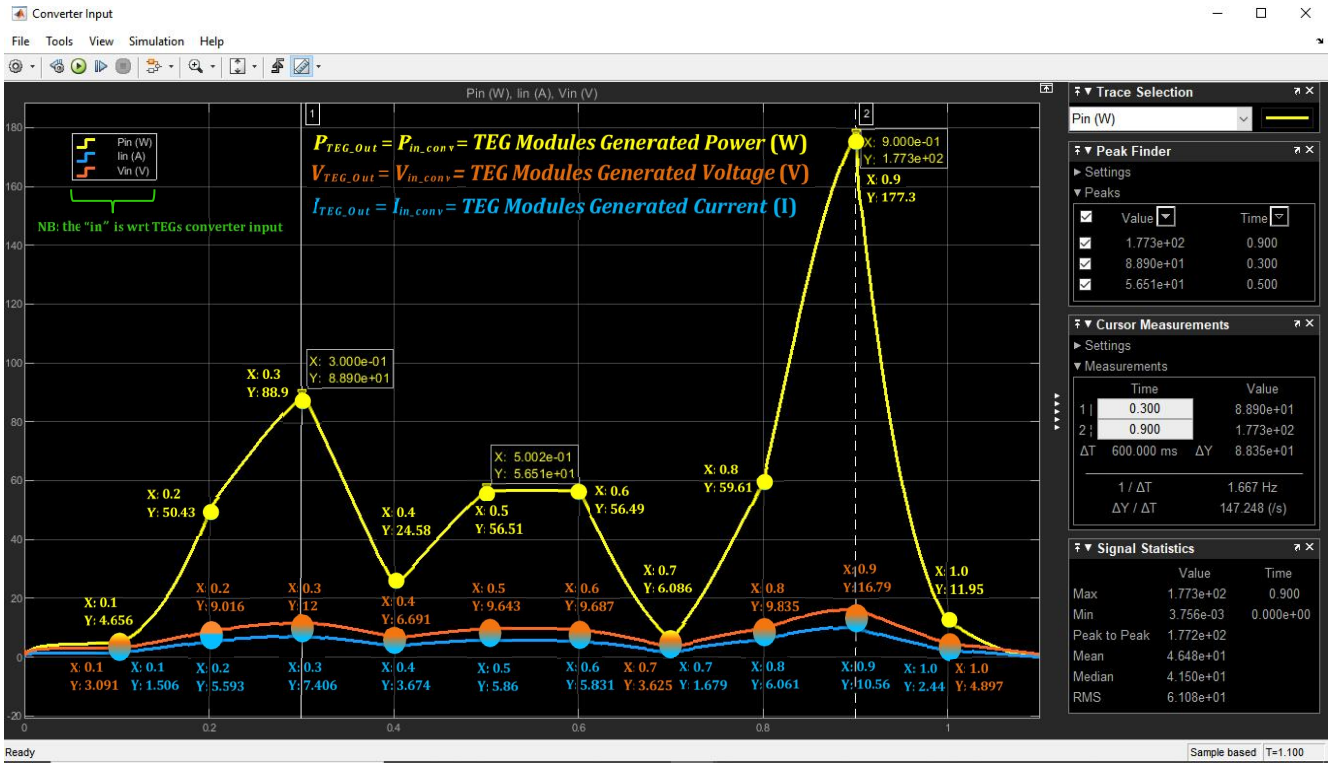

(e) 36 TEGs output power, voltage and current dynamics as the TEGs temperatures and 10 configurations auto change as simulation progresses

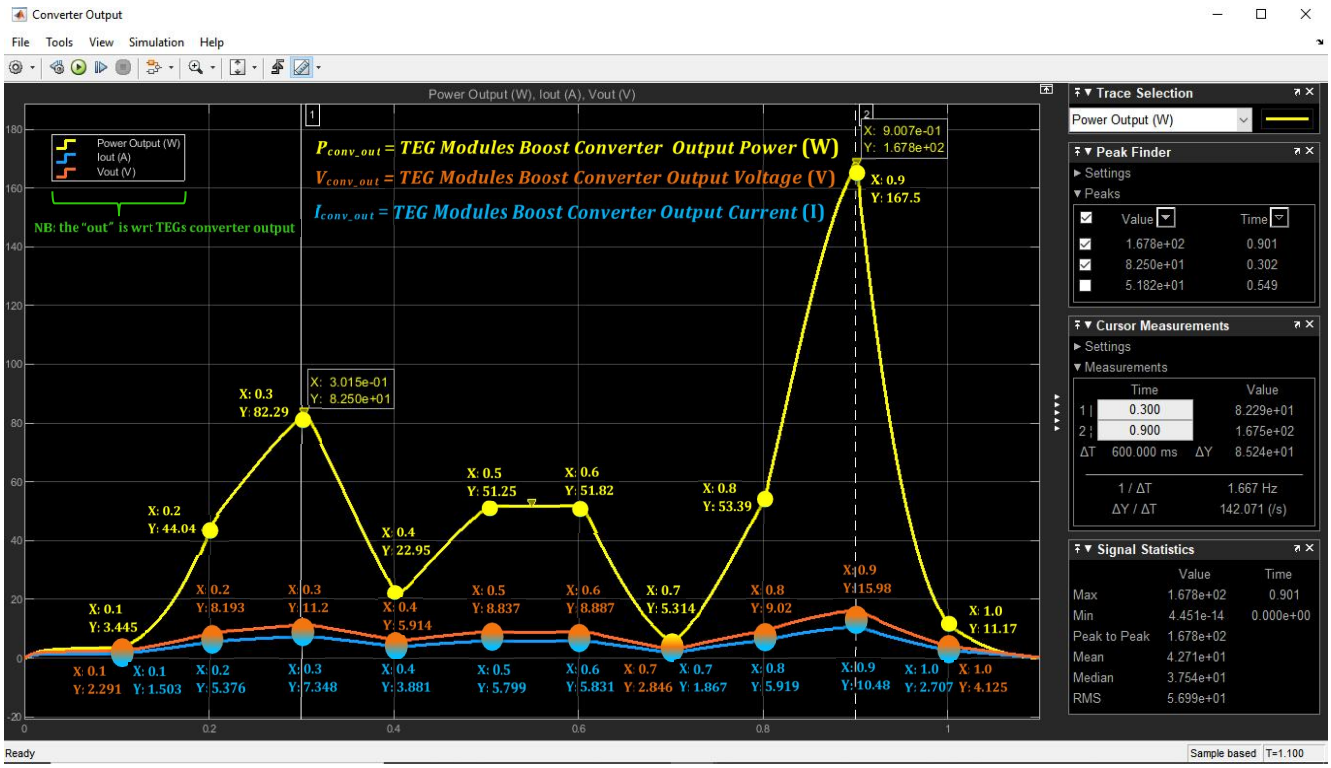

(f) 36 TEGs boost converter output power, voltage and current dynamics as the TEGs temperatures and the TEGs 10 configurations auto change

Figure 5.11: TEGs temperatures (T_h, T_c and ΔT) and 10 different configurations, losses, ideal parameters, input and output parameters dynamic simulations

5.2.4 TEGs and TECs Static and Dynamic Simulations Results Discussions

The TEGs / TECs simulations results shown in Section 5.2.3 are engaged below in their following respective sub-sections.

5.2.4.1 TEGs Parameters Steady-state (Static) Simulation Results Discussion

Some of the crucial TEGs parameters simulated in Section 5.2.3.1. and the significance of the results are herein asserted. As exemplified in Figure 5.3, a TEGs generated power P_o is proportional to its temperature difference ΔT and output current I; however, I above 5A (in this case) will decrease P_o – which is because of the TEGs internal Ohmic heating as a result of the increasing output current I. The ΔT, P_o and I optimum operation points are emphasized in green in Figure 5.3. In Figure 5.4, a TEGs conversion efficiency η is directly proportional to current output I up to ~5A maximum (in this case) and decreases later as highlighted in green. It should be noted that η is as well directly proportional to P_o. However, TEG P_o is reciprocally proportional to its p-n thermocouple resistance r and as well to the total internal resistance R_t of TEG modules, though pro rata to I up to ~5A (in this case) as portrayed in Figure 5.5. At this optimal point; R_t or R is 0Ω, I is ~5A maximum and P_o is ~105W as highlighted in green. In Figure 5.6, the TEGs current output I is proportional directly to the TEGs absorbed heat Q_h (at temperature T_h on the TEG hot-side) which in turn is directly dependent on the TEG ΔT. Figure 5.6 pictured the optimum point stressed-out in green. It should be noted these results are not specific to a particular TEGs connections, they just fundamentally present a holistic theoretical understanding on what TEGs physical parameters must be taken into considerations, how they are interrelated, their associated dynamics and technical limitations and how they can be practically traded-off or optimized for optimal performance when designing TEGs power supply systems.

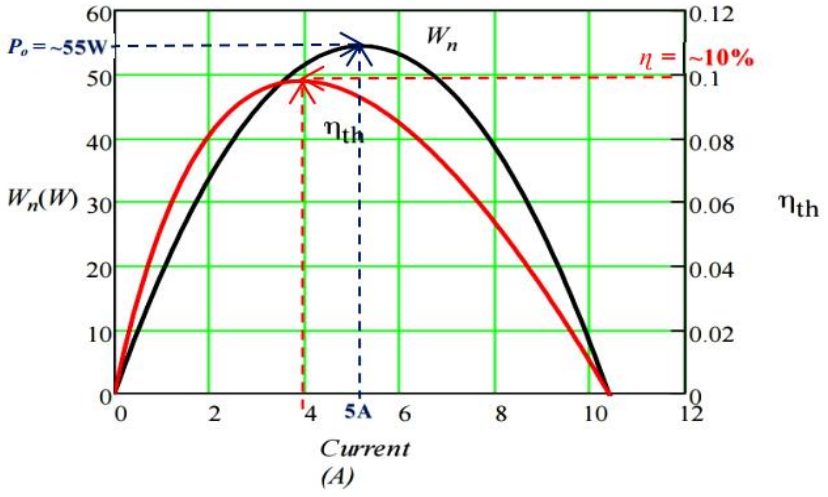

Figure 5.12: Model validation with Lee (2016): TEG (i) output power P_O= ~55W vs output current I = ~5A validating my Figure 5.3 result and (ii) conversion efficiency η= ~10% vs output current I= ~ 4A validating my Figure 5.4 result

Depicted in Figure 5.12, is a result of a typical TEG model simulated with Mathcad using TEG standard specifications from typical manufacturers data-sheet as presented in Lee (2016). This was used as a benchmark to validate my TEGs model simulation accuracy − which is very close, besides a few discrepancies due to minor simulation settings differences. In light of this, my implemented TEGs model can be used and developed further to simulate TEGs of any amount, including any series and parallel connections − which is one of this research highlights.

5.2.4.2 TECs Parameters Steady-state (Static) Simulation Results Discussion

Some of the critical TECs parameters simulated in Section 5.2.3.2 and the importance of the results are herein articulated. Figure 5.7 illustrates that TECs Q_c on TECs cold-side T_c, is inversely pro rata to ΔT but directly pro rata to I_{in} up to a maximum point, after which Q_c starts dropping. The reasons are due to i) Joule heating (the more I_{in}, the more the internal heating effect) and also ii) the second law of thermodynamics − simply put, heat flows from a hotter to a colder body; in this regards, the heating caused by the increasing I_{in}, increases the TECs internal temperature up to a temperature more than that surrounding the TECs hot-side T_h; consequently, heat now starts to flow from the TECs hot-side to its cold-side, thus making the cooling process (heat pumping) on the TECs cold-side inefficient. In Figure 5.7 and highlighted in red, the Q_c, ΔT and I_{in}; display three optimal operation points depending on the TECs design constraints / priorities. In option 1, Q_c is 115.677W with a ΔT of 1°C and I_{in} of 6A. In option 2, Q_c is 110.668W with a ΔT of 19°C and I_{in} of 14A. In option 3, Q_c is 105.664W with a ΔT of 4°C and I_{in} of 16A. As evident, either ΔT and or I_{in} depending on the design constraints, can be optimized by either minimizing the TECs ΔT and or maximizing TECs I_{in} to increase Q_c within max operational limits. In Figure 5.8, P_{in} and I_{in} are directly proportionally which will initially increase Q_c, until a certain maximum limit, after which increasing P_{in} and I_{in} drop Q_c − contrary to ΔT which is inversely pro rata to Q_c. The optimal operation point is highlighted in red. Figure 5.9 shows a TECs P_{in} vs I_{in} vs R. Normally R is set fixed when designed by the manufacturer but now, with R_t introduced, R can be fairly altered and if it is matched to R_s, maximum power will be transferred to the TEC(s); therefore, optimizing P_{in} and maximizing Q_c as highlighted in red. Figure 5.10 demonstrates how *CoP* akin to Q_c; increases with decreasing ΔT and initially with increasing I up to a maximum value and then starts decreasing as current I increases as shown variously in Figure 5.10. Depending on the design constraints, two optimal *CoP* operation points are evident as highlighted in red − in optimal operation point 1, a *CoP* of 3.3763 is achieved by minimizing I_{in} to 1.8644A and maximizing ΔT to 9.322°C; whereas in optimal operation point 2, a *CoP* of 3.3638 is attained by maximizing I_{in} to 2.9831A and minimizing ΔT to 0°C. Finally, my TECs model is reasonably validated by comparing a specific Q_c of Figure 5.7 with that of Figure 5.13 as shown. The discrepancy is due to different TECs parameters setting. In sum, understanding the theory of

TECs parameters and taking the various operational dynamics involved into considerations are very crucial in TECs design and performance.

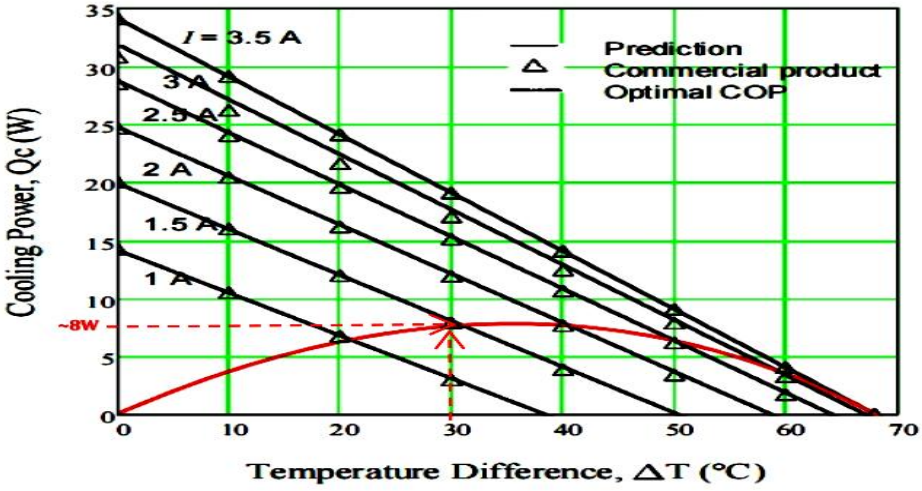

Figure 5.13: Model validation with Lee (2016) − with TEC cooling power Q_c=~8W vs input current I= ~1.5A vs ΔT= ~30°C to validate my TECs Q_c in Figure 5.7 result, with cooling power Q_c = ~16W vs input current I=~2A vs ΔT= ~30°C

5.2.4.3 TEGs Parameters Dynamic (Transients) Simulation Results Discussion

Some of the critical TEGs dynamics simulated in Section 5.2.3.3 and the importance of the results are herein discussed. The TEGs temperatures and modules electrical connections dynamics were simulated, in which beginning with the TEGs temperature dynamics, various arbitrary temperatures on the TEGs hot and cold sides as demonstrated in Figure 5.1b and Figure 5.11a, as well as summarized in Table 5.1, were dynamically simulated using time-series inputs and the various output results recorded. As expected, the TEGs generated power, voltage and current increased with increasing T_h and DT but with decreasing T_c.

Table 5.1: TEGs time-series input dynamic simulation results summary

Parameters	Matlab / Simulink Simulation Time										Matlab / Simulink Simulation Time										Parameters
	0.1	0.2	0.3	0.4	0.5	0.6	0.7	0.8	0.9	1.0	0.1	0.2	0.3	0.4	0.5	0.6	0.7	0.8	0.9	1.0	
Figure 5.11a	**TEG modules T_h, T_c and DT dynamic temperature inputs in °C**										**36 TEG modules generated (terminal) power, voltage and current**										**Figure 5.11e**
TEGs T_h	60	120	125	75	100	80	65	85	200	150	4.656	50.43	88.9	24.58	56.51	56.49	6.086	59.61	177.3	11.95	***P_{TEG_Out}* (W)**
TEGs T_c	10	20	25	30	35	15	40	0	5	45	3.091	9.016	12	6.691	9.643	9.687	3.625	9.835	16.79	4.897	***V_{TEG_Out}* (V)**
TEGs DT	50	100	100	45	65	65	25	85	195	105	1.506	5.593	7.406	3.674	5.86	5.831	1.679	6.061	10.56	2.44	***I_{TEG_Out}* (A)**
Figure 5.11b	**36 TEG modules in 10 dynamic T_s, T_p, T_t and R_t auto configuration**										**36 TEG modules internal resistance power, voltage and current**										**Figure 5.11d**
T_s	36	18	12	9	6	6	4	3	2	1	54.86	13.72	6.096	3.429	1.524	1.524	0.677	0.381	0.169	0.0423	***TEG_{Rtint}* (Ω)**
T_p	1	2	3	4	6	6	9	12	18	36	124.5	429	334.3	46.28	52.33	51.82	1.909	14	18.88	0.2519	***$PTEG_{Rtint}$* (W)**
T_t	36	36	36	36	36	36	36	36	36	36	82.63	76.71	45.15	12.6	8.93	8.887	1.137	2.309	1.788	0.0103	***$VTEG_{Rtint}$* (V)**
***R_t* (Ω)**	54.86	13.72	6.096	3.429	1.524	1.524	0.677	0.381	0.169	0.0423	1.506	5.593	7.406	3.674	5.86	5.831	1.679	6.061	10.56	2.44	***$ITEG_{Rtint}$* (A)**
Figure 5.11c	**36 TEG modules ideal (if TEG_{Rtint} = 0) power, voltage and current**										**36 TEG modules boost converter output power, voltage and current**										**Figure 5.11f**
***TEG_{PocM}* (W)**	129.1	479.4	423.2	70.86	108.8	108.3	7.995	73.61	196.1	12.2	3.445	44.04	82.29	22.95	51.25	51.82	5.314	53.39	167.5	11.17	***P_{conv_out}* (W)**
***TEG_{Voc}* (V)**	85.72	85.72	57.15	19.29	18.57	18.57	4.763	12.14	18.57	5	2.291	8.193	11.2	5.914	8.837	8.887	2.846	9.02	15.98	4.125	***V_{comv_out}* (V)**
***TEG_{Ioc}* (A)**	1.506	5.593	7.406	3.674	5.86	5.831	1.679	6.061	10.56	2.44	1.503	5.376	7.348	3.881	5.799	5.831	1.867	5.919	10.48	2.707	***I_{conv_out}* (A)**

The TEG modules quantity used and most vitally in series, parallel and mixed connection were simulated, whereby as shown in Figure 5.1b and Figure 5.11b, as well as summarized in Table 5.1; 36 TEGs were arbitrary chosen and then arranged in 10 different combinations to study the setup effects of the various arrangements and when matched to a 1.524Ω electrical load. Each arrangement gives a different R_t, consequently giving different generated powers, voltages and currents. Figure 5.11c depicts the TEGs ideal power, voltage and current generated; assuming the TEGs R_t or TEG_{Rtint} is negligible. Figure 5.11d shows the power loss, voltage drop and Ohmic current due to the presence of TEG_{Rtint}. Finally, Figures 5.11e and 5.11f, show the resultant output power, voltage and current supplied to the DC-DC boost converter and from it. As evident, more TEG modules increased the output values; however, what is more insightful is how TEGs opt to be arranged and matched to R_L to obtain maximum power transfer.

5.2.5 Summary

South Africa has been experiencing electrical power outages which is getting worst during winter periods. Sustainable energy is becoming popular to supplement the grid and for private use. In view of this, I proffer thermoelectricity as an alternative energy source (TEGs) as well as an energy efficient load (TECs) for household applications that require low DC power, cooling and heating. However, TEG and TEC require multiple units connected in series and or in parallel to provide decent output and cooling powers respectively. Usually, the perception would be trying to utilise more with the hope to get more power; however, my findings assert this is not really the case, as i) TEG and TEC temperature difference ΔT and current parameters have performance dynamics which must be operated within strict optimal operation limits to guarantee efficiency and ii) TEGs and TECs total internal resistance R_t changes − increases when connected in series and decreases when connected in parallel; hence, the overall power /efficiency will be affected, especially if the source and load resistances are not matched to transfer maximum power. In essence, this study major contributions include a structured meticulous mathematical presentations with focus on TEG and TEC modules total resistance R_t, when more than one TEG and TEC module are connected in series and or in parallel combinations, followed by a detailed TEGs and TECs modeling using Matlab / Simulink. Forbye, the TEGs and TECs models were used to simulate and investigate some thermoelectricity profound parameters performance dynamics, R_t losses and to validate some of their operation points with industry standard models. Various large scale practical studies of TEGs and TECs in Liu *et al.* (2014), Ebrahimi and Derakhshan (2018), Giwa *et al.* (2019), Abhijith *et al.* (2020), Fauzan *et al.* (2020), Hu *et al.* (2020), Afshari (2021), Aljibory *et al.* (2021) and Rösch *et al.* (2021) were examined and in light of their results, the future work will include embarking on an actual lab design, testing my implemented models with them and refining accordingly while taking the physical dynamics into account. Thereafter, a practical pilot 1kW implementation shall be devised for a household combined cooling, heating and power (CCHP) system − as an alternative energy option to the RSA energy crisis.

5.3 Thermoelectric Generators (TEGs) Modules − Optimum Electrical Configurations and Performance Determination

In South Africa by and large Africa, load shedding has made renewable energy trendy and now paramount, due to its environmental friendliness and sustainability. This section focuses on alternative energy based-on thermoelectricity, particularly thermoelectric generators (TEGs). From the literature review, there is less emphasis on how and what multiple TEGs configuration is best for optimum operations. In light of this, Matlab and Simulink were employed to institute a theoretical framework that can comprehensively be easily used to model and simulate thermoelectricity parameters to determine TEGs optimal electrical matching configurations and performance. The main findings brought forth to conclude my study are; the multiple TEGs used should be a) of the same model with the same or approximate internal resistance, b) in a configuration whereby the TEGs total resistance equals the load electrical resistance, as doing so ensures maximum power is transferred between the source (TEGs) and the electrical load and c) preferably in a square electrical array, as this configuration ensures, i) the total source resistance of the TEGs, irrespective of the modules quantity used, approximates that of a unit TEG (meaning the overall TEG modules simply becomes now one big powerful TEG) and ii) the TEGs power, voltage and current operations are optimal.

5.3.1 Introduction

According to Bayendang *et al.* (2020b), South Africa like most African countries, is currently having an unstable national grid, which is affecting homes and businesses electricity supplies. As a result, renewable and alternative energy sources demands are on the rise to augment the electricity grid. In this regard, thermoelectricity is investigated as a potential alternative for basic household energy use − such as power, lighting and cooling / heating. Thermoelectricity as examined in Bayendang *et al.* (2020b), constitutes the Seebeck, Peltier and Thomson effects. The latter has trivial practical use, therefore the practical focus is on the Seebeck and Peltier effects. Seebeck effect entails production of DC power from heat using a TEG, whereas Peltier effect entails cold / heat generation from DC electricity depending on the applied voltage polarity across a TEC. This study focuses on TEGs. Reviewed in Twaha *et al.* (2016), TEG module DC power can be enhanced by properly matching the TEG internal resistance to the electrical load, increasing the TEG hot-side temperature and lowering the TEG cold side temperature, increasing the heat flux density, increasing the number of TEG units, using DC to DC power converters and energy management control techniques etc. With research gaps identified in Lesage *et al.* (2013), Twaha *et al.* (2016), Kwan *et al.* (2018), Bayendang *et al.* (2020b) and Koketsu and Tanzawa (2021); i now zoom-in on TEGs source to load resistance matching with focus on using an in/finite TEGs amount. Proceeding the introduction is a brief TEGs applicable maths, followed by TEGs modelling and simulation using Matlab / Simulink, in which 100 TEGs are simulated in ten different series and or parallel configurations to determine an

optimum electrical configuration with respect to the size of the electrical load and finally the simulated results are presented, comparatively engaged, validated and the closing remarks are drawn to end the study.

5.3.2 TEGs Mathematics and Modeling

From analysing Twaha *et al.* (2016) and Bayendang *et al.* (2020b) extensive literature review, in both articles, multiple TEG modules are connected in series and or in parallel to increase the output power. However, there is little or no emphasis on the significance of the TEG modules actual configurations. It should be noted that a TEG is a voltage source and to transfer maximum power between a source and load, the source and load resistances or impedances must matched. A TEG is not an ideal voltage source; as a result, it's imperative its internal resistance is considered when connecting multiple TEGs to increase their DC output power − as the internal resistance will either increase, decrease or stays approximately the same depending on the quantity of TEGs and the configuration used, which will consequently affects the TEG output power. TEG maths is extensively presented in Bayendang *et al.* (2020c) and I developed it further to study the total resistance and power output when multiple TEGs are connected in series and or parallel.

5.3.2.1 TEGs Basic Mathematics

It's worth noting that connecting TEGs in series to boost the output voltage, also boosts the TEGs total internal resistance and connecting in parallel to increase the output current, also decreases the total internal resistance. TEGs steady-state mathematics is developed as follows:

- The thermoelectric (TE) device p-n junction thermocouples unit resistance (r) in ohm is:

$$r = \frac{L\rho}{A} \qquad (\Omega) \tag{5.56}$$

where L is the TEG p-n junction thermocouple length in meter (m), ρ is the TEG electrical resistivity in Ωm and A is the TEG p-n junction thermocouple area in metre squared (m^2).

- The TE device (TEG) module unit resistance (R) in (ohm) is calculated as:

$$R = r\,n \qquad (\Omega) \tag{5.57}$$

where n which differs, is the TEG's manufacturer p-n junction thermocouples quantity used.

- The TEG module(s) or TEG(s) total resistance (R_t) in (Ω) can be derived as:

$$R_t = r\,n\frac{T_s}{T_p} = R\frac{T_s}{T_p} \qquad (\Omega) \tag{5.58}$$

where T_s and T_p are the TEGs respective amount in series and in parallel. NB: for equation (5.58) to be valid, all the TEGs modules used must be of the same type or model to ensure their R is very identical.

- The TEG module(s) generated current (I) in ampere is calculated as:

$$I = \frac{nS\Delta T}{R_L + R_t} \quad \text{(A)} \tag{5.59}$$

where S is the TE device Seebeck coefficient in V/K, R_L is the electrical load resistance connected to the TEG(s) output and ΔT is the TEG(s) temperature difference in °C or K.

- The TEG module(s) generated voltage (V_o) in volt is derived as:

$$V_o = IR_L = n[S\Delta T] - IR_t \quad \text{(V)} \tag{5.60}$$

where $\Delta T = T_h - T_c$ is the TEG(s) temperature difference in °C or kelvin in which T_h and T_c are respectively the temperatures on the TEG hot and cold sides in °C or K and I in ampere is the output current through the TEG(s) and is normally responsible for the TEG(s) internal Ohmic or Joule heating − which will affects the internal working of the TEG if not controlled within a certain optimal value.

- Heat absorbed on the TEG module(s) hot-side (Q_h):

For the TEG(s) to generate power, the TEG(s) hot-side must be at a high temperature T_h to absorb more heat and create a constant heat flux (Q_h) in watt.

$$Q_h = n[(SIT_h) + (K\Delta T)] - 0.5I^2R_t \quad \text{(W)} \tag{5.61}$$

where K is the TEG(s) thermal conductance in (W/K)

- Heat emitted on the TEG module(s) cold-side (Q_c):

For the TEG(s) to generate power, the TEG(s) cold-side must be at a lower temperature T_c to dissipate the heat Q_c in watt.

$$Q_c = n[(SIT_c) + (K\Delta T)] + 0.5I^2R_t \quad \text{(W)} \tag{5.62}$$

- TEG module(s) generated power (P_o)

The TEG(s) output power in watt, is the difference between Q_h and Q_c or the product of the generated voltage and current.

$$P_o = Q_h - Q_c = n[(SI\Delta T)] - I^2R_t \quad \text{(W)} \tag{5.63}$$

$$P_o = IV_o = n[(SI\Delta T)] - I^2R_t \quad \text{(W)} \tag{5.64}$$

- TEG(s) conversion efficiency (η)

This is the ratio of the TEGs output power and the heat absorbed on the TEG(s) hot-side.

$$\eta = P_o / Q_h \tag{5.65}$$

It should be noted that the above sets of equations are just the fundamental mathematical expressions necessary to define a TEG and for use to formulate the case for connecting more than one TEG in series and in parallel to generate more power. The major electrical difference between a TEG and TEG(s) is their electrical resistance R_t and consequently it will affects the output voltage, current and power productions.

5.3.2.2 TEGs Modelling and Simulations

In Section 5.3.2.1, TEGs fundamental equations of interests were examined with keen emphasis on the total internal resistance R_t − which was derived and further used to develop and express in terms of R_t the standard TEG equations to now cover the case for TEG(s). These equations were henceforth modeled in Matlab and Simulink to establish a TEG(s) model that can be used to simulate and determine optimal TEGs configurations. The detailed modeling is above the scope of this study. Represented in Figure 5.14a is the main TEGs simulated model, in which an infinite amount of TEGs configurations and the TEGs parameters expressed in Section 5.3.2.1, can be configured and simulated to obtain TEG(s) optimum results − the idea is to match the source and load resistances. Usually R_L is first set and the simulation is executed to iteratively check and match the TEGs total internal resistance for maximum power transfer at different simulation times which correspond to the different TEGs configurations. Lets assume a heat energy harvesting system is to be designed to use “X” amount of TEGs modules, normally in the literature, it’s a matter of dividing the total output power required by the amount of power a TEG can generate to get the “X” amount of TEGs required. In-depth research on the optimal number and in what optimum configurations with respect to the load is lacking. Lets further assume this computed “X” amount of TEGs happens to be 102.3 or 97.6. In the literature, it’s also a matter of just rounding down to 102 or up to 98 and further connecting the TEGs in series / parallel to get the needed output power − which might not be

efficient / optimal. In this regard, I hereby advance the case for using multiple TEGs, whereby emphasis on the TEGs optimal electrical configurations with respect to the electrical load must first be determined. Table 5.2 portrays a typical TEG standard thermoelectric parameters (datasheets TG12-4 and TGM-127-1.4-2.5) and lets assumed instead of normally using 102 or 98 TEGs; 100 TEGs is proffered, from which the 100 TEGs is further analyzed in 10 different electrical configurations as exemplified in Table 5.3.

Table 5.2: A TEG module typical manufacturer parameters of interest

S (μV/K)	r (mΩ)	n	R (Ω)	Z (K^{-1})	ZT	T_h (°C)	T_c (°C)	V_{out} (V)	I_{out} (A)	P_{out} (W)
375	12	127	1.524	0.00191	0.7125	200	50	3.558	2.353	8.371

My rationale is to take for example the 100 TEG modules, find the factors of 100 (1, 2, 4, 5, 10, 20, 25, 50, 100) and arrange them in different series and parallel combinations pairs to get 10 unique configurations from 100, as shown in Table 5.3. By using equation (5.58) to compute the total resistance R_t for each of this configurations (C) denoted C1-C10, each gives different R_t. The following conditions must be met i) all the TEGs used must be the same to have similar r or R, ii) for each configuration (C1-C10), the load resistance R_L must be changed to match each TEGs configuration R_t to obtain maximum power for that specific configuration and iii) all other parameters/factors must be unaltered to ensure the same input test parameters for each C1-C10. The TEGs in series are denoted TEG_S and in parallel TEG_P. NB: The same rationale applies to thermoelectric coolers (TECs); however, unlike TEG which is a voltage source that supplies DC power, TEC is an electrical load that needs DC power supplied to it. Asserted in Section 5.3.3 are the simulation results. It should be noted this is a theoretical study with key focus on studying TEGs source to load electrical resistance matching and maximum power transfer based on TEG modules different electrical configurations (10 in this case) only and no other factors (dynamics) are of interest in this particular study.

Table 5.3: Analyzing multiple TEGs / TECs (e.g. 100) in 10 different configurations (C1 - C10)

	C1	C2	C3	C4	C5	C6	C7	C8	C9	C10
TEG_S	100	50	25	20	10	10	5	4	2	1
TEG_P	1	2	4	5	10	10	20	25	50	100
$R_t = R_L$ (Ω)	152.4	38.1	9.525	6.096	1.524	1.524	0.381	0.24384	0.06096	0.01524

5.3.3 TEGs Optimal Electrical Configurations Determination Simulations Results

Figures 5.14 − 5.23 show the 100 TEGs 10 unique electrical configurations to determine the optimal setup.

5.3.3.1 TEGs Configuration 1 (C1): R_t = 152.4Ω

C1 simulation result has the following settings: $TEG\_S=T_s=100$; $TEG\_P=T_p=1$; $R_L=152.4\Omega$.

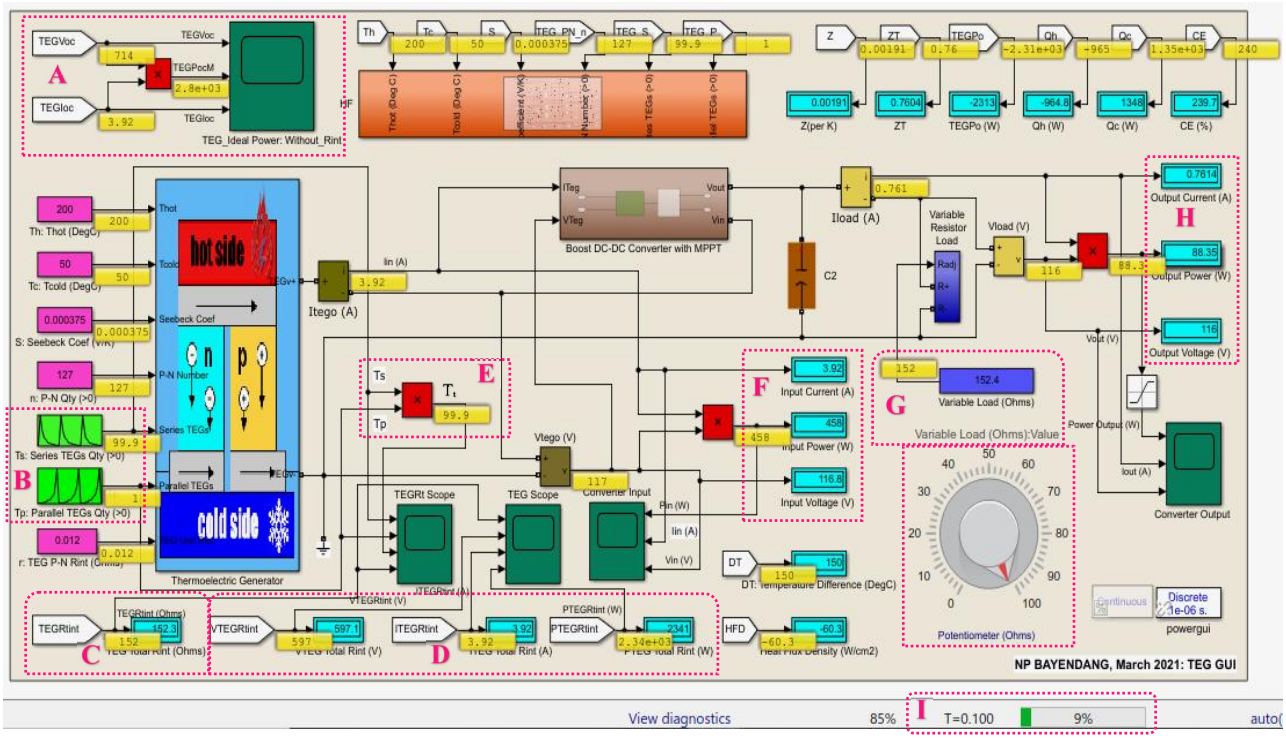

(a)

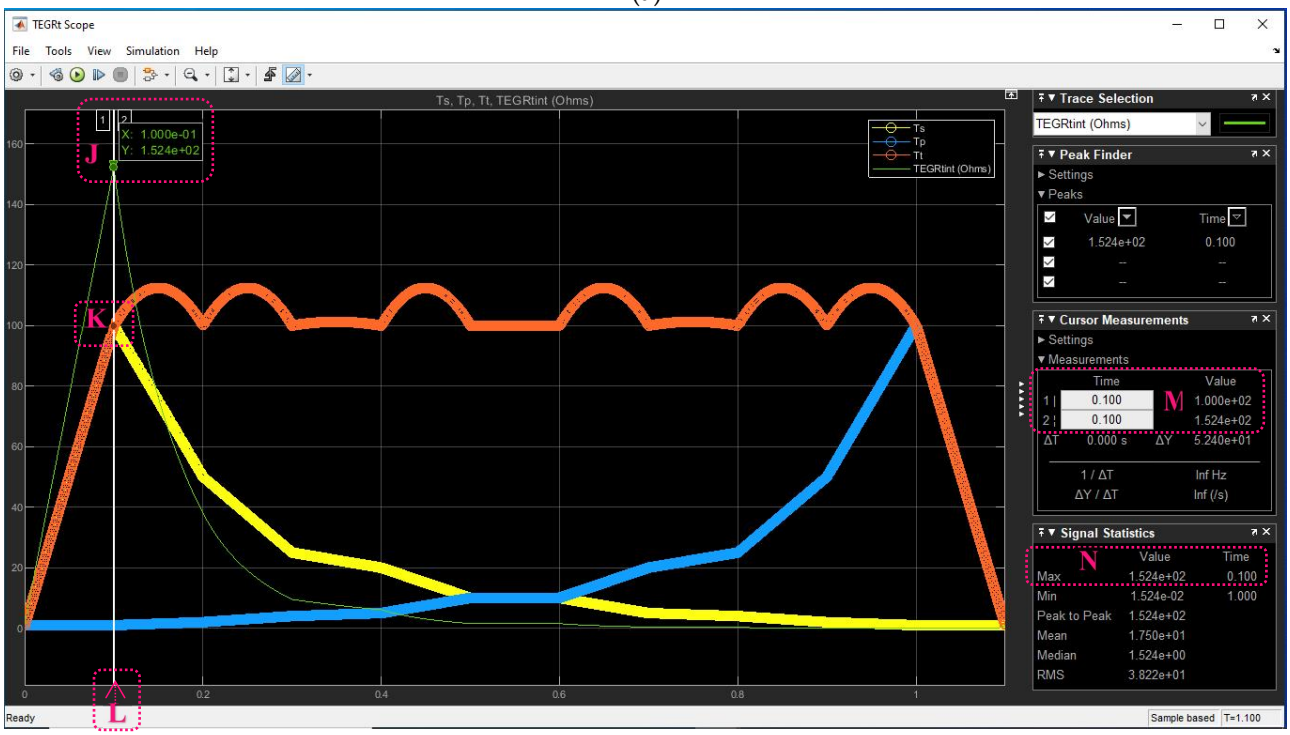

(b)

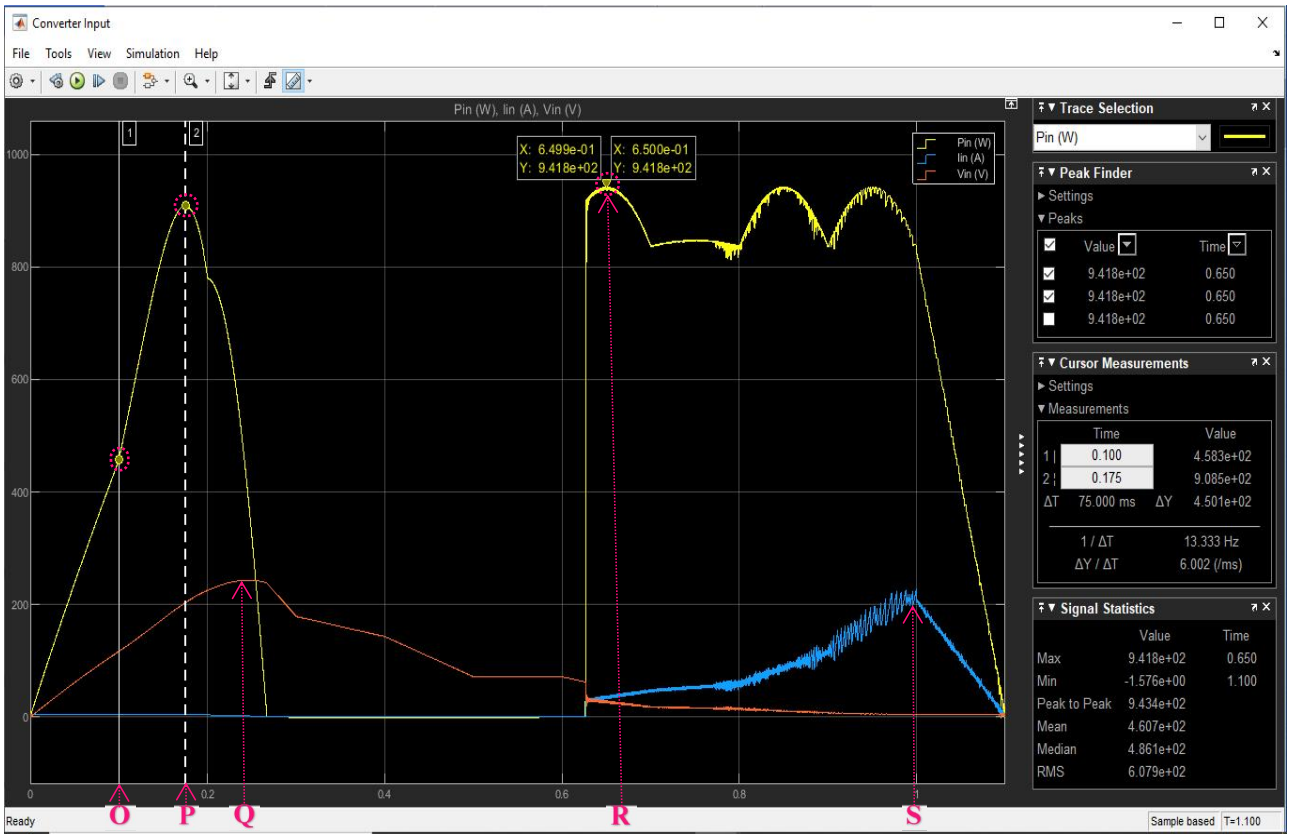

(c)

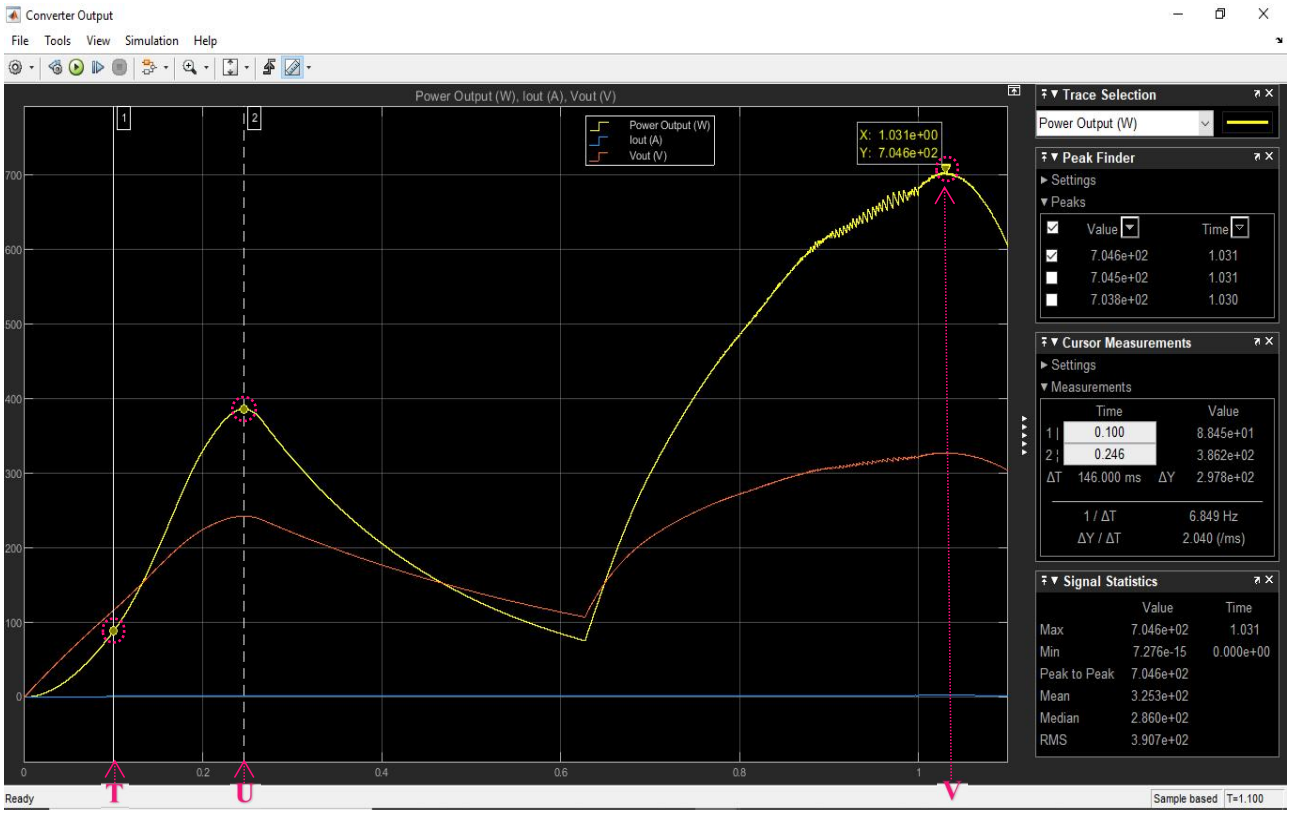

(d)

Figure 5.14: TEGs configuration 1; $R_t = R_L = 152.4\Omega$ simulation results − note the points of interest highlighted A to V: (**a**) TEGs user's interface; (**b**) T_s, T_p, T_t and R_t dynamics; **(c)** TEGs converter's input; **(d)** TEGs converter's output.

5.3.3.2 TEGs Configuration 2 (C2): $R_l = 38.1\Omega$

C2 simulation result has the following settings: $TEG\_S=T_s=50$; $TEG\_P=T_p=2$; $R_L=38.1\Omega$.

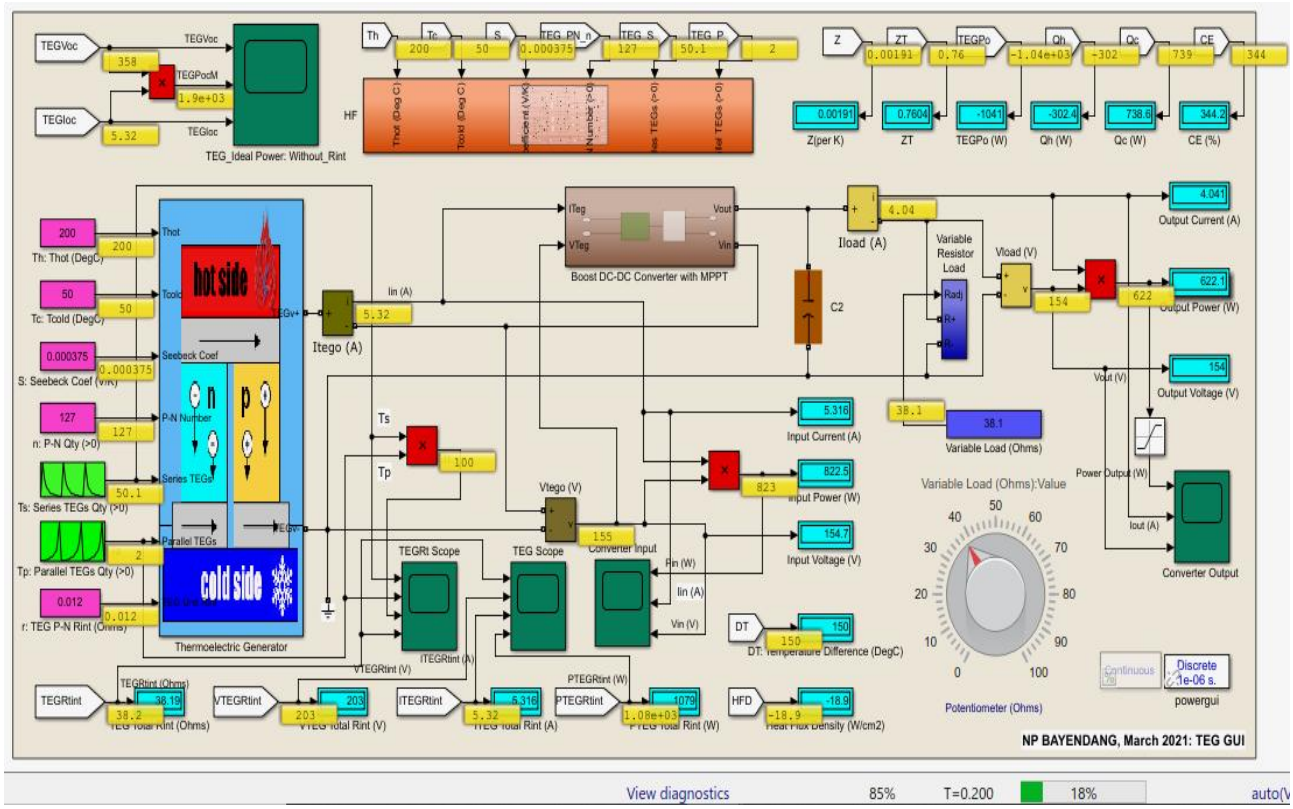

(a)

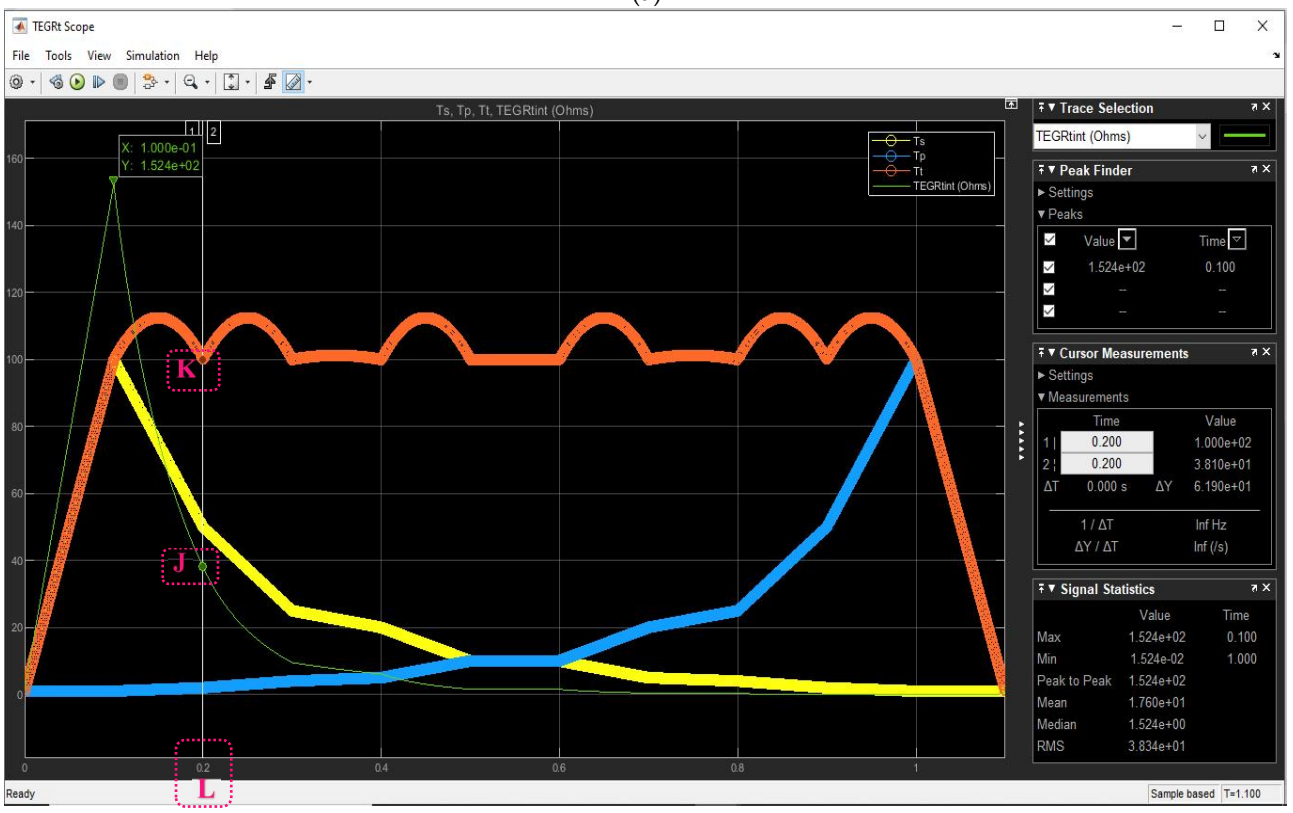

(b)

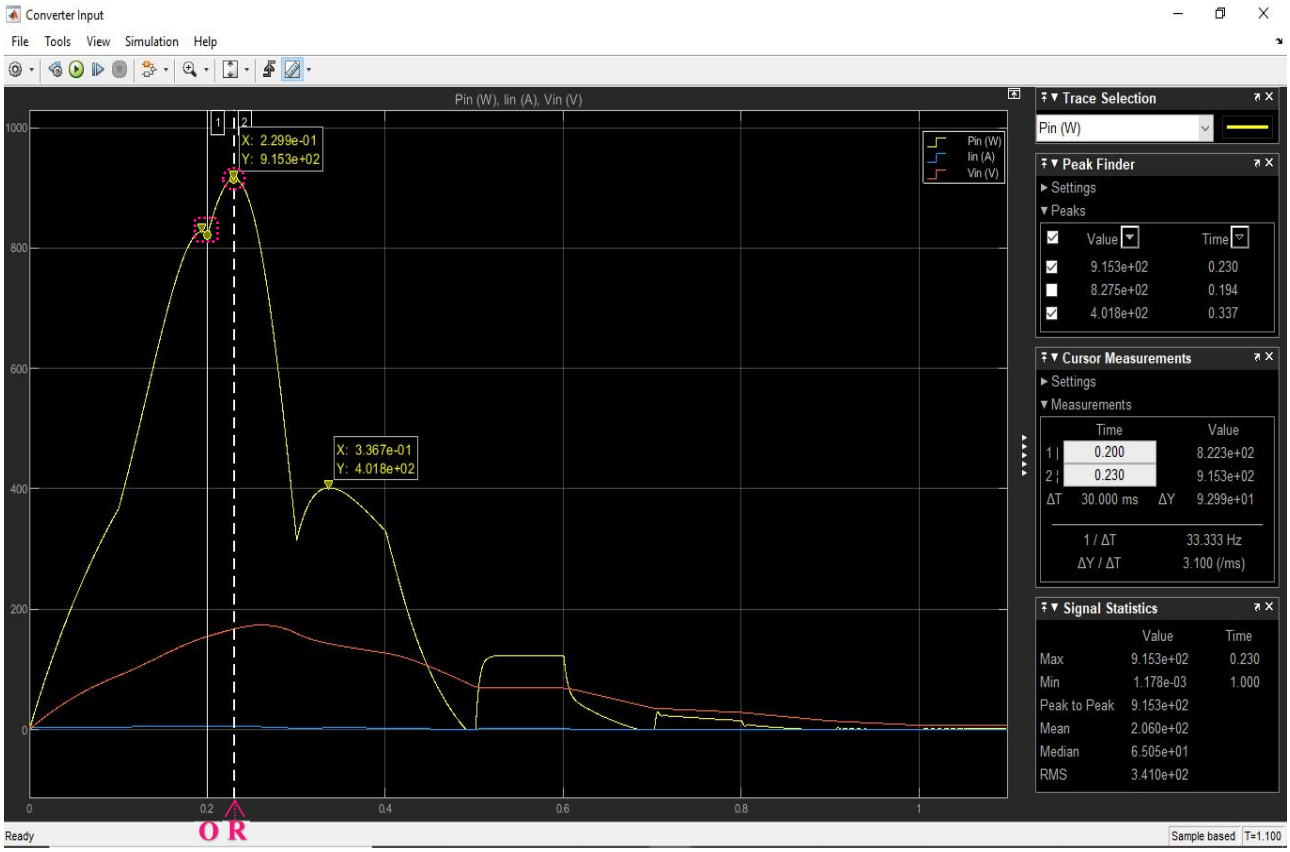

(c)

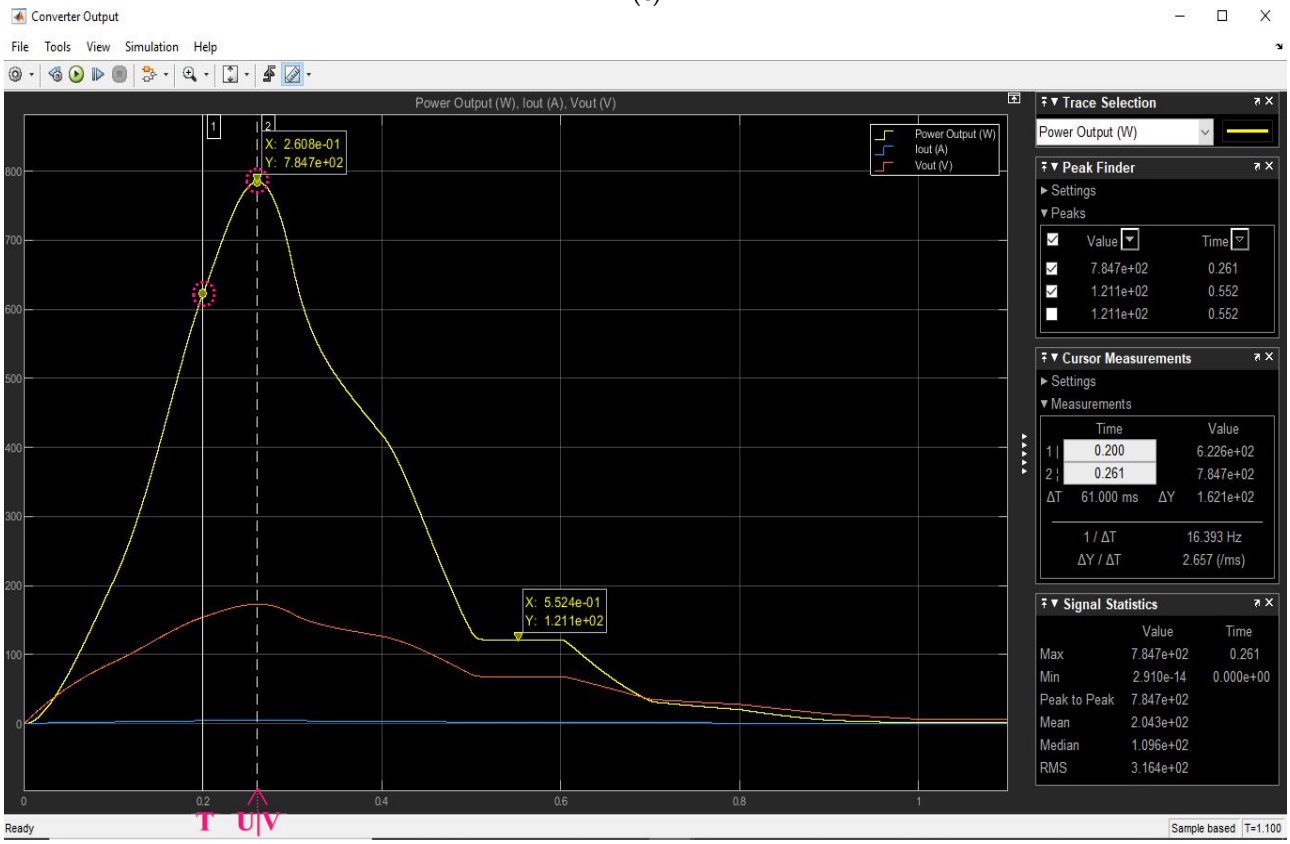

(d)

Figure 5.15: TEGs configuration 2; $R_t = R_L = 38.1\Omega$ simulation results − note the points of interest highlighted A to V: (**a**) TEGs user's interface; (**b**) T_s, T_p, T_t and R_t dynamics; **(c)** TEGs converter input; **(d)** TEGs converter output.

5.3.3.3 TEGs Configuration 3 (C3): R_l = 9.525Ω

C3 simulation result has the following settings: $TEG\_S=T_s=25$; $TEG\_P=T_p=4$; $R_L=9.525\Omega$.

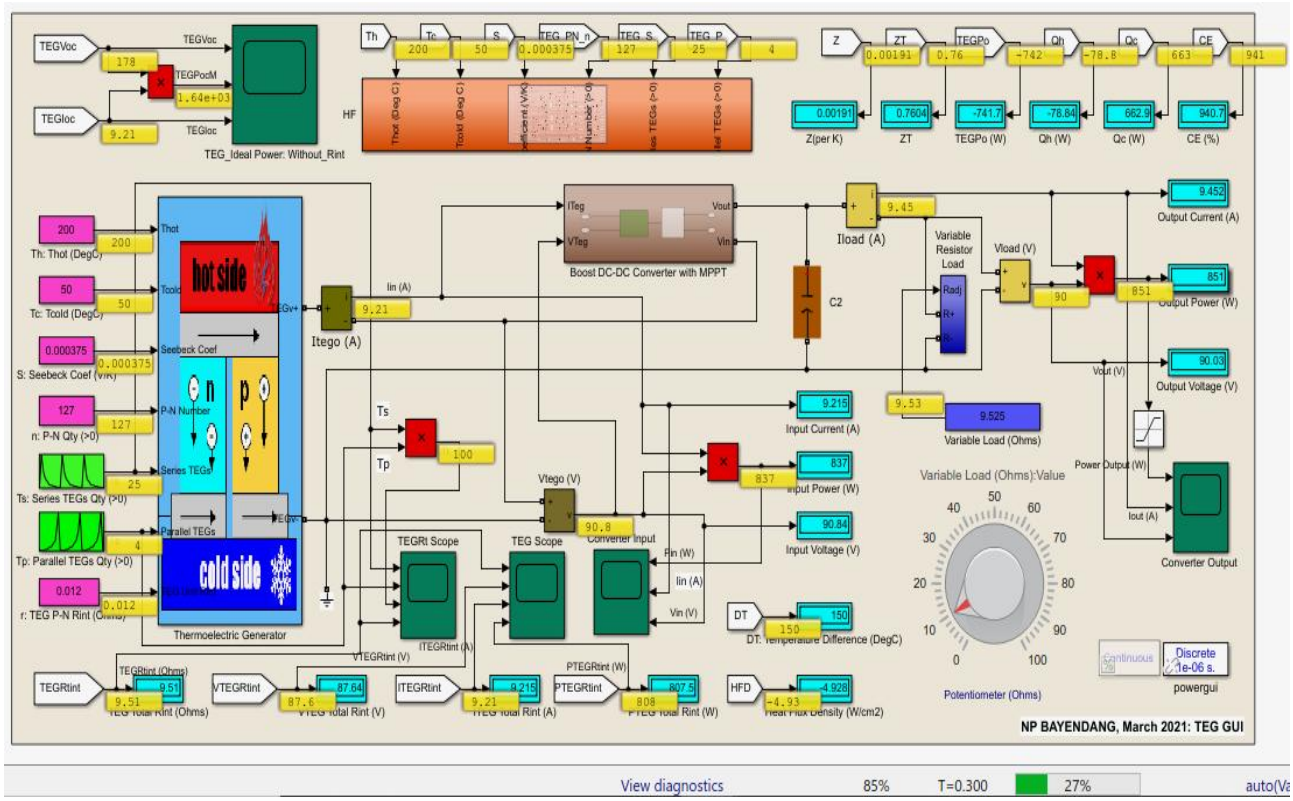

(**a**)

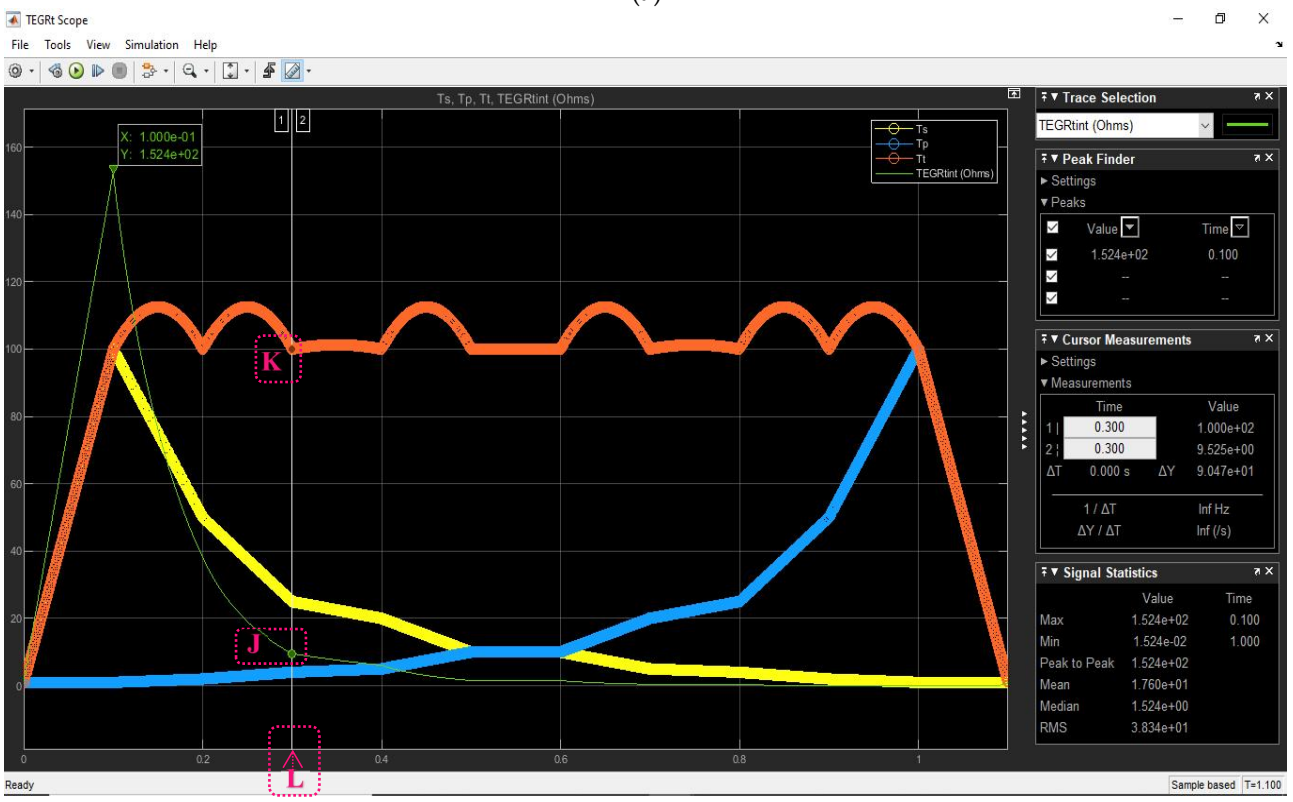

(**b**)

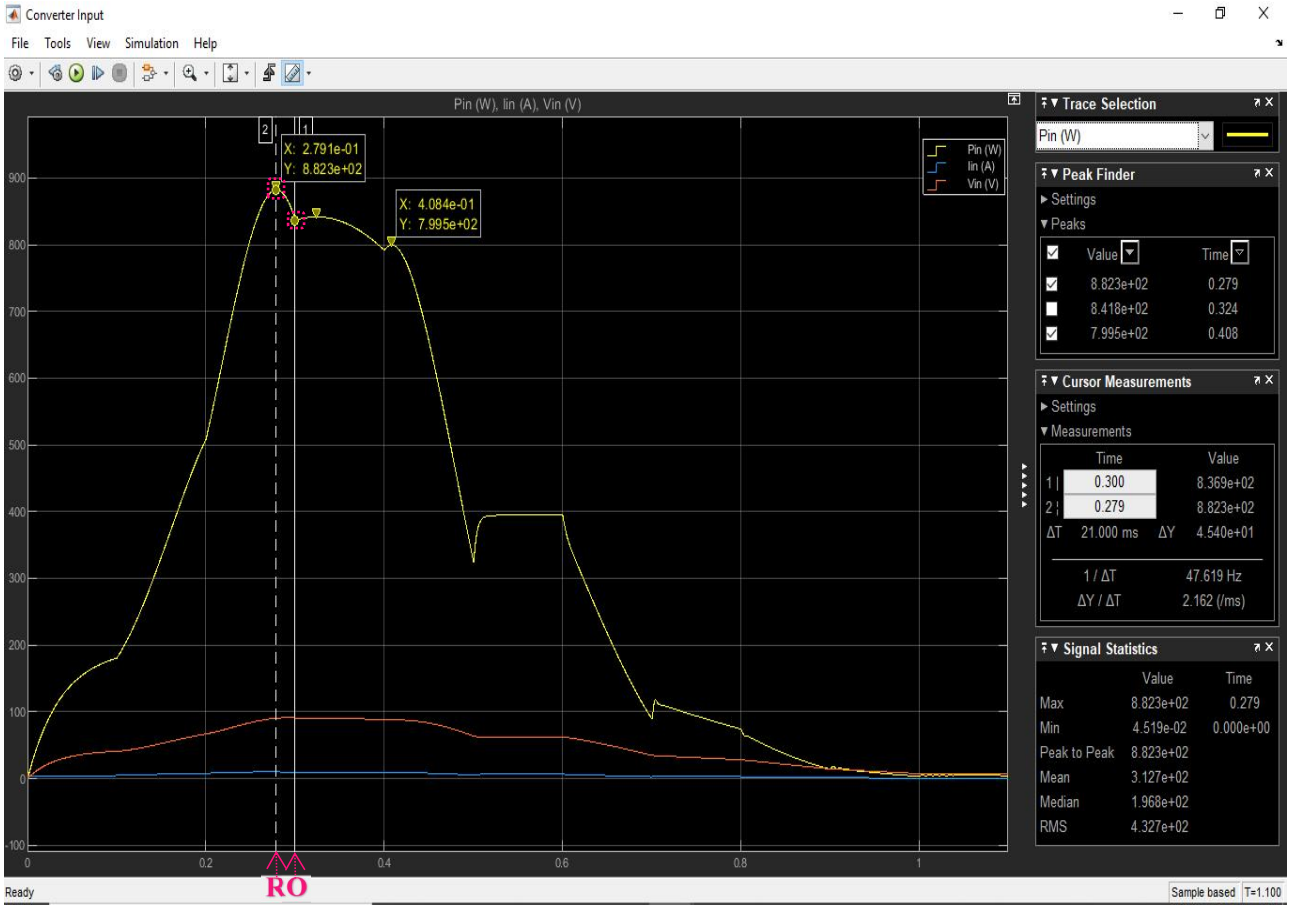

(c)

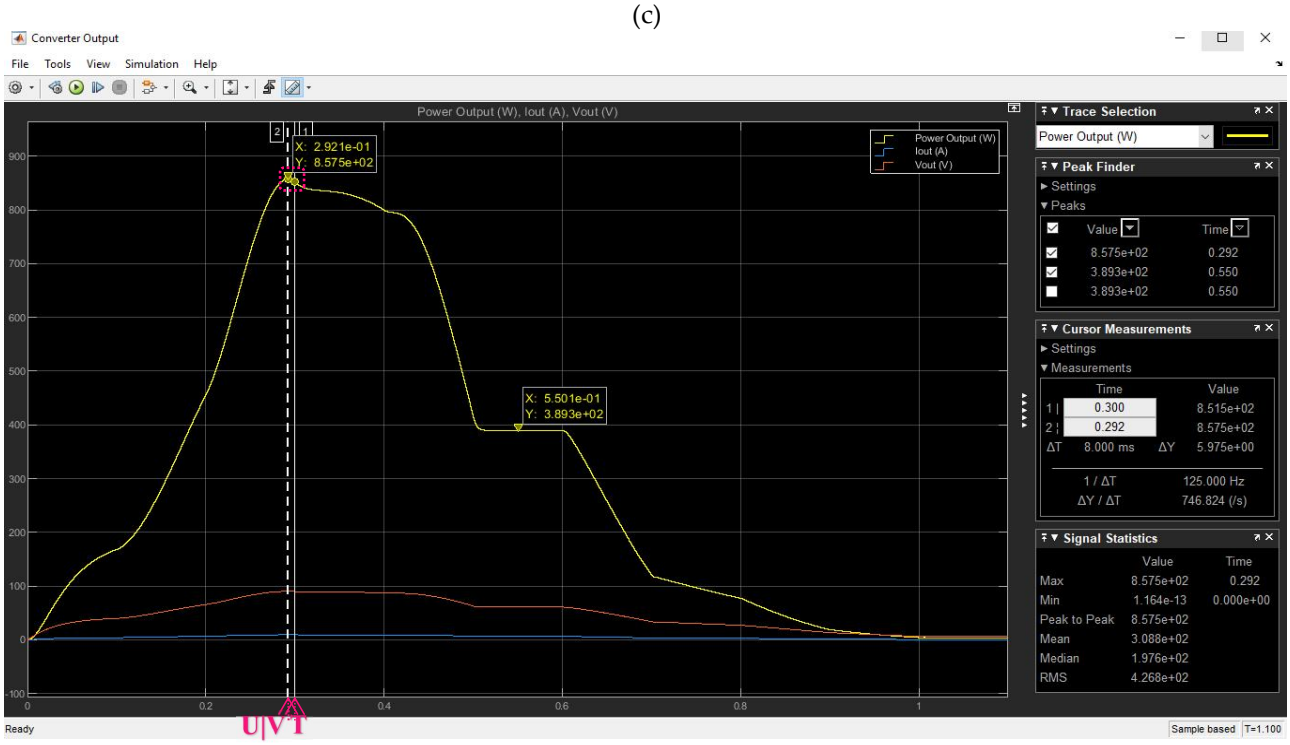

(d)

Figure 5.16: TEGs configuration 3; $R_t = R_L = 9.525\Omega$ simulation results − note the points of interest highlighted A to V: **(a)** TEGs user's interface; (**b**) T_s, T_p, T_t and R_t dynamics; **(c)** TEGs converter input; **(d)** TEGs converter output.

5.3.3.4 TEGs Configuration 4 (C4): R_l = 6.096Ω

C4 simulation result has the following settings: $TEG\_S=T_s=20$; $TEG\_P=T_p=5$; $R_L=6.096\Omega$.

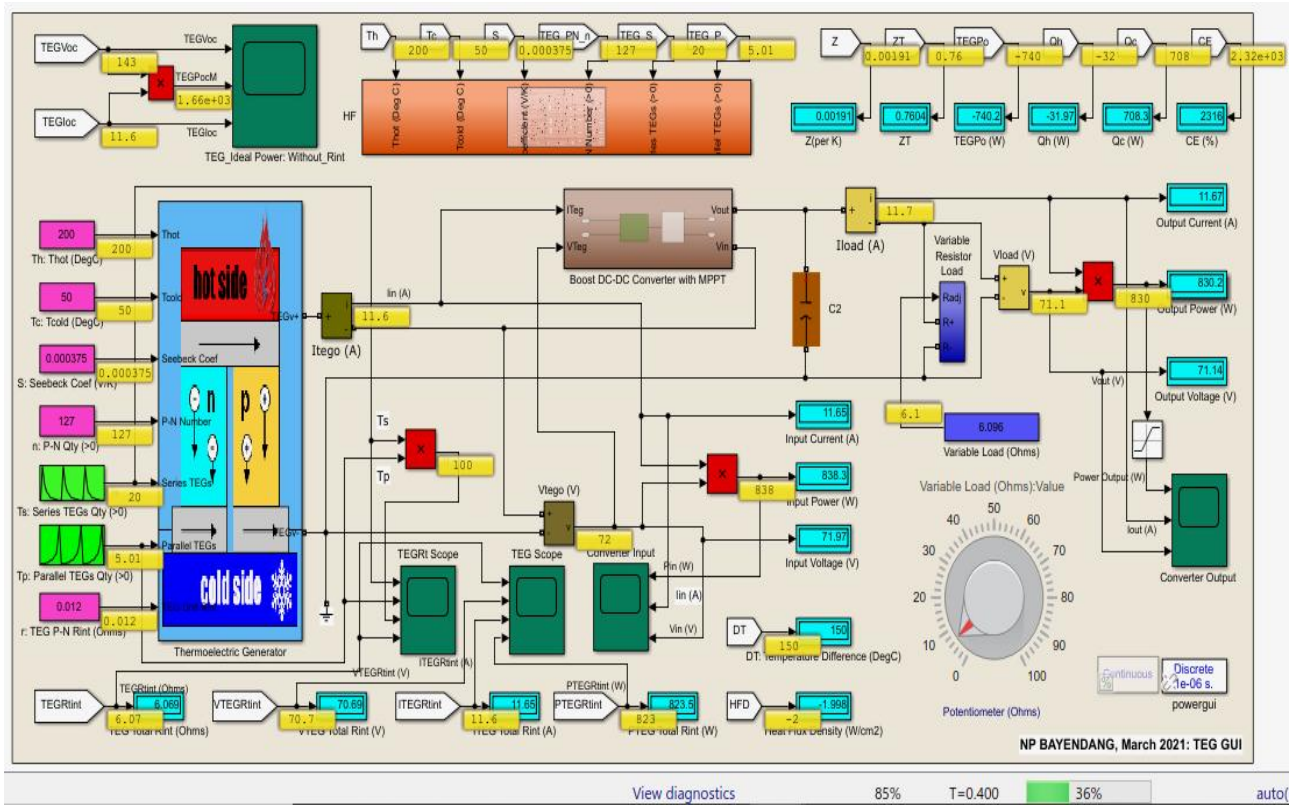

(**a**)

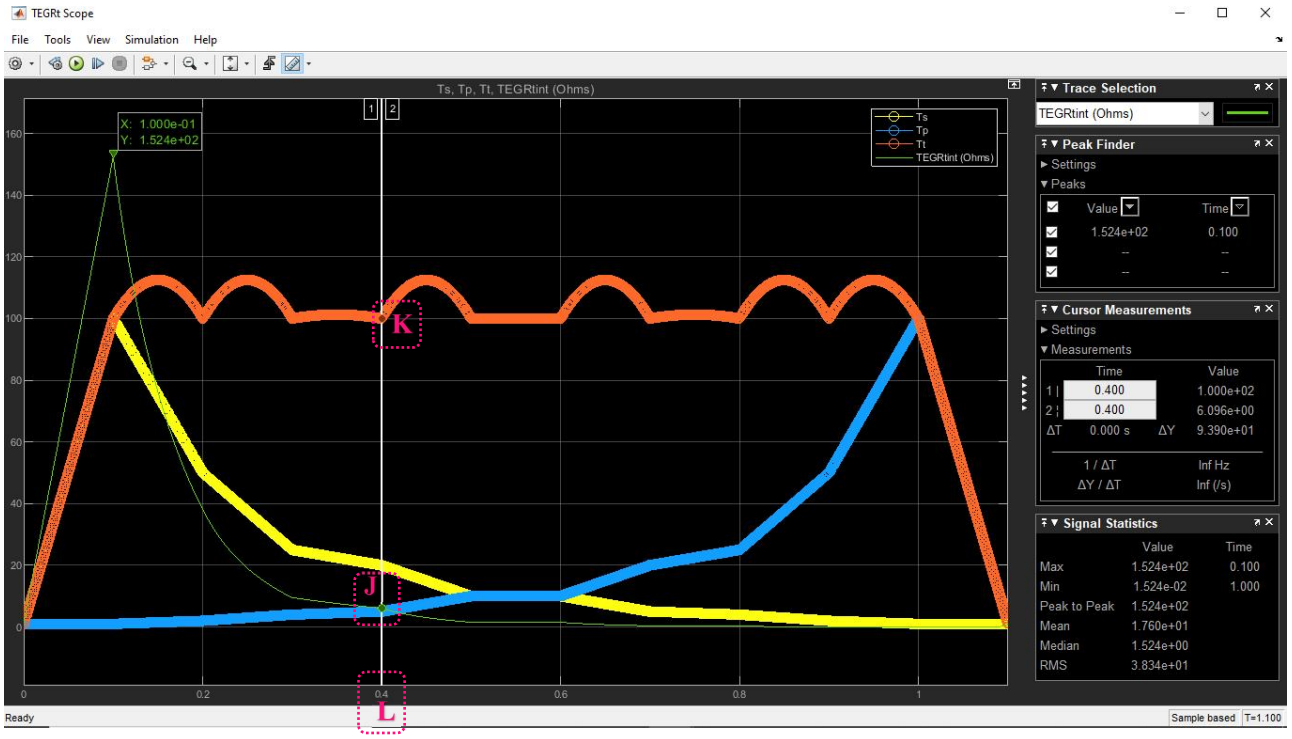

(**b**)

(c)

(d)

Figure 5.17: TEGs configuration 4; $R_t = R_L = 6.096\Omega$ simulation results − note the points of interest highlighted A to V: **(a)** TEGs user's interface; (**b**) T_s, T_p, T_t and R_t dynamics; **(c)** TEGs converter input; **(d)** TEGs converter output.

5.3.3.5 TEGs Configuration 5 (C5): R_t = 1.524Ω

C5 simulation result has the following settings: $TEG\_S=T_s=10$; $TEG\_P=T_p=10$; $R_L=1.524\Omega$.

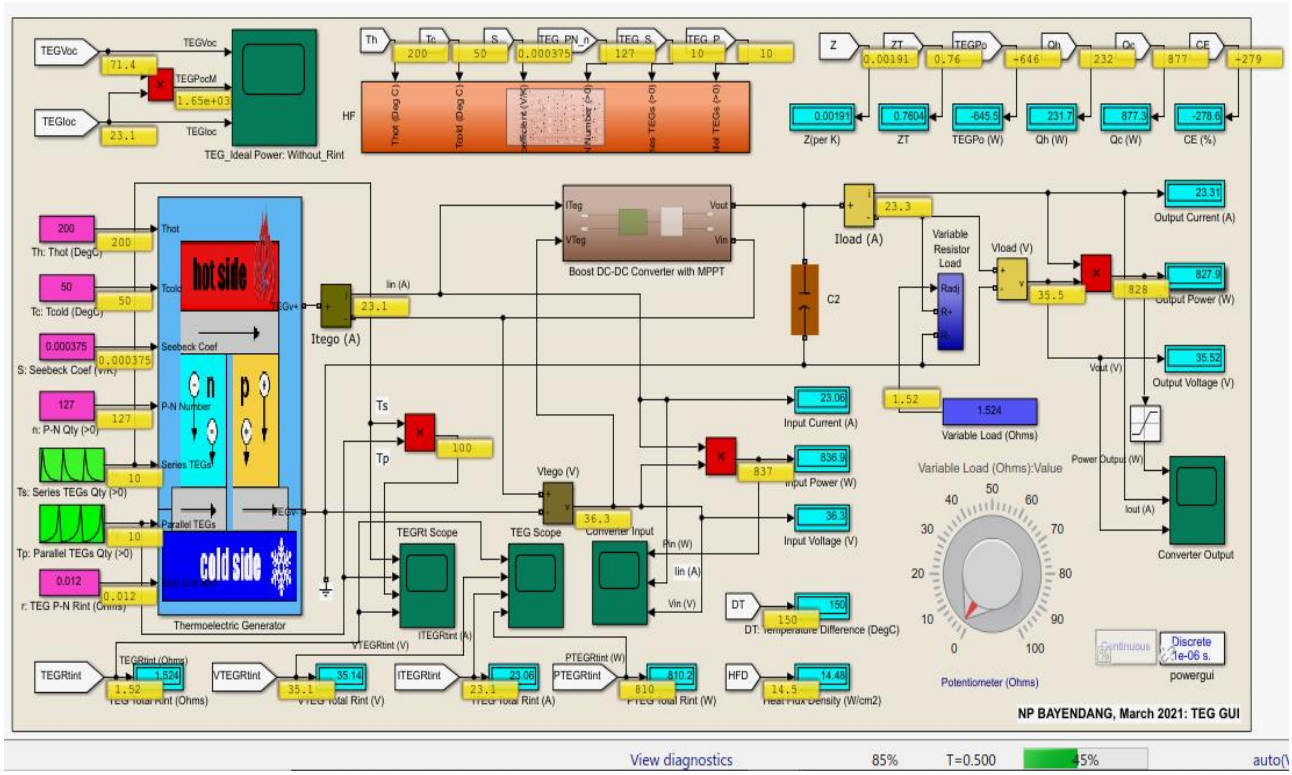

(**a**)

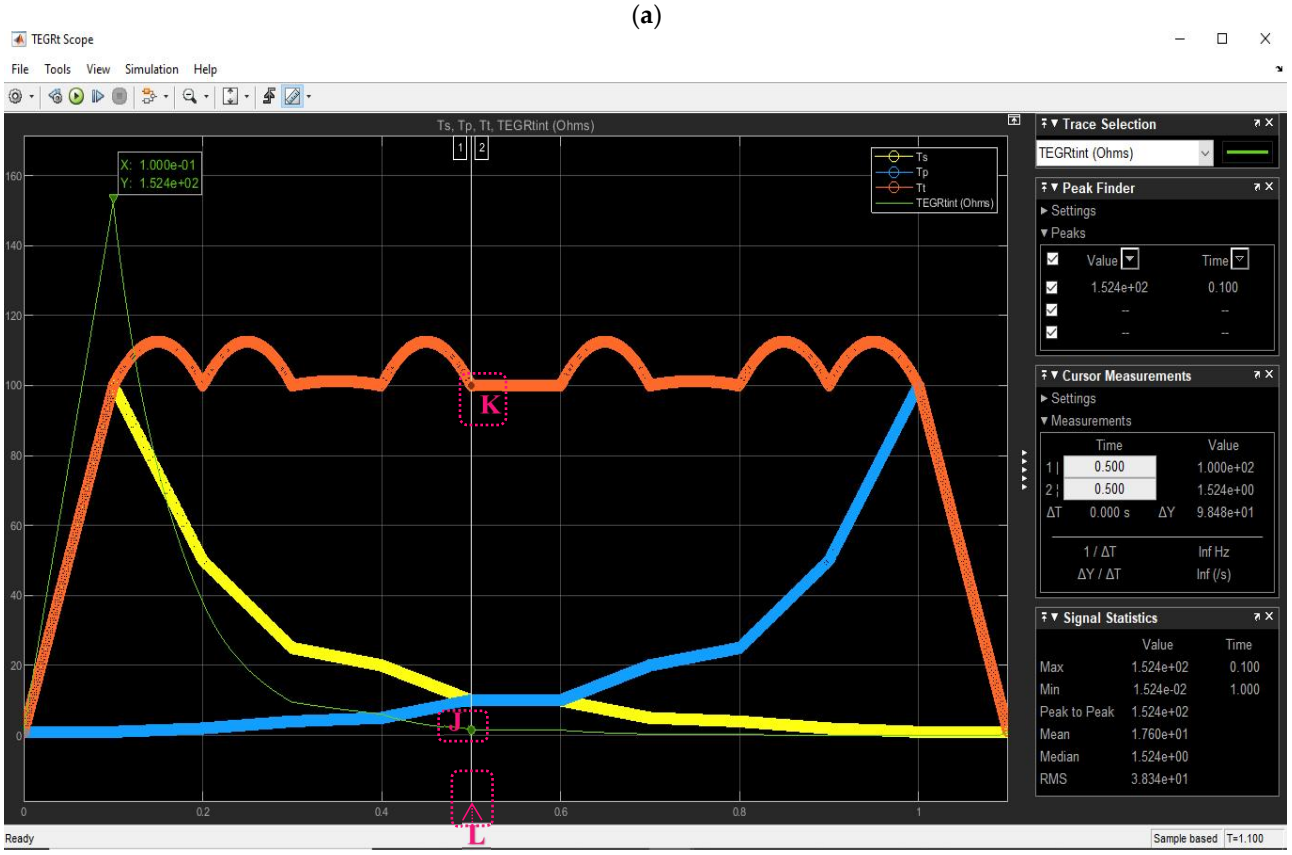

(**b**)

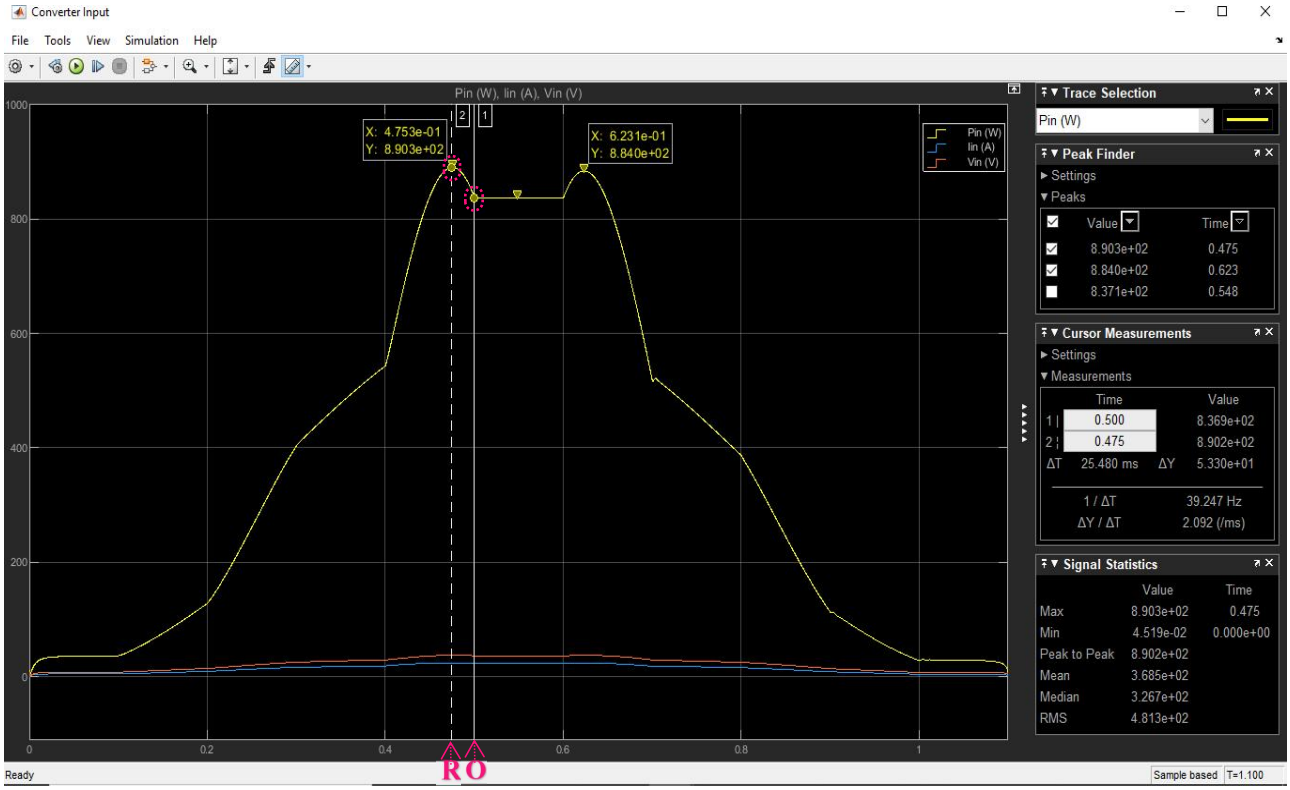

(c)

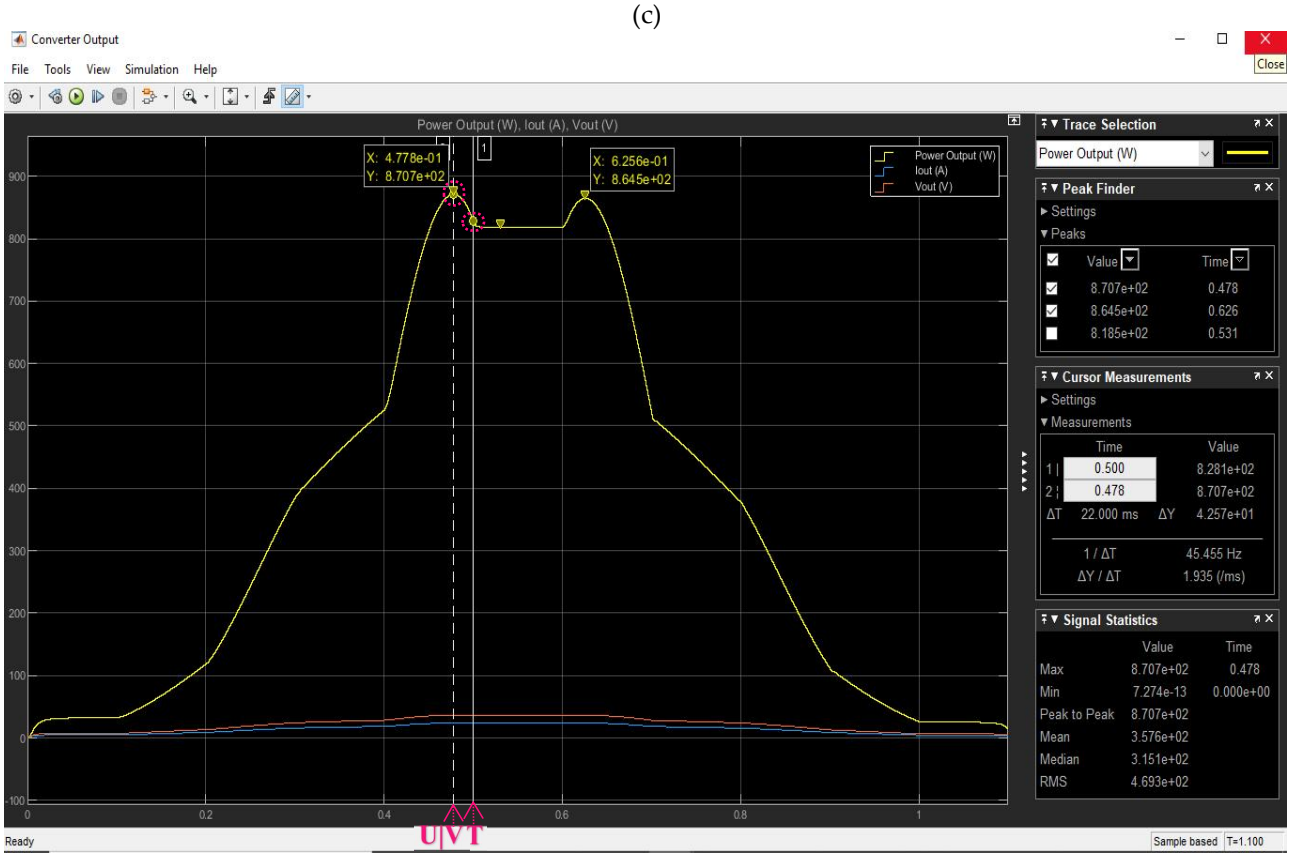

(d)

Figure 5.18: TEGs configuration 5; $R_t = R_L = 1.524\Omega$ simulation results − note the points of interest highlighted A to V: **(a)** TEGs user's interface; **(b)** T_s, T_p, T_t and R_t dynamics; **(c)** TEGs converter input; **(d)** TEGs converter output.

5.3.3.6 TEGs Configuration 6 (C6): R_t = 1.524Ω

C6 simulation result has the following settings: $TEG\_S=T_s=10$; $TEG\_P=T_p=10$; $R_L=1.524\Omega$.

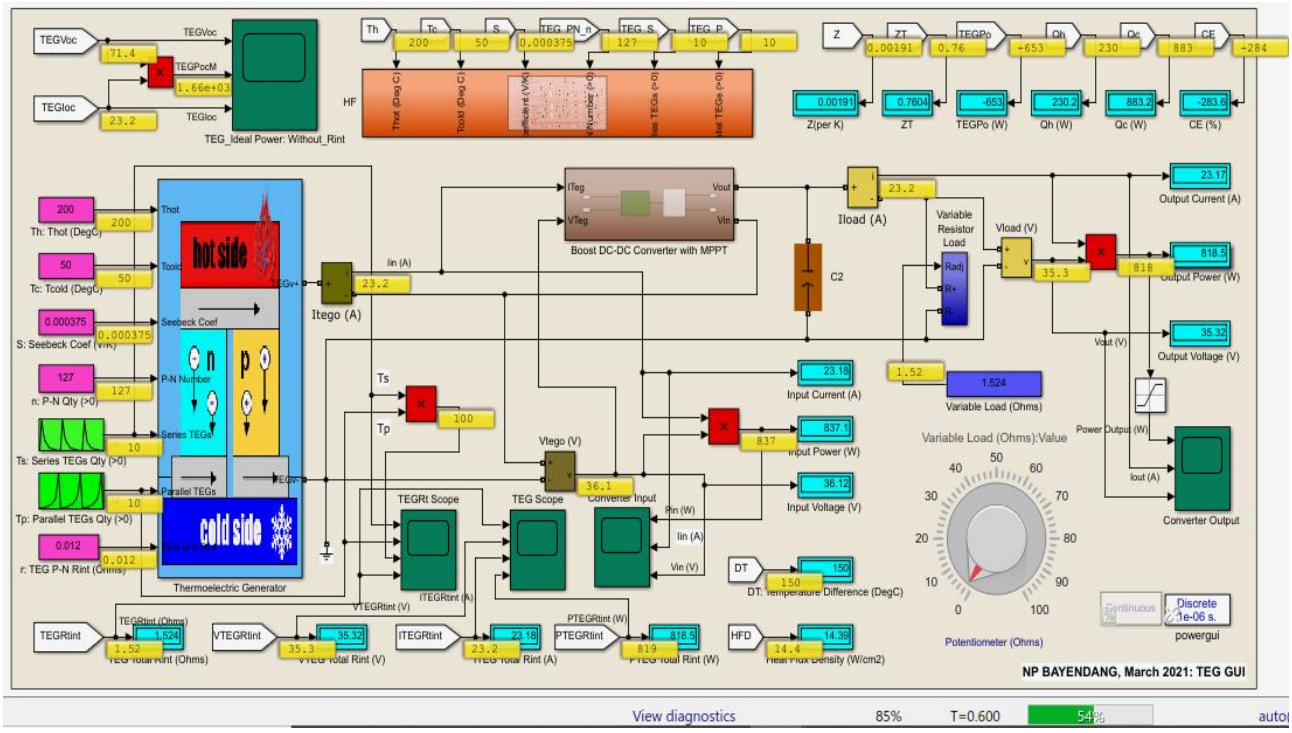

(**a**)

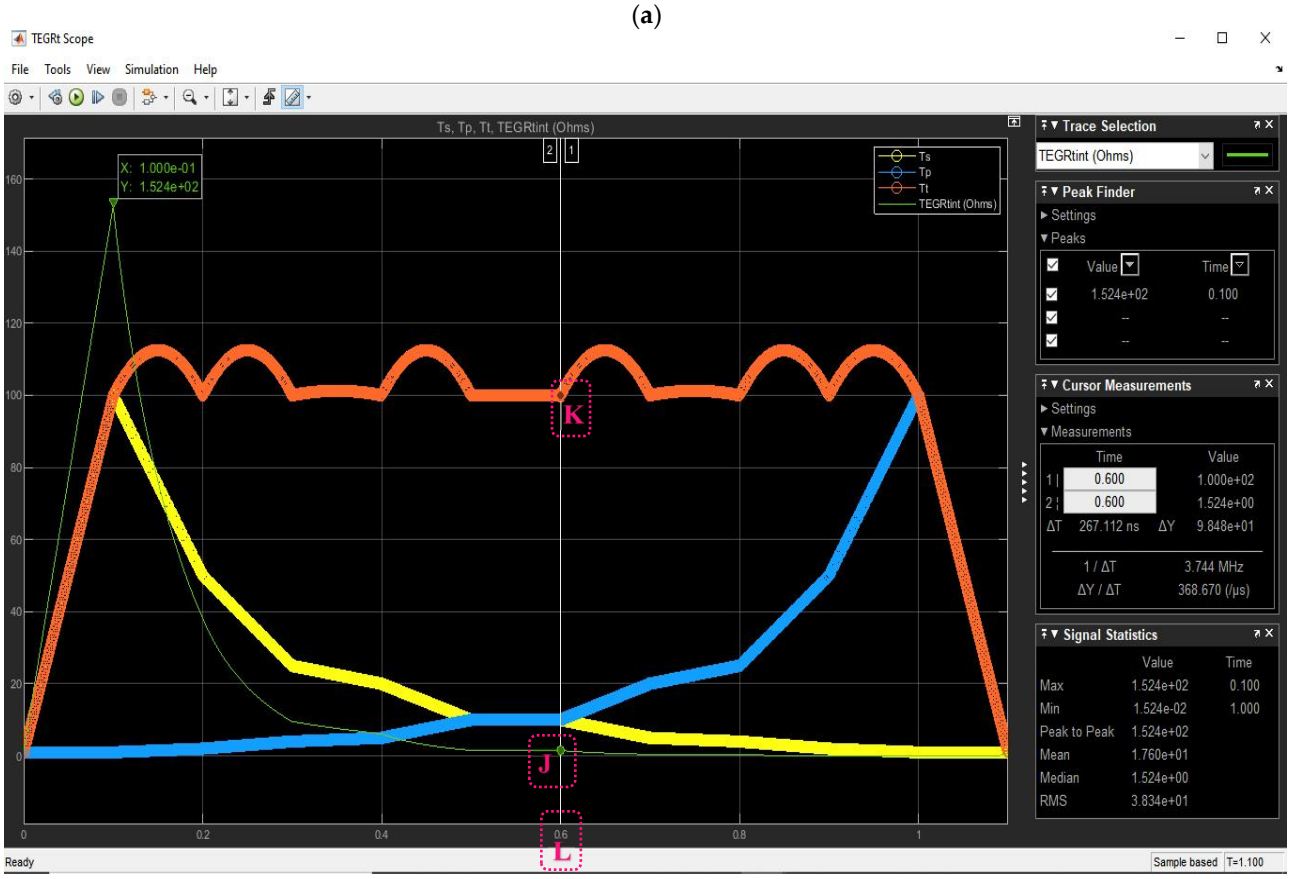

(**b**)

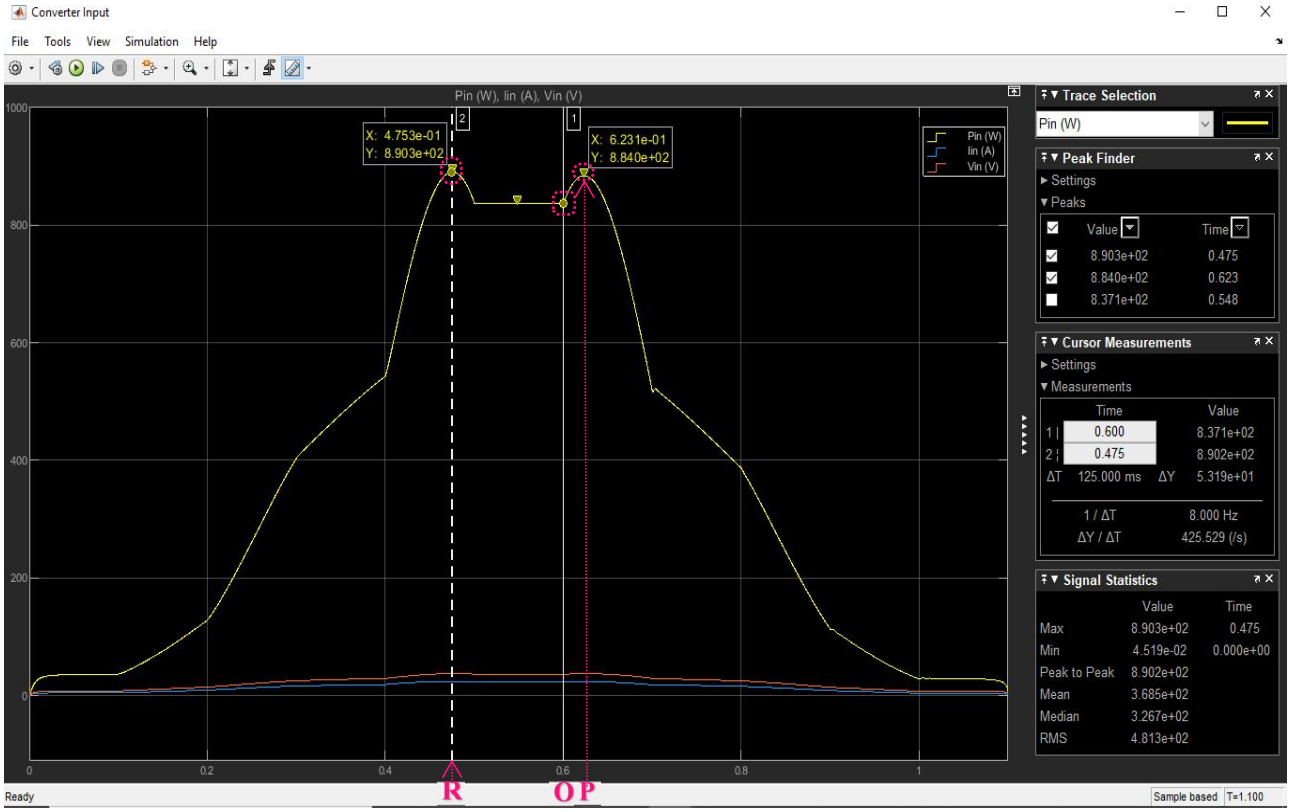

(c)

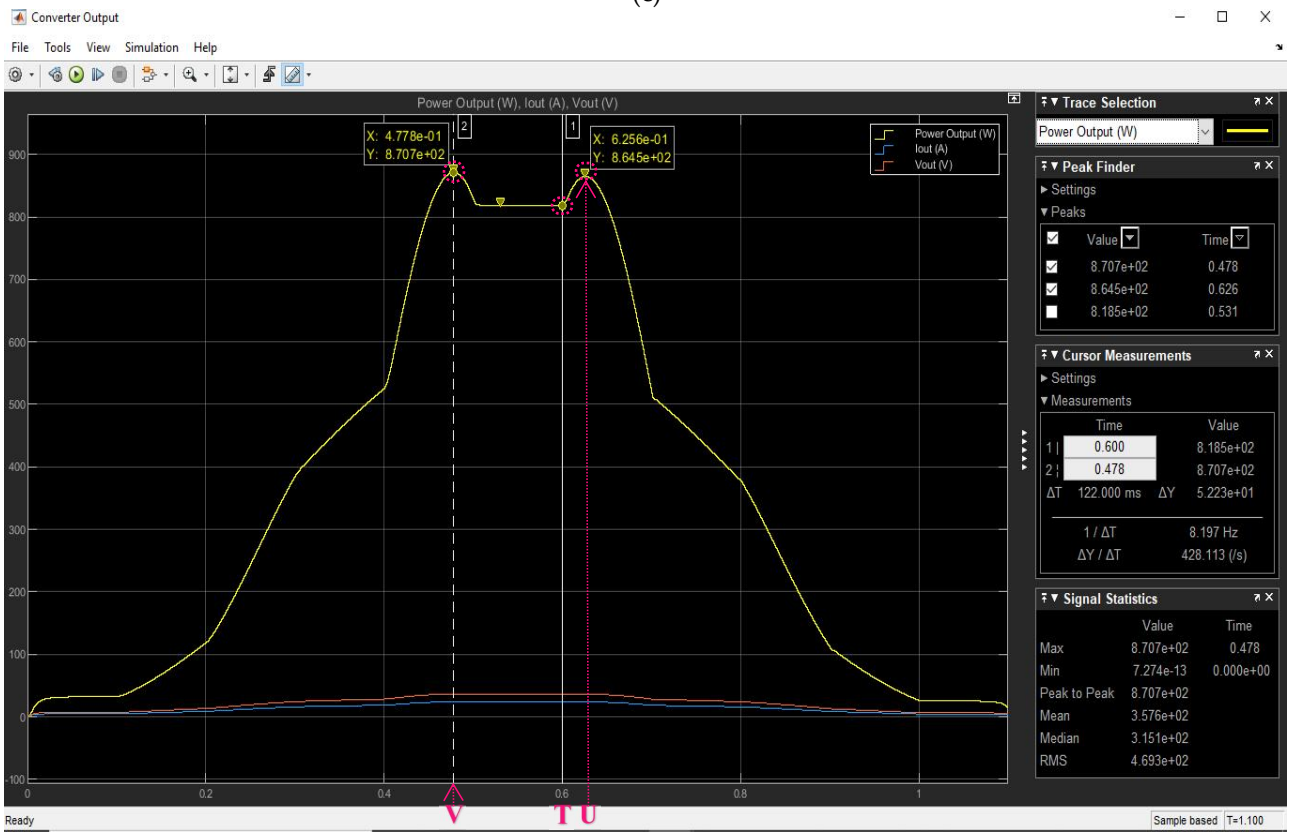

(d)

Figure 5.19: TEGs configuration 6; $R_t = R_L = 1.524\Omega$ simulation results − note the points of interest highlighted A to V: **(a)** TEGs user's interface; (**b**) T_s, T_p, T_t and R_t dynamics; **(c)** TEGs converter input; **(d)** TEGs converter output.

5.3.3.7 TEGs Configuration 7 (C7): R_t = 0.381Ω

C7 simulation result has the following settings: $TEG\_S=T_s=5$; $TEG\_P=T_p=20$; $R_L=0.381\Omega$.

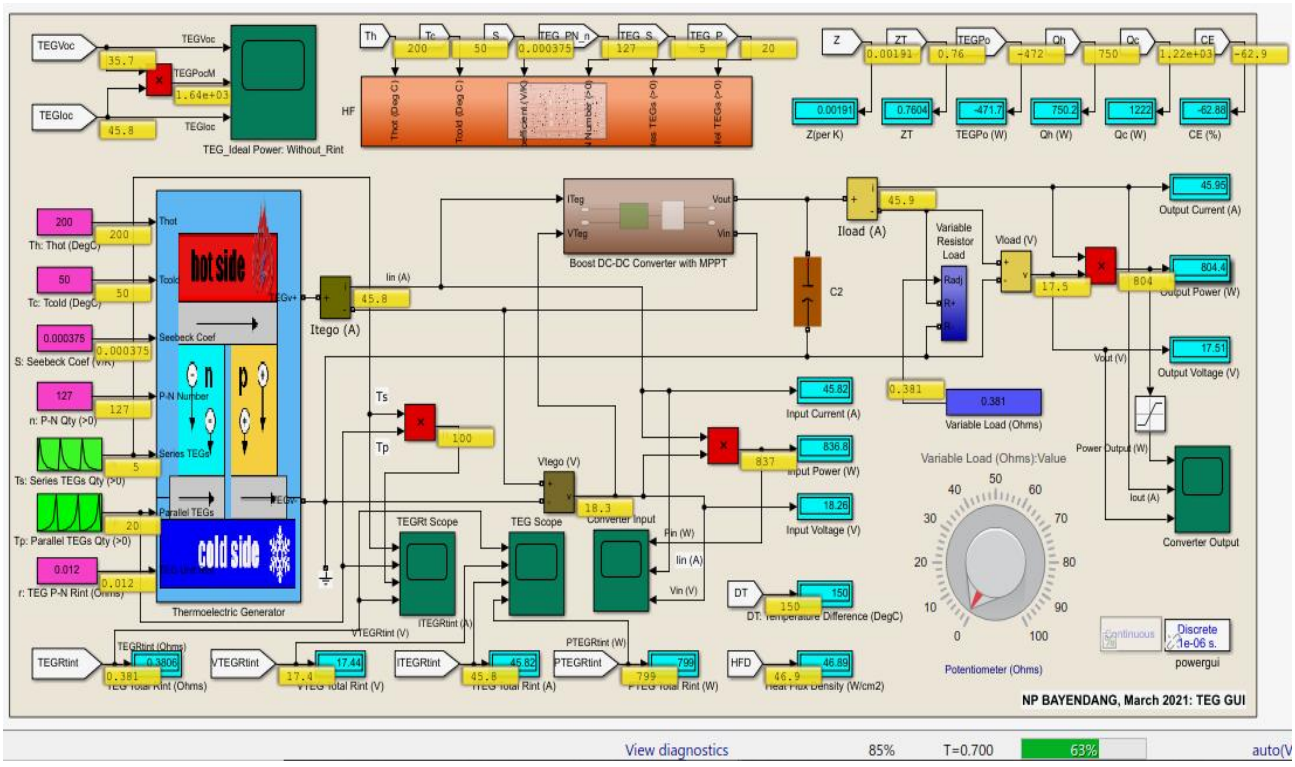

(**a**)

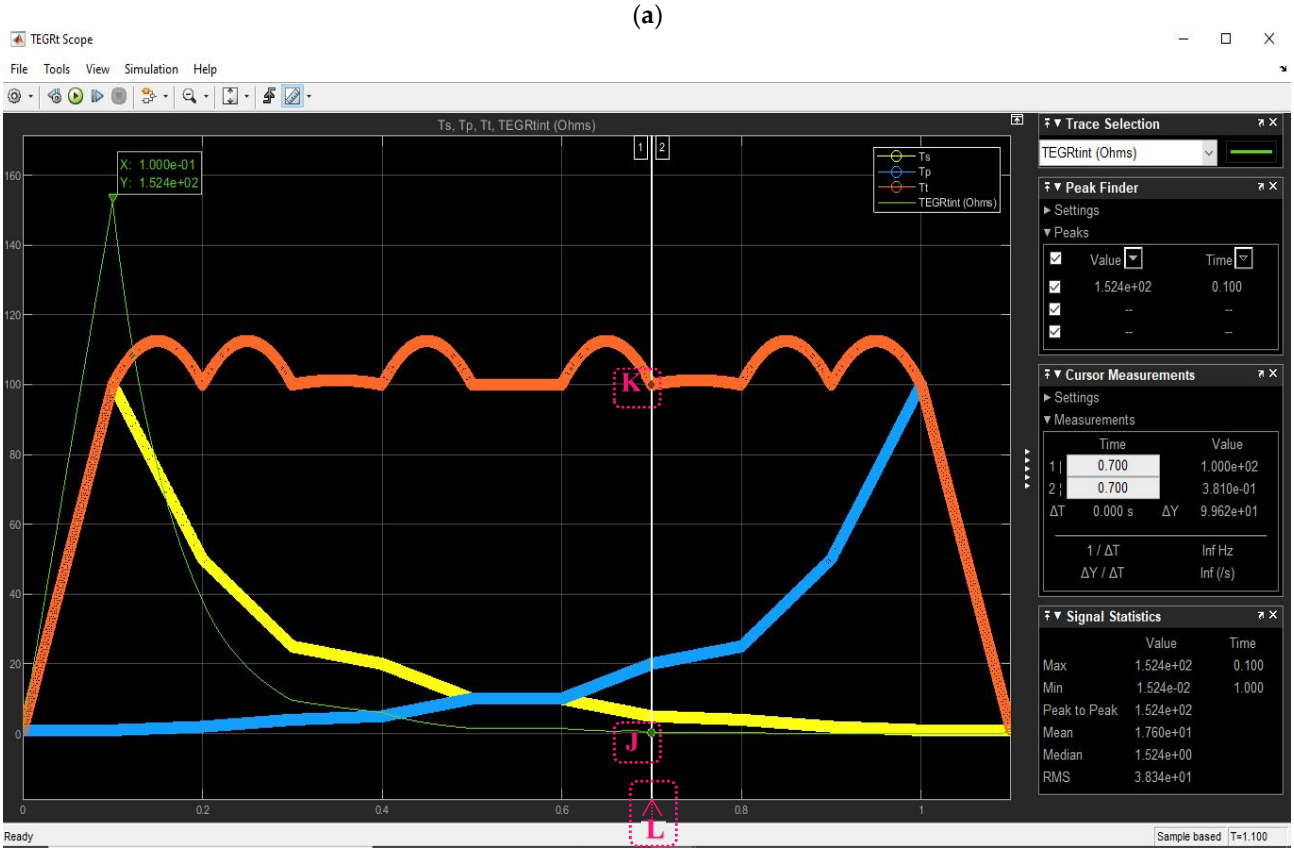

(**b**)

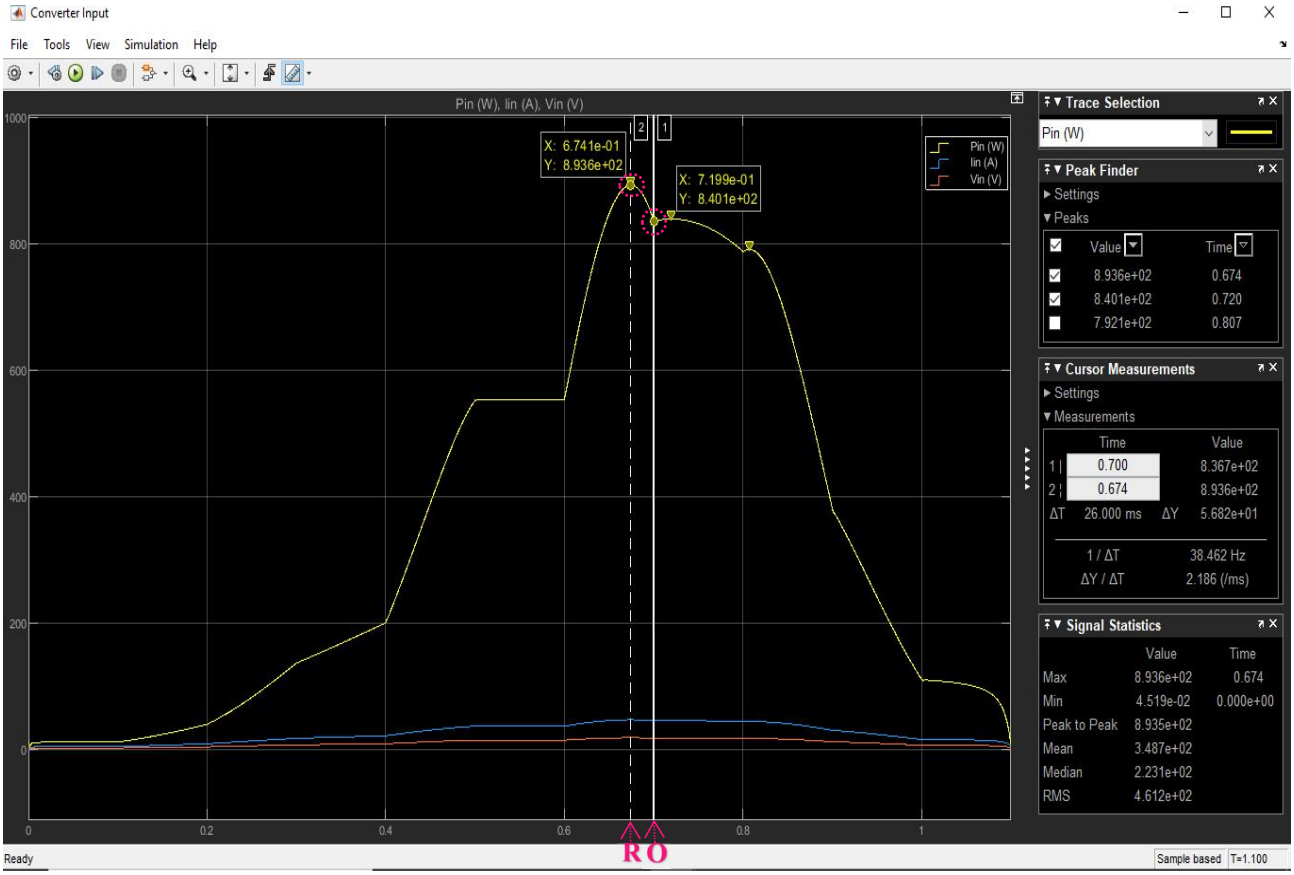

(c)

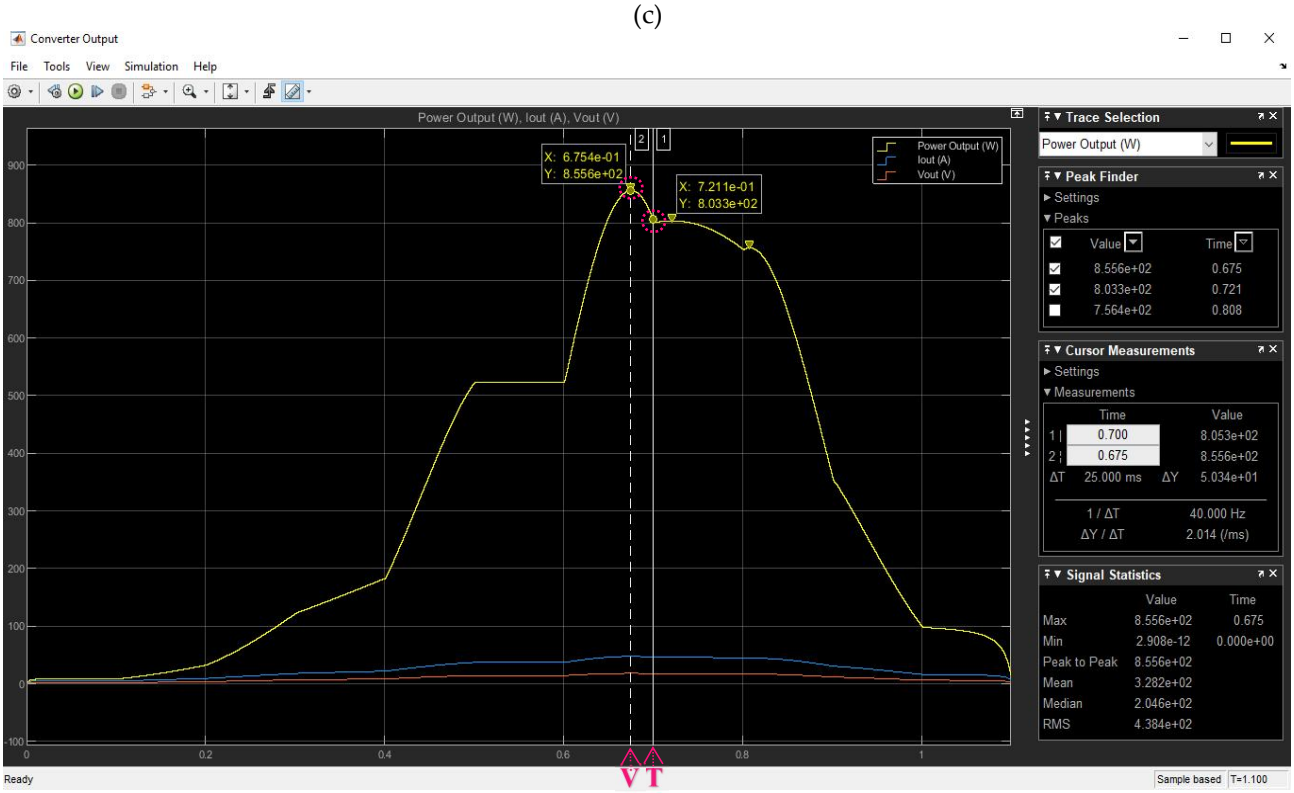

(d)

Figure 5.20: TEGs configuration 7; $R_t = R_L = 0.381\Omega$ simulation results − note the points of interest highlighted A to V: **(a)** TEGs user's interface; **(b)** T_s, T_p, T_t and R_t dynamics; **(c)** TEGs converter input; **(d)** TEGs converter output.

5.3.3.8 TEGs Configuration 8 (C8): R_t = 0.24384Ω

C8 simulation result has the following settings: $TEG\_S=T_s=4$; $TEG\_P=T_p=25$; R_L=0.24384Ω.

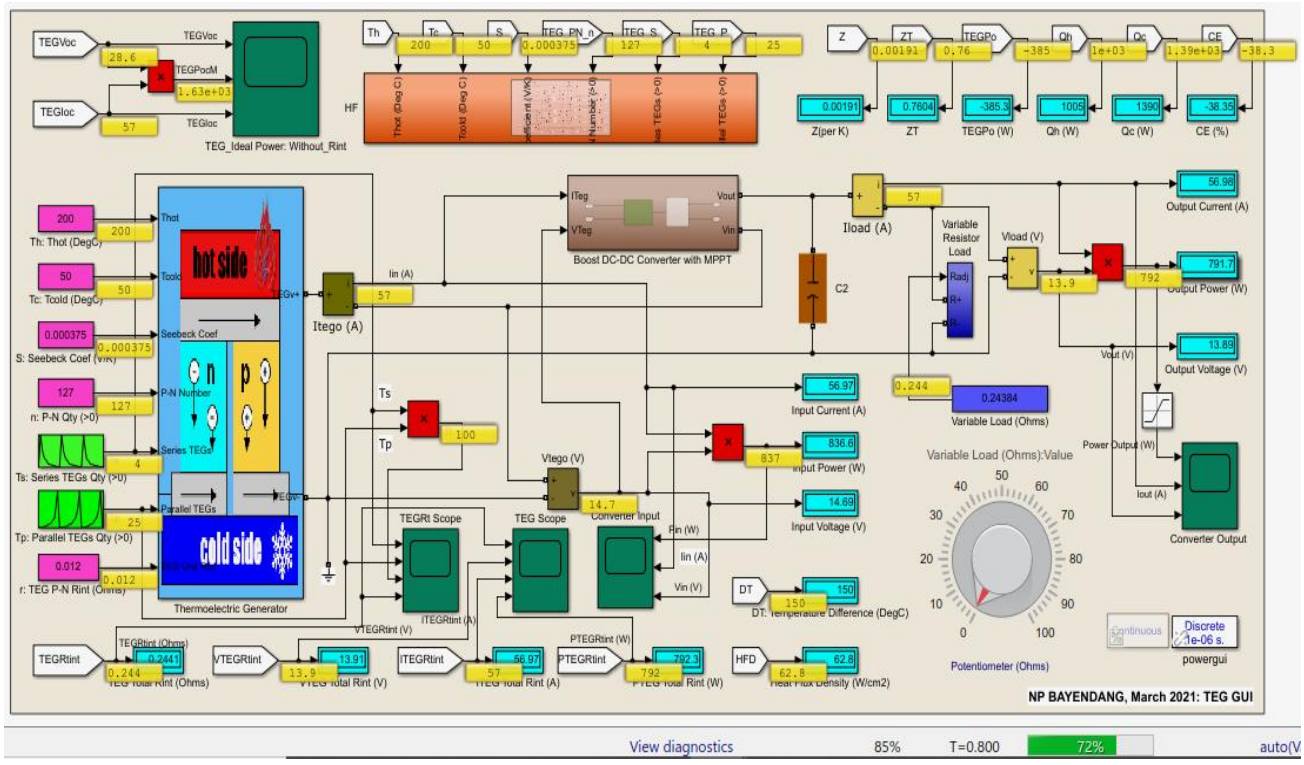

(**a**)

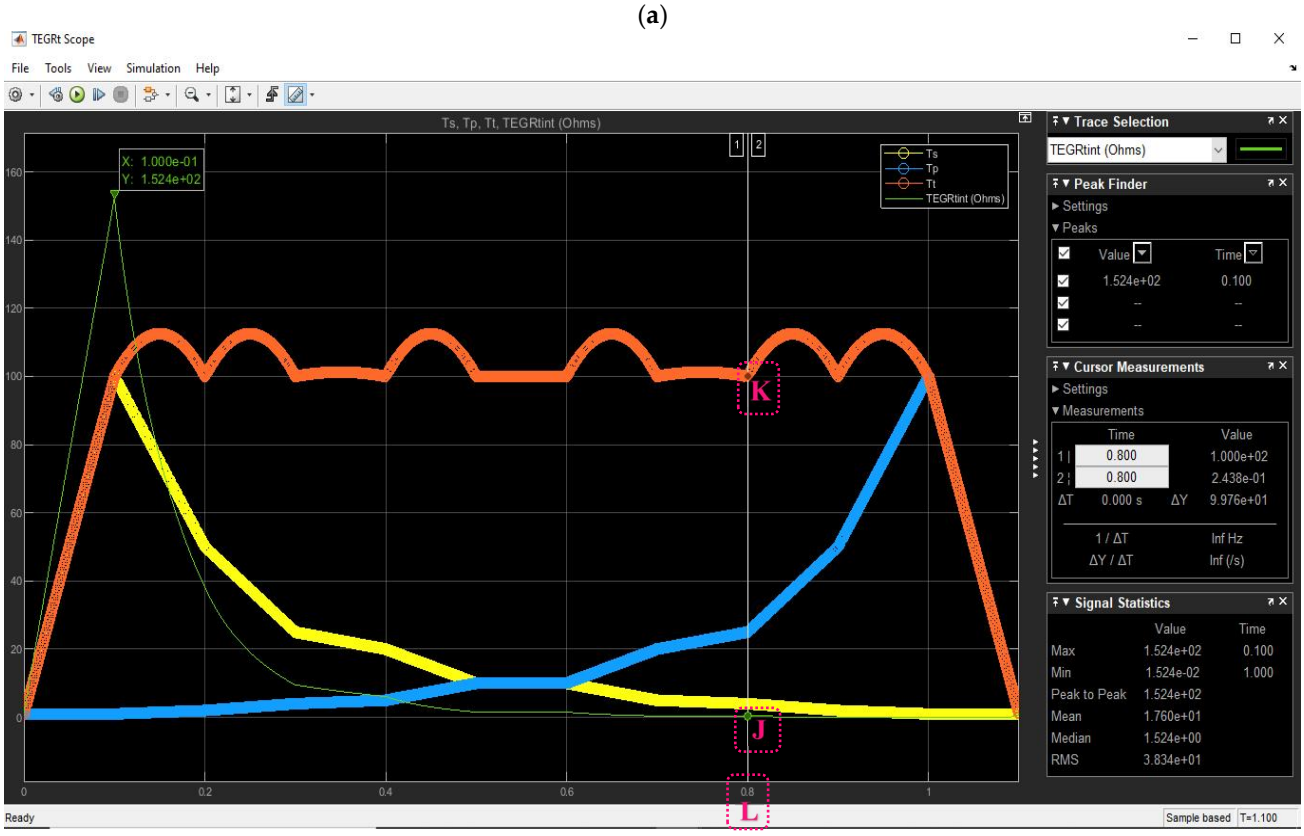

(**b**)

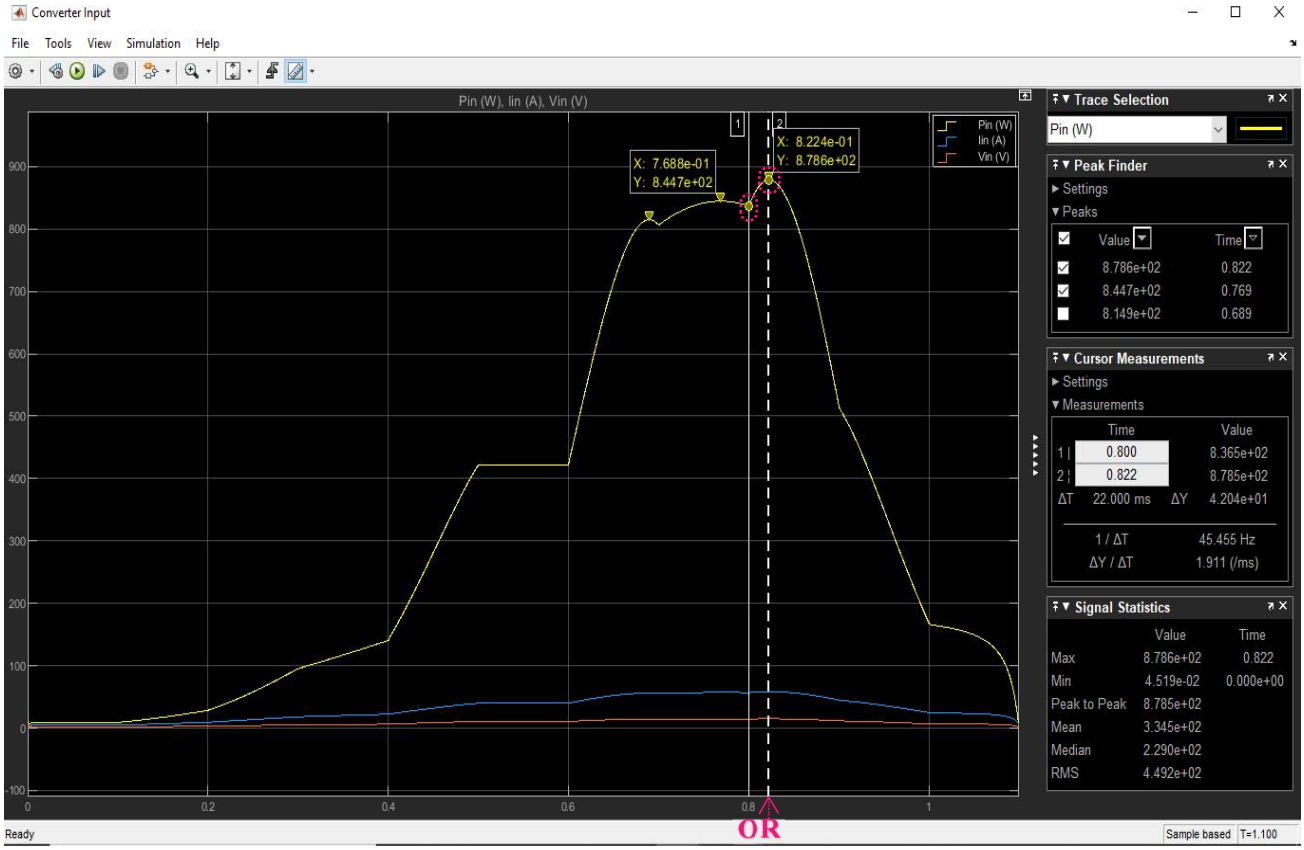

(c)

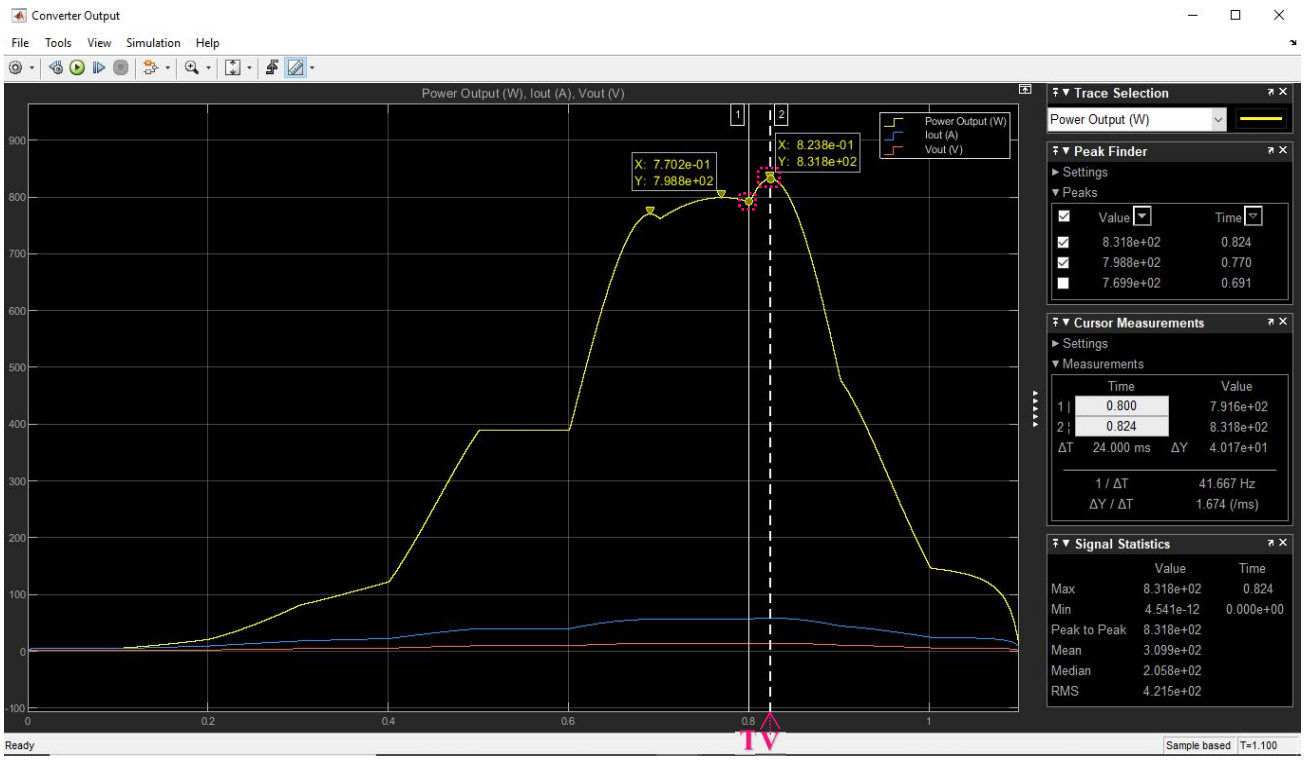

(d)

Figure 5.21: TEGs configuration 8; $R_t = R_L = 0.24384\Omega$ simulation results − note the points of interest highlighted A to V: **(a)** TEGs user's interface; (**b**) T_s, T_p, T_t and R_t dynamics; **(c)** TEGs converter input; **(d)** TEGs converter output.

5.3.3.9 TEGs Configuration 9 (C9): R_t = 0.06096Ω

C9 simulation result has the following settings: $TEG\_S=T_s=2$; $TEG\_P=T_p=50$; $R_L=0.06096\Omega$.

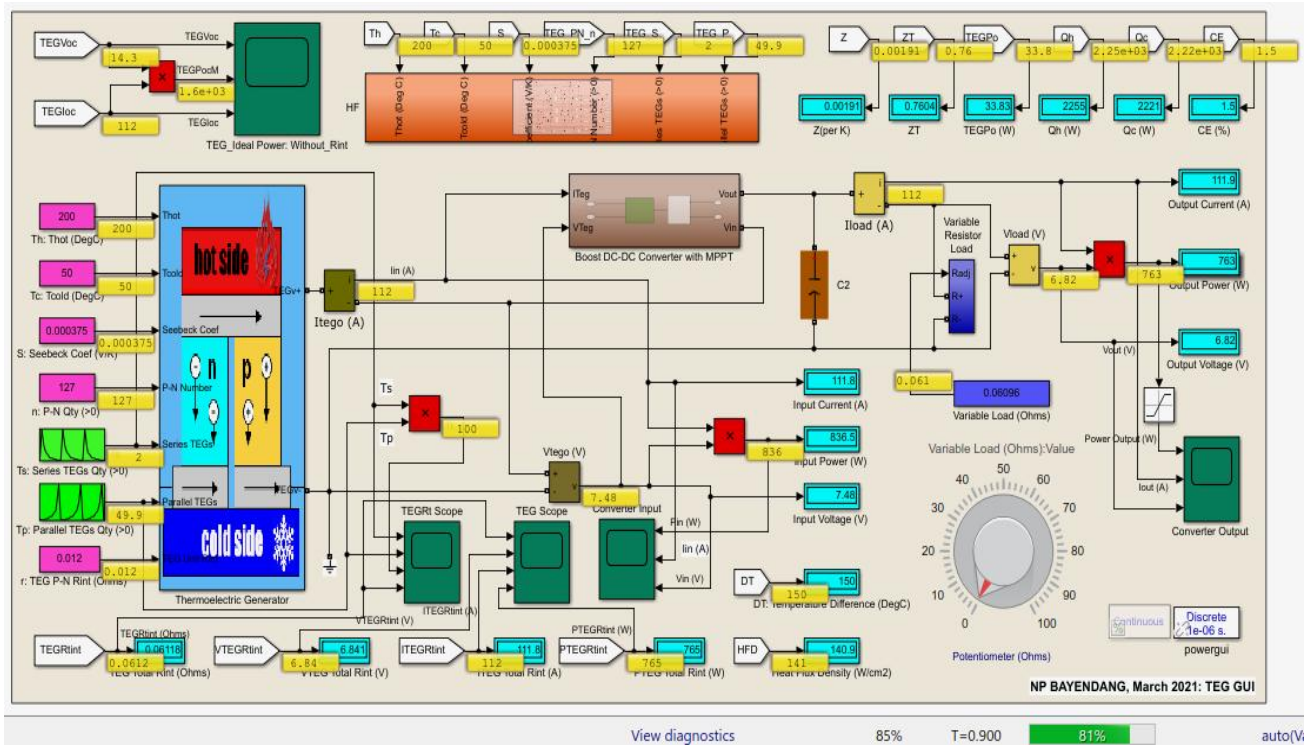

(**a**)

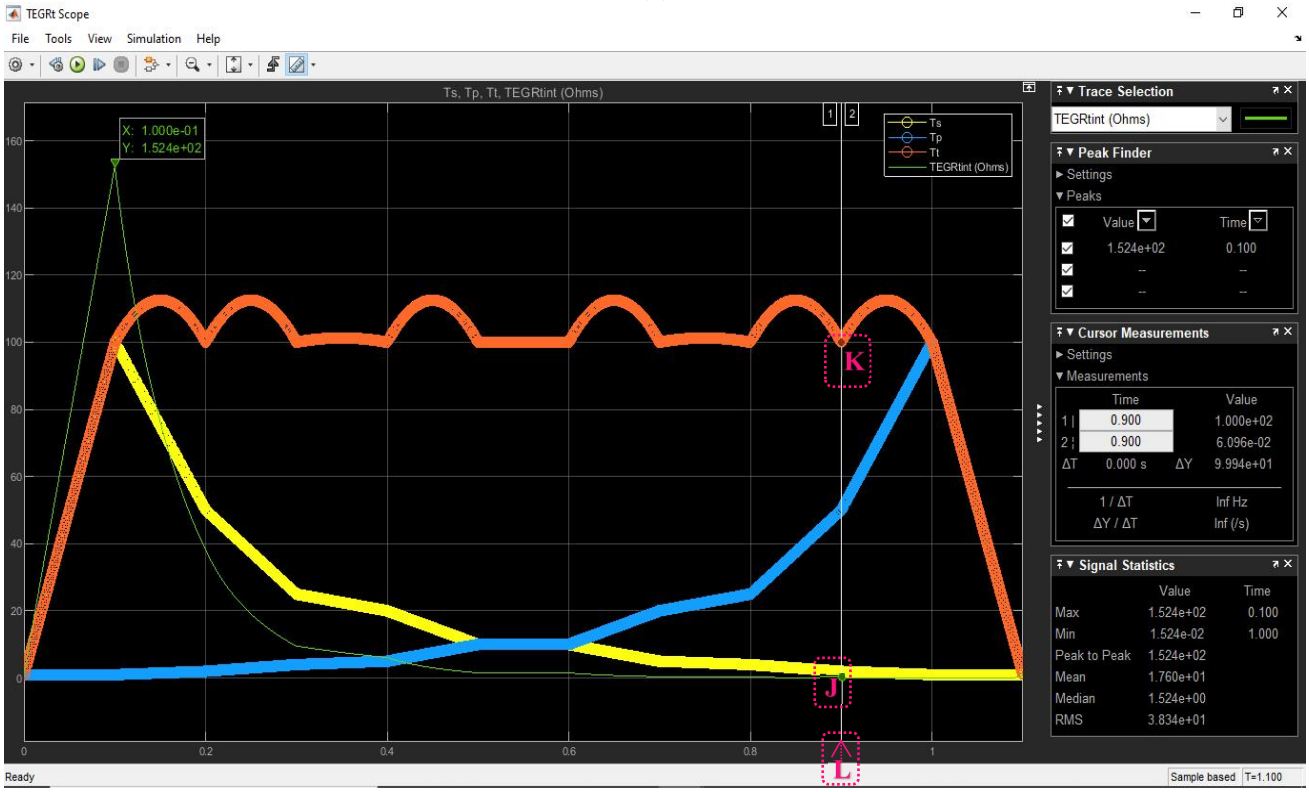

(**b**)

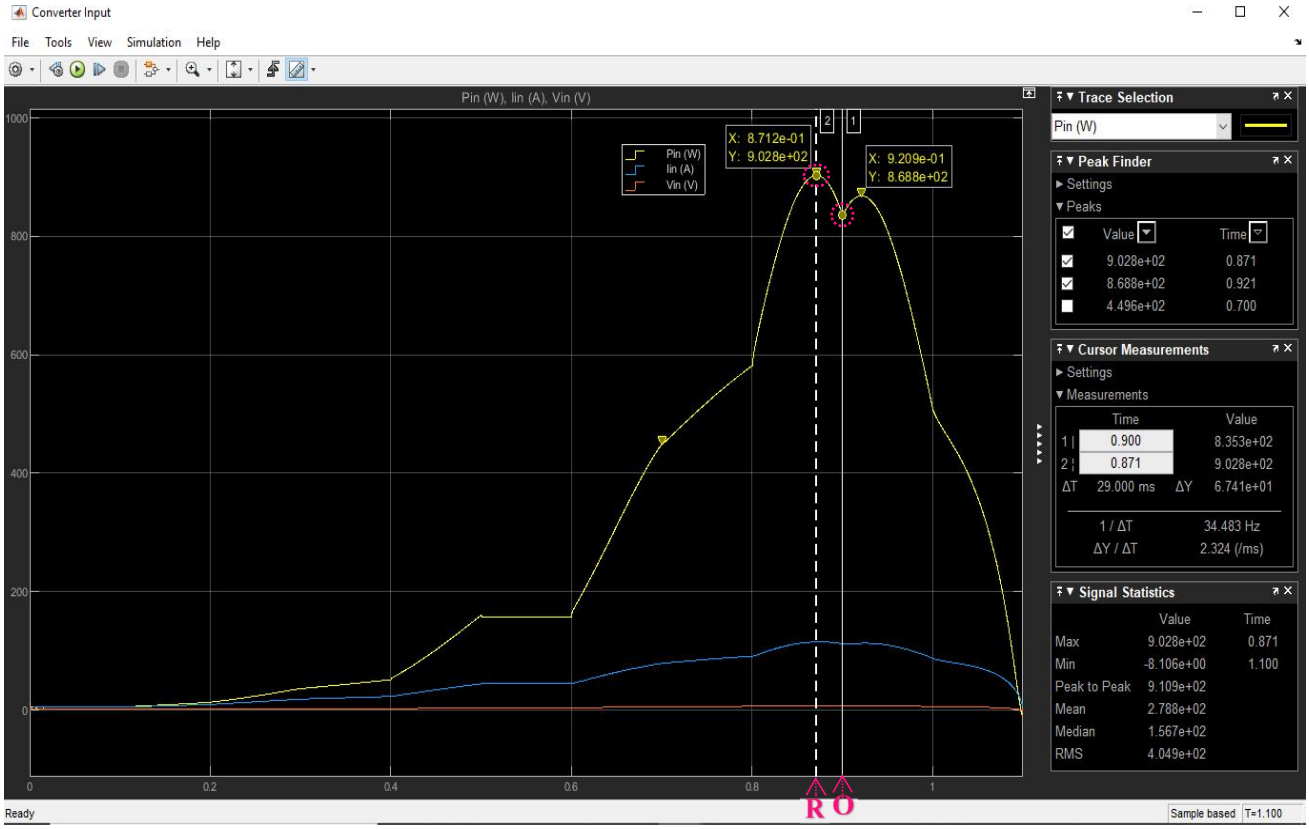

(c)

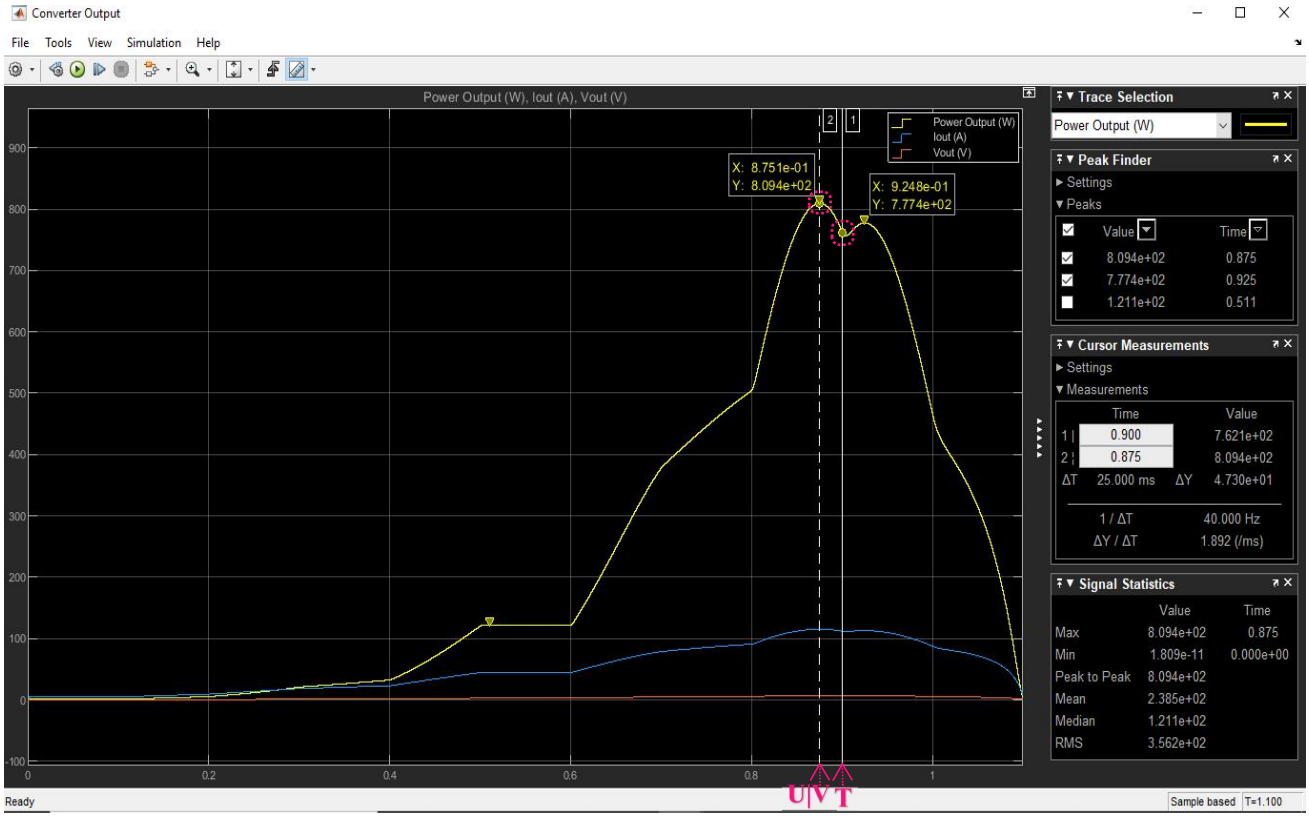

(d)

Figure 5.22: TEGs configuration 9; $R_t = R_L = 0.06096\Omega$ simulation results − note the points of interest highlighted A to V: **(a)** TEGs user's interface; **(b)** T_s, T_p, T_t and R_t dynamics; **(c)** TEGs converter input; **(d)** TEGs converter output.

5.3.3.10 TEGs Configuration 10 (C10): R_t = 0.01524Ω

C10 simulation result has the following settings: $TEG\_S=T_s=1$; $TEG\_P=T_p=100$; $R_L=0.01524\Omega$.

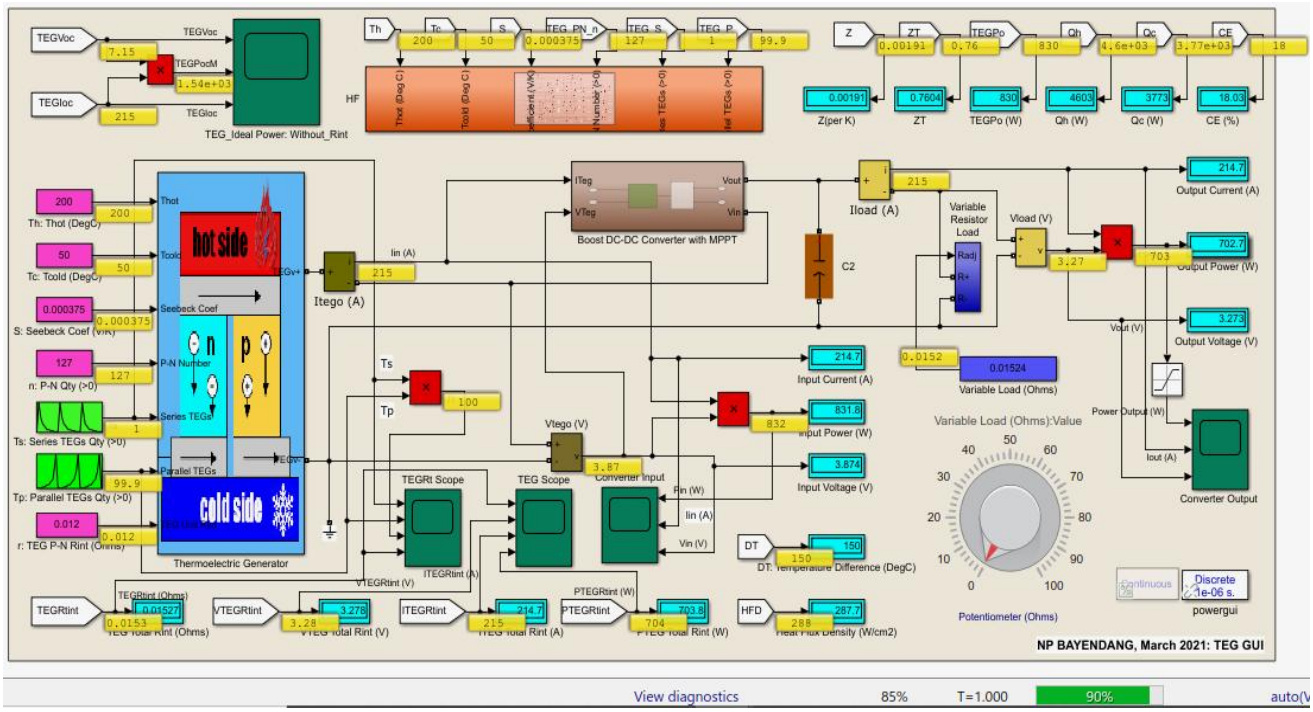

(**a**)

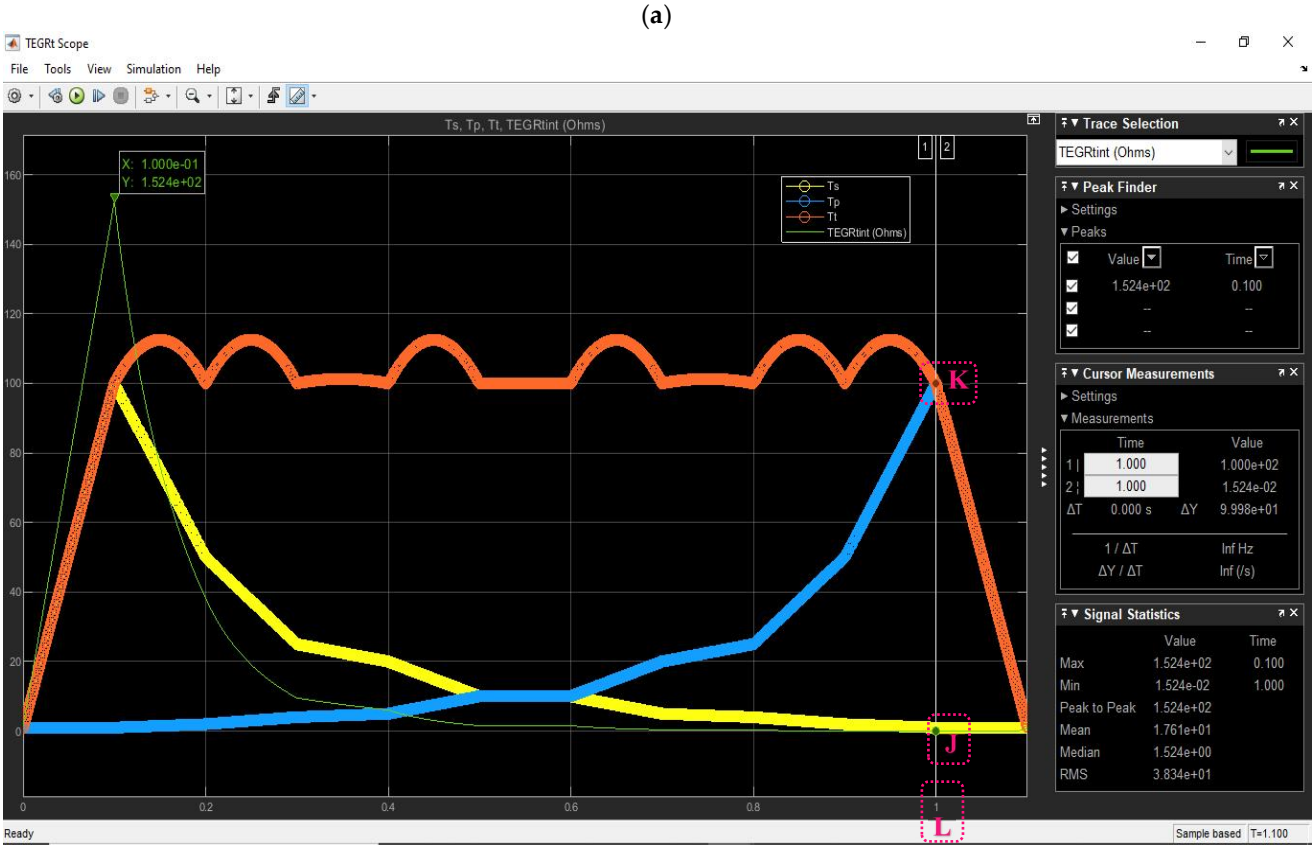

(**b**)

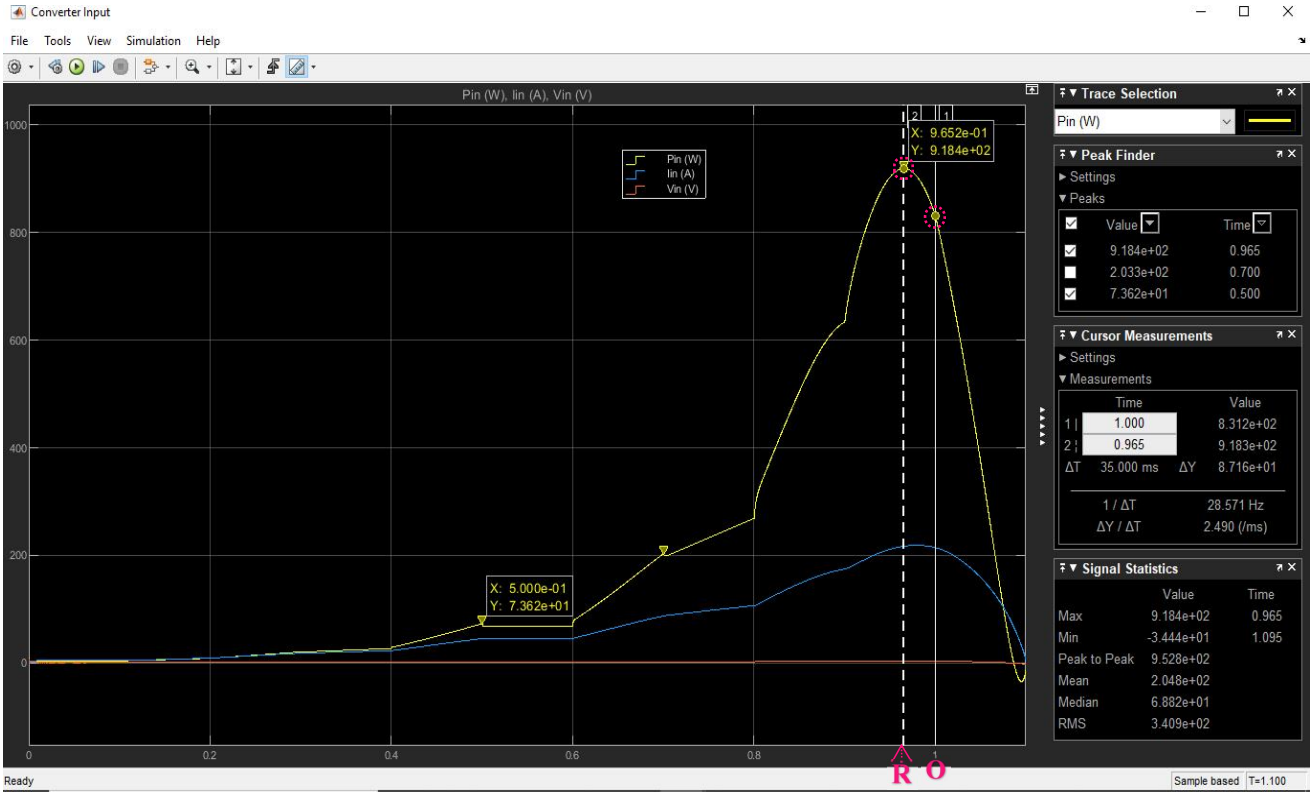

(c)

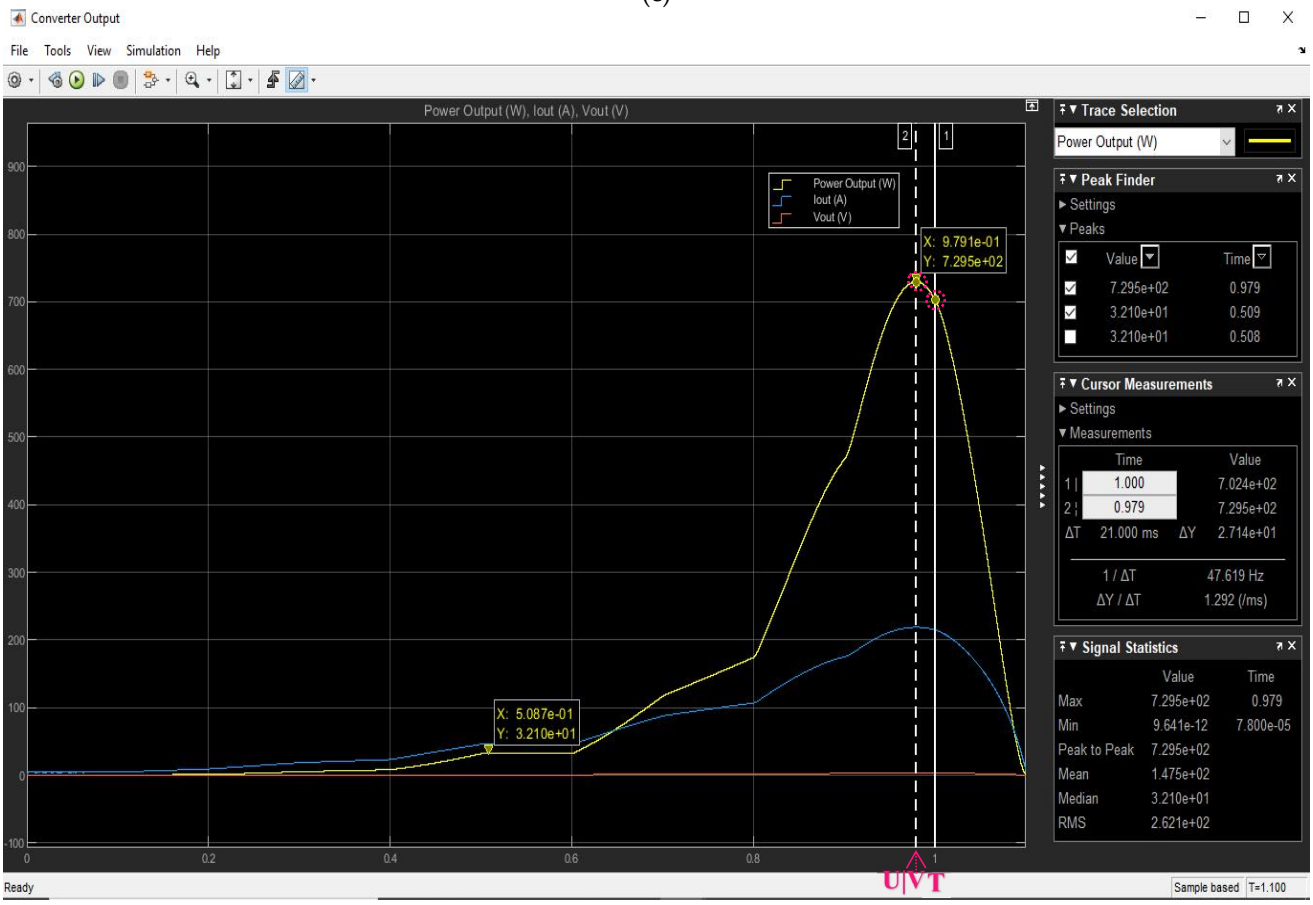

(d)

Figure 5.23: TEGs configuration 10; $R_t = R_L = 0.01524\Omega$ simulation results − note the points of interest highlighted A to V: **(a)** TEGs user's interface; (**b**) T_s, T_p, T_t and R_t dynamics; **(c)** TEGs converter input; **(d)** TEGs converter output.

Table 5.4: TEGs optimal configuration determination simulation results summary

Simulation Parameters Settings				Simulated Measurements	TEGs Conv_Pin (W), Vin (V) & Iin (A)			TEGs Conv_Po (W), Vo (V) & Io (A)			TEGs series, parallel, total & int resistance				TEGs Conv Eff (%)
C	TEG-S	TEG-P	$R_L(\Omega)$		P_{TEG_Ci}/Time	V_{TEG_Ci}/Time	I_{TEG_Ci}/ Time	P_{TEG_Co}/Time	V_{TEG_Co}/Time	I_{TEG_Co}/Time	T_s/Time	T_p/Time	T_t/Time	R_t (Ω)/ Time	
C1	100	1	152.4	Peak	941.8 / 0.65	243.4 / 0.246	226.6 / 1	704.6 / 1.031	327.7 / 1.031	2.15 / 1.031	100 / 0.1	100 / 1	112.5 / 0.15	152.4 / 0.1	74.814
				MPP	908.5 / 0.175	203.5 / 0.175	4.465 / 0.175	386.2 / 0.246	242.6 / 0.246	1.592 / 0.246	100 / 0.1	1 / 0.1	100 / 0.1	152.4 / 0.1	42.509
				Actual	458.3 / 0.1	116.9 / 0.1	3.92 / 0.1	88.45 / 0.1	116.1 / 0.1	0.7618 / 0.1	100 / 0.1	1 / 0.1	100 / 0.1	152.4 / 0.1	19.299
C2	50	2	38.1	Peak ǀ *MPP	915.3 / 0.23	173.7 / 0.261	5.609 / 0.174	*784.7 / 0.261	172.9 / 0.261	4.538 / 0.261	100 / 0.1	100 / 1	112.5 / 0.15	152.4 / 0.1	85.731
				Actual	822.3 / 0.2	154.8 / 0.2	5.312 / 0.2	622.6 / 0.2	154 / 0.2	4.042 / 0.2	50 / 0.2	2 / 0.2	100 / 0.2	38.1 / 0.2	75.714
C3	25	4	9.525	Peakǀ *MPP	882.3 / 0.279	91.16 / 0.292	9.833 / 0.268	*857.5 / 0.292	90.37 / 0.292	9.488 / 0.292	100 / 0.1	100 / 1	112.5 / 0.15	152.4 / 0.1	97.189
				Actual	836.9 / 0.3	90.84 / 0.3	9.213 / 0.3	828.4 / 0.3	88.83 / 0.3	9.326 / 0.3	25 / 0.3	4 / 0.3	100 / 0.3	9.525 / 0.3	98.996
C4	20	5	6.096	Peak ǀ *MPP	887.4 / 0.423	73.68 / 0.431	12.1 / 0.419	*871.6 / 0.431	72.89 / 0.431	11.96 / 0.431	100 / 0.1	100 / 1	112.5 / 0.15	152.4 / 0.1	98.219
				Actual	837.1 / 0.4	71.94 / 0.4	11.64 / 0.4	830.3 / 0.4	71.14 / 0.4	11.67 / 0.4	20 / 0.4	5 / 0.4	100 / 0.4	6.096 / 0.4	99.187
C5	10	10	1.524	Peak ǀ *MPP	890.3 / 0.475	37.22 / 0.477	23.93 / 0.473	*870.7 / 0.478	36.43 / 0.478	23.9 / 0.478	100 / 0.1	100 / 1	112.5 / 0.15	152.4 / 0.1	97.798
				Actual	836.9 / 0.5	36.29 / 0.5	23.06 / 0.5	828.1 / 0.5	35.53 / 0.5	23.31 / 0.5	10 / 0.5	10 / 0.5	100 / 0.5	1.524 / 0.5	98.948
C6	10	10	1.524	Peak	890.3 / 0.475	37.22 / 0.477	23.93 / 0.473	870.7 / 0.478	36.43 / 0.478	23.9 / 0.478	100 / 0.1	100 / 1	112.5 / 0.15	152.4 / 0.1	97.798
				MPP	884 / 0.623	37.09 / 0.625	23.84 / 0.621	864.5 / 0.625	36.3 / 0.625	23.82 / 0.625	10 / 0.6	10 / 0.6	100 / 0.6	1.524 / 0.6	97.794
				Actual	837.1 / 0.6	36.12 / 0.6	23.18 / 0.6	818.5 / 0.6	35.32 / 0.6	23.17 / 0.6	10 / 0.6	10 / 0.6	100 / 0.6	1.524 / 0.6	97.778
C7	5	20	0.381	*MPP	*893.6 / 0.674	18.85 / 0.674	47.39 / 0.674	*855.6 / 0.675	18.06 / 0.675	47.39 / 0.675	100 / 0.1	100 / 1	112.5 / 0.15	152.4 / 0.1	95.747
				Actual	836.7 / 0.7	18.25 / 0.7	45.84 / 0.7	805.3 / 0.7	17.52 / 0.7	45.97 / 0.7	5 / 0.7	20 / 0.7	100 / 0.7	0.381 / 0.7	96.247
C8	4	25	0.24384	*MPP	*878.6 / 0.822	15.04 / 0.822	58.41 / 0.823	*831.8 / 0.824	14.24 / 0.824	58.40 / 0.824	100 / 0.1	100 / 1	112.5 / 0.15	152.4 / 0.1	94.673
				Actual	836.5 / 0.8	14.68 / 0.8	56.96 / 0.8	791.6 / 0.8	13.89 / 0.8	56.98 / 0.8	4 / 0.8	25 / 0.8	100 / 0.8	0.2438 / 0.8	94.632
C9	2	50	0.06096	Peak ǀ *MPP	902.8 / 0.871	7.845 / 0.867	115.2 / 0.875	*809.4 / 0.875	7.024 / 0.875	115.2 / 0.875	100 / 0.1	100 / 1	112.5 / 0.15	152.4 / 0.1	89.654
				Actual	835.3 / 0.9	7.475 / 0.9	111.8 / 0.9	762.1 / 0.9	6.816 / 0.9	111.8 / 0.9	2.00 / 0.9	50 / 0.9	100 / 0.9	0.06096 / 0.9	91.237
C10	1	100	0.01524	Peak ǀ *MPP	918.4 / 0.965	4.268 / 0. 949	218.8 / 0.979	*729.5/ 0.979	3.334 / 0.979	218.8 / 0.979	100 / 0.1	100 / 1	112.5 / 0.15	152.4 / 0.1	79.432
				Actual	831.2 / 1	3.872 / 1	214.7 / 1	702.4 / 1	3.272 / 1	214.7 / 1	1.00 / 1	100 / 1	100 / 1	0.01524 / 1	84.504

Table 5.5: TEGs R_T & ideal powers, voltages & currents optimal configuration determination simulation results summary

Simulation Parameters Settings				Simulated Measurements	TEG(s) Internal Power (W), Voltage (V), Current(A) & Resistance (Ω)				TEG(s) Ideal Power (W), Voltage (V) & Current (A)			TEGs Source Eff (%)
C	TEG-S	TEG-P	$R_L(\Omega)$		P_{TEG_Int} / Time	V_{TEG_Int} / Time	I_{TEG_Int} / Time	R_{TEG_Int} / Time	P_{TEG_OC} / Time	V_{TEG_OC} / Time	I_{TEG_OC} / Time	
C1	100	1	152.4	Peak	2342 / 0.1	597.5 / 0.1	226.6 / 1	152.4 / 0.1	2843 / 0.114	714.4 / 0.1	226.6 / 0.1	33.127
				MPP	2342 / 0.1	597.5 / 0.1	3.92 / 0.1	152.4 / 0.1	2843 / 0.114	714.4 / 0.1	4.28 / 0.114	31.956
				Actual	2342 / 0.1	597.5 / 0.1	3.92 / 0.1	152.4 / 0.1	2801 / 0.1	714.4 / 0.1	3.92 / 0.1	16.362
C2	50	2	38.1	Peak	2581 / 0.109	624.8 / 0.1	5.609 / 0.174	152.4 / 0.1	3043 / 0.123	714.4 / 0.1	5.609 / 0.174	30.079
				Actual	1075 / 0.2	202.4 / 0.2	5.312 / 0.2	38.1 / 0.2	1897 / 0.2	357.2 / 0.2	5.312 / 0.2	43.347
C3	25	4	9.525	Peak	3154 / 0.129	673.5 / 0.1	9.833 / 0.268	152.4 / 0.1	3427 / 0.138	714.4 / 0.1	9.833 / 0.268	25.745
				Actual	808.5 / 0.3	87.76 / 0.3	9.213 / 0.3	9.525 / 0.3	1645 / 0.3	178.6 / 0.3	9.213 / 0.3	50.875
C4	20	5	6.096	Peak	3321 / 0.134	686.5 / 0.1	12.1 / 0.419	152.4 / 0.1	3525 / 0.141	714. 4 / 0.1	12.1 / 0.419	25.174
				Actual	825.4 / 0.4	70.93 / 0.4	11.64 / 0.4	6.096 / 0.4	1662 / 0.4	142.9 / 0.4	11.64 / 0.4	50.367
C5	10	10	1.524	Peak	3619 / 0.144	706.5 / 0.1	23.93 / 0.473	152.4 / 0.1	3691 / 0.147	714.4 / 0.1	23.93 / 0.473	24.121
				Actual	810.5 / 0.5	35.15 / 0.5	23.06 / 0.5	1.524 / 0.5	1647 / 0.5	71.44 / 0.5	23.06 / 0.5	50.814
C6	10	10	1.524	Peak	3619 / 0.144	706.5 / 0.1	23.93 / 0.473	152.4 / 0.1	3691 / 0.147	714.4 / 0.1	23.93 / 0.473	24.121
				Actual	818.5 / 0.6	35.32 / 0.6	23.18 / 0.6	1.524 / 0.6	1656 / 0.6	71.44 / 0.6	23.18 / 0.6	50.549
C7	5	20	0.381	Peak	3719 / 0.148	711.8 / 0.1	47.39 / 0.674	152.4 / 0.1	3743 / 0.149	714.4 / 0.1	47.39 / 0.674	23.874
				Actual	800.6 / 0.7	17.46 / 0.7	45.84 / 0.7	0.381 / 0.7	1637 / 0.7	35.72 / 0.7	45.84 / 0.7	51.112
C8	4	25	0.24384	Peak	3732 / 0.149	712.4 / 0.1	58.41 / 0.823	152.4 / 0.1	3750 / 0.149	714.4 / 0.1	58.41 / 0.823	23.429
				Actual	791.3 / 0.8	13.89 / 0.8	56.96 / 0.8	0.2438 / 0.8	1628 / 0.8	28.57 / 0.8	56.96 / 0.8	51.382
C9	2	50	0.06096	Peak	3750 / 0.15	713.3 / 0.1	115.2 / 0.875	152.4 / 0.1	3758 / 0.15	714.4 / 0.1	115.2 / 0.875	24.023
				Actual	761.4 / 0.9	6.813 / 0.9	111.8 / 0.9	0.06096 / 0.9	1597 / 0.9	14.29 / 0.9	111.8 / 0.9	52.304
C10	1	100	0.01524	Peak	3754 / 0.15	713.5 / 0.1	218.8 / 0.979	152.4 / 0.1	3761 / 0.15	714.4 / 0.1	218.8 / 0.979	24.419
				Actual	702.3 / 1	3.272 / 1	214.7 / 1	0.01524 / 1	1533 / 1	7.144 / 1	214.7 / 1	54.220

Tables 5.4 and 5.5 summarised the TEGs simulation results. Table 5.5 detailed simulation results are found in Supplementary A - J. *MPP means MPP is also Peak. NB: C3 TEGs converter efficiency with dynamic simulation gave 101.74% (an anomaly), which was troubleshooted with static simulation to give 98.996%.

It should be noted that, the points named and highlighted A - V on Figure 5.14, also apply to the same unnamed points/positions on Figures 5.15 - 5.23; though, the only difference is the value each point has on their respective figures is now different due to their respective configurations. Furthermore, the points named J, K, L, O, P/R, T and U/V; will have different positions (but the same designation and meaning) as

well as different values depending on the respective simulated TEGs electrical configurations. Finally, the points named W - Z on Figures 5.25 - 5.34 have the same meaning on their respective figures, though the only difference is their position and value, since the simulation results all have different TEG configurations. The meaning of each point and results interpretation are discussed next in details.

5.3.4 TEGs Optimal Electrical Configurations Determination Simulation Results Discussion

It's prudent I first clarify the various simulation parameters nomenclatures used as well as the meaning and significance of the various points highlighted and labeled A-Z. The parameter R_t is the TEG(s) total resistance. This parameter is also electrically the same as the TEGs internal resistance termed *TEGRtint* in the simulation and R_{TEG_Int} in Table 5.5. Furthermore, at maximum power point (MPP), this parameter is approximately equal to R_L − which is the variable load resistor in the simulation. The TEGs in series denoted TEG_S, is the same as the designation T_s in the simulation. Likewise, the TEGs in parallel denoted TEG_P, is the same as the designation T_p. In the simulation, T_t is the total TEGs quantity as per a configuration. NB, T_t is different from R_t − the latter defines the TEGs total resistance, whereas the former defines the TEGs total amount (quantity) used. The TEGs output voltage denoted (V_o) in the mathematical analysis, is the same as the TEGs converter input voltage designated V_{in} in the simulation and V_{TEG_Ci} in Table 5.4. The same applies to the TEGs output current (I), being the same as the TEGs converter input current designated I_{in} in the simulation and I_{TEG_Ci} in Table 5.4. Furthermore, the TEGs output power (P_o), is the same as the TEGs converter input power designated P_{in} in the simulation and P_{TEG_Ci} in Table 5.4. The TEGs converter output voltage designated V_{out} in the simulation and V_{TEG_Co} in Table 5.4; are the same as the load voltage. The same applies to the TEGs converter output current designated I_{out} in the simulation and I_{TEG_Co} in Table 5.4; which are the same as the load current. Furthermore, the TEGs converter output power designated P_{out} in the simulation and P_{TEG_Co} in Table 5.4; are the same as the load power. It should be noted that the same current that flows through the TEGs R_t, is the same as the current that flows through R_L − since R_t and R_L are electrically in series. The TEGs internal power P_{TEG_Int}, voltage V_{TEG_Int}, current I_{TEG_Int} and resistance R_{TEG_Int} as denoted in Table 5.5, are respectively the same as *PTEGRtint*, *VTEGRtint*, *ITEGRtint* and *TEGRtint* as used in the simulation. The TEGs ideal power P_{TEG_OC}, voltage V_{TEG_OC} and current I_{TEG_OC} as denoted in Table 5.5, are respectively the same as *TEGPocM*, *TEGVoc* and *TEGIoc* as designated in the simulation. The simulated measurement field in Tables 5.4 and 5.5, has three kinds of measurement namely; Peak, MPP and Actual. The peak value is the highest measurement recorded anywhere and at any time (from 0 - 1.1) in the simulation. For example, 941.8/0.65 in Table 5.4 in configuration C1 at corresponding 0.1 simulation time, I recorded a peak or maximum TEGs output power of 941.8W at simulation time of 0.65. However, Table 5.4 in configuration C1 at corresponding 0.1 simulation time, recorded respective peak voltage and current as 243.4/0.246 and 226.6/1. As can be seen, the peak power is not the product of the

peak voltage and current at C1, because the peak power, voltage and current can occur at different simulation times (0.65, 0.246 and 1 in this case); even though TEGs configuration under testing was C1 that corresponds to simulation time 0.1. The MPP value is the measurement recorded at maximum power point at the same simulation time instant (e.g. 0.175), which however doesn't correspond to the TEGs configuration number (e.g. C1). NB: TEGs configuration number C1 - C10, correspond to simulation time 0.1 - 1. For example: Table 5.4 in configuration C1 at corresponding 0.1 simulation time, recorded respective MPP power, voltage and current as 908.5 / 0.175, 203.5 / 0.175 and 4.465 / 0.175. As can be seen, the MPP power, voltage and current occurred at the same simulation time of 0.175, consequently the MPP power is a product of the MPP voltage and current. However, the simulation time of 0.175 when the MPP parameters values were measured, don't correspond to the TEGs configuration number C1 corresponding simulation time of 0.1 in this case. The actual value (the research focus) is the measurement recorded at exactly the same simulation time (e.g. 0.1) which must correspond to its respective TEGs configuration (e.g. C1) in this case. For example, Table 5.4 in TEGs configuration C1 at corresponding 0.1 simulation time, recorded respective actual power, voltage and current as 458.3 / 0.1, 116.9 / 0.1 and 3.92 / 0.1. As can be seen, the actual power is the product of the actual voltage and current − which all 3 occurred at the same simulation time of 0.1, which also corresponds to the TEGs C1 configuration.

The simulation highlighted points of interest labeled A-Z, where applicable in Figures 5.14−5.23 and in Figures 5.25−5.34, are clearly defined and explained as follows:

- **Point A:** This is the TEGs ideal power (W), voltage (V) and current (A) parameters; respectively (*TEGPocM* = P_{TEG_OC}, *TEGVoc* = V_{TEG_OC} and *TEGIoc* = I_{TEG_OC}). TEGs ideal or open circuit parameters are the maximum power, voltage and current that can be produced assuming TEGs has no internal resistance; that is $R_t = 0$. This means all the power, voltage, current produced will be delivered to the load, which in reality is not the case due to R_t. That is, TEG ideal power is the sum of the TEG internal resistance power (power lost as heat due to R_t Joule or Ohmic heating) and TEG output power (power delivered to the load). This is an interesting parameter, as it reveals i) the maximum power that TEG(s) can produce and ii) the effects of TEG(s) total internal resistance R_t − the smaller the R_t, the more the TEGs output power. These ideal parameters results are abridged in Table 5.5 and detailed in Figures 5.14a−5.23a and Figures 5.25−5.34.

- **Point B:** This is the series (T_s = *TEG_S*) and parallel (T_p = *TEG_P*) TEG(s). They are used to choose the number (infinite) of TEGs to be connected in series and or parallel. Connecting more TEGs in series (T_s) increases the TEGs output voltage and connecting more in parallel (T_p) increases the TEGs output current. However, connecting more TEGs in series also increases the TEGs internal resistance (*TEGRtint* = R_t), which as a result inefficiently affects (decreases) the TEGs output voltage, current and power, since the increase in *TEGRtint* increases the voltage drop over it, consequently increases the power loss

($P=V_{TEGRtint}^2/TEGRtint$). However, connecting more TEGs in parallel also decreases the TEGs internal resistance ($TEGRtint = R_t$), which as a result affects (decreases) the TEGs output voltage and power, since the decrease in *TEGRtint* decreases the voltage drop; however, it increases the output current which consequently increases the power loss ($P=I_{TEGRtint}^2 TEGRtint$) due to Joule or Ohmic heating. It should be noted that a TEG akin a battery, is a voltage source and a good or ideal voltage source is one with respectively very little or no internal (source) resistance, which is practically impossible. Therefore, a balance has to be made and one way is connecting the TEGs in series and in parallel to optimize both the TEGs outputs voltage and current. However, it's prudent to first ascertain R_L to ensure whatever configuration of T_s and T_p, gives a *TEGRtint* or R_t that matches R_L for efficient direct maximum power transfer − without extra devices. Of course in practice, a boost DC-DC converter with energy management is paramount for reliable performance; however, first ensuring matching R_t to R_L boost the system efficiency.

- **Point C:** This is the TEGs total internal resistance ($TEGRtint = R_t$) and the most vital TEGs electrical parameter. R_t is the total electrical resistance resulting from connecting multiple T_s and or T_p. When $R_t = R_L$, maximum power shall be transferred from the TEGs to the load, though, maximum power don't exactly happens at $R_t = R_L$ due to non-linearity of TEG.

- **Point D:** This is the TEGs total internal voltage (*VTEGRtint*), current (*ITEGRtint*) and power (*PTEGRtint*) as a result of the TEGs total internal resistance *TEGRtint* or R_t. Without R_t, all the power generated by the TEGs, can be delivered to the load. Therefore, by minimizing R_t, the TEGs power to the load can be maximally and efficiently delivered.

- **Point E:** This simply illustrates the product of T_s and T_p to give T_t − which is the total number of TEGs used. T_t (TEGs total amount) is different from R_t (TEGs total resistance).

- **Point F:** This is the actual TEGs output or better, generated power (P_{in}), voltage (V_{in}) and current (I_{in}) as designated in the simulation, which is the same as the TEGs converter input power (P_{TEG_Ci}), voltage (V_{TEG_Ci}) and current (I_{TEG_Ci}) as assigned in Table 5.4. NB: It will be the output power, voltage and current delivered directly to the load (if there wasn't a boost converter) and it is practically the difference between the TEGs ideal and internal parameters. $P_{in}=TEGPocM-PTEGRtint;$ $V_{in}=TEGVoc-VTEGRtint$ and $I_{in}=TEGIoc-ITEGRtint.$

- **Point G:** This is the TEGs electrical load resistance (R_L). Without the boost converter in between, R_L connects directly to the TEGs output (practically to R_t or *TEGRtint*). For maximum power transfer, with or without the boost converter, R_L should equals R_t, which in reality is actually not the case. Usually in the simulation, R_L as per a specific TEGs configuration (e.g. C1) is first calculated and set ($R_L = 152.4\Omega$ for C1) and the simulation executed, during which the values of T_s, T_p, T_t and R_t are observed as they change and

once at the corresponding simulation time of 0.1; T_s = ~100, T_p = ~1, T_t = ~100 and R_t = ~152.4Ω which theoretically necessitate maximum power transfer to be attained at this instance.

- **Point H:** This is the TEGs boosted output with maximum power point tracking (MPPT) power (P_{out}), voltage (V_{out}) and current (I_{out}) delivered directly to the load R_L as designated in the simulation − which is the same as the TEGs boost converter / MPPT output power (P_{TEG_Co}), voltage (V_{TEG_Co}) and current (I_{TEG_Co}) as designated in Table 5.4.

- **Point I:** This is the simulation time (from 0 to 1.1 or better from 0.1 to 1) which should correspond to the respective TEGs configurations of C1 to C10. That is, once at simulation time 0.1 with R_L=152.4Ω, the TEGs configuration will automatically be exactly at C1 in which T_s = ~100, T_p = ~1, T_t = ~100 and R_t = ~152.4Ω; at simulation time 0.2 with R_L=38.1Ω, the TEGs configuration will automatically be exactly at C2 whereby T_s = ~*50*, T_p =~*2,* T_t = ~100 and R_t = ~38.1Ω and so forth till simulation time 1, corresponding to C10.

- **Point J:** This is the dynamic R_t value with respect to each TEGs configuration C1 − C10. Mindful that the TEGs R_t value and position will respectively change downwards and to the right as the simulation progresses from simulation time 0.1 to 1 for C1 to C10.

- **Point K:** This is the T_t (product of T_s and T_p) value with respect to each TEGs configuration C1-C10. It should be noted that the value will approximately stays the same (e.g. T_t = ~100) while the position will change to the right as the simulation progresses from simulation time 0.1 for C1 to 1 for C10 correspondingly. However, at non C1-C10 values, T_t will be at maximum of ~112.5.

- **Point L:** This is the same as Point I; however, the only difference is this keeps tracks of the simulation time on the graphs whereas, Point I keeps track of GUI simulation time.

- **Point M:** This shows cursors 1 and 2 measurements value and the simulation time the measurements were made. At certain instances, these cursors 1 and 2 measurements parameters, values and simulation times will vary depending on the investigation made.

- **Point N:** This simply displays the measurement statistics. However, of interest here is the peak or maximum value and the corresponding simulation times of occurrence.

- **Point O:** This indicates the simulated TEGs converter input power actual measurements value at the simulation times 0.1 to 1 corresponding to C1 to C10. This is the simulated TEGs output power measurement critical research test point of interest.

- **Point P:** This indicates the simulated TEGs converter input power MPP measurements value at the simulation times 0.1 to 1 corresponding to C1 to C10. This is the simulated TEGs output power measurement first control research point of interest.
- **Point Q:** This indicates the simulated TEGs output voltage peak measurement.

- **Point R:** This indicates the simulated TEGs converter input power peak measurements value at the simulation times 0.1 to 1 corresponding to C1 to C10. This is the simulated TEGs output power measurement second control research interest point.

It should be noted that the actual, MPP and peak simulated measurements in the context of this research article are merely reasonable terminologies used herein to define and differentiate the three measurements for the sake of ease of understanding and explanation. There are instances (e.g. C1) where the peak as well as MPP measurements don't accurately conforms to their definitions used here, as the peak readings at times obeys MPP definition. Also, MPP can be a peak value but don't obey the peak definition.

- **Point S:** This indicates the simulated TEGs output current peak measurement.

- **Point T:** This indicates the simulated TEGs converter output power actual measurements value at the simulation times 0.1 to 1 corresponding to C1 to C10. This is the simulated TEGs boost converter load (terminal) power measurement critical research test point of interest. Please note carefully the difference between Point T and Point O.

- **Point U:** This indicates the simulated TEGs converter output power MPP measurements value at the simulation times 0.1 to 1 corresponding to C1 to C10. This is the simulated TEGs boost converter load (terminal) power measurement first control research interest point. Please note carefully the difference between Point U and Point P.

- **Point V:** This indicates the simulated TEGs converter output power peak measurements value at the simulation times 0.1 to 1 corresponding to C1 to C10. This is the simulated TEGs boost converter load (terminal) power measurement second control research interest point. Please note carefully the difference between Point V and Point R.

NB: U|V means the output power measurement could either be considered MPP or Peak measurement.

Finally, the following four points (W−Z) of interest apply to Supplementary A−J (that is Figures 5.25 − 5.34) and are defined and explained as follows:

- **Point W:** This signifies the simulated TEGs internal resistance (*TEGRtint*) power peak measurements value at the simulation times 0.1 to 1 corresponding to C1 to C10. *PTEGRtint* is a very vital parameter, as it demonstrates the effects of the source internal resistance which is very crucial for a voltage source. The more the *TEGRtint*, the more of the generated TEGs power will be dissipated as heat, causing TEGs to be less powerful and very inefficient.

- **Point X:** This signifies the simulated TEGs internal resistance (*TEGRtint*) power actual measurements value at the simulation times 0.1 to 1 corresponding to C1 to C10. At C1, W equals X, as the *PTEGRtint* measurement is at maximum corresponding to C1. However, X value will always be less than W value and X will decrease from left to right for subsequent C2 − C10 configurations tests, corresponding to simulation times 0.2 − 1.

- **Point Y:** This signifies the simulated TEGs ideal power (*TEGPocM* or P_{TEG_OC}) peak measurements value at the simulation times 0.1 to 1 corresponding to C1 to C10. *TEGPocM* is a very vital parameter, as it demonstrates the effects of the source internal resistance *TEGRtint*, which is very crucial for a voltage source. Without *TEGRtint*, all the generated TEGs power will be theoretically delivered to the load, causing the TEGs to be very powerful. However, this is hardly the case in practice, as the thermoelectric elements used have intrinsic resistance and minimising *TEGRtint* will therefore enhance TEGs performance.

- **Point Z:** This signifies the simulated TEGs ideal power (*TEGPocM* or P_{TEG_OC}) actual measurements value at the simulation times 0.1 to 1 corresponding to C1 to C10 − meaning, Z value will always be less than Y value and Z will decrease from left to right for subsequent C2 − C10 configurations tests, corresponding to simulation times 0.2 − 1. NB: subtracting *PTEGRtint* from *TEGPocM* will give the TEGs real output or load power.

With the above clarity, the simulated TEGs configurations results presented in Section 5.3.3 are discussed.

5.3.4.1 TEGs Configuration 1 (C1): R_t = 152.4Ω

In TEGs C1 as displayed in Figure 5.14a, R_L is first calculated and set to 152.4Ω and the simulation ran while noticing the T_s, T_p, T_t and R_t values changing. At exactly 0.1 simulation time; T_s, T_p, T_t and R_t should respectively exactly read 100, 1, 100, 152.4Ω as shown in Figures 5.14a and 5.14b. The TEGs converter associated input and output powers, voltages and currents are portrayed in Figures 5.14c and 5.14d, as well as the TEGs internal power, voltage, current and resistance pictured in Figure 5.25a and finally the TEGs ideal power, voltage and current depicted in Figure 5.25b. Theses results are summarised in Tables 5.4 and

5.5 including also the TEGs boost converter efficiency (calculated as: (P_{TEG_Co} / P_{TEG_Ci}) x 100) and the TEGs source efficiency (calculated as: (P_{TEG_Ci} / P_{TEG_OC}) x 100). NB: the TEGs boost converter input and output powers MPP respectively occurred but at 0.175 and 0.246 simulation times instead of 0.1, corresponding to TEGs configuration C1. Furthermore, proceeding the MPP value and from simulation time 0.27, the TEGs internal resistance voltage and current as shown in Figure 5.25a, the TEGs ideal power and current as shown in Figure 5.25b and the TEGs converter P_{in} and I_{in} as shown in Figure 5.14c, dropped to zero until after 0.6 simulation time. These TEGs parameters dynamic symbolizes the effect if the TEGs source internal resistance *TEGRtint* or R_t is connected to an electrical load R_L of 152.4Ω and then matched and mismatched.

5.3.4.2 TEGs Configuration 2 (C2): R_t = 38.1Ω

In TEGs C2 as displayed in Figure 5.15a, R_L is first computed and set to 38.1Ω and the simulation executed while observing the T_s, T_p, T_t and R_t values changing. At exactly 0.2 simulation time; T_s, T_p, T_t and R_t should exactly read 50, 2, 100, 38.1Ω respectively as shown in Figures 5.15a and 5.15b. The TEGs converter associated input and output powers, voltages and currents are portrayed in Figures 5.15c and 5.15d, as well as the TEGs internal power, voltage, current and resistance pictured in Figures 5.26a and finally the TEGs ideal power, voltage and current depicted in Figure 5.26b. Theses results are summarised in Tables 5.4 and 5.5 including the TEGs boost converter efficiency and the TEGs source efficiency. NB: the TEGs boost converter P_{in} and P_{out} MPP respectively occurred but at 0.23 and 0.261 simulation times instead of 0.2 − corresponding to TEGs configuration C2. The TEGs converter P_{in}, V_{in} and I_{in} are shown in Figure 5.15c, the TEGs converter P_{out}, V_{out} and I_{out} are portrayed in Figure 5.15d, the TEGs internal resistance, power, voltage and current are shown in Figure 5.26a and the TEGs ideal power, voltage and current are depicted in Figure 5.26b. These TEGs parameters dynamics symbolizes the effect if the TEGs *TEGRtint* or R_t is connected to a load R_L of 38.1Ω and then matched and mismatched.

5.3.4.3 TEGs Configuration 3 (C3): R_t = 9.525Ω

In TEGs C3 as shown in Figure 5.16a, R_L is first calculated and set to 9.525Ω and the simulation executed while observing the T_s, T_p, T_t and R_t values changing. At exactly 0.3 simulation time; T_s, T_p, T_t and R_t should exactly respectively read 25, 4, 100, 9.525Ω as shown in Figures 5.16a and 5.16b. The TEGs converter associated input and output powers, voltages and currents are portrayed in Figures 5.16c and 5.16d, as well as the TEGs internal power, voltage, current and resistance pictured in Figures 5.27a and finally the TEGs ideal power, voltage and current depicted in Figure 5.27b. Theses results are summarised in Tables 5.4 and 5.5 including the TEGs boost converter efficiency (NB: this value with dynamic simulation gave 101.74%

for C3 − which is an anomaly and was investigated with static simulation to correctly give 98.996%) and the TEGs source efficiency. NB: the TEGs boost converter P_{in} and P_{out} MPP respectively occurred but at 0.279 and 0.292 simulation times instead of 0.3, corresponding to TEGs configuration C3. The TEGs converter P_{in}, V_{in} and I_{in} are shown in Figure 5.16c, the TEGs converter P_{out}, V_{out} and I_{out} are portrayed in Figure 5.16d, the TEGs internal resistance, power, voltage and current are shown in Figure 5.27a and the TEGs ideal power, voltage and current are depicted in Figure 5.27b. These TEGs parameters dynamics symbolizes the effect if the TEGs *TEGRtint* or R_t is connected to a load R_L of 9.525Ω and then matched and mismatched.

5.3.4.4 TEGs Configuration 4 (C4): R_t = 6.096Ω

In TEGs C4 as shown in Figure 5.17a, R_L is first computed and set to 6.096Ω and the simulation executed while watching the T_s, T_p, T_t and R_t values changing. At exactly 0.4 simulation time; T_s, T_p, T_t and R_t should respectively exactly read 20, 5, 100, 6.096Ω as shown in Figures 5.17a and 5.17b. The TEGs converter associated input and output powers, voltages and currents are portrayed in Figures 5.17c and 5.17d, as well as the TEGs internal power, voltage, current and resistance pictured in Figures 5.28a and finally the TEGs ideal power, voltage and current depicted in Figure 5.28b. Theses results are summarised in Tables 5.4 and 5.5 including the TEGs boost converter efficiency and the TEGs source efficiency. NB: the TEGs boost converter P_{in} and P_{out} MPP respectively occurred but at 0.423 and 0.431 simulation times instead of 0.4, corresponding to TEGs configuration C4. The TEGs converter P_{in}, V_{in} and I_{in} are shown in Figure 5.17c, the TEGs converter P_{out}, V_{out} and I_{out} are portrayed in Figure 5.17d, the TEGs internal resistance, power, voltage and current are shown in Figure 5.28a and the TEGs ideal power, voltage and current are depicted in Figure 5.28b. These TEGs parameters dynamics symbolizes the effect if the TEGs *TEGRtint* or R_t is connected to a load R_L of 6.096Ω and then matched and mismatched.

5.3.4.5 TEGs Configuration 5 (C5): R_t = 1.524Ω

In TEGs C5 as shown in Figure 5.18a, R_L is first computed and set to 1.524Ω and the simulation executed while watching the T_s, T_p, T_t and R_t values changing. At exactly 0.5 simulation time; T_s, T_p, T_t and R_t should exactly respectively read 10, 10, 100, 1.524Ω as shown in Figures5.18a and 5.18b. The TEGs converter associated input and output powers, voltages and currents are portrayed in Figures 5.18c and 5.18d, as well as the TEGs internal power, voltage, current and resistance pictured in Figure 5.29a and finally the TEGs ideal power, voltage and current depicted in Figure 5.29b. Theses results are summarised in Tables 5.4 and

5.5 including the TEGs boost converter efficiency and the TEGs source efficiency. NB: the TEGs boost converter P_{in} and P_{out} MPP respectively occurred but at 0.475 and 0.478 simulation times instead of 0.5, corresponding to TEGs configuration C5. The TEGs converter P_{in}, V_{in} and I_{in} are shown in Figure 5.18c, the TEGs converter P_{out}, V_{out} and I_{out} are portrayed in Figure 5.18d, the TEGs internal resistance, power, voltage and current are shown in Figure 5.29a and the TEGs ideal power, voltage and current are depicted in Figure 5.29b. These TEGs parameters dynamics symbolizes the effect if the TEGs *TEGRtint* or R_t is connected to a load R_L of 1.524Ω and then matched and mismatched.

5.3.4.6 TEGs Configuration 6 (C6): R_t = 1.524Ω

In TEGs C6 as shown in Figure 5.19a, R_L is first calculated and set to 1.524Ω and the simulation executed while noticing the T_s, T_p, T_t and R_t values changing. At exactly 0.6 simulation time; T_s, T_p, T_t and R_t should respectively exactly read 10, 10, 100, 1.524Ω as shown in Figures 5.19a and 5.19b. The TEGs converter associated input and output powers, voltages and currents are portrayed in Figures 5.19c and 5.19d, as well as the TEGs internal power, voltage, current and resistance pictured in Figure 5.30a and finally the TEGs ideal power, voltage and current depicted in Figure 5.30b. Theses results are summarised in Tables 5.4 and 5.5 including the TEGs boost converter efficiency and the TEGs source efficiency. NB: the TEGs boost converter P_{in} and P_{out} MPP respectively occurred but at 0.623 and 0.625 simulation times instead of 0.6, corresponding to TEGs configuration C6. The TEGs converter P_{in}, V_{in} and I_{in} are shown in Figure 5.19c, the TEGs converter P_{out}, V_{out} and I_{out} are portrayed in Figure 5.19d, the TEGs internal resistance, power, voltage and current are shown in Figure 5.30a and the TEGs ideal power, voltage and current are depicted in Figure 5.30b. These TEGs parameters dynamics symbolizes the effect if the TEGs *TEGRtint* or R_t is connected to a load R_L of 1.524Ω and then matched and mismatched.

5.3.4.7 TEGs Configuration 7 (C7): R_t = 0.381Ω

In TEGs C7 as shown in Figure 5.20a, R_L is first computed and set to 0.381Ω and the simulation executed while observing the T_s, T_p, T_t and R_t values changing. At exactly 0.7 simulation time; T_s, T_p, T_t and R_t should exactly respectively read 5, 20, 100, 0.381Ω as shown in Figures 5.20a and 5.20b. The TEGs converter associated input and output powers, voltages and currents are portrayed in Figures 5.20c and 5.20d, as well as the TEGs internal power, voltage, current and resistance pictured in Figure 5.31a and finally the TEGs ideal power, voltage and current depicted in Figure 5.31b. Theses results are summarised in Tables 5.4 and

5.5 including the TEGs boost converter efficiency and the TEGs source efficiency. NB: the TEGs boost converter P_{in} and P_{out} MPP respectively occurred but at 0.674 and 0.675 simulation times instead of 0.7, corresponding to TEGs configuration C7. The TEGs converter P_{in}, V_{in} and I_{in} are shown in Figure 5.20c, the TEGs converter P_{out}, V_{out} and I_{out} are portrayed in Figure 5.20d, the TEGs internal resistance, power, voltage and current are shown in Figure 5.31a and the TEGs ideal power, voltage and current are depicted in Figure 5.31b. These TEGs parameters dynamics symbolizes the effect if the TEGs *TEGRtint* or R_t is connected to a load R_L of 0.381Ω and then matched and mismatched.

5.3.4.8 TEGs Configuration 8 (C8): R_t = 0.24384Ω

In TEGs C8 as shown in Figure 5.21a, R_L is first computed and set to 0.24384Ω and the simulation executed while watching the T_s, T_p, T_t and R_t values changing. At exactly 0.8 simulation time; T_s, T_p, T_t and R_t should respectively exactly read 4, 25, 100, 0.24384Ω as shown in Figures 5.21a and 5.21b. The TEGs converter associated input and output powers, voltages and currents are portrayed in Figures 5.21c and 5.21d, as well as the TEGs internal power, voltage, current and resistance pictured in Figures 5.32a and finally the TEGs ideal power, voltage and current depicted in Figure 5.32b. Theses results are summarised in Tables 5.4 and 5.5 including the TEGs boost converter efficiency and the TEGs source efficiency. NB: the TEGs boost converter P_{in} and P_{out} MPP respectively occurred but at 0.822 and 0.824 simulation times instead of 0.8, corresponding to TEGs configuration C8. The TEGs converter P_{in}, V_{in} and I_{in} are shown in Figure 5.21c, the TEGs converter P_{out}, V_{out} and I_{out} are portrayed in Figure 5.21d, the TEGs internal resistance, power, voltage and current are shown in Figure 5.32a and the TEGs ideal power, voltage and current are depicted in Figure 5.32b. These TEGs parameters dynamics symbolizes the effect if the TEGs *TEGRtint* or R_t is connected to load R_L of 0.24384Ω and then matched and mismatched.

5.3.4.9 TEGs Configuration 9 (C9): R_t = 0.06096Ω

In TEGs C9 as shown in Figure 5.22a, R_L is first computed and set to 0.06096Ω and the simulation executed while noticing the T_s, T_p, T_t and R_t values changing. At exactly 0.9 simulation time; T_s, T_p, T_t and R_t should exactly respectively read 2, 50, 100, 0.06096Ω as shown in Figures 5.22a and 5.22b. The TEGs converter associated input and output powers, voltages and currents are portrayed in Figures 5.22c and 5.22d, as well as the TEGs internal power, voltage, current and resistance pictured in Figures 5.33a and finally the TEGs ideal power, voltage and current depicted in Figure 5.33b. Theses results are summarised in Tables 5.4 and

5.5 including the TEGs boost converter efficiency and the TEGs source efficiency. NB: the TEGs boost converter P_{in} and P_{out} MPP respectively occurred but at 0.871 and 0.875 simulation times instead of 0.9, corresponding to TEGs configuration C9. The TEGs converter P_{in}, V_{in} and I_{in} are shown in Figure 5.22c, the TEGs converter P_{out}, V_{out} and I_{out} are portrayed in Figure 5.22d, the TEGs internal resistance, power, voltage and current are shown in Figure 5.33a and the TEGs ideal power, voltage and current are depicted in Figure 5.33b. These TEGs parameters dynamics symbolizes the effect if the TEGs *TEGRtint* or R_t is connected to load R_L of 0.06096Ω and then matched and mismatched.

5.3.4.10 TEGs Configuration 10 (C10): R_t = 0.01524Ω

In TEGs C10 as shown in Figure 5.23a, R_L is first computed and set to 0.01524Ω and the simulation executed while noticing the T_s, T_p, T_t and R_t values changing. At exactly 1 simulation time; T_s, T_p, T_t and R_t should exactly respectively read 1, 100, 100, 0.01524Ω as shown in Figures 5.23a and 5.23b. The TEGs converter associated input and output powers, voltages and currents are portrayed in Figures 5.23c and 5.23d, as well as the TEGs internal power, voltage, current and resistance pictured in Figures 5.34a and finally the TEGs ideal power, voltage and current depicted in Figure 5.34b. Theses results are summarised in Tables 5.4 and 5.5 including the TEGs boost converter efficiency and the TEGs source efficiency. NB: the TEGs boost converter P_{in} and P_{out} MPP respectively occurred but at 0.965 and 0.979 simulation times instead of 1, corresponding to TEGs configuration C10. The TEGs converter P_{in}, V_{in} and I_{in} are shown in Figure 5.23c, the TEGs converter P_{out}, V_{out} and I_{out} are portrayed in Figure 5.23d, the TEGs internal resistance, power, voltage and current are shown in Figure 5.34a and the TEGs ideal power, voltage and current are shown in Figure 5.34b. These TEGs parameters dynamics symbolizes the effect if the TEGs *TEGRtint* or R_t is connected to load R_L of 0.01524Ω and then matched and mismatched.

5.3.5 Results Validations

My TEGs simulated model/results were scientifically validated where possible in fairly two ways, as follows:

5.3.5.1 Analytical, Numerical and Graphical Simulated Results Comparisons

With this approach, a simple TEGs resistance (R_t), power, voltage, current and TEGs T_s, T_p and T_t comparisons were done between the calculations in Table 5.3 with their corresponding simulated numeric and graphical results demonstrated in Figures 5.14 - 5.23 as well as Figures 5.25 - 5.34 and finally the

summary in Tables 5.4 and 5.5. These results exactly correlated each other confirming the results validity of the different TEGs configurations, with focus on the source to load resistance matching and maximum power transfer. NB: any other parameters or dynamics or factors irrespective of their relevance, are not the focus of this study and therefore were simply treated as ideal / constants and not taken into considerations.

5.3.5.2 Simulated Results Comparisons with Applicable Results of Past Studies

The next phase of my research is to do a practical implementation, which as can been seen would be extensive, considering the quantity of TEGs involved and the various configurations (10) as well as finding actual TEGs with the exact simulated specifications. Furthermore, vital practical aspects are to be considered and though they'll influence the practical results; notwithstanding, they'll still be treated as constants and will thus have no effect on the actual TEGs source to load maximum power transfer comparisons of the different TEGs configurations − which is the main dynamic focus of this study. So, it's reasonable to say in as much a practical implementation is necessary, it's not critical for use to validate this study aims, as basic electrical maths and simulation results validate it. Nevertheless, various past studies results relevant to my study were analysed and their findings where applicable to my study were compared and engaged as follows. In Liu *et al.* (2014a), a 500W TEG system was practically designed using 96-100 TEG modules to convert geothermal heat to power. The number of thermocouples *n* used in each TEG was 127. These are the only two parameters the same as in my study. They reported that 500W of output power was attained when the temperature difference was 200℃. My study temperature difference is 150℃. What is interesting and the more reason my study is relevant is the type of TEGs configuration used − they didn't mention it, perhaps had they used the right optimal TEG configuration with respect to the given electrical load, the generated power would've been more, hence the aim for my study. It's worth mentioning that 500W is closest to my configuration C1 (the least optimal configuration) which produces ~ 458W. I'm not sure whether this was the configuration they used as details weren't given − it would've been useful had all the technical details used were given in their study for me to compare and benchmark my study with. Similarly in Liu et al. (2014b), a 1kW TEG system was practically designed using 600 TEG modules to convert geothermal heat to power. The number of thermocouples *n* used in each TEG was 127 − this is the only technical parameter the same as mine. The temperature difference was 120℃ and lower than mine. The configuration used was not mentioned; however, they indicated that with more temperature difference, up to 2kW of power could be attained. Furthermore, they also highlighted that it's cheaper to generate the same DC power using TEGs

compared to using solar system. In Suter *et al.* (2012), a 1kW TEG power system to convert geothermal heat to electricity was modeled. The number of thermocouples *n* used in each TEG was 127 − this is the only technical parameter the same as mine. The temperature difference was 200K or 200℃ (note, temperature difference in kelvin is the same as in degree ℃). The exact configuration was not mentioned besides that it was an array of 10 - 50 of about 550 TEGs (it's worth mentioning that they didn't used TEG but TEC modules − both can be used interchangeably, though TEC if used as TEG, its hot-side maximum temperature should be below 200℃). Other studies of interest that involved use of multiple TEGs to generate power though not having the same approach, aims and specifications as my study include; Zhao *et al.* (2021) whereby the use of TEGs to recover waste heat from automobile exhaust with focus on temperature distribution, TEG module surface area and the cold-side cooling fluid (air and water) were examined; Ramírez *et al.* (2019) in which 20 TEGs in two series pairs of 10 each were used to recover heat in diesel engines with focus on temperature − with the pair of TEGs exposed to hot temperature generating more power compared to the pair of TEGs exposed to cold temperature; Orr *et al.* (2016) in which various car heat recovery systems with heat pipes were examined whereby 38 high temperature TEGs were used to generate 750W of power in a BMW car, another TEG array (quantity not mentioned) in Ford car was used to generate 400W, followed by a Renault car with a TEG array (quantity not mentioned) to produce 1kW and finally a Honda consisting of 32 TEGs to generate 500W; LaGrandeur *et al.* (2006) whereby a 750W TEG system of different thermocouple materials produced different results with more power/current produced with higher temperature on the TEG hot-side; Massaguer *et al.* (2014) in which an electro-thermal dynamics of series-parallel TEGs was modeled and experimented and the results showed the electrical interconnections of TEGs with respect to an electrical load has significant effect on their power output − supporting my study; Li *et al.* (2019) covered optimising the number of TEGs used and the distribution pattern for waste heat recovery, in which the number of TEGs (306) in a 18 x17 array were assessed and their findings portrayed that the central TEGs generate more power compared to peripheral TEGs (which have less temperature exposure) suggesting that more TEGs may not necessarily increase the output power or efficiency if poorly exposed to a hot temperature and finally Ezzitouni *et al.* (2021) investigated the mismatched when 80 series/parallel connected TEGs are used for heat recovery and revealed that connecting all TEGs in series is less efficient relative to the TEGs connected in groups of two or four as exemplified in Figure 5.24, which affirms why my C1 configuration is less efficient compared to the other configurations.

This is because connecting TEGs in series increases resistance R_t which is bad for a voltage source and therefore causes proportional power loss as heat. In Ezzitouni *et al.* (2021), it is also stated that mismatched affects TEGs power output and a particular interconnection choice depends on TEGs load, which supports my findings that the electrical load value must first be determined, thus why my study articulated an optimal TEGs configuration analysis must first be done to choose an optimal connection whose source resistance matches the load to ensure maximum power is transferred. This concludes my validation and gives a rough practical perspective considering other factors and dynamics not covered in my study. Furthermore, not every configuration aspects of my study was validated due to lack of experimented data or similar studies (which indicates originality of my study); however, the few aspects validated gave promising results and my next research will be to conduct several experiments for all ten (10) configurations and correlate my results.

5.3.6 Summary

South Africa has been experiencing electricity rationing due to an unstable national grid. Renewable energy is gaining traction to augment the grid and for personal use. As an alternative, I advance the case for thermoelectricity with focus on R_t when using multiple TEGs devices. A modest mathematical presentation for multiple TEGs was expressed, proceeded by modeling with Matlab/Simulink. The TEGs model was used to simulate and ascertain TEGs functionality. Thereafter, 100 TEGs were used in 10 different configurations C1−C10 to determine TEGs optimal configuration. It was realised that C1 at corresponding simulation time of 0.1 has the most TEG boost converter input and output voltages of ~116V but worst source resistance ($TEGRtint = R_t = 152.4\Omega$), worst TEG converter input and output powers of ~458W and ~88W respectively and worst TEG boost converter and source efficiencies of ~19% and ~16% respectively; due to most of the power wasted in the very high *TEGRtint.* C3 with $TEGRtint = R_t = 9.525\Omega$ and C4 with $TEGRtint = R_t = 6.096\Omega$, gave approximately 99% TEG boost converter efficiency and more than 50% source efficiency. C3 and C4 configurations are recommended where multiple TEGs are to be connected in series to increase the output voltage. C5 and C6 are of interests, as their $TEGRtint = R_t = R = 1.524\Omega$, which is exactly the R of a unit TEG − meaning C5 or C6 is an even setup, which simply changes a unit TEG to a bigger TEG with the same manufacturer R specification but now with more voltage and current capabilities. Also C5 and C6 have more or less the same performance, though with slight differences. C5 has a TEG boost converter efficiency of ~98.9% whereas C6 has a TEG boost converter efficiency of ~97.8%. Their respective source efficiencies are ~50.8% and 50.5%. Though C5 and C6 have been presented here differently and with slight performance differences, it's just for theoretical explanation, as in practice C5=C6 with the same setup and results. Where both high output voltage and current are paramount, C5 or C6 is recommended. C7 and C8 with respective $TEGRtint = R_t = 0.381\Omega$ and 0.024384, respectively gave a TEG boost converter efficiency of ~96.2% and

~94.6%; whereas C7 and C8 have a TEG source efficiency of ~51.11% and ~51.38% respectively. These C7 and C8 configurations are advisable where multiple TEGs are to be connected in parallel to increase the TEGs output current. Finally C10 with *TEGRtint* = R_t = 0.01524Ω gave the most output current with the highest TEGs source efficiency of ~54.3%; however, it has a TEG boost converter efficiency of ~84.5%. It should be noted that C10 R_t is approximately equal to the TEG p-n thermoelectric element resistance r of 0.012Ω; therefore, operating TEGs at this configuration will not only limit its practical performance, but will also affects it longevity due to the very high current and consequent Joule heating involved. C2 and C9 have average performances, though just respectively better than C1 and C10. It's worth mentioning that the TEGs boost converter MPP output power, voltage and current simulation times are all synchronized unlike the TEGs boost converter MPP input power, voltage and current simulation times, which are different except in C7 and C8. The TEGs boost converter / MPPT removed some ripples and stabilized the output. In sum, while it's good and tempting to functionally connect TEGs in series or in parallel to respectively increase the output voltage and current, it's better to understand their dynamics as well as the practical optimal operation points / limits and best to determine which TEGs configurations can give optimal performance. In light of this, this research findings conclude that the TEG load resistance R_L must first be established, from which different TEGs configurations can be experimented to compute different values of R_t and to determine a TEGs configuration with an optimal or suitable source resistance R_t that matches the load to ensure maximum power is transferred to it. However, in as much R_t should equals R_L to ensure transfer of maximum power, from my simulation results, TEG(s) maximum power is not transferred at exactly $R_t = R_L$ but at slightly more or less. The next logical step is to do a physical design and refine / benchmark my simulations with, taking now into considerations the physical challenges such as thermal management (over-heating)/ heat loss and the thermal resistances associated when heatsinks are added on the TEGs hot and cold sides.

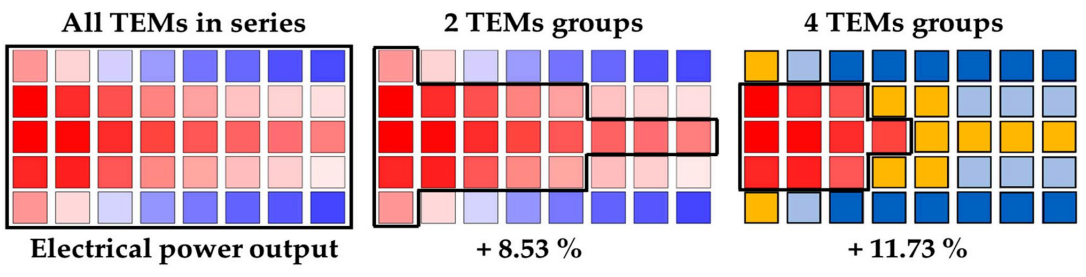

Figure 5.24: TEGs electrical connections power output in three setups (adapted from Ezzitouni *et al.*, 2021)

5.3.7 Supplementary Results

Herein contains the TEG ideal parameters (output power, voltage and current) without the TEG internal resistance (TEGRtint) − assuming it's zero (which in practice is not the case) and as well the power loss, voltage drop and current due to the TEGRtint. As evident, TEGRtint drastically increases TEG inefficiency.

Supplementary A

TEGs Configuration 1 (C1): R_t = 152.4Ω

C1 simulation result has the following settings: TEG_S=T_s=100; TEG_P=T_p=1; R_L=152.4Ω.

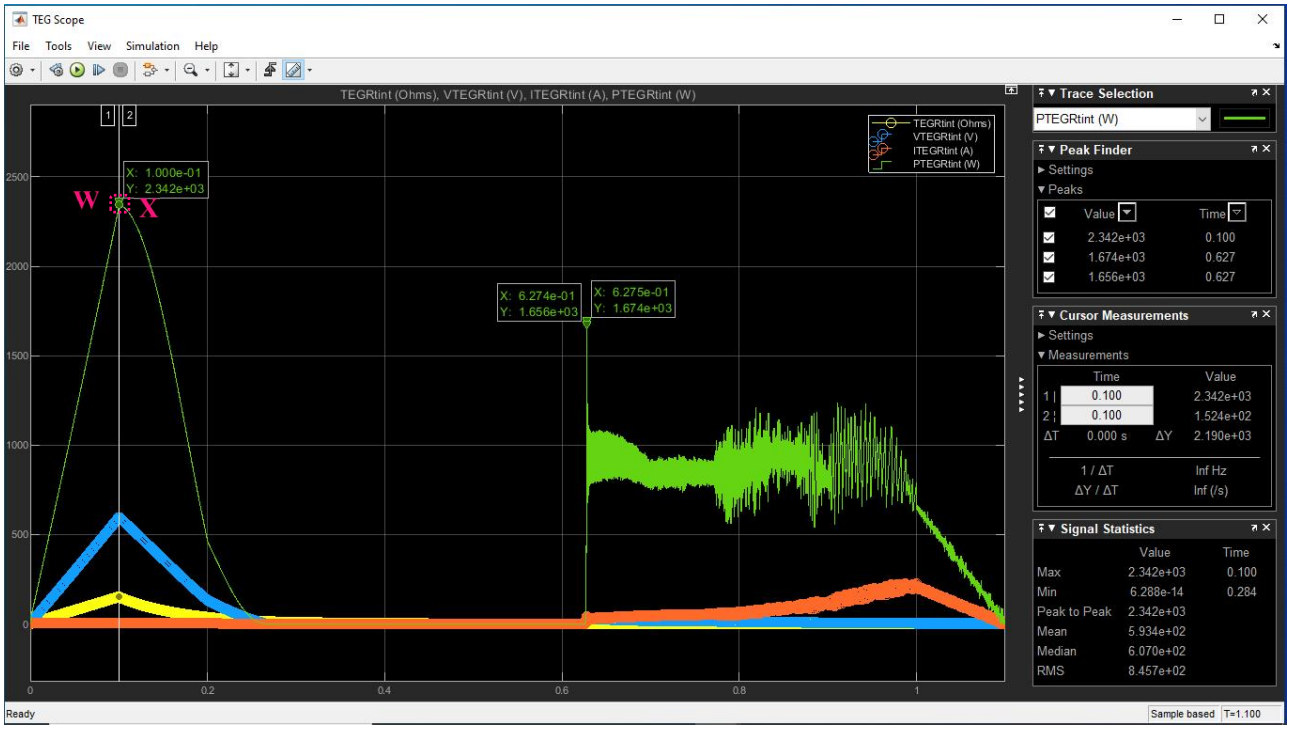

(**a**)

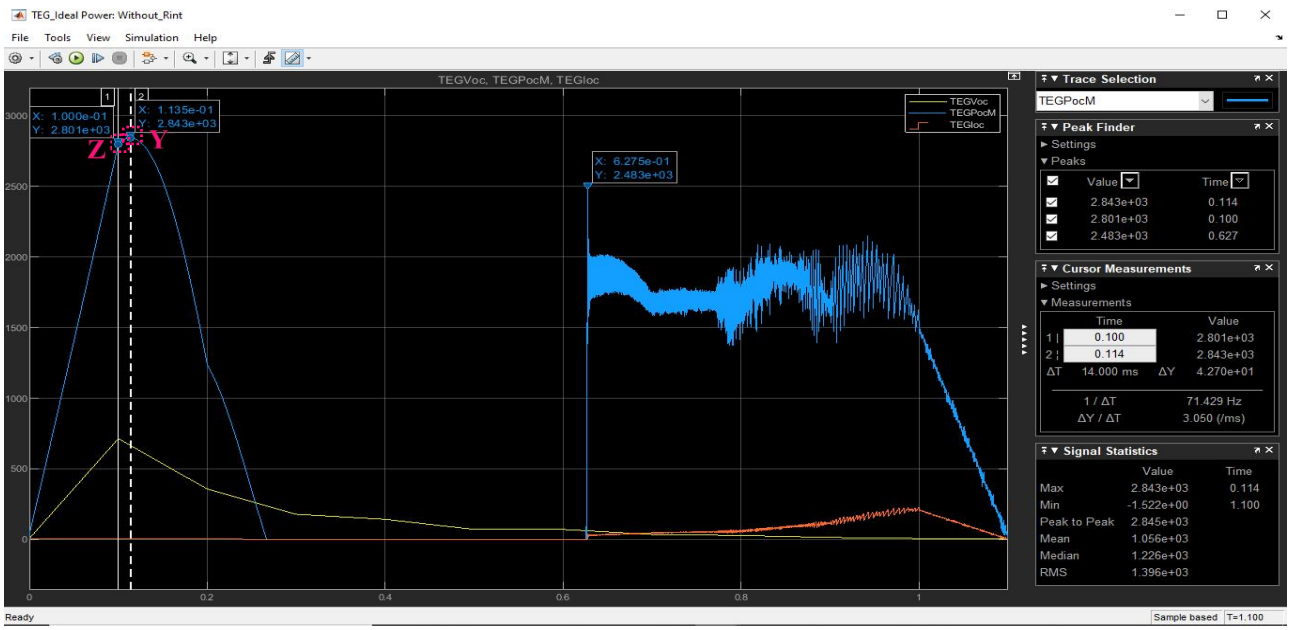

(**b**)

Figure 5.25: TEGs configuration 1; R_t = R_L = 152.4Ω simulation results − note the points of interest highlighted W to Z: (**a**) TEGs internal resistance (i.e. R_t), power, voltage and current; (**b**) TEGs ideal power, voltage and current.

Supplementary B

TEGs Configuration 2 (C2): $R_t = 38.1\Omega$

C2 simulation result has the following settings: $TEG\_S=T_s=50$; $TEG\_P=T_p=2$; $R_L=38.1\Omega$.

(**a**)

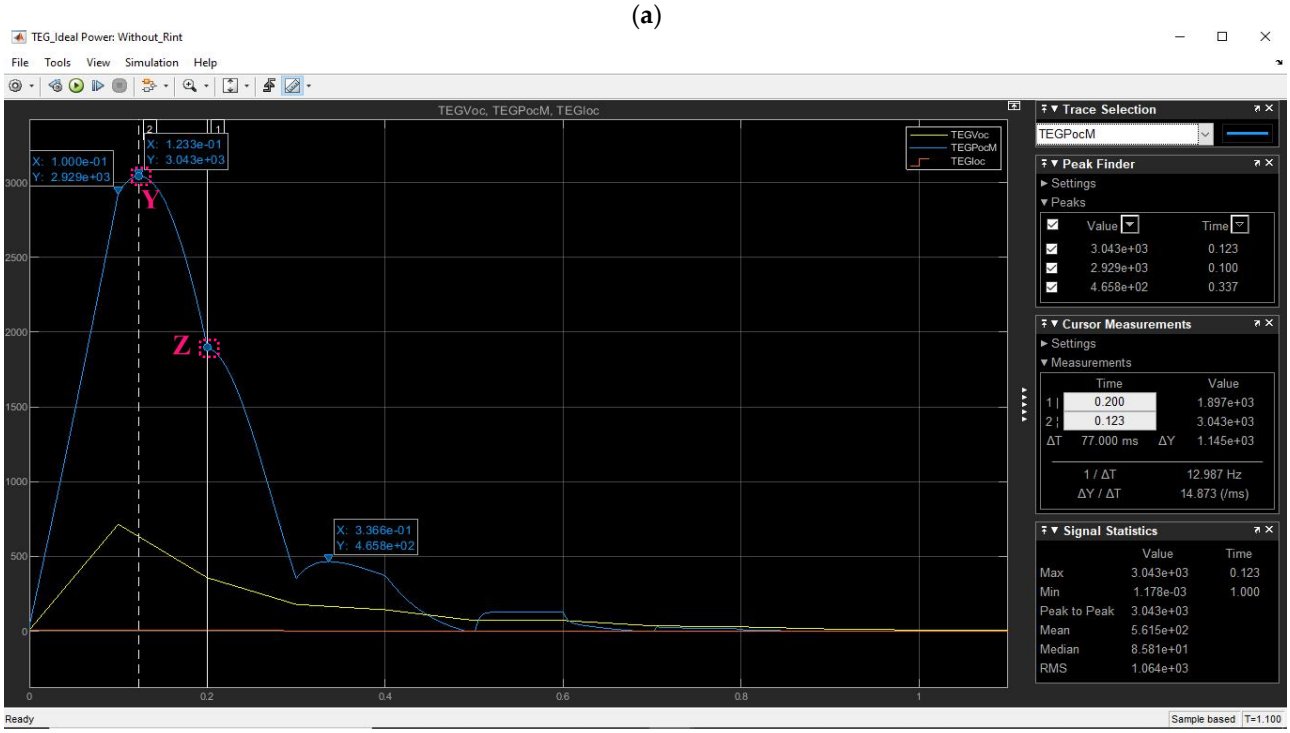

(**b**)

Figure 5.26: TEGs configuration 2; $R_t = R_L = 38.1\Omega$ simulation results − note the points of interest highlighted W to Z: (**a**) TEGs internal resistance (i.e. R_t), power, voltage and current; (**b**) TEGs ideal power, voltage and current.

Supplementary C

TEGs Configuration 3 (C3): $R_t = 9.525\Omega$

C3 simulation result has the following settings: $TEG\_S=T_s=25$; $TEG\_P=T_p=4$; $R_L=9.525\Omega$.

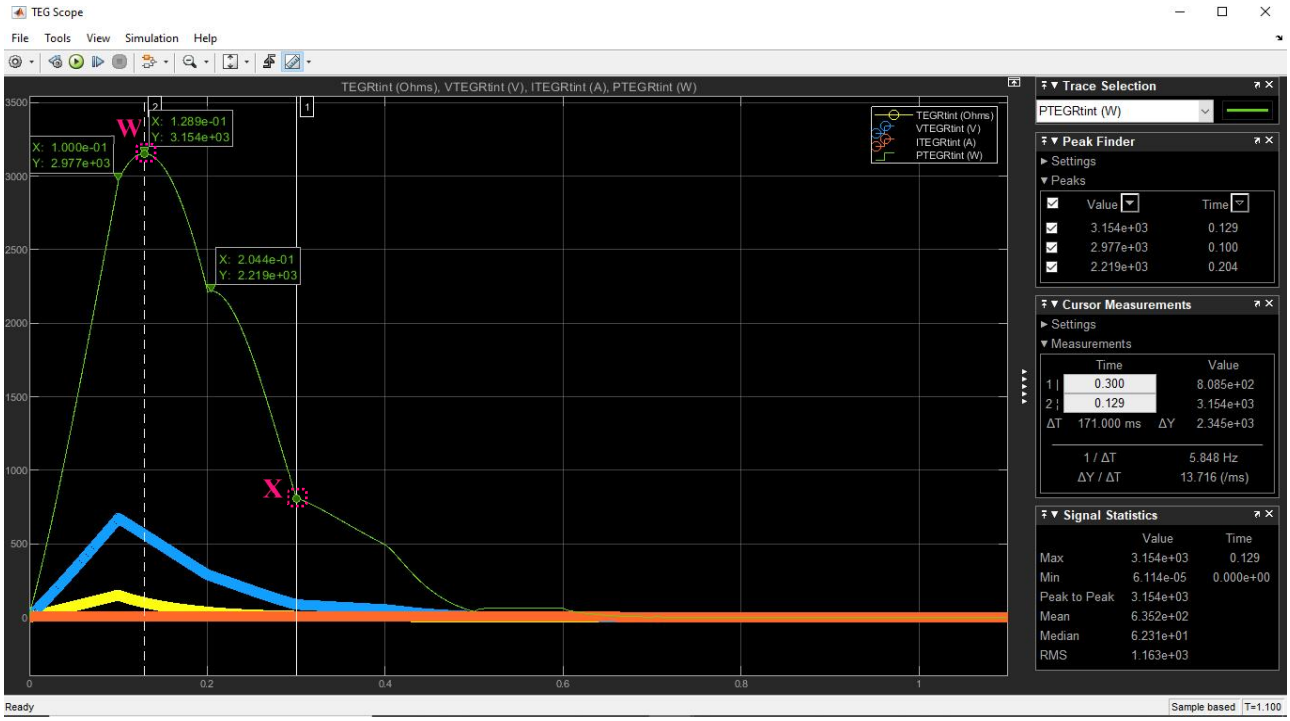

(**a**)

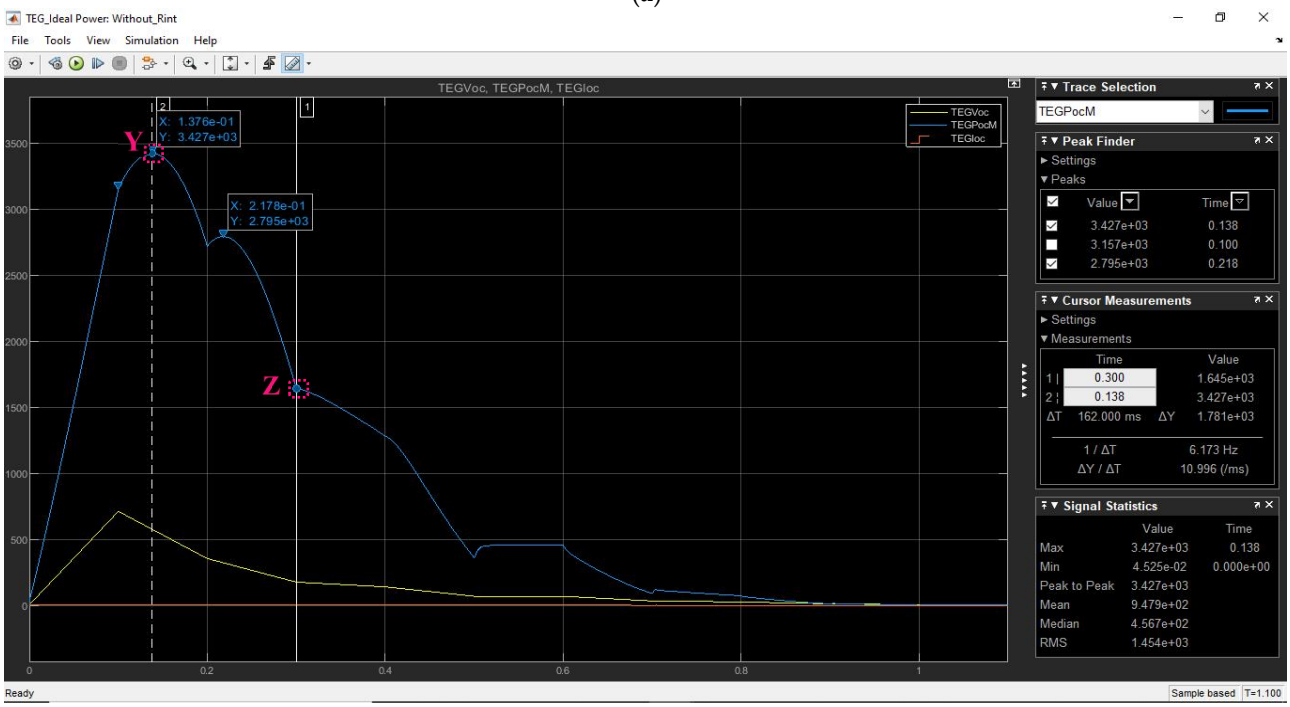

(**b**)

Figure 5.27: TEGs configuration 3; $R_t = R_L = 9.525\Omega$ simulation results − note the points of interest highlighted W to Z: (**a**) TEGs internal resistance (i.e. R_t), power, voltage and current; (**b**) TEGs ideal power, voltage and current.

Supplementary D

TEGs Configuration 4 (C4): $R_t = 6.096\Omega$

C4 simulation result has the following settings: $TEG\_S=T_s=20$; $TEG\_P=T_p=5$; $R_L=6.096\Omega$.

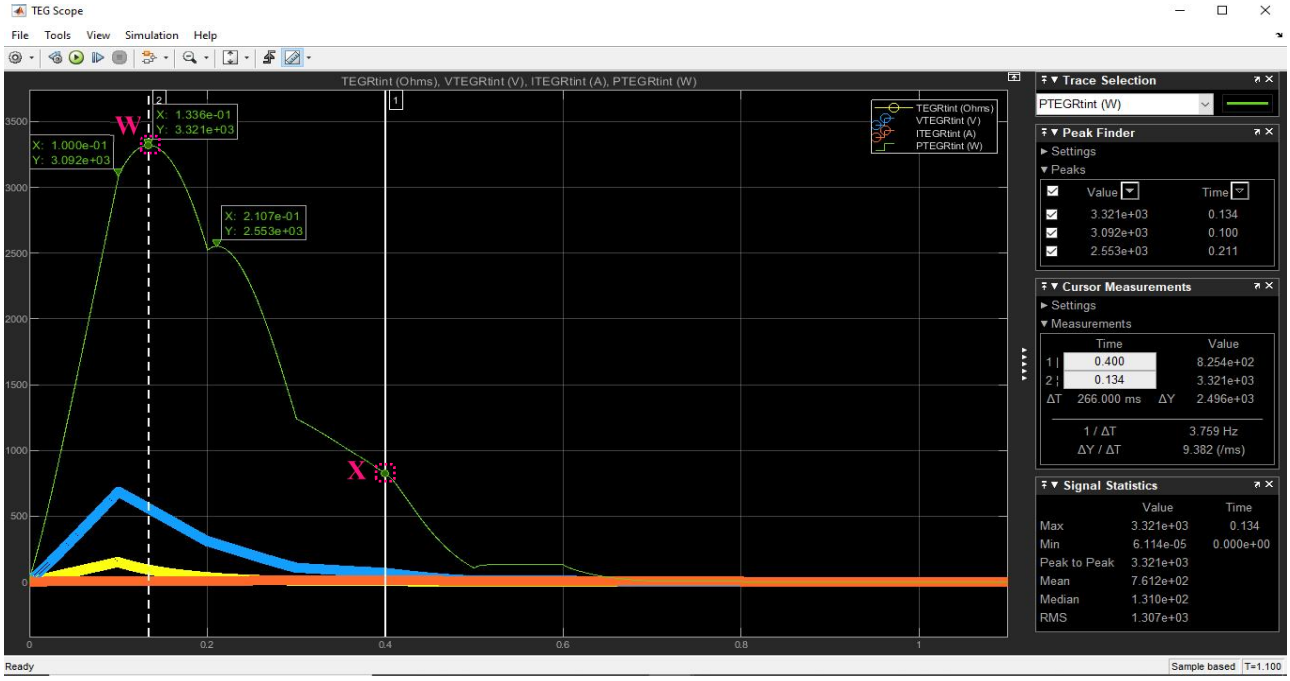

(**a**)

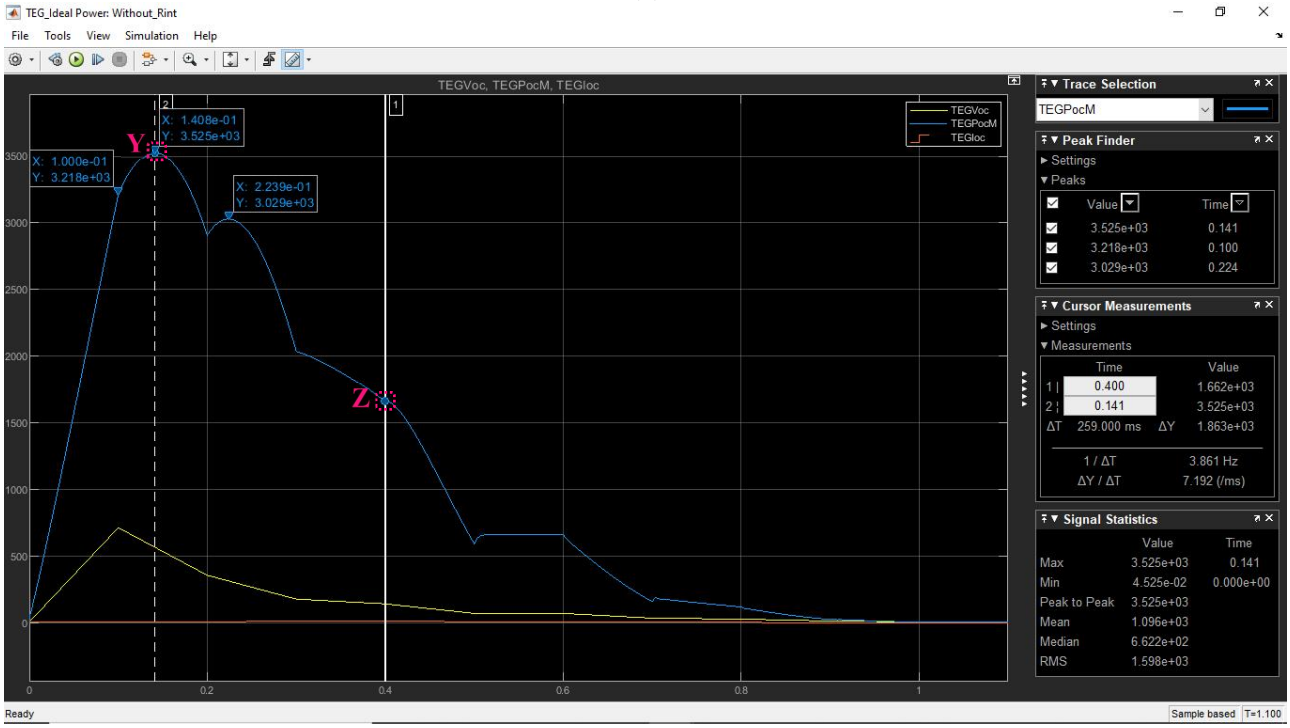

(**b**)

Figure 5.28: TEGs configuration 4; $R_t = R_L = 6.096\Omega$ simulation results − note the points of interest highlighted W to Z: (**a**) TEGs internal resistance (i.e. R_t), power, voltage and current; (**b**) TEGs ideal power, voltage and current.

Supplementary E

TEGs Configuration 5 (C5): R_t = 1.524Ω

C5 simulation result has the following settings: TEG_S=T_s=10; TEG_P=T_p=10; R_L=1.524Ω.

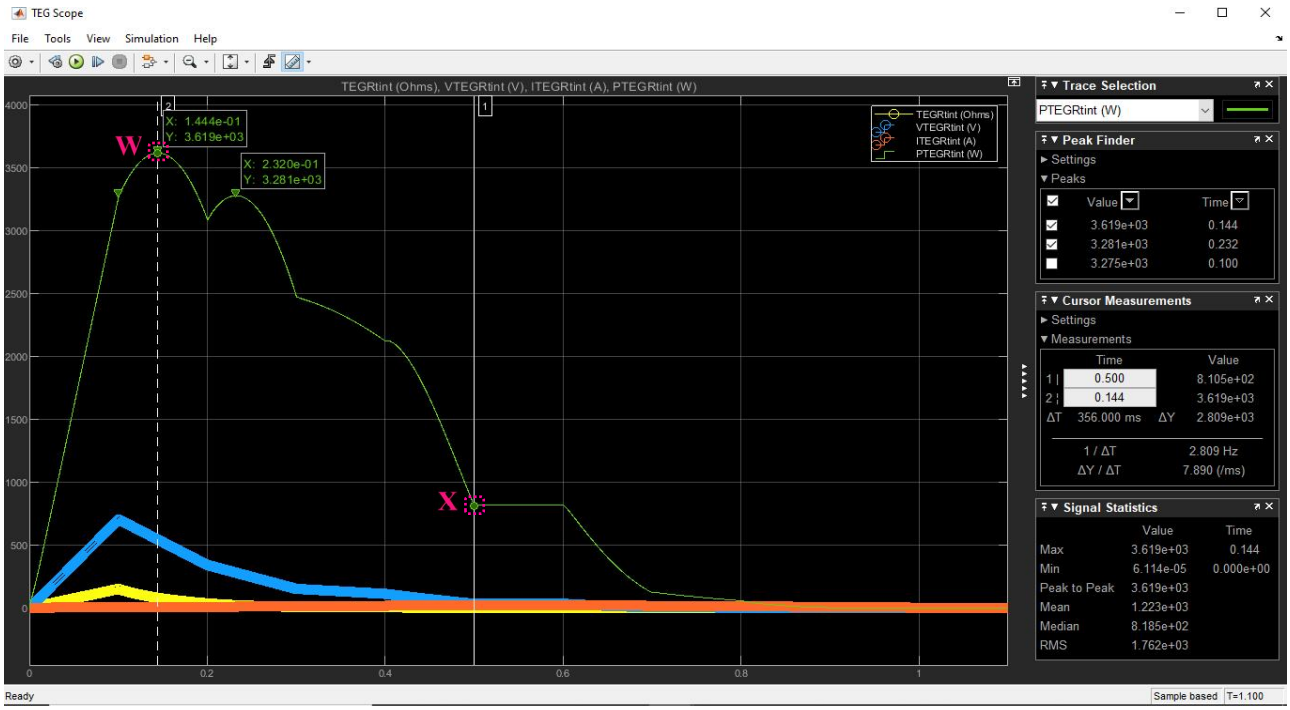

(**a**)

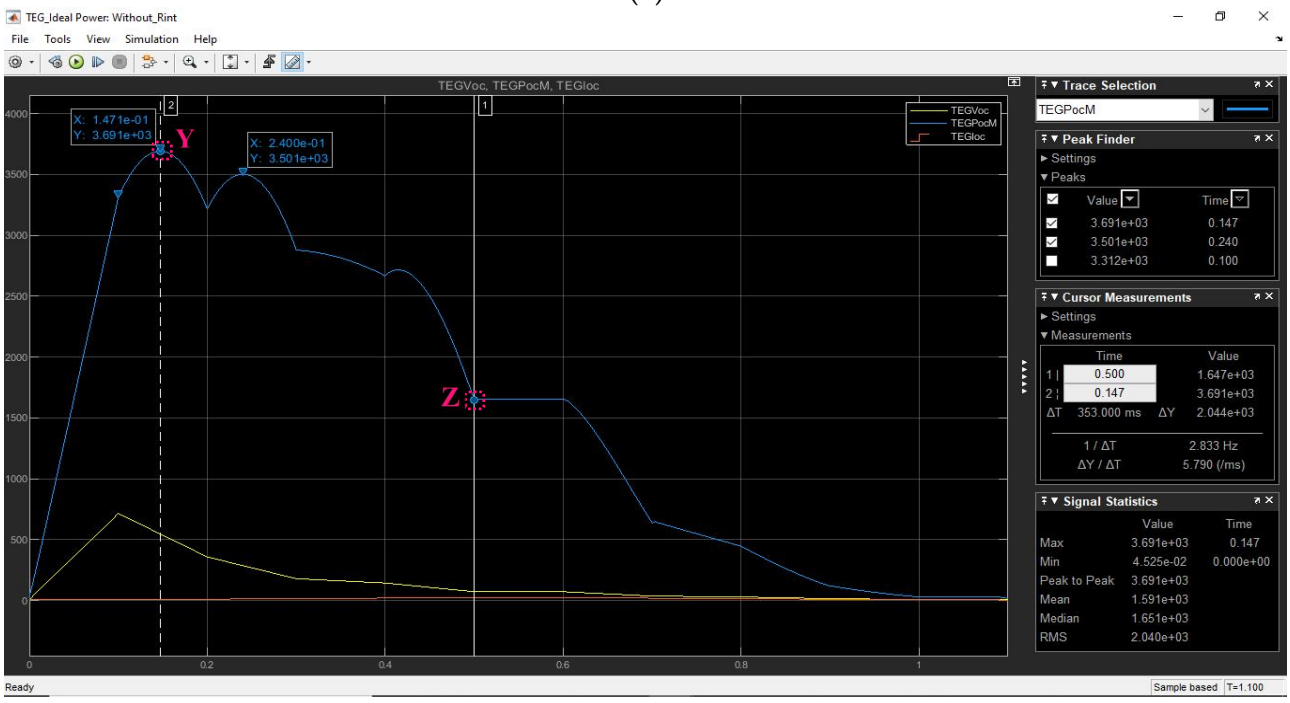

(**b**)

Figure 5.29: TEGs configuration 5; R_t = R_L = 1.524Ω simulation results − note the points of interest highlighted W to Z: (**a**) TEGs internal resistance (i.e. R_t), power, voltage and current; (**b**) TEGs ideal power, voltage and current.

Supplementary F

TEGs Configuration 6 (C6): R_t = 1.524Ω

C6 simulation result has the following settings: $TEG\_S=T_s=10$; $TEG\_P=T_p=10$; R_L=1.524Ω.

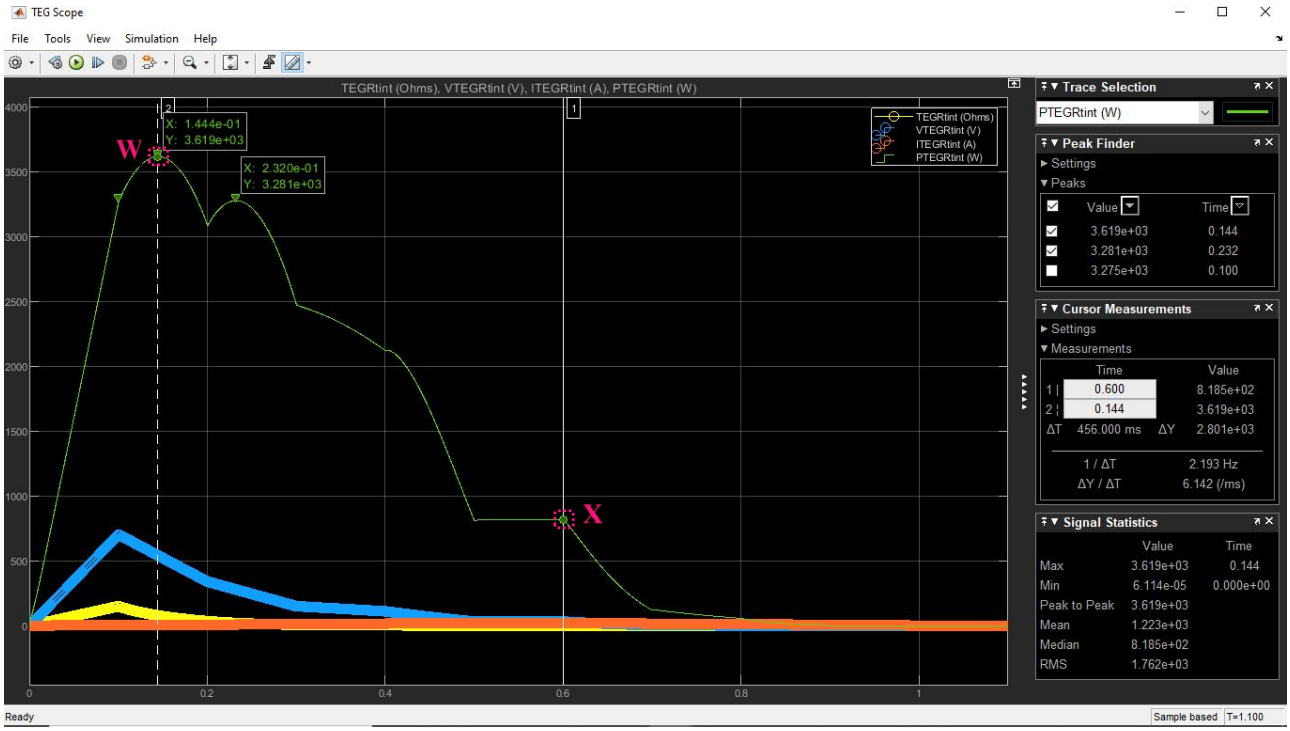

(**a**)

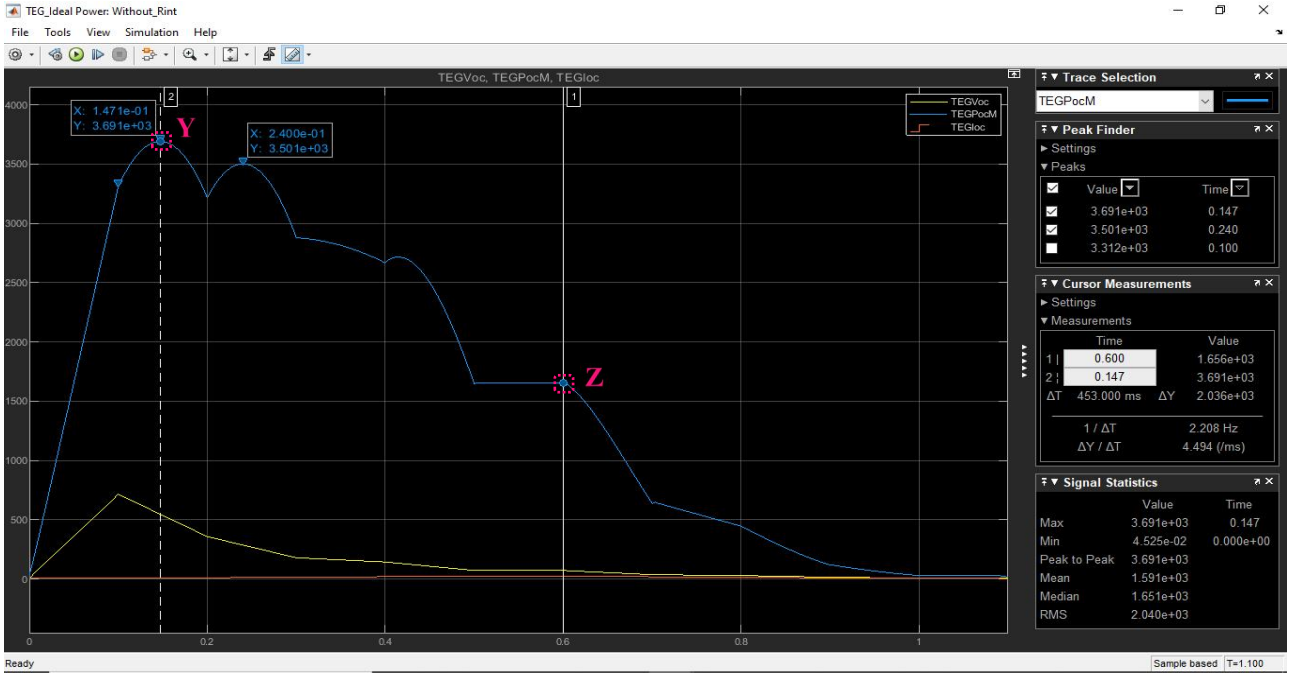

(**b**)

Figure 5.30: TEGs configuration 6; $R_t = R_L$ = 1.524Ω simulation results − note the points of interest highlighted W to Z: (**a**) TEGs internal resistance (i.e. R_t), power, voltage and current; (**b**) TEGs ideal power, voltage and current.

Supplementary G

TEGs Configuration 7 (C7): $R_t = 0.381\Omega$

C7 simulation result has the following settings: $TEG\_S=T_s=5$; $TEG\_P=T_p=20$; $R_L=0.381\Omega$.

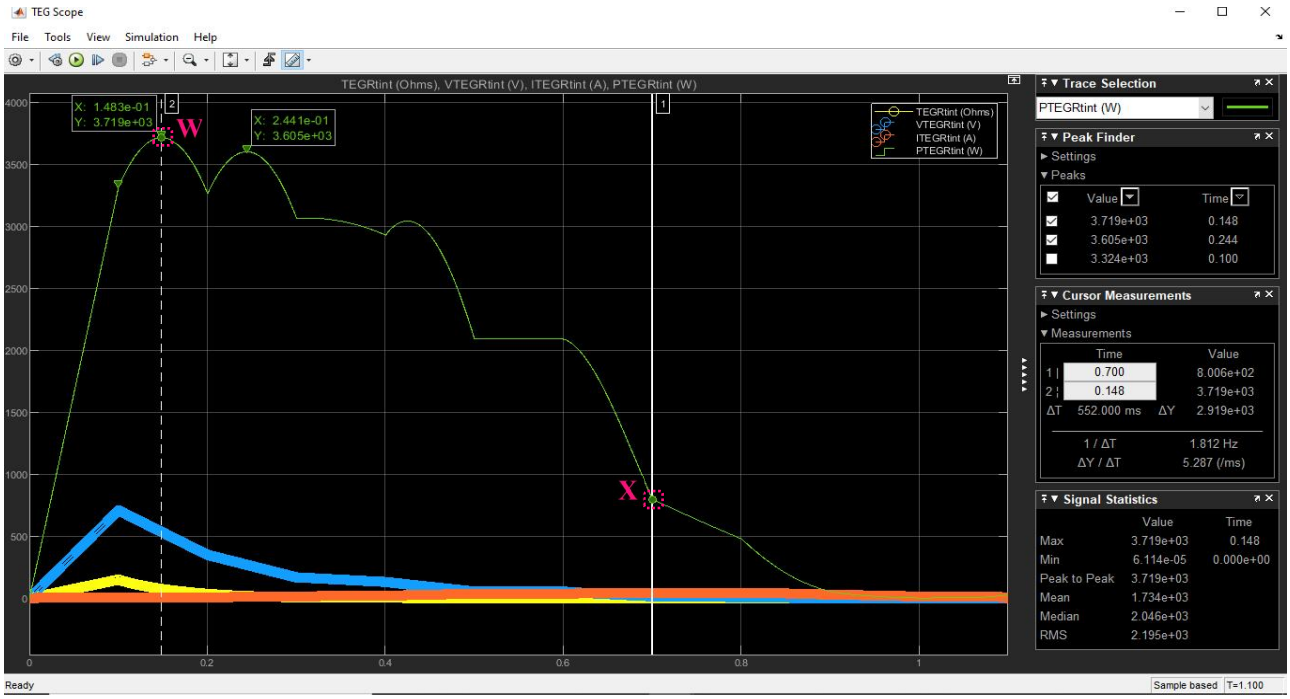

(**a**)

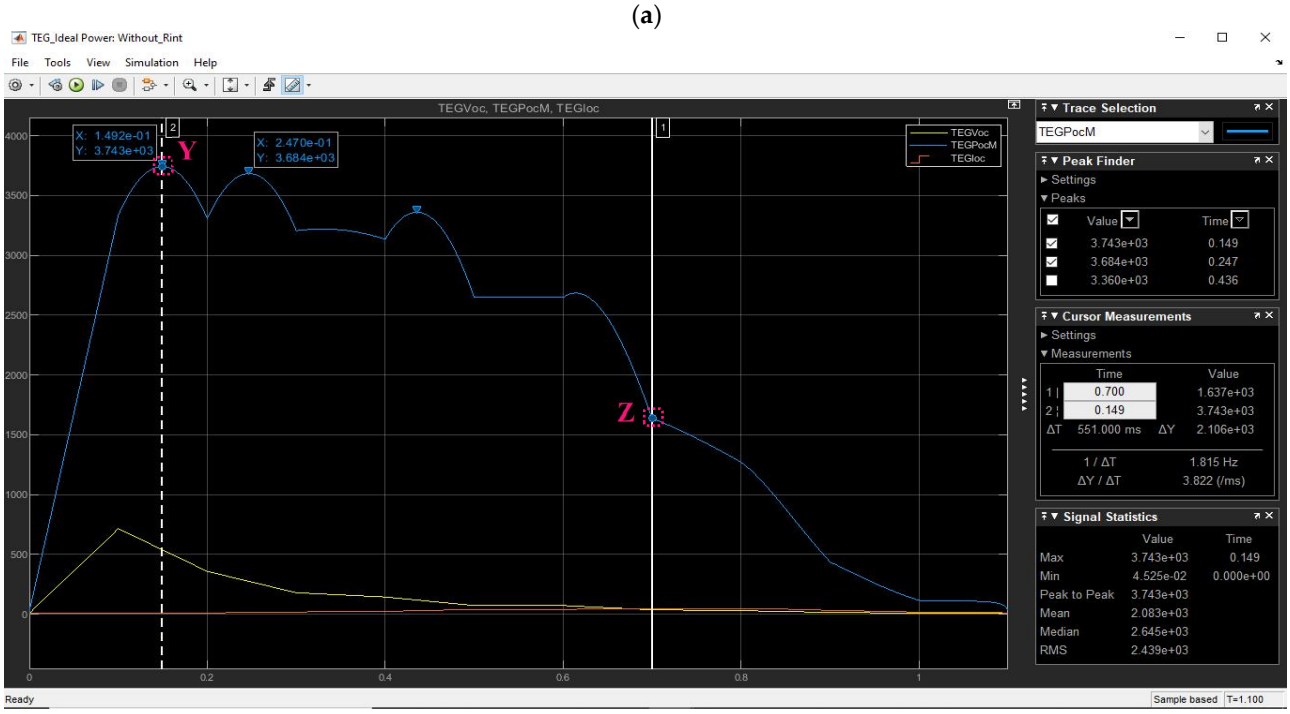

(**b**)

Figure 5.31: TEGs configuration 7; $R_t = R_L = 0.381\Omega$ simulation results − note the points of interest highlighted W to Z: (**a**) TEGs internal resistance (i.e. R_t), power, voltage and current; (**b**) TEGs ideal power, voltage and current.

Supplementary H

TEGs Configuration 8 (C8): R_t = 0.24384Ω

C8 simulation result has the following settings: $TEG\_S=T_s=4$; $TEG\_P=T_p=25$; R_L=0.24384Ω.

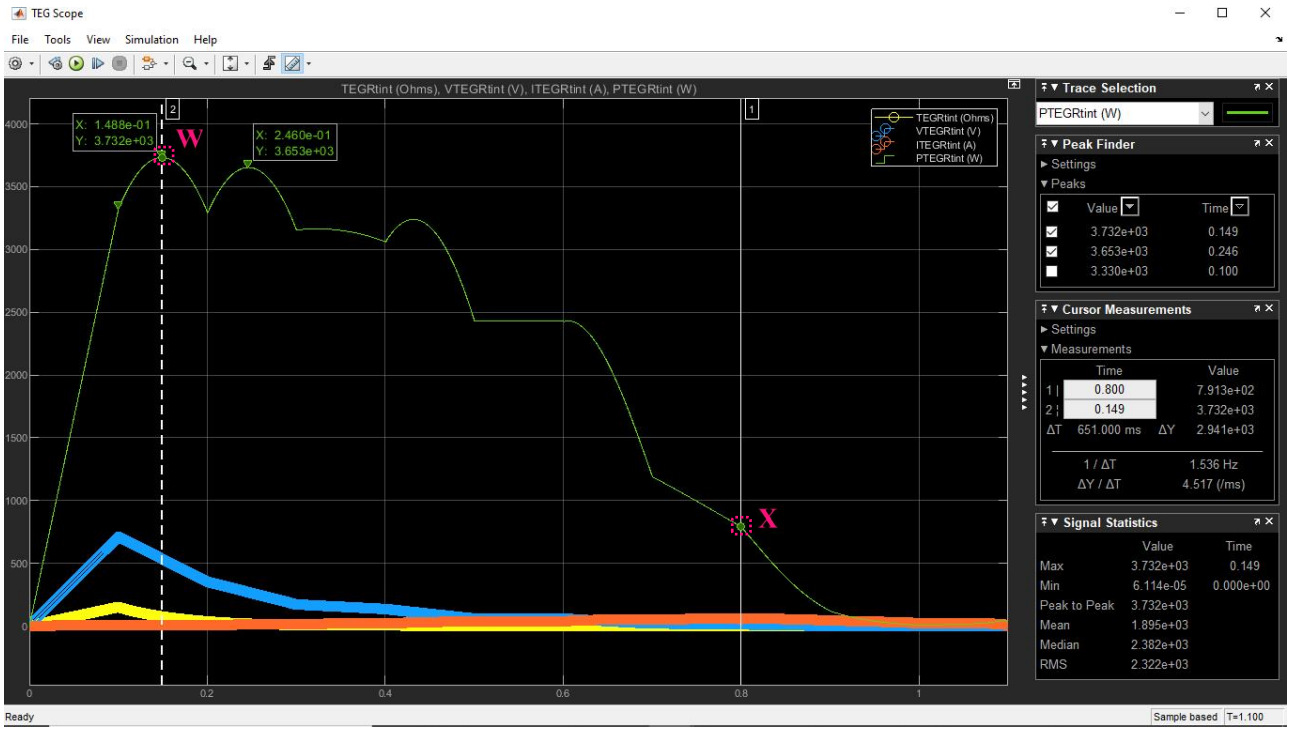

(**a**)

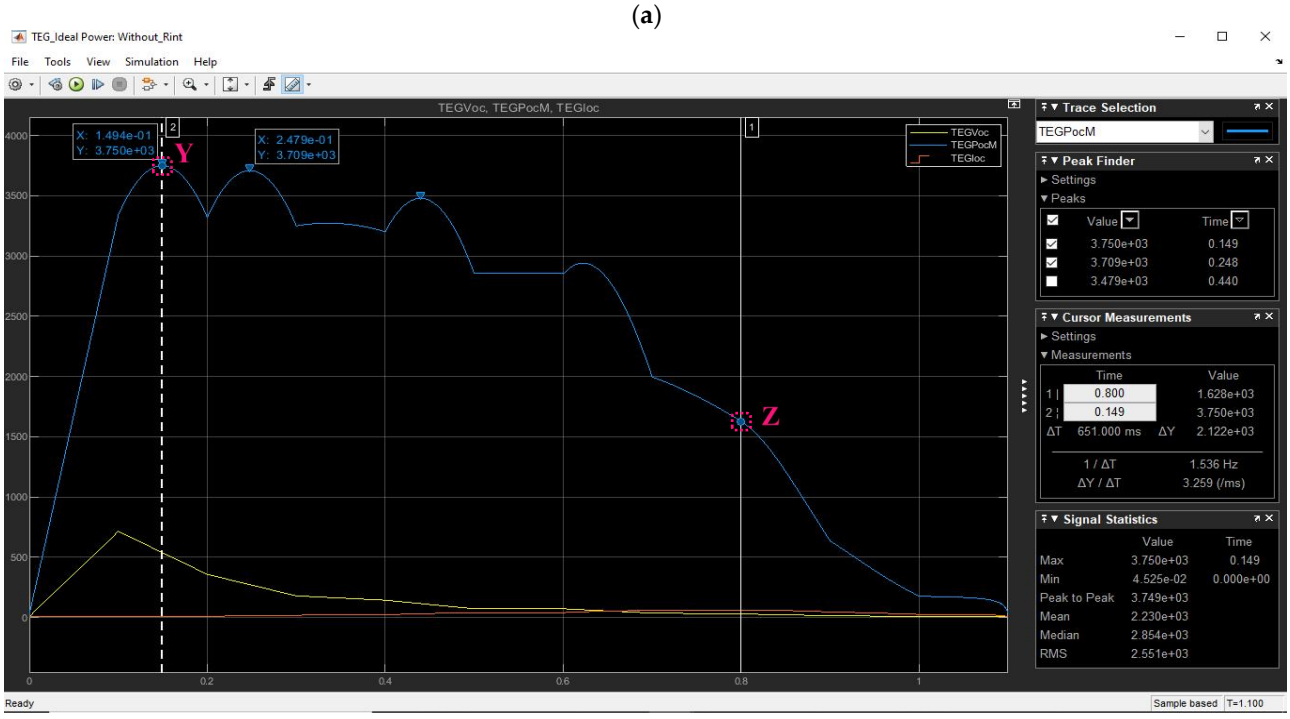

(**b**)

Figure 5.32: TEGs configuration 8; $R_t = R_L$ = 0.24384Ω simulation results − note the points of interest highlighted W to Z: (**a**) TEGs internal resistance (i.e. R_t), power, voltage and current; (**b**) TEGs ideal power, voltage and current.

Supplementary I

TEGs Configuration 9 (C9): R_t = 0.06096Ω

C9 simulation result has the following settings: $TEG\_S=T_s=2$; $TEG\_P=T_p=50$; R_L=0.06096Ω.

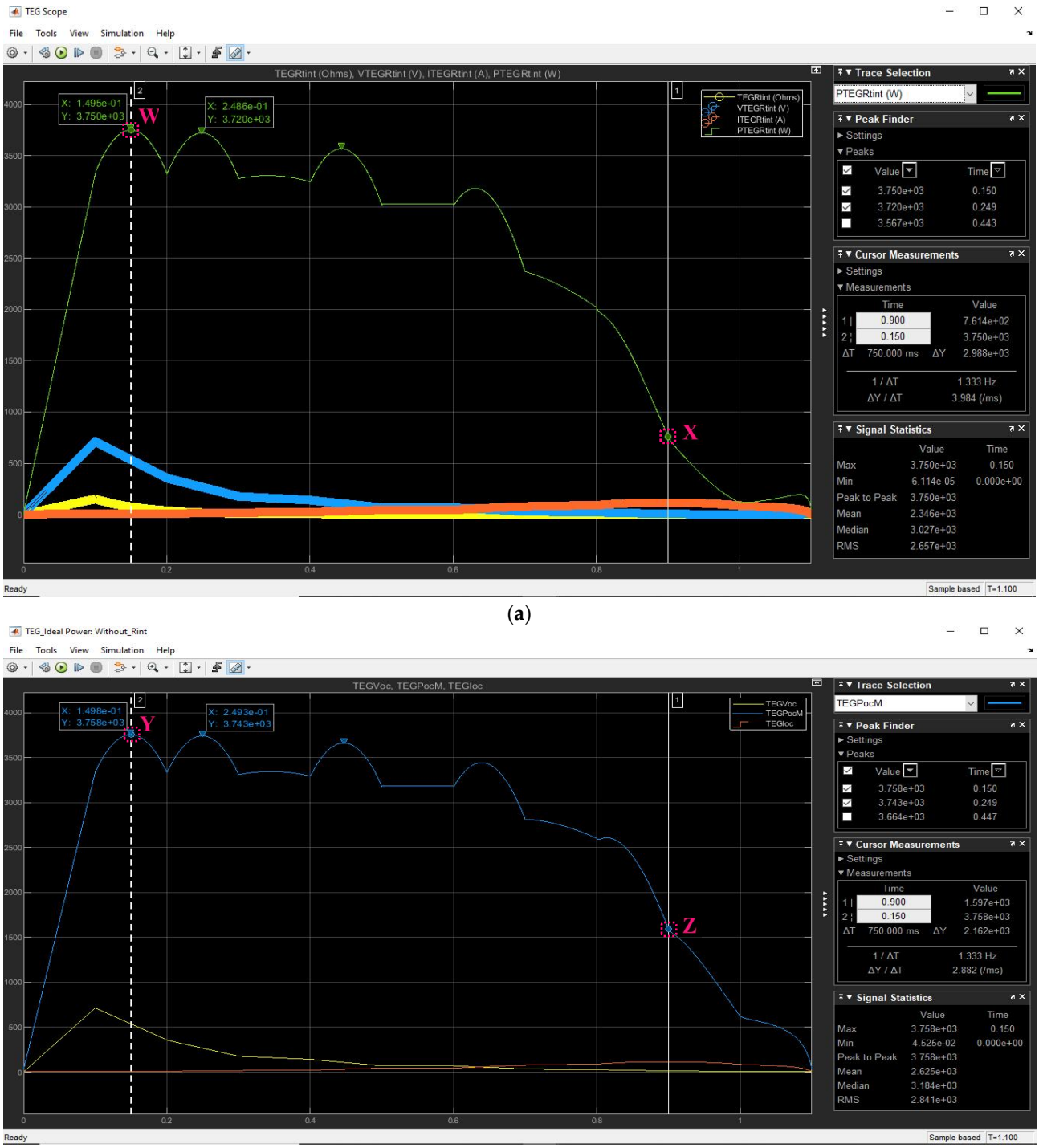

(**a**)

(**b**)

Figure 5.33: TEGs configuration 9; $R_t = R_L$ = 0.06096Ω simulation results − note the points of interest highlighted W to Z: (**a**) TEGs internal resistance (i.e. R_t), power, voltage and current; (**b**) TEGs ideal power, voltage and current.

Supplementary J

TEGs Configuration 10 (C10): $R_t = 0.01524\Omega$

C10 simulation result has the following settings: $TEG\_S = T_s = 1$; $TEG\_P = T_p = 100$; $R_L = 0.01524\Omega$.

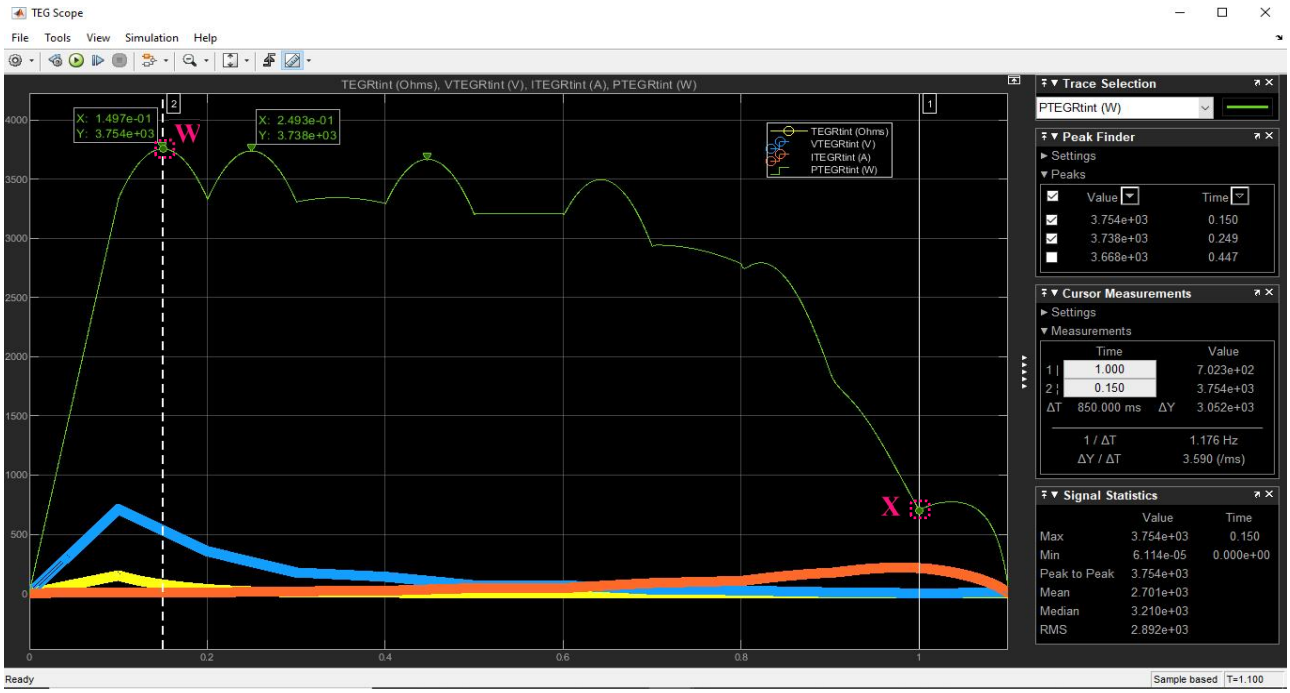

(**a**)

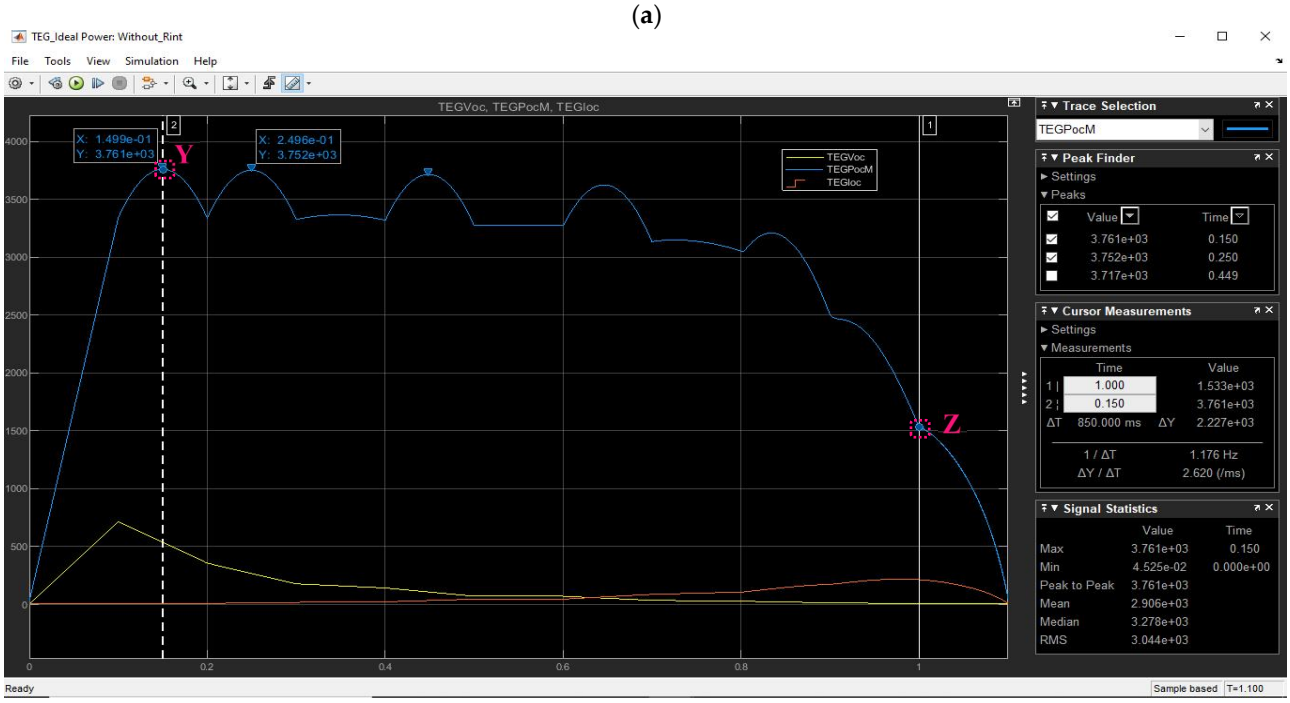

(**b**)

Figure 5.34: TEGs configuration 10; $R_t = R_L = 0.01524\Omega$ simulation results − note the points of interest highlighted W to Z: (**a**) TEGs internal resistance (i.e. R_t), power, voltage and current; (**b**) TEGs ideal power, voltage and current.

CHAPTER 6

GENERAL DISCUSSIONS and CONCLUSIONS

6.1 Overview

Sustainable energy is unarguably becoming the future for energy security especially in the developing world and in this regards Africa and South Africa in this context. In light of this, my research was set out to examined the problem of energy inefficiency associated with hybrid energy systems and proffer improved solutions. An extensive literature review was conducted on CCHP systems, fuel cells, thermoelectricity and power converters as well as energy management systems to understand the research problem better and to establish best practices that can be applied to offer alternative solutions. Furthermore, thermoelectricity with focus on TEG and TEC was primal to my research and was theoretically treated in details and all the highlights of the several findings realised, are herein holistically discussed to summarise and conclude my research merits.

6.2 My Review Articles / Publications Summary Discussions and Conclusions

My review article on combined cold, heat and power (CCHP) systems and fuel cells (FCs) commenced by stating the prevailing electricity crisis in South Africa as basis for the study. Thirty four CCHP systems including the internal combustion engine (ICE), the Stirling engine, biomass, micro-turbine, solar and biogas, photovoltaic (PV) and gas-turbine, wind turbine, photovoltaic and micro-turbine, solid oxide and phosphoric acid fuel cells (FCs), ICE and thermoelectric generator (TEG), low temperature (LT) polymer electrolyte membrane (PEM), inlet air throttling gas-turbine, ground source heat pump (GSHP) micro gas-turbine and PV, ICE and GSHP, ICE with dehumidification and refrigeration, 5kW PEM FC, thermoelectric cooler (TEC) and LT PEM FC, Stirling engine and molten carbonate fuel cell, organic Rankine cycle (ORC), solar thermal (ST), geothermal, integrated energy systems (IES), power and heat storage systems, energy conversion systems, thermodynamic and thermo-economic optimization strategies, working fluids based on Hydrogen, Helium as well as Ammonia, H2O, CO2 etc were investigated and from these CCHP system types reviewed, the fuel cells based CCHP Systems were of most interests and particularly PEM FC. Consequently, FCs were further investigated whereby the popular six kinds of FCs were compared from which the PEM FC was preferred because of its practical popularity. However, PEM FC like all FCs, are susceptible to FCs fuel starvation phenomenon and therefore, six fuel cells assisted schemes were examined, from which the fuel cell assisted

with super-capacitor and battery technique is the most widely applied. In sum, the study significance entails investigations of assorted CCHP systems, FCs and their novelties and applications thereof to formulate a unique research model of an innovative alternative energy efficient CCHP system based-on fuel cells, Li-ion battery, ultra-capacitor and thermoelectricity as well as energy management system using Matlab and Simulink.

My review paper on thermoelectricity began by introducing the ongoing South Africa electricity crisis followed by thermoelectricity, in which eighteen miscellaneous applicable case studies were structurally analysed in detailed. The aim was to establish best practices for the R&D of an efficient thermoelectric (TE) and fuel cell (FC) CCHP system. The examined literature reviews, covered studies that focused on thermoelectricity principle, highlighting TE devices basic constructions, TEGs and TECs as well as investigations on the applications of thermoelectricity with FCs, whereby thermoelectricity was applied to recover waste heat from FCs to boost the power generation capability by ~7 – 10%. Furthermore, non-stationary TEGs whose generated power can be increased by pulsing the DC-DC power converter, showed that an output power efficiency of 8.4% is achievable and that thicker TEGs with good area coverage can efficiently harvest waste heat energy in dynamic applications. TEG and TEC exhibit duality and the higher the TEG temperature difference, the more the generated power – which can be stabilised using MPPT technique with a 1.1% tracking error. A comparison study of TEG and solar energy demonstrated that TEG generates more power compared to solar cells of same size, though more expensively. TEG output power and efficiency in a thermal environment can be maximised simultaneously if its heat flux is stable but not the case if its temperature difference is stable. The review concluded with a TEC LT-PEM-FC hybrid CCHP system capable of generating 2.79kW of electricity, 3.04kW of heat and 26.8W of cooling with a total efficiency of ~77% and fuel saving of 43.25%. The aforementioned presentation was the contribution brought forward, as it heuristically highlighted miscellaneous thermoelectricity studies / parameters of interests in a single manuscript, which further established that practical applications of thermoelectricity is possible and can be innovatively applied together with FC for efficient CCHP applications − this endorsed my research hypothesis.

My review manuscript on power converters and EMS for fuel cells CCHP applications started by highlighting that energy insecurity and electrical energy in particular, is a progressive pressing societal crisis in South Africa and Africa. In this regard, the article articulated a structural review of forty four different power converters and EMS research case studies to reasonably choose and develop a suitable FC power converter

and EMS scheme for a hybrid FC CCHP system for households / commercial applications. From the review, it was observed that the power converters based on IBC / variants and as well isolated boost converters were of interests. IBC are simple, more robust, good for ripples reduction and peak power applications. However, the fundamental IBC topology is not isolated and adding isolation transformers offers protection but increases the costs and size. Likewise, EMS techniques can be grouped under rule-based, learning-based and optimization-based but the most popular EMS strategy used with power converters are the MPPT and PI controller. Furthermore, FCs can also be modularized with each FC sub-module having its own power converters and EMS scheme to increase the system efficiency. In sum, there is no method that is flawless − choosing a particular approach and trading-off different features depend on the targeted applications and the research objectives; whether to maximize efficiency, robustness, safety, performance etc and minimize costs, size, noise, complexity etc. For my research project, power converters based-on IBC variants and BDC with EMS based on MPPT and or PID controller for use with FC, Li-ion battery, ultra-capacitor and thermoelectric devices were considered to investigate further the postulated CCHP system. The contributions brought forward are i) an apt single reference study that presents a quick topological insight and synopsis of assorted FCs power converters as well as EMS and ii) my proffered FC CCHP system undergoing research to offer an innovative energy efficient solution for basic household energy (electricity, heating, cooling and lighting).

In summary, the various literature reviews covered an extensively examined and structurally presented CCHP systems, fuel cells, thermoelectricity, power converters and EMS articulations. The crux of a CCHP system lies in its prime mover, from which FC based types and in particular PEM FC and specifically HT-PEM-FC CCHP system is of interest. The FC fuel starvation phenomenon and popularly applied solutions were examined and an alternative solution using thermoelectricity which doubles as a FC-TE hybrid CCHP system is proposed. However, FCs and TEG power sources are low voltage DC and are unstable; therefore necessitates inclusion of power converters as well as EMS and storage capabilities to enable reliable connection to a load for maximum power transfer. In these regards, some key pros and cons were advanced as my research findings, which were used to model the postulated FC-TE CCHP system in a bid to devise an efficient model that can be used to implement and develop further a practical innovative FC CCHP system.

6.3 My Research Articles / Publications Summary Discussions and Conclusions

My publication on TEG modeling started by briefly introducing the ongoing electricity crisis in South Africa followed by the assorted renewable energy and power sources provisions as the innovative solutions being sought after, with keen focus on waste heat and in particular low grade waste heat which is abundantly produced in various settings and notably in domestic, commercial, industrial, vehicles and appliances. This low grade waste heat energy sources make them suitable for use with TEG – a thermoelectric device that converts heat to DC electricity based-on Seebeck effect. The mathematical analysis of thermoelectricity with emphasis on TEG was examined, developed and elaborately presented to determine how much power can be generated and from what optimal TEG parameters. A unique TEG model in Matlab / Simulink was developed incorporating these improvements and the advance implementation was also simulated with realistic TEG specifications from different manufacturers and the generated results confirmed that, to get maximum output power (P_o) and efficiency (η) from TEGs, ΔT must be highest, which will increase the output current I until it has no confirmatory effect on η. These outcomes were analysed in conformity with information reported in scholarly TEGs publications and datasheets. The research highlights were asserted as the scientific contributions to conclude the study. The recommendation is to practically implement my research findings to correlate the TEG mathematical and simulated analyses, whereby the TEG(s) shall be used with fuel cells to innovatively and efficiently convert waste heat to power in a larger FC-CCHP system.

My paper on TEC modeling began by also briefly introducing the ongoing electricity crisis in South Africa followed by the diverse renewable energy / power sources being commissioned as potential solutions. However, some of these energy/power sources are not apt for heavy loads, one of which is heat pumps – it is therefore prudent to devise energy efficient coolers and of interest is TEC – a thermoelectric device that converts power to cold based-on Peltier effect. This low power DC load makes its many cooling applications suitable for use with renewable power. The mathematical analysis of thermoelectricity with emphasis on TEC(s) was investigated, developed and extensively expressed to determine how much heat absorption (Q_c) and CoP can be produced and from what optimal TEC parameters. A novel TEC model in Matlab / Simulink was implemented incorporating these advancements and the original TEC implementation was simulated by using realistic TEC specifications from various TECs manufacturers and the generated results affirmed that, to get max cooling power (Q_c) and CoP from TECs, ΔT must be lowest and input current I should be increased

until it has no affirmative effect on Q_c. These results were analysed in consistency with information published in diverse scholarly TECs articles, books and datasheets. Highlights of the study were asserted as the scientific contributions to conclude the research. The recommendation is to practically implement my research findings to correlate the TEC simulated and mathematical analyses, whereby the TEC(s) shall be used with fuel cells to efficiently generate cold from DC power in a larger combined cooling, heating and power (CCHP) system.

My article on TEG with heatsinks modeling started by stating South Africa has been facing unreliable electrical power supply which is becoming unbearable and sustainable energy is transcending to be the future and to complement the national grid and for private use. As a result, I researched thermoelectricity as an alternative energy source (TEG) for household applications requiring low DC power and lighting. However, practical TEG use requires heatsinks to work efficiently and reliably but regrettably adding heatsinks add thermal resistances, which consequently degrades the TEG efficiency as well as its output power. I investigated various techniques, especially dimensional analysis and shortlisted the approach by Lee (2013) − which converts thermal resistance to convection conductance, making it easier for practical use. However, the formulations in Lee (2013) could not find the exact analytical formulas to directly calculate T_{s1} and T_{s2}; as a result, he used numerical analysis (a bit cumbersome) which I developed further by introducing *DTs* to simplify and derive novel simple and accurate analytical formulas that can be applied to compute T_{s1} and T_{s2} directly. Furthermore, these simple formulas were further simplified to obtain simpler analytical equations for T_{s1} and T_{s2}. Finally, my simplest T_{s1} and T_{s2} formulas and their optimal relationships were established. These formulas were all verified with chosen optimal values and all gave approximate results that correlated each other. I further used these newly introduced formulas to model, numerically simulate and plotted various characteristics curves of Q_{s1}, Q_{s2}, P_{os}, T_{s1}, T_{s2} and *Eff** against R_r vs N_k vs *DTs* using Matlab and Simulink. These results were articulated variously in both 2D and 3D plots and finally the outcomes were comparatively discussed and validated among each other and as well with results asserted in Lee (2013). In Lee (2013), P_{os} of 0.045 is optimal with N_k=0.3 at R_r=1.7, contrary to my study which gave optimal P_{os} of 0.0474483 at N_k=0.25 using my simple equations; however, using my simpler equations, it gave optimal P_{os} of 0.0716775 at N_k=0.3. Notwithstanding, my simple equations gave P_{os} of 0.0451302 at N_k=0.3 (though not optimal in my case) which corresponds exactly to optimal P_{os} value of 0.045 with N_k=0.3 as in Lee (2013). In addition, the magnitude of P_{os} and *Eff** are more (almost doubled) using my simpler equations, compared to using my simple equations.

Furthermore, the optimal values of P_{os} and Eff^* using both my "simple" and "simpler" equations, respectively occurred at different values of R_r. In sum, Eff^* is best at very low N_k values. The highlights of this study were marked in the various presented figures and tables and it's worth mentioning that, DTs=0.8 for this set of optimal values, is rightly only equal to T_{s1} - T_{s2} = ~0.8 only at R_r=1.7 and N_k=0.3 as optimally established and not at any other values when used in both my simple and simpler equations. Finally, in as much as my newly introduced simpler analytical formulas for T_{s1} and T_{s2} didn't give P_{os} and Eff^* results correlating those in Lee (2013) and that of my newly introduced analytical simple equations (that gave accurate results the same as those in Lee, 2013), I suggest my simpler equations can always be used as first approximation to quickly find T_{s1} and T_{s2} values as well as Q_{s1} and Q_{s2} values which have been accurately validated using my simple equations and also with Lee (2013). In sum, T_{s1} and T_{s2} are the most vital, as they are those that can be easily practically manipulated to achieve the other values; however, first ascertaining the electrical load or R_r value is most paramount to achieve optimal result, as a TEG as well TEC, are non-linear devices whose dynamics must be well understood before embarking on a practical design − which is the recommended next phase of my research, to validate and refine the study practically and then to implement a 1kW household CCHP system.

My manuscript on TEC with heatsinks modeling began by briefly highlighting the ongoing South Africa energy crisis and the need for renewable energy/power sources and as well energy efficient loads. As a result, alternative energy based on thermoelectricity and with focus on TEC was investigated to determine optimal TEC design with heatsinks when considering a good practical implementation. However, heatsinks introduce thermal resistances which negatively affect the TEC performance. Dimensional analysis, in particular the approach that easily converts TEC thermal conductance to convection conductance was researched as the optimisation tact to facilitate an optimal practical design. I developed this method from Lee (2013) and introduced new analytical formulas to compute the TEC optimal dimensionless cold and hot sides temperature. These formulas were verified using analytical, numerical and graphical solutions with the aid of an easy TEC with heatsinks model implemented using Matlab and Simulink. The optimal results were validated with Lee (2013) research using TEC manufacturers typical parameters value used in the industry. These outcomes define the research impacts, from which a physical design can be done and the new TEC model benchmark with for further use to devise and implement a clean energy efficient cooling and or heating device or system.

My paper on TEGs and TECs optimal operation point investigation started by noting South Africa has been experiencing electrical power outages which is getting worst during winter periods and sustainable energy is becoming popular to supplement the grid and for private use. In view of this, i proffer thermoelectricity as an alternative energy source (TEGs) as well as an energy efficient load (TECs) for household applications that require low DC power, cooling and heating. However, TEG and TEC require multiple units connected in series and or in parallel to provide decent output and cooling powers respectively. Usually, the perception would be trying to utilise more with the hope to get more power; however, my findings assert this is not really the case, as i) TEG and TEC temperature difference ΔT and current parameters have performance dynamics which must be operated within strict optimal operation limits to guarantee efficiency and ii) TEGs and TECs total internal resistance R_t changes − increases when connected in series and decreases when connected in parallel; hence, the overall power / efficiency will be affected, especially if the source and load resistances are not matched to transfer maximum power. In essence, my research major contributions herein include a structured meticulous mathematical presentations with focus on TEG and TEC modules total resistance R_t, when more than one TEG and TEC module are connected in series and or in parallel combinations, followed by a detailed TEGs and TECs modeling using Matlab / Simulink. Forbye, the implemented TEGs and TECs models were used to simulate and investigate some thermoelectricity profound parameters performance dynamics, R_t losses and to validate some of their optimal operation points with industry standard models.

My article on TEGs optimum electrical configuration, as usual indicated South Africa has been experiencing electricity rationing due to an unstable national grid. Renewable energy is gaining traction to augment the grid and for personal use. As an alternative, I advance the case for thermoelectricity with focus on R_t when using multiple TEGs devices. A modest mathematical presentation for multiple TEGs was expressed, proceeded by modeling with Matlab/Simulink. The TEGs model was used to simulate and ascertain TEGs functionality. Thereafter, 100 TEGs were used in 10 different configurations C1−C10 to determine TEGs optimal performance. It was realised that C1 at corresponding simulation time of 0.1 has the most TEG boost converter input and output voltages of ~116V but worst source resistance ($TEGR_{tint} = R_t = 152.4\Omega$), worst TEG converter input and output powers of ~458W and 88W respectively and worst TEG boost converter and source efficiencies of ~19% and ~16% respectively; due to most of the power wasted in the very high $TEGR_{tint}$. C3 with $TEGR_{tint} = R_t = 9.525\Omega$ and C4 with $TEGR_{tint} = R_t = 6.096\Omega$, gave about 99% TEG boost converter efficiency and more than 50% source efficiency. C3 and C4 configurations are recommended where multiple

TEGs are to be connected in series to increase the output voltage. C5 and C6 are of interests, as their $TEGR_{tint} = R_t = R = 1.524\Omega$, which is exactly the R of a unit TEG − meaning C5 or C6 is an even setup, which simply changes a unit TEG to a bigger TEG with the same manufacturer R specification but now with more voltage and current capabilities. Also, C5 and C6 have more or less the same performance though with slight differences. C5 has a TEG boost converter efficiency of ~98.9% whereas C6 has a TEG boost converter efficiency of ~ 97.8%. Their respective source efficiencies are ~50.8% and 50.5%. Though C5 and C6 have been presented here differently and with slight performance differences, it's just for theoretical explanation, as in practice C5=C6 with the same setup and results. Where both high output voltage and current are paramount, C5 or C6 is recommended. C7 and C8 with respective $TEGR_{tint} = R_t = 0.381\Omega$ and 0.024384, respectively gave a TEG boost converter efficiency of ~96.2% and 94.6%; whereas C7 and C8 have a TEG source efficiency of ~51.11% and ~51.38% respectively. These C7 and C8 configurations are advisable where multiple TEGs are to be connected in parallel to increase the TEGs output current. Finally C10 with $TEGR_{tint} = R_t = 0.01524\Omega$ gave the most output current with the highest TEGs source efficiency of 54.3%; however, it has a TEG boost converter efficiency of ~84.5%. It should be noted that C10 R_t is approximately equal to the TEG p-n thermoelectric element resistance r of 0.012Ω; therefore, operating TEGs at this configuration will not only limit its practical performance, but will also affects it longevity due to the very high current and consequent Joule heating involved. C2 and C9 have average performances, though just respectively better than C1 and C10. It's worth mentioning that the TEGs boost converter MPP output power, voltage and current simulation times are all synchronized unlike the TEGs boost converter MPP input power, voltage and current simulation times, which are different except in C7 and C8. The TEGs boost converter / MPPT removed some ripples and stabilized the output. In sum, while it's good and tempting to functionally connect TEGs in series or in parallel to respectively increase the voltage and current outputs, it's better to understand their dynamics as well as the practical optimal operation points / limits and best to determine which TEG configurations can give optimal performance. In light of this, this research findings concluded that the TEG load resistance R_L must first be established, from which different TEGs configurations can be experimented to compute different values of R_t and to determine a TEGs configuration with an optimal or suitable source resistance R_t that matches the load to ensure maximum power is transferred to it. However, in as much R_t should equals R_L to ensure transfer of maximum power, from my simulation results, TEG(s) maximum power is not transferred at exactly $R_t = R_L$ but at slightly more or less − which is due to the linear (at low current) and non-linearity (at high current) of TEGs.

CHAPTER 7

RECOMMENDATIONS

7.1 Overview

One of the biggest shortcoming of my research was the lack of practical implementations, because of CPUT's procurement department not being able to process and buy the components on time to enable the physical experimentation. The bill of materials was submitted in January / February 2021 but the procurement was done only around June / July 2021! So, hopefully CPUT's procurement department also becomes efficient in future!

7.2 Future Research

Once the components are bought, the next logical step shall be to do a physical design and refine / benchmark my simulations with, by taking into considerations physical challenges such as thermal management (over-heating) and the thermal resistances associated by adding heatsinks on the TEGs and TECs sides as well as temperature fluctuations on the TEGs and TECs. Figures 7.1 - 7.4 exemplify the preliminary concept designs of some of the practical setups of the experiments that were to be conducted to validate my Matlab models.

Furthermore, various large scale practical applications of TEGs and TECs were examined and in light of the results, future work will include embarking on a practical pilot 1kW implementation of a CCHP system as an alternative renewable energy option to the energy crisis for households and small commercial establishments. Should resources permit, a HT PEM FC shall be the prime mover in addition to other low grade heat sources.

Model-based designs with hardware-in-the-loop shall also be performed, in which the software models implemented in Matlab and Simulink can be optimised and converted to tokenised firmware and finally to hardware. The idea is to have a CCHP systems or some of its components on a chip (field programmable gate array), where the various parameters can be tested and optimised in real-time as if it was the real system or components. Achieving this will speed developments time and costs as well as realisation of a more efficient and robust CCHP system, which is more flexible and advanced. It should be noted that this was one of the objectives of my research and was part of the topic but left out due to the components procurement problem. So, hopefully, this becomes another interesting future research aspect and surely be made a reality!

Experiment 1: Investigating the effect of TEG modules RESISTANCE in Series, Series & Parallel and Parallel configurations with all the TEG setups having the same SQUARE dimension

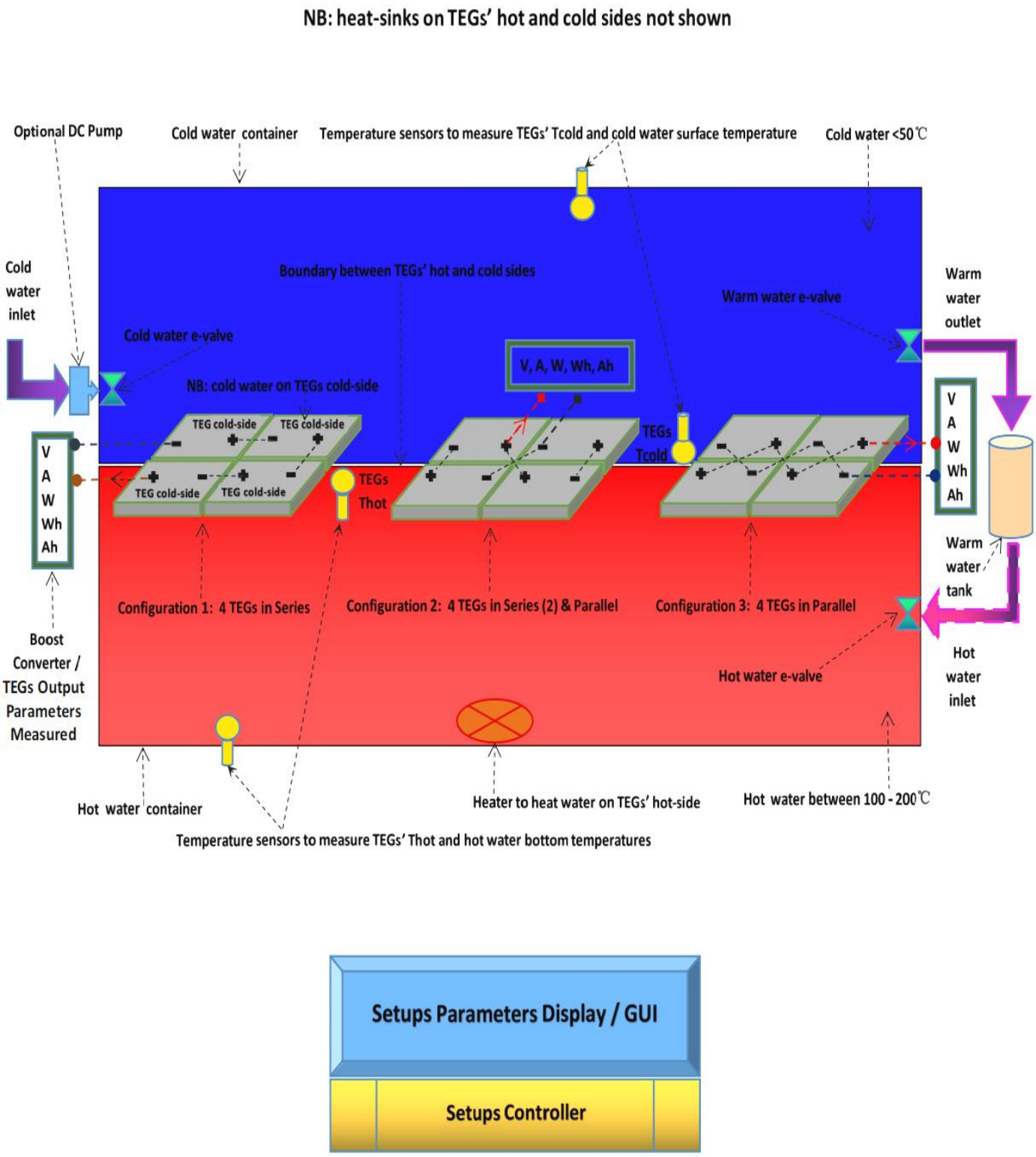

Figure 7.1: Investigating TEGs in different electrical configurations with all the TEGs having the same square setup dimension

Experiment 2: **Investigating the effect of TEG modules RESISTANCE in Series, Series & Parallel and Parallel configurations with all the TEG setups having same RECTANGULAR dimension**

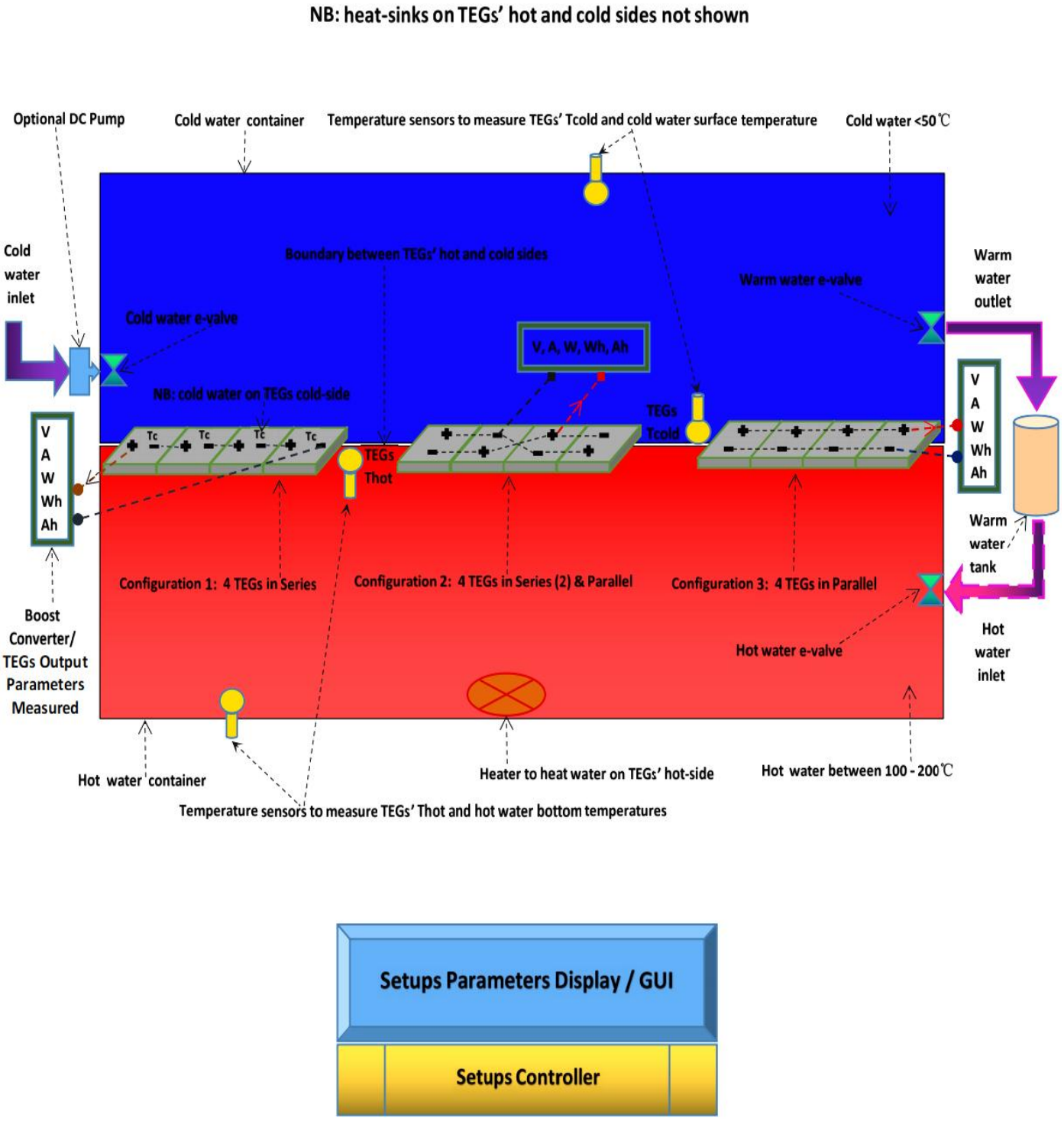

Figure 7.2: Investigating TEGs in various electrical configurations with all the TEGs having the same rectangular setup dimension

Experiment 3: Investigating the effect of TEC modules RESISTANCE in Series, Series & Parallel and Parallel configurations with all the TEC setups having the same SQUARE dimension

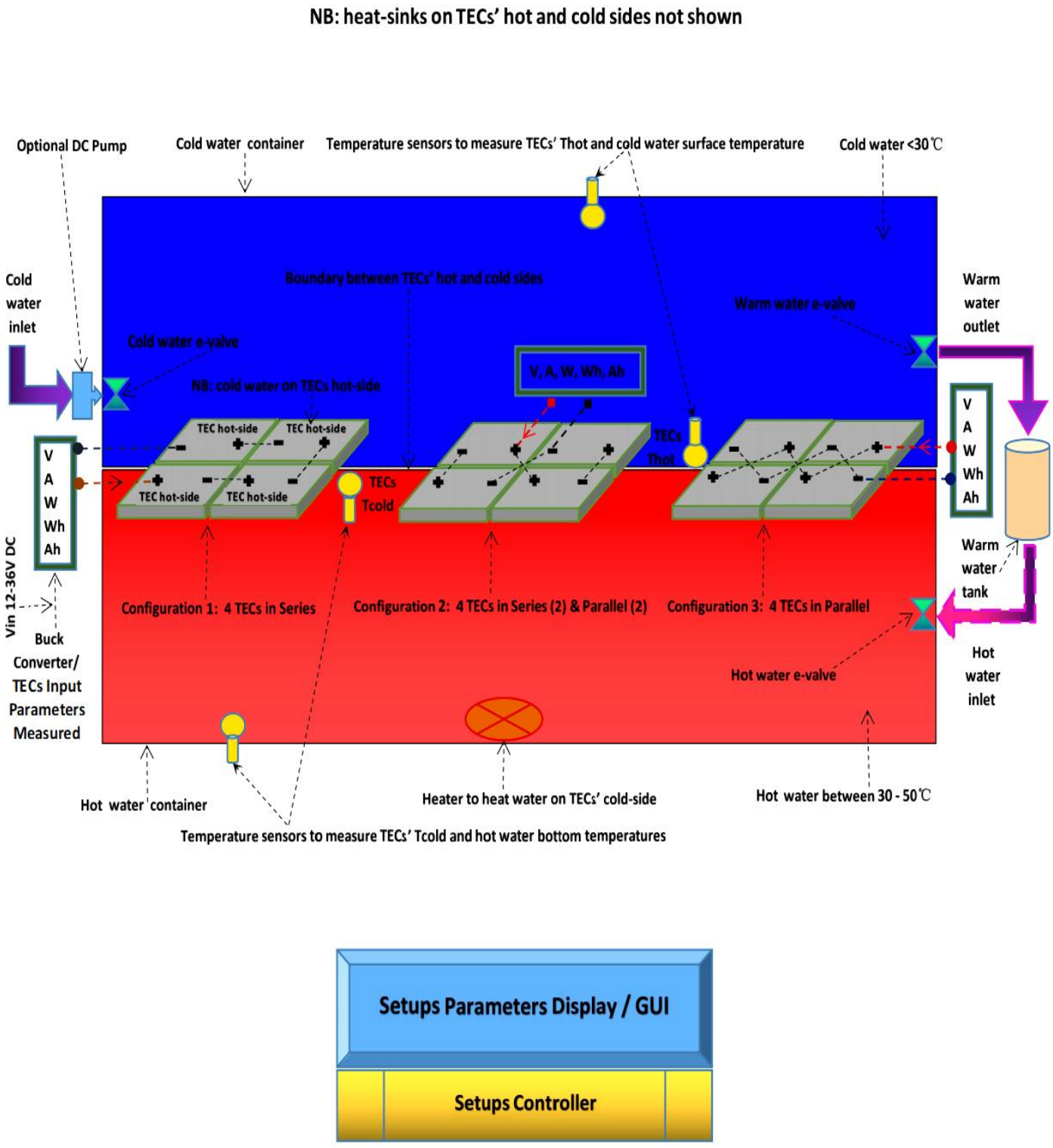

Figure 7.3: Investigating TECs in different electrical configurations with all the TECs having the same square setup dimension

Experiment 4: Investigating the effect of TEC modules RESISTANCE in Series, Series & Parallel and Parallel configurations with all the TEC setups having same RECTANGULAR dimension

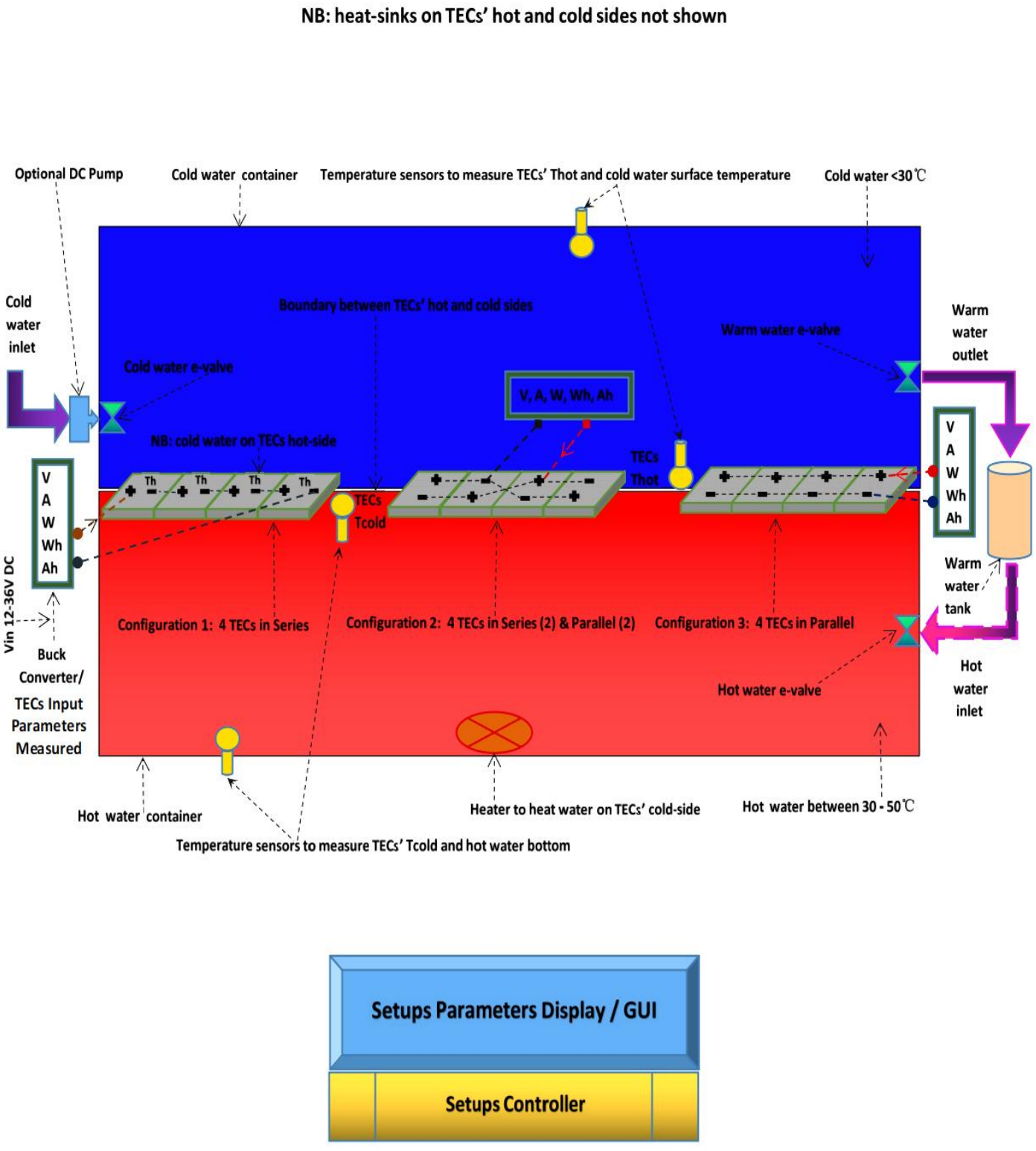

Figure 7.4: Investigating TECs in various electrical configurations with all the TECs having the same rectangular setup dimension

BIBLIOGRAPHY

A

Abdelhakim, A. & Blaabjerg, F. 2020. Current-fed modular multilevel converter (CMMC) for fuel cell and photovoltaic integration. 2020 IEEE 21st *Workshop on Control and Modeling for Power Electronics (COMPEL)*, Aalborg, Denmark, 1-6. DOI: 10.1109/COMPEL49091.2020.9265695.

Abhijith, V.B., Narayanaswamy, K., Pooja, C.M., Prasad, S.V. & Sambhu, R. 2020. Household application of thermoelectric generator in the field of propagating power from waste heat. *AIP Conference Proceedings,* 2297, 020010. DOI: https://doi.org/10.1063/5.0031699.

Abolhosseini, S., Heshmati, A. & Altmann, J. 2014. A Review of Renewable Energy Supply and Energy Efficiency Technologies, http://ftp.iza.org/dp8145.pdf.

Afshari, F. 2021. Experimental and numerical investigation on thermoelectric coolers for comparing air-to-water to air-to-air refrigerators. *Journal of Thermal Analysis and Calorimetry*, 144, 855–868. DOI: https://doi.org/10.1007/s10973-020-09500-6.

Ahmed, O.A. & Bleijs, J.A.M. 2013. Power flow control methods for an ultra-capacitor bidirectional converter in DC micro-grids – a comparative Study. *Renewable and Sustainable Energy Reviews*, 26, 727–738. DOI: https://doi.org/10.1016/j.rser.2013.06.021.

Aljibory, M.W., Hashim, H.T. & Abbas, W.N. 2021. A review of solar energy harvesting utilising a photovoltaic–thermoelectric integrated hybrid system. *IOP Conference Series: Materials Science and Engineering, 4th International Conference on Engineering Sciences (ICES 2020)*, 1067, Kerbala, Iraq. DOI:10.1088/1757-899X/1067/1/012115.

Ando Junior, O.H., Calderon, N.H. & De Souza, S.S. 2018. Characterization of a thermoelectric generator (TEG) system for waste heat recovery. *Energies*, 11, 1555. DOI:10.3390/en11061555.

Apertet Y., Ouerdane H., Goupil C. & Lecoeur P. 2014. Influence of thermal environment on optimal working conditions of thermoelectric generators. *Journal of Applied Physics,* 116, 144901.

Arazi, M., Payman, A., Camara, M.B. & Dakyo, B. 2020. Energy management in a multi-source system using isolated DC-DC resonant converters. *2020 22nd European Conference on Power Electronics and Applications* (EPE'20 ECCE Europe), Lyon, France, 1-7. DOI: 10.23919/EPE20ECCEEurope43536.2020.9215662.

Artal-Sevil, J.S., Domínguez-Navarro, J.A., Bernal-Ruiz, C. & Coronado-Mendoza, A. 2020. Power flow control through differential power processing to improve reliability in hybrid systems based on PEM-Fuel Cell. *2020 15th International Conference on Ecological Vehicles and Renewable Energies (EVER)*, Monte-Carlo, Monaco, 1-12. DOI: 10.1109/EVER48776.2020.9243125.

Ates, Y., Uzunoglu, M., Erdinc, O. & Vural, B. 2009. A Wavelet-ADALINE network based load sharing and control algorithm for a FC/UC hybrid vehicular power system. *Proceedings of the 2009 International Conference on Clean Electrical Power*, Capri, Italy, 591–94. DOI: 10.1109/ICCEP.2009.5211976.

B

Badea, N., Vlad, C. & Stolan, A. 2010. Comparative study of energy performance for two mCCHP systems used in domestic residence. *2010 3rd International Symposium on Electrical and Electronics Engineering (ISEEE)*, Galati; 321–326. DOI: 10.1109/ISEEE.2010.5628489.

Barhoumi, E.M., Okonkwo, P.C., Belgacem, I.B. & Zghaibeh, M. 2020. MPPT control of an interleaved boost converter for a polymer electrolyte membrane fuel cell applications. *2020 International Conference on Electrical and Information Technologies (ICEIT)*, Rabat, Morocco, 1-5. DOI: 10.1109/ICEIT48248.2020.9113228.

Bayendang, N.P., Kahn, M.T., Balyan, V. & Draganov, I. 2020a. CCHP systems analysis with emphasis on fuel cells, thermoelectricity and power converters. *2020 5th International Conference on Smart and Sustainable Technologies (SpliTech)*; Split, Croatia; 1–9. https://doi.org/10.23919/SpliTech49282.2020.9243720.

Bayendang, N.P., Kahn, M.T. & Balyan, V. 2020b. A structural review of thermoelectricity for fuel cells CCHP applications. *Hindawi Journal of Energy,* Volume 2020, 1-23. https://doi.org/10.1155/2020/2760140.

Bayendang, N.P., Kahn, M.T., Balyan, V., Draganov, I. & Pasupathi, S. 2020c. A comprehensive thermoelectric cooler (TEC) modelling. *AIUE Congress 2020: International Conference on Use of Energy*, Cape Town, South Africa, 1-7. http://dx.doi.org/10.2139/ssrn.3735378.

Bayendang, N.P., Kahn, M.T., Balyan, V., Draganov, I. & Pasupathi, S. 2020d. A comprehensive thermoelectric generator (TEG) modelling. *AIUE Congress 2020: Energy and Human Habitat Conference*, Cape Town, South Africa, 1-7. http://doi.org/10.5281/zenodo.4289574.

Bayendang, N.P., Kahn, M.T. & Balyan, V. 2021a. Power converters and EMS for fuel cells CCHP applications: A structural and extended review. *Adv. Sci. Technol. Eng. Syst. J.* 6(3): 54-83. http://dx.doi.org/10.25046/aj060308.

Bayendang, N.P., Kahn, M.T. & Balyan, V. 2021b. Simplified thermoelectric cooler (TEC) with heatsinks modeling and simulation using Matlab and Simulink based-on dimensional analysis. *AIUE Congress 2021: 2nd Energy and Human Habitat Conference*, Cape Town, South Africa, 1-8. https://www.ssrn.com/abstract=3900757.

Bayendang, N.P., Kahn, M.T. & Balyan, V. 2021c. Simplified thermoelectric generator (TEG) with heatsinks modeling and simulation using Matlab and Simulink based-on dimensional analysis. *AIMS Energy*, 9(6):1213-1240. http://dx.doi.org/10.3934/energy.2021056.

Bayendang, N.P., Kahn, M.T. & Balyan, V. 2022a. Thermoelectric generators (TEGs) and thermoelectric coolers (TECs) modeling and optimal operation points investigation. *Adv. Sci. Technol. Eng. Syst. J.* 7(1):60-78. http://dx.doi.org/10.25046/aj070107.

Bayendang, N.P., Kahn, M.T. & Balyan, V. 2022b. Thermoelectric generators (TEGs) modules − Optimum electrical configurations and performance determination. *Undergoing publication production*. [Accepted: March 9, 2022]. *AIMS Energy.*

Bazin, P., Beranger, B., Ecrabey, J., Garnier, L. & Mercier, S. 2020. Smart fuel cell module (6.5 kW) for a range extender application. *2020 22nd European Conference on Power Electronics and Applications (EPE'20 ECCE Europe)*, Lyon, France, 1-8. DOI: 10.23919/EPE20ECCEEurope43536.2020.9215856.

Bell, L.E. 2008. Cooling, heating, generating power and recovering waste heat with thermoelectric systems. *Science 321*, 1457. DOI: 10.1126/science.1158899.

Belovski, I.R. & Aleksandrov, A.T. 2019. Examination of the characteristics of a thermoelectric cooler in cascade. *2019 X National Conference with International Participation (ELECTRONICA)*, 1-4. DOI: 10.1109/ELECTRONICA.2019.8825631.

Bessarabov, D., Human, G., Kruger, A.J., Chiuta, S., Modisha, P.M., Du Preez, S.P., Oelofse, S.P., Vincent, I., Van Der Merwe, V., Langmi, H.W., Ren, J. & Musyoka, N.M. 2017. South African Hydrogen Infrastructure (HySA Infrastructure) for fuel cells and energy storage: Overview of a Project's Portfolio. *International Journal of Hydrogen Energy*, 42, 13568 – 13588.

Bhaskar, M.S., Ramachandaramurthy, V.K., Padmanaban, S., Blaabjerg, F., Ionel, D.M., Mitolo, M. & Almakhles, D. 2020. Survey of DC-DC non-isolated topologies for unidirectional power flow in fuel cell vehicles. *IEEE Access*, 8, 178130 – 178166. DOI: 10.1109/ACCESS.2020.3027041.

Bizon, N. 2011. A new topology of fuel cell hybrid power source for efficient operation and high reliability. *Journal of Power Sources*. 196(6): 3260 – 3270. DOI: 10.1016/j.jpowsour.2010.11.049.

Boettner, D.D., Paganelli, G., Guezennec, Y.G., Rizzoni, G. & Moran, M.J. 2002. Proton exchange membrane fuel cell system model for automotive vehicle simulation and control. *Journal of Energy Resource Technology*. 124(1): 20 – 27. DOI: 10.1115/1.1447927.

Boukoberine, M.N., Zhou, Z., Benbouzid, M. & Donateo, T. 2020. Frequency separation-based power management strategy for a fuel cell-powered drone. *2020 2nd International Conference on Smart Power & Internet Energy Systems (SPIES)*, Bangkok, Thailand, 209-214. DOI: 10.1109/SPIES48661.2020.9242975.

Bozchalui, M.C. & Sharma, R. 2012. Optimal operation of commercial building micro-grids using multi-objective optimization to achieve emissions and efficiency targets. *2012 IEEE Power and Energy Society General Meeting*, San Diego, California, USA; 1–8. DOI: 10.1109/PESGM.2012.6345600.

Brown, J.S. & Domanski, P.A. 2014. Review of alternative cooling technologies. *Applied Thermal Engineering,* 64(1 – 2): 252 – 262. DOI: 10.1016/j.applthermaleng.2013.12.014.

C

Cao, Y., Wang, Q., Wang, Z., Jermsittiparsert, K. & Shafiee, M. 2020. A new optimized configuration for capacity and operation improvement of CCHP system based on developed owl search algorithm. *Energy Reports* 6, 315-324. https://doi.org/10.1016/j.egyr.2020.01.010.

Carvalho, A. & Outeiro, M.T. 2011. Matlab in model-based design for power electronics systems. *Engineering education and research using Matlab*. DOI: 10.5772/21144.

Casano, G. & Piva, S. 2012**.** Parametric thermal analysis of the performance of a thermoelectric generator. 6th European thermal sciences conference (Eurotherm 2012), Poitiers, France. *Journal of Physics*: Conference Series, 395(1): 2156. DOI: 10.1088/1742-6596/395/1/012156.

Casteleiro-Roca, J.L., Barragán, A.J., Segura, F., Calvo-Rolle, J.L. & Andújar, J.M. 2019. Fuel cell output current prediction with a hybrid intelligent system. *Complexity*, *Special Issue*: *Advanced Controls in Complex Clean Energy Devices, Subsystems, and Processes,* Volume 2019. https://doi.org/10.1155/2019/6317270.

Cernaianu, M.O. & Gontean, A. 2013. Parasitic elements modelling in thermoelectric modules. *IET Circuits Devices Systems*, 7(4): 177–184. DOI: 10.1049/iet-cds.2012.0351.

Chahartaghi, M. & Sheykhi, M. 2019. Energy, environmental and economic evaluations of a CCHP system driven by Stirling engine with helium and hydrogen as working gases. *Energy*, 174, 1251-1266. https://doi.org/10.1016/j.energy.2019.03.012.

Champier, D. 2017. Thermoelectric generators: A review of applications. *Energy Conversion and Management*, 140, 167-181. https://doi.org/10.1016/j.enconman.2017.02.070.

Chandan, A., Hattenberger, M., El-kharouf, A., Du, S., Dhir, A., Self, V., Pollet, B.G., Ingram, A., Bujalski, W. 2013. High temperature (HT) polymer electrolyte membrane fuel cells (PEMFC) – a review. *Journal of Power Sources*; 231, 264 – 278. https://doi.org/10.1016/j.jpowsour.2012.11.126.

Charris, D., Gómez, D. & Pardo, M. 2019. A portable thermoelectric energy harvesting unit to power up outdoor sensors and devices. *2019 IEEE Sensors Applications Symposium (SAS*), 1-6. DOI: 10.1109/SAS.2019.8705985.

Chein, R. & Huang, G. 2004. Thermoelectric cooler application in electronic cooling. *Applied Thermal Engineering*, 24(14–15): 207-2217. https://doi.org/10.1016/j.applthermaleng.2004.03.001.

Chen, J., Li, K., Liu, C., Li, M., Lv, Y., Jia, L. & Jiang, S. 2017. Enhanced efficiency of thermoelectric generator by optimizing mechanical and electrical structures. *Energies*. 10: 1329. DOI: 10.3390/en10091329.

Chen, P., Jiang, Z., Tang, Z. & Guan, L. 2016. Effect of electricity feed-in tariff on the planning of CCHP Micro-systems. *2016 IEEE PES Asia-Pacific Power and Energy Engineering Conference (APPEEC).* Xi'an, China; 875–879. DOI: 10.1109/APPEEC.2016.7779620.

Chen, W. & Lin, Y. 2018. Performance comparison of thermoelectric generators using different materials. *10th International Conference on Applied Energy (ICAE2018)*, 22-25, Hong Kong, China.

Chen, X., Wang, Y., Cai, L. & Zhou, Y. 2015. Maximum power output and load matching of a phosphoric acid fuel cell-thermoelectric generator hybrid system. *Material Science: Journal of Power Sources.* 294 (2015): 430 - 436. DOI: 10.1016/J.JPOWSOUR.2015.06.085.

Chen, X., Zhou, H., Li, W., Yu, Z., Gong, G., Yan, Y., Luo, L., Wan, Z. & Ding, Y. 2018. Multi-criteria assessment and optimization study on 5kW PEMFC based residential CCHP system. *Energy Conversion and Management*; 160, 384–395. https://doi.org/10.1016/j.enconman.2018.01.050.

Chen, J., Li, K., Liu, C., Li, M., Lv, Y., Jia, L. & Jiang, S. 2017. Enhanced efficiency of thermoelectric generator by optimizing mechanical and electrical structures. *Energies*, 10, 1329. DOI: 10.3390/en10091329.

Chen, J., Lin, B., Wang, H. & Lin, G. 2000. Optimal design of a multi-couple thermoelectric generator, *Semiconductor, Science and Technology*, 2000, 15(2): 184–188, doi: 10.1088/0268-1242/15/2/318.

Cheng, L., Liu, C., Huang, R. & Li, H. 2016. An optimal operating strategy for CCHP in multi-energy carrier system. *IEEE Power and Energy Society General Meeting (PESGM)*, Boston, MA, USA; 1–5. DOI: 10.1109/PESGM.2016.7741902.

Corcau, J., Dinca, L., Adochiei, I. & Grigorie, T.L. 2019. Modeling and simulation of an aerodrome electrical power source based on fuel cells. *2019 E-Health and Bioengineering Conference (EHB)*, Iasi, Romania, 2019, 1-4. DOI: 10.1109/EHB47216.2019.8969870.

Cozzolino, R. 2018. Thermodynamic performance assessment of a novel Micro-CCHP system based on a low temperature PEMFC power unit and a half-effect Li/Br absorption chiller. *Energies*, *MDPI, Open Access Journal*. 11(2): 1–21. https://doi.org/10.3390/en11020315.

D

Delshad, M. & Farzanehfard, H. 2011. A new soft switched push pull current fed converter for fuel cell applications. *Energy Conversion and Management*, 52(2): 917–923. https://doi.org/10.1016/j.enconman.2010.08.019.

Dos Santos Guzella, M., Dos Santos, G.R., Cabezas-Gómez, L., Campo, A. & Monteiro Guimarães, L.G. 2021. Numerical simulation of the two-dimensional heat diffusion in the cold substrate and performance analysis of a thermoelectric air cooler using the lattice Boltzmann method. *Int. J. Appl. Comput. Math* 7, 130. https://doi.org/10.1007/s40819-021-01073-8.

E

Eberhard, A., Gratwick, K., Morella, E. & Antmann, P. 2017. Independent power projects in Sub-Saharan Africa: investment trends and policy lessons, *Energy Policy*, 108, 390-424. DOI: 10.1016/j.enpol.2017.05.023.

Ebrahimi, M. & Derakhshan, E. 2018. Design and evaluation of a micro combined cooling, heating, and power system based on polymer exchange membrane fuel cell and thermoelectric cooler. *Energy Conversion and Management*; 171, 507–517. https://doi.org/10.1016/j.enconman.2018.06.007.

Eckardt, B., März, M., Hofmann, A., Gräf, M. & Ungethüm, J. 2005. High power buck-boost DC/DC converter for automotive power-train application. *2005 Official Proceedings of the International Conference of Power Electronics, Intelligent Motion, Power Quality: PCIM 2005* Europe, Nürnberg, Germany, 685. http://publica.fraunhofer.de/documents/N-46644.html.

Efstathiou, D.S., Petrou, A.K., Spanoudakis, P., Tsourveloudis, N.C. & Valavanis, K.P. 2012. Recent Advances on the Energy Management of a Hybrid Electric Vehicle. *2012 20th Mediterranean Conference on Control & Automation (MED)*, Barcelona, Spain, 896–901. DOI: 10.1109/MED.2012.6265752.

EG&G Technical Services, Inc. 2004. Science applications international corporation: U.S. Department of Energy Office of Fossil Energy, National Energy Technology Laboratory. *Fuel Cell Handbook*, West Virginia, USA, 7th Edition.

Elarusi, A., Attar, A. & Lee, H. 2017. Optimal design of a thermoelectric cooling /heating system for a car seat climate control (CSCC). *Journal of Electronic Materials*, 46(1): 1984-1995.

Emadi, A., Ehsani, M. & Miller, J.M. 2003. *Vehicular electric power systems: Land, Sea, Air and Space Vehicles*, Roca Raton, Florida, USA, CRC Press, 1st Edition.

Ezzitouni, S., Fernández-Yáñez, P., Rodríguez, L.S., Armas, O., De las Morenas, J., Massaguer, E. & Massaguer, A. 2021. Electrical modelling and mismatch effects of thermoelectric modules on performance of a thermoelectric generator for energy recovery in diesel exhaust system. *Energies*, 14, 3189. https://doi.org/10.3390/en14113189.

F

Fanjul, L.M.P. 2006. Design Considerations for DC-DC Converters in Fuel-cell Systems, PhD Thesis, Texas A&M University, USA.

Farmani, F., Parvizimosaed, M., Monsef, H., Rahimi-Kian, A. 2018. A conceptual model of a smart energy management system for a residential building equipped with CCHP system, *International Journal of Electrical Power & Energy Systems*, 95, 523-536. https://doi.org/10.1016/j.ijepes.2017.09.016.

Fathabadi, H. 2018. Novel fuel cell/battery/super-capacitor hybrid power source for fuel-cell hybrid electric vehicles. *Energy*, 143, 467 – 477. https://doi.org/10.1016/j.energy.2017.10.107.

Fauzan, M.Y., Muyeen, S.M. & Islamc, S. 2020. Experimental modelling of grid-tied thermoelectric generator from incinerator waste heat. *International Journal of Smart Grid and Clean Energy*. DOI: 10.12720/sgce.9.2.304-313.

Felgner, F., Exel, L., Nesarajah, M. & Frey, G. 2014. Component-oriented modeling of thermoelectric devices for energy system design. *IEEE Transactions on Industrial Electronics*, 61(3): 1301-1310. DOI: 10.1109/TIE.2013.2261037.

Flores-Niño, C.Y., Olivares-Robles, M.A. & Loboda, I. 2015. General approach for composite thermoelectric systems with thermal coupling: the case of a dual thermoelectric cooler. *Entropy*, 17, 3787-3805. DOI: 10.3390/e17063787.

G

Gao, X. 2014. HT-PEM fuel cell system with integrated thermoelectric exhaust heat recovery. PhD Thesis, Department of Energy Technology, Aalborg University, Denmark.

Gao, J., Li, M., Hu, Y., Chen, H. & Ma, Y. 2019. Challenges and developments of automotive fuel cell hybrid power system and control. *Science China Information Sciences*, 62(5). https://doi.org/10.1007/s11432-018-9690-y.

Garcia-Saez, I., Mendez, J., Ortiz, C., Loncar, D., Becerra, J.A. & Chacartegui, R. 2019. Energy and economic assessment of solar Organic Rankine Cycle for combined heat and power generation in residential applications, *Renewable Energy*, 140(2019): 461–476. https://doi.org/10.1016/j.renene.2019.03.033.

Giwa, S.O., Nwaokocha, C.N., Layeni, A.T. & Olaluwoye, O.O. 2019. Energy harvesting from household heat sources using a thermoelectric generator module. *Nigerian Journal of Technological Development*, 16(3). http://dx.doi.org/10.4314/njtd.v16i3.6.

Goldsmid, H. 1995. Conversion Efficiency and Figure-of-merit. CRC Handbook of Thermoelectrics. 19-25.

Gonnet, A., Jorge, S.G., Busada, C. & Solsona, J. 2019. Power converter topology for conditioning a fuel cells battery voltage. *2019 Argentine Conference on Electronics (CAE)*, Mar del Plata, Argentina, 2019, 9-14. DOI: 10.1109/CAE.2019.8709157.

Grotsch, M., Mangold, M. & Kienle, A. 2009. Analysis of the coupling behaviour of PEM fuel cells and DC-DC converters. *Energies*, 2, 71-96. DOI: 10.3390/en2010071.

H

Haddad, C., Périlhon, C., Danlos, A., François, M. & Descombes, G. 2014. Some efficient solutions to recover low and medium waste heat: competitiveness of the thermoacoustic technology. *Energy Procedia*, 50, 1056 –1069.

Hannan, M.A., Azidin, F.A. & Mohamed, A. 2014. Hybrid electric vehicles and their challenges: a review. *Renewable and Sustainable Energy Reviews*, 29, 135-50. https://doi.org/10.1016/j.rser.2013.08.097.

Hannan, M.A., Azidin, F.A. & Mohamed, A. 2012. Multi-sources model and control algorithm of an energy management system for light electric vehicles. *Energy Converters Management*, 62, 123–30. https://doi.org/10.1016/j.enconman.2012.04.001.

Hao, J., Qiu, H., Ren, J., Ge, Z., Chen Q. & Du, X. 2020. Multi-parameters analysis and optimization of a typical thermoelectric cooler based on the dimensional analysis and experimental validation. *Energy*, 205, 118043. https://doi.org/10.1016/j.energy.2020.118043.

Hasani, M. & Rahbar, N. 2015. Application of thermoelectric cooler as a power generator in waste heat recovery from a PEM fuel cell: An Experimental Study. *International Journal of Hydrogen Energy,* 40 (2015): 15040 - 15051.

He, J., & Tritt, T.M. 2017. Advances in thermoelectric materials research: Looking back and moving forward. *Science*, 357 (6358). DOI: 10.1126/science.aak9997.

He, W., Zhang, G., Zhang, X., Ji, J., Li, G. & Zhao, X. 2015. Recent development and application of thermoelectric generator and cooler. *Applied Energy*, 143(C), 1–25. DOI: 10.1016/j.apenergy.2014.12.075.

He, W., Wang, S. & Yang, Y. 2016. Optimal heat exchanger dimensional analysis under different automobile exhaust temperatures for thermoelectric generator system. CUE2016-Applied Energy Symposium and Forum 2016: Low carbon cities & urban energy systems, *Energy Procedia,* 104, 366–371. DOI: 10.1016/j.egypro.2016.12.062.

Hong, M., Zheng, K., Lyv, W., Li, M., Qu, X., Sun, Q., Xu, S., Zou, J. & Chen, ZG. 2020. Computer-aided design of high-efficiency GeTe-based thermoelectric devices. *Energy & Environmental Science,*13, 1856-1864. https://doi.org/10.1039/D0EE01004A.

Hong, M., Lyu, W., Wang, Y., Zou, J. & Chen, Z.G. 2020. Establishing the golden range of Seebeck coefficient for maximizing thermoelectric performance. *American Chemical Society,* 142(5): 2672–2681. https://doi.org/10.1021/jacs.9b13272.

Hoogers, G. 2002. Fuel Cell Technology Handbook, Florida, US, CRC Press LLC, 1st Edition.

Hu, X., Jiang, C., Fan, X., Feng, B., Liu, P., Zhang, Y., Li, R., He, Z., Li, G. & Li, Y. 2020. Investigation on waste heat recovery of a nearly kilowatt class thermoelectric generation system mainly based on radiation heat transfer. *Energy Sources, Part A: Recovery, Utilization, and Environmental Effects.* https://doi.org/10.1080/15567036.2020.1829190.

Huangfu, Y., Ma, R., Liang, B. & Li, Y. 2015. High power efficiency buck converter design for standalone wind generation system. *International Journal of Antennas and Propagation*, Volume 2015, Special Issue: Recent Advances in Theory and Applications of Electromagnetic Metamaterials. http://dx.doi.org/10.1155/2015/751830.

Hubbard, W.A., Mecklenburg, M., Lodico, J.J., Chen, Y., Ling, X.Y., Patil, R., Kessel, W.A., Flatt, G.J.K., Chan, H.L., Vareskic, B., Bal, G., Zutter, B. & Regan, B.C. 2020. Electron-Transparent thermoelectric coolers demonstrated with nanoparticle and condensation thermometry, *ACS Nano,* 14(9): 11510-11517. DOI: 10.1021/acsnano.0c03958.

Huston, J., Wyatt C., Nichols, C., Binder, J.M. & Holcomb, F.H. 2004. Application of thermoelectric devices to fuel cell power generation: demonstration and evaluation. US Army Corps of Engineers, Engineer Research and Development Centre, Washington DC, USA.

I

İnci, M., Büyük, M., Demir, M.H. & İlbey, G. 2021. A review and research on fuel cell electric vehicles: Topologies, power electronic converters, energy management methods, technical challenges, marketing and future aspects. *Renewable and Sustainable Energy Reviews*, 137. DOI: https://doi.org/10.1016/j.rser.2020.110648.

Ioffe, AF. 1957. Semiconductor thermoelements and thermoelectric Cooling (London, UK: Infosearch Limited).

J

Jafari, M., Malekjamshidi, Z. & Lu, D.D. & Zhu, J. 2019. Development of a fuzzy-logic-based energy management system for a multiport multioperation mode residential smart micro-grid. *IEEE Transactions on Power Electronics*, 34(4), 3283-3301. DOI: 10.1109/TPEL.2018.2850852.

Jeong, Y., Rorrer, R.A.L., Lee, B. & Park, J. 2019 A novel control scheme for high efficiency fuel cell power systems in parallel structure. *2019 IEEE Energy Conversion Congress and Exposition (ECCE)*, Baltimore, MD, USA, 940-946, DOI: 10.1109/ECCE.2019.8912856.

Ji, J., Ding, Z., Xia, X., Wang, Y., Huang, H., Zhang, C., Peng, T., Wang, X., Nazir, M.S., Zhang, Y., Liu, B., Jia, X., Li, R. & Wang, Y. 2020. System design and optimisation study on a novel CCHP system integrated with a hybrid energy storage system and an ORC, *Complexity*, Volume. 2020, 1-14. https://doi.org/10.1155/2020/1278751.

Jia, J., Chen, H., Liu, H., Ai, T., Li, H. 2021. Thermodynamic performance analyses for CCHP system coupled with organic Rankine cycle and solar thermal utilization under a novel operation strategy. *Energy Conversion and Management*, 239, 2021, 114212, https://doi.org/10.1016/j.enconman.2021.114212.

Jiang, R., Qin, F.G.F., Yin, H., Yang, M., Xu, Y. 2017. Thermo-economic assessment and application of CCHP system with de-humidification and hybrid refrigeration. *Applied Thermal Engineering*, 125, 928–936. https://doi.org/10.1016/j.applthermaleng.2017.07.048.

K

Kabalo, M., Blunier, B., Bouquain, D. & Miraoui, A. 2010. State-of-the-Art of DC-DC Converters for fuel cell vehicles. *2010 IEEE Vehicle Power and Propulsion Conference*, Lille, France. DOI: 10.1109/VPPC.2010.5729051.

Kabutey, F.T., Zhao, Q., Wei, L., Ding, J., Antwi, P., Quashie, F.K, & Wang, W. 2019. An overview of plant microbial fuel cells (PMFCs): Configurations and applications. *Renewable and Sustainable Energy Reviews*, 110: 402–414. https://doi.org/10.1016/j.rser.2019.05.016.

Katkus, T. 2015. Design and construction of high temperature thermoelectric power generator module characterisation system. Master's thesis. Institute for Superconducting and Electronic Materials, University of Wollongong, Australia. http://ro.uow.edu.au/theses/4499.

Kavyapriya, S. & Kumar, R.K. 2020. Modeling and simulation of DC-DC converters for fuel cell system," international journal of engineering and advanced technology (IJEAT), 9(3). DOI: 10.35940/ijeat.C5754.029320.

Khaligh, A. & Li, Z. 2010. Battery, ultra-capacitor, fuel cell and hybrid energy storage systems for electric, hybrid electric, fuel cell, and plug-in hybrid electric vehicles: state of the art. *IEEE Transaction on Vehicle Technology*, 59(6): 2806 – 2814. DOI: 10.1109/TVT.2010.2047877.

Kim, H.S., Liu, W., Chen, G., Chu, C.W. & Ren, Z. 2015. Relationship between thermoelectric figure of merit and energy conversion efficiency. PNAS. 112(27): 8205–8210. www.pnas.org/cgi/doi/10.1073/pnas.1510231112.

Kirubakaran, A., Shailendra, J., & Nema, R.K. 2009. The PEM fuel cell system with DC/DC boost converter: Design, modeling and simulation. *International Journal of Recent Trends in Engineering*, 1(3). DOI: 01.ijepe.01.01.05.

Kiziroglou, M.E., Becker, T.H., Wright, S.W., Yeatman, E.M., Evans, J.W. & Wright, P.K. 2016. Thermoelectric generator design in dynamic thermoelectric energy harvesting. *Journal of Physics*: Conference Series 773 (2016) 012025. DOI: 10.1088/1742-6596/773/1/012025.

Koketsu, K. & Tanzawa, T. 2021. Design of a charge pump circuit and system with input impedance modulation for a flexible-type thermoelectric generator with high-output impedance. *Electronics*, 10, 1212. https://doi.org/10.3390/electronics10101212.

Kolli, A., De-Bernardinis, A., Khatir, Z., Gaillard, A., Béthoux, O. & Hissel, D. 2015. Part-load control strategy of a 20kW SiC power converter for embedded PEM FC multi-stack architectures. *IECON 2015 - 41st Annual Conference of the IEEE Industrial Electronics Society*, Yokohama, Japan, 4627-4632. DOI: 10.1109/IECON.2015.7392821.

Kolli, A., Gaillard, A., De Bernardinis, A., Bethoux, O., Hissel, D. & Khatir, Z. 2015a. A review on DC/DC converter architectures for power fuel cell applications. *Energy Conversion and Management*, 105, 716-730. https://doi.org/10.1016/j.enconman.2015.07.060.

Kolli, A., Gaillard, A., De Bernardinis, A., Bethoux, O., Hissel, D. & Khatir, Z. 2015b. Design and control of a high frequency six-phase interleaved DC/DC converter based on SiC power MOSFETs for a PEMFC. *6th International Conference on Fundamentals and Development of Fuel Cells (FDFC 2015)*, Toulouse, France.

Kraa, O., Ghodbane,H., Saadi, R., Ayad, M.Y., Becherif, M., Aboubou, V. & Bahri, M. 2015. Energy Management of fuel cell / super-capacitor hybrid source based on linear and sliding mode control. *International Conference on Technologies and Materials for Renewable Energy, Environment and Sustainability, TMREES15, Energy Procedia*, 74, 1258–1264. https://doi.org/10.1016/j.egypro.2015.07.770.

Kwan, T.H., Wu, X. & Yao, Q. 2018. Bidirectional operation of the thermoelectric device for active temperature control of fuel cells. *Applied Energy*, *222*, 410-422, https://doi.org/10.1016/j.apenergy.2018.04.016.

L

LaGrandeur, J., Crane, D., Hung, S., Mazar B. & Eder, A. 2006. Automotive waste heat conversion to electric power using Skutterudite, TAGS, PbTe and BiTe, *25th International Conference on Thermoelectrics*. 343-348. DOI: 10.1109/ICT.2006.331220.

Leahy, M.J., Connolly, D., & Buckley, D.N. 2010. Wind energy storage technologies, *WIT Transactions on State of the Art in Science and Engineering*, 44. DOI: 10.2495/978-1-84564-205-1/21.

Lee, H. 2010. Thermal Design: Heat Sinks, Thermoelectrics, Heat Pipes, Compact Heat Exchangers and Solar Cells. John Wiley & Sons, Inc., Wiley, New Jersey, USA, 1st Edition, 648 pages.

Lee, H. 2016. Thermoelectrics: Design and Materials, 464 pages, ISBN-13: 978-1118848951, John Wiley Inc. New Jersey, USA.

Lee, H. 2013. Optimal design of thermoelectric devices with dimensional analysis. *Applied Energy*, 106, 79-88. https://doi.org/10.1016/j.apenergy.2013.01.052.

Lemes, Z., Vath, A., Hartkopf, T., Mancher, H. 2006. Dynamic fuel cell models and their application in hardware in the loop simulation. *Journal of Power Sources*. 154: 386–393. https://doi.org/10.1016/j.jpowsour.2005.10.032.

Lesage, F.J., Pelletier, R., Fournier, L., Sempels, É.V. 2013. Optimal electrical load for peak power of a thermoelectric module with a solar electric application, *Energy Conversion and Management*, 74, 51-59, https://doi.org/10.1016/j.enconman.2013.05.008.

Li, B., Hu, P., Zhu, N., Lei, F., Xing, L. 2019. Performance analysis and optimization of a CCHP-GSHP coupling system based on quantum genetic algorithm. *Sustainable Cities and Society*; 46: 101408. https://doi.org/10.1016/j.scs.2018.12.036.

Li, J., Liu, J., Yan, P., Li, X., Zhou, G. & Yu, D. 2021. Operation optimization of integrated energy system under a renewable energy dominated future scene considering both independence and benefit: A Review. *Energies*, 14(4): 1103. https://doi.org/10.3390/en14041103.

Li, S., Lam, K.H. & Cheng, K.W.E. 2017. The thermoelectric analysis of different heat flux conduction materials for power generation board. *Energies*, 10, 1781. DOI: 10.3390/en10111781.

Li, X., Dong, Y. & Zou, Y. 2017. Energy management of CCHP micro-grid considering demand-side management. 32nd *Youth Academic Annual Conference of Chinese Association of Automation (YAC)*, Hefei, China, 240–245. DOI: 10.1109/YAC.2017.7967412.

Li, Z. & Xu, Y. 2017. Dynamic dispatch of grid-connected multi-energy micro-grids considering opportunity profit. *2017 IEEE Power & Energy Society General Meeting*, Chicago, IL, USA, 1–5. DOI: 10.1109/PESGM.2017.8274205.

Li, Q., Yang, H., Han, Y., Li, M. & Chen, W. 2016. A state machine strategy based on droop control for an energy management system of PEMFC-battery, super-capacitor hybrid tramway. *International Journal of Hydrogen Energy*, 41(36): 16148 – 16159. https://doi.org/10.1016/j.ijhydene.2016.04.254.

Li, X., Xie, C., Quan, S, Shi, Y. & Tang, Z. 2019. Optimization of thermoelectric modules' number and distribution pattern in an automotive exhaust thermoelectric generator. *IEEE Access*, 7, 72143-72157. DOI: 10.1109/ACCESS.2019.2919689.

Li, W., Paul, M.C., Montecucco, A., Knox, A.R., Siviter, J., Sellami, N., Meng, X., Fernandez, E.F., Mallick, T.K., Mullen, P., Ashrafa, A., Samarelli, A., Llin, L.F., Paul, D.J., Gregory, D.H., Gao, M., Sweet, T., Azough, F., Lowndes, R. & Freer, R. 2015. Multiphysics simulations of a thermoelectric generator, the 7th *International Conference on Applied Energy – ICAE2015, Energy Procedia*, 75 (2015): 633 – 638. DOI: 10.1016/j.egypro.2015.07.473.

Lineykin, S., Ruchaevski, I. & Kuperman, A. 2014. Analysis and optimization of TEG-heatsink waste energy harvesting system for low temperature gradients. *2014 16th European Conference on Power Electronics and Applications*, Lappeenranta, Finland, 1-10. DOI: 10.1109/EPE.2014.6910778.

Lineykin, S. & Ben-Yaakov, S. 2006. A simple and intuitive graphical approach to the design of thermoelectric cooling systems. *37th IEEE Power Electronics Specialists Conference*, Jeju, Korea (South), 1-5, 2006. DOI: 10.1109/pesc.2006.1712075.

Lingmin, C., Jiekang, W., Changjie, L., Huiling, T., Xiaoming, M., Kangxing, L. 2021. A configuration optimization framework for renewable energy systems integrating with electric-heating energy storage in an isolated tourist area. *Wiley: Energy Science and Engineering*. 9(6): 865-883. https://doi.org/10.1002/ese3.864.

Lingmin, C., Jiekang, W., Fan, W., Huiling, T., Changjie, L., Yan, X. 2020. Energy flow optimization method for multi-energy system oriented to combined cooling, heating and power. *Energy*, 211, 118536. https://doi.org/10.1016/j.energy.2020.118536.

Liu, W.D., Yang, L., Chen, Z.G. & Zou, J. 2020. Promising and Eco-Friendly Cu2X-Based Thermoelectric Materials: Progress and Applications. *Wiley: Advanced Materials*, 32 (8): 1905703. https://doi.org/10.1002/adma.201905703.

Liu, C., Chen, P. & Li, K. 2014a. A 1kW thermoelectric generator for low-temperature geothermal resources. 39th *proceedings workshop on geothermal reservoir engineering*, Stanford University, Stanford, California, USA, 24-26, SGP-TR-202. https://pangea.stanford.edu/ERE/pdf/IGAstandard/SGW/2014/Li.pdf [Date Accessed: July 7 - August 3, 2021].

Liu, C., Chen, P. & Li, K. 2014b. A 500W low-temperature thermoelectric generator: design and experimental study. *International Journal of Hydrogen Energy*. 39(28): 15497-15505. https://doi.org/10.1016/j.ijhydene.2014.07.163.

Liu, H., Xu, L., Hu, Z., Li, J., Jiang, H. & Ouyang, M. 2020. Experimental study and performance analysis on high power fuel cell system. *IECON 2020 The 46th Annual Conference of the IEEE Industrial Electronics Society*, Singapore, 2031-2035. DOI: 10.1109/IECON43393.2020.9254802.

Livint, G., Horga, V., Ratoi, M. & Albu, M. 2011. Control of hybrid electrical vehicles, electric vehicles. *Electric Vehicles – Modelling and simulation*. DOI: 10.5772/16637, Croatia: InTech.

Lombardo, W., Sapienza, A., Ottaviano, S., Branchini, L., De Pascale, A., Vasta, S. 2021. A CCHP system based on ORC cogenerator and adsorption chiller experimental prototypes: Energy and economic analysis for NZEB applications, *Applied Thermal Engineering*, 183, Part 2, 116119, https://doi.org/10.1016/j.applthermaleng.2020.116119.

Lu, S., Li, Y. & Xia, H. 2018. Study on the configuration and operation optimization of CCHP coupling multiple energy system. *Energy Conversion and Management*; 177: 773–791. DOI: http://dx.doi.org/10.1016/j.enconman.2018.10.006.

Lu, X., Zhao, D., Ma, T., Wang, Q., Fan, J. & Yang, R. 2018. Thermal resistance matching for thermoelectric cooling systems. *Energy Conversion and Management*, 169, 186-193. https://doi.org/10.1016/j.enconman.2018.05.052.

Luo, C., Wang, R., Yu, W. & Zhou, W. 2020. Parametric study of a thermoelectric module used for both power generation and cooling. *Renewable Energy,* 154, 542-552. https://doi.org/10.1016/j.renene.2020.03.045.

M

Ma, H., Zhang, P., Chen, Z., Shen, K., Wang, C. & Ren, H. 2020. Operation Simulation of the CCHP-ORC based distributed energy system in a shopping mall. *2020 5th International Conference on Power and Renewable Energy (ICPRE)*, 179-183, Shanghai, China. DOI: 10.1109/ICPRE51194.2020.9233299.

Madkhali, H.A., Hamil, A. & Lee, H. 2017. Validation, optimization of a solar thermoelectric generator model. *Journal of Electronic Materials*. DOI: 10.1007/s11664-017-5723-2, 2017.

Mahmud, K.H., Yudistirani, S.A. & Ramadhan, A.I. 2017. Analysis of Power characteristics of model thermoelectric generator (TEG) small modular. *International Journal of Scientific & Technology Research,* 6(4).

Mamur, H. & Çoban, Y. 2020. Detailed modeling of a thermoelectric generator for maximum power point tracking. *Turkish Journal of Electrical Engineering & Computer Sciences,* 28: 124–139, https://doi.org/10.3906/elk-1907-166.

Mani, P.I. 2016. Design, modelling and simulation of a thermoelectric cooling system (TEC). Master's Thesis, Western Michigan University, Kalamazoo, Michigan, USA.

Mao, Y., Wu, J. & Zhang, W. 2020. An effective operation strategy for CCHP system integrated with photovoltaic/thermal panels and thermal energy storage. *Energies*, 13, 6418. DOI: 10.3390/en13236418.

Maraver, D., Sin, A., Sebastián, F. & Royo, J. 2013. Environmental assessment of CCHP (combined cooling heating and power) systems based on biomass combustion in comparison to conventional generation. *Energy*, 57: 17–23. https://doi.org/10.1016/j.energy.2013.02.014.

Martinez, J.S., Hissel, D., Pera, M.C. & Amiet, M. 2011. Practical control structure and energy management of a test bed hybrid electric vehicle. *IEEE Transactions on Vehicular Technology*, 60(9): 4139–4152. DOI: 10.1109/TVT.2011.2169821.

Martin-Lozano, A., Barrado, A., Rodriguez-Lorente, A., Lázaro, A. & Fernández, C. 2020. Energy management system optimization for a fuel cell hybrid vehicle based on power losses minimization. *IEEE 14th International Conference on Compatibility, Power Electronics and Power Engineering (CPE-POWERENG)*, Setubal, Portugal, 402-408. DOI: 10.1109/CPE-POWERENG48600.2020.9161482.

Massaguer, E., Massaguer, A., Pujol, T., Gonzalez, J.R. & Montoro, L. 2017. Modelling and analysis of longitudinal thermoelectric energy harvesters considering series-parallel interconnection effect. *Energy*, 129, 59-69. https://doi.org/10.1016/j.energy.2017.04.061.

Mehrpooya, M., Sayyad, S. & Zonouz, M.J. 2017. Energy, exergy and sensitivity analyses of a hybrid combined cooling, heating and power (CCHP) plant with molten carbonate fuel cell (MCFC) and Stirling engine. *Journal of Cleaner Production*, 148: 283–294. https://doi.org/10.1016/j.jclepro.2017.01.157.

Melnikov, A.A., Kostishin, V.G. & Alenkov, V.V. 2017. Dimensionless model of a thermoelectric cooling device operating at real heat transfer conditions maximum cooling capacity mode. *Journal of Electronic Materials*, 46, 2737–2745, 2017. DOI: 10.1007/s11664-016-4952-0.

Meseguer, J., Pérez-Grande, I. & Sanz-Andrés, A. 2012. Thermoelectric cooling. *Spacecraft Thermal Control*, 263–273, https://doi.org/10.1533/9780857096081.263.

Miao, N., An, P., Yue, C., Yu, B., Zhao, G. & Fu, Y. 2020. Research ideas for the capacity configuration of CCHP system. *2020 IEEE/IAS Industrial and Commercial Power System Asia (I&CPS Asia)*, 8-14, Weihai, China. DOI: 10.1109/ICPSAsia48933.2020.9208366.

Ming, G., Onifri, M., Lin, Z. & Ma, J. 2011. Experimental studies on a CCHP system based on a micro-turbine. *2011 2nd International Conference on Mechanic Automation and Control Engineering*, Hohhot, China, 2159–2162. DOI: 10.1109/MACE.2011.5987405.

Ming, Z., Qiqi, Q., Haojing, W., Yuming, G., Liang, G., Jian, Z., Huadong, Z. 2015. Economy benefit comparison of CCHP system and conventional separate supply system. *2015 8th International Conference on Intelligent Computation Technology and Automation (ICICTA)*, Nanchang, China; 2015. 402–406. DOI: 10.1109/ICICTA.2015.107.

Miyazaki, R., Mishima, T. & Lai, C.M. 2020. Coupled inductor-assisted current-fed snubber-less zero-current-soft switching high step-up DC-DC converter for fuel cell power interface. *2020 IEEE 9th Global Conference on Consumer Electronics (GCCE)*, Kobe, Japan, 797-801. DOI: 10.1109/GCCE50665.2020.9291776.

Mohammadi, K. & Powell, K. 2020. Thermodynamic and economic analysis of different cogeneration and trigeneration systems based on carbon dioxide vapor compression refrigeration systems. *Applied Thermal Engineering*, 164. https://doi.org/10.1016/j.applthermaleng.2019.114503.

Moqsud, MA., Yoshitake, J., Bushra, Q.S., Hyodo, M., Omine, K. & Strik, D. 2015. Compost in plant microbial fuel cell for bioelectricity generation. *Waste Management*; 36: 63–69. https://doi.org/10.1016/j.wasman.2014.11.004.

Motahhir, S., Abdelaziz, E.G. & Derouich, A. 2017. MIL and SIL and PIL tests for MPPT algorithm. *Cogent Engineering*, 4(1). https://doi.org/10.1080/23311916.2017.1378475.

Motapon, S.N., Dessaint, L. & Al-Haddad, K. 2014. A comparative study of energy management schemes for a fuel-cell hybrid emergency power system of More-Electric Aircraft. *IEEE Transactions on Industrial Electronics*, 61(3), 1320-1334. DOI: 10.1109/TIE.2013.2257152.

Müller, E., Zabrocki, K., Goupil, C., Snyder, G.J. & Seifert, W. 2017. Functionally graded thermoelectric generator and cooler elements. *In Materials, Preparation, and Characterization in Thermoelectrics* (Chapter 4, pp 36). CRC Press, Boca Raton, 1st Edition (2012). https://doi.org/10.1201/b11891.

Mungporn, P., Yodwong, B., Thounthong, P., Nahid-Mobarakeh, B., Takorabet, N., Guilbert, D., Bizon, N., Kumam, P. & Kaewprapha, C. 2019. Model-Free control of multiphase interleaved boost converter for fuel cell/reformer power generation. *2019 Research, Invention, and Innovation Congress (RI2C)*, Bangkok, Thailand, 1-6. DOI: 10.1109/RI2C48728.2019.8999919.

Musleh, M.A., Topriska, E., Jack, L. & Jenkins, D. 2017. Thermoelectric generator experimental performance testing for wireless sensor network application in smart buildings. *MATEC Web of Conferences* 120, 08003. DOI: 10.1051/71200matecconf/2018003.

Mwaniki, F.M. 2014. High voltage boost DC-DC converter suitable for variable voltage sources and high power photovoltaic application, Master of Engineering Dissertation, University of Pretoria, South Africa. http://hdl.handle.net/2263/37320.

N

National Planning Commission (NPC), South Africa Department of Planning, Monitoring and Evaluation. 2018. NPC Economy Series: Energy. https://static.pmg.org.za/180101NPC_Energy_Paper.pdf [Date Accessed: 10 Dec 2021].

Naveen, R., Revankar, P.P. & Rajanna, S. 2020. Integration of renewable energy systems for optimal energy needs - a review. *International Journal of Renewable Energy Research*, 10(2).

Nehrir, M.H., Wang, C. & Shaw S.R. 2006. Fuel cells: promising devices for distributed generation. *IEEE Power and Energy Magazine 2006*; 4(1): 47–53. DOI: 10.1109/MPAE.2006.1578531.

Noh, Y.-S., Seo, J.-II., Choi, W.-J., Kim, J.-H., Phuoc, H.V., Kim, H.-S., Lee, S.-G. 2021. 17.6A re-configurable dc-dc converter for maximum TEG energy harvesting in a battery-powered wireless sensor node. *2021 IEEE International Solid-State Circuits Conference (ISSCC)*. 266-268. DOI: 10.1109/ISSCC42613.2021.9365811.

Nomnqa, MV. 2017. Design of a domestic high temperature proton exchange membrane fuel cell cogeneration system: modelling and optimisation. Doctor of Engineering Thesis, Cape Peninsula University of Technology, Cape Town, South Africa.

Nozu, R., Lizuka, M., Nakanishi, M. & Kotani, MJ. 2009. Investigation of the life process of the electric double layer capacitor during float charging. *Journal of Power Sources*; 186: 570–579. https://doi.org/10.1016/j.jpowsour.2008.10.025.

Nymand, M. & Andersen, M.A.E. 2008. A new approach to high efficiency in isolated boost converters for high-power low-voltage fuel cell applications. *2008 13th Power Electronics and Motion Control Conference.* Poznan, Poland, 2008, 127-131, https://doi.org/10.1109/EPEPEMC.2008.4635255.

O

Orr, B., Akbarzadeh, A., Mochizuki M. & Singh, R. 2016. A review of car waste heat recovery systems utilising thermoelectric generators and heat pipes. *Applied Thermal Engineering*. 101, 490-495. https://doi.org/10.1016/j.applthermaleng.2015.10.081.

Ouddah, N., Boukhnifer, M. & Raisemche, A. 2013. Two control energy management schemes for electrical hybrid vehicle. *2013 Proceedings of the 10th International Multi-conference on Systems, Signals & Devices (SSD13)*, Hammamet, Tunisia. DOI: 10.1109/SSD.2013.6564135.

Outeiro, M.T. & Carvalho, A. 2013. Methodology of Designing Power Converters for Fuel-cell Based Systems: A Resonant Approach. *New Developments in Renewable Energy*. http://dx.doi.org/10.5772/54674.

P

Paladini, V., Donateo, T., De Risi, A. & Laforgia, D. 2007. Super-capacitors fuel-cell hybrid electric vehicle optimization & control strategy development. *Energy Conversion and Management*. 48(11): 3001-3008. https://doi.org/10.1016/j.enconman.2007.07.014.

Parikhani, T., Azariyan, H., Behrad, R., Ghaebi, H., Jannatkhah, J. 2020. Thermodynamic and thermoeconomic analysis of a novel ammonia-water mixture combined cooling, heating, and power (CCHP) cycle, *Renewable Energy*. 145, 1158-1175. https://doi.org/10.1016/j.renene.2019.06.100.

Parise, R.J. & Jones, G.F. 2002. Fuel cell thermal management with thermoelectric coolers. *2002 37th Inter-society Energy Conversion Engineering Conference (IECEC)*.

Park, J., Lee, H. & Bond, M. 2014. Uninterrupted Thermoelectric Energy Harvesting using Temperature-Sensor-based Maximum Power Point Tracking System. *Energy Conversion and Management*, 86, 233–240. DOI: 10.1016/j.enconman.2014.05.027.

Petsagkourakis, I., Tybrandt, K., Crispin, X., Ohkubo, I., Satoh, N. & Mori, T. 2018. Thermoelectric materials and applications for energy harvesting power generation. *Science and Technology of Advanced Materials*, 19(1): 836-862. DOI: 10.1080/14686996.2018.1530938.

Pollet, B.G., Pasupathi, S., Swart, G., Mouton, K., Lototskyy, M., Williams, M., Bujlo, P., Ji, S., Bernard, J.B. & Linkov, V. 2014. Hydrogen South Africa (HySA) Systems Competence Centre: Mission, objectives, technological achievements and breakthroughs. *International Journal of Hydrogen Energy*, 39(8): 3577-3596 https://doi.org/10.1016/j.ijhydene.2013.11.116.

Powers, W.F. & Nicastri, P.R. 2000. Automotive vehicle control challenges in the 21st century. *Control Engineering Practice,* 8(6): 605 – 18. https://doi.org/10.1016/S0967-0661(99)00199-9.

Prabhakaran, P. & Agarwal, V. 2020. Novel Four-port DC–DC converter for interfacing solar pv–fuel cell hybrid sources with low-voltage bipolar dc micro-grids. *IEEE Journal of Emerging and Selected Topics in Power Electronics*, 8(2), 1330-1340. DOI: 10.1109/JESTPE.2018.2885613.

Pratt, J.W., Klebanoff, L.E., Munoz-Ramos, K., Akhil, A.A., Curgus, D.B. & Schenkman, B.L. 2011. Proton Exchange Membrane Fuel Cells for Electrical Power Generation On-Board Commercial Airplanes, SAND2011-3119, Unlimited Release Printed.

Q

Qiu, P., Mao, T., Huang, Z., Xia, X., Liao, J., Agne, M.T., Gu, M., Zhang, Q., Ren, D., Bai, S, Shi, X., Snyder, G.J. & Chen, L. 2019. High-efficiency and stable thermoelectric module based on liquid-like materials. *Joule*, 3(6): 1538-1548. https://doi.org/10.1016/j.joule.2019.04.010.

Qu, Z., Ma, T., Yu, X. & Wang, Q. 2018. Parametric study on thermoelectric power generator and micro-turbine combined power generation system. *Chemical Engineering Transactions*, 70, 61–66. https://doi.org/10.3303/CET1870011.

R

Rahbar, N. & Asadi, A. 2016. Solar intensity measurement using a thermoelectric module; experimental study and mathematical modelling. *Energy Conversion and Management,* 129, 344–353.

Ramírez, R., Gutiérrez, A.S., Cabello, Eras, J.J., Valencia, K., Hernández, B. & Forero, J.D. 2019. Evaluation of the energy recovery potential of thermoelectric generators in diesel engines, *Journal of Cleaner Production*, 241, 118412. https://doi.org/10.1016/j.jclepro.2019.118412.

Rathode, K.S., Sharma, S.K. & Shringi, S. 2019. Performance analysis of PV & fuel cell based grid integrated power system. *2019 International Conference on Communication and Electronics Systems (ICCES)*, Coimbatore, India, 970-975. DOI: 10.1109/ICCES45898.2019.9002090.

Ravi, D., Letha, S.S., Samuel, P. & Reddy, B.M. 2018. An overview of various DC-DC converter techniques used for fuel cell based applications. *2018 International Conference on Power Energy, Environment and Intelligent Control (PEEIC)*, Greater Noida, India, 16-21. DOI: 10.1109/PEEIC.2018.8665465.

Rösch, A.G., Gall, A., Aslan, S., Hecht, M., Franke, L., Mallick, M.M., Penth, L., Bahro, D., Friderich, D. & Lemme, U. 2021. Fully printed origami thermoelectric generators for energy-harvesting. *npj Flex Electrons,* 5(1). https://doi.org/10.1038/s41528-020-00098-1.

S

Salimi, M., Radmand, F. & Firouz, M.H. 2021. Dynamic modeling and closed-loop control of hybrid grid-connected renewable energy system with multi-input multi-output controller," in Journal of Modern Power Systems and Clean Energy, 9(1), 94-103. DOI: 10.35833/MPCE.2018.000353.

Schaltz, E. & Rasmussen, P.O. 2008. Design and comparison of power systems for a fuel cell hybrid electric vehicle. *IEEE Industry Applications Society Annual Meeting*. Edmonton, AB, Canada, 1–8. DOI: 10.1109/08IAS.2008.184.

Seyezhai, R., Anitha, R., Mahalakshmi, S. & Bhavani, M. 2013. High gain interleaved boost converter for fuel cell applications. *Bulletin of Electrical Engineering and Informatics*, 2(4): 265-271. DOI: https://doi.org/10.11591/eei.v2i4.192.

Shen, Z., Wu, S. & Xiao, L. 2015. Theoretical analysis on the performance of annular thermoelectric couple. *Energy Conversion and Management*, 89, 244–250.

Shi, XL, Tao, X, Zou, J & Chen, Z.G. 2020. High-Performance Thermoelectric SnSe: Aqueous Synthesis, Innovations and Challenges. *Advanced Science,* 7(7), 1902923. https://doi.org/10.1002/advs.201902923.

Singh, J., Kuchroo, P., Bhatia, H. & Sidhu, E. 2016. Floating TEG based solar energy harvesting system. *2016 International Conference on Automatic Control and Dynamic Optimization Techniques (ICACDOT)*, 763-766. DOI: 10.1109/ICACDOT.2016.7877689.

Sorlei, I.S., Bizon, N., Thounthong, P., Varlam, M., Carcadea, E., Culcer, M., Iliescu, M. & Raceanu, M. 2021. Fuel cell electric vehicles — A brief review of current topologies and energy management strategies. *Energies*, 14(1), 252. DOI: https://doi.org/10.3390/en14010252.

Stockholm, J., Goupil, C., Maussion, P. & Ouerdane, H. 2015a. Transient thermoelectric generator: an active load story. *Journal of Electronic Materials, Institute of Electrical and Electronics Engineers*, 44 (6): 1768-1772. DOI: 10.1007/s11664-014-3545-z. hal-01308074.

Stockholm, J., Wojciechowski, K., Leszczynski, J., Witek, K., Guzdek, P. & Kulawik, J. 2015b. Thermoelectric generator with an active load. *12th European Conference on Thermo-electrics. Materials Today: Proceedings 2* (2015), 744 – 750.

Stockholm, J.G. 2016. Non-stationary thermoelectric generators. http://dx.doi.org/10.5772/66421. Intech.

Su, Z., Sun, B., Zhang, C., Wei, D., Xu, P. & Sha, C. 2016. Optimal operation strategy of biomass and solar CCHP system. *2016 35th Chinese Control Conference (CCC)*, Chengdu, China, 8612–8616. DOI: 10.1109/ChiCC.2016.7554731.

Suárez-Velázquez, G.G., Mejia-Ruiz, G.E. & García-Vite, P.M. 2020. Control and grid connection of fuel cell power system. *2020 IEEE International Autumn Meeting on Power, Electronics and Computing (ROPEC)*, Ixtapa, Mexico, 1-5. DOI: 10.1109/ROPEC50909.2020.9258729.

Suh, K. & Stefanopoulou, A.G. Coordination of converter and fuel cell controllers. 2005. *Proceedings of the 2005 IEEE International Symposium on, Mediterrean Conference on Control and Automation Intelligent Control,* Limassol, Cyprus. DOI: 10.1109/.2005.1467076.

Sulaiman, M.S., Mohamed, W.A.N.W., Singh, B. & Ghazali, M.F. 2017. Validation of a waste heat recovery model for a 1kW PEM fuel cell using thermoelectric generator. *IOP Conf. Series: Materials Science and Engineering,* 226, 012148. DOI: 10.1088/1757-899X/226/1/012148

Sulaiman, N., Hannan, M.A., Mohamed, A., Majlan, E.H. & Wan Daud, W.R. 2015. Review on energy management system for fuel cell hybrid electric vehicle: Issues and challenges. *Renewable and Sustainable Energy Reviews*, 52: 802–814. https://doi.org/10.1016/j.rser.2015.07.132.

Sullivan, O.A. 2012. Embedded thermoelectric devices for on-chip cooling and power generation. MSc Thesis. Georgia Institute of Technology, Atlanta, USA.

Sundstrom, O. & Stefanopoulou, A. 2006. Optimal power split in fuel cell hybrid electric vehicle with different battery sizes, drive cycles and objectives. *2006 IEEE Conference on Computer Aided Control System Design, 2006 IEEE International Conference on Control Applications*, *2006 IEEE International Symposium on Intelligent Control*, Munich, Germany, 1681–1688. DOI: 10.1109/CACSD-CCA-ISIC.2006.4776894.

Suter, C., Jovanovic, Z.R. & Steinfeld, A. 2012. A 1kW thermoelectric stack for geothermal power generation – modeling and geometrical optimization, *Applied Energy*, 99, 379-385. https://doi.org/10.1016/j.apenergy.2012.05.033.

T

Tani, A., Camara, M.B., Dakyo, B. & Azzouz, Y. 2013. DC/DC and DC/AC converters control for hybrid electric vehicles energy management ultra-capacitors and fuel cell. *IEEE Transactions on Industrial Informatics*, 9(2), 686–696. DOI: 10.1109/TII.2012.2225632.

Taniguchi, A., Akita, T., Yasuda, K. & Miyazaki, Y. 2004. Analysis of electro-catalyst degradation in PEMFC caused by cell reversal during fuel starvation. *Journal of Power Sources,* 130: 42–49. https://doi.org/10.1016/j.jpowsour.2003.12.035.

Teffah, K., Zhang, Y. & Mou, X. 2018. Modelling and experimentation of new thermoelectric cooler–thermoelectric generator module. *Energies*, 11, 576. DOI:10.3390/en11030576.

Terasaki, I. 2011. Thermal conductivity and thermoelectric power of semiconductors. *Comprehensive Semiconductor Science and Technology*, 1, 326–358. https://doi.org/10.1016/B978-0-12-803581-8.00771-2.

Thomas, S., Zalbowitz, M. & Cruz, J. 1999. Fuel Cells – green power, Los Alamos National Laboratory, Los Alamos, New Mexico, USA.

Thounthong, P., Chunkag, V., Sethakul, P., Sikkabut, S., Pierfederici, S. & Davat, B. 2011. Energy management of fuel cell / solar cell / super-capacitor hybrid power source. *Journal of Power Sources*, 196, 313–324. https://doi.org/10.1016/j.jpowsour.2010.01.051.

Thounthong, P., Rael, S. & Davat, B. 2008. Control strategy of fuel cell and super-capacitors association for a distributed generation system. *IEEE Transactions on Industrial Electronics*, 54(6): 3225 – 3233. DOI: 10.1109/TIE.2007.896477.

Thounthong, P. & Sethakul, P. 2007. Analysis of a fuel starvation phenomenon of a PEM fuel cell. *Power Conversion Conference* - Nagoya, Japan. DOI**:** 10.1109/PCCON.2007.373048.

Thounthong, P., Pierfedereci, S., Martin, J.P., Hinaje, M. & Davat, B. 2010. Modelling and control of fuel-cell super-capacitor hybrid source based on differential flatness control. *IEEE Transaction on Vehicle Technology*, 59 (6): 2700–2710. DOI: 10.1109/TVT.2010.2046759.

Tichagwa, A. 2013. Micro combined heat and power management for a residential system. Master Thesis, University of Cape Town, South Africa.

Tritt, T.M. 2002. Thermoelectric materials: principles, structure, properties, and applications. *Encyclopedia of Materials: Science and Technology* (Second Edition), 1–11. https://doi.org/10.1016/B0-08-043152-6/01822-2.

Tsai, H.L. & Lin, J.M. 2010. Model building and simulation of thermoelectric module Matlab/Simulink. *Journal of Electronic Materials.* 39(9). DOI: 10.1007/s11664-009-0994-x.

Twaha, S., Zhu, J., Yan, Y. & Li, B. 2016. A comprehensive review of thermoelectric technology: materials, applications, modelling and performance improvement. *Renewable and Sustainable Energy Reviews,* 65, 698-726, https://doi.org/10.1016/j.rser.2016.07.034.

U

Uzunoglu, M. & Alam, M.S. 2008. Modelling and analysis of an FC/UC hybrid vehicular power system using a novel-wavelet-based load sharing algorithm. *IEEE Transaction on Energy Conversion,* 23(1): 263–272. DOI: 10.1109/TEC.2007.908366.

V

Van der Walt, M.L., Van den Berg, J. & Cameron, M. 2017. South Africa Department of Energy, State of renewable energy in South Africa. http://www.energy.gov.za/files/media/Pub/2017-State-of-Renewable-Energy-in-South-Africa.pdf. [Date accessed: 21 June 2021].

Vigneshwaran, S. & Vijayalakshmi, R. 2016. High efficiency DC/DC buck-boost converters for high power DC system using adaptive control. *American-Eurasian Journal of Scientific Research*, 11(5): 381-389. DOI: 10.5829/idosi.aejsr.2016.11.5.22957.

Vining, C.B. 2009. An inconvenient truth about thermoelectric. *Nature Materials*, 8(83).

W

Wan, Q., Teh, Y. & Mok, P.K.T. 2016. Analysis of a re-configurable TEG array for high efficiency thermoelectric energy harvesting. *IEEE Asia Pacific Conference on Circuits and Systems (APCCAS)*, 662-665. DOI: 10.1109/APCCAS.2016.7804084.

Wang, J.L., Wu, J.Y., Zheng, C.Y. 2014. Simulation and evaluation of a CCHP system with exhaust gas deep-recovery and thermoelectric generator. *Energy Conversion and Management*, 86: 992–1000. https://doi.org/10.1016/j.enconman.2014.06.036.

Wang, R., Guo, Y., Liu, K., Wang, J. & Dai, L. 2018. Performance analysis of building Hydrogen comprehensive utilization system based on CCHP system of Hydrogen fuel cell. *2nd IEEE Conference on Energy Internet and Energy System Integration (EI2)*, Beijing, China, 1–6. DOI: 10.1109/EI2.2018.8582349.

Wang, W., Cionca, V., Wang, N., Hayes, M., O'Flynn, B. & O'Mathuna, C. 2013. Thermoelectric energy harvesting for building energy management wireless sensor networks. *International Journal of Distributed Sensor Networks,* Volume 2013, 1-14. http://dx.doi.org/10.1155/2013/232438.

Wang, X., Zhao, X.L., Fu, L. & Bo, C.J. 2016. Research on configuration and operation of the CCHP system applicable to active distribution network. *IEEE International Conference on Power System Technology (POWERCON)*, Wollongong, NSW, Australia, 1–6. DOI: 10.1109/POWERCON.2016.7753991.

Wang, Z., Han, W., Zhang, N., Su, B., Liu, M. & Jin, H. 2018. Analysis of inlet air throttling operation method for gas turbine in performance of CCHP system under different operation strategies. *Energy Conversion and Management,* 171: 298–306. http://dx.doi.org/10.1016/j.enconman.2018.05.072.

Wang, H. 2019. Design and control of a 6-phase interleaved boost converter based on SiC semiconductors with EIS functionality for fuel cell electric vehicle. PhD Thesis, UBFC and UTBM, Belfort, France.

Wongvisanupong, K. & Hoonchareon, N. 2013. Optimal scheduling of hybrid CCHP and PV operation for shopping complex load. *2013 10th International Conference on Electrical Engineering/ Electronics, Computer, Telecommunications and Information Technology*, Krabi, Thailand, 1–6. DOI: 10.1109/ECTICon.2013.6559594.

Wu, D., Han, Z., Liu, Z., Li, P., Ma, F., Zhang, H., Yin, Y. & Yang, X. 2021. Comparative study of optimization method and optimal operation strategy for multi-scenario integrated energy system. *Energy,* 217, 119311. https://doi.org/10.1016/j.energy.2020.119311.

Wu, D, Zuo, J., Liu, Z., Han, Z., Zhang, Y., Wang, Q. & Li, P. 2019. Thermodynamic analyses and optimization of a novel CCHP system integrated organic Rankine cycle and solar thermal utilization. *Energy Conversions and Management*. 196, 453–466, https://doi.org/10.1016/J.ENCONMAN.2019.06.020.

Wu, D.W. & Wang, R.Z. 2006. Combined cooling, heating and power: a review. *Progress in Energy and Combustion Science*, 32(5-6): 459–495. https://doi.org/10.1016/j.pecs.2006.02.001.

X

Xiao, D. & Wang, Q. 2012. The research of energy management strategy for fuel cell hybrid vehicle. *International Conference on Industrial Control and Electronics Engineering*, Xi'an, China, 931–934. DOI: 10.1109/ICICEE.2012.247.

Xie, C.J., Quan, S.H. & Chen, Q.H. 2008. Multiple model control for hybrid power system of fuel cell electric vehicle. *IEEE Vehicle Power and Propulsion Conference*, Harbin, China. DOI: 10.1109/VPPC.2008.4677527.

Xing, Y., Liu, R., Liao, J., Zhang, Q., Xia, X., Wang, C., Huang, H., Chu, J., Gu, M., Zhu, T., Zhu, C., Xu, F., Yao, D., Zeng, Y., Bai, S., Uher, C. & Chen, L. 2019. High-efficiency half-heusler thermoelectric modules enabled by self-propagating synthesis and topologic structure optimization. *Energy & Environmental Science*, 12 (11): 3390-3399. https://doi.org/10.1039/C9EE02228G.

Xu, A.D., Lin, S., Lei, J.Y., Jing, Z.X., Liao, M.Y., Shen, Z., He, X.Y. & Wu, Q.H. 2014. Operation optimization model for micro-turbine based CCHP systems. *2014 IEEE PES General Meeting | Conference & Exposition*, National Harbor, Maryland, USA,1–5. DOI: 10.1109/PESGM.2014.6939384.

Y

Ye, L. & Yi, L. 2011. Optimal design of distributed CCHP system. *Proceedings 2011 International Conference on Transportation, Mechanical, and Electrical Engineering (TMEE), Changchun*, 1961–1965. DOI: 10.1109/TMEE.2011.6199599.

Yildiz, F., Coogler, K.L. & Crockford, B. 2013. An applied comparison study: solar energy vs thermoelectric energy. *120th ASEE Annual Conference & Exposition*.

Youn, H.S., Yun, D.H., Lee, W.S. & Lee, I.O. 2020. Study on boost converters with high power-density for hydrogen-fuel-cell hybrid railway system. *Electronics*, 9(5): 771. DOI: https://doi.org/10.3390/electronics9050771.

Yu, A., Chabot, V. & Zhang, J. 2013. Electrochemical super-capacitors for energy storage and delivery: fundamentals and applications, Boca Raton, USA: CRC Press, 1st Edition.

Yusop, A.M., Mohamed, R. & Ayob, A. 2013. Model building of thermoelectric generator exposed to dynamic transient sources. *5th International Conference on Mechatronics (ICOM'13). IOP Conference Series: Materials Science and Engineering*, 53, 012015. DOI:10.1088/1757-899X/53/1/012015.

Z

Zandi, M., Payman, A., Martin, J.P., Pierfederici, S., Davat, B. & Meibody-Tabar, F. 2011. Energy management of a fuel cell / super-capacitor / battery power source for electric vehicular applications. *IEEE Transactions on Vehicular Technology*, 60(2): 433–443. DOI: 10.1109/TVT.2010.2091433.

Zare, V. & Takleh, H.R. 2020. Novel geothermal driven CCHP systems integrating ejector transcritical CO2 and Rankine cycles: thermodynamic modeling and parametric study. *Energy Conversion and Management*, 205. https://doi.org/10.1016/j.enconman.2019.112396.

Zhang, J., Cao, S., Yu, L., Zhou, Y. 2018. Comparison of combined cooling, heating and power (CCHP) systems with different cooling modes based on energetic, environmental and economic criteria. *Energy Conversion and Management*, 160: 60–73. https://doi.org/10.1016/j.enconman.2018.01.019.

Zhang, K., Li, X.R. & Liu, J.M. 2019. Research on minimum schedulable power optimization of CCHP system. *2019 IEEE Innovative Smart Grid Technologies - Asia (ISGT Asia)*. Chengdu, China; 4210–4214. DOI: 10.1109/ISGT-Asia.2019.8881422.

Zhang, Q., Cui, G., Zhang, L. & Guan, X. 2006. Energy integration and economical optimization of small scale CCHP system. *2006 International Technology and Innovation Conference (ITIC 2006)*, Hangzhou, China, 2198–2203. DOI: 10.1049/cp:20061136.

Zhang, X, Li, H., Liu, L, Bai, C., Wang, S., Song, Q., Zeng, J., Liu, X. & Zhang, G. 2018. Optimization analysis of a novel c.ombined heating and power system based on biomass partial gasification and ground source heat pump. *Energy Conversion and Managemen*t, 163: 355–370. https://doi.org/10.1016/j.enconman.2018.02.073.

Zhang, Y., Huangfu, Y., Liu, W. & Guo, L. 2019. An energy management strategy based on state machine with power compensation for photovoltaic-PEMFC-lithium battery power system. *2019 IEEE International Conference on Industrial Technology (ICIT)*, Melbourne, VIC, Australia, 2019, 1675-1680. DOI: 10.1109/ICIT.2019.8843696.

Zhao, D., Wang, H., Ullah, K.Z., Chen, J.C., Gabrielsson, R., Jonsson, M., Berggren, M. & Crispin X. 2016. Ionic Thermoelectric Super-capacitors. *Energy & Environmental Science*, 9(4): 1450-1457. https://doi.org/10.1039/c6ee00121a.

Zhao, H., Hu, E., Wang, Z., Song, X., Guo, J., Shen, Z., Xing, Y. & Ren, F. 2018. Optimal configuration of grid connected micro-grid considering CCHP and analysis of energy saving and emission reduction. *2018 2nd IEEE Conference on Energy Internet and Energy System Integration (EI2)*, Beijing, China, 1–9. DOI: 10.1109/EI2.2018.8581657.

Zhao, D. & Tan, G. 2014. A review of thermoelectric cooling: Materials, modelling and applications. *Applied Thermal Engineering*, 66(1–2): 15-24. https://doi.org/10.1016/j.applthermaleng.2014.01.074.

Zhao, Y., Fan, Y., Ge, M., Xie, L., Li, Z., Yan, X. & Wang, S. 2021. Thermoelectric performance of an Exhaust Waste Heat Recovery System based on Intermediate Fluid under different Cooling Methods. *Case Studies in Thermal Engineering*, 23, 100811. https://doi.org/10.1016/j.csite.2020.100811.

Zheng, C.H., Lee, C.M., Huang, Y.C. & Lin, W.S. 2013. Adaptive optimal control algorithm for maturing energy management strategy in fuel–cell/Li-ion/super-capacitor hybrid electric vehicles. *9th Asian Control Conference*, Istanbul, Italy, 1–7. DOI: 10.1109/ASCC.2013.6606091.